UNIVERSIDAD AUTONOMA DE MADRID

DEPARTAMENTO DE FÍSICA DE MATERIALES

FACULTAD DE CIENCIAS

Crystal Growth & Technology, Device Fabrication, and Material Properties of Cd(Zn)Te for Radiation Detector Applications

PhD Dissertation

Jerome Crocco

Thesis Advisor

Pr. Ernesto Dieguez

Thesis Tribunal

Pr. José García Solé

Pr. Pedro Hidalgo

Dr. José-Manuel Perez

Pr. Michael Fiederle

Pr. Jan Franc

This page intentionally left blank.

Acknowledgements

First, foremost, and above all I must thank my wife Marie for here unending support, encouragement, love, and patience. This life would not have been realized without you by my side. I also give thanks for my son, Lucas, who has made me both physically and mentally a stronger person. To my Mother and my Father, many thoughts come to mind. Thank you for encouraging in me a sense of curiosity. To my family in Spain and for all of their support over the past three years, I am indebted with gratitude: especially the constant support of my Mother and Father in law´s, and their family. For Ernesto, I must admit I am constantly surprised by how positive and supportive you have been of this investigation. Without your intensity, this work would not have been carried out with such velocity. I also thank each of my colleagues in CGL Verónica Carcelen, Hakima Bensalah, Qian Zheng, Andrés Black, Axa Pinneiro, and Juan Medina.

For a great deal of technical work which has been carried out in the laboratory, I must also acknowledge SEGAINVEX for their technical support in the construction of the VGF furnace used in this work, especially the expertise of Nuria Diaz, Juan Antonio Higuera Romero, Manuel García Fernández, and Ramon Martin. For his help in the development of electrode patterning, I must also give acknowledgment to Eduardo Ruiz of the Microelectronics department at UAM. We have spent many hours, and failed many times to achieve our goal.

I would also like to acknowledge the support provided by the COCAE framework as well as the Spanish MAT2009-08592 program funded by MICINN. These programs provided the opportunity for my interaction with investigators across the E.U. Most importantly, the discussions I have had with Pr. Michael Fiederle, Dr. Alex Fauler from the Freiburger Materialforschungszentrum research institute of the Albert-Ludwig University of Freiburg, as well as Dr. Haris Lambropoulos from the Institute of Chalkis

I would like to acknowledge the collaboration of several institutes and scientists who have also aided me in making various measurements for the scientific investigations which have been carried out. Rutherford backscattering spectroscopy measurements were carried out at the Instituto Tecnológico e Nuclear in the Unidade de Física e Aceleradores in Portugal by Dr. Vitoria Corregidor. Surface photo-voltage spectroscopy, photo-induced current spectroscopy, hot probe measurements and Kelvin force probe measurements were carried

out during a pre-doctoral stay at the PHoS research laboratory in the University of Bologna, Italy in collaboration with Antonio Castaldini, Dr. Beatrice Fraboni, Dr. Daniela Cavalcoli, and Dr. Anna Cavallini. Glow Discharge Mass Spectroscopy measurements were taken through collaboration with the National Research Council (NRC) in Canada with the support of Brad Methven. Cathodoluminescence measurements have been carried out at the materials science faculty of the University of Cumplutense, Madrid with the endless support of Dr. Pedro Hidalgo. Spectroscopic gamma ray measurements of Cd(Zn)Te devices have been carried out at the Centro de Investigation Energéticas Medioambientales y Tecnológicas (CIEMAT) in Madrid with the technical expertise of Oscar Vela and Dr. Jose-Manuel Perez. Scanning electron microscopy, Energy Dispersive X-ray spectroscopy, FTIR, and ion coupled plasma mass spectroscopy measurements have been carried out in SIDI of the material science faculty of the Universidad de Autonoma de Madrid. Photoconductivity measurements have been carried out at the Charles University in Prague by Pr. Jan Franc, Pr. Vladmir Babenstov.

PUBLISHED AND PRESENTED WORKS

The papers which have been published through the course of this investigation are presented here. The papers for which I have published (or am in the process of publishing) as first Author are presented first. This section is followed by works which have been carried out through both internal and external collaborative efforts over the past three years. Finally, also included are collaborative publications which are currently under review.

1.1 Original Publications

1. **Influence of SiC Pedestal in the Growth of 50mm Cd(Zn)Te by Vertical Gradient Freeze Method**. **J. Crocco**, H. Bensalah, Q. Zheng, V. Carcelén, E. Diéguez. In Press. http://dx.doi.org/10.1016/j.jcrysgro.2011.11.047.

2. **Study of the Effects of Edge Morphology on Detector Performance by Leakage Current and Cathodoluminescence**. **J. Crocco**, H. Bensalah, Q. Zheng, F. Dierre, P. Hidalgo, J. Carrascal, O. Vela, J. Piqueras, E. Dieguez. 2010 IEEE Trans. Nucl. Sci. 2011 (58) Issue: 4 1935 – 1941.

3. **Detector surface preparation of Cd0.9Zn0.1Te for electrode patterning**. **J. Crocco**, Q. Zheng, H. Bensalah, E. Dieguez. Appl. Surf. Sci. 258 (2012) 2948– 2952

4. **Influence of Dynamic Temperature Adjustments During Growth on the Material Properties of Cd(Zn)Te Radiation Devices. J. Crocco**, A. Castaldini, B. Fraboni, D. Cavalcoli, H. Bensalah, Q. Zheng, A. Cavallini, E. Dieguez. J. Crystal Growth. *Submitted 2012.*.

5. **Investigation of Crystal Growth of 50mm Cd(Zn)Te Using SiC Pedestal and pBN Crucible. J. Crocco**, A. Black, H. Bensalah, Q. Zheng, V. Carcélen, E. Dieguez. *Submitted 2012.*

6. **Influence of Carbon Coated pBN Crucible on Crystal Growth of Cd0.9Zn0.1Te for Radiation Detector Applications. J. Crocco**, V. Carcelen, B. Methven, I. Gallardo, H. Bensalah, Q. Zheng, I. Rivas, F. Moreno, O. Vela, E. Dieguez. *Submitted 2011.*

7. **Investigation of Asymmetries of Cd(Zn)Te Detectors Investigated Using PICTS, RBS, SPS, and Gamma Ray Spectroscopies. J. Crocco**, H. Bensalah, Q. Zheng, V. Corregidor, A. Castaldini, B. Fraboni, D. Cavacoli, A. Cavallini, O. Vela, E. Dieguez. *Submitted 2012.*

Collaborative Publications

8. **Concentration of uncompensated impurities as a key parameter of CdTe and Cd(Zn)Te crystals for Schottky diode X-ray detectors**. L A Kosyachenko, C P Lambropoulos, T Aoki, E Dieguez, M Fiederle, D Loukas, O V Sklyarchuk, O L Maslyanchuk, E V Grushko, V M Sklyarchuk, **J Crocco** and H Bensalah. 2012 *Semicond. Sci. Technol.* **27** 015007

9. **The COCAE Detector: An Instrument for Localization—Identification of Radioactive Sources. C.P. Lambropoulos**, T. Aoki, **J. Crocco**, E. Dieguez, C. Disch, A. Fauler, M. Fiederle, D. Hatzistratis, V.A. Gnatyuk, K. Karafasoulis, L.A. Kosyachenko, S.N. Levytskyi , D. Loukas, O.L. Maslyanchuk, A. Medvids , T. Orphanoudakis, I. Papadakis, A. Papadimitriou, K. Papakonstantinou, C. Potiriadis, T. Schulman, V.V. Sklyarchuk, K. Spartiotis, G. Theodoratos, O.I. Vlasenko, K. Zachariadou, E. Zervakis. IEEE Trans. In Nucl. Sci. 2011 (58) Issue: 5 2363 - 2370

10. **Increased Radiation Hardness of Cd(Zn)Te by Laser Radiation**. A. Medvid, A. Mychko, E. Dauksta, Y. Naseka, **J. Crocco**, E. Dieguez. IEEE Nucl. Sci. Sym. 2010 Conference Record N36-189.

11. **Study of Ammonium Fluoride Passivation Time on Cd(Zn)Te Bulk Crystal Wafers**. H. Bensalah**, J. Crocco**, V. Carcélen, J. L. Plaza, Q. Zheng, L. Marchini, M. Zanichelli, G. Domínguez, L. Soriano, and E. Diéguez. Cryst. Res. Technol., 1 – 5 (2011).

12. **Deposition of Nanometric Double Layers Ru/Au,Ru/Pd, and Pd/Au onto Cd(Zn)Te by the Electroless Method.** Q. Zheng, F. Dierre, V. Corregidor, R. Fernandez-Ruiz, **J. Crocco**, H. Bensalah, E. Alves, E. Dieguez. J. Crystal Growth (2011), In Press. http://dx.doi.org/10.1016/j.jcrysgro.2011.04.014

13. **Influence of Surface Preparation on Cd(Zn)Te Nuclear Radiation Detectors**. Q. Zheng, F. Dierre, **J. Crocco**, V. Carcelen, H. Bensalah, J.L. Plaza, E. Dieguez. App. Surf. Sci., 257 (2011) 8742– 8746

14. **Study of Effects of Polishing and Etching Processes on Cd(Zn)Te Surface Quality**. A. Bensouici, V. Carcelen, J.L. Plaza, S. De Dios, N. Vijayan, **J. Crocco**, H. Bensalah, E. Dieguez, M. Elaatmani. J. Crystal Growth 312 (2010) 2098–2102.

15. **Pt Coldfinger improves quality of Bridgman-grown Cd0.9 Zn0.1Te:Bi crystals**. V. Carcelén, K. H. Kim, G.S. Camarda, A.E. Bolotnikov, A. Hossain, G. Yang, **J. Crocco**, H. Bensalah, F. Dierre, E. Diéguez and R. B. James. J. Crystal Growth 338 (2012) 1–5.

16. **The effect of etching time on the Cd(Zn)Te surface**. H. Bensalah, J.L. Plaza**, J. Crocco**, Q. Zheng, V. Carcelen, A. Bensouici, E. Dieguez. App. Surf. Sci. 257 (2011) 4633–4636.

17. **Comparison of radiation detector performance for different metal contacts on Cd(Zn)Te deposited by electroless deposition method.** Q. Zheng, F. Dierre, M. Ayoub, **J. Crocco**, H. Bensalah, V. Corregidor, E. Alves, R. Fernandez-Ruiz, J. M. Perez, E. Dieguez. Cryst. Res. Technol. 46, No. 11, 1131 – 1136 (2011).

Other Publications: Under Review

18. **Effect of Superheating and fast cooling on Te inclusions of $Cd_{0.9}Zn_{0.1}Te$:In Crystals Grown by Vertical Gradient Freezing.** H. Bensalah, J. Crocco, V. Carcelén, A. Black, Q. Zheng, J.L. Plaza, E. Diéguez. *Submitted 2012.*

19. **Comprehensive study of semi-insulating Cd(Zn)Te grown by the Bridgman method.** J V. Babentsov, J. Franc, J.Zázvorka, P., E. Dieguez, J. Crocco, M. V. Sochinskyi, R. B. James**.** *Submitted 2011*.

20. **Electroless Deposition of Au, Pt, or Ru Metallic Film Layer on Cd(Zn)Te**. Q. Zheng, F. Dierre, V. Corregidor, **J. Crocco**, H. Bensalah, J.L. Plaza, E. Alves, E. Dieguez, Thin Solid Films, *Submitted.*

21. **Investigation of Generation of Defects due to Metallisation on Cd(Zn)Te Detectors**. Q. Zheng, F. Dierre, J. Franc, J. Crocco, H. Bensalah, V. Corregidor, E. Alves, E. Ruiz, O. Vela, J.M. Perez, E. Dieguez, J. Phys. D: Appl. Phys. *Submitted*

Conferences Attended/Presented

2011. **IEEE Nuclear Science Symposium**, Valencia, Spain. Oral Presentation. **Influence of SiC Pedestal in the Growth of 50mm Cd(Zn)Te by Vertical Gradient Freeze Method**. **J. Crocco**, A. Black, H. Bensalah, Q. Zheng, V. Carcélen, E. Dieguez.

2011. **IEEE Nuclear Science Symposium**, Valencia, Spain. Poster Presentation. **Influence of Carbon Coated pBN Crucible on Crystal Growth of Cd0.9Zn0.1Te for Radiation Detector Applications.** **J. Crocco**, V. Carcelen, B. Methven, B. Fraboni, I. Gallardo, H. Bensalah, Q. Zheng, F. Moreno, E. Dieguez

2011. **International Workshop on Crystal Growth Technology 5**, Berlin Germany, Poster Presentation. **Challenges for Improving the Bulk Growth of Cd(Zn)Te.** **J. Crocco**, H. Bensalah, Q. Zheng, V. Carcelén, E. Diéguez.

2010. **IEEE Nuclear Science Symposium**, Knoxville, TN, USA. Oral Presentation. **Study of the Effects of Edge Morphology on Detector Performance by Leakage Current and Cathodoluminescence**. **J. Crocco**, H. Bensalah, Q. Zheng, F. Dierre, P. Hidalgo, J. Carrascal, O. Vela, J. Piqueras, E. Dieguez.

This page intentionally left blank.

Thesis Contents

Commonly Used Acronyms

AFM	Atomic Force Microscope
ASIC	Application Specific Integrated Circuit
BF	Brightfield
BN	Boron Nitride
BNC	Bayonet Neill–Concelman type RF Connector
BSE	Backscattered electron
CAD	Computer assisted drafting
CB	Conduction Band
CBM	Conduction Band minimum
CCD	Charge coupled device
CCE	Charge collection efficiency
CFT	Capillary force template
CGL	Crystal Growth Laboratory of UAM
CH_3COOH	Acetic Acid
CIEMAT	Centro de Investigaciones Energeticas, Medioambientales, y Tecnologicas
CL	Cathodoluminescence
CMP	Chemical mechanical planarization
COCAE	Cooperation across Europe
COREMA	Cooperation Across Europe for Cd(Zn)Te Based Security Instruments
CRSS	Critically resolved sheer stress
CVD	Chemical Vapor Deposition
DC	Direct Current
DF	Darkfield
DI	Deionized Water
EDS	Energy dispersive X-ray spectroscopy
EMF	Electromotive force
FAM	Free abrasive machining
FET	Field effect transistor
FF	First to freeze
FWHM	Full width at half maximum
GDMS	Glow discharge mass spectroscopy
GUI	Graphical user interface
HF	Hydrofluoric acid
HNO3	Nitric Acid
ICP	Inductively coupled plasma
ICP-MS	Inductively coupled plasma mass spectroscopy
ID	Inner diameter
III-V	Class of semiconductors
II-VI	Class of semiconductors
IR	Infrared
I-V	Current Voltage

KFPM	Kelvin Force Probe Microscopy
LED	Light emitting diode
LEL-3	Lateral edge lapping using 3 micron alumina
LEL-9	Lateral edge lapping using 9 micron alumina
LEP-1	Lateral edge polishing using 1 micron diamond
LEP-3	Lateral edge polishing using 3 micron alumina
LEP-CP	Lateral edge polishing using chemical polishing agent
MCA	Multi-channel analyzer
MeOH	Methanol
NIR	Near infrared
pBN	pyrolytic boron nitride
PCB	printed circuit board
PE Sensor	pyro electric sensor
PICTS	Photo-induced current transient spectroscopy
PL	Photoluminescence
RBS	Rutherford backscatter spectroscopy
RMS	Root mean square
RPM	Revolutions per minute
SCR	Space charge region
SEGAINVEX	Electrical, mechanical, and glass shop of the UAM
SEM	Scanning electron microscope
SiC	Silicon Carbide
SLI	Solid liquid interface
SPS	Surface photo-voltage spectroscopy
SPV	Surface photo-voltage
TCE	Trichloroethylene
THM	Travelling heater method
TTV	Total thickness variation
UAM	Universidad Autonoma de Madrid
VB	Valence band
VBM	Valence band minimum
VGF	Vertical gradient freeze method
VGF-1	Vertical gradient freeze furnace 25mm
VGF-2	Vertical gradient freeze furnace 50mm
XPS	X-ray photoelectron spectroscopy
XRD	X-ray diffraction

This page intentionally left blank.

Chapter I

Background and Significance of the Problem

This page intentionally left blank.

1 INTRODUCTION TO RADIATION DETECTION

Section Contents

The instrumentation for the detection of high energy radiation is a field of technological interest which has developed rapidly in recent years. It has only been over the course of the past century that the technological effort for the development of high energy radiation detectors has begun. At the turn of the 19th century, the foundation for nuclear physics was beginning to be laid, while some of the first instruments for the detection of nuclear radiation were first being developed.

One hundred years later, after the turn of the 20th century some of the first pixelated spectroscopic semiconductor detectors are being integrated into satellite systems for space exploration, CT scanner systems for nuclear imaging in medical applications, as well as many other high technology fields requiring high resolution spectroscopic devices operable under ambient conditions. This increasing demand of solid-state spectrometers has initiated an international effort to develop large volume semiconductor materials for detector applications.

Cadmium Zinc Telluride ($Cd_{0.9}Zn_{0.1}Te$, referred to as Cd(Zn)Te throughout this thesis) is one of the semiconductor compounds which has received the most attention for room temperature spectroscopic applications. However, there still exist several challenges to obtaining large volumes of detector grade material for deployment in space-based or clinical-based applications.

1.1 Introduction (English)

The thesis is divided into four chapters, each with individual sub-sections. The first chapter is an introduction and discusses the objectives of the thesis within the framework of the COCAE project, which has supported this work. The second chapter discusses the experimental methods which have been implemented, as well as the experimental equipment which has been designed/built during the course of investigation. The theoretical background of the characterization and measurement techniques is elaborated to some extent, based on how much each method has been used in this work.

Chapters 3 and 4 represent the original results which have been obtained through this investigation. Chapter 3 has been structured to first discuss crystal growth aspects including 1) material synthesis and melt homogenization, 2) development of new novel crucible materials for crystal growth, 3) the effects of temperature adjustments made during growth cycle, 4) the scaling of crystal growth capacity for growth of 50mm diameter ingots,

and 5) the development of a 2D model for simulation of the crystal growth process to explain observed experimental phenomenon.

In Chapter 4, the emphasis is now the fabrication of radiation devices and improving/understanding their operation. This chapter is broken up into sections which describe 1) surface preparation and electrode patterning processes 2) effect of surface morphology on leakage current 3) deep levels introduced by the fabrication process 4) effects of crystallographic twinning on the electrical properties of radiation devices and 5) asymmetry in CZT radiation devices related with the A-face and B-face surfaces.

The appendix of the thesis discusses a separate project which has also been completed during this investigation, related with the design of a 30kW furnace for the growth of PV silicon. The furnace is currently under construction, and this chapter discusses the design considerations taken into account including electrode design, recirculating water system, linear motion systems, and crucible/insulation design.

1.2 Introducción (Español)

El primer capítulo sirve a modo de introducción y en él se analizan los objetivos de la tesis en el marco del proyecto COCAE, que ha apoyado este trabajo. El segundo capítulo describe los métodos experimentales que se han empleado, así como el equipo experimental que ha sido diseñado / construido durante el curso de la investigación. La base teórica de las técnicas de caracterización y medición se elabora en cierta medida, basado en la cantidad de cada método ha sido utilizado en este trabajo.

Los capítulos 3 y 4 presentan los resultados originales que se han obtenido a través de esta investigación. El capítulo 3 se ha estructurado para discutir primero los aspectos de crecimiento de cristales, incluyendo 1) la síntesis de material y la homogeneización del fundido, 2) desarrollo de nuevos crisoles basados en materiales innovadores en el campo de crecimiento de cristales, 3) los efectos de los ajustes de temperatura realizados durante el ciclo de crecimiento, 4) el escalado de la técnica de crecimiento para la obtención de lingotes de 50 mm de diámetro, y 5) el desarrollo de un modelo en 2D para la simulación del proceso de crecimiento de los cristales que sirva como apoyo a la explicación de los fenómenos observados experimentalmente.

El capítulo 4 está enfocado en la fabricación de dispositivos de radiación y la mejora/comprensión de su funcionamiento. Este capítulo está dividido en secciones que

describen 1) preparación de la superficie y los procesos de modelado de electrodos 2) Efecto de la morfología de superficie sobre la corriente de fuga 3) niveles profundos introducidos por el proceso de fabricación 4) los efectos de maclado cristalográfico sobre las propiedades eléctricas de los dispositivos de radiación y 5) asimetría en los dispositivos de radiación CZT relacionados con las superficies cara A y cara B.

El apéndice de la tesis discute un proyecto independiente que también se ha completado durante esta investigación, relacionado con el diseño de un horno de 30 kW para el crecimiento de silicio adecuado para la industria fotovoltaica. El horno está actualmente en construcción, y en este capítulo se describen las consideraciones de diseño tomadas en cuenta, incluyendo diseño de los electrodos, el sistema de recirculación de agua, sistemas de movimiento lineal, y el diseño del crisol / aislamiento.

1.3 Historical Perspective

To better understand the development of compound semiconductors, such as those based on Cd(Zn)Te and how this material derives its importance relative to the currently available technologies, a brief summary of the historical development of the instrumentation used for nuclear imaging is presented.

High energy radiation, in the form of X-rays was first discovered by Wilhelm Conrad Roentgen in 1895 during the course of some experiments using vacuum tubes, when he observed the fluorescence of a barium-platinum cyanide screen induced by X-rays emitted by his experimental apparatus (1). When he placed his hand between the screen and the X-ray source, he created the first X-ray of a human hand. He found that these rays did not reflect or refract the same way as optical photons, nor were they affected strongly by magnetic fields.

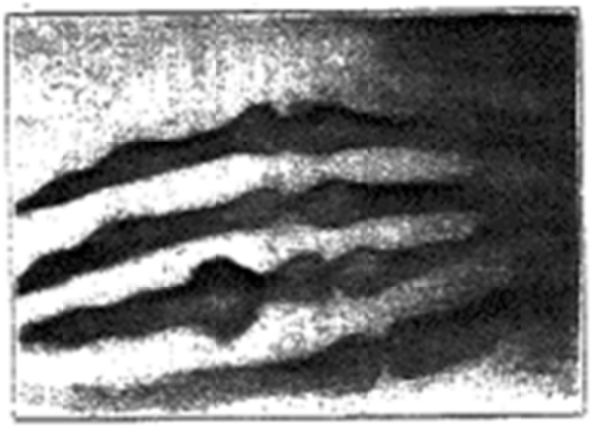

Figure 1 X-ray of the hand of Ms. Roentgens hand with ring, adapted from (1)

In 1897, the piezoelectric electrometer was developed by Pierre and Marie Curie for the study of spontaneous radioactivity in Radon, which led to their being awarded the Nobel Prize in Physics in 1903. The system developed by the Curies for the study of radioactivity consisted of physical weights which were applied to a piezoelectric material to offset the voltage produced by the ionizing radiation. The energy of the incident radiation therefore could be related to the piezo-electric properties of the material and the associated counterweight. Presented in **Figure 2** is the original equipment used for this investigation, and the experimental arrangement. The system consisted of several components including a sample ionization chamber, a Quadrant electrometer, a light source, and the piezoelectric crystal with compensating weights.

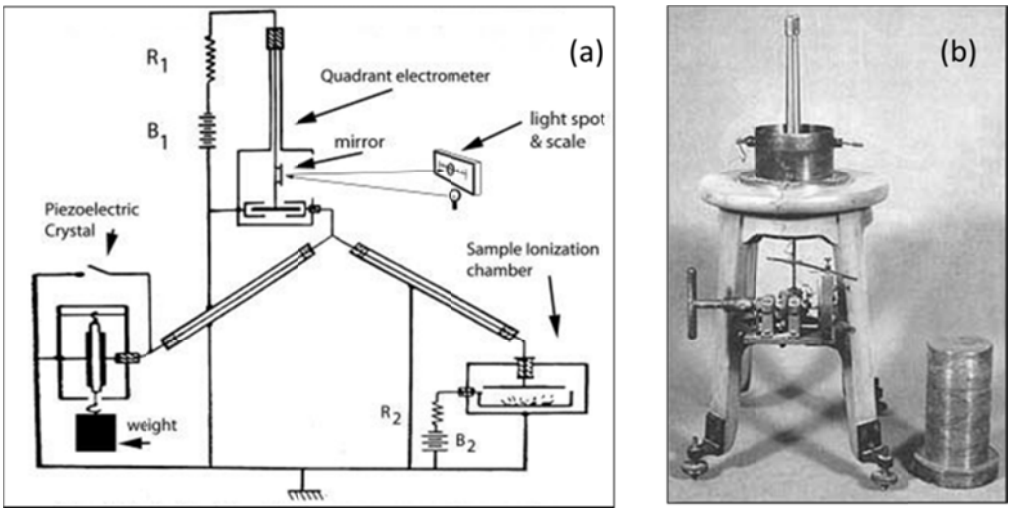

Figure 2 (a) experimental arrangement used by Pierre and Marie Curie for the study of spontaneous radioactivity in Radon. (b) actual experimental equipment used.

The years between 1900 and 1950 saw the development of a range of different configurations of Electroscopes for the detection of radioactive materials. While many of the electroscopes had their own unique advantages, they relied upon similar physical principles. These electroscopes were used for measuring electric charge through the mechanical forces acting between two charged bodies. This charging of the instrument is brought about by the radioactivity of the material being studied. The Lind Electroscope which was developed by Sam Lind for measurement of Radon is presented below in **Figure 3**(a), as are other electroscope designs developed during the same time period.

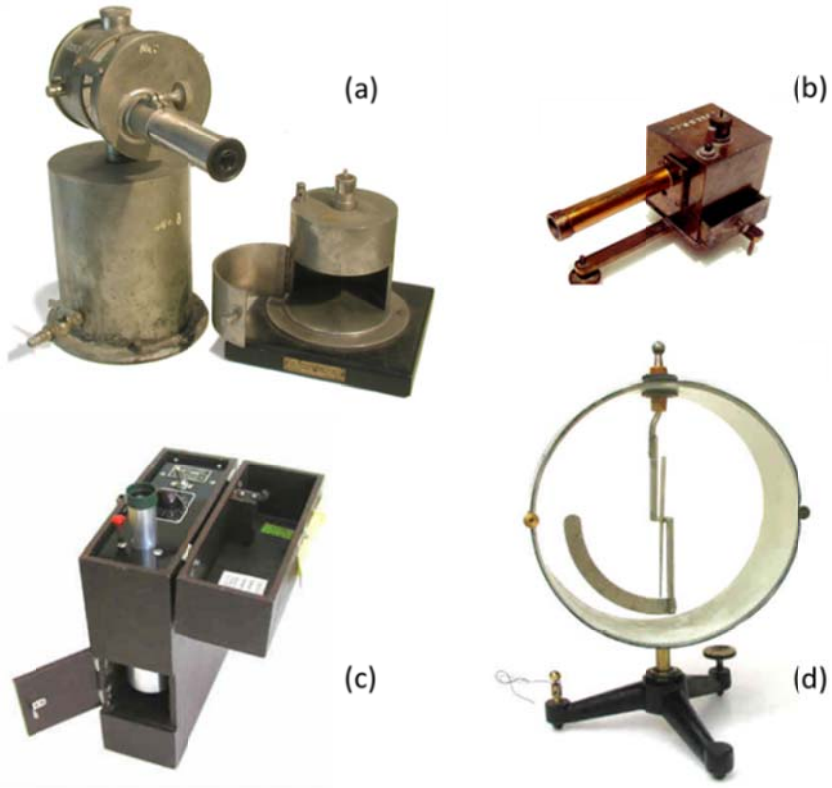

Figure 3 Electroscopes developed between early 1900´s and 1950s (a) Lind Electroscope c1925 used for measurement of Radon (b) Electroscope developed for measurement of Uranium c1920-1930 (c) Fred C. Henson Lauritsen Electroscope c1947-1955 (d) Braun electroscope c1900.

Other important activities in the field of radiation detection and measurement include the development of materials and systems for radiation dosimetry. Some of the first dosimeters were constructed from photographic plates which change color in response to incident radiation. Higher intensities of radiation result in a larger change in the materials color. In the 1950s, color dosimeters were developed using a colored disk of barium platinocyanide, which turns darker when exposed to x-rays. Using standardized color scales which correspond to different levels of exposure, the degree of exposure could be determined. Dosimeters can be found in various forms such as radiographic films, gels, or even ionization chambers. It is important that materials used for dosimetry applications exhibit a large dynamic range, high spatial resolution, small directional dependence, a flat energy response, and linearity of the signal over a large range.

Presented in **Figure 4** is a diagram illustrating the basic operational characteristics of Geiger Mueller counter, which was also used for the determination of radioactivity, but without the need of photolithographic plates. In its most basic form, this instrument

consisted of an ionization chamber filled with BF_3 gas, a cylindrical tube whose outer wall served as the cathode and a fine wire stretched along the axis of the cylinder serving as the anode. The fill gas would absorb the radiation through interactions with the nuclei of the gas while the Geiger counter would detect this interaction as the ionized nucleus would drift towards the cathode under the applied electric field.

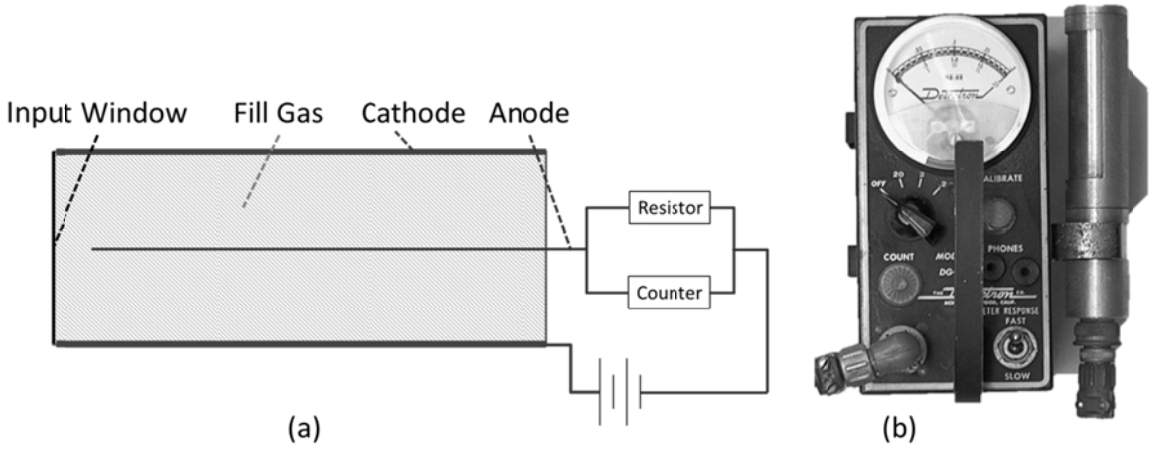

Figure 4 (a) Operation diagram of a Geiger Mueller counter (b) Geiger Mueller counter fabricated by Detection.

The development of scintillator crystals has taken place over the past 50 years for radiation detection. Scintillating materials are a special class of materials which exhibit luminescence when excited by ionizing radiation. A substantial amount of research and development has been invested into the preparation of scintillation crystals for spectroscopic applications. In the mid-1940s - 1950s, the first single crystal scintillator camera was introduced by groups such as Anger at the University of California and Curran and Baker from University of Strathclyde, Britain. This camera consisted of the passive scintillator crystal coupled to photomultiplier (PM) tubes. The PM tubes absorb the light emitted by the scintillator crystal and re-emit electrons via the photoelectric effect. Subsequent amplification of the electronic signal gives rise to an electrical pulse which may be used for obtaining information regarding the radioactive source which is exciting the scintillating crystal. Moreover, the intensity of the radioactive source, is proportional to the intensity of the luminescence, which is also proportional to the intensity of the pulse output.

Presented in **Figure 5** are Hal Anger and the first scintillation camera on display at the Fifth Annual Meeting of The Society of Nuclear Medicine 1958 in Los Angeles. Also presented is the geometry of materials used in the camera for creating an image, illustrating

the operating principles of the device. The collimator is a higher density material (for example lead) which serves as a patterned aperture to restrict the direction from which the high energy photon may reach the scintillator crystal. The light produced by the optical scintillation is detected by the photo-multiplier tube.

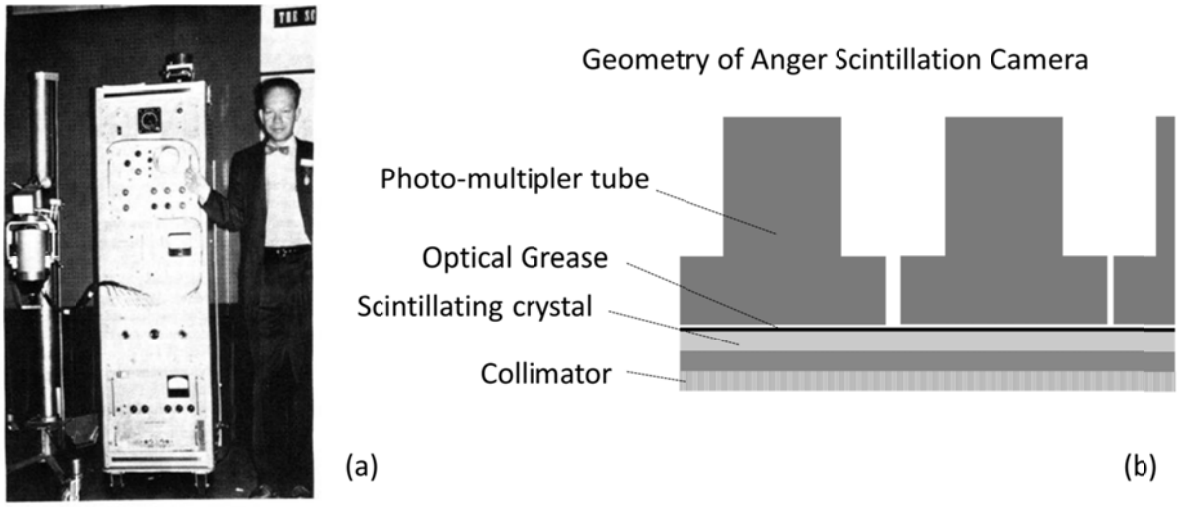

Figure 5 (a) Hal Anger and his first scintillation camera displayed at the Fifth Annual Meeting of The Society of Nuclear Medicine 1958 in Los Angeles, adapted from (2) (b) basic geometry of scintillation camera.

Calorimetric devices have also been rapidly developed over the past several decades for high energy detection applications such as those pertaining to Astrophysics. X-ray calorimeters may function in several different modalities, but the principles of their operation are similar. One common configuration of this calorimeter device relies upon measuring the temperature increase in a material with known heat capacity. The interaction between the energy of the incident photon and the absorbing material is related by the materials thermal properties i.e. heat capacity, diffusivity, and thermal conductivity.

Typically, calorimeter devices should be opaque to X-rays with a sufficiently low heat capacity so that for small amounts of energy deposited, a measureable signal may be extracted. Furthermore, they are typically operated at low temperatures such that the energy deposited by the X-ray is large compared to the background heat transfer. Presented in **Figure 6** is one of the more sophisticated X-ray micro-calorimeter devices which have been developed by the X-ray Calorimeter group at the Astrophysics Science Division of NASA. The incident X-ray with Energy E, is absorbed by the absorber material. For materials with sufficiently low heat capacitance, the change in temperature can be

measured using a thermistor to determine the energy of the X-ray. The heat sink is used for restoring the absorber to equilibrium temperature via the thermal bridge.

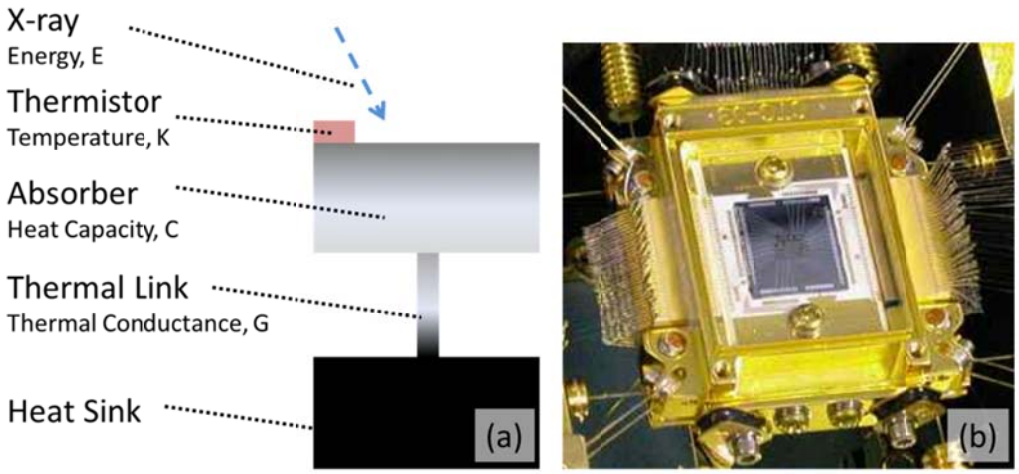

Figure 6 (a) Basic geometry of calorimeter devices used for measurement of X-ray. (b) X-ray micro-calorimeter device developed at Astrophysics Science Division of NASA

Starting in the 1960s and following to present day, the development of solid state semiconductor detectors for the detection of high energy radiation has received a great deal of attention. Semiconductor based detectors offer several appealing advantages compared with the other competing technologies. Their compact size compared to scintillator or gas filled ion-chamber configurations makes them more easily integrated into complex array structures. Second, the relatively high atomic mass, or ´´Z´´ value, of semiconductor compounds corresponds to increased photoelectric absorption and stopping power of the incident radiation. This means that there is greater charge collection efficiency of the device. Third, the direct generation of electron-hole pairs from incident radiation means a linear device response. And finally, all types of high energy particles may be detected, both ionized particles as well as photons. In the next section, a brief description of semiconductor based detectors will be discussed.

1.4 Semiconductor Detector Materials

Semiconducting and Semi-insulating materials used for the detection of high energy particles offer several benefits to the detection of high energy radiation. These benefits include a high Z value, a corresponding high density, and the potential for high resistivity materials. Presented in **Table 1** is a summary of the different material properties for various semiconductor materials which are under investigation as possible detectors for

nuclear imaging applications. As can be seen from this table, some materials such as GaAs and PbI_2 suffer from intrinsic material properties, other detector material such as Si are transparent to the higher energy X-rays due to its low Z value, whereas Ge requires liquid nitrogen cooling due to its low bandgap and correspondingly lower resistivity at room temperature.

Table 1 Material properties of several candidates for X-ray and gamma ray detection.

Material	Z	Density ($g\ cm^{-3}$)	Bandgap (eV)	Ionization Energy (eV)	Comments
GaAs	31/33	5.32	1.43	4.2	Limited by native defects
InP	49/15	4.79	1.35	4.2	
CdSe	48/34	5.8	1.73	-	
PbI_2	82/53	6.2	2.55	4.9	Poor Charge mobility
GaSe	31/34	4.55	2.03	4.5	
Ge	32	5.3	0.67	2.95	Requires LN2 cooling
Si	16	2.3	1.11	3.62	Transparent to HEX-rays
HgI_2	80/53	6.36	2.13		R&D Stage
Cd(Zn)Te	48/30/52	5.9	1.64	4.43-4.64	Growth & Cost

Wide bandgap semiconductors offer the possibility for achieving compact radiation devices operable at room temperature, without the need for cooling to cryogenic temperatures. This is due to the lower leakage current of the device under bias, which is a consequence of increasing separation between the valence and conduction bands. However, it is also important that the material have sufficiently high atomic number. Presented below in **Figure 7** is a diagram illustrating the required material thicknesses of various semiconductor compounds for stopping a 60keV photon. For these reasons, semiconductor compounds such as HgI_2 and Cd(Zn)Te which are closest to being ideal materials have been the subject of intense investigation over the past twenty years.

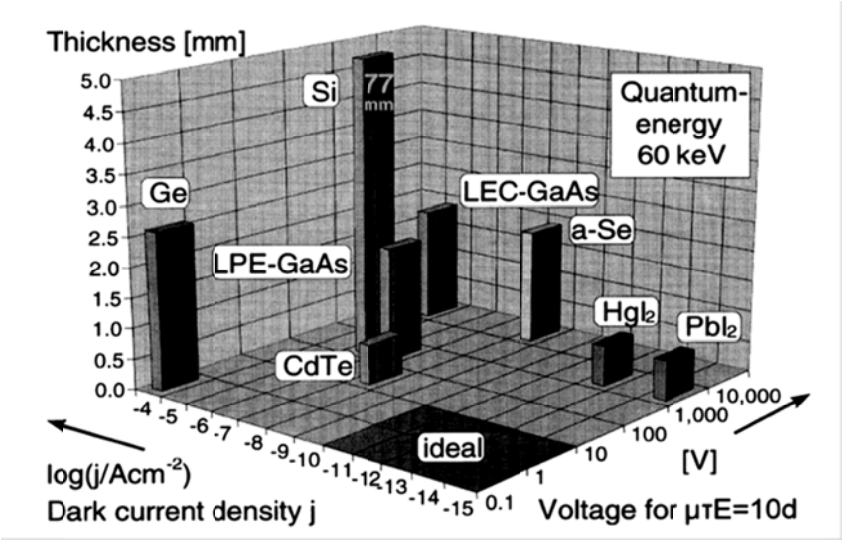

Figure 7 Thickness required for 90% absorption at 60 keV for different semiconductors are shown with the dark current densities and voltages needed for good charge collection adapted from (3).

With respect to Cd(Zn)Te, a great deal of progress has been made with respect to crystal growth and device preparation for spectroscopic analysis of nuclear radiation. Indeed Cd(Zn)Te based spectrometer technology has reached sufficient maturity to be integrated into advanced systems used in space exploration, medicine, and homeland security applications

For example, the HEX-payload which consists of 4cm x 4cm x 5mm Cd(Zn)Te devices with a 16 x 16 pixelated array have been recently integrated into the Chandrayaan-1 spacecraft which launched in Oct. 2008. The so-called HEX payload is intended for the study of X-ray spectra with energies higher than 10keV i.e. radioactive decay of U and Th on the lunar surface, excess of ^{210}Pb. The NuSTAR spectroscopic Telescope Array uses a deployable mast and a Wottler Type 1 lens for telescopic observation using (4) 32x32 pixelated Cd(Zn)Te arrays in conjunction with an ASIC designed by Caltech. This system has an expected launch date of early 2012. The Astro-H exploration telescope with an expected lunch date in early 2014, will use Silicon strip detectors in conjunction with 1mm thick Cd(Zn)Te detectors. Presented in **Figure 8** is a single pixelated Cd(Zn)Te detector mounted to the PCB board which will be incorporated into the NuSTAR telescope.

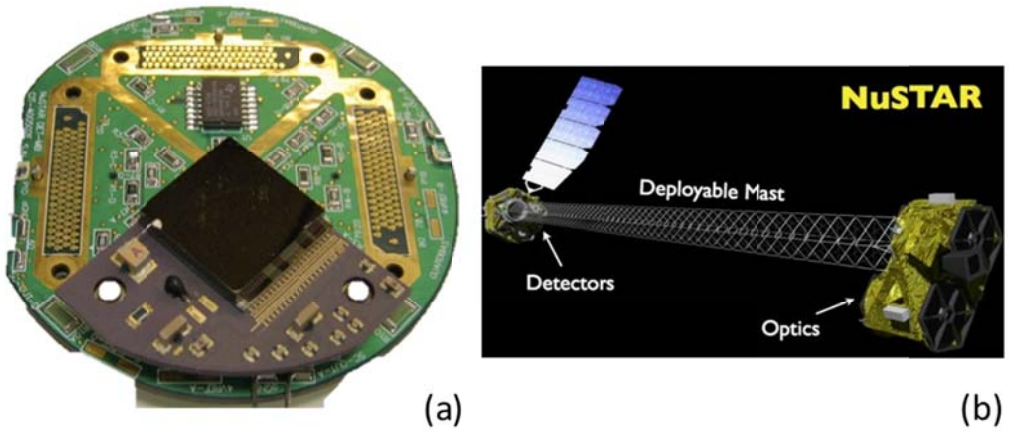

Figure 8 (a) Pixelated Cd(Zn)Te detector mounted to the PCB board which will be incorporated into the NuSTAR telescope (b)

One of the factors which distinguish detector size requirements for space exploration applications is that novel optics may be used for focusing of the high energy photons. In the absence of scattering, X-rays propagate in straight lines and therefore for medical applications a detector which is the same size or larger than the target organ is ideal. The limited volume of single crystals with uniform properties prohibits the development of such large arrays. To overcome this limitation therefore, the detectors may be placed side by side as shown in **Figure 9**. Using such an arrangement and implementing electro-mechanical systems, these sensors may be used for scanning panoramic images of the body.

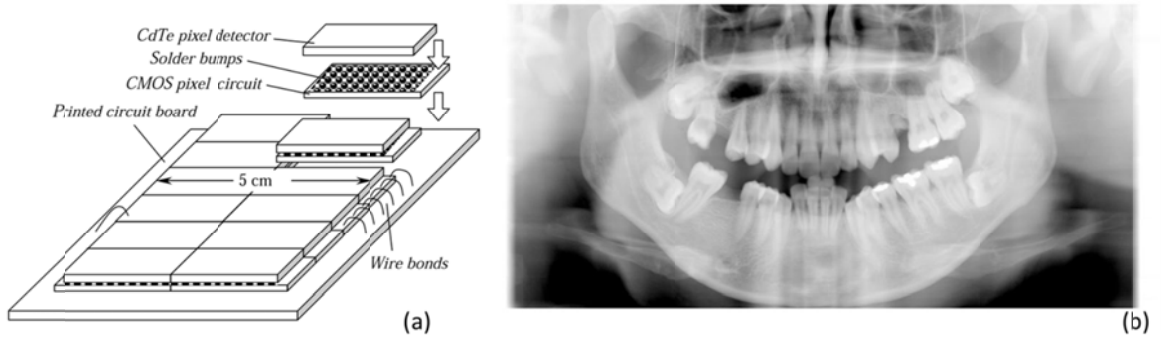

Figure 9 (a) Semiconductor sensor modules mounted side by side in a tiled format and coupled with electro-mechanical systems may be used for scanning images of the body (b) A panoramic projection of the human skull acquired using AJAT CMOS-CdTe camera, adapted from (4)

Despite these more recent developments, obtaining large volumes of uniform and high quality material continues to be one of the limiting factors affecting cost and availability of large detector arrays. Indeed, some of the largest single crystal Cd(Zn)Te detectors which have been reported are 6 cm^3 pixelated Cd(Zn)Te devices and have been produced in

relatively low quantities (5). Indeed, improvements in material synthesis and technological development of crystal growth are crucial to obtaining high quality high resistivity detector grade material.

Furthermore, even though the crystal growth process plays such a fundamental role in determining the material properties of a device, there exist a wide range of competing technologies used for crystal growth. These methods include, but are not limited to Horizontal and Vertical Bridgman (6) (7) (8) (9) (10), Vertical Gradient Freeze (11) (12), High Pressure Bridgman (13), Electro-dynamic Gradient Freeze (14), Travelling Heater Method (15) (16), Vapor Phase Transport (17) (18), Solid State Recrystallization (19), De-wetted Crystal Growth (20), as well as several other modified furnace geometries and experimental arrangements (21) (22) (23). In addition to this, the experimental geometries, the types of refractory materials used, and the crystal growth programs vary substantially between investigators using the same experimental arrangement.

The physical size of the Cd(Zn)Te grown using each technique also varies substantially due to the different types of process restraints and growth rates achievable. Presented in **Table 1** are the physical dimensions of Cd(Zn)Te crystals which have been produced using methods which exhibit the most commercial viability.

Table 2 Physical dimensions of Cd(Zn)Te crystals grown using different methods.

Method	Diameter	Length	Reference
High Pressure Bridgman/EDG	140 mm	>100mm	(13)
Travelling Heater method	100 mm	300 mm	(24)
Vapor Phase Transport	50mm	1-5 mm	(18)

There are also many challenges to producing functioning radiation devices from Cd(Zn)Te grown by any of the aforementioned methods. Indeed, the experimental processes applied to device fabrication present substantial obstacles to achieving material suitable for spectroscopic applications. The methods used for electrical contact deposition and surface preparation, the electrode geometry, the operating mode of the device, as well as the electrical connections to the measurement circuitry all play an important role influencing the performance of the radiation detector.

1.5 COCAE Project- Compton Scattering Camera

The objective of this thesis investigation was the development of detector grade Cd(Zn)Te crystals for spectroscopic gamma ray imaging. Specifically, the material which was grown during this investigation was used for the development of a Compton camera in conjunction with a collaborative European project title COCAE.

The COCAE project was intended to develop technologies for nuclear radiation detection and whose principle aim was the development of a portable instrument with the capacity for detection and identification of radioactive sources, with a range of meters. Using currently available technology, this kind of detection and identification is either time consuming, expensive, or error-prone. Development of a Compton camera, a technology whose principles are inspired by high energy astrophysics, is intended to address these issues.

Examples where the speedy and accurate acquisition of such information is valuable apart from the case of a hypothetical terrorist attack are the melting of a strong radioactive sources in scrap metal refineries/recycling facilities, the theft of a radioactive source, or the dispersion of a radioactive substance due to malfunction of a nuclear power plant. Other applications include

- Border security & inspections (end users: Custom officers, Regulatory authorities)
- Security and inspections at recycling factories (end users: Operators, Custom officers)
- Nuclear waste management facilities and decommissioning of nuclear reactors (end users group: Operators of, Regulatory authorities)
- Emergency response (end users: First response teams (fire brigade)

Development of the Compton camera was a multi-disciplinary program which required the development of several technologies provided by separate institutions as shown in **Figure 10**. Indeed, the organization of the COCAE project required the development of (i) high quality spectrometer grade crystals based on Cd(Zn)Te, (ii) electrode patterning technology for fabrication of pixelated devices, (iii) pixel electronic readout ASIC, (iv) bump bonding technology for bonding the pixelated device to the ASIC, (v) integrated camera housing, and (vi) source localization software for detection of distance, direction, and activity of radioactive sources. Indeed, one of the objectives of the program was to develop the capability to detect sources up to 2 meters with an uncertainty less than 10%.

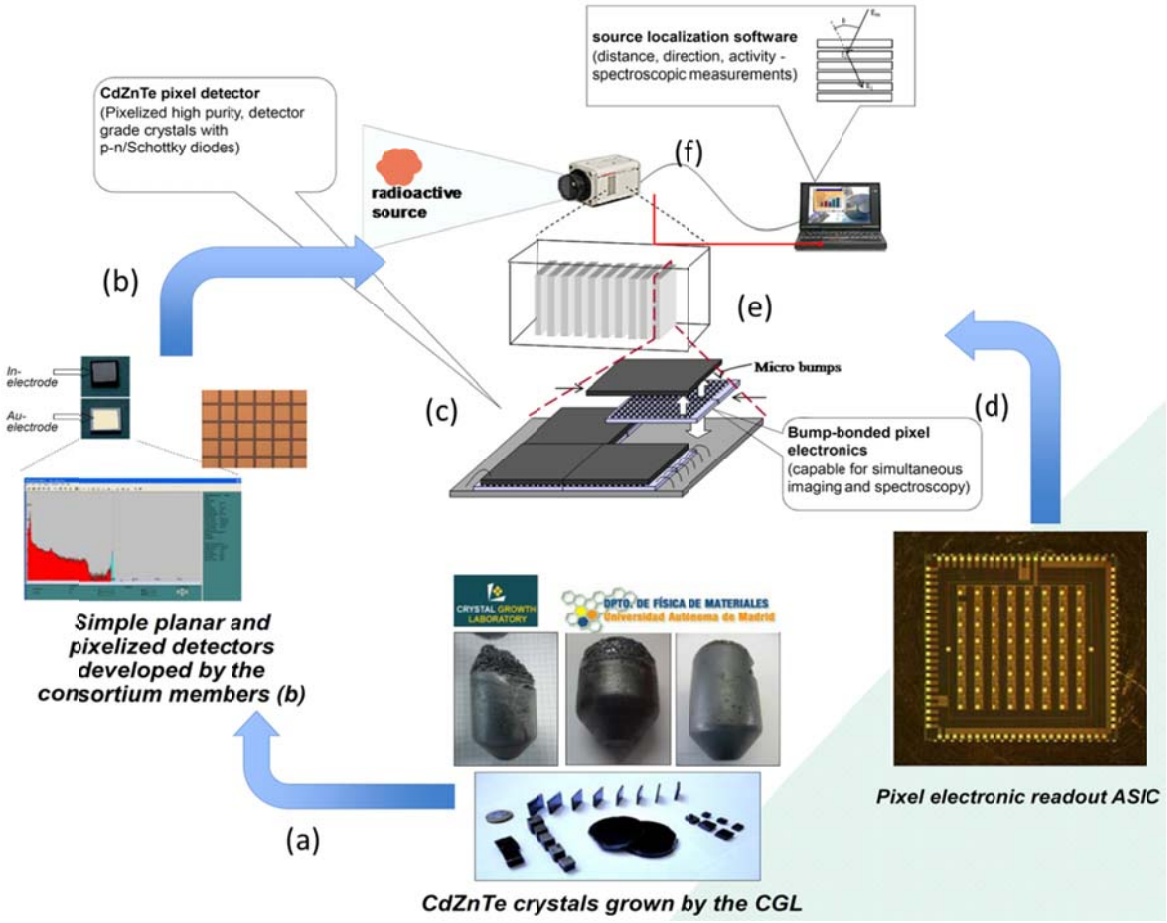

Figure 10 Organizational structure of COCAE project. (a) Crystals grown by the Crystal growth lab (b) tested as planar/Shottkey detectors or fabricated into pixelated detectors (c) bump bonded to pixel electronics using the (d) pixel electronic ASIC and (e) arranged into an array of stacked detectors in order to function as a Compton camera (f)

The instrument is shown schematically in **Figure 11**. It has ten parallel planar layers placed 2 cm apart the one from the other and made of pixilated 2 mm thick Cd(Zn)Te crystals occupying an area of 4 cm 4 cm. Each detector's layer consists of a two dimensional array of pixels (100 x 100) of 400μm pitch, bump-bonded on a two dimensional array of silicon readout CMOS circuits. Supporting printed circuit boards (PCBs) house the hybrid detectors along with additional processing circuitry. The "qualitative" performance criterion for the COCAE detector was to determine a Cs-137 source of 1 mCi located on its symmetry axis at a distance of 1 m with 5% uncertainty within 1 min.

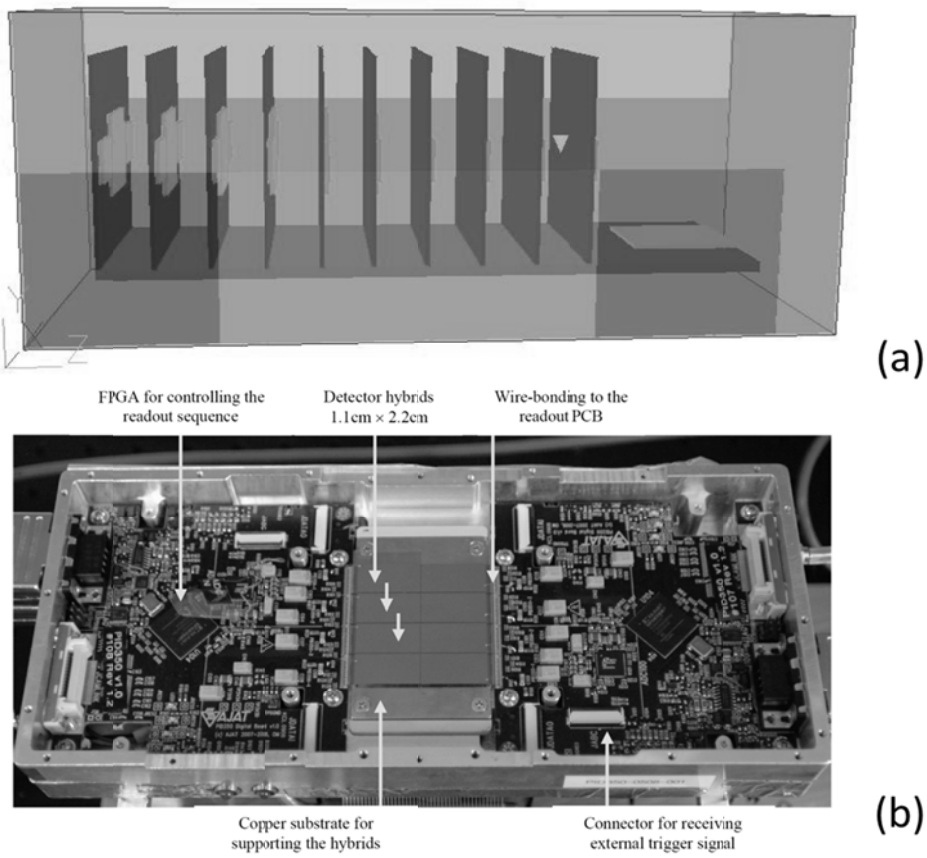

Figure 11 COCAE Compton camera (a) consisting of 10 parallel planar layers placed 2 cm (b) single layer constructed from 2 mm thick Cd(Zn) with dimensions 1.1 x 2.2 cm.

The Cd(Zn)Te source material used for producing these detectors was developed within the COCAE collaboration. Specifically, 0.75kg Cd(Zn)Te ingots were grown by the Crystal Growth Laboratory in support of these developments. The effort to produce crystals of sufficient quality for the development of this camera is the focus of this thesis investigation. The detectors were harvested from the as-grown crystals, hybridized with the CMOS ASIC of the PID350 module provided by the COCAE members, and integrated into the Compton camera. Presented below in **Figure 12** are three PID350 modules assembled.

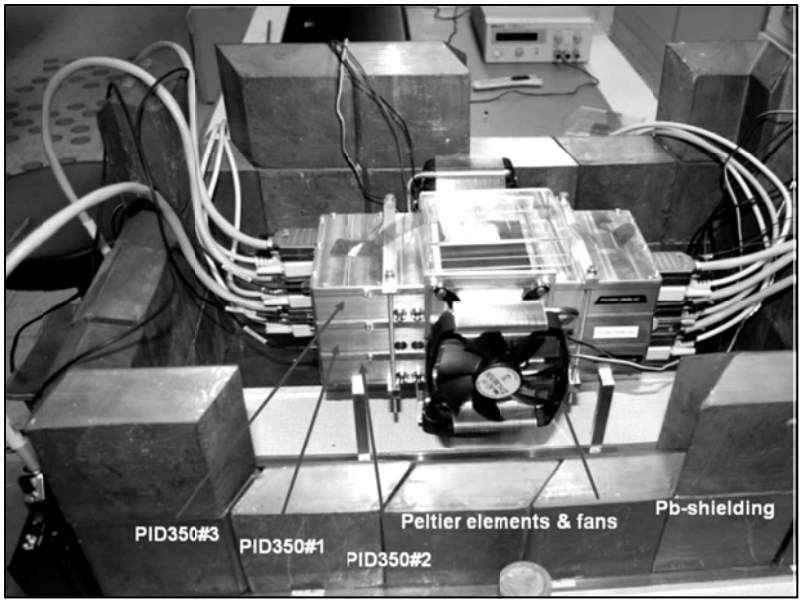

Figure 12 COCAE detector with integral Peltier cooling and fan cooling system, and lead shielding.

1.6 Thesis Objectives

The objective of this thesis has been focused on (i) the development of crystal growth protocol for achieving large volumes of spectrometer grade crystals and (ii) development of detector fabrication protocol for improving the spectroscopic performance of planar and pixelated devices. Both of these objectives are oriented around the development of a high performance Compton camera which has been previously described.

The first chapter of this thesis discusses some of the important material properties of Cd(Zn)Te including the intrinsic and extrinsic defects associated with crystal growth, as well the electrical and transport properties of semi-insulating radiation devices.

The second chapter of this thesis provides a complete list of the experimental methods which have been used in this investigation. This includes (i) the design, construction and testing of various crystal growth technologies which form a crucial part of this thesis investigation, (ii) the experimental methods used for measuring gamma response of detectors, and (iii) the implementation of characterization techniques for the scientific investigations.

The third chapter details advances in crystal growth of Cd(Zn)Te made during this thesis. Included in this chapter are results pertinent to (i) melt homogenization (ii) crystal growth, (iii) development of novel crucible technologies as well as, (iv) the results obtained for scaling the growth capacity to 50mm diameter, 0.75kg charges and (v) the development

of a numerical model for simulation of the crystal growth process. The development of this technology has laid the groundwork for obtaining large volumes of crystals required by the COCAE project.

The fourth chapter provides a detailed description of the progress which has been made with respect to the fabrication of radiation devices based on Cd(Zn)Te. The first section represents the investigation of state-of-the-art commercial detectors. Specifically, four spectrometer grade planar radiation detectors were purchased and characterized extensively in terms of their electrical and optical properties. This first study is intended to serve as a benchmark for reference to future investigations

The original studies carried out in Chapter IV covers several topics including (i) the development of instrumentation and protocol for ingot slicing, wafer lapping and polishing, surface etching and cleaning, electrode deposition, and electrode patterning (ii) investigation of the effects of lateral surface morphology on radiation device performance (iii) the effect of structural defects and the introduction of new deep centers into semi-insulating Cd(Zn)Te radiation devices (iv) the effects of crystallographic twinning on radiation detectors and (v) investigation of asymmetrical distribution of surface states present on oriented as well as non-oriented Cd(Zn)Te radiation devices.

The general conclusions reached during the course of this investigation are summarized in the concluding remarks of each chapter.

Finally, additional work which has been carried out during this thesis is presented in the Appendices. These additional works include the development of a 30kW Heat Exchange Method (HEM) furnace for the growth of poly-crystal silicon for PV applications.

2 MATERIAL PROPERTIES OF CD(ZN)TE RADIATION DEVICES

Section Contents

2.1 Introduction

During the last three decades semi-insulating CdTe and $Cd_xZn_{1-x}Te$ materials have continued to play a dominant role as room temperature semiconductor devices used for high energy radiation detectors covering a broad energy range from a few keV to MeV.

In general, the high atomic number of Cd(Zn)Te semiconductor (Z_{Cd} = 48, Z_{Te} = 52) provides a high quantum efficiency in comparison with Si and other semiconducting materials used for detector applications. The large band gap energy (E_g ~ 1.6 eV) results in a low concentration of carriers which permits room temperature operability. In this section, the bulk material properties of Cd(Zn)Te are discussed with an emphasis on the structural and electrical properties affecting radiation device performance.

2.2 Crystal Structure

The structure of Cd(Zn)Te consists of two interpenetrating FCC sub-lattices, one of which is occupied by Cd or Zn atoms and the other occupied by Te atoms, as presented below in **Figure 13**. This is referred to as the Zinc Blende Structure. The lattice of cations in a zinc blende crystal (in this case Cd^{2+}, Zn^{2+}) is a FCC lattice of the same dimension as the anion sub-lattice (in this case Te^{2-}). The Bravais lattice for this structure consists of a two point basis which is shifted ¼ bond length in the (111) direction.

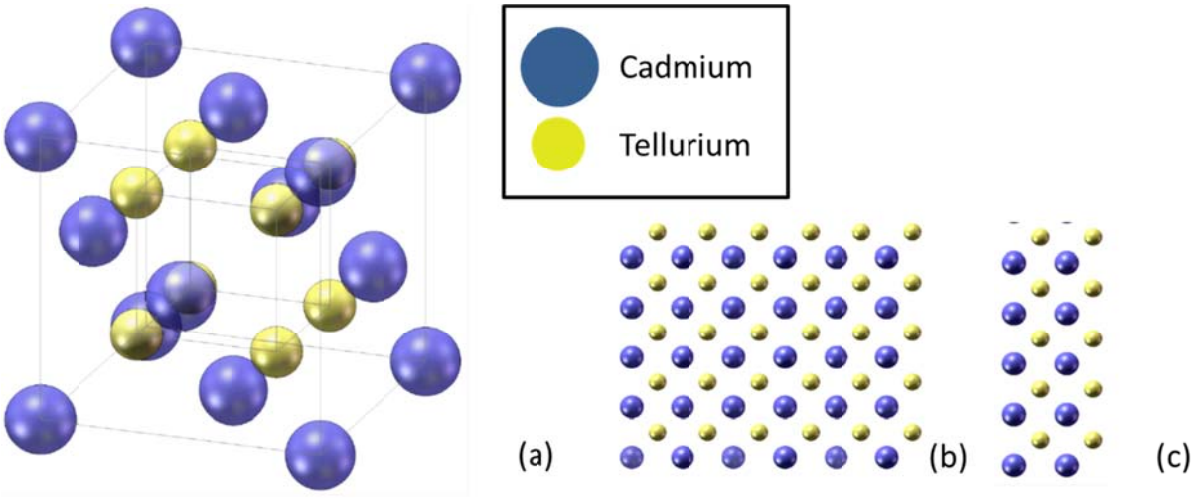

Figure 13 (a) Zinc blende structure of Cd(Zn)Te consisting of two interpenetrating FCC sub-lattices (b) Crystal structure viewed from (100) and (b) (010) plane.

Each FCC unit cell may be described using primitive vectors

Equation 1 $$\boldsymbol{a} = \frac{\mathbf{1}}{\mathbf{2}}\boldsymbol{y} + \frac{\mathbf{1}}{\mathbf{2}}\boldsymbol{z} \qquad \boldsymbol{b} = \frac{\mathbf{1}}{\mathbf{2}}\boldsymbol{x} + \frac{\mathbf{1}}{\mathbf{2}}\boldsymbol{z} \qquad \boldsymbol{c} = \frac{\mathbf{1}}{\mathbf{2}}\boldsymbol{x} + \frac{\mathbf{1}}{\mathbf{2}}\boldsymbol{y}$$

When the FCC basis describing the periodicity of the lattice is Fourier transformed into k-space, a Wigner-Seitz cell of the reciprocal lattice may also be constructed. The basis for the reciprocal lattice follows the vector relationships presented in **Equation 2**. In general, for an FCC lattice with lattice constant $\boldsymbol{a}$, it can be shown that the reciprocal lattice will have spacing 4π/a. As a result, for decreasing lattice spacing, the volume of the Wigner-Seitz cell of the reciprocal lattice will increase.

Equation 2 $$\boldsymbol{a}^* = \mathbf{2}\boldsymbol{\pi}\frac{\boldsymbol{b}\times\boldsymbol{c}}{\boldsymbol{a}\cdot\boldsymbol{b}\times\boldsymbol{c}} \qquad \boldsymbol{b}^* = \mathbf{2}\boldsymbol{\pi}\frac{\boldsymbol{c}\times\boldsymbol{a}}{\boldsymbol{a}\cdot\boldsymbol{b}\times\boldsymbol{c}} \qquad \boldsymbol{c}^* = \mathbf{2}\boldsymbol{\pi}\frac{\boldsymbol{a}\times\boldsymbol{b}}{\boldsymbol{a}\cdot\boldsymbol{b}\times\boldsymbol{c}}$$

Presented in **Figure 14** is the Wigner-Seitz cell of the Fourier transformed FCC lattice (i.e. BCC lattice) with the high symmetry points named following the conventions proposed by (25). The lattice point Γ is located at the origin (0,0,0) and represents the lattice point, or nuclei in this case, about which the Wigner-Seitz cell has been constructed. The symmetry point L is located at (½,½,½) and represents the zone edge following the (111) axis, $\vec{\Lambda}$. The symmetry point X is located at (0,0,1) and represents the zone edge along the (100) axis $\vec{\Delta}$. The symmetry point K is situated at (¾,¾,0) and represents the zone edge along the (110) axis, $\vec{\mathrm{E}}$.

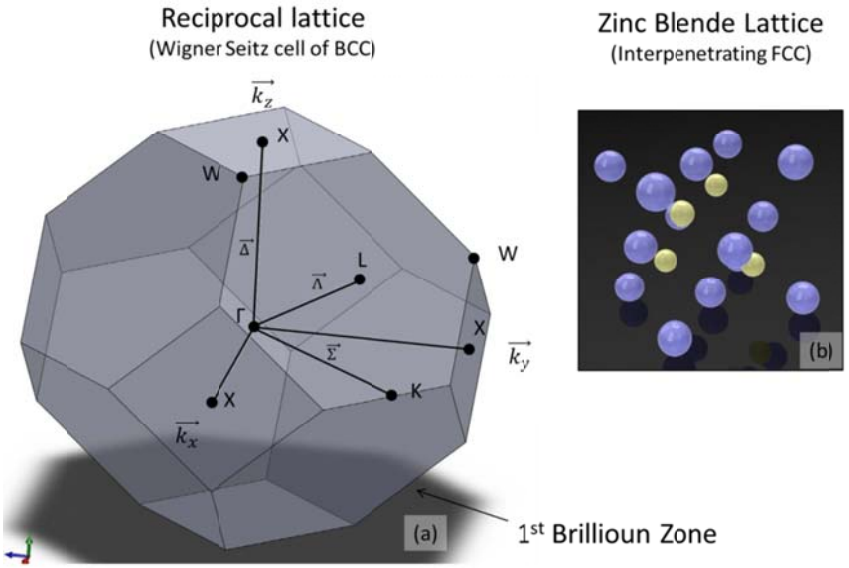

Figure 14 (a) 1st Brillion Zone for FCC crystal constructed (b) Zinc blende crystal structure.

This Zinc blende structure of Cd(Zn)Te is shared by other semiconductors including group (IV) Si, Ge, (III-VI) GaAs, GaP, and (II-VI) HgCdTe. As may be seen in **Figure 15**, CdTe is a direct gap semiconductor which has the largest lattice parameter of II-VI compounds and forms a single phase from CdTe to ZnTe (26). Indeed, introducing Zinc content into the CdTe crystal structure has the effect of increasing the bandgap while decreasing the lattice constant of the material.

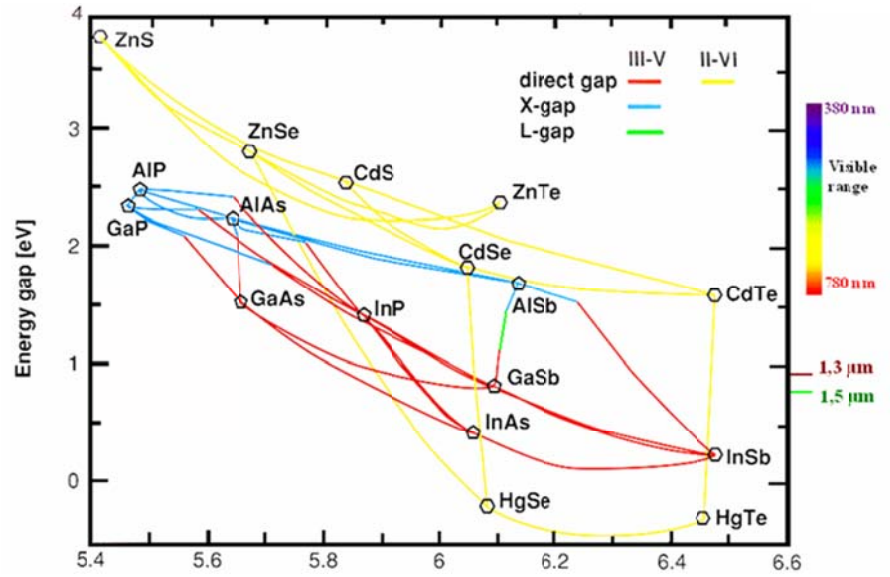

Figure 15 Lattice constant and bandgap energy for a of III-V and II-VI semiconductor compounds (27)

The covalent nature of the bond between Cd and Te plays a significant role in the bulk properties of Cd(Zn)Te. The Cd-Te ionicity has been reported to be 0.55 between Cd^{2+} and Te^{2-} (28) and is one of the largest in the II-VI family of semiconductors. With increasing ionicity in the solid state, the energy of defects, such as vacancies, is reduced (29) and the tendency towards a hexagonal structure is increased. Indeed as will be discussed later, point defects such as vacancies are one of the dominant defects in Cd(Zn)Te affecting charge transport properties.

The Cd(Zn)Te lattice constant, which depends on the concentration of zinc, may be estimated using a linear approximation from Vegard's Law given by **Equation 3**, where a_1 and a_2 are lattice constants of CdTe and ZnTe respectively. Vergard´s law is an approximate empirical rule which posits a linear relationship between the alloy

concentration and the lattice constant for semiconductor materials. Using the lattice constant data for ZnTe and CdTe (30) a lattice constant of 6.441Å for $Cd_{0.9}Zn_{0.1}Te$ may be derived.

Equation 3 $$a(x) = a_1(1 - x) + a_2 \cdot x$$

As previously mentioned, the effect of incorporating Zinc into the CdTe crystal decreases the lattice constant of the material while increasing the bandgap energy. This is a direct consequence of the smaller atomic radii of Zinc with respect to Cadmium. Indeed, the higher bandgap energy leads to the possibility for achieving higher resistivity detector materials, as will be discussed later. Furthermore, because of the higher binding energy of ZnTe with respect to CdTe, the lattice is strengthened which results in a higher shear modulus (see **Table 3**, page 37). As a result, the addition of Zinc should correspond to lower dislocation densities and sub-grain boundaries. This has been verified experimentally by (31).

2.3 A-Face / B-face

When taking into account the crystal structure of a material, it is important to also consider how the positions of the Cd and Te atoms in the lattice affect the surface properties. Indeed, near the surface of the crystalline solid, the periodicity condition is no longer valid. As a result, the free energy at the surface will depend to a large extent on the surface composition.

For a CdTe wafer harvested along the (111) direction, one surface will terminate in primarily Te-atoms while the opposite surface will terminate in primarily Cd-atoms. This asymmetric feature of the surface arises from the periodic nature of the unit cell constructed from two different atoms. As a result, one surface will exhibit a more cationic nature, while the opposite surface will exhibit more anionic nature. As may be seen in **Figure 16**, the surface which terminates in Te (anion) is referred to as the (111)B surface, while the surface terminating in Cd (cation) is referred to as the (111)A surface.

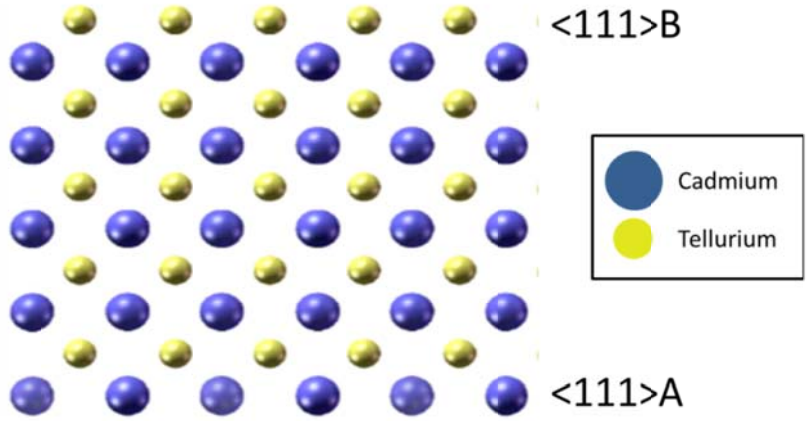

Figure 16 Surface termination following the (111) direction for CdTe.

Indeed this surface polarity has been observed to have a strong effect on the performance of radiation detectors by several groups. For example, differences in device leakage current have been reported to depend on crystal polarity such that a gamma response could only be obtained when the Au anode was on the Cd-rich face (32). T. Takeuchi *et al* proposes that surface barriers at the (111)B face show recombination preferred processes for n-type (111) oriented materials, evidenced by the Current-Voltage characteristics (33). They have provided experimental evidence that the top-most atoms of the (111)A are Cd bonded to O, while the top most atoms of CdTe(111)B are Cd and Te atoms. This asymmetry in the device performance has also been investigated here and is presented in Chapter 4 of this thesis.

2.4 Cd(Zn)Te Mechanical Properties

The hardness and dislocation density for Cd(Zn)Te has depends inversely on the bond length of the constituent elements (34). The incorporation of Zn into the CdTe structure strengthens the crystal lattice as a result of the Zn-Te ionicity being smaller than the Cd-Te iconicity. The Zn-Te bond length is shorter, the energy of defect formation higher, and the resultant density of dislocations lower. This increases the stability of the compound and correspondingly the shear modulus. In general, the energy of defect formation increases with the addition of Zn and the hardness is increased. The hardness for both CdTe and ZnTe compounds is between 55 – 145 kg/mm^2 (0.54GPa – 1.42GPa) and 90 – 225kg/mm^2 (0.882-2.26GPa) respectively.

Nano-hardness and elastic modulus were measured by Zhang et al (35) for Cd(Zn)Te as a function of orientation: (111), (101), and (110) for $Cd_{0.96}Zn_{0.04}Te$ and $Cd_{0.9}Zn_{0.1}Te$, to illustrate the effects of Zn on the Cd(Zn)Te. As Zinc has a smaller electron radius than Cd, and because both elements are from the same IIb family of metals, the Zn-Te bond is stronger, resulting in higher hardness and elastic modulus. The hardness values fall within the range reported by (34). Presented below in **Table 3** are some of the properties for CdTe and ZnTe reported in literature (36) and which have been discussed.

Table 3 Mechanical properties of CdTe and ZnTe.

Material Property	CdTe	ZnTe
Hardness (kg/mm^2)	55-145	90-225
Bond Length 300K (nm)	0.6482	0.6103
Band Gap at 300K (eV)	1.474	2.394
Density (kg/m^3)	5860	5650
Shear Modulus (Nm^{-2})	1.83×10^{10}	2.86×10^{10}
Bulk Modulus (Nm^{-2})	4.9×10^{10}	6.18×10^{10}
Elastic Modulus (Nm^{-2})		
C11	7.34×10^{10}	9.98×10^{10}
C12	3.68×10^{10}	4.28×10^{10}
C44	2.74×10^{10}	4.04×10^{10}

2.5 Stopping Power

One of the principal advantages of Cd(Zn)Te as a detector for high energy radiation is its high average atomic number of Z≈50 which is associated with the ´´stopping power´´ of the material. This property of Cd(Zn)Te leads to greater interaction between the lattice and incident radiation, resulting in a higher overall charge collection efficiency.

Increasing atomic number of a material increases attenuation of high energy radiation, or stopping power. From a detector standpoint this is of paramount importance in terms the number of interactions which take place within the detector of a given thickness. Presented in **Figure 17**a is the attenuation coefficient for Cd(Zn)Te as a function of incident photon energy up to 0.5MeV. For heavier nuclei such as HgI_2 or TlBr, the attenuation coefficient is higher whereas for lighter nuclei such as Si or GaAs the attenuation is lower. In general, for higher energy photons, the materials become more transparent.

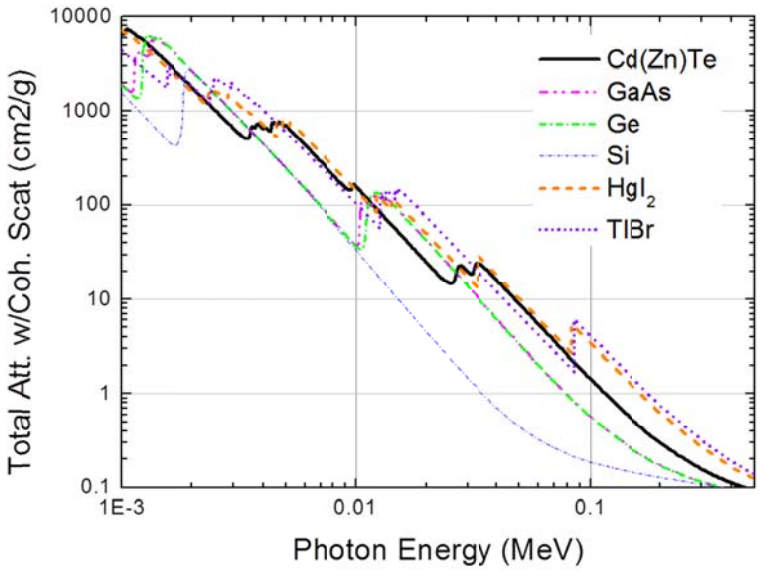

Figure 17 Attenuation Coefficient for Cd(Zn)Te as a function of photon energy compared with other semiconductor materials (37).

In general, attenuation of X-rays or gamma rays within matter may be divided into three distinct categories: photoelectric absorption, Compton scattering, and pair production. For lower energy radiation, photoelectric absorption plays a dominant role in the attenuation of radiation up to 0.5MeV. All of the energy of the incident photon is absorbed by the electrons of the nuclei, and the produced photoelectron will have energy equal to the energy of the incident photon minus the binding energy of the atom, following **Equation 4**. Whereas the incident photon is an un-charged particle, the photoelectron will gradually lose its energy through Coulomb force interactions with the lattice, creating a cloud of electron hole pairs as energy is transferred away from the photoelectron. The quantity of electron-hole pairs generated depends on the energy of the incident photon, as well as the electron-hole pair production energy required by the material. The electron decay from the excited state to its original state produces an X-ray characteristic of the material which may be re-absorbed or may exit from the detector volume.

Equation 4 $$K.E_{Photoelectron} = E_{photon} - E_{B.E.}$$

The photoelectric cross sections of the atoms comprising the detector material play an important role. Shown in **Figure 18**, greater photoelectric absorption is achieved with increasing atomic number. Furthermore, the attenuation increases strongly near the K-edge

of each atom. This is because photons having energy above the binding energy of the K-shell electrons are more likely to be absorbed. For Cd, Zn, and Te the K-edge is located near 26keV, 10keV, and 31keV as can also be seen below (38) (37).

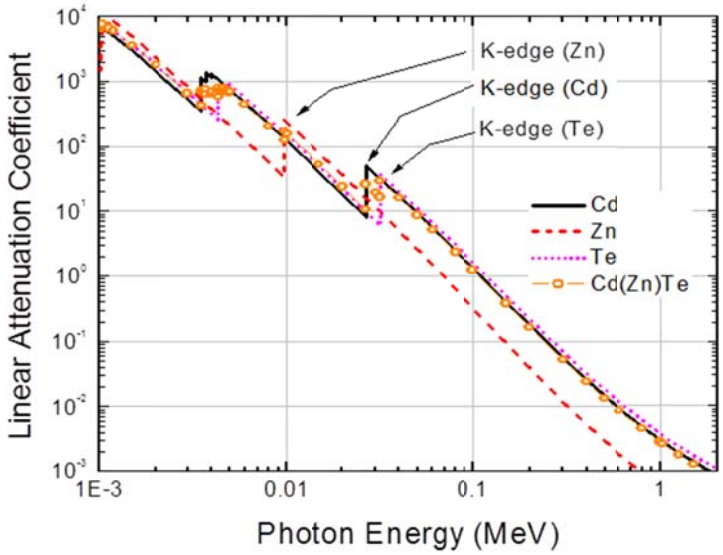

Figure 18 Photoelectric attenuation coefficients of Cd, Zn, Te, and Cd(Zn)Te for low energy photons. Data obtained from NIST database for attenuation coefficients (37).

Compton scattering is another important kind of interaction which results from the non-elastic charge transfer between a photon and an orbital electron. As may be seen in **Figure 19**, for energies between 0.01MeV and 0.5MeV the attenuation due to photoelectric absorption decreases by several orders of magnitude while incoherent scattering, or Compton scattering, increases. Using a classical mechanics model for in-elastic collision, the angle of interaction between the photon and the electron will determine the amount of energy which is transferred to the electron following Equation 5 where $\boldsymbol{E_1}$ is the incident energy of the photon, $\boldsymbol{E_2}$ is the photon energy after scattering and charge transfer, and θ is the angle of the scattering event.

Equation 5 $$\boldsymbol{E_1 - E_2 = \frac{h}{m_e c}\left(1 - Cos(\theta)\right)}$$

In the absence of scattering, X-rays and gamma rays travel in straight lines. In the Compton effect, the scattering angle will determine the energy loss of the photon, and

gained by the electron. The electron will again lose energy through coulomb force interactions with the lattice, creating a cloud of electron hole pairs.

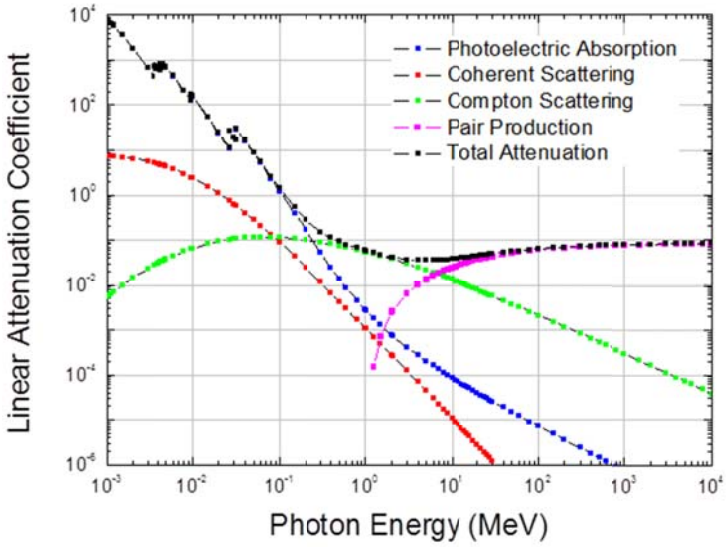

Figure 19 Total attenuation coefficient of Cd(Zn)Te due to elastic or coherent scattering, photoelectric absorption, Compton scattering, and pair production (37).

For photons with energy between 0.15MeV and 2MeV, Compton scattering plays a significant role in determining the amount of charge deposited within the material by the gamma ray. For energies higher than 1MeV however, the Compton effect begins to decrease as pair production begins to play a more dominant role. Electron-Positron pairs may be generated by a photon with energy above 1.02MeV. The positron may then subsequently decay through annihilation with an electron, producing two gamma rays with energy 0.511MeV. These gamma rays are free to interact with the lattice either through photoelectric absorption or Compton scattering, or they may leave the detector volume altogether.

2.6 Crystalline Defects in Cd(Zn)Te

Advancements in crystal growth and device fabrication processes require a strong working knowledge of defects and defect formation in Cd(Zn)Te. These defects may be introduced by the crystal growth process, or by subsequent cutting and polishing of the material, or may even be native defects. A description of the most pertinent defects to Cd(Zn)Te are presented here.

2.6.1 Point Defects

Defects in crystalline semi-insulating materials such as Cd(Zn)Te introduce energetic levels into the bandgap of the material. Point defects strongly influence the statistics of occupation of both the deep and shallow centers, which determines to a large extent the resistivity of the material. To control the electronic properties of Cd(Zn)Te, it is important to understand the nature of these point defects (donor or acceptor behavior) in order to counteract any negative impact on device performance they might have. Presented in Figure 20 are several of the more dominant point defects found in Cd(Zn)Te. Point defects and their impact on Cd(Zn)Te radiation devices have been studied in detail, and more details are presented in Chapters 3 and 4.

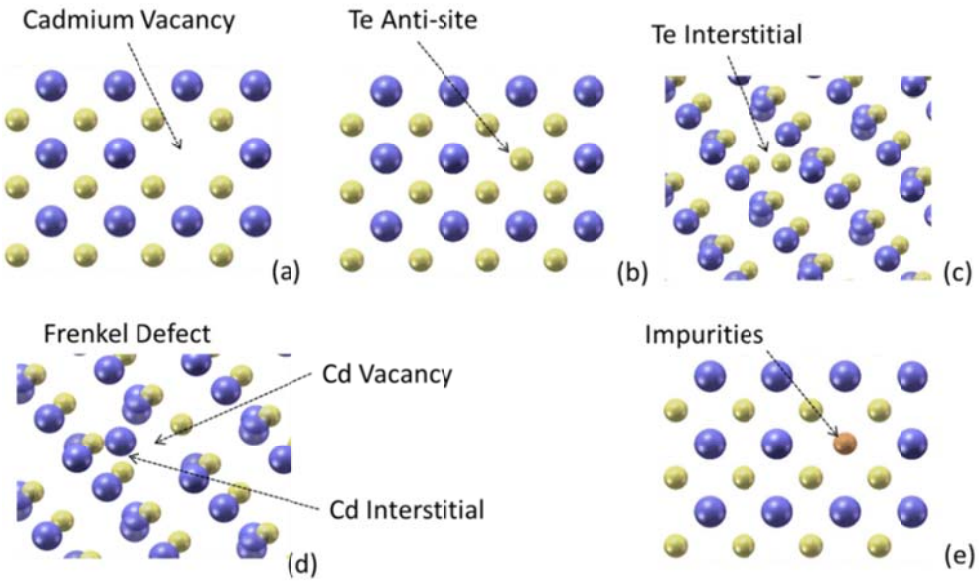

Figure 20 Different types of point defects found in Cd(Zn)Te **(**a) Cadmium vacancy (b) Te anti-site (c) Te-interstitial (d) Frenkel defect (e) impurity

V_{Cd} are indeed one of the more important point defects in Cd(Zn)Te, and may exist as ionized V_{Cd}^{--}, or as V_{Cd} - impurity complexes. The doubly ionized V_{Cd} has been attributed as the energy level responsible for the pinning of the Fermi level near mid-gap. The energy and capture cross section of the latter complex may vary to some degree depending on the type of impurity atom involved, and for these reasons is referred to as the A-center family. V_{Te} and ionized V_{Te+} as well as impurities such as C, Au, and Cu have been attributed to introducing electronic levels into the bandgap. For more information on these defects in Cd(Zn)Te the reader is referred to (39) (40) (41) (42) (12) (43) (44) (45) (46).

The point defects in Cd(Zn)Te have been studied by a wide range of investigators using an even wider range of experimental techniques. Presented in **Table 4** are the deep centers in Cd(Zn)Te following the naming conventions proposed by both (39) and (42) and presented in **Figure 17** are the position of the defect levels situated in the bandgap of Cd(Zn)Te.

Table 4 Deep centers present in Cd(Zn)Te which have been investigated in this work.

Naming Convention (39)	(42)	Energy (eV)	Cross Section (cm^{-3})	Character	Proposed Origin of Defect
A_0	**P1**	0.12	2×10^{-16}	Acceptor	A-center
A		0.14	1×10^{-16}	Acceptor	V_{Cd}
A_1		0.15	4×10^{-17}	Acceptor	V_{Zn} / impurities on Cd sites
B	**P2**	0.19-0.22	3×10^{-16}	Acceptor	Attributed to growth process (THM) / V_{Te}
C	**P3**	0.25-0.29	8×10^{-17}	Acceptor	Zinc related defect, C, Si
D	**P4**	0.32-0.41	8×10^{-16}	Acceptor	Te_{Cd}
E	**P5**	0.43	1×10^{-14}	Acceptor	V_{Cd} / Structural defects/ Stress
F	**P6**	0.57-0.60	8×10^{-14}	Acceptor	V_{Zn}? / unknown
G		0.64-0.67	2×10^{-13}	Donor	Doubly ionized Cd_i^{++}
H	**P7**	0.76	6×10^{-13}	Acceptor	V_{Cd} – impurity complex /transition element
H1	**P8**	0.79	4×10^{-14}	Donor	Metallic impurities
I	**P9**	1.10	9×10^{-11}	Donor	V_{Te}^{+}

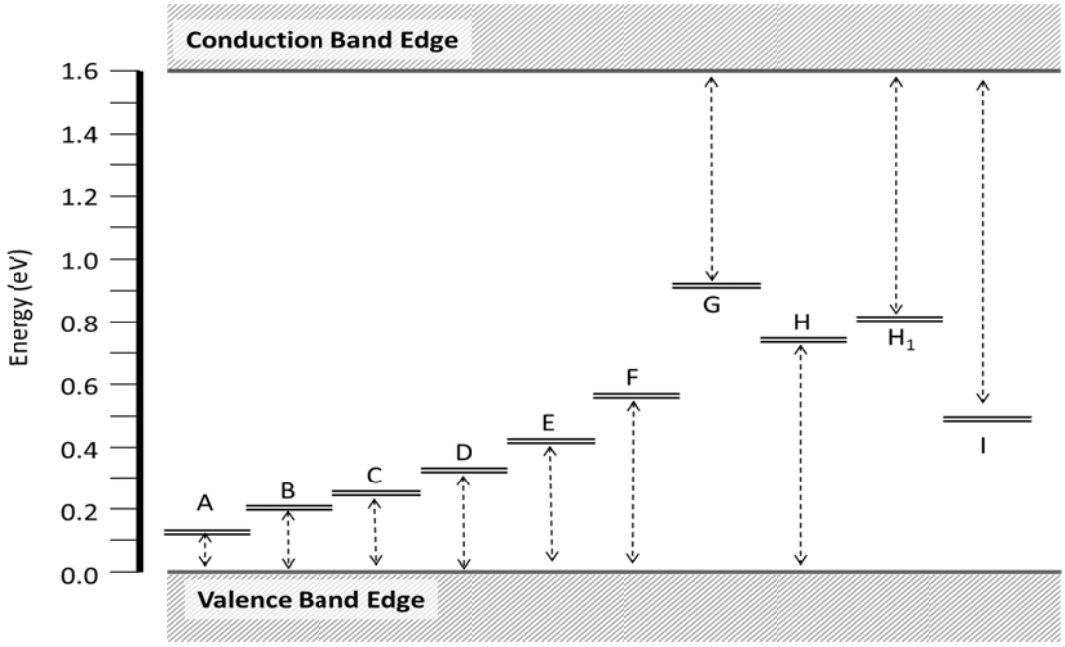

Figure 21 Deep centers observed in Cd(Zn)Te using naming conventions proposed by Castaldini (39).

2.6.2 Second Phase Inclusions/Precipitates

Second phase particles in Cd(Zn)Te and how these crystalline defects affect detector performance have received a great deal of attention over the past two decades. Indeed, these particles have been shown to have a strong impact on detector transport properties. It is important however, to distinguish between the two major kinds of second phase particles found in Cd(Zn)Te. Te-inclusions are larger second phase particles within the Cd(Zn)Te matrix, roughly several microns in diameter, originating from morphological instabilities of the growth interface. Te-precipitates are smaller second phase particles which arise from the diffusion, segregation, and retrograde solubility of Te in the Cd(Zn)Te matrix.

The formation of inclusions may be understood by taking into account crystal growth of Cd(Zn)Te has been carried out using Te-rich melts, where there is an excess of Te with respect to Cd. As a result, within the molten Cd(Zn)Te liquid, there are particles or droplets of Te which become associated. As crystal growth begins, these droplets of Te become trapped as the solid liquid interface propagates through the melt. Indeed, inclusions originate at the growth interface as consequence of morphological instability in the growth process (47) (48) (49). If we consider that the melting point of Te is close to 450ºC, the Te-droplet must remain liquid throughout the growth process, until low temperatures are reached.

Once the Te-inclusion is within the solid Cd(Zn)Te matrix, it is possible that the particle may break apart into smaller inclusions and diffuse throughout the Cd(Zn)Te ingot. In fact the proper choice of superheating and post-growth annealing conditions may be used to reduce the size of second phase inclusions.

Presented Figure 22 are typical inclusions found in Cd(Zn)Te wafers grown in this work, and studied using EDS spectroscopy to confirm their elemental composition. Characteristic X-rays emitted by Cd, Zn, and Te, demonstrate that these inclusions contain no Cd, a small amount of Zinc, and are predominantly composed of Te.

Not only the size, but also the density of Te-inclusions is important. The diffusion of inclusions throughout the Cd(Zn)Te matrix is limited by structural features such as grain boundaries, sub-grains, and twin boundaries which may act as physical barriers hindering migration. It has also been demonstrated that Te inclusions may selectively getter impurities such as Na, Ag, In and Bi (50). This gettering mechanism of the Te-inclusions

may originate from diffusion during crystal growth and segregation during the crystal cooling cycle.

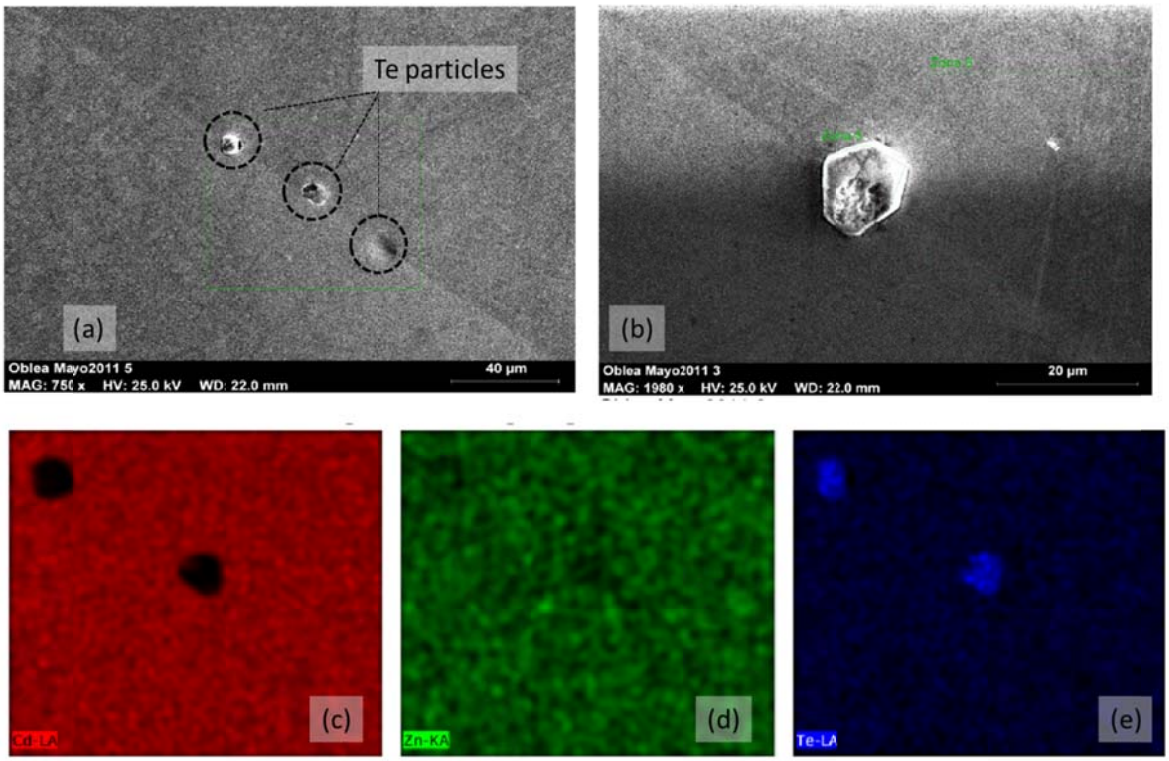

Figure 22 Te-inclusion at the surface of Cd(Zn)Te wafer. (a) SEM image of Cd(Zn)Te surface with three Te-inclusions present, two of which are slightly buried within the Cd(Zn)Te matrix (b) Higher magnification of exposed Te- particle (c-e) EDX images of the surface illustrating the absence of Cd, the presence of Zn and the abundance of Te in these particles.

Te-inclusions play a prominent role on the optical and electronic properties of devices (47) (51) (48) (49) (52).. Indeed, charge trapping and distortion of the electric field due to Te-inclusions has been observed. The minimum permissible size of Te-inclusions in Cd(Zn)Te is not well defined, but is also related with their density. It is ideal that the inclusions not be more than 10 microns in diameter, as they begin to strongly affect the charge collection efficiency as scattering centers and recombination centers in Cd(Zn)Te. It is also important to realize that the spatial trapping region extends far beyond the size of the second phase particle, associated with their dislocation fields. (53) (54).

Te-precipitates are a second type of second phase particles found in Cd(Zn)Te materials. Precipitation of Te may be considered as a group of 5 neighboring Te atoms, formed in the early stages of growth, and created in the solid phase during the cooling phase (47). More than 90% of the *excess* Te will precipitate, in consequence of the

retrograde solubility of Te (48) (53) (55) (56). Their formation is also controlled by the diffusion of Te through the ingot (49).

Te precipitates can be 10-50 nm in diameter in size, and may be composed of roughly 50-80% Te (57). Different structures of Te-precipitates have been observed depending of the concentration of Te. For precipitates with a higher the concentration of Te, the features have a more elliptical the shape, whereas in precipitates with lower concentrations of Te, the geometry is more linear (58). Dislocation fields surrounding precipitates also act as trapping centers (59) , and degrade detector performance.

2.6.3 Dislocations

Presented in **Figure 23** are these two types of idealized dislocation structures. Dislocations are a 2-dimensional and 3-dimensional crystallographic defect which gives rise to a distortion of the crystal lattice producing a stress field localized around the defect. Dislocations may be generally classified as either edge-dislocation or screw dislocation, though dislocations in real materials are usually a combination of the two kinds. These classifications are derived from the relationship of the dislocation line with the Burgers vector. In edge-dislocations, the burgers vector and the dislocation line are perpendicular, whereas for screw-dislocations the burgers vector and the dislocation line are parallel.

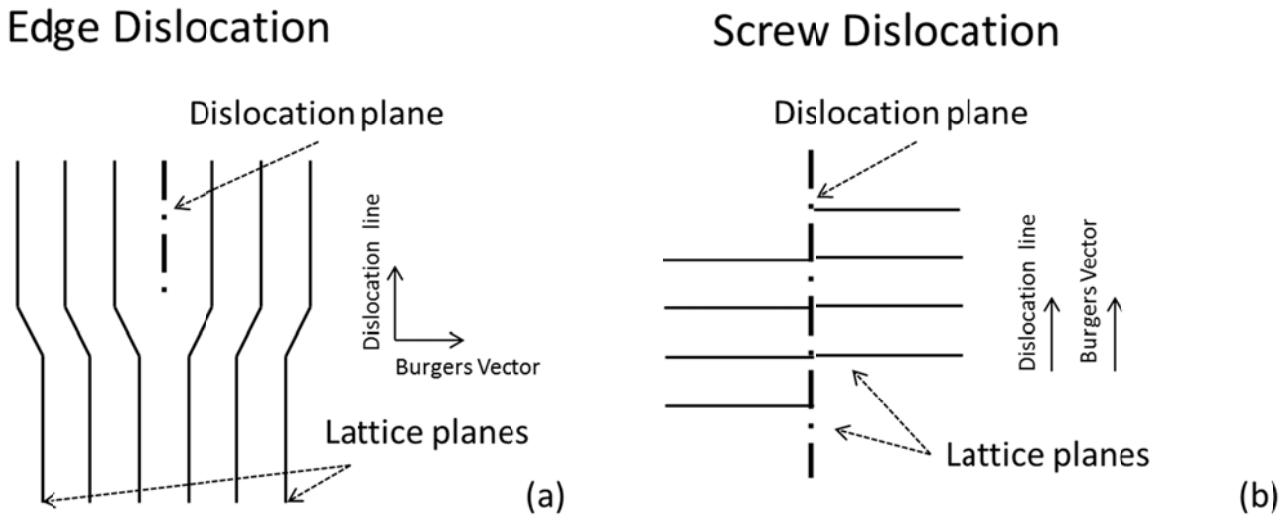

Figure 23 (a) edge dislocations (b) screw dislocations in ordered crystalline materials.

In the case of Cd(Zn)Te, dislocation fields may also be associated with the structural changes induced by second-phases such as Te-inclusions. For larger diameter Te-inclusions, the induced dislocation field extends far beyond the boundaries of the inclusion surface. Using X-ray topography methods, the dislocation field surrounding a Te-inclusion has been investigated, to demonstrate the negative impact of both the inclusions and the associated dislocation field on electrical transport properties of the material (49).

Dislocations may be generated due to thermally induced stress at the ampoule wall or even through the application of induced stress into the sample (60). Thermo-mechanical strain induced by high thermal gradients during solidification and cool down are other possible sources for dislocations (11).

The density of dislocations in Cd(Zn)Te material may be revealed by measurement of the etch pit density (EPD) following the etch for <111> oriented samples. In the etching developed by Nakagawa (61), a correspondence between deformation induced dislocations observed in n-type CdTe and etch pits was revealed. This etching measurement is one indicator of material quality as the presence of dislocations degrades detector performance. For a good quality sample, the EPD value is normally in the range of 10^3-10^4 cm^{-2}.

2.6.4 Voids & Pipes

Void and pipe defects in Cd(Zn)Te are large macroscopic 3-dimensional defects with a hollow tubular shape, which can be large enough to be seen upon visible inspection. It is possible that these defects are related to the trapping of Cd gas, due to fluctuations in the growth condition, and may be related with high growth rates. Suppression of these defects can be achieved through correct choices of thermal profiles, crucible materials, and growth cycle, such as those presented in this thesis. Presented in Figure 24 are some examples of void defects which were present in crystals grown at the start of this investigation, under growth conditions which had not yet been optimized. Through implementation of controlled crystal growth rate and improved refractory materials, these defects were systematically eliminated from the growth process.

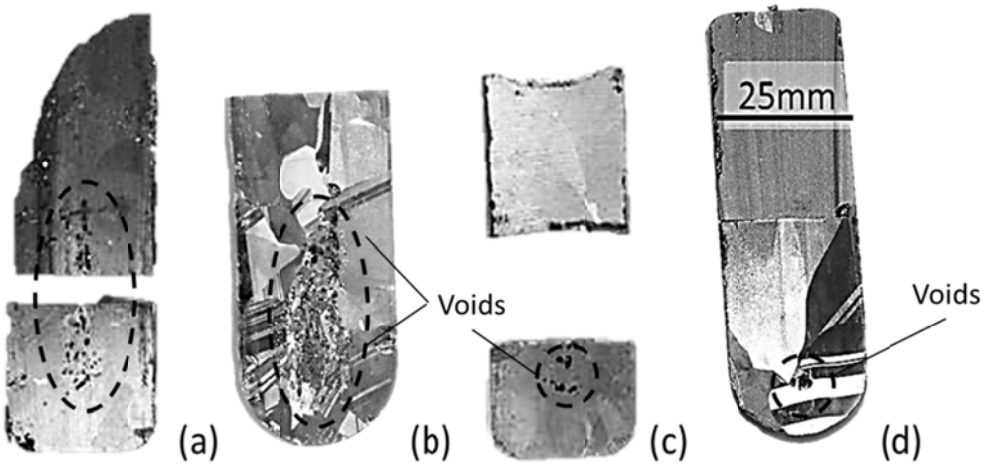

Figure 24 High concentrations of voids in Cd(Zn)Te grown in four ingots at the start of this investigation.

2.6.5 Twinning

Due to the crystallographic symmetry group of the Zinc Blende structure (F43m), twinning in Cd(Zn)Te may be expressed by (1) rotation of the of the lattice by 180º about the <111> orientation or (2) rotated 250.53° about the (011) plane (62) (63). Presented in Figure 25 is an example of twinning in Cd(Zn)Te such that the crystal lattice is rotated by 180º about the <111> orientation. As may be seen, this type of defect disrupts the periodicity of the crystal.

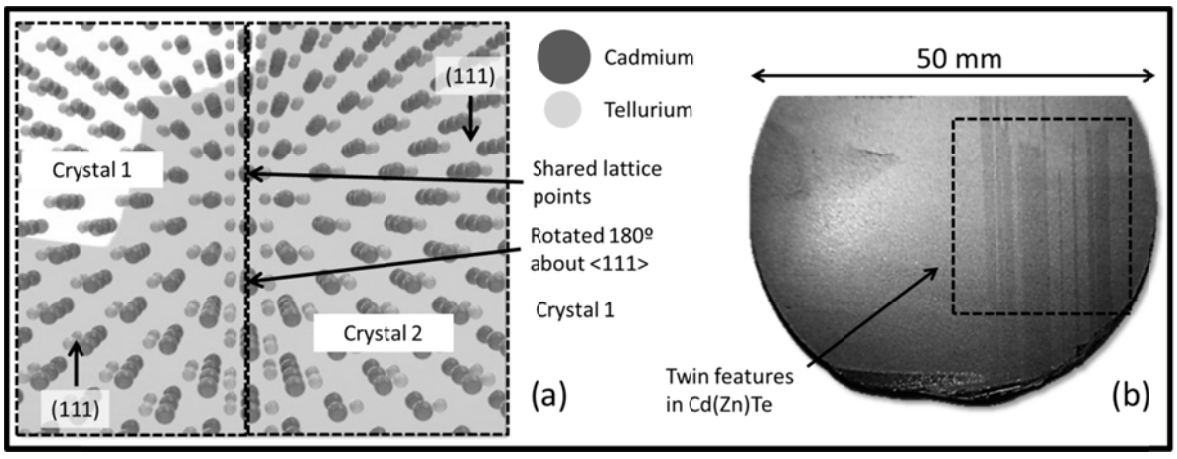

Figure 25 (a) Twinning in Cd(Zn)Te by rotation about the <111> plane by 180º and (b) actual twin features in Cd(Zn)Te wafer

While the structural properties of twinning may have a negligible impact on the electrical properties of Cd(Zn)Te devices, these twins may act as gettering planes, to which

higher concentrations of impurities and dislocations may diffuse. Furthermore, the rotation of the crystal structure by 180º about the <111> direction also changes the direction of the Cd-Te electric dipole. As a result, both faces of an oriented <111> sample may exhibit the A-face and B-face terminations as was discussed in 2.3 and was illustrated in **Figure 16**. This feature of twinning in Cd(Zn)Te is investigated further in Chapter 4 Section 6.

2.6.6 Grain Boundaries

The 2-dimensional **s**urface which divides two or more crystal volumes containing different crystallographic orientation may be referred to as a grain boundary. Grain boundaries, in general, have the effect of decreasing the thermal and electrical conductivity of a material, a result of the boundary surface functioning as gettering sites for impurities, second phase inclusions, and dislocations.

Grain boundaries may be classified into two different groups depending on the angle of orientation between the two grains. Low angle grain boundaries (LAGB) occur when there is only a small angle between the two grains resulting from a small mis-orientation less than 10º. The LAGB may be further sub-divided into two idealized classes: tilt grain boundaries and twist grain boundaries. In the case of tilt grain boundaries, the orientation of the crystal is changed through the introduction of dislocations. These dislocations reduce the energy of elastic deformation of the lattice, and provide a mechanism for changing the crystallographic orientation. Twist grain boundaries may be formed by the coupling of screw dislocations resulting in a rotation of the crystallographic orientation by some angle. These two cases are shown schematically in Figure 26 for Cd(Zn)Te. High angle grain boundaries occur when there are much larger angles between the two grains and can induce larger concentrations of dislocations and crystalline defects as a result.

For Cd(Zn)Te, these grain boundaries may be formed at the very early stages of growth wherein nucleation of several grains occurs, or later on due to instabilities at the growth interface. Nucleation of more than a single grain may occur if the crystal is grown using high growth velocities, under high temperature gradients, or may also be a result of the melt convection and latent heat extraction properties. Presented in Figure 27 is a Cd(Zn)Te crystal grown early in this work using a high crystal growth rate near 1 mm-hr^{-1}. As may

be seen, the as grown crystal suffers from large voids present in the first to freeze tip, very small crystal grain sizes, and cracks propagating from the void sites throughout the ingot.

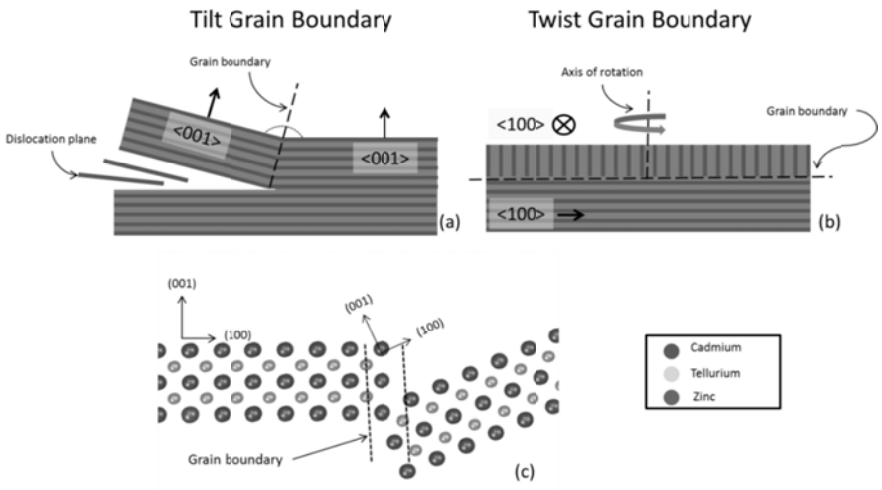

Figure 26 (a) tilt grain boundaries induced by dislocation planes and (b) twist grain boundaries induced by rotation of the grain. (c) Tilt grain boundary between two crystallographic orientations in Cd(Zn)Te normal to the (100) projection.

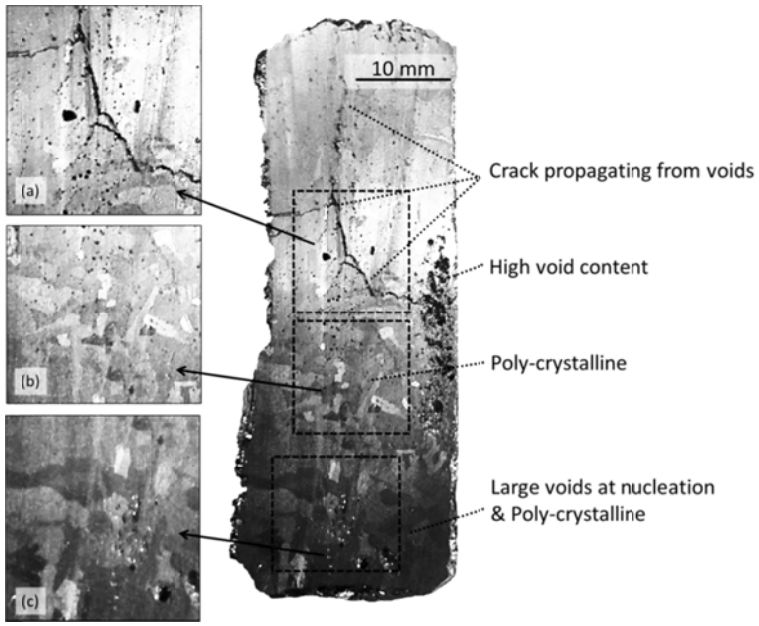

Figure 27 Crystal grown using high crystal growth rate with (a) cracks propagating through the crystal (b) very small crystal grain sizes and (c) voids and multiple grains present at the first to freeze region.

While reasonable counting efficiency may be obtained within each individual grain, detector response is substantially reduced along the grain boundaries. Indeed, these grain boundaries have the effect of limiting the charge transport properties of the material. This

may be due to the weak bonding characteristics at the grain boundaries, or may be related to the higher concentration of impurities and dislocations found at these boundaries. Therefore, it is important that large enough single grains are grown to increase the detector volume which may be harvested. In general, small grain sizes are one of the limiting factors prohibiting the fabrication of large volume detectors for radiation detection applications.

2.6.7 Cracks

Large macroscopic defects such as fissures and cracking may be associated with the thermal-mechanical stresses imparted by the ampoule, or the cool down phase. As may be seen in Figure 27, cracking may propagate through an ingot due to excessively high densities of voids or inclusions. Such high densities of voids near the ampoule wall may be indeed associated with the crucible material. The ingot presented in **Figure 27** was grown using a quartz ampoule such that the melt was in direct contact with the quartz. Furthermore, mechanical stresses imparted into the sample during post-growth processing such as ingot slicing, dicing, grinding, and polishing also may induce cracking. Through appropriate choices of growth temperatures, crucible materials, and cooling, these defects have been systematically eliminated.

2.7 Electrical Properties

In the following section, the electrical and optical properties of Cd(Zn)Te will be developed. The purpose of this section is to introduce the properties of Cd(Zn)Te which make this material suitable as a for applications requiring room temperature gamma ray spectroscopy. For these reasons, concepts related with band structure, density of states, and the Fermi distribution functions will be developed to underline the concepts pertinent to achieving semi-insulating material.

2.7.1 Band Structure

In crystalline solids, electrons and holes are confined to bands. These bands are formed through the splitting of atomic energy levels and may be described by the Pauli exclusion principle as the isolated atoms are brought together to form a system. The total number of quantum states does not change as the crystal is formed. However, because each electron must have a unique set of quantum numbers, the discrete atomic energy levels must now be split into bands. For a sufficiently large number of atoms, these bands may be

considered to be quasi-discrete due to the small separation of energy levels. It is precisely this splitting of the bands which gives rise to the forbidden bandgap in semiconductor materials.

Neglecting the core levels, the valence band represents specific lattice sites at which electrons are bound. The lowest unoccupied band, the conduction band, provides the mechanism for conduction. When electrons occupy the valence band, they do not contribute to the electrical conductivity of the material. Being fermions, electrons cannot carry any current in a filled band as they may only occupy empty states.

For semiconducting materials, at T=0ºK, the valence band is full and the conduction band is empty. However, as thermal energy is increased with temperature, some electrons may become excited to the conduction band and may contribute to the electrical conductivity of the material. The larger the bandgap of the material, the more thermal energy is required for electrons to become excited into the conduction band. A general depiction of the band structure of semiconductor and metals at T=0ºK is shown in **Figure 28**. It is also useful to define here the concepts of work function (Φ) and electron affinity (χ) which are important material properties. The work function (Φ) represents the amount of energy required to remove an electron from the material, whereas the electron affinity represents the amount of energy to remove an electron from the conduction band to the vacuum level.

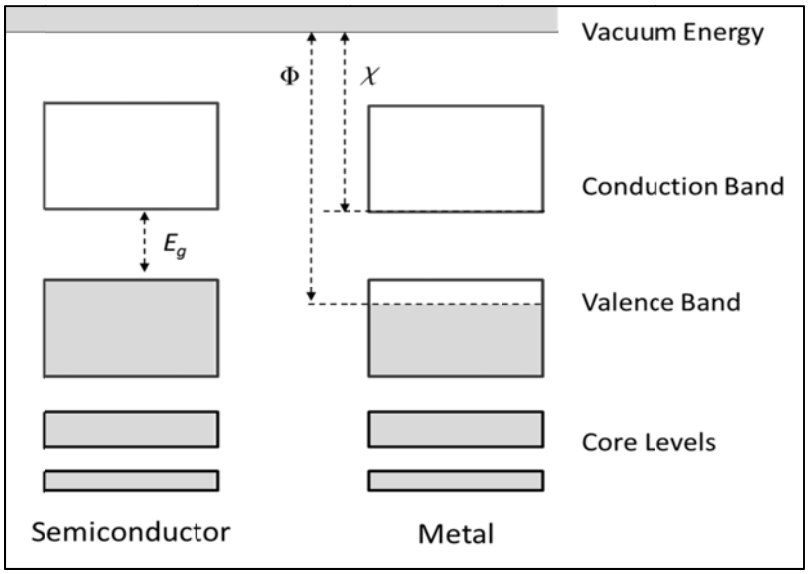

Figure 28 Generalized band structure of semiconductors and metals.

The band structure of a crystalline solid refers to the energy-momentum relationship and may be obtained by solving the Schrodinger equation of an approximate one-electron problem. Because the electrical potential V(r) is periodic with the lattice, the solutions take the general form of periodic Bloch functions **Equation 7**. Using this convention, any momentum $\boldsymbol{k}$ may be reduced to some point in the Brillouin Zone.

Equation 6
$$\left[\frac{\hbar^2}{2m}\nabla^2 + V(r)\right]\phi_k(r) = E_k\phi_k(r)$$

Equation 7
$$\phi_k(r) = e^{jk\cdot r}U_n(k,r)$$

The most simplified 1-D model used for generating the band structure of crystalline solids using an idealized quantum-mechanical system is the Kroenig-Penney model. This model consists of an infinite array of potential barriers with period $\boldsymbol{a}$ and potential barrier width $\boldsymbol{b}$. Using the Bloch functions to evaluate the Schrödinger equation in 1-D, the solutions to the Schrodinger equation will take the general form of **Equation 8**, where $\alpha^2 = 2mE/\hbar^2$ and β=$\alpha^2 - 2mV_0/\hbar^2$.

Equation 8
$$u_1(x) = Ae^{i(\alpha-k)x} + Be^{-i(\alpha-k)x}$$
$$u_2(x) = Ce^{i(\beta-k)x} + De^{-i(\beta-k)x}$$

Taking into account the periodic boundary conditions of the problem, 4 sets of equations can be used for solving four unknowns, namely the coefficients. A,B,C, and D. In general, a non-trivial solution will exist if the determinant of this 4 x 4 linear combination of equations equals zero i.e. if the equations are linearly independent. Evaluation of this determinant, and working under the assumptions that 1) $b \to 0$, $V \to \infty$, and $V \cdot b \to finite$ leads to the analytical relationship presented in **Equation 9** (64). It is important to realize that this relationship sets forth the values for $\boldsymbol{k}$ and $\boldsymbol{\alpha}$ which may be used to obtain a real solution to the Schrodinger equation. This relation is plotted in **Figure 29**. When the left had side of **Equation 9** is equal to the right hand side, the $\boldsymbol{k}$ and $\boldsymbol{\alpha}$ requirements are satisfied.

Equation 9 $$\left(\frac{m \cdot V_0 \cdot b \cdot a}{\hbar^2}\right)[sin(\alpha \cdot a)/\alpha \cdot a] + cos(\alpha \cdot a) = cos(k \cdot a)$$

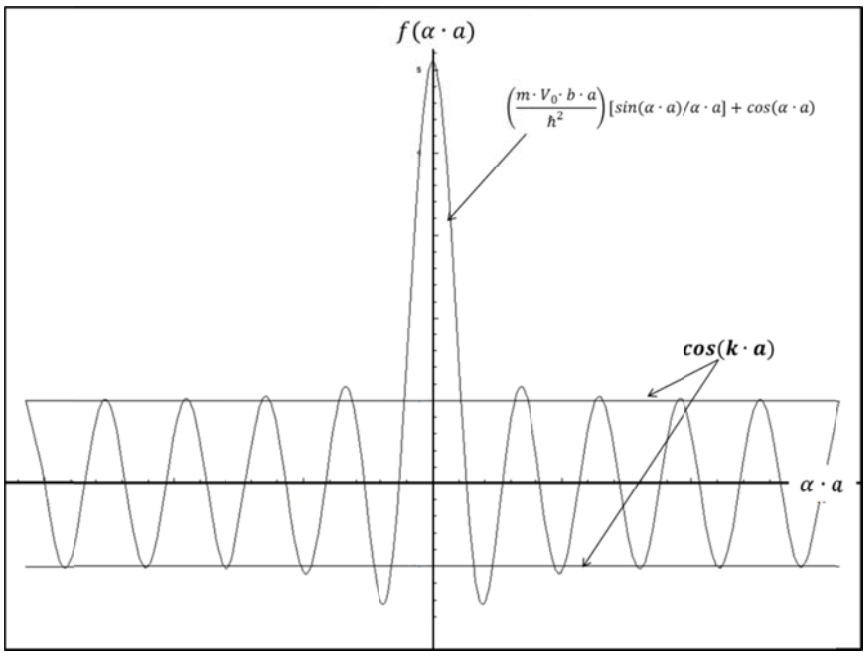

Figure 29 Graphical representation of analytical relationship necessary to obtain a solution to the Schrodinger equation

This simplified pedagogical method however, is not sufficient for capturing the band-structure arising from the more complex 3-D electric potentials present in compound semiconductors and alloys. Numerical methods for calculating band structure have been developed over the past decades including the Orthogonalized Plane-Wave method, Pseudo-potential method, Augmented Plane wave method, Tight-Binding method (TBM), and k•p method, as well as others.

As one example, Koster and Slater published their paper on the tight binding method as early as 1954 (65). This method relies upon perturbative methods for approximating electronic band structure. First, known atomic orbitals of isolated atoms are used as a basis for expanded Bloch functions to solve Schrodinger's equation. As the isolated atoms are brought together into, these atomic orbitals are no longer valid as their potential changes due to band splitting. However considering that the s- and p-type character of the bonds remains in-tact, a perturbative term is introduced which effectively increases the electrical potential and helps retain the atomic orbitals approximations validity.

The Schrodinger equation is then cast in the form of a secular determinant shown in **Equation 10**, using the Bloch functions $\psi(k)$ which have been constructed using the atomic orbitals, $\phi_{m,j}$, as a basis to construct an N x N matrix, and solving for the coefficients $C_{m,j}$. It is important to notice that for the 3-D case, there are 8 sets of basis functions, associated with the electrons in the s, p_x, p_y, and p_z orbitals each with spin up and spin down configurations. More details on this method are presented in (64).

Equation 10 $$\left|\langle \boldsymbol{\phi}_{m^*,j^*} | \boldsymbol{H} - \boldsymbol{E} | \, \boldsymbol{\psi}(\boldsymbol{k}) \rangle\right| = \boldsymbol{0}$$

Equation 11 $$\boldsymbol{\psi}(\boldsymbol{k}) = \sum_{\boldsymbol{R}} \sum_{\boldsymbol{m=1}}^{\boldsymbol{4}} \sum_{\boldsymbol{j=1}}^{\boldsymbol{2}} \boldsymbol{C_{m,j}} \, \boldsymbol{\phi_{m,j}}\left(\boldsymbol{r} - \boldsymbol{r_j} - \boldsymbol{R_i}\right) \boldsymbol{e^{ikR_i}}$$

In the Tight Binding Method (TBM), however, the approximation assumes degeneracy of the electron spin. As a result, the band-structure calculated using the TBM will show 6-fold degeneracy at the top of the valence band including the effects of spin. It is well known that for essentially all semiconductors, the top of the valence band is 4-fold degenerate with another band displaced by a small energy below the valence band edge. In Silicon, for example this displacement is the smallest of all semiconductors being only 0.044eV, whereas for III-V semiconductors this spin-orbit splitting can reach as high as 0.82eV for InSb (64).

The electron-spin provides a means for the valence electron of the orbital to interact with the magnetic field produced through its orbital motion. For essentially all semiconductors, the top of the valence band is primarily p-type states, and so the spin-orbit coupling is expected to have a stronger affect in this region (as opposed to the s-type states in the conduction band). In the case of Cd(Zn)Te, the upper valence edge would correspond to the Tellurium bonds, whereas the lower conduction band edge would correspond to the Cadmium orbitals.

Presented in **Figure 30** is the band structure for CdTe calculated using the k•p and pseudo-potential methods (66) (67). For both methods, the bandgap occurs at the high symmetry point Γ, and exhibits a direct gap character. Splitting of the heavy and light holes about Γ is evident for the k•p method. The exact position of the valence band edge, however differs for different methods used.

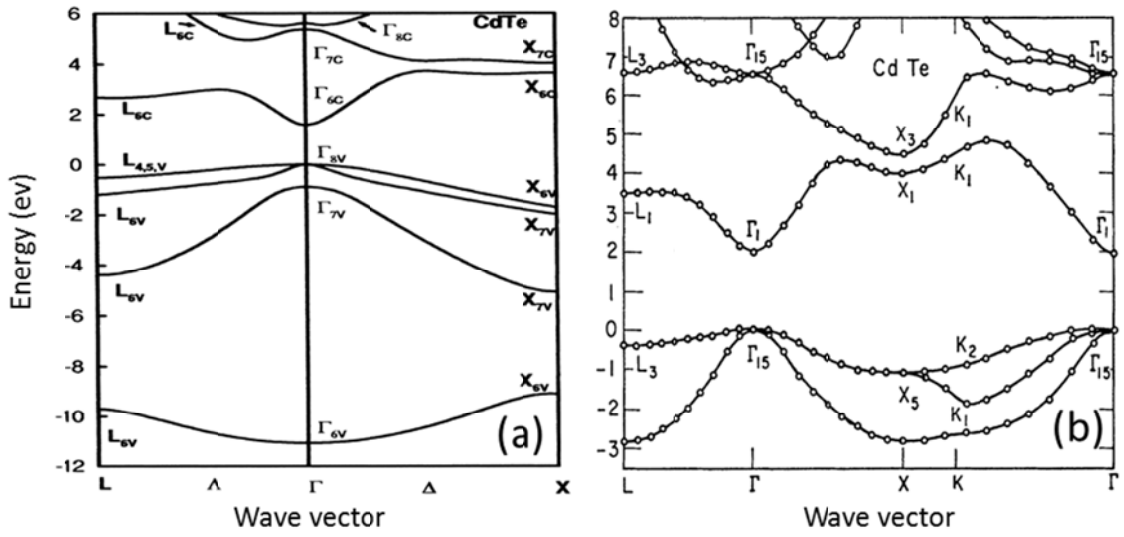

Figure 30 Band structure of CdTe calculated using (a) the k•p method (66) and (b) the Pseudo-potential method (67)

2.7.2 Density of States & Occupation Statistics

The charge carriers present in a semi-insulating or semiconducting material are derived principally from the bandgap of the material, the associated density of state (DOS) function, and the Fermi-Dirac Distribution.

The DOS function may be derived using an infinite potential well with dimensions $0 \leq x \leq a$, $0 \leq y \leq b$, and $0 \leq z \leq c$, and potential barrier $V \rightarrow \infty$. Application of the 3-dimensional Schrodinger equation and the boundary conditions $u(0) = 0$ yields solutions with the form given in **Equation 12**, and the corresponding energy relation given in **Equation 13**. (68)

Equation 12

$$u(x) = A_1 \cdot \sin\left(\frac{k_x x}{a}\right) \sin\left(\frac{k_y y}{b}\right) \sin\left(\frac{k_z z}{c}\right) \qquad \text{n=1, 2, 3 . . .}$$

$$k_x = \frac{n\pi}{a}, \quad k_y = \frac{n\pi}{b}, \quad k_z = n\pi/c$$

Equation 13

$$E_n = \left(\frac{{n_x}^2}{a} + \frac{{n_y}^2}{b} + \frac{{n_z}^2}{c}\right) \pi^2 \hbar^2 / 2m$$

A Fermi-sphere in k-space is defined as a sphere with radius k_f whose volume represents the minimum number of states required to contain all of the electrons representing the average energy of the crystal. Division of this Fermi-sphere, by the actual volume of the potential well, yields the number of possible states within a Fermi-sphere,

where V represents the physical volume of the potential well with dimensions. a×b×c. As can be seen in **Equation 14**, increasing the diameter of the Fermi-sphere increases the total number of states, as does decreasing the size of the potential well. The factors 2 and 1/8 represent multiplicative factors to account for electron spin, and to reduce the volume of the sphere to octet sections to remove redundancies.

Equation 14

$$N = \frac{V_{Fermi\ Sphere}}{V_{Single\ State}} = 2 \cdot \frac{1}{8} \cdot \frac{{}^{4}/_{3}\pi {k_f}^3}{{}^{\pi^3}/_{V}} = \frac{V \cdot {k_f}^3}{3\pi^2}$$

If the electron density of a material is known, the Fermi level of the material may be derived using **Equation 15** in conjunction with the derived Fermi-sphere radius. The term n represents the known electron density.

Equation 15

$$E_f = \frac{\hbar^2}{2m} \cdot {k_f}^2 = \frac{\hbar^2}{2m} \cdot \left(\frac{n \cdot 3\pi^2}{V}\right)^{2/3}$$

The Density of States function G(E) is defined as the number of states per energy, per unit volume. This relation is expressed in **Equation 25**, where the chain rule has been used. Applying this relation to a semiconductor requires substituting the effective mass m^* for **m**, and the Energy term for the near band edge $E = E - E_c$. This gives the total number of allowed states per unity energy and volume in a semiconductor. Presented in **Equation 16** is the density of states for the conduction band energies (64) (68).

Equation 16

$$\begin{aligned} G_c(E) &= \frac{dN}{dE} \cdot \frac{1}{V} = \frac{dN}{dk}\frac{dk}{dE} = \frac{dE^{3/2}}{dE} \cdot \frac{2m}{\hbar^2} \cdot \frac{V}{3\pi^2} \cdot \frac{1}{V} \\ &= \frac{m\sqrt{2m}}{\hbar^3\pi^2}\sqrt{E} \\ &= \frac{m^*\sqrt{2m^*}}{\hbar^3\pi^2}\sqrt{E - E_c} \end{aligned}$$

It is not enough, however, to have the density of states to describe the occupation of bands by electrons. Indeed, the DOS function only provides information regarding the

number of states available for electrons to occupy. Indeed, the number of ways (W_i) a given number of electrons (N_i) may occupy a given number of states (S_i) with distinct energies (E_i) plays a fundamental role in determining the temperature dependent optical and electrical properties of a material. This relationship may be expressed for a single energy level using the statistical relationship presented in **Equation 17** (64).

Equation 17

$$\boldsymbol{W = S_i!/(S_i - N_i)! \cdot N_i}$$

When more than one level is considered, the number of ways the electrons may be organized increases as the product of the W_i factors. Taking the natural log of each side of the equation produces **Equation 18**.

Equation 18

$$\boldsymbol{ln(W) = \prod_i ln[W_i] = \sum_i ln[S_i!] - ln[S_i - N_i!] - ln[N_i!]}$$

Using Stirling´s approximation which states ln(x!) → x•ln(x) +1, the chain rule which states d/dx(x•ln[x]) = ln[x]+1, and the relation d•ln[x])= dx/x, and after differentiation with respect to the number of electrons N_i, **Equation 19** is obtained,.

Equation 19

$$\begin{aligned} \boldsymbol{d(ln[W])/dN_i} &= \boldsymbol{\sum_i ln[S_i - N_i] - ln[N_i]} \\ &= \boldsymbol{\sum_i ln\left[\frac{S_i}{N_i} - 1\right]} \end{aligned}$$

The probabilities to this point, describe the total number of permutations of available electrons and states. However, taking into account that we are searching for real physical solutions, we would like the solution which is most probable. Therefore we want to maximize the total number of ways (W_i) the electrons can be organized to give the same solution, with respect to the total number of electrons. This is a simple maximization problem and is determined by setting **Equation 19** equal to zero. Introducing undetermined multipliers of the form found in **Equation 20**, taking into account the real physical properties of our system (constant number of electrons and total system energy)

and by applying these constraints using **Equation 21**, the statistics of occupation now require that **Equation 22** be satisfied for all *i*.

Equation 20 $$\sum_i -\alpha \cdot dN_i = 0 \quad \sum_i -\beta \cdot E_i dN_i = 0$$

Equation 21 $$\sum_i N_i = constant \rightarrow \frac{d\sum_i N_i}{dN_i} = 0 \qquad \frac{d\sum_i E_i N_i}{dN_i} = 0$$

Equation 22 $$ln\left[\frac{S_i}{N_i} - 1\right] - \alpha - \beta \cdot E_i = 0$$

Equation 23 may be satisfied by the Fermi function which describes the relationship between the number of available levels, the number of electrons in the system, and the thermal energy associated with temperature. This function is expressed in **Equation 22**, where $\alpha = E_f/kT$ and $\beta = 1/kT$ (64) (68) .

Equation 23 $$\frac{S_i}{N_i} = F(E) = \frac{1}{1+e^{\alpha+\beta E_i}}$$

The DOS function has been derived for electrons in the conduction band (**Equation 16**) and may also be derived for holes in the valence band, taking into account the larger effective mass of holes. Furthermore, using **Equation 23** the occupation statistics for electrons has been derived. Using these two equations together, precisely how the electrons and holes populate the conduction and valence bands may be determined for Cd(Zn)Te.

Presented in **Figure 31**a are the effects of temperature and Fermi level position on the occupation statistics. With increasing temperature, the probability that electrons will occupy energy levels greater than the E_f increases, which can be seen by higher occupation probabilities for energies larger than the Fermi level.

For a fixed temperature (i.e. 300K) increasing the Fermi level position within the bandgap also raises the energy of the highest occupied energy as can be seen from **Figure 31**b. **Figure 31**c illustrates how for semi-insulating materials such as Cd(Zn)Te, the valence band is fully occupied and the conduction band is empty when the Fermi level is in the mid-gap position.

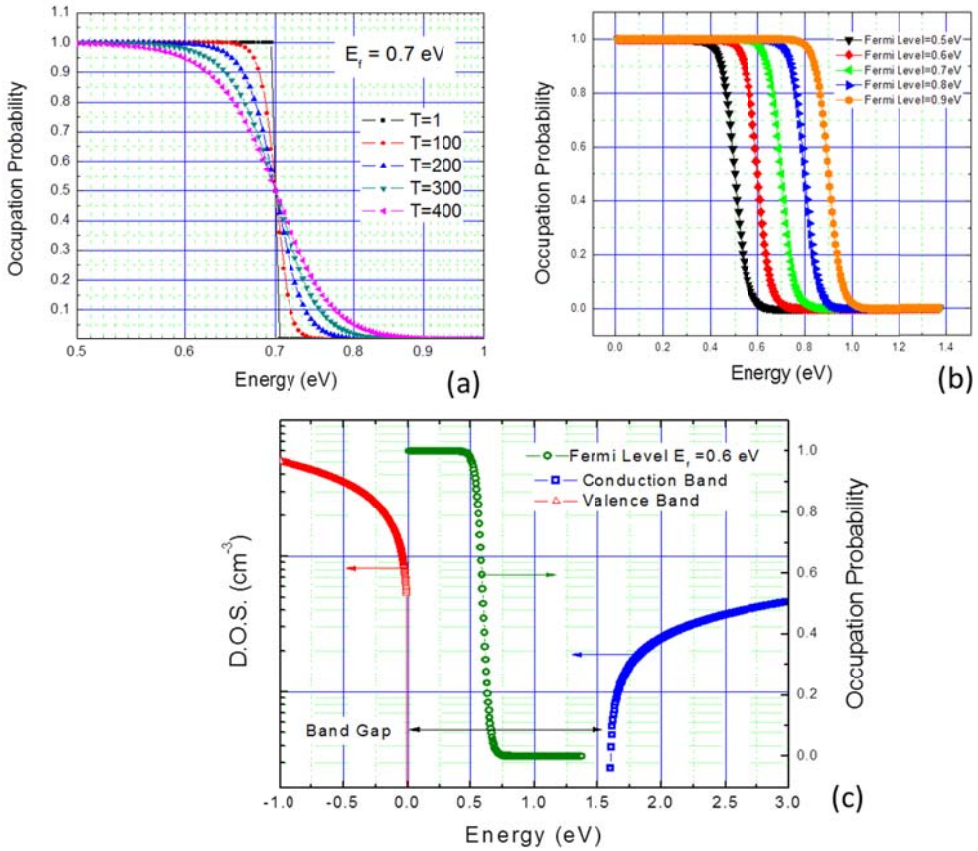

Figure 31 (a) Effect of increasing temperature on the Fermi level occupation statistics (b) Effect of increasing Fermi-level energy on occupation statistics and (c) occupation statistics for with a near mid-gap Fermi-level.

2.7.3 Electrical Resistivity

The density of states and the Fermi level are directly related to the electrical properties of a semiconducting or in the case of Cd(Zn)Te semi-insulating material. The intrinsic carrier density of a semiconductor may be expressed following Equation 24, where N_c and N_v is the density of states in the conduction and valence bands, E_g is the bandgap, and kT is the thermal energy (69).

Equation 24
$$n_i = \sqrt{N_c N_v} \cdot e^{-E_g/2kT}$$

For Cd(Zn)Te with a bandgap near 1.56eV at 300K, this corresponds to an intrinsic carrier concentration of 2.2×10^5 cm^{-3}. The electrical resistivity may be classically described using Equation **25** for intrinsic and non-intrinsic materials, where q is the electric charge (1.6E10^{-19} C), n and p the carrier concentrations, and μ_n and μ_p are the electron and hole mobilities respectively. From this simple equation it may be observed how reducing the concentration of carriers has the effect of increasing the resistivity of the material. Presented in **Figure 32** are the intrinsic carrier concentrations for Si, GaAs, and Cd(Zn)Te

and the corresponding electrical resistivity. Due to the low resistivity of Si and GaAs, X-ray and gamma-ray detectors based these materials must be cooled to low temperatures in order to reduce dark current produced by carrier drift. This cooling of the material reduces the intrinsic carrier concentration following **Equation 24** by changing the occupation probability associated with the Fermi distribution function.

Equation 25 $$\rho = \frac{1}{q \cdot n_i \cdot (\mu_n + \mu_p)} \; or \; \frac{1}{q \cdot (n \cdot \mu_n + p \cdot \mu_p)}$$

With increasing Zn content, there is also an increase in the bandgap, which further decreases net carrier concentration. It has been shown experimentally that the bandgap energy in Cd(Zn)Te follows **Equation 26**, where the *x*-value represents the composition of Zinc in the alloy (70). This arises from less electrons becoming thermally excited to the conduction band. This has also been demonstrated by other researchers working with Cd(Zn)Te (71).

Equation 26 $$E_g = 1.5045 + 0.631 \cdot x + 0.128 \cdot x^2$$

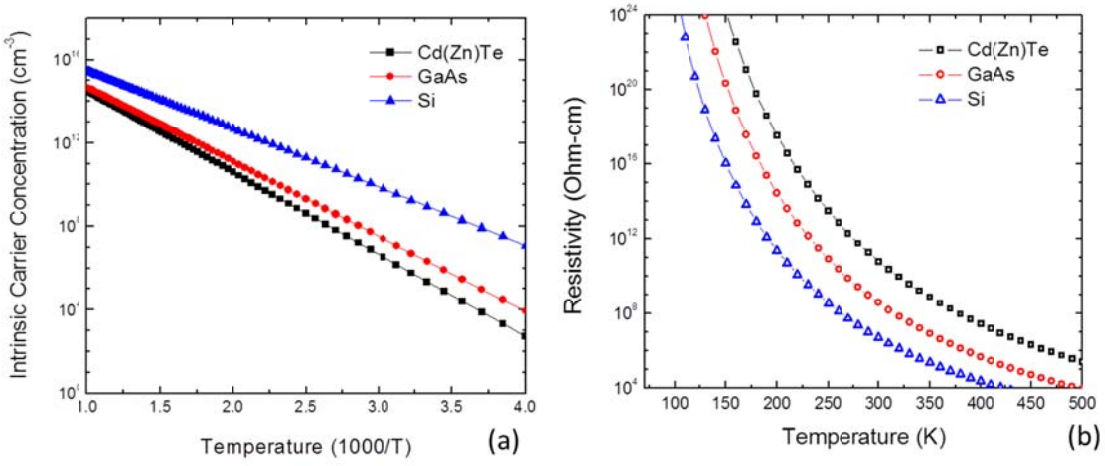

Figure 32 Intrinsic carrier concentrations for Cd(Zn)Te, GaAs, and Si.

This predicted dependence of zinc concentration with resistivity and bandgap energy is presented in **Figure 33**. The experimental data which is also reported in this graph corresponds to detectors which have been fabricated as part of this thesis investigation.

These results are in agreement with others which have been presented elsewhere (72). In general, increasing resistivity in Cd(Zn)Te is observed with increasing Zinc content. The fact that these detectors exhibit higher resistivity than is theoretically predicted may be associated with surface states influencing charge transport properties of the planar devices.

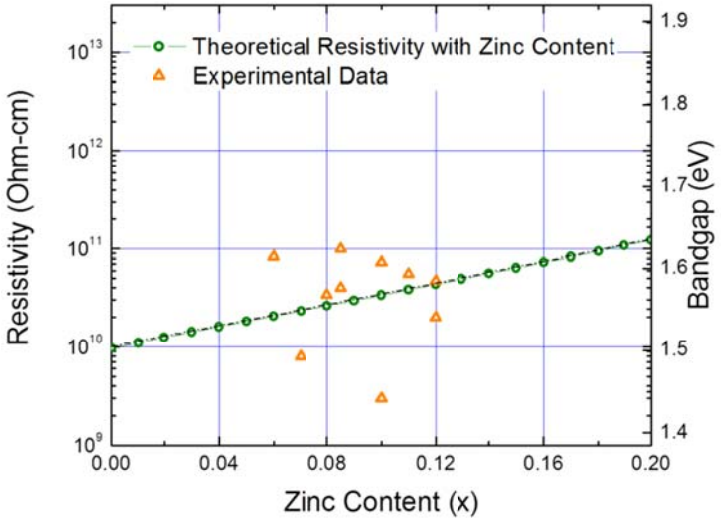

Figure 33 Theoretical dependence of zinc content on resistivity and bandgap with some experimental values which have been measured in this work from several different crystals.

From the bulk resistivity, the voltage required to achieve fully depleted devices may be calculated using Equation 27, where ϵ_0 is the dielectric permittivity of free space, $\boldsymbol{\epsilon_s}$ is the dielectric permittivity of Cd(Zn)Te, N_a and N_d are the concentrations of acceptor and donor levels in the crystal, $\boldsymbol{\mu}$ is the mobility, $\boldsymbol{\rho}$ the bulk resistivity, V the applied bias, and V_{bi} the built in voltage. Due to the low concentration of carriers, very low electric fields are required to achieve a fully depleted device.

Equation 27

$$W = \sqrt{2 \cdot \epsilon_0 \cdot \epsilon_s \frac{N_a + N_d}{N_a \cdot N_d} \cdot (V + V_{bi})}$$
$$= \sqrt{2 \cdot \epsilon_0 \cdot \epsilon_s \cdot \rho \cdot \mu \cdot (V + V_{bi})} \approx \sqrt{2\epsilon_0 \epsilon_s \rho \mu V}$$

2.8 Transport Properties

High resistivity is not the only requirement for material to be suitable for detector applications. Indeed, Cd(Zn)Te based radiation devices are often affected by incomplete

collection of photon-generated carriers, which ultimately limits detector performance. If there is a considerable amount of charge loss occurring in the detectors, it will ultimately reduce the energy resolution of the device. One of the factors affecting charge collection in Cd(Zn)Te radiation devices is the charge mobility.

Starting from equilibrium, the distribution of electrons within a semiconductor may be described using the Fermi-Dirac distribution presented in **Equation 22**. Changes in this equilibrium may give rise to changes in the occupation statistics as a result of several factors including (1) electron diffusion through the material (2) electron drift due to an external electric field or (3) scattering of the electrons. These changes in equilibrium may be represented using **Equation 28**, where $\boldsymbol{f^0}$ represents the equilibrium distribution. The first term $-v_k \nabla_r f^0$ represents the diffusion of electrons due to a spatial gradient, ∇_r, in the distribution function, while the $\frac{e}{\hbar}(\boldsymbol{F} + \boldsymbol{v_k} \times \boldsymbol{B})$ term represents electron drift under the presence of external electrical (F) and magnetic (B) fields (64).

Equation 28

$$\left.\frac{df^0}{dt}\right|_{diffusion} + \left.\frac{df^0}{dt}\right|_{drift} + \left.\frac{df^0}{dt}\right|_{scattering} = 0$$

$$\Longrightarrow -\boldsymbol{v_k}\nabla_r \boldsymbol{f^0} - \frac{\boldsymbol{e}}{\hbar}(\boldsymbol{F} + \boldsymbol{v_k} \times \boldsymbol{B}) = \left.\frac{\boldsymbol{df^0}}{\boldsymbol{dt}}\right|_{\boldsymbol{scattering}}$$

The distribution function $\boldsymbol{f_k}$ is the distribution after some event has occurred, producing a change in the occupation statistics of the energy levels. This distribution function is equal to the equilibrium distribution $\boldsymbol{f^0}$ plus some perturbative factor $\boldsymbol{g_k}$. This perturbative approach is used taking into account a uniform temperature across an infinite crystal to determine this distribution function $\boldsymbol{f_k}$.

It is important that the scattering induced change in the equilibrium distribution function has an exponential form such that the perturbation decays following some time constant τ (referred to as the relaxation time). This relation may be expressed as follows in **Equation 29** and represents the amount of time required to restore equilibrium.

Equation 29 $$\left.\frac{df_k}{dE_k}\right|_{scattering} = \frac{dg}{dt} = \frac{g_k}{\tau}$$

Using this relationship, it may be shown that the distribution function follows **Equation 30** (or represented in k-space in **Equation 31**) (64)

Equation 30 $$f_k = f^0(E - e \cdot \tau \cdot v_k \cdot F)$$

Equation 31 $$f_k = f^0(k - e \cdot \tau \cdot F/\hbar)$$

These changes in the occupation statistics caused by diffusion, an external applied field, or scattering effectively shift the equilibrium distribution by some vector quantity in k-space ($k - e \cdot \tau \cdot F/\hbar$). Indeed, when an electric field is applied to a semiconductor, the relationship between the effective mass of the electron/hole and the time constant of the perturbation event gives rise to the electron mobility parameter. This change in the momentum is described by **Equation 31**. The factor $-e \cdot \tau/m^*$ represents the mobility of the electron when an external applied electric field (64).

Equation 32 $$\partial p = \hbar \partial k = -e \cdot \tau \cdot F/m^*$$

For a n-electron system, under an external electric field, F, this gives rise to a current density which is described by **Equation 33**.

Equation 33 $$J = n \cdot e^2 \cdot \tau \cdot F/m^*$$

It is important to comment that the effect of introducing acceptor/donor impurities, or crystallographic defects into the material will increase the scattering or in the relaxation time constant. This will decrease the mobility of the electrons/holes, and degrade the electrical properties. From the perspective of transport properties, it is important that high purity starting materials are used, and crystallographic defects are minimized.

2.8.1 Mobility Lifetime Product

Indeed, the mobility of electrons and holes in semiconductor devices used for x-ray and gamma spectroscopy is a fundamental figure of merit. This parameter is often determined in conjunction with electron/hole lifetime by measuring the change in the photo-peak position of alpha particles as a function of bias voltage. Using the Hecht equation, which is presented in **Equation 34**, the charge collection efficiency, Q^*, at the anode/cathode may be related to the velocity (ν) and lifetime (τ) of the electrons and holes generated at a distance x_i from the anode of a Cd(Zn)Te detector of thickness W. In the case of planar test device geometries such as those used in this work, the charge induced on the surface of the anode and cathode is equal. This electron lifetime-mobility may be determined for using alpha particles which are strongly absorbed at the surface, to eliminate the contribution from holes and to eliminate variance in the depth of interaction parameter, W.

Equation 34
$$Q^* = eN_0\left[\frac{v_h t_h}{W}\left(1 - e^{-x_i/v_h t_h}\right)dx_e + \frac{v_e t_e}{W}\left(1 - e^{W - x_i/v_e t_e}\right)\right]$$

Factors effecting the CCE of a radiation detector can be attributed to structural in-homogeneities (grain boundaries), point defects (vacancies or interstitials which behave as acceptors/donors), second phase inclusions, or deep levels introduced by impurities in the crystal. Despite the advantages, $Cd_{1-x}Zn_xTe$ solid solutions have lower homogeneity and more kinds of structure defects than CdTe.

Imperfections in the crystalline structure exhibit electrical activity and may be responsible for changes in the density of free carriers. The concentration of free carriers represents a source of electrical noise in a device under electronic bias, and essentially decreases the energy discrimination of X-ray and gamma-ray radiation and other uncharged and charged particles.

Presented in

Table 5 are electrical properties for Cd(Zn)Te grown by High Pressure Bridgman technique from (48). It is fairly accepted that the electrical properties of as-grown material are affected strongly by the growth technique. It has been claimed that while crystals grown by traditional Bridgman and Vertical Gradient Freeze techniques may have better

structural characteristics, while the important values for the electrical resistivity and gamma-ray response for these crystals are lower (73).

Table 5 Typical electrical properties for $Cd_{0.9}Zn_{0.1}Te$ grown by High Pressure Bridgman technique, data adapted from (48)

Property	Nominal	Actual
Zn Composition (%)	10	5-13
Band gap RT (eV)	1.56	1.53-1.58
Resistivity ($x10^{10}$ Ω-cm)	3.0	1.7-4.0
Intrinsic carrier concentration ($x10^5$ cm^{-3})	2.0	1.0-4.0
$\mu\tau_e$ ($x10^3$ cm^2/V)	2.5	0.5-5.0
$\mu\tau_h$ ($x10^3$ cm^2/V)	2.0	0.2-5.0

2.8.2 Electrical Compensation

In real crystals, to achieve high resistivity Cd(Zn)Te material suitable for gamma ray spectroscopy applications, electrical compensation of the material is required to achieve charge neutrality. This is due to several factors, including both extrinsic factors such as the purity of starting materials as well as intrinsic factors including point defects in Cd(Zn)Te.

While the purity of starting materials has advanced significantly over the past 20 years, the highest quality material input is only 7N pure (99.99999%), which is considered low when compared with the purity which can be obtained with Si 12N pure (99.999999999%). Indeed, this purity level in Cd(Zn)Te is determined by the net concentration of impurities not exceeding 100ppb. Spectroscopic methods such as Glow Discharge Mass Spectroscopy may be used for this determination of material purity. As a result, there exists a background concentration of impurities which may act as either an acceptors or donors. This behavior of the impurities has the effect of moving the Fermi level of the semiconductor, and can change the electrical properties of the material substantial. One of the major challenges of this thesis has been to obtain high resistivity material suitable for detector applications.

Indeed, when impurities are introduced into a crystal, the Fermi level must change to preserve electrical neutrality. The total number of ionized donors and acceptors is again determined using the Fermi-Dirac distribution function, presented in Equation 35. In these equations, a degeneracy factor, g, is used. For acceptors, which are located above the valence band and interact with the holes, this degeneracy factor is 4, due to the degeneracy

of the VB at k=0, and the up-and down spin electron configurations. For donor levels, the degeneracy factor is 2. As an illustrative example, acceptor impurities introduced in a concentration of 1×10^{15} at/cm^3 into the crystal lattice, and producing a level with activation energy $E_a = E_v + 0.2eV$ in the bandgap at 300K, would produce 1.6×10^7 ionized acceptors. In the case of donors, using the same concentration and activation energy would correspond to 2×10^6 ionized donors.

Equation 35

$$N_a^- = N_a \frac{1}{1+[g^{-1} \cdot exp(E_a - E_f/kT)]}$$
$$N_d^+ = N_d \frac{1}{1+[g \cdot exp(E_d - E_f/kT)]}$$

In order to fulfill the electrical neutrality condition in an n-type semiconductor (such as those investigated in this work), the total negative charge must be equal to the total positive charge present in the material. This relation is presented in **Equation 36**, for donor impurities added to crystalline solid. The terms on the left hand side of the equation represent the total number of electrons, whereas the terms on the right hand side of the equation represent the total number of ionized donors and the total number of holes. For a given set of N_c, N_d, N_v, E_c, E_d, E_v, and T, the Fermi-level of the semiconductor may be determined (69).

Equation 36

$$N_C \cdot e^{(E_C - E_f/kT)} = N_d^+ \frac{1}{1+[g \cdot exp(E_a - E_f/kT)]} + N_V \cdot e^{(E_f - E_V/kT)}$$

When impurity atoms or donor/acceptor defects are introduced into the crystal, the law of mass action is retained such that the product n•p remains constant. Crystallographic defects such as V_{cd} or Te_{Cd} sites present in the as-grown material are on the order of ~10^{14} cm^{-3} and contribute significantly to the electronic properties of the bulk i.e. decreasing carrier lifetimes, mobilities, and overall charge collection at the detector level.

One approach to obtain high resistivity material is to attempt control the compensation of deep and shallow acceptors. Compensation doping is a technique used for counteracting the deleterious effects of native defects to achieve electrical neutrality. Using this

approach, the resistivity of the material may be controlled by adjusting the net carrier density and pinning the Fermi level near the mid-gap. This may be accomplished by using a precise amount of a specific dopant to establish a balance between shallow and deep level impurities (74).

2.8.3 Compensation of Native defects

Cd vacancies (V_{Cd}) are the dominant native shallow acceptor defect (*sA)* with a concentration ~10^{11} – 10^{15} cm^{-3} in Cd(Zn)Te, depending to a large extent of the experimental methods. This particular defect plays an important role in the electrical compensation and carrier trapping in Cd(Zn)Te. When the V_{cd} is paired with shallow donors (*sD*), they form a complex named the "A-center".

The shallow donors (*sD*s) are located just below the conduction band. Possible donors in Cd(Zn)Te are include elements from group IIIA (Al, Ga, In) which occupy Cd sites, and group VIIA (Cl, Br and I) which occupy Te sites (75) (76). These *sD*s form complexes with the shallow acceptors (*sAs)* such as V_{Cd}, to form A-centers. Shallow acceptors, located above the valence band include from group IA (Li, Na and K) which occupy Cd sites and from group IB (Cu, Ag, Au) which occupy Te sites.

Increasing the concentration of A-center complexes to reduce the deleterious effects of V_{Cd} is one approach to achieving high resistivity material. Indeed, the A-centers are too shallow at $E_a = E_v + 0.1\text{-}0.2$ eV to strongly affect the occupation statistics of the deep levels (77). The In atom (shallow donor) is used to fill the V_{Cd}^{-2} (shallow acceptor). One mechanism for electrical compensation that has been proposed is the following (78) (50) (79). First, the Indium dopant is attracted to a doubly ionized Cadmium vacancy

1 $In + V_{Cd}^{-2} = In_{Cd}^{+} + 3e^{-}$

Where In_{Cd}^{+} is now an ionized shallow donor. Second, the shallow Donor In_{Cd}^{+} attracts one V_{Cd}^{-2} shallow acceptor, to form an acceptor complex:

2 $In_{Cd}^{+} + V_{Cd}^{-2} = [In_{Cd}^{+}V_{Cd}^{-2}]^{-}$

Finally, an electrically neutral complex is formed.

3 $In_{Cd}^{+} + [In_{Cd}^{+}V_{Cd}^{-2}]^{-} = [2In_{Cd}^{+}V_{Cd}^{-2}]^{0}$

It is in this third step where the acceptor complex and the neutral complex are responsible for the compensation effect in Cd(Zn)Te. This coupling helps reduce the problematic effect of cadmium vacancies.

3 CHAPTER SUMMARY

This chapter has presented the historical development of radiation devices over the past several decades, and has emphasized the importance of semiconductor based radiation devices. The advantages of Cd(Zn)Te as a radiation device have presented which include high resistivity, room temperature operability, and high density and stopping power. The challenges to producing detector grade material have also presented, which include the suppression of deleterious point defects, crystallographic defects such as dislocations and grain boundaries, as well as large macroscopic defects such as voids.

4 BIBLIOGRAPHY

1. *On a new kind of rays.* **Wilhelm Rontgen, translated by Arthur Stanton.** 1896, Nature, Vol. 53, p. 274.

2. *The Anger Scintillation Camera Becomes of Age.* **Myers, W. G.** 1979, J. Nucl. Med. , Vol. 20, pp. 565-567.

3. *Requirements on amorphous semiconductors for medical x-ray detectors.* **M. Hoheisel, L. B atz.** 2000, J. Non-Cryst. Sol., Vols. 266-269, pp. 1152-1157.

4. **Schulman, Tom.** *Si, CdTe and CdZnTe radiation detectors for imaging applications.* Faculty of Science, University of Helsinki, Finland. Helsinki : Yliopistopaino, 2006. Thesis. ISBN 952-92-0428-0.

5. *The First Polaris 3-D CdZnTe Detector Array System.* **Z. He, F. Zhang.** Honolulu : s.n., 2007. IEEE Nuclear Science Symposium and Medical Imaging.

6. *Growth of high resistivity CdTe and (Cd,Zn)Te crystals.* **M. Fiederle, V. Babentsov, J. Franc, A. Fauler, J.P. Konrath.** 2003, Cryst. Res. Technol., Vol. 38, p. 588.

7. *Characterization of CdTe Crystals Grown by the Bridgman Method.* **M. Fiederle, A. Fauler, V. Babenstov, J. Franc, J. Konrath, M. Webel, J. Ludwig, K.W. Benz.** 2003, Nuc. Inst. and Meth. in Phys. Res. A, Vol. 509, pp. 70-75.

8. *Boron Oxide Encapsulated Vertical Bridgman Grown CdZnTe Crystals as X-Ray Detector Material.* **A.Zappettini, M.Zha, L.Marchini, D.Calestani, R.Mosca, E.Gombia, L.Zanotti, M.Zanichelli, M.Pavesi, N.Auricchio, E.Caroli.** 4, IEEE Trans. Nucl. Sci., Vol. 56, p. 1.

9. *Improvements in Production of CZT Crystals Grown by the Bridgman Method.* **H.L. Glass, A.J. Socha, C.L. Parfeniuk, D.W. Bakken.** 1998, J. Crystal Growth, Vol. 184/185, pp. 1035-1038.

10. *Basic problems of vertical Bridgman growth of CdTe.* **P. Rudolph, M. Mühlberg.** 1993, Mater. Sci. & Eng. B, Vol. 16, p. 8.

11. *Characterization of 100 mm Diameter CZT Single Crystals Grown by the Vertical Gradient Freeze Technique.* **T. Asahi, O. Oda, Y. Taniguchi, A. Koyama.** 1995, J. Crystal Growth, Vol. 149, pp. 23-29.

12. *Defect Structure of High Resistive CdTe:In Prepared by Vertical Gradient Freeze.* **J. Franc, V. Babensotv, M. Fiederle, E. Belas, R. Grill, K. W. Benz, P. Hoeschl.** 3, 2004, IEEE Trans. Nucl. Sci., Vol. 51.

13. *Advances in the High-pressure Crystal Growth Technology of Semi-insulating CdZnTe for Radiation Detector Applications.* **C. Szeles, S. Cameron, J. Ndap, M. Reed.** San Diego : s.n., 2003. SPIE Conference on Hard X-Ray, Gamma-Ray and Neutron Detector Physics V.

14. *Development of the High-Pressure Electro-Dynamic Gradient.* **C. Szeles, et. al.** 6, 2004, J. Electron. Mater., Vol. 33, p. 742.

15. *Characterization of detector-grade CdZnTe crystals grown by the Travelling Heater method.* **S.A. Awadalla, et al.** 2010, J. Crystal Growth, Vol. 312 , pp. 507-513.

16. *Spectral Response of THM Grown CdZnTe Crystals.* **H. Chen, et al.** 3, 2008, IEEE Trans. Nucl. Sci, Vol. 55.

17. *Vapor-Phase Growth of Bulk Crystals of Cadmium Telluride and Cadmium Zinc Telluride on GaAs Seed.* **J. T. Mullins, B. J. Cantwell, A. Basu, Q. Jiang, A. Choubey, A.W. Brinkman, and B.K. Tanner.** 2008, J. Electron. Mater., Vol. 37, p. 1460.

18. *Crystal growth of large-diameter bulk CdTe on GaAs wafer seed plates.* **J.T. Mullins, B.J. Cantwell, A. Basu, Q. Jiang, A. Choubey, A.W. Brinkman.** 7-9, 2008, J. Crystal Growth, Vol. 310, pp. 2058-2061.

19. *Seed-free growth of (1 1 1) oriented CdTe and CdZnTe crystals by solid-state recrystallization.* **S. Hassani, A. Lusson, A. Tromson-Carli, R. Triboulet.** 2003, J. Crystal Growth, Vol. 249, pp. 121-127.

20. *Dewetting application to CdTe single crystal growth on earth.* **N. Chevalier, P. Dusserre, J. Garandet, T. Duffar.** 2004, J. Crystal Growth, Vol. 261, pp. 590-594.

21. *Growth of High Purity CdTe Single Crystals by Vertical Zone Melting.* **R. Triboulet, Y. Marfaing.** 1973, J. Electrochem. Soc. Sol. Stat. Sci. and Tech., Vol. 120, p. 1260.

22. *Full encapsulated CdZnTe crystals by the vertical Bridgman method.* **M. Zha, A. Zappettini, D. Calestani, L. Marchini, L. Zanotti, C. Paorici.** 7-9, 2008, J. Crystal Growth, Vol. 310, p. 2072.

23. **V. Carcelen, N. Vijayana, E. Dieguez, A. Zappettini, M. Zha, L. Sylla, A. Fauler, M. Fiederle.** 11, 2008, J. Optoelectron. Adv. M, Vol. 10, pp. 3135 – 3140.

24. *THM Growth and Characterization of 100 mm Diameter CdTe Single Crystals.* **H. Shiraki, M. Funaki, Y. Ando, A. Tachibana, S. Kominami, R. Ohno.** 4, 2009, IEEE Trans. Nucl. Sci., Vol. 56, pp. 1717-1723.

25. **Brillouin, L.** *Wave Propagation in Periodic Structures.* New York : Dover, 1963.

26. *Elastic Properties of Diamond-Type Semiconductors.* **Keyes, R.** J. Appl. Phys, Vol. 33, p. 3371.

27. Semiconductor Technology . [Online] Christian-Albrechts-University of Kiel. http://www.tf.uni-kiel.de/matwis/amat/semitech_en/kap_2/backbone/r2_3_1.html.

28. *Fundamentals of the CdTe and CdZnTe bulk growth.* **Triboulet, R.** 5, 2005, Phys. Stat. Sol. (c), Vol. 2, pp. 1556-1565.

29. *J. Cryst. Growth.* **Vérié, C.** 1998, Beryllium substitution-mediated covalency engineering of II–VI alloys for lattice elastic rigidity reinforcement, Vol. 184, p. 1061.

30. [ed.] P. Capper. *Properties of Narrow Gap Cadmium-based components.* London : Institution of Electricla Engineers, 1997.

31. *Solution hardening and dislocation density reduction in CdTe crystals by Zn addition.* **K. Guergouri, R. Triboulet, A. Tromson-Carli, and Y. Marfaing.** 1988, J. Cryst. Growth, Vol. 86, p. 61.

32. *Light-Induced Tellurium Enrichment on CdZnTe Crystal Detected by Raman Spectroscopy.* **S. Hawkins, E. Villa-Aleman, M. C. Duff, D. Hunter, A. Burger, M. Groza, V. Buliga, D. Black.** 9, 2008, J. Electron. Mater., Vol. 37.

33. *Surface barriers formation mechanisms of the chemically etched CdTe(111) polar surfaces and gold interfaces.* **T. Takeuchi, T. Kore-eda, A. Ebina.** 1996, Appl. Surf. Sci., Vol. 100/101, pp. 596-600.

34. *Effects influencing the structural integrity of semiconductors and their alloys.* **Sher, A., et al., et al.** 1, s.l. : J. Vac. Sci. & Tech. A, 1985, Vol. 3, p. 105.

35. *Chemical mechanical polishing and nanomechanics of semiconductor CdZnTe single crystals.* **Zhang, Z., et al., et al.** 105023, 2008, Semicnd. Sci. Technol., Vol. 23, p. 9pp.

36. *Electronic, lattice vibration and mechanical properties of CdTe, ZnTe, MnTe, MgTe, HgTe and their ternary alloys.* **S. Mnasri, S. Abdi-Ben Nasrallah, N. Sfina, N. Bouarissa, and M. Said.** 2009, Semicond. Sci. Technol. , Vol. 24, p. 095008.

37. XCOM Database. *NIST.* [Online] National Institute of Standards and Technology. http://physics.nist.gov/PhysRefData/Xcom/html/xcom1.html.

38. *Extended X-ray absorption fine structure (EXAFS) at the K edge of cadmium (26.7 keV) with synchrotron radiation.* **G. Dalba, P. Fornasini, E. Burattini.** 5, 1983, J. Phys C: Sol. State. Phys., Vol. 16, p. L165.

39. *Deep Energy Levels in CdTe and CdZnTe.* **A. Castaldini, A. Cavallini, and B. Fraboni, P. Fernandez, J. Piqueras.** 4, 1998, J. Appl. Phys., Vol. 83, p. 4.

40. *Cathodoluminescence and photoinduced current transient spectroscopy studies of defects in Cd0.8Zn0.2Te.* **A. Castaldini, A. Cavallini, B. Fraboni, L. Polenta, P. Fernandez, J. Piqueras.** 11, 1996, Phys. Rev. B, Vol. 54, p. 7622.

41. *Properties of CdZnTe crystals grown by High Pressure Bridgman.* **A. Drighil, R. Adhiri, C. Sribi, M. Mousstad, K. Cherkaoui, G. Marrakchi, A. Zerrai, M. Zazoui.** 1, 1999, M. J. Cond. Matter, Vol. 2.

42. *CdTe and CdZnTe for nuclear detectors: facts and fictions.* **P. Fougeres, P. Siffert, M. Hageali, J. M. Koebel, R. Regal.** 1999, Nucl. Instr. Meth. Phys. Res. A, Vol. 428, pp. 38-44.

43. *Effects of copper in high resistivity CdTe.* **B. Biglari, M. Samimi, M. Hage-Ali, J.M. Koebel, P. Siffert.** 4, 1988, J. Crystal Growth, Vol. 89, pp. 428-434.

44. *Detailed characterization of deep centers in CdTe: Photoionization and thermal ionization properties.* **T. Takebe, J. Sarie, H. Matsunami.** 1, 1982, J. Appl. Phys., Vol. 53, p. 457.

45. *Defective states induced in CdTe and CdZnTe detectors by high and low energy neutron irradiation.* **A. Cavallini, B. Fraboni, W. Dusi, M. Zanarini.** 5, 2003, J. Appl. Phys., Vol. 94.

46. *Point defects in CdZnTe Crystals Grown by Different Techniques.* **R, Gul, A. Bolotnikov, H. K. Kim, R. Rodriguez, K. Keeter, Z. Li, G. Gu, R. B. James.** 3, 2011, J. Electron. Mater., Vol. 40, p. 274.

47. **Camarda GS, Bolotnikov AE, Carini GA, James RB.** Effects of tellurium precipitates on charge collection in CZT nuclear radiation detectors. *Countering nuclear and radiological terrorism, Chapter 4.* s.l. : Springer, 2006, p. Chapter 4.

48. *Growth and properties of semi-insulating CdZnTe for radiation detector applications.* **C. Szeles, M.C. Driver.** 1, San Diego : SPIE, 1998, Vol. 3446.

49. *Advances in the Crystal Growth of Semiinsulating CdZnTe for Radiation Detector Applications.* **C. Szeles, S. E. Cameron, J. Ndap, W. C. Chalmers.** 5, 2002, IEEE Trans. Nucl. Sci., Vol. 49, pp. 2535-2540.

50. *Effects of In doping on the properties of CdZnTe single crystals.* **G. Yang, W. Jie, Q. Li, T. Wang, G. Li, H. Hua.** 3-4, 2005, J. Crys. Grwth, Vol. 283, pp. 431-437.

51. *Crystal Growth and Characterization of Detector Grade CZT Crystals.* **M. Fiederle, A. Fauler, Z. Zwerger.** 2007, IEEE Trans. on Nucl. Sci., Vol. 54, p. 769.

52. *Impurity gettering effect of Te inclusions in CdZnTe single crystals.* **Yang G, Bolotnikov AE, Cui Y, Camarda GS, Hossain A and James RB.** 1, 2008, J. Crystal Growth, Vol. 311, pp. 99-102.

53. *Performance limiting defects in CdZnTe detectors.* **A.E. Bolotnikov, G.S. Camarda, A.G Carini, Y. Cui, K.T. Kohman.** 4, 2007, IEEE Trans. Nucl. Sci, Vol. 54, pp. 821-827.

54. *Factors affecting energy resolution of coplanargrid CdZnTe detectors.* **P.N. Luke, M. Amman, J.S. Lee.** 3, 2004, IEEE Trans. Nucl. Sci., Vol. 51, pp. 1199-1203.

55. *Synchrotrom X-ray based characterization of CdZnTe crystals.* **M.C. Duff, D.B. Hunter, P. Nuessle, D.R. Black, H. Burdette, J. Woicik, A. Burger, M. Groza.** 8, 2007, J. Electron. Mater., Vol. 36, pp. 1092-1097.

56. *Recent Progress in CdZnTe Crystals.* **A. Koyama, A. Hichiwa, R. Hirano.** 6, 1999, J. Elec. Mater., Vol. 28, pp. 683-687.

57. *Properties of Cd 1−x Zn x Te crystals grown by high pressure Bridgman for nuclear detection.* **P. Fougeres, et al.** 1998, J. Crystal Growth, Vol. 184/185, pp. 1313-1318.

58. *Nanostructures of defects in CdZnTe single crystals.* **Li, G.** 1, 2008, J. Crystal Growth, Vol. 311, pp. 85-89.

59. *Effect of Te precipitates on the performance of CdZnTe detectors.* **A.G. Carini, A.E. Bolotnikov, G.S. Camarda, G.W. Wright, R.B. James.** 2006, Appl. Phys. Lett., Vol. 88, pp. 143515-1-3.

60. *The effect of dislocations on CdZnTe single crystal IR transmittance.* **G. Zha, W. Jie, Q. Li, Z. Wang, Y. Xu, D. Zeng.** 2006, Mater. Sci. in Semicond. Proc., Vol. 9, pp. 160-163.

61. *Observations of dislocations in CdTe by Cathodoluminescence microscopy.* **K. Nakagawa, K. Maeda and S. Takeguchi.** 1979, Appl. Phys. Lett., Vol. 34, pp. 574-575.

62. **K. Durose, G.J. Russell.** 1990, J. Cryst. Growth, Vol. 101, p. 246.

63. **K.F. Hulme, J.B. Mullin.** 1962, Solid State Electron, Vol. 5, p. 211.

64. **Singh, J.** *Electronic and Opto-electronic properties of semiconductor structures.* Cambridge, 2003 : Cambridge University Press, 2003. 978-0-511-07863-7.

65. *Simplified LCAO Method for the Periodic Potential Problem.* **J.C. Slater, G.F. Foster.** 6, 1954, Phys. Rev., Vol. 94, p. 1498.

66. *Energy-band structure of CdTe and Si.* **K. Boujdaria, O. Zitouni.** 2004, Sol. State Comm., Vol. 129, pp. 205-210.

67. *M. Cohen, T.K. Bergstresser.* **Structures, Band Structures and Pseudopotential Form Factors for Fourteen Semiconductor of the diamond and Zinc Blende.** 2, 1966, Phys. Rev., Vol. 141, pp. 789-796.

68. **Neamen, Donald.** *Semiconductor Physics and Devices.* Crawfordsville, IN : McGraw Hill, 2003. 0-07-232107-5.

69. *Pysics and Properties of Semiconductors.* **Sze, S.M.** New York : Wiley, 1981. ISBN O-471-09837-X.

70. *A comparison of techniques for nondestructive composition measurements in CZT substrates.* **S. P. Tobin, J. P. Tower, P. W. Norton, D. Chandler-Horowitz, P. M. Amirtharaj, V. C. Lopes, W. M. Duncan, A. J. Syllaios, C. K. Ard and N. C. Giles,.** 5, J. Electron. Mater., Vol. 24, p. 697.

71. *Surface photovoltage spectroscopy analyses of CZT.* **D. Cavalcoli, B. Fraboni, A. Cavallini.** 2008, J. App. Phys., Vol. 103, p. 043713.

72. *State of the art of (Cd,Zn)Te as gamma detector.* **Fiederle, M., et al., et al.** 3, 1999, Journal of Crystal Growth, Vol. 197, pp. 635-640.

73. *Advances in the crystal growth and device fabrication technology of CdZnTe room temperature radiation detectors.* **Szeles, C.** 3, 2004, IEEE Trans. Nucl. Sci., Vol. 51, pp. 1242-1249.

74. *Distribution of zinc, resistivity, and photosensitivity in a vertical Bridgman grown Cd1−xZnxTe ingot.* **Babenstov, V., et al., et al.** 15, 2008, Journal of Crystal Growth, Vol. 310, pp. 3482-3487.

75. *Electrical compensation in CdTe and Cd0.9Zn0.1Te by intrinsic defects.* **Krsmanovic, N.** R16279, 2000, Phys. Rev. B, Vol. 62.

76. *Correlation between the low-temperature PL spectra and Cd0.9Zn0.1Te quality.* **Li, G., Zhang, X. and Jie, W.** 1, 2005, Semicond. Sci. Technol., Vol. 20, pp. 86-89.

77. *Compensation and deep levels in II–VI compounds.* **Castaldini, A., et al., et al.** 1-3, 1996, Material Science and Engineering B, Vol. 42, pp. 302-305.

78. *Temperature dependence of photoluminescence properties of In-doped cadmium zninc telluride.* **T.Wang, et al.** 2008, J.Mater.Res.,, Vol. 23, p. 1389.

79. *Upgrading of CdZnTe by annealing with pure Cd and Zn metals.* **Li, G., et al., et al.** 3, 2006, Semicond. Sci. Technol., Vol. 21, pp. 392-396.

This page intentionally let blank.

Chapter II

Experimental Methods

This page intentionlly left blank

Chapter II Content

This page intentionally left blank.

1 INTRODUCTION

In order to demonstrate real improvements made in crystal growth and detector fabrication, it was necessary to develop both crystal growth technology as well as device processing protocol. Moreover, both the methods and equipment which have been developed through this investigation required intense study in order to evaluate their relative merits. To develop a deeper understanding of the experimental methods which have been implemented throughout this thesis, a description of each the technology and characterization methods which have been implemented are presented.

This chapter is divided into three sections based on these three important experimental approaches undertaken in this work. The first section describes in detail the design, construction, testing of furnaces and furnace components used for crystal growth of Cd(Zn)Te. Due to the importance of the measurements, spectroscopic gamma ray measurement considerations applied to Cd(Zn)Te is discussed in the second Section. The third section presents technical summaries of each of the characterization techniques used in this work.

This page intentionlly left blank

2 DEVELOPMENT OF CRYSTAL GROWTH TECHNOLOGY

Section Contents

This page intentionally left blank.

2.1 5-zone Vertical Gradient Freeze Furnace (VGF-1)

A five-zone Vertical Gradient Freeze (VGF) furnace was used for growing more than 20 crystals 25m in diameter. Presented below in **Figure 1** is the actual VGF system which has been used. The hot zone of the system consisted of five independent 1kW furnace elements each 10cm in height. The temperature inside each zone is measured using a type-S thermocouples placed along the inner wall located at the center of each zone. High temperature refractory wool was used for improving thermal insulation of the furnace.

A linear actuation system was also used for positioning the crystal growth ampoule inside the furnace. This system consisted of a linear column actuated by a stepper motor which was controlled by a computer program. This positioning system was coupled to a quartz pedestal, upon which the growth ampoule would be placed. This quartz pedestal consisted of a central quartz/SiC pedestal, intended to support the weight of the ampoule at high temperatures, surrounded by a separate set of a type-S thermocouples for measuring the temperature gradients near the ampoule wall. A second DC motor was housed inside the linear actuator column head and provided the capability for rotation of the ampoule during the process.

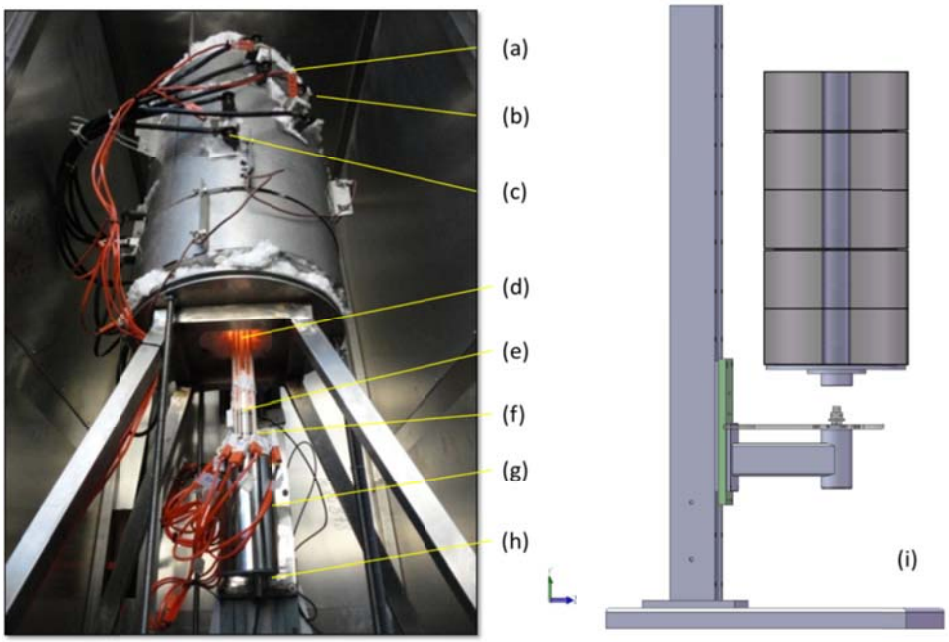

Figure 1 Left: VGF 1 system used for the growth of 23mm ingots. (a) high temperature silicone cables used for power transmission (b) type-s thermocouples used for measuring furnace temperature (c) furnace element contact extensions protruding from furnace casing (d) furnace pedestal near opening of VGF furnace (closing insulation has been removed for photo) (e) quartz pedestal with circumferentially arranged thermocouples, (f) quartz pedestal coupled to DC motor (g) linear actuation head/DC motor housing (h) linear actuation column (i) side view of 5-zone VGF furnace with linear actuation column.

Using this existing system for the growth of 25mm ingots, improved control over growth rate and temperature profile stability were achieved. The circumferentially located thermocouples were key elements for measuring the temperature near the ampoule wall during the growth cycle. In addition, the linear actuation system designed for this system provided better accuracy and resolution of displacement than previous systems used in the laboratory.

2.2 6-Zone Vertical Gradient Freeze Furnace (VGF-2)

A larger diameter Vertical Gradient Freeze furnace was designed and built during this thesis investigation to increase the quantity and quality of material synthesized in the laboratory, specifically for the COCAE project which was the focus of this investigation. This experimental system was designed to employ three Eurotherm controllers for operating six independent furnace zones, for the growth of up to 1kg Cd(Zn)Te ingots 50mm in diameter.

The electronics used for controlling each temperature set point and operating power of each zone consisted of (i) Eurotherm 2604 temperature controller (ii) a Eurocube thyristor unit connected to (iii) 1kW transformer. The Eurotherm temperature controller sends signal pulses to the Eurocube triac whose conductivity is mediated by a voltage gate. This control circuit is presented in **Figure 2**.

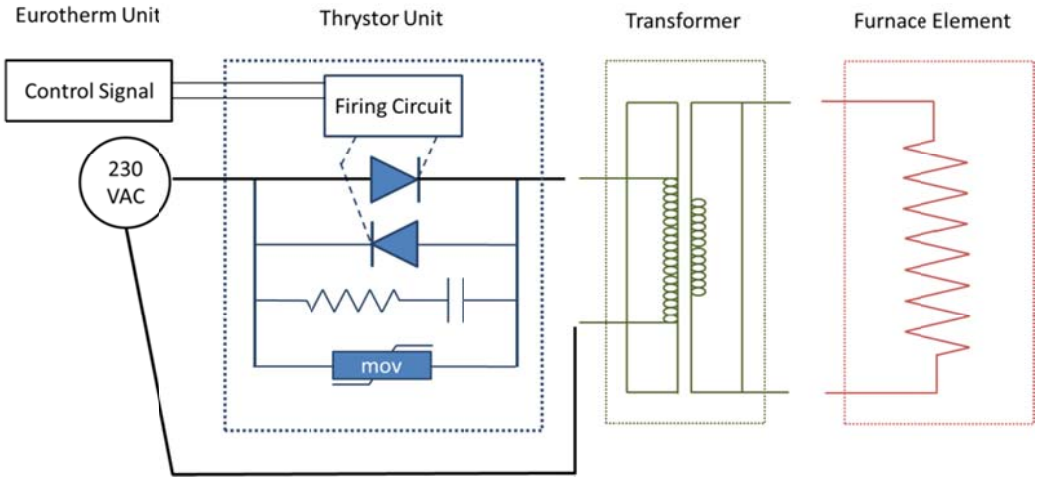

Figure 2 Electrical circuit diagram for connection of single zone of VGF-2 Furnace.

Presented in **Figure 3** is the guiding principle of the thyristor, which illustrates the bi-stable DC functionality, which allows current to pass only in a single direction. A thyristor is normally

a set of alternating type-n and type-p semiconductor layers, consisting of three p-n junctions. Correspondingly, this structure will conduct only so long each junction is forward biased.

When a negative voltage reaches the first p-type layer, no current will flow. When the voltage changes to positive however, the 1st junction will be forward biased, while the 2nd will be reverse-biased. For low voltages, no current will flow through this structure. For positive voltages exceeding the breakdown voltage of the semiconductor, an avalanche breakdown mechanism will occur at the 2nd Junction, and as a result the current will begin to flow. The purpose of the gate, which is actuated by the Eurotherm controller, is to reduce the threshold for this breakdown to occur, providing a mechanism for controlling current.

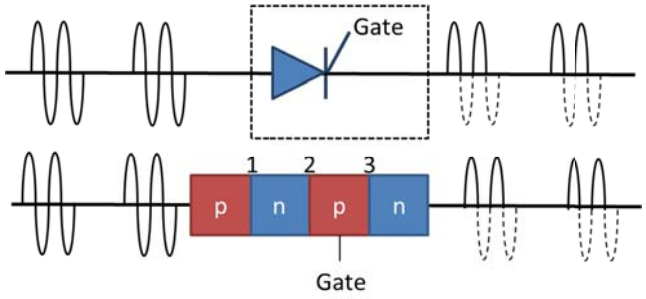

Figure 3 Basic operating principle of a thyristor used for modulating AC voltage

To take advantage of the entire output power of the power source, the thyristor unit is actually comprised of two inversely oriented thyristors connected in parallel. Using this configuration it is possible to set the primary voltage of the transformer from Zero to the nominal value of the voltage source. Additional features integrated into the Thyristor unit, and presented in **Figure 2**, include an RC filter for elimination of current spikes in the transformer, as well as a metal oxide ´´varistor´´ whose resistance changes with applied bias. This latter component absorbs voltage spikes in the circuit from causing damage.

The output of the thyristor is connected directly to the primary voltage of the transformer. This connection provides the capacity for changing the energy from the voltage source into current, which is used in turn for resistive heating the furnace element. A typical diagram of the transformer circuit element is presented in **Figure 4**.

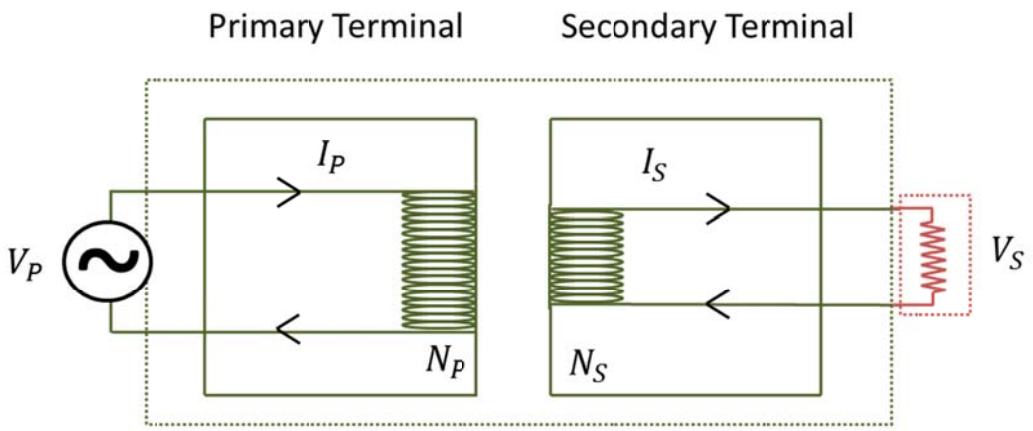

Figure 4 Transformer element circuit diagram. The votlage and current applied ot the primary terminal, composed of N_p turns is reduced to a lower voltage and higher current at the secondary terminal.

The current and voltage relation for the primary and secondary terminals of the transformer may be expressed using Equation 1, where V_P and V_S is the voltage applied at the primary terminal and output at the secondary terminal, I_P and I_S are the current at the primary and secondary terminals, and $N_{P,S}$ represents the number of turns of the primary and secondary coils respectively. From this relation it may be observed that decreasing the voltage at the secondary terminal by using a step-down transformer results in a proportional increase in current. For the VGF-2 furnace, a 1kW transformer was used to step down the voltage from 230V to 12V.

Equation 1 $$\frac{V_S}{V_P} = \frac{N_S}{N_P} = \frac{I_P}{I_S}$$

Presented in **Figure 5** is an individual Kanthal furnace element which was directly to the secondary terminals of the transformers. As may be seen from this figure, each heating element consists of a vacuum formed ceramic fiber with an integral Kanthal heating element. Each furnace element was fitted with modified Kanthal extensions to increase convective cooling of the electrodes, permitting greater dissipation of heat. Indeed, in the absence of this convective cooling, the Kanthal electrodes would reach excessively high temperatures through thermal conduction, beyond the operating limit of the silicone jacket encapsulating the cables.

The unique properties of Kanthal make this material suitable for temperatures up to 1600ºC. However, a steep increase in electrical resistivity with temperature is in fact an important

characteristic to take into account for Kanthal electrodes. Also, the material is very brittle at low temperatures meaning that mechanical vibrations or excessive amperage may create forces sufficient to rupture the elements. Indeed, at low temperatures the vibrations of the Kanthal coils associated with the applied AC voltage was notable, and power outputs substantially lower than 100% were used.

Presented below in **Figure 6** is the 3D CAD design of the VGF furnace, which has been designed, built, tested, and implemented in this investigation. Similar to the VGF-1 furnace, the mechanical system incorporated several elements for process control including type-S thermocouples for temperature control, a linear actuation column for vertical displacement of the ampoule, as well as coupling to a DC motor for rotational stirring of the melt. One of the differences was that an extra furnace zone was introduced to provide the capability for Cd-over-pressure control.

The control of the furnace was achieved using software and hardware developed at SEGAINVEX in conjunction with the electrical cabinet presented in **Figure 7**. The various elements comprising the electrical cabinet used for controlling the furnace temperature include six 1kW single phase transformers, (6) thyristor units, used in conjunction with two Eurotherm temperature controllers, connections for thermocouple terminations, communication ports, and circuit breaking elements. All of this hardware is housed in a rigid steel enclosure with protective slotted panels which also provide convective cooling of the transformers.

The Graphical User Interface (GUI) for controlling each furnace was developed by SEGAINVEX as an interface between the crystal grower and the Eurotherm temperature controller. Additional software for controlling the positioning and rotation of the ampoule was also developed, but is not presented here. Presented in **Figure 8** is the VGF-2 GUI which provides the capacity to program each of the temperature ramps for each zone of the furnace. The output power of each zone at a given temperature is also actively measured and may be displayed in one of the windows. This information regarding output powers is useful for the development of simulation models of the crystal growth cycle and estimation of heat transfer coefficients.

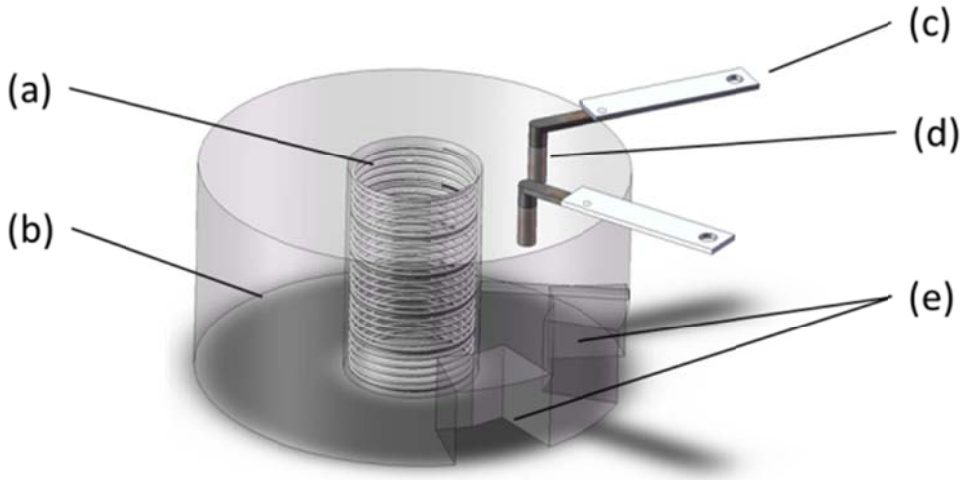

Figure 5 Single furnace element used in the construction of the VGF-2 furnace (a) 75mm bore & Kanthal spiral (b) refractory alumina insulation (c) Kanthal extensions (d) Kanthal electrodes (e) refractory cut-outs used for stacking furnace elements

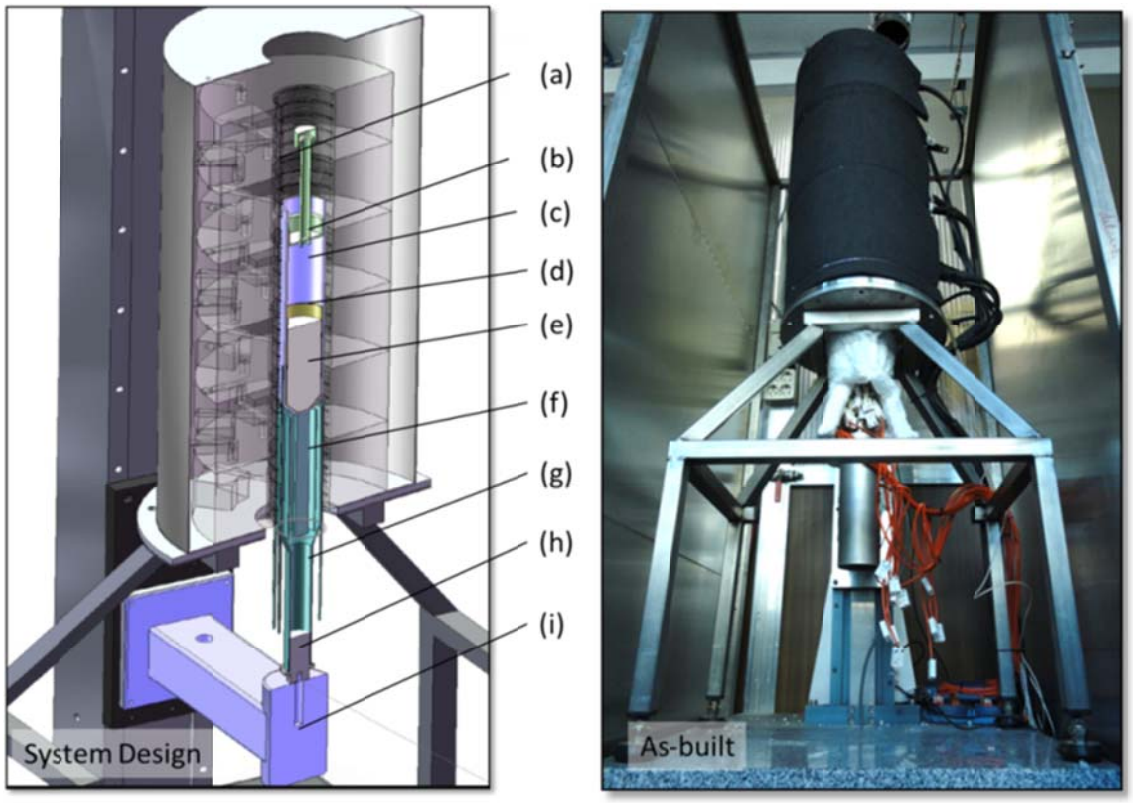

Figure 6 The 6 Zone VGF Furnace designed, assembled, and implemented in this thesis investigation. (a) Cd-reservoir for over-pressure control, (b) quartz ampoule sealing cup, (c) quartz ampoule, (d) pBN crucible, (e) Cd(Zn)Te ingot, (f) quartz/SiC pedestal, (g) quartz pedestal taper for coupling to DC motor and circumferentially oriented thermocouples, (h) DC motor shaft, (i) linear actuation column head and DC motor housing.

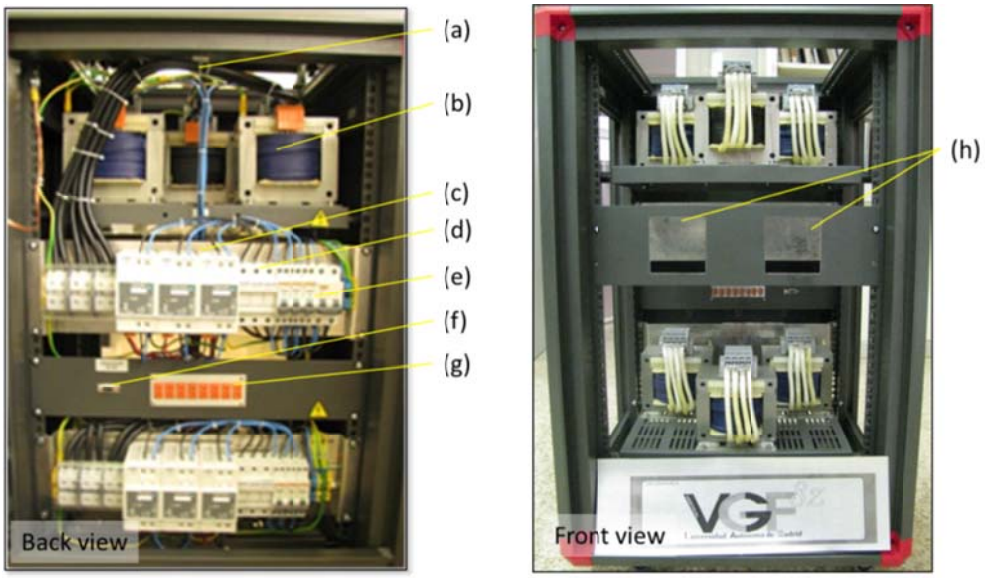

Figure 7 Electrical cabinet of VGF-2 system. (a) High temperature silicone leads going to VGF-2 furnace zones, (b) 1kW Transformer, (c) thyristor unit, (d) - (e) circuit breakers and fuses, (f) data communication port, (g) thermocouple ports, (h) panel with cut-outs for Eurotherm hardware.

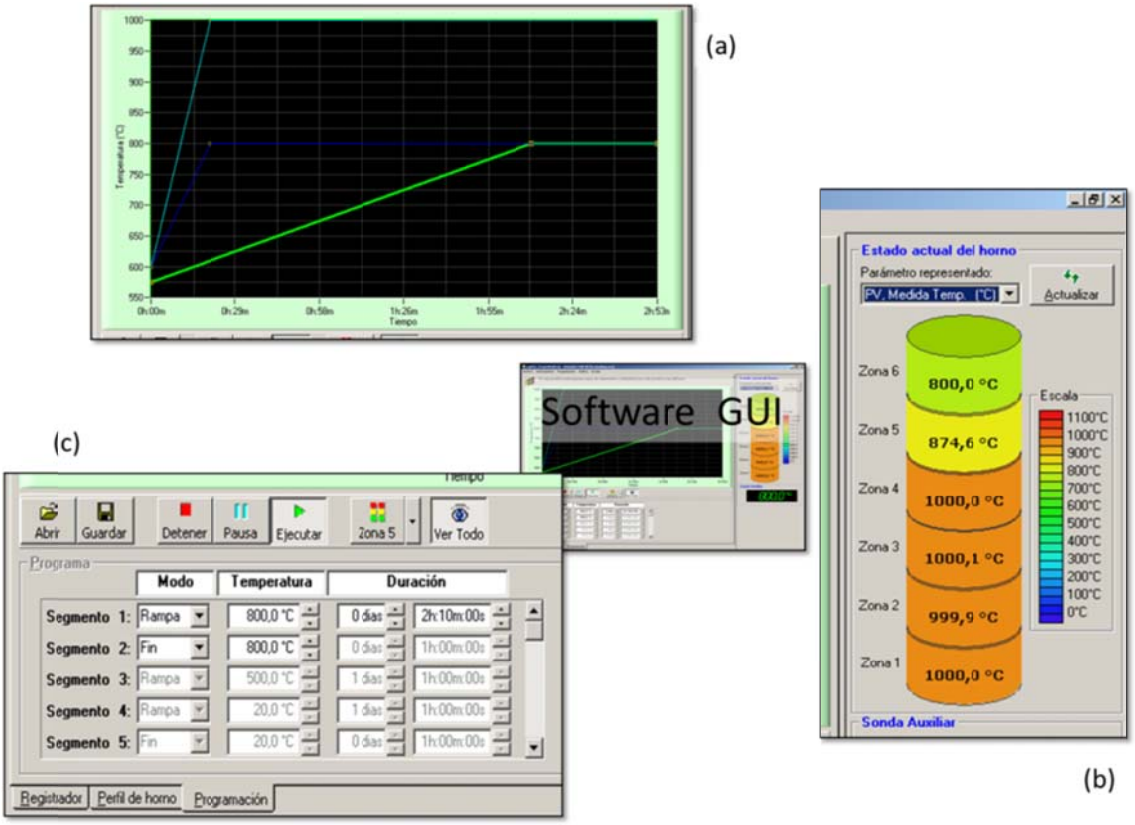

Figure 8 Software GUI used for controlling VGF-2 furnace consisting of (a) temperature plot window illustrating the programmed temperature ramps, (b) furnace status window displaying information related to the furnace temperature, output power, set-point, and (c) the program window were the temperature ramps are created to form a growth recipe.

2.2.1 Furnace Insulation

A significant amount of consideration must be taken into account into both the design and construction of a furnace. For the temperature range of interest, it was necessary to used type S thermocouples (T/Cs) for the measurement of temperature gradients inside the furnace. The T/Cs were distributed along the vertical axis of the furnace to determine the axial temperature profile.

Each zone of the VGF-2 system was assembled and sealed using a high temperature silicate to convection and heat loss through the small air gaps separating each zone. Additionally, Alumina wool refractory was used to insulate and stabilize the furnace temperatures. Indeed, the use of insulation can have a profound impact on the temperature stability inside the furnace.

To illustrate the effect of furnace insulation on temperature profile stability, three trials were carried out, and are presented in **Figure 9**. For the first trial, no insulation was used to cover the top and bottom of the furnace. A strong convective current was observed and results in large temperature fluctuations inside the furnace and high operating powers. These fluctuations in the temperature would correspond to a very un-stable solid liquid interface during the growth cycle.

For the second trial, only the top of the furnace was covered in order to stop this convective flow from pushing through the furnace. Finally, in the third trial, both the top and bottom of the furnace were well insulated. Presented below in **Figure 9** are the temperature measurements for Zone-2 of the VGF-2 furnace during the course of each trial.

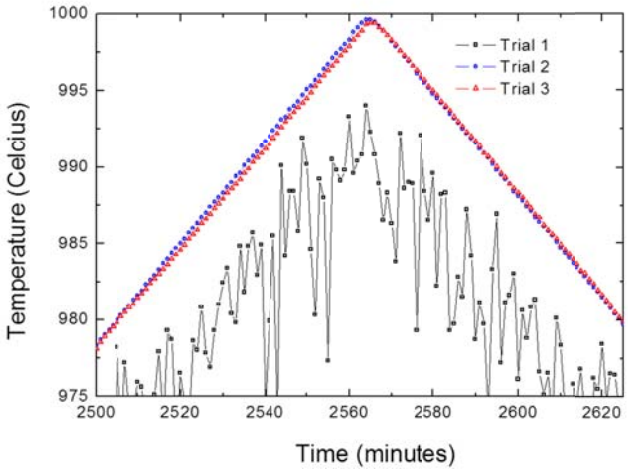

Figure 9 Thermocouple profiles for non-insulated furnace, furnace with insulation at top of furnace, and furnace with insulation at both top and bottom of furnace profile.

The strong temperature fluctuations would have a profound effect on the stability of crystal growth and resultant crystal quality. For this reason, a large emphasis was placed on reducing convective flows, and maximizing thermal isolation using various high temperature refractory materials.

Shown below in **Figure 10** are output powers for each thyristor unit controlling each zone of the furnace, under a second set of thermal boundary conditions, with the temperature set points of each Zone 1-4 at 1000ºC, the set point of Zone 6 was 800ºC, and no power was supplied to Zone 5.

In the first trial shown in **Figure 10**(a), no alumina refractory was used to insulate the bottom of the furnace opening. After adding a single layer of alumina refractory to insulate the system shown in **Figure 10**(b), the output power of Zone 1 dramatically dropped from 82.4% to 63.0%. Zone 2 remained the same, Zone 3 dropped 1%, and Zone 4 dropped almost 2.4%. After adding a second layer of insulation and tightly fastening with Kanthal wire, the output power from Zone 1 dropped only 1.4% and for all of the other zones, less than 1%, as shown in **Figure 10**c. An example of the alumina refractory wrapped around the quartz pedestal, as well as the abovementioned data is presented below along with the furnace set points used for these tests (d). It is important to note that these, as well as other tests not mentioned, helped identify stable operating parameters for enhancing control over the crystal growth cycle.

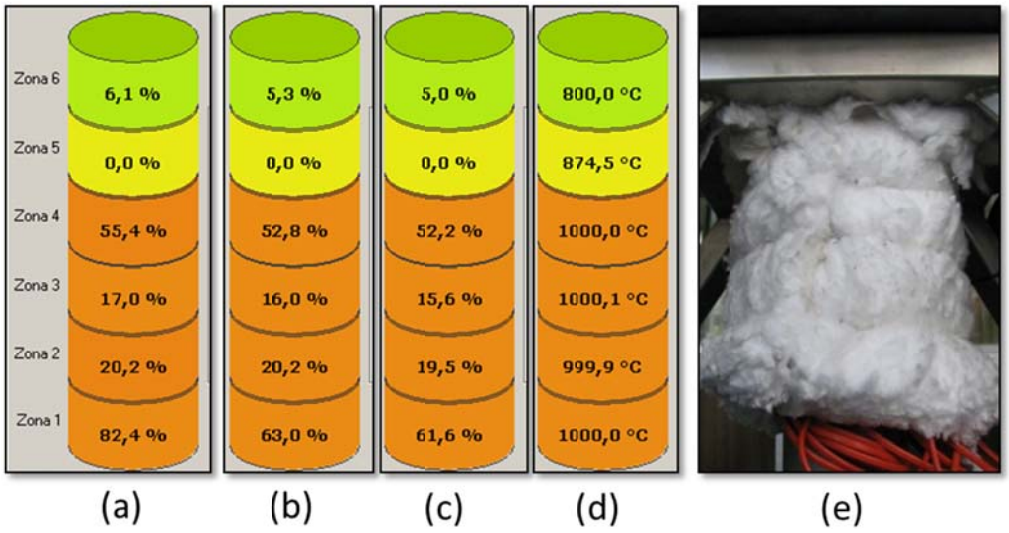

Figure 10 Output power of thyristor of each zone with (a) no insulation at bottom of furnace, (b) with one layer alumina refractory at bottom of furnace, (c) with two layers alumina refractory at bottom of furnace, (d) temperature set points for each furnace, and (e) example of 1 layer alumina refractory.

2.2.2 Thermocouples

Each thermocouple for both the VGF-1 and VGF-2 furnaces had to be made in the laboratory to meet the custom requirements of the furnace. The thermocouples (T/Cs) used in this work are Type-S Platinum-Platinum Rh(10%) thermocouples, with a wire diameter of 0.55mm. The specific wire used follows the standard BS EN 60584-2 Class 1. This standard requires that for temperatures $t \leq 1000^{o}C$, the readout is accurate to $\pm$ 1 ^{o}C and for $t > 1000^{o}C$, the accuracy of the T/Cs decreases to $\pm 1 + 0.003 \times (T\text{-}1000^{o}C)$. This means that for the growth of Cd(Zn)Te, which occurs between 1100-1130ºC, the error in the measurement is $\pm$ 1.3ºC.

The thermo-electric junction of each T/C was created in the laboratory using an acetylene-oxygen torch to union the two wires. The cable connected to the T/C's used for measurement were electrically compensated copper which takes into account the voltage offset induced by the Copper-Platinum metallurgical junction. Robust T/C's with fiberglass jacketing and ceramic plugs were used near hot components of the furnace, while T/C data loggers were used for collecting and logging data. Typical T/C's which have been constructed here are shown below in **Figure 11**. The T/C wires are placed within a high temperature, double slotted alumina sheath.

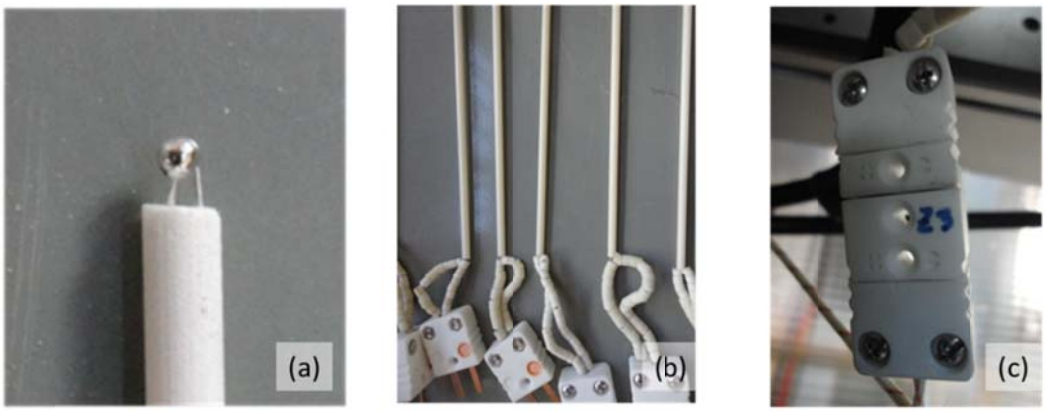

Figure 11 (a) Pt:Pt (Rh10%) metal junction which produces EMF. (b) Dual bore ceramic tubes with leads protected by ceramic beads. (c) High temperature ceramic T/C connectors

2.2.3 Design and Development of Furnace Pedestal

A great deal of effort was invested into the development of a furnace pedestal for supporting growth ampoules. Indeed, all of the quartz, pBN, and pedestal components were designed, built, tested, and implemented in the course of this investigation. The desired pedestal for crystal growth would incorporate the capability for rotation, vertical translation, while contributing

favorably to growth conditions i.e. facilitate the extraction of latent heat arising from the crystal growth process. Several prototypical furnace pedestals were fashioned from quartz and stainless steel components. Shown below in **Figure 12** are the pedestals fabricated for both the VGF-1 and VGF-2 growth furnaces.

The stainless steel component was specifically designed for coupling of the DC motor to the quartz pedestal. This coupling was achieved using a 50mm stainless steel rod, with two O-ring grooves for alignment, the ampoule's deviation from the axis of rotation was limited by the intrinsic straightness of the Quartz ampoule.

Alumina wool refractory and smaller diameter quartz tubes were layered to provide a robust support structure. A sintered silicon carbide (SiC) rod was also integrated into the pedestal. The incorporation of the SiC pedestal was intended to increase the thermal gradient and axial heat flow during the growth process and more details on this behavior are presented in Chapter 3 Section 7.

The quartz pedestal was mounted to a vertical linear actuator using a custom motor housing block. A DC motor within the housing provided ampoule rotation both clockwise and counterclockwise. The entire vertical actuation system was mounted to a granite anti-vibration table in order to minimize vibrations transferred from the external environment to the solid-liquid interface of the crystal growth. Shown below in **Figure 13** are the vertical translation/rotation components of the VGF-1 furnace, with the furnace pedestal inside the furnace. In this photograph, the insulation covering the bottom of the furnace has been removed. A similar vertical actuation/rotational system was also incorporated into the VGF-2 system.

Shown below in **Figure 14** are images of the two types of pedestals which have been used in this thesis investigation. In both VGF systems (VGF-1 and VGF-2), the thermocouples used for measuring temperature gradients were located circumferentially around the sealed ampoule, and distributed about the axial direction. A micrometer accurate to 0.01mm was used for locating each thermocouple vertically, while each thermocouple was fixed into place using a high temperature silicate paste. The quartz pedestal was the first type of pedestal investigated due to its compatibility with high temperatures. The SiC pedestal was further investigated due to its high thermal conductivity properties, and for increasing the temperature gradient at the first to freeze tip. These properties of SiC are further discussed in Chapter 3, Section 6 and 7.

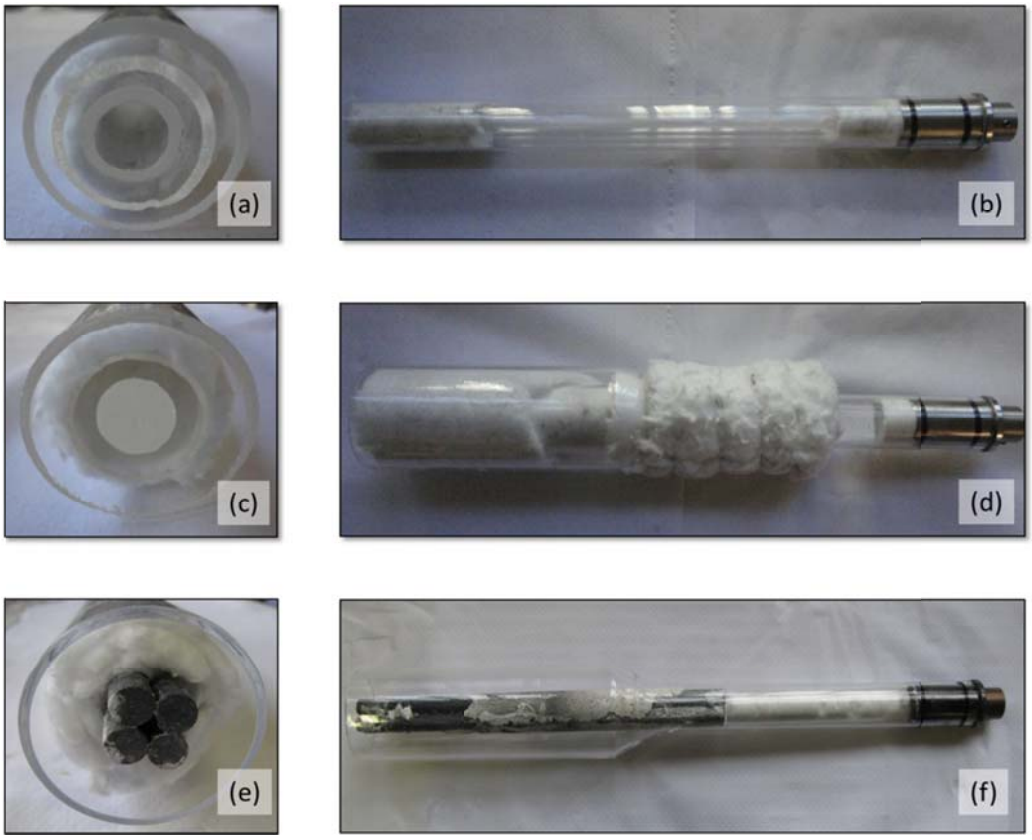

Figure 12 (a) & (b) Quartz pedestal for 25mm diameter ampoule (c) & (d) quartz pedestal for 50mm ampoule, (e) & (f) SiC/Quartz pedestal for 50mm ampoule.

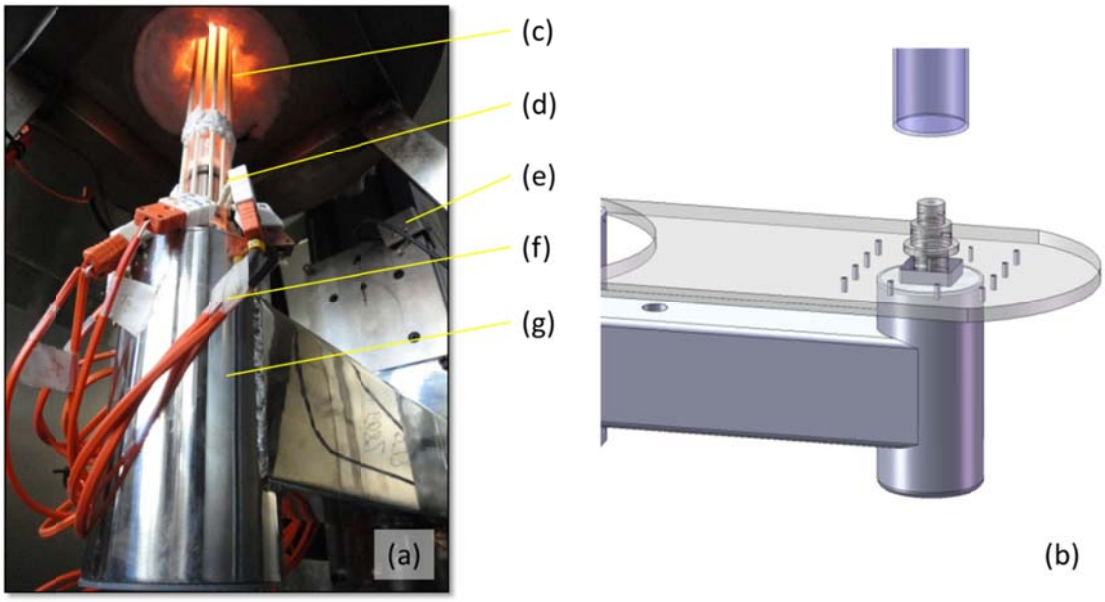

Figure 13 (a) Electrical-mechanical system used for vertical actuation and rotation for VGF-1 (b) 3D model design of system (c) quartz pedestal with circumferentially arranged thermocouples (d) quartz pedestal coupling to rotational DC motor (e) vertical actuation limit switch (f) thermocouple connections (g) DC motor housing and linear actuation head.

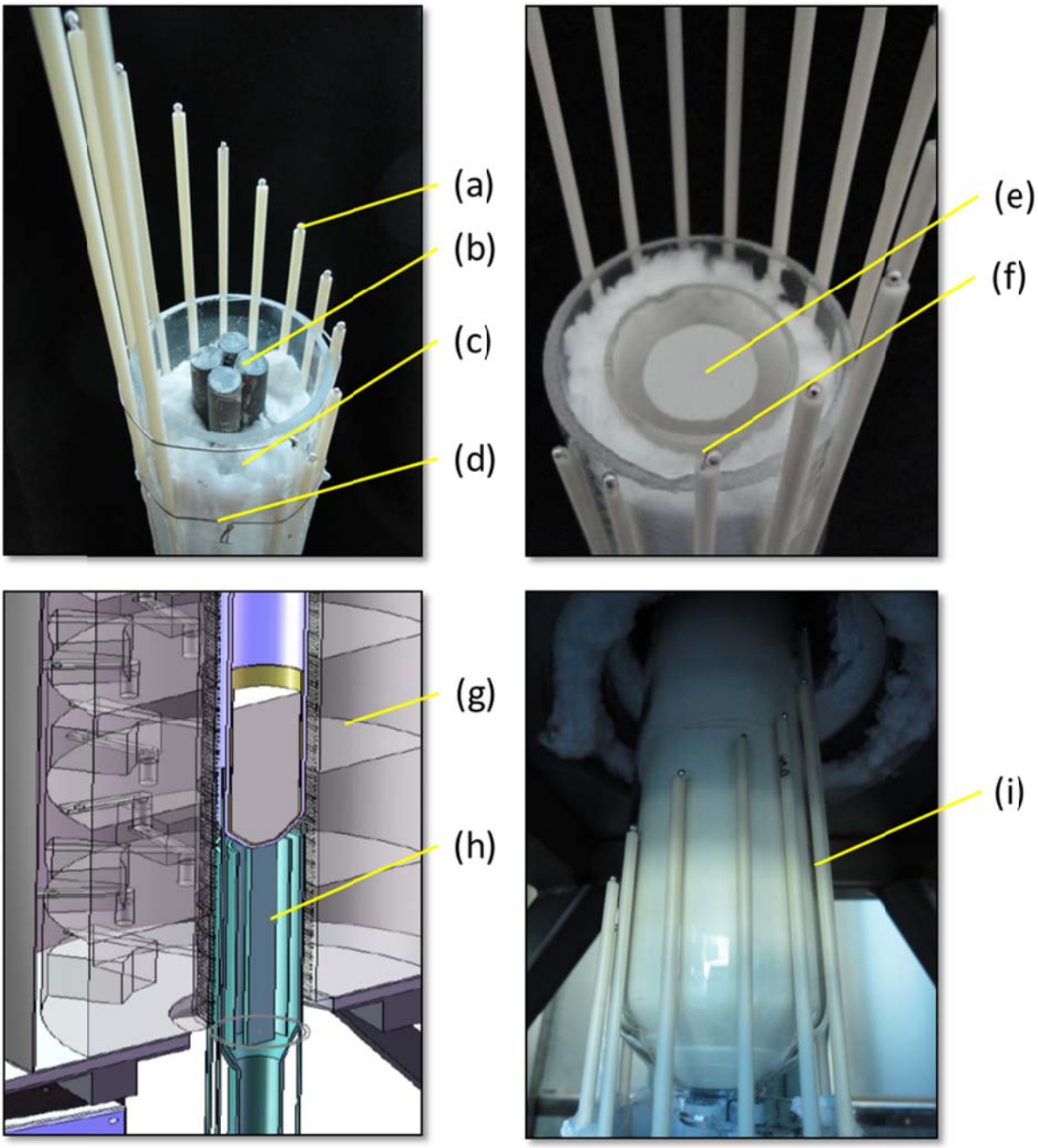

Figure 14 Quartz pedestal used for mounting ingot and measuring temperature gradients throughout the growth process. (a) Type S thermocouple, (b) sintered SiC pedestal (c) Quartz support (d) Kanthal wire for fixing in place (e) Quartz pedestal (f) alumina refractory wool (g) Cd(Zn)Te ingot positioned between Zone 2 and Zone 3 of furnace (h) pedestal support (i) pBN crucible &Quartz ampoule placed onto pedestal.

2.3 Development of Vacuum Carbon Coating System

In Bridgman and Vertical Gradient Freeze (VGF) crystal growth techniques, it is common to use a sealed quartz ampoule for charging Cd(Zn)Te. To prevent interaction, sticking, or diffusion of chemical impurities between the quartz ampoule and the Cd(Zn)Te melt, different methods exist. One of the most commonly used methods is to deposit a layer of carbon on the quartz surface.

The reaction between Cadmium Oxide (CdO) and Silicon in the sidewall is favorable to the formation of cadmium metal-silicate ($CdSiO_3$). During the carbon deposition at elevated temperatures, the carbon layer actually functions to getter any excess O_2 and H_2O. As a result, the carbon layer physically prevents CdO from contacting the inner ampoule wall (1). Furthermore, the carbon layer functions as a mechanical barrier and prevents impurities from the quartz from diffusing into the melt during growth.

The carbon layer is typically quite thin however, on the order of microns, and there is some doubt whether or not this carbon layer effectively blocks impurities from the quartz from diffusing into the ingot. In fact a typical growth cycle is on the order of 200 to 300 hours at temperatures above 1100ºC which makes the diffusion of impurities into the melt quite possible.

To eliminate these potential sources of impurities from the growth process, it was necessary to 1) study the current state of the technology in the laboratory and 2) improve the carbon coating technology using a vacuum carbon coating system. Finally, it is important to also mention here that this vacuum coating system has also been used for carbon coating of pBN crucibles. This new crucible material shows considerable promise as is discussed in Chapter 3, Section 3.

2.3.1 Open Carbon Coating System

To prevent diffusion and species migration from the crucible to the Cd(Zn)Te charge, a layer of carbon can be used to coat ampoule or crucible walls using a method of pyrolytic carbon coating. This technique is used to create a thin carbon barrier between the crucible wall and charge. The production of carbon from hydrocarbon molecules can be described using the following equation.

Equation 2

$$2 \cdot (CH_3)_2CO \xrightarrow{Heat} 6 \cdot C + 2 \cdot H_2O + H_2$$

This pyrolysis can be accomplished experimentally in several ways. One simple method is to place an open quartz ampoule directly into a furnace which is maintained at a temperature of 1000°C. After a short time when the temperature inside of the ampoule is relatively uniform, a small amount of acetone (~40-100μL) may be dropped into the quartz ampoule using a micro-pipette. Almost immediately, the carbon atoms of the acetone molecule deposit a carbon layer on the wall of the quartz ampoule (substrate) also producing hydrogen gas. It is important to also comment that carbon flakes also form as a result of the cracked acetone molecule not nucleating on the surface of the ampoule, but in the air. An experimental schematic for this simple approach is presented in **Figure 15**.

The open tube technique has many experimental drawbacks. First, there are many sources of contamination as the system is ´open´. Any airborne sources of contamination can easily become deposited onto the wall of the ampoule. Second, due to the nature of the rapid phase transition of liquid hydrocarbon to carbon film, the carbon layer formed is often non-uniform and exhibits polyp-shape morphology as presented in **Figure 15**. The film is on the order of 1μm in thickness with 'polyp' shaped carbon formations, and exhibits a low density. These factors decrease the carbon layers utility as a mechanical barrier to diffusing impurities and gettering of O_2 and H_2O. In fact, it seems unlikely that these types of films act as efficient barriers to the diffusion of impurities when one considers that the crystal growth cycle takes place at near 1100ºC and may last over 200 hours.

2.3.2 Vacuum Carbon Coating System

More uniform carbon films could be achieved through the implementation of a vacuum carbon coating system. The system developed in this thesis was designed to have two zones each capable of reaching more than 1000ºC. Additionally, the furnace is capable of rocking 180º, which provides the capability for loading and unloading ampoules without moving the experimental vacuum apparatus. A compression fitting is used for connecting the quartz ampoules to the vacuum pumps (both rotary and turbo-molecular pumps may be used). A liquid nitrogen trap sits between the ampoule and the vacuum pumps. The hydrocarbon (Acetone) is loaded from the bottom, with a needle valve to regulate mass flow. Finally, a bourdon gauge and a pressure relieve valve are mounted to prevent positive pressures from building up inside the system. Several of the system components which have been custom designed for this work are presented in **Figure 16**.

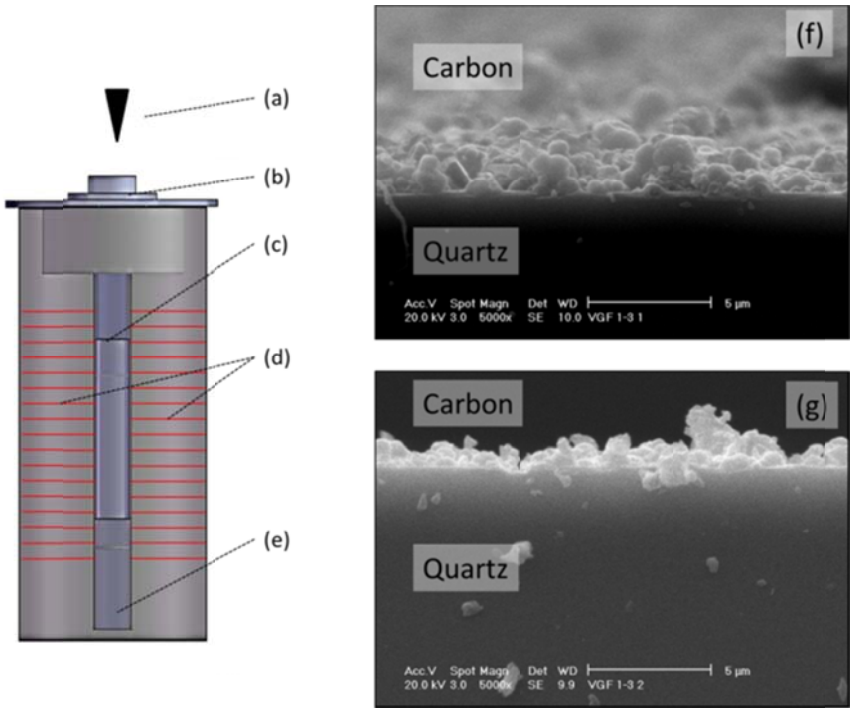

Figure 15 Typical carbon film obtained using open carbon coating system as shown on the left. The open carbon coating system is typically composed of (a) a micropipette for dropping acetone into ampoule, (b) furnace opening, (c) quartz ampoule for carbon coating, (d) furnace heating elements at 1000ºC, and (e) protective quartz enclosure. The resulting films which have been obtained after this coating process are shown in (f) and (g)

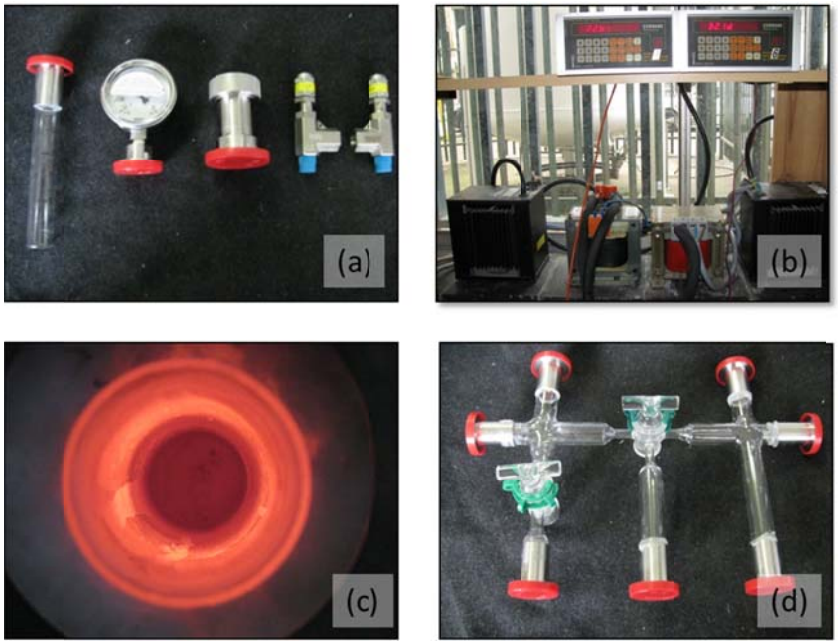

Figure 16 (a) Ampoule cuvette, bourdon gauge, compression fitting, and over pressure release valves, compression fitting, (b) temperature controllers, thyristors, and transformers, (c) inside bore of 2-Zone furnace, (d) prototype glass chamber developed for carbon coating.

The 3-D design and the experimental apparatus designed, constructed, and tested in this investigation is shown in **Figure 17.** Using this closed system, it was possible to coat the quartz ampoule under vacuum, from the gas phase directly to the solid phase. A typical process would include the following steps. First, a vacuum is created inside the ampoule and the temperature of the furnace is raised to 1000ºC. The valve of the vacuum system is then closed in order to separate the vacuum pumping system from the carbon deposition process. The valve connecting the Acetone to the vacuum system slowly opened to allow the vapor pressure of the hydrocarbon to enter into the evacuated ampoule. When this valve is opened, carbon deposition upon the inner wall of the ampoule proceeds. The pressure within the closed system is monitored using a Bourdon gauge. When the pressure inside the ampoule approaches ambient pressure levels, the valve connecting the vapor pressure of the Acetone to the vacuum system is closed to separate the hydrocarbon source from the vacuum pumps. The valve connecting the vacuum system is then re-opened to again establish vacuum inside the system. A liquid nitrogen trap prevents particulates from reaching the pumping system.

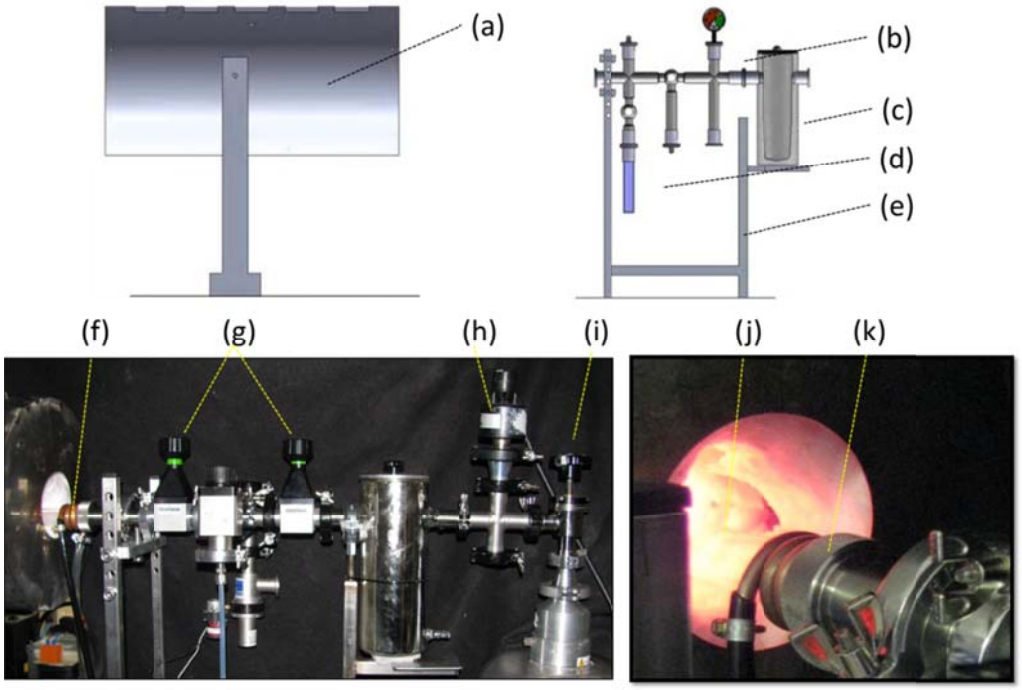

Figure 17 System design of vacuum carbon coating system incorporating (a) a 2-zone 5kW rocking furnace, (b) bourdon gauge for positive and negative pressure measurements, (c) liquid nitrogen vacuum trap, (d) vessel for acetone, (e) mechanical support structure for system and the experimental system constructed at CGL, (f) water cooling coil, (g) vacuum valves for controlling vacuum/acetone over pressure, (h) turbo-pump vacuum gauge, (i) turbo-pump, (j) evacuated ampoule/crucible, and (k) compression fitting.

Presented in **Figure 18**, the pressure change is at the onset of carbon deposition is at first rapid as the vapor pressure of the hydrocarbon fills the evacuated ampoule and carbon deposition proceeds. However, after the first 5 minutes, this change in pressure slows considerably. The increase in vessel pressure may be associated with the build-up of CO_2, H_2O, as well as water vapor which are a byproduct of the pyrolytic process described above in **Equation 2**. As may be seen, the system may be run for nearly 1 hr before a vacuum needs to be re-established in the system.

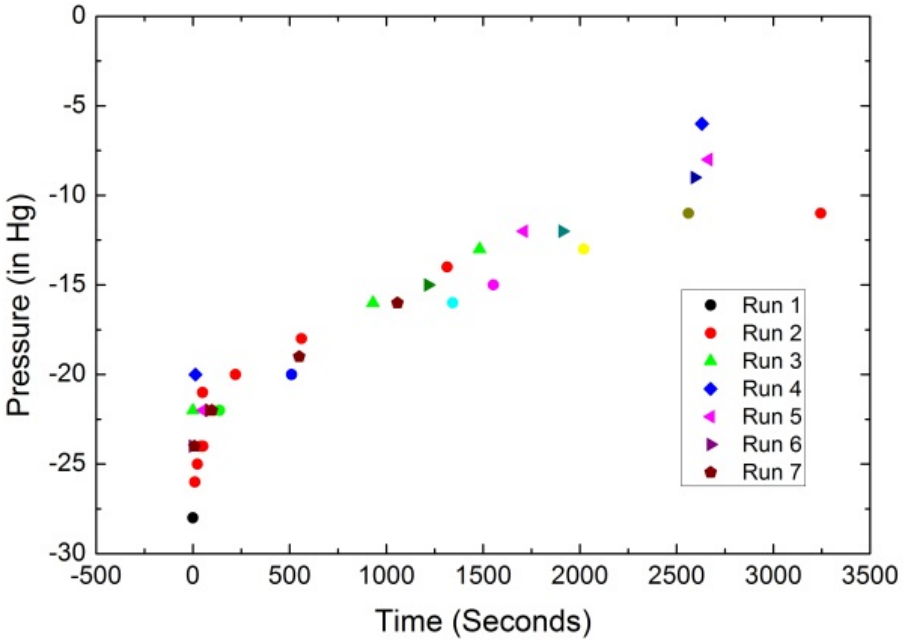

Figure 18 Pressure change inside the quartz ampoule a function of a time. The pressure build up is likely associated with the build-up in the concentration of CO_2 and H_2 gases as well as water vapor.

2.3.3 Quartz Ampoule Preparation

To prepare ampoules for graphitization (both open and closed methods) the following procedure was used (for both 24mm diameter and 50mm diameter quartz ampoules). First the ampoules were thoroughly rinsed using Alconox detergent to remove residual salts and surface contaminants. This step was followed by a thorough rinsing with DI water, Trichloroethylene, Methanol, and Acetone (DI, TCE, MeOH, Acetone). The ampoules were etched using HCl : HNO_3 acid solution in a ratio of 3:1 for a period of 24 hours, followed by DI, TCE, MeOH, Acetone. The ampoules were next chemically etched using Hydroflouric acid for a period of 3 hours, followed by DI, TCE, MeOH, Acetone rinsing. The cleaned and dried ampoules were loaded into the horizontal vacuum carbon coating system and sealed via a compression vacuum

fitting. The furnace was raised to 1000°C for pyrolytic coating of the ampoule. Immediately following the carbon coating, the crucibles were rinsed with DI, TCE, MeOH, and Acetone to remove residual carbon flakes which did not adhere to the surface of the quartz ampoule wall. Shown below in **Figure 19** are images of a 50mm diameter ampoule x 240mm long, at various stages of the process described above.

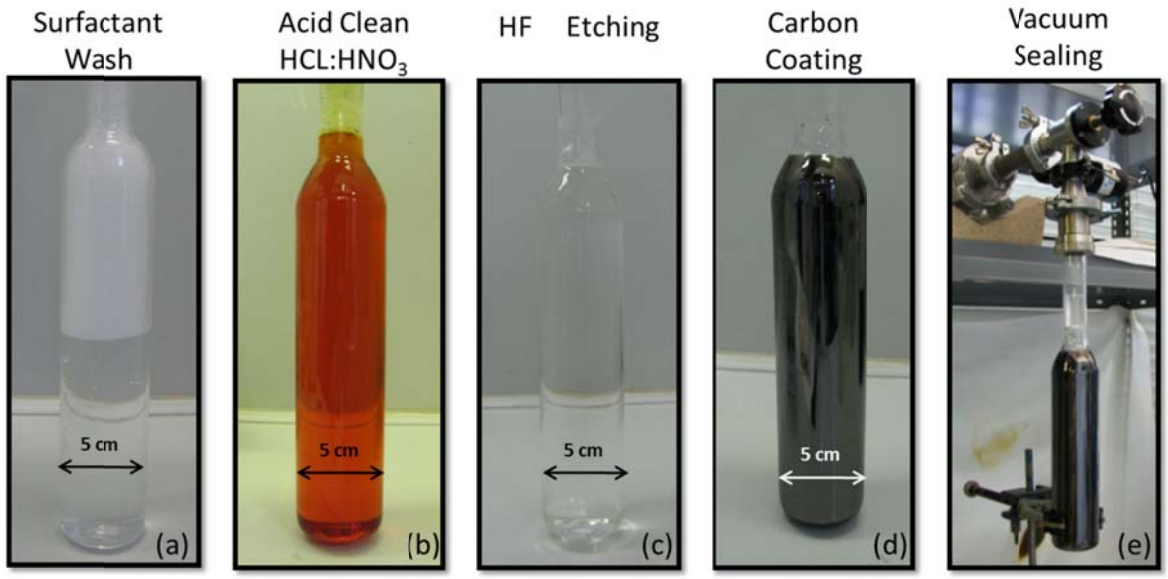

Figure 19 Ampoule preparation for carbon coating of quartz. (a) Ampoule being cleaned with Alconox detergent, (b) acid cleaning using $HCl:HNO_3$ solution, (c) quartz etching using HF acid, (d) after carbon coating, and (e) after charging with Cd(Zn)Te the ampoule is immediately placed under vacuum.

2.3.4 Carbon Film Characterization

The thickness of the carbon films were measured using secondary electron images from a Scanning Electron Microscope (SEM) Hitachi S-3000N, coupled to an energy dispersive X-ray (EDS) analyzer by Oxford Instruments, INCAx-sight model. Energy dispersive X-ray analysis confirmed the location of the carbon on the quartz (SiO_2). The quartz ampoule was cut open, and small shards from various axial positions were cleaved. Only pieces from the first 8 cm were chosen, as these are the regions in which crystal growth and melt interactions take place. Representative images for the study are presented below in **Figure 20**. In general, the data suggests: (1) The thickness of each film can be controlled by controlling quantity of hydrocarbon (i.e. Acetone), (2) The morphology of the film has been improved, exhibiting planar smooth surfaces instead of polyp shaped formations associated the open carbon coating

approach, and (3) The density of each film is increased due to lower growth rates and increased 2-dimensional growth

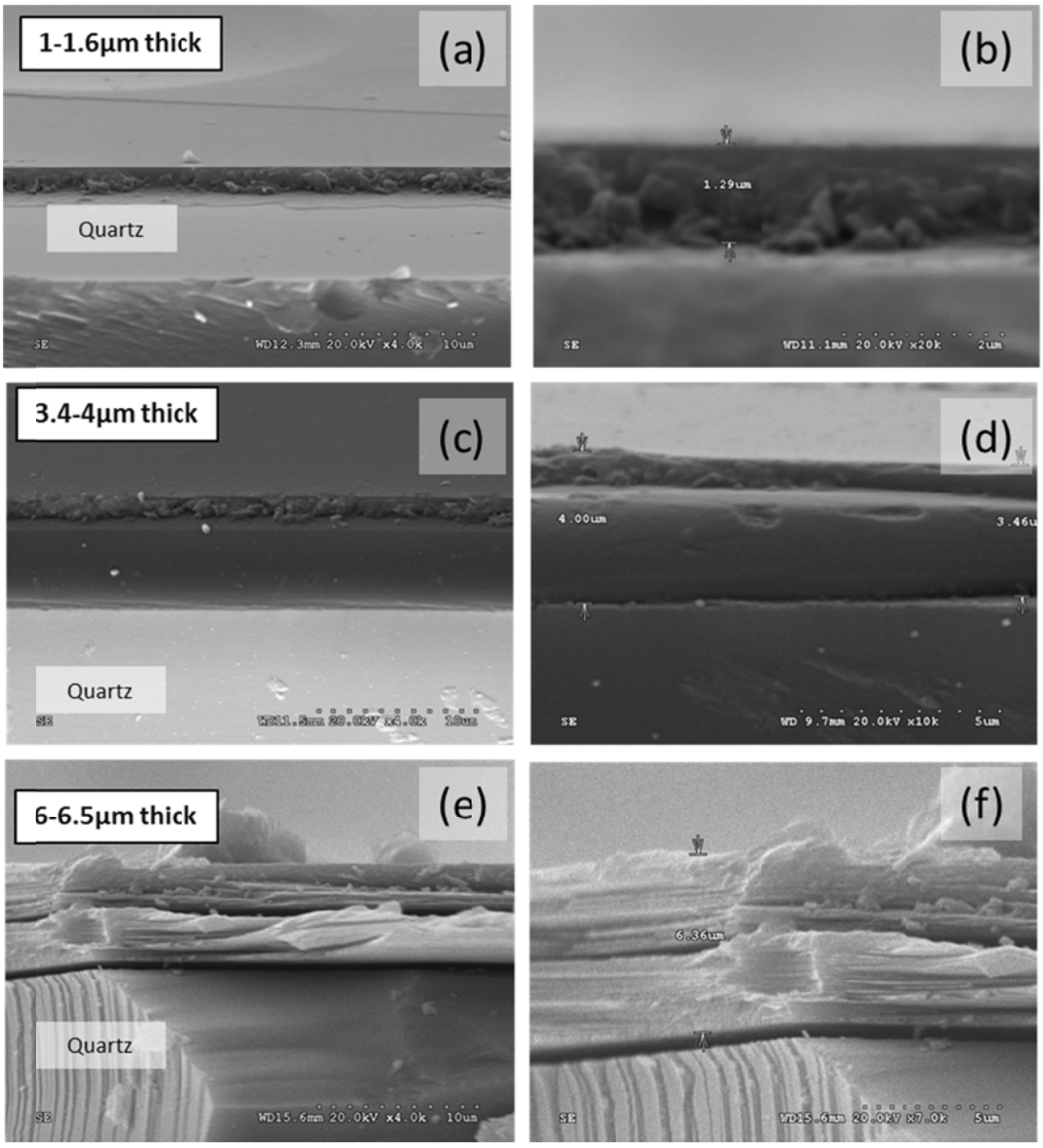

Figure 20 SEM Images of carbon coated quartz ampoules with thicknesses of (a) 1-2µm, (b) 3-4µm, and (c) 6-7 µm

The surface area of the carbon coated region of each ampoule was measured after each experiment. For a known volume of Acetone used in the deposition experiment, the data could be normalized to the volume of acetone used per unit aria or mL/cm. This was to correlate the measured thickness of the carbon film deposited with the known quantity of acetone used.

Because the system could be normalized, it would also help for calculating carbon film thicknesses of arbitrary geometries, larger size ampoules, or on materials in which cross sections may be difficult to measure. However, it was observed that the thicker coatings (6μm) tended to exhibit a substantial degree of flaking and the adhesion of the film to the quartz surface was not as robust as desired.

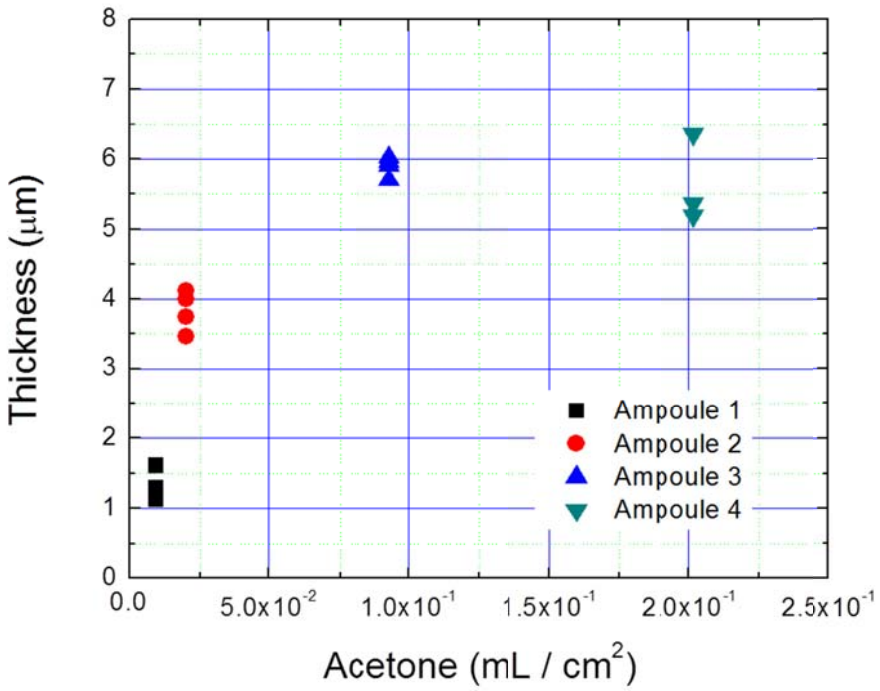

Figure 21 Thickness of carbon coating as a function of the normalized hydrocarbon quantity (mL / cm^2)

A system for carbon coating has been designed, tested, and the results of carbon films grown using this system are presented. Control over the thickness of the carbon film has been demonstrated, and films as thick as 6μm have been grown. In this thesis this system has also been used for carbon coating both quartz and pBN crucible materials.

This page intentionally left blank.

3 DEVICE OPERATION AND MEASUREMENT

Section Contents

3.1 Experimental Apparatus

To minimize the effects of temperature variations on leakage current in Cd(Zn)Te based detectors, the temperature within the room where measurements were made was controlled and maintained at 20º C at all times. Presented in **Figure 22** is the experimental fixture used for mounting Cd(Zn)Te radiation detectors and connecting with the A250 pre-amplifier for measurement. The (4) PCB boards each contain the FET and A250 charge sensitive pre-amplifier. The cathode of a detector was connected to high voltage, while the anode of the detector was connected using a short wire to the input of the FET.

On the walls of the fixture are BNC connections used for connecting the cathode of the detector to the bias voltage and for connecting the output of the A250 pre-amplifier with the input of the Ortec Dual Spec Amp 855 post-amplifier. All connections were made using 50 Ω coaxial cables, with BNC terminations. These are all important considerations to ensure there is impedance matching between all connections and to avoid reflections in the cable.

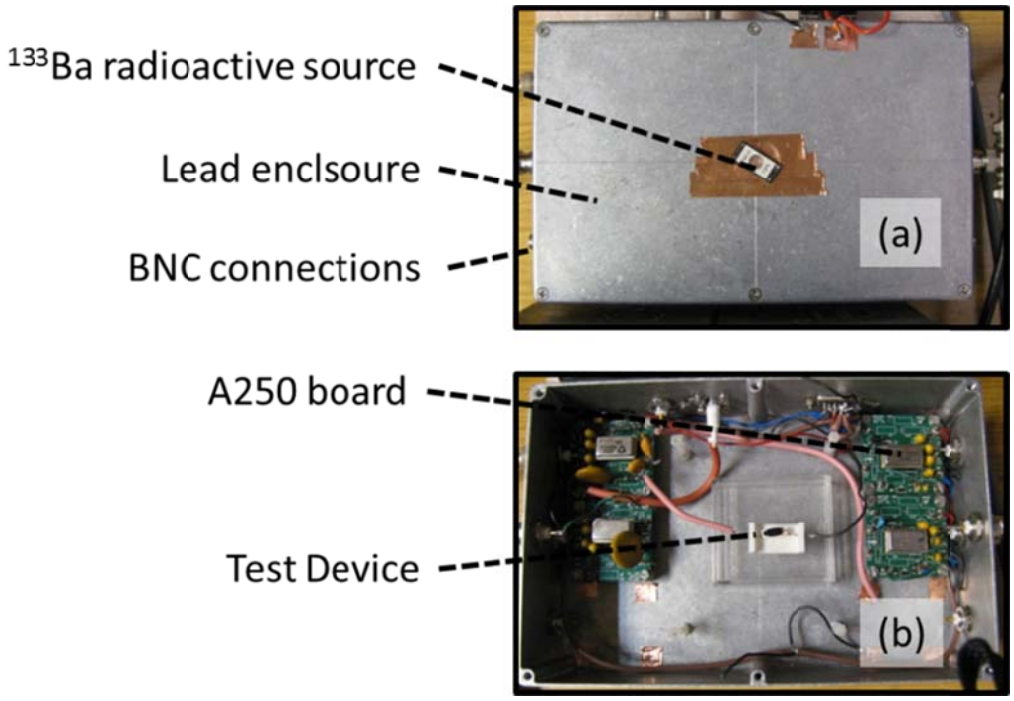

Figure 22 Experimental configuration for gamma measurement (a) lead enclosure closed during measurement and (b) lead enclosure opened showing the various electronic components used for measurement

Detector measurements were carried out in pulsed detector modes, as opposed to current modes or mean square voltage (MSV) modes. For this mode to function properly, it is important

that the time constant of the charge sensitive preamplifier is substantially larger than the time constant of the detector.

The detector itself was mounted on a custom Teflon fixture with a gold coated mounting plate (anode) and was contacted using a gold cantilever (cathode), presented in **Figure 23**. This test fixture was designed and built in this investigation for both I-V and spectroscopy measurements. The Teflon fixture was placed within a lead test box with each electrode connected to an AMPTEK A250 preamplifier.

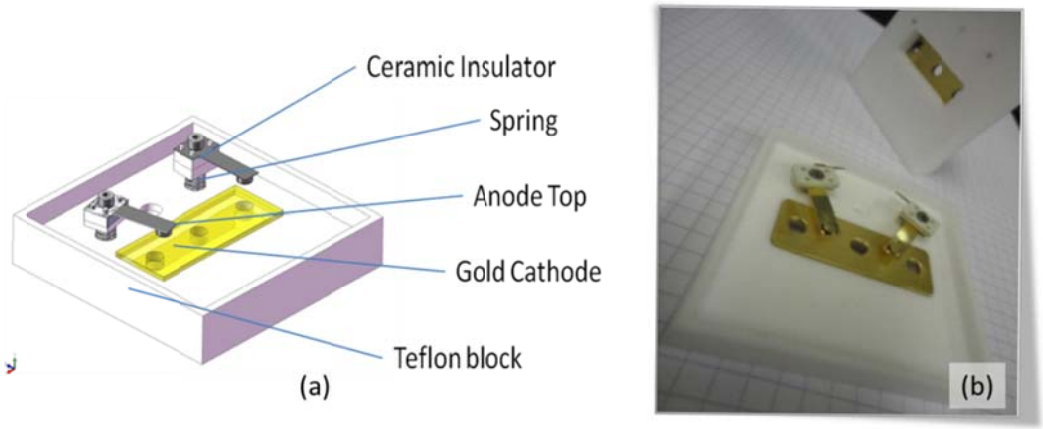

Figure 23 Detector test fixture used for characterizing material quality for planar detectors.

3.2 Measurement Considerations

Several experimental considerations must be given for the measurement of solid state detectors. From the mechanical point of view, these considerations include appropriate shielding and enclosures using absorbing materials. However, there are several considerations which must also be made for minimization of electronic noise in a system used for such precise measurements.

One important parameter has to do with the electronic noise introduced by the detector into the electronics. N_{tot} is the total noise introduced by the detector into the measurement system. N_i is the noise generated due to leakage current of the device, and can be minimized by selecting detectors with high resistivity, or even by lowering the temperature of the detector and FET. N_c is the noise due to detector capacitance, cable capacitance, and stray capacitance, and may be reduced for example by using a short connection between detector and pre-amplifier, or by using

low capacitance coaxial connections. These factors are related to the total noise by Equation 3. Indeed, methods to reduce this electronic noise have been investigated in Chapter 4, Section 4 for real radiation devices.

Equation 3 $$N_{tot} = \sqrt{(N_i^2) + (N_c^2)}$$

The type of Field Effect Transistor (FET) used in the measurement system also plays a role in the electronic noise. Actually, nearly all the noise generated in the FET + A250 preamplifier arrangement is due to the FET. The FET noise performance as a function of detector capacitance and shaping time constants in the post amplifier are usually given in the specifications, and the FET should be matched to the detector and to the application. In general, it is common to choose a FET with large trans-conductance, while matching the FET input capacitance to the detector capacitance. A large trans-conductance ensures the current flowing into the FET is efficiently changed into a voltage pulse. The FET used for all measurements presented here was the FET ID 2SK152. The dependency of noise in the A250 module on parameters such as FET package, detector capacitance, and shaping time in the post-amplifier are presented in **Figure 24**. These results show that for low capacitance materials, such as high resistivity Cd(Zn)Te which has a Capacitance on the order or 2 pF, the 2SK152 is a suitable FET and results in the lowest noise introduced into the measurement system.

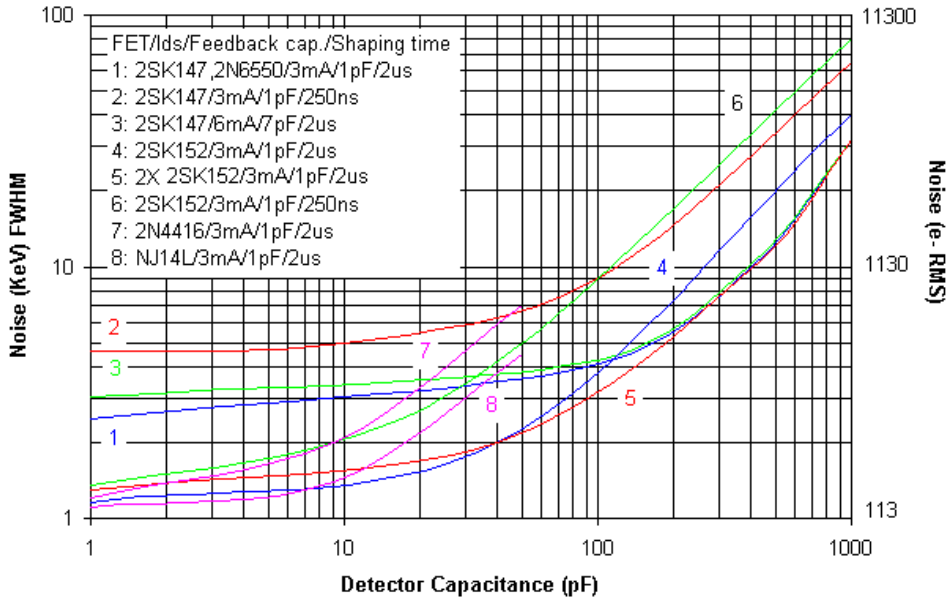

Figure 24 A250 Noise, measured in FWHM (KeV) as a function of detector capacitance.

The preamplifier feedback resistor is another integral component of the A250 pre-amplifier package. The resistor is placed in parallel with the feedback capacitor. This resistor serves as a source of noise in the electronics, and for this reason, should be as large a resistor as possible. In the A250 package, the internal feedback resistor is 300 Mega-ohms.

The post amplifier and its shaping time constant are yet another integral system component which influences the electronic noise in the system. For room temperature measurements of solid state detectors typical shaping time constants are between 0.5 and 3 μ-seconds. For lower temperature measurements, the shaping time is increased. The effect of shaping time on the electronic noise is presented somewhat qualitatively in **Figure 24**. By comparing lines 4 (blue) and 6 (green), the effect of decreasing the shaping time from 2μs to 250ns results in an increase in RMS noise by a factor of 2-3. This also depends on the device capacitance.

Additional considerations to reduce noise may include lowering the temperature of the detector-FET package in order to reduce leakage current and capacitance in the detector while increasing the trans-conductance of the FET. To achieve this, thermoelectric or even cryogenic systems can be used, however such methods were not employed for the investigation presented here.

3.2.1 A250 Noise Calibration

The A250 pre-amplifier used for signal amplification in the gamma ray spectroscopy measurements has been tested for electronic noise. Presented in **Figure 25** is the circuit diagram for the experiment. This was achieved experimentally using an Ortec 814FP to pulse a small test capacitor, which in turn injects a small quantity of known charge to the input of the A250 preamplifier. The A250 charge-sensitive pre-amplifier and the post amplifier are tested together, as the noise characteristics of the A250 pre-amplifier are associated with the timing constants which are used in the post amplifier. The post amplifier is used not only for amplification of the A250, but also functions as a band-pass filter to block unwanted frequencies. The post amplifier used in this work was the Ortec Dual Spec Amp 855. A Tektronix DP04104 oscilloscope was used for verification and accurate measurement of the pulse height of the 814FP.

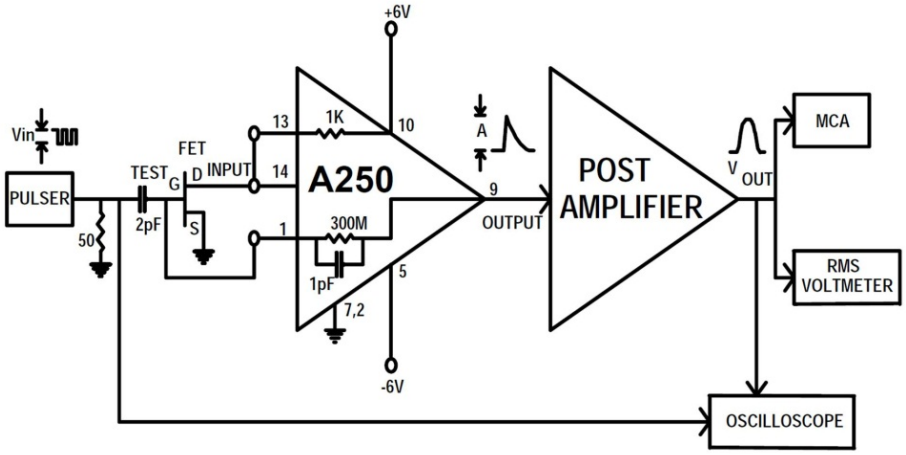

Figure 25 Electronic noise measurement circuit diagram. From left to right: The 814FP pulser injects a pulse onto the test capacitor. The A250 pre-amplifier responds to this charge via an FET at the input. The output of the A250 is shaped in the Post amplifier, whose output is read by the MCA card.

For solid-state detectors, there is a linear relationship between the deposited energy of an incident gamma ray and the number of electrons generated within the material. This relationship may be expressed for Cd(Zn)Te detectors using **Equation 4** where $\boldsymbol{x}$ represents the number of generated electrons and $\boldsymbol{y}$ represents the energy of the incident gamma ray. The parameter $\boldsymbol{E_{e-h}}$ is describes the energy for generating an electron-hole pair in Cd(Zn)Te, and takes a value of 4.64 eV. Not all of the incident gramma ray energy produces ionized electrons, but also interacts with the crystal lattice. Therefore, there is also some dependence of this parameter on temperature.

Equation 4 $$\boldsymbol{x \cdot E_{e-h} = y}$$

For the experimental methods used for calibration described above, it is important to select a test pulse which will induce the same charge on the test capacitor as the gamma ray would introduce in the bulk material. Therefore, the total amount of charge induced by a gamma ray must first be calculated in order to determine appropriate test pulse amplitude.

From the relationship presented in **Equation 4**, the total charge induced by an incident gamma ray with energy $\boldsymbol{650\ keV}$ may be calculated by solving for the total number of electrons generated by a $\boldsymbol{650\ keV}$ gamma ray. Multiplying the total number of electrons by their elementary charge yields the total induced charge, following **Equation 5**.

Equation 5

$$\boldsymbol{Q = \frac{650\ keV}{4.64\ eV} \cdot e \approx 140{,}000\ \cdot 1.60217 \cdot 10^{-19}}$$

From this relationship, it is possible to determine the test pulse amplitude injected into the test capacitor to simulate an incident gamma ray with an energy of $650\ keV$. This number was chosen based on the desired operation characteristics of the COCAE detector, described in Chapter 1. Using Equation 6, the induced charge may be expressed as the product of the pulse height of the pulser measured in mV, and $C_t = 2pF$ is the capacitance of the of the test capacitor which injects charge into the charge sensitive pre-amplifier.

Equation 6

$$\boldsymbol{Q = V \cdot C_t = 22.4 \cdot 10^{-15}}$$

Therefore, the pulse height required to produce a total charge $22.4 \cdot 10^{-15}\ C$ using a test capacitor with capacitance $C_t = 2pF$ to inject charge into the charge sensitive pre-amplifier is $V = 11.2\ mV$.

The output of the A250 preamplifier was connected to an Ortec Dual Spec Amp 855, with a shaping constant of 1.5μs. The post amplifier was connected to the input of the Multi-Channel Analyzer (MCA). Using the 814FP Pulser as the input, a spectra of the pulse could be obtained. Using the APTEC software package for analysis of spectra acquired using the MCA card, the FWHM of the test pulse could be calculated.

Presented in **Figure 26** are the spectra obtained for 0 V and 400 V applied to the FET shown in **Figure 25**. The value of 400 V was selected because it is an average working potential used with the system in gamma ray spectroscopy, and it is a more practical to measure noise in the A250 preamplifier under normal working bias.

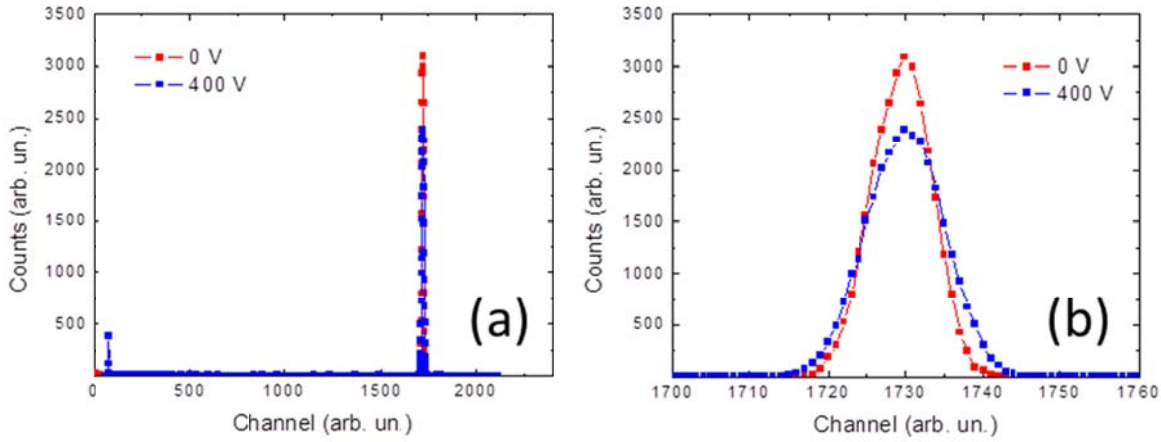

Figure 26 Spectra acquired using Ortec 814FP Pulser to simulate 650 keV gamma ray.

Each spectrum was acquired using APTEC software in order to derive the FWHM of the pulse at 0 V and at 400 V bias. The FWHM for 0 V bias was 0.54% or 3.51keV, while the FWHM for a 400 V bias was 0.7% or 4.55keV. The formation of charge can be considered a Poisson process and for N charge carriers, and can be related to the FWHM using **Equation 7**. The electronic background noise level for the instrumentation used for gamma ray spectroscopy has therefore been determined to be 322 e^- and 417 e^- with respect to each biasing condition.

Equation 7 $$\boldsymbol{\sigma = \frac{FWHM}{2.35}}$$

3.2.2 Planar Test Device Measurement

Understanding the electrical circuitry used in the measurement of Cd(Zn)Te based radiation detection devices is of great importance for correctly understanding the behavior of measured devices. Presented below in **Figure 27** is a diagram of the electronics used for testing planar Cd(Zn)Te devices in this work.

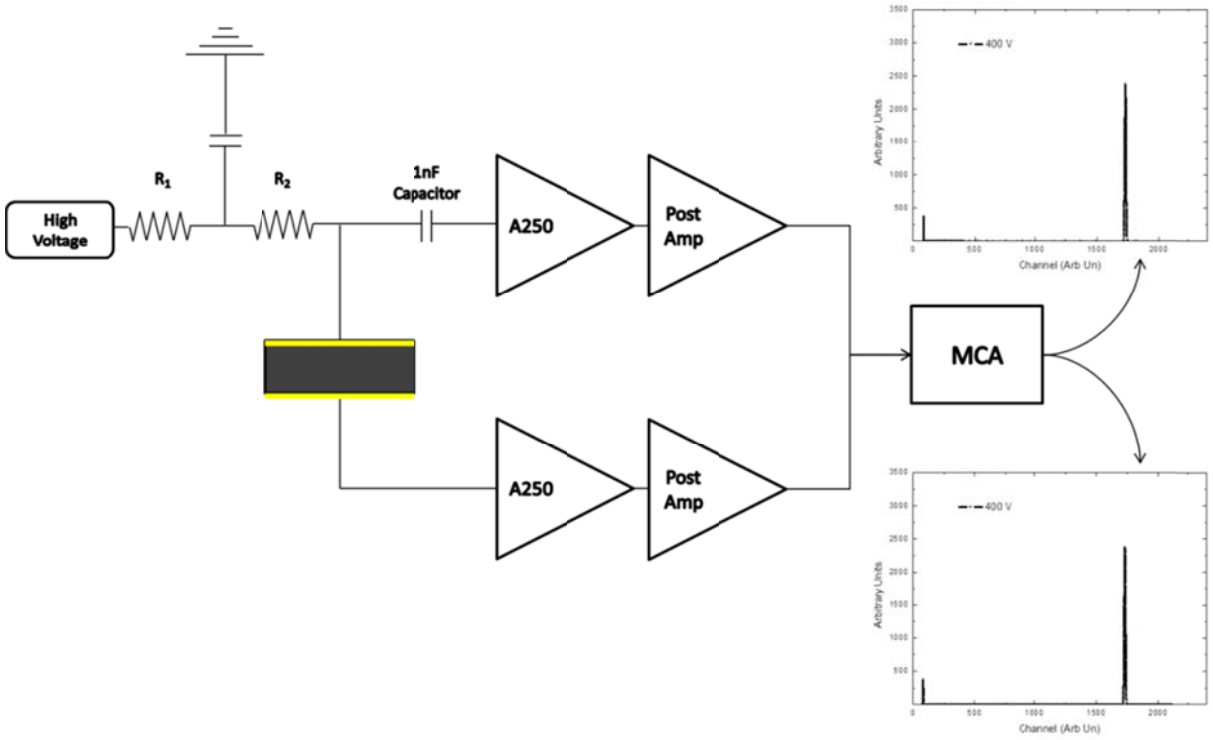

Figure 27 Experimental arrangement and electrical circuit for testing planar Cd(Zn)Te gamma ray devices.

For this experimental arrangement, a high voltage power supply is connected to the cathode of the Cd(Zn)Te device and the radiation source is placed such that the high energy photons enter the device through the cathode. The working voltage for each device varies, to some degree depending on device quality, but typical electric fields between 1000 and 3000 V / cm are common.

Charge is deposited into the Cd(Zn)Te device by the high energy photons through various interactions such as photoelectric absorption and Compton scattering processes. The test devices used in this work were studied using a 1μCi radioactive ^{133}Ba source. This value corresponds to 37,000 Bq which has the units of sec^{-1}. Indeed, this represents the number of decays which occur every second and is the activity of the material.

For each 4.64eV of energy deposited into the Cd(Zn)Te device, an electron-hole pair is created. This is the ionization energy for Cd(Zn)Te and varies for different semiconductors. The electron hole pair each in turn drifts under the influence of the external electric field towards the anode and cathode respectively. The motion of this charge under the influence of an electric field gives rise to current within the device. However the energy deposited is proportional to charge, which is the integral of current. Therefore, the charge sensitive A250 preamplifier

produces a voltage step which is directly proportional to the integral of the current produced in the device.

This process of integration is demonstrated graphically in **Figure 25**, where the current produced by an 81keV photon (i.e. of ^{133}Ba) in a 2mm thick Cd(Zn)Te device under an applied electric field of 3000 V/cm has been simulated. In the ideal scenario, the total current produced within the device would be the sum of the current produced by both motion of electrons (52.5nA) and holes (4.67nA). Under normal operating conditions, however, the current pulse exhibits decay due to several factors including trapping and scattering of the charge by defects and impurities in the crystal.

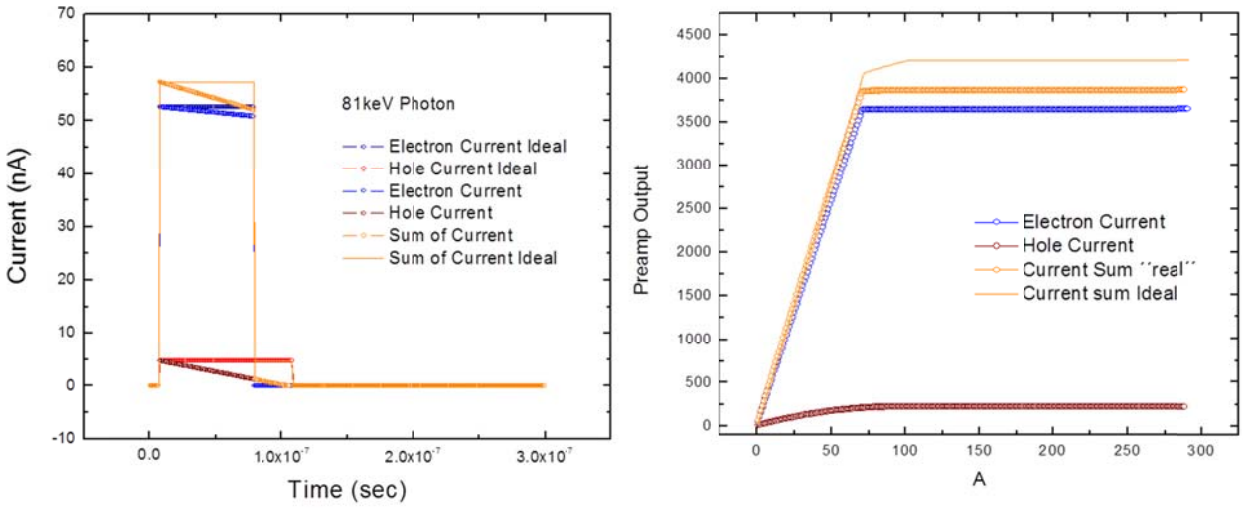

Figure 28 (Left) Current produced by electron-hole drift after photon interaction in device (Right) Voltage step produced by charge sensitive preamplifier, which is proportional to deposited energy.

The step voltage output by the A250 preamplifier is then sent to the linear amplifier. To preserve the amplitude of the preamplifier pulse, the shaping constant must be large compared with the preamplifier rise time. The difference between the pulse shape amplitude using a finite shaping time constant and using an infinite shaping time constant is referred to as the ballistic deficit. Amplified pulses can then be sorted and binned by the Multi-channel Analyzer for generation of gamma spectra.

3.2.3 Charge Collection Efficiency & Interaction Depth

For test devices with planar symmetric electrodes, the charge induced by the electron and holes on the anode and cathode is equal. Using the Hecht equation, which is presented in **Equation 8**, the charge collection efficiency, Q^*, at the anode/cathode may be related to the velocity (ν) and lifetime (τ) of the electrons and holes within the Cd(Zn)Te matrix. For planar test device geometries, the charge induced on the surface of the anode and cathode is equal.

Equation 8

$$Q^* = e \cdot N_0 \left[\frac{v_h t_h}{W} \left(1 - \exp\left(\frac{-x_i}{v_h t_h} \right) \right) dx_e + \frac{v_e t_e}{W} \left(1 - \exp\left(\frac{W - x_i}{v_e t_e} \right) \right) \right]$$

For the simple case where electron and hole mobility lifetime products are equal, and for planar test device geometries, optimal charge collection efficiency, or CCE, occurs for electron-hole pairs generated in the center of the detector, equidistant between the anode and cathode. For increasing detector width, W, the CCE decreases as trapping and recombination processes start to play a larger role in charge loss. This is illustrated graphically in **Figure 28**(a), where the electron and hole currents slowly decay throughout the current pulse. For increasing electron and hole mobility lifetime product, however, comes increasing CCE.

For Cd(Zn)Te materials, the difference in the electron and hole mobility-lifetime products has been reported to be up to two orders of magnitude. In such a case where the $\mu_e\tau_e$ product of is significantly larger than the $\mu_h\tau_h$ product, the Hecht relation also proves useful. Presented in **Figure 29**(b) is the CCE calculated using a 3000 V/cm electric field, for various ratios of $\nu_e\tau_e$: $\nu_h\tau_h$. The value of $\nu_h\tau_h$ used in these calculations was kept constant at $6\text{x}10^{-6}$ cm^2/V, and the value of $\nu_e\tau_e$ was increased through a range of values. From this data it is also clear how the charge collection efficiency is strongly limited by the poor $\nu_h\tau_h$ product of the holes. As a result, the maximum in the CCE is shifted towards the cathode of the device due to the increasing $\nu_e\tau_e$ product. What this means is that events occurring near the cathode are more readily detected than events occurring near the anode.

The depth of interaction is therefore of paramount importance for compound semiconductors such as Cd(Zn)Te for which the poor $\nu_h\tau_h$ product of the holes limits ultimately the CCE. Presented in **Figure 30**(a) is the attenuation coefficient for Cd(Zn)Te as a function of incident photon energy up to 100keV. For photons with an energy of 31keV, the attenuation coefficient

of Cd(Zn)Te is near 19.7 cm^2/g. For higher energies near 81keV however, the material is more transparent as the attenuation coefficient is near 2.55 cm^2/g (2).

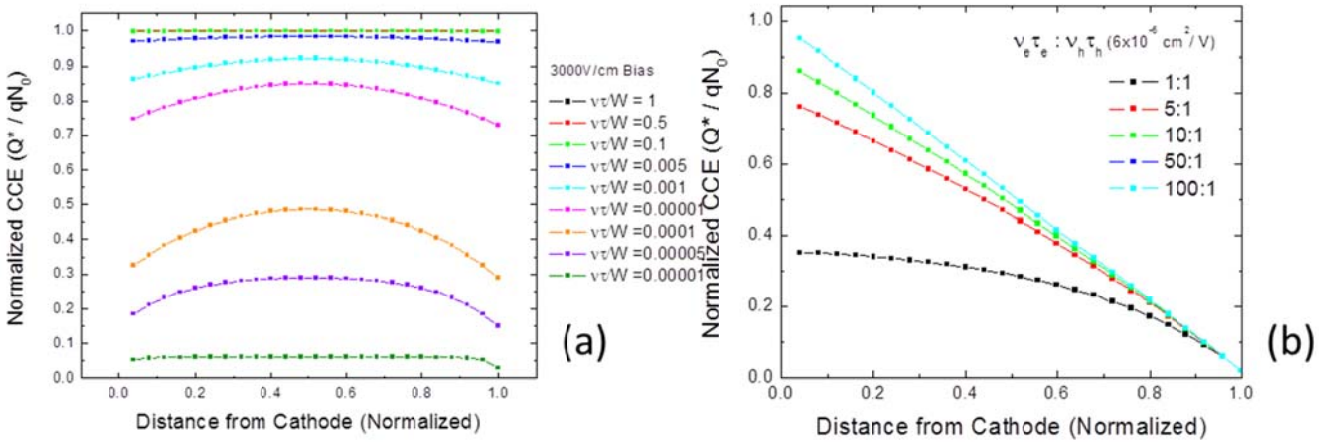

Figure 29 Left: Charge Collection Efficiency for case were electron and hole mu-tao products $\mu_h\tau_h = \mu_e\tau_e$ plotted for various ratios of $v\tau/W$. Right: Charge Collection Efficiency for material with non-equal electron and hole mu-tao products $\mu_h\tau_h \neq \mu_e\tau_e$.

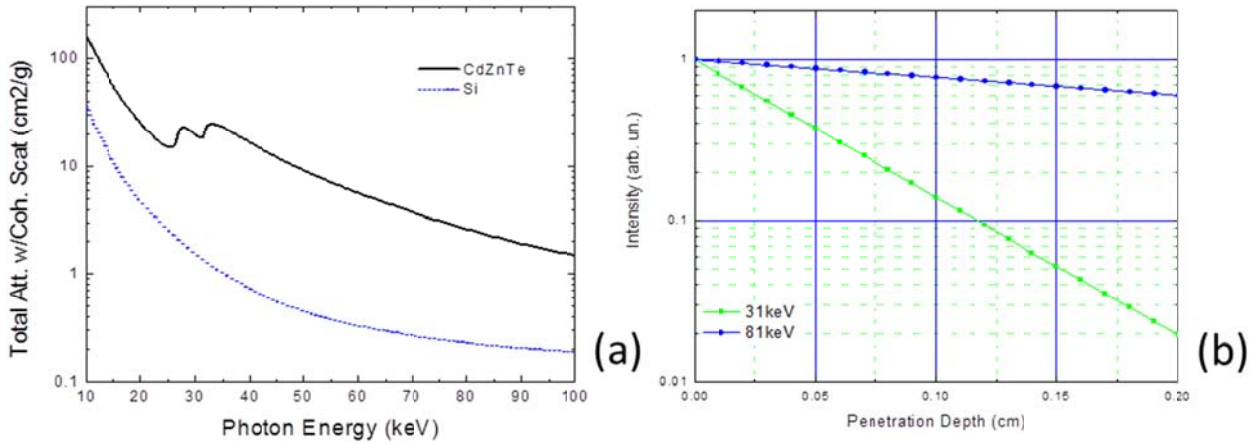

Figure 30 (a) Attenuation Coefficient for Cd(Zn)Te as a function of photon energy. The attenuation coefficient of Si is included for comparison. (b)Attenuation of 31keV (green) and 81keV (blue) photons in Cd(Zn)Te.

Using **Equation 9**, dependence of attenuation (α) on the intensity of radiation passing through Cd(Zn)Te may be determined. Attenuation of 31keV and 81keV photons in Cd(Zn)Te is presented in **Figure 30**(b), using the attenuation coefficients obtained from the data in **Figure 30(a)**. It is interesting to note that within the first 0.2 cm the intensity of the 31keV is reduced by nearly 2 orders of magnitude, whereas the intensity of the 81keV reduces by less than a factor of 2.

Equation 9 $$\boldsymbol{I = I_0 \cdot exp(-\alpha \cdot x)}$$

This page intentionally left blank.

4 EXPERIMENTAL CHARACTERIZATION TECHNIQUES

Section Contents

4.1 Introduction

The use of several advanced characterization techniques has been necessary for the study of the electrical, optical, and structural properties of Cd(Zn)Te. This section presents a brief technical description of the experimental methods, measurements, and theory used throughout this work. The techniques have been divided into three classes corresponding to microscopy methods, spectroscopic methods, and methods used for characterization of the electrical properties.

4.2 Microscopy Methods

4.2.1 Infrared and Optical Microscopy

A Nikon 90i Microscope was tested, purchased, and implemented during the course of this investigation specifically for optical characterization of both bulk and surface properties of Cd(Zn)Te detector materials. Presented in **Figure 31** is the microscope used for this work. This system was comprised of two distinct light sources for illuminating from the top and back side of the specimen. Several different objectives were used for the characterization of surface and bulk properties, ranging 1x magnification to 20x magnification. Furthermore, a 3-axis motorized stage with stepper motor functionality was used extensively for producing 2-D optical surface mappings.

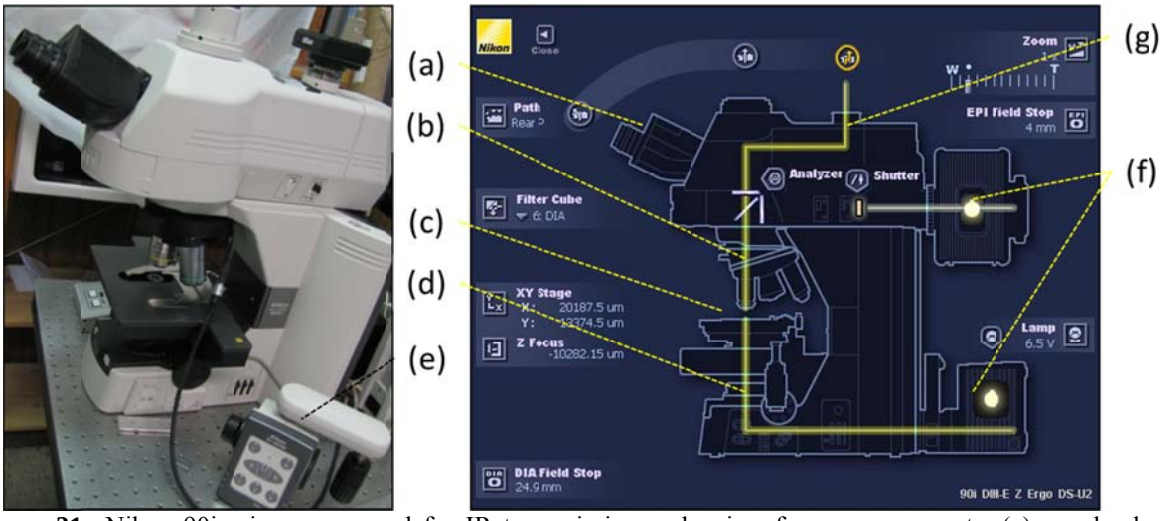

Figure 31 Nikon 90i microscope used for IR transmission and epi-surface measurements. (a) occular lens (b) objective turret and objectives (c) Frame (d) condensor lens (e) stage controller and focus wheel (f) light source (g) external camera.

Several cameras were evaluated in terms of their price and performance with respect to Cd(Zn)Te including a high performance Luca R 604 low-light imaging camera and a Rolera-ZR

NIR Digital CCD camera. The Nikon DS-Qi-1 camera was used for imaging. This is a 1.5MP camera, with integrated Peltier cooling to 10ºC lower than ambient. The image is displayed in 1280x1024 format, and the camera exposure time could range from 1msec to 600sec.

For evaluation of the surface morphology bright-field (BF), dark-field (DF), and phase-contrast filter cubes were purchased. In the BF imaging mode, differences in absorption at the surface of the sample is used for differentiating materials or features at the surface. This mode has been used in conjunction with the phase-contrast filter cube for imaging of surface morphology and surface roughness.

The DF optical configuration is a complementary microscopy technique which offers several advantages to the BF configurations. The principle advantage of the DF technique is due to the placement of an opaque disc below the condenser lens within the microscope objective. This opaque disc blocks the light directly reflected by the wafer surface from reaching the condenser lens, and ultimately the CCD. Only light which is scattered at oblique angles is able to pass into the condenser lens and through to the camera or ocular lens. As a result, this technique is highly sensitive to scattered light whether it is from scratches, particulates, or other surface non-uniformities. For surfaces which are very rough and exhibit a large degree of scattering, the differences between DF and BF microscopy are not as significant. However for more specular surfaces, DF mode is orders of magnitude more sensitive to scratches and particulate matter.

Te-inclusions present within the bulk have been studied using the transmission mode of the microscope. Presented in **Figure 32** are examples of the large variation of inclusions which have been measured in different samples. Indeed, though present in similar densities, the larger inclusions play a more significant role in reducing the overall charge collection efficiency of radiation devices. In the optical regime, the second-phase inclusions also act as scattering centers of the IR light, to which the Cd(Zn)Te matrix is transparent.

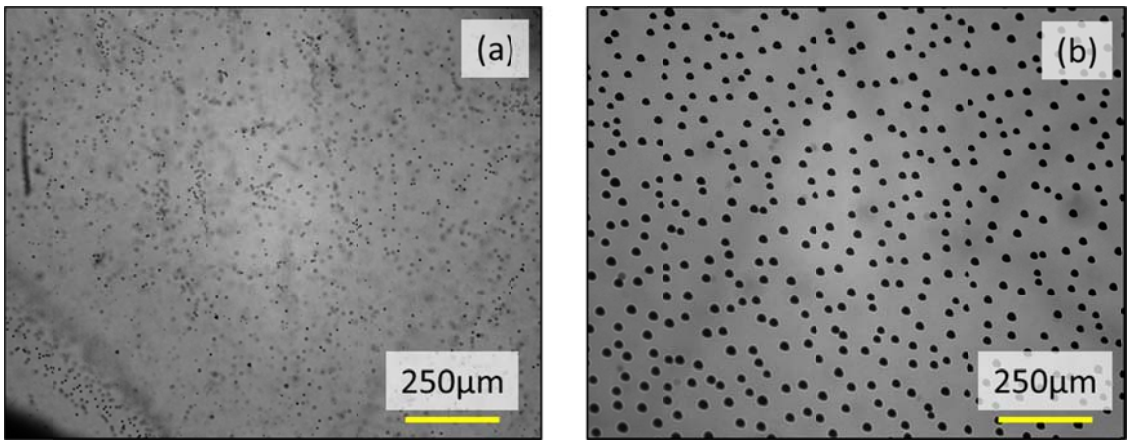

Figure 32 Te-Inclusions present in Cd(Zn)Te were present in a wide range of shapes and sizes. Presented here are Te-inclusion of (a) small diameter and (b) larger diameter.

The use of Nikon's NIS-elements software provided the capability to recognize and sort objects according to their size/diameter, providing a more quantitative analysis of the surface/transmission. Presented in **Table 1** is the algorithm applied to the samples presented in **Figure 32**. While the densities appear similar, the second sample exhibits a larger diameter of the inclusions. This software has also been applied for the analysis of Te-Inclusion densities associated with the superheating processes investigated in Chapter 3, Section 1, and for the analysis of surface contamination introduced during surface preparation which is presented in Chapter 4, Section 3. This experimental technique was extensively used for preliminary material characterization and evaluation, in conjunction with resistivity mapping data, for selection of the highest quality materials from which to fabricate radiation devices.

Table 1 NIS-Elements software used for characterization of Te-Inclusions in Cd(Zn)Te providing information on the density, and meen diameter for a given sample area.

Sample	Precipitates	Histogram Data	Te Density (cm^2)	Mean Diameter (micron)
(a)	254	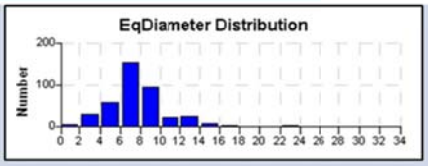	2.54×10^5	6
(b)	428	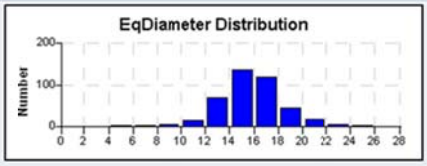	4.28×10^5	16

4.2.2 Cathodoluminescence

Cathodoluminescence (CL) is a surface sensitive characterization technique used for studying the electrical and optical properties of materials. The method relies upon (1) excitation of surface and bulk states using an energetic beam of electrons, and (2) the subsequent decay of these occupied surface states to and the emission of photons in the optical region and (e) selection, detection, and amplification of the analog signal produced by these photons.

A diagram of the CL instrument is presented below in **Figure 33**. The CL instrument in its reduced form consists of an electron gun, an elongated beam path for beam refinement focusing and scanning, a sample surface used for producing the luminescence, a coated parabolic mirror for recollecting the luminescent photons, a monochromator for energy selection, a detector sensitive to the energy range of interest, and a signal amplification system. As can be seen, even in CL secondary electrons and backscattered electrons are produced, however these emissions are not detected as the image is produced only by the luminescence of the surface states. By changing the monochromator settings, the luminescence intensity as a function of energy may be determined.

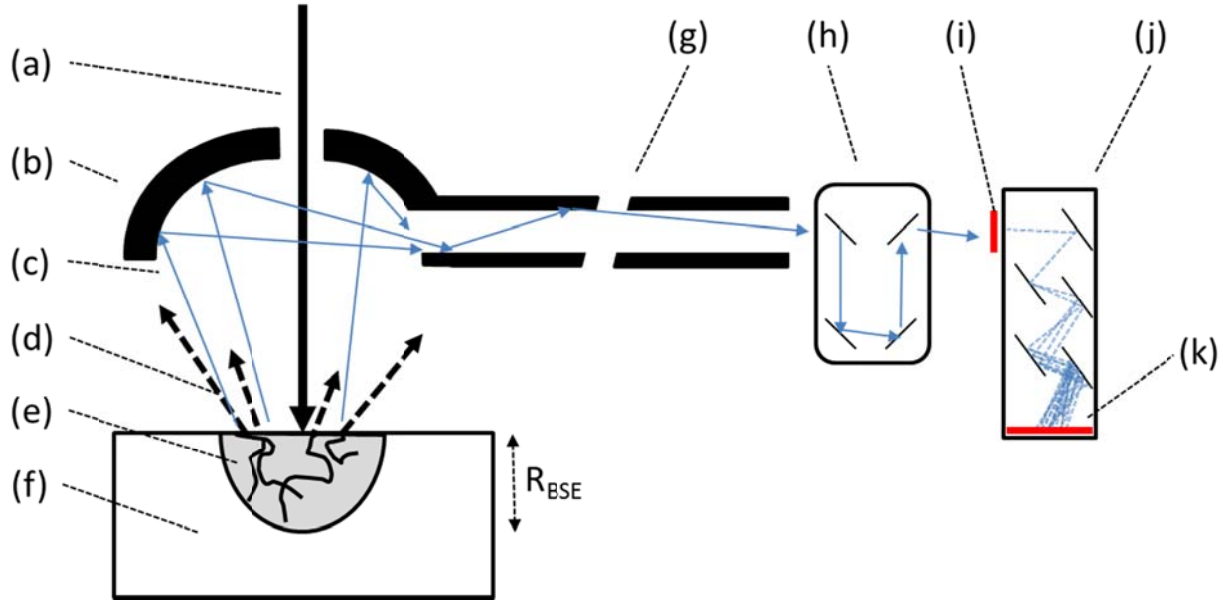

Figure 33 Schematic diagram of cathodoluminescence technique consisting of (a) electron beam, (b) parabolic mirror with pinhole pass-thru for electron beam, (c) photons produced by luminescence of the sample surface, (d) back scattered and secondary electrons, (e) interaction volume of the electrons in the material, (f) sample, (g) fiber optic cable for coupling of parabolic lens to monochromator, (h) monochromator, (i) photo-sensitive material for producing electrons, (j) dynode, (k) collecting anode.

The electron gun consists of an electron source (via thermionic emission for example), a beam condenser (Wehnelt cylinder), and an anode plate for accelerating these free electrons

down the beam path. This beam bath normally consists of a condenser lens used to reduce the diameter of the electron beam, as well as scanning coils which electromagnetically raster the beam for producing 2D images. A final electromagnetic lens is used for reducing the spot size of the beam.

The accelerated electrons impinging on the sample surface will penetrate to some depth. This relationship between the depth of interaction and the energy of the electrons may be described the analytical expression presented in **Equation 10** where R is the radius of penetration into the sample, A is the atomic weight (mol^{-1}), Z is the atomic number, E is the incident energy in keV, and ρ is the density. In the case of Cd(Zn)Te, taking into account excitation was carried out under an acceleration of 20keV for all CL measurements, this corresponds to a penetration depth close to 1.3 μm.

Equation 10 $$R_{BSE} = \frac{0.007}{Z^{0.9}\rho} \cdot A \cdot {E_0}^{1.67}$$

The measurements presented in this thesis were realized using an FEI-INSPECT and a Hitachi 2500 Scanning Electron Microscope in conjunction with a R5509 Hamamatsu photomultiplier tube used for CL detection. Electrons were accelerated under a 20kV potential difference for producing luminescence. The Cd(Zn)Te samples were investigated at low temperatures, being cooled to a temperature of 90K. A typical CL measurement of the n-type Cd(Zn)Te material which has been investigated in this work is presented in **Figure 34**. As may be seen, this technique provides the ability to measure the presence/absence of electronic levels in the bandgap i.e. Energy < 1.6eV.

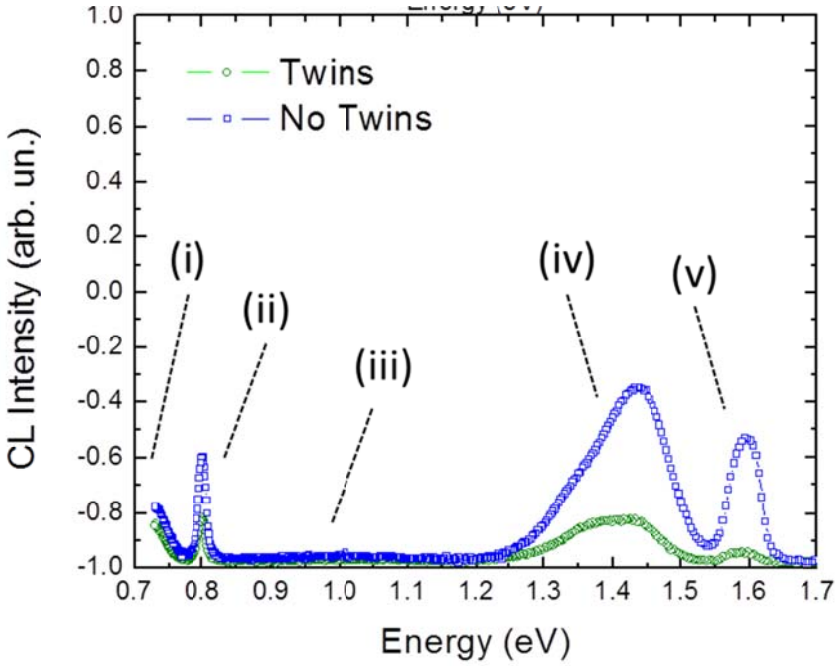

Figure 34 Typical CL spectra for n-type Cd(Zn)Te devices which have been grown in this work. Differences in the electronic properties of devices becomes evident through luminescent techniques such as CL. (i) Trap H associated with pinning of the Fermi level (ii) donor defect possibly associated with In in crystal (iii) donor defect possibly associated with ionized V_{Te} (iv) A-center, donor character (v) band to band transition.

4.2.3 Atomic Force Microscopy

Using a Park Systems XEI-100 Atomic Force Microscope (AFM), it is possible to image and measure sample surface roughness in both contact and non-contact mode. Presented in **Figure 35** is the AFM system used and a schematic diagram of the various system components. The AFM consists of a piezoelectric modulator which vibrates a small cantilever at a fixed frequency. As this cantilever is brought close to the sample surface, electrostatic interaction between the surface and cantilever changes the phase and amplitude of the oscillating cantilever. These changes are detected by the systems closed loop servo controller, which maintains a fixed distance between the sample surface and the cantilever tip. Sweeping of the cantilever across the surface of the sample produces individual line scans, each of which are assembled into images of the sample surface.

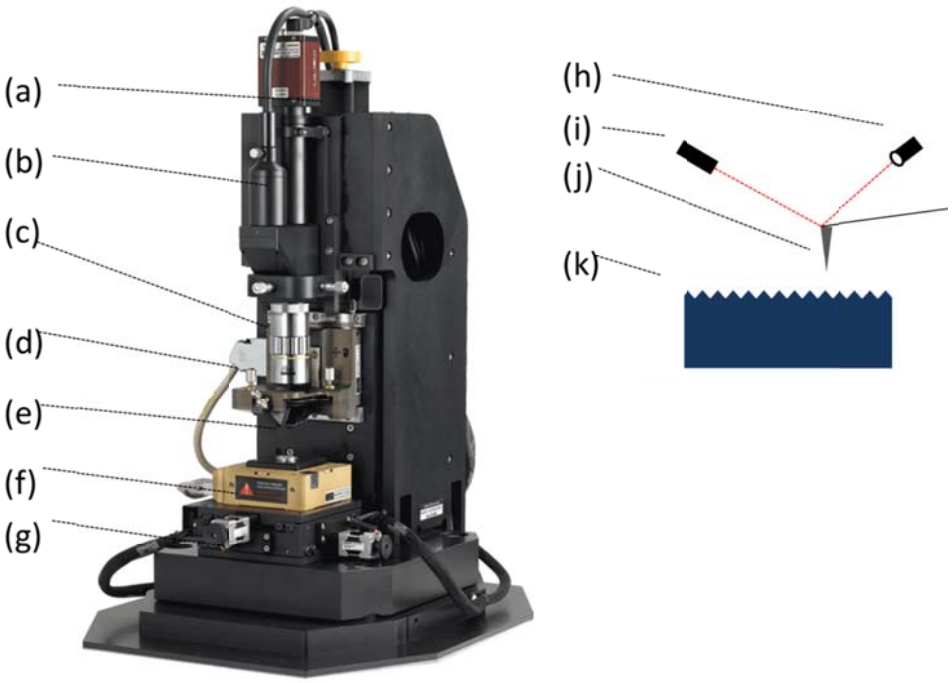

Figure 35 Parks XEI-100 AFM used in this work for investigation of morphology of Cd(Zn)Te. (a) Z-servo motor, (b) light source, (c) microscope objective, (d) laser diode course and fine adjustment knobs, (e) AFM tip, (f) x-y scanning stage, (g) x-y servo motors, (h) photodiode, (i) laser diode, (j) AFM tip with, (k) sample surface.

The AFM may be operated in contact mode or non-contact mode, both of which are determined by the cantilevers position with respect to the surface. The surfaces in this work have been primarily investigated using the non-contact mode of the atomic force microscope. The benefits of the non-contact mode atomic force microscopy include no tip wear, no sample damage, and improved accuracy of the AFM measurement. In addition, for the measurement of Cd(Zn)Te surfaces, the scan rate of the probe, the probe itself, as well as the size of the scan were all important consideration for obtaining good images, free from experimental artifacts. Presented in **Figure 36** are some commonly encountered artifacts which may be due to non-uniformities in the surface distorting the measurement or due to the mechanical scanning of the cantilever across the surface. Indeed, if the cantilever is scanning at a high frequency, when the tip of the cantilever encounters a protruding feature, the nuclear interaction will strongly deflect the cantilever and as a result will broaden the surface feature as can be seen on **Figure 36**(a).

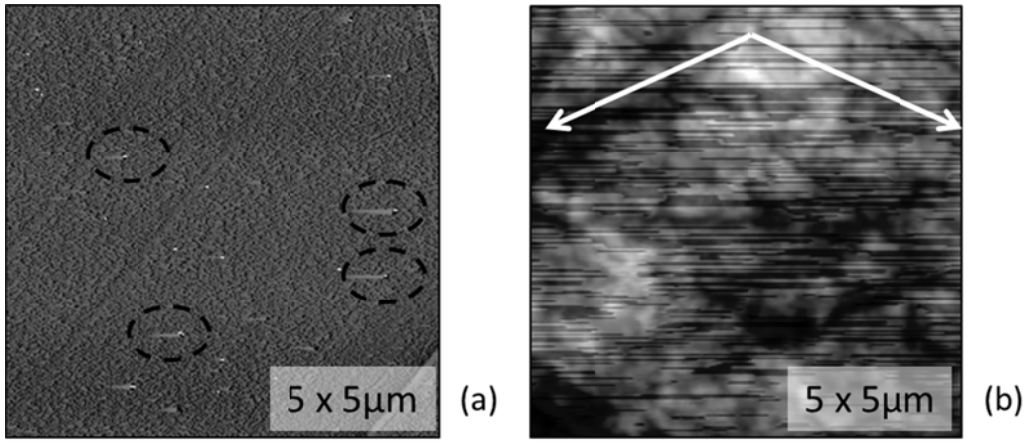

Figure 36 AFM scans which exhibit various kinds of experimental artifacts such as (a) ´´comet tails´´ associated with surface features (b) and artifacts associated with the scanning motion of the cantilever.

Using the contact mode of the AFM, it was not possible to obtain artifact free images of the Cd(Zn)Te surface. The non-contact probes used in this work were the DD-ACTA probe, manufactured by AppNano, and is presented in **Figure 37**. These non-contact tips were comprised of pyramidal shaped Silicon, with a 100nm boron doped diamond coating at the tip for improved hardness and electrical conductivity. Furthermore, the backside of the tip was coated with 30nm thick Al film to improve reflectivity and thus the laser signal on the photodiode. These tips are 35µm in width, 125µm in length, approximately 4 µm in thickness, and resonate at a frequency between 200-400kHz (3).

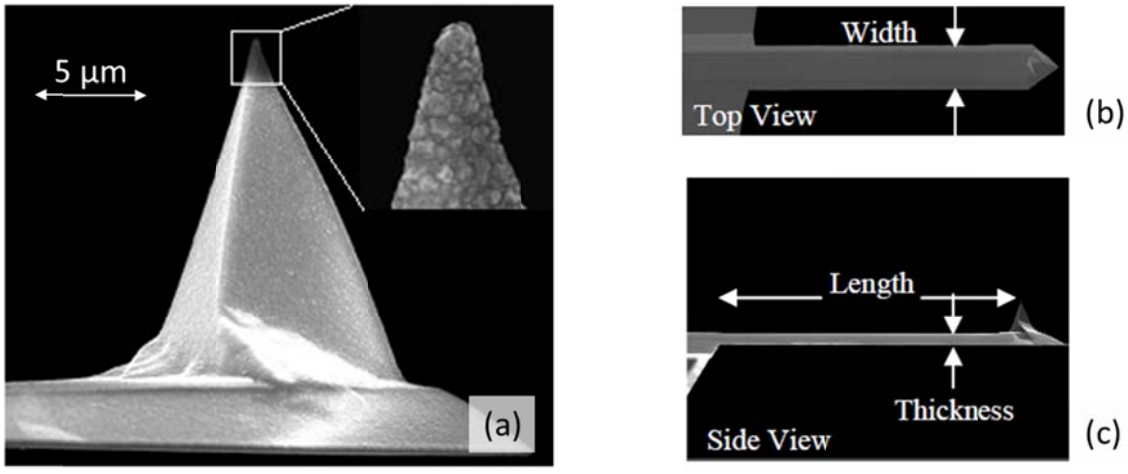

Figure 37 ACTA AFM tip which was used for producing high resolution AFM images of polished, etched, and prepared Cd(Zn)Te surfaces. (a)-(c) SEM images of AFM probe tip taken from (3).

Presented in **Figure 38** is a typical AFM image which has been constructed through the assembly of 1-D line-scans, to produce 2-D topographic data. To achieve such high quality images, the AFM was operated in non-contact mode, using a high resolution Non-contact ACTA AFM cantilever previously discussed, and using a scan rate between 0.1 - 0.3Hz. Despite the high density of surface features present in this particular sample, the broadening associated with tip-deflection was minimized.

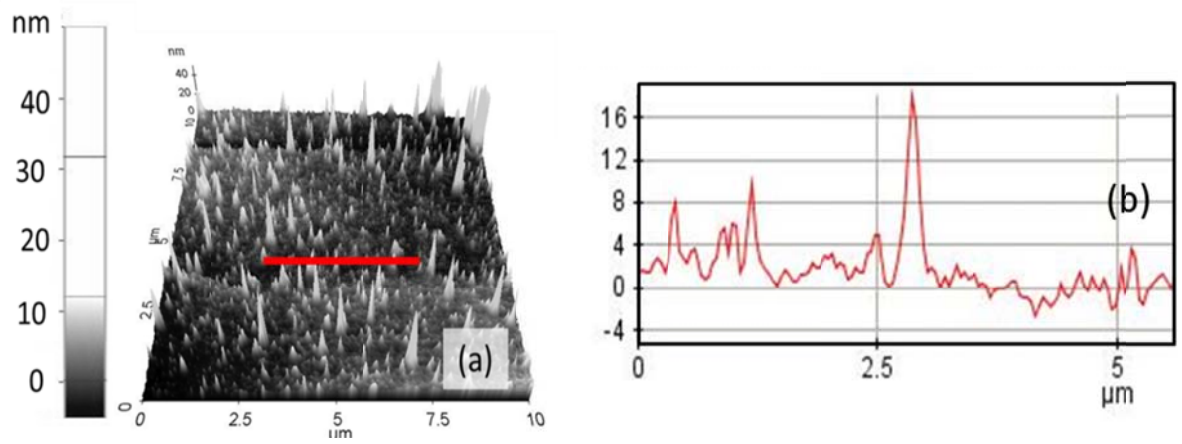

Figure 38 (a) 2-D topographic data produced by AFM from an array of (b) 1-D line scan of surface.

In general, the AFM is an industry standard for measuring the surface roughness, regularly reported over a 10µm x 10µm area, and is useful for measuring nanometer-scale surface features. Surface roughness is often characterized in terms of RMS roughness. For 1-D line scans, this may be represented following Equation 11 where R_{RMS} is and the term z_i represents the height of the i´th point of the line.

Equation 11

$$R_{RMS} = \sqrt{\frac{1}{n}\sum_{i=1}^{N}(z_i)^2}$$

4.2.4 Kelvin Force Probe Microscopy

The work function of Cd(Zn)Te surfaces were also investigated using Kelvin Force Probe Microscopy (KPFM) methods. These measurements were taken to analyze local changes in the surface work function associated with twinning and micro-scratch defects in the surface. The KPFM technique is based on the mechanical principles of AFM, however the work-function is measured by using the cantilever as the reference electrode that forms a capacitor with the surface of the semiconductor. The cantilever is scanned laterally across the surface, maintaining a constant offset from the surface. This constant offset is achieved by nulling the force induced by the changes in morphology.

Presented in **Figure 39** is the band diagram of a metal and a semiconductor before and after the cantilever and surface are in electrical contact. Indeed, when the cantilever and semiconductor surface are connected the circuit is that of a capacitor. The subsequent alignment of the Fermi level in the semiconductor, $E_{F,S}$, to the Fermi level of the metal, $E_{F,M}$, gives rise to an electrostatic potential termed the contact potential, $\Phi_{C.P.}$.

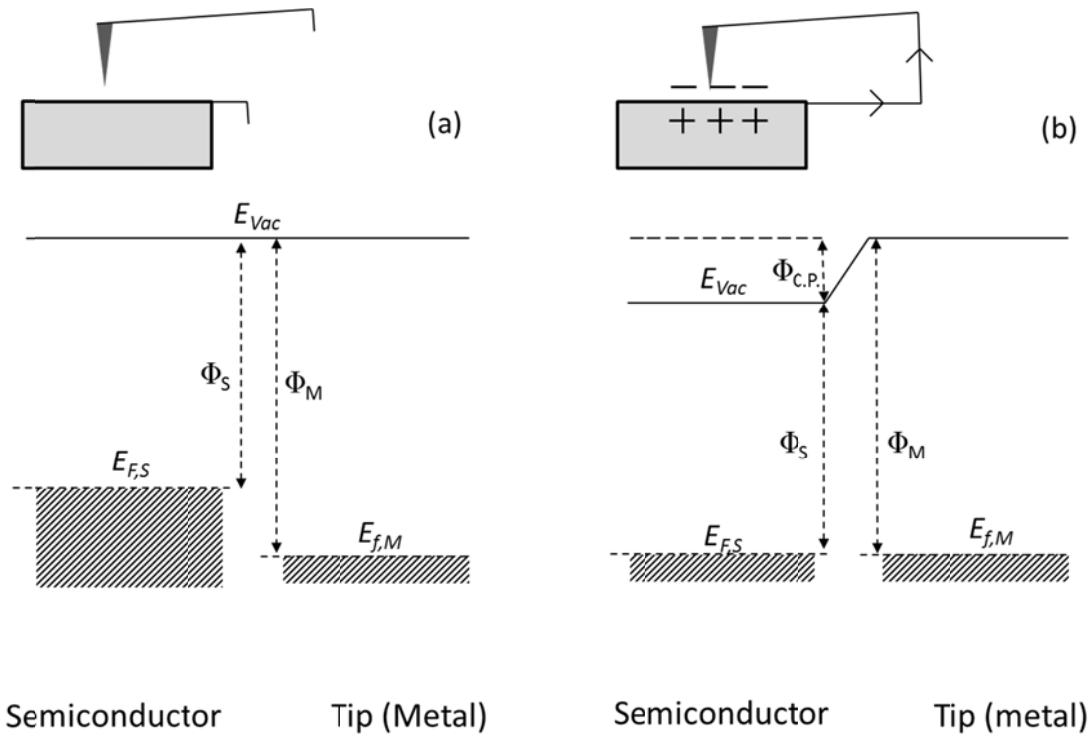

Figure 39 Band diagram of semiconductor surface and metal before contact (a) and after contact (b) where E_{Vac} is the vacuum level, E_C is the conduction band edge, E_V is the valence band edge, $E_{F,S}$ is the Fermi level of the semiconductor, $E_{f,M}$ is the Fermi level of the metal, Φ_S, Φ_M, $\Phi_{C.P.}$ are the semiconductor and metal work-function, and the contact potential respectively.

To achieve this experimentally, a silver paste was used for connecting the surface of the semiconductor to KPFM system. The experimental system and connection to the sample surface are presented in **Figure 40**. Once the surface of the sample was connected to the KPFM system, the measurement head with integrated laser, photodiode, and cantilever may be mounted for carrying out the measurement.

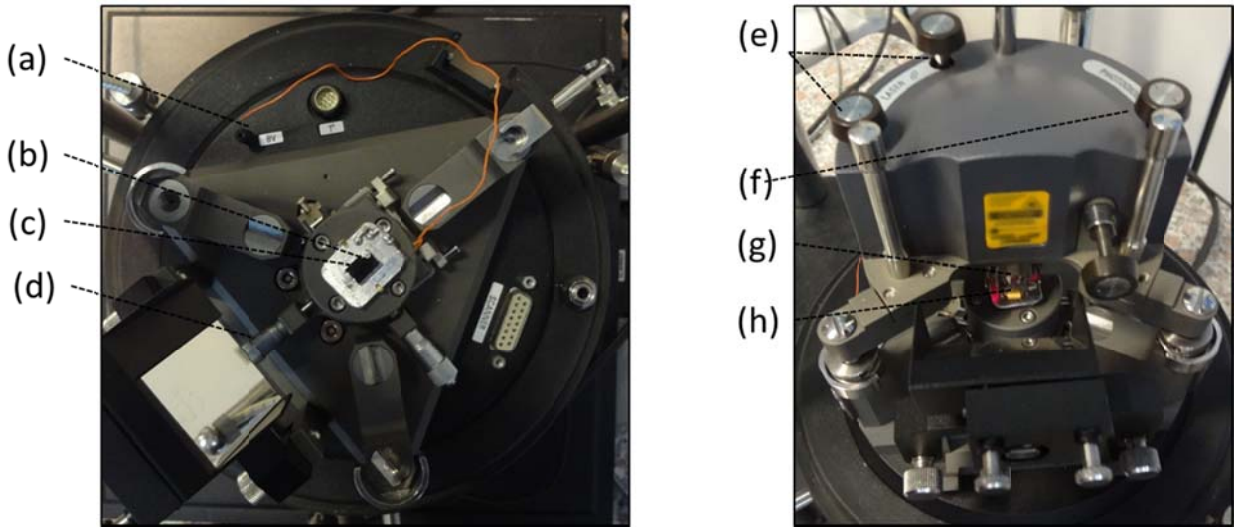

Figure 40 The KPFM system (a) was connected to the sample (b) using a small drop of silver paste (c). The sample stage provided lateral positioning of the sample. The laser adjustment knobs (e) and photodiode adjustment knob (f) provided the ability to optimize the signal to noise ratio of the laser reflected from the cantilver (g) located just above the sample (h).

For the measurement, the cantilever is not driven using a piezoelectric, as is the case for the AFM, but an AC voltage is applied at the tips resonant frequency (i.e. 48kHz). When there is a DC potential difference between the tip of the cantilever and the surface, the sum of the AC and DC voltages will cause the cantilever to vibrate. This origin of this force may be expressed using **Equation 12**, where C_z represents the capacitance between the probe and the surface, V_{DC} represents voltage a DC voltage offset, and V_{AC} represents the AC voltage with resonant frequency of the cantilever tip, ω_0. From this equation it is important to notice that the only term which resonates at the resonant frequency is the term with both V_{DC} and V_{AC} components (4).

Equation 12

$$\begin{aligned} F &= \frac{1}{2} C_z \cdot V^2 \\ &= \frac{1}{2} C_z \cdot [V_{DC} + V_{AC} sin(\omega_0 t)]^2 \\ &= \frac{1}{2} C_z \cdot \left[2 \cdot V_{DC} V_{AC} sin(\omega_0 t) - \frac{1}{2} V_{AC}^2 cos(2\omega_0 t)\right] \end{aligned}$$

In the case of the actual KPFM measurement, a DC bias is applied to offset the contact potential and minimize the cantilever oscillations. Furthermore, an AC-voltage with frequency 2ω is also applied to provide that the cantilever oscillates with changes in the surface potential. This sum of DC and AC voltages may be described using **Equation 13**.

Equation 13

$$V = (V_{DC} - \varphi_{C.P.}) + V_{AC} sin(\omega_2 t)$$

In general, the V_{DC} potential required to minimize the oscillations of the cantilever essentially forms a nulling circuit is applied throughout the measurement. This vibration of the cantilever is detected using the laser diode/photodiode arrangement which has been presented in **Figure 35**. The potential offset required to null the cantilever may be measured as the cantilever scans across horizontally across the sample surface producing a profile of the V_{DC} potential offset. This value of V_{DC} required to null the force corresponds directly to the contact potential between the tip and the sample presented in **Figure 39**.

Using calibration samples with a known work function permits the determination of the surface work function following **Equation 14**, where the difference between the known work function of the tip, and the known contact potential gives rise to the work function of the surface. In practice, however this is quite difficult due to changes in the Fermi level between two different samples. While calibration samples were not available during the current investigation, the relative work function of the surface with respect to itself has been investigated. The phenomena and its effects on Cd(Zn)Te radiation detectors is further investigated in Chapter 4, Section 4.

Equation 14

$$\varphi_M - \varphi_{C.P} = \varphi_S$$

For work-function measurements, a CSG30/PT coated cantilever tip was used, which had a tip radius of 30 nm, a tip height of 14-16nm, was conductively coated with Platinum, and had resonant frequency at 48 kHz. Also, for these work function measurements it was taken into account that the topography roughness should be much smaller than the tip radius. This is due to the surface capacitance, $C_{x,y}$, of the sample influencing the tip-surface capacitance C_z which acts on the cantilever force according to **Equation 12**. For high surface roughness, the total capacitance of the cantilever-surface circuit follows **Equation 15**, which applies for capacitors acting in series.

Equation 15 $$\boldsymbol{C_{Tot} = \left(C_z \cdot C_{x,y}\right)/\left(C_z + C_{x,y}\right)}$$

4.3 Spectroscopic Methods

4.3.1 Surface Photo-Voltage Spectroscopy

The Surface Photo-Voltage Spectroscopy method has been used extensively in this thesis and a section describing in detail the theory and experimental procedures associated with this equipment is warranted. Indeed, a system has been designed at the Crystal Growth Lab in Madrid during the course of this investigation and which is presented below.

The surface photo-voltage measurement is a surface state characterization technique that has been developed over the past several decades. It was first discovered by Brittain in 1947, with later publications in the1950s, by Brattain and Bardeen on the effects of surface illumination of the surface voltage (5) (6) (7). In the 1970s, work carried out by Gatos on the effects of sub-bandgap illumination of the surface voltage helped demonstrate the capability of the measurement technique (8). The 1980s and a1990s showed a further increase in the application of this measurement technique for characterizing the chemical, structural, and optical properties of a wide range of surfaces (9) (10).

Some advantages of this method for studying the surface states for Cd(Zn)Te are that it is (i) a non-contact method, (ii) is highly sensitive to surface properties, (iii) it can be used for the determination of bandgap energy as well as majority carrier type, and (iv) it may be used for the determination of the type of trap transition i.e. the recombination takes place between conduction or valence bands.

This section will present some of the theory associated with the SPV method, as well as some of the experimental conditions which have been used to improve the spectroscopy of Cd(Zn)Te materials.

4.3.1.1 Gap States & Charge Distribution

In the bulk lattice of an ideal semiconductor crystal, the probability of finding an electron in any of the unit cells is equal, and is a consequence of imposed 3-dimensional symmetry. The abrupt termination of the crystal lattice at the surface, however, introduces an asymmetry into the crystalline periodicity. This asymmetry imposes new boundary conditions on the electron wave function, and as a result introduces surface states, or gap states, which do not exist in the bulk. In reality, many factors contribute to the concentration of surface states including non-stoichiometry at the surface, surface reconstruction, damage imparted by mechanical or chemical polishing processes, adsorbed impurities.

The charge stored within a gap state is expressed differently for donor states and acceptor states. For acceptor states, the charge is proportional to the number of occupied states n_t. For donor states, the charge found within the state is proportional to the number of unoccupied states. This is represented using Equation 16, where N_t is the total number of gap states.

Equation 16

$$\boldsymbol{Q_{donor} = e \cdot (N_t - n_t)} \qquad \boldsymbol{Q_{acceptor} = e \cdot n_t}$$

The charge within each gap state must be supplied by the bulk, and therefore the net carrier density near the surface will be different from the average bulk carrier density. This difference in carrier density produces what is called a Space Charge Region (SCR). This departure from equilibrium implies the existence of an electric field at the surface giving rise to a surface potential different than the potential in the bulk. As a consequence, there is a bending of the conduction and valence bands corresponding to the magnitude of this surface potential (a positive surface potential corresponds to downward bent bands).

The charge within the surface state, Q_{SS}, and the SCR are related by taking into account that the bulk supplies all of the necessary charge. Therefore, Equation 17 states that for all of the charge within the gap states at the surface, there should be an equal and opposite net charge in the space charge region.

Equation 17 $$\boldsymbol{Q_{SS} = -Q_{SCR}}$$

In general, only three types of conditions exist for this redistribution of charge between the bulk and the surface states. When the majority carrier concentration is larger at the surface than its bulk value, it is referred to as **accumulation**. When the majority carrier concentration is smaller than the bulk equilibrium, but still larger than the minority carrier concentration, it is referred to as **depletion**. When the majority carrier concentration is smaller than the minority carrier concentration at the surface, it is referred to as **inversion**.

For n-type material, which is the material under the present study, accumulation would therefore correspond to an increase in carriers at the surface, creating a lower surface potential. Depletion occurs as the surface potential increases. Therefore, a higher surface state density will correspond to larger band bending, and as a result, greater charge transfer between the surface and the bulk are required to establish equilibrium. It is precisely these changes in the surface potential which are measured by the SPV method.

4.3.1.2 Sub-bandgap SPV in Cd(Zn)Te

In order to remove Band to Band absorption at the surface, sub-bandgap energies are used for excitation of the gap states (i.e. $\lambda < 1.6$eV). The carrier exchange between the gap states and valence/conduction bands induce changes in the surface potential via optical transitions. In reality, both bulk and surface states may be excited and the SPV signal is a combination of both.

These positive and negative changes in surface potential are illustrated in **Figure 41**, where the dotted line corresponds to the surface potential after absorption. In a depleted type n-semiconductor, such as those used in the current study, $\boldsymbol{Q_{SS}}$ is negative and $\boldsymbol{Q_{SCR}}$ is positive. When the energy of incident photons is sufficient i.e. $h\nu \geq E_c - E_t$, the value $\boldsymbol{Q_{SS}}$ becomes less negative as electrons are first excited from the trap, E_t, to the conduction band, and are subsequently swept into the bulk by the electric field at the surface. As a result, the space charge region becomes less depleted and $\boldsymbol{Q_{SCR}}$ becomes less positive. It is important to also note that a strong decrease of the SPV signal in the above band gap region is mainly due to electron hole recombination at the surface

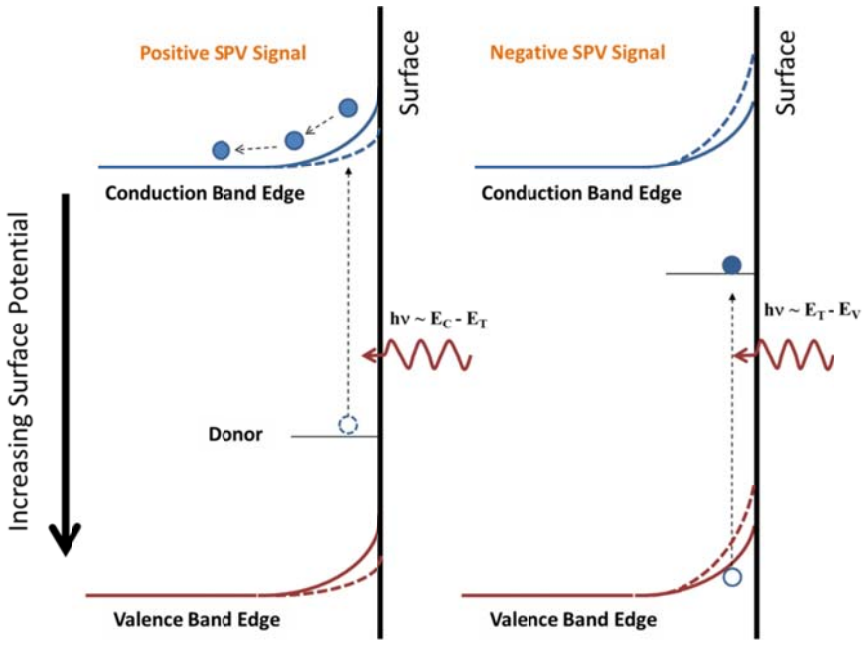

Figure 41 Surface band bending diagram of n-type material for (a) excitation of electron from trap level to conduction band using sub-bandgap energy light and (b) excitation of electron from valence band to trap level.

SPV has been a technique implemented in Cd(Zn)Te for measuring alloy composition as well as bandgap energy (11). Just as the lattice parameter changes with increasing Zinc concentration, the bandgap of the Cd(Zn)Te alloy also increases. One of the reasons Zinc is added to the CdTe system for radiation detector applications is to increase the resistivity through increasing the bandgap energy. This is discussed in greater detail in Chapter 1, Section 2.

Non-destructive and non-invasive methods for determination of the bandgap energy, is therefore of great interest. Using room temperature photo-reflectance measurements, in conjunction with lattice parameter measurements, it has been shown that the bandgap energy in Cd(Zn)Te follows **Equation 18** (12), where x represents the atomic Zinc content. This has also been demonstrated by other researchers working with Cd(Zn)Te (13). For different alloy compositions of $Cd_{1-x}Zn_xTe$, the corresponding bandgap energy and lattice constant have been calculated and are presented in **Table 2**. In order to achieve accurate determination of Zinc content, the light source and the detector must have sufficiently high spectral resolution i.e. determination of *x* value less than $\pm$ 0.01. See reference (14) for further details.

Equation 18
$$E_g = 1.5045 + 0.631 \cdot x + 0.128 \cdot x^2$$

Table 2 Bandgap energy as a function of Zinc composition in the ternary alloy $Cd_{1-x}Zn_xTe$

$Cd_xZn_{1-x}Te$ Alloy Composition	Bandgap Energy (eV)
0	1.5045
0.01	1.510823
0.02	1.517171
0.03	1.523545
0.04	1.529945
0.05	1.53637
0.06	1.542821
0.07	1.549297
0.08	1.555799
0.09	1.562327
0.1	1.56888

4.3.1.3 Experimental Apparatus

The SPV system used in this work consisted of a Quartz-Tungsten lamp, a SPEX 500M Spectrometer, a Standford Research Systems SR830 DSP Lock in Amplifier, a SCITEC Instruments optical chopper, and an Infratec pyro-electric detector (for calibration of variations in photon flux). The sample mounting system consisted of a AD820AR FET amplifier package, a faraday cage, and an optically transparent electrically conducting probe for measuring the photo-induce voltage near the surface. The SPV signal is fed through the high impedance field-effect transistor preamplifier and is measured by a lock-in amplifier. Presented in **Figure 42** is the experimental apparatus used in this work.

A quartz tungsten lamp was used as a light source for the spectral measurements. One advantage of using these lamps has to do with their broad emission between 300nm (ultraviolet) and 1400 nm (infrared). An optical lens was used for collimating the light before entering the Monochromator.

Some of the drawbacks of this type of light source have to do with filament decomposition, and intensity darkening from evaporated tungsten residue on the quartz. Also, the output intensity of the filament depends on the voltage applied to the Tungsten filament. As a result the luminance and color temperature of tungsten lamps can vary significantly. For controlling the voltage applied to the light source, a ELC AL924A DC power supply was used for regulating voltage and maintaining a constant applied voltage between experiments. To compensate for changes in the spectra photon flux measurements were completed after each experiment for

normalization of spectra, and for detecting changes in the spectra (no observable changes were observed however, during the three months of experiments which were carried out).

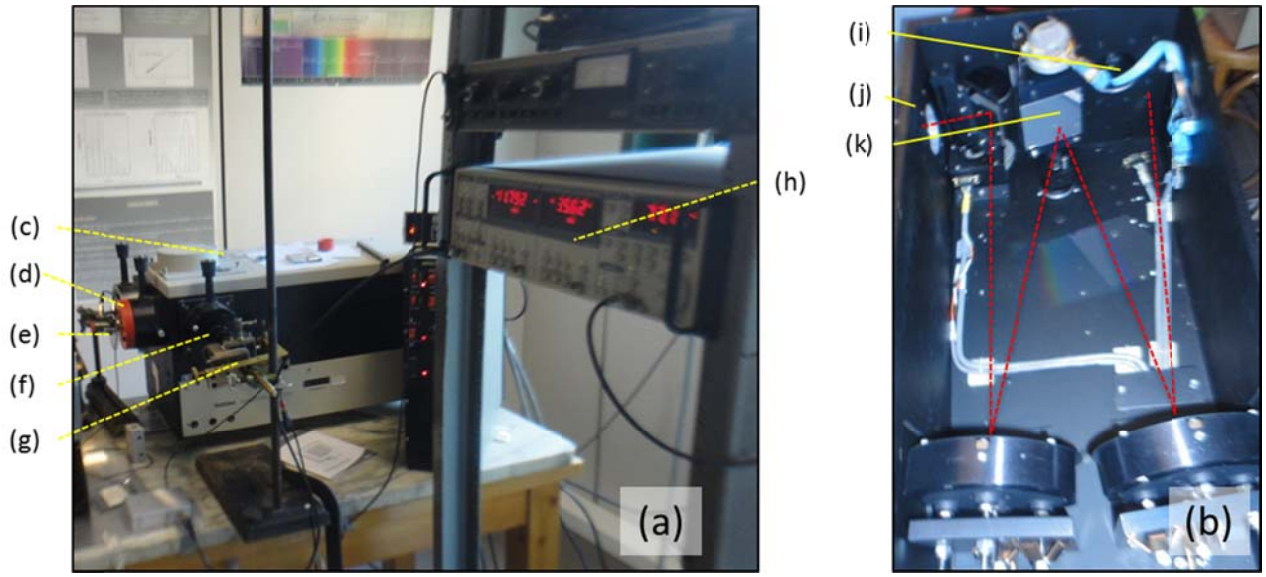

Figure 42 (a) Experimental configuration for surface photo-voltage measurements, (b) inside SPEX 500M monochromator, (c) SPEX 500M monochromator, (d) pyro-electric sensor, (e) optical chopper, (f) SPEX 500M exit slits, (g) sample mounting, (h) DSP SR830 Lock in amplifier, (i) lamp entrance slits, (j) exit slits, (k) diffraction grating.

For measuring variations in the photon flux produced by the light source, a pyro-electric detector based on Lithium Tantalate ($LiTaO_3$) was used (InfraTec). When light is absorbed by the detector crystal, the change in temperature modifies the position of the atoms such that the polarization of the material changes. This change in polarization produces a proportional electric charge, and this electric charge is directly proportional to the number of photons impinging on the detector crystal. An optical chopper is used in line with the quartz tungsten lamp during measurement. The pyro-electric detector is integrated with a high impedance resistor and FET package for changing the induced charge into a measureable signal.

4.3.1.4 Experimental Conditions

The accurate determination of Zinc content or surface properties requires high spectral resolution. The SPEX 500M monochromator has a focal length of 0.5 meters, and a spectral range between 0-1.5 μm. The linear dispersion of the system is 1.6nm / mm slits, and the corresponding resolution of the system is 0.02nm. However, system resolution depends on the

type of diffraction grating, and slits width used. It was important to investigate how these experimental parameters such as the monochromator diffraction grating and slits affected experimental measurement conditions.

The monochromator was first calibrated using the spectral lines from a Hg vapor lamp. The lamp was placed closely to the entrance of the monochromator and a pyro-electric (PE) sensor was used for measuring the response as a function of wavelength. Both spectral lines located at 546nm, and 436nm showed local maxima in the PE sensor output, consistent with the Hg vapor lamp emission spectra.

For the region of the electromagnetic spectrum investigated here, the response of the pyro-electric detector used for calibration is independent of wavelength and is sensitive only to the number of photons impinging on the detector. Fluctuations in source intensity as a function of wavelength can therefore be detected and eliminated. Specifically, the spectra may be normalized for variations in photon flux, taking into account the variation in the photon flux determined using the PE sensor.

Two types of monochromator gratings were studied. Using a 750nm diffraction grating (1200 gratings mm^{-1}) the linear dispersion of the monochromator is 1.96nm/mm slits width, whereas for the 350nm diffraction grating (600 gratings mm^{-1}), the linear dispersion is 3.94nm/mm slits width.

The photon flux obtained using each grating is presented in **Figure 43**. The low photon flux above 1.65eV is due to an optical filter which is used to cut-off photons above this energy. Each diffraction grating used has a local maximum near 1.62eV and for this reason there is a local increase in photon flux in this region (it is not related to the light source). After 1.55eV, there is a steady increase up to the lamps maximum output intensity (near 1.1-1.3eV). It is also important to observe that using the 750nm diffraction grating, there is a higher, more uniform photon flux. This higher photon flux is important for obtaining a stronger response in the material. Changes in the photon flux are also less dynamic over the range of interest, which would correspond to less measurement artifacts. For these reasons the 750nm diffraction grating proved to be advantageous for measuring Cd(Zn)Te surfaces.

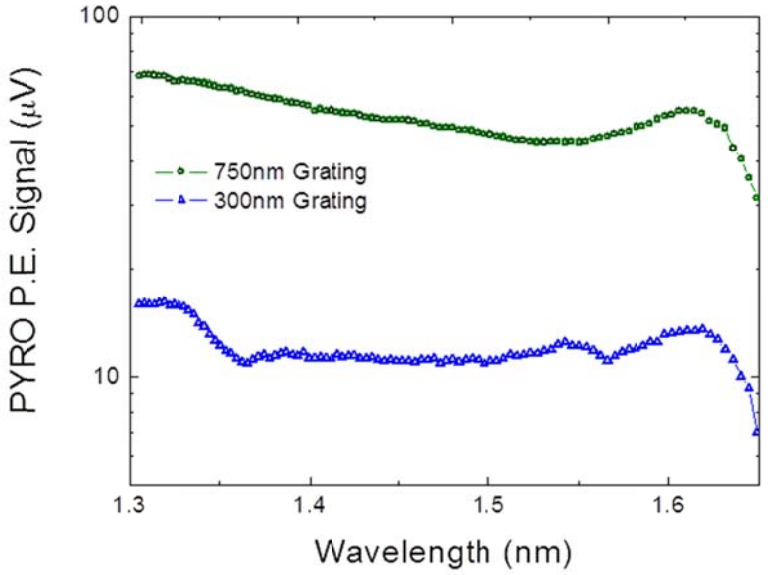

Figure 43 Spectral response of Pyro-electric detector to Quartz Tungsten lamp using two different diffraction gratings.

The 750nm diffraction grating provides superior spectral resolution, as well as a higher photon flux than the 300nm grating. However, the spectral resolution of the system also depends on the width of the input and output slits of the monochromator. The slit width of the monochromator is usually selected to achieve the desired spectral resolution, or bandwidth, as well as for adjusting the intensity of the light source.

Examples of the spectral resolution obtainable using different slit widths are presented in **Table 3**. To identify good working conditions for obtaining a high signal to noise ratio, different slits widths were tested. The spectral resolution defined by the SPEX500M monochromator is 3.94nm/1mm slits width.

Table 3 Dependence of spectral resolution of SPEX500 monochromator on exit/entrance slits

Slits Width	*Spectral Resolution (nm)*	*Energy Resolution (meV)*
2000 μm	7.88	16.2
1500 μm	5.91	11.4
1000 μm	3.94	7.6
500 μm	1.97	3.8
250 μm	0.985	1.9
100 μm	0.394	0.8

Changing the slits of the monochromator and its effect on the photon flux at the monochromator output is presented in **Figure 44**. In general, the photon flux decreases exponentially with decreasing slits, while the general shape of the spectra (derived from the quartz-tungsten lamp, diffraction grating, and low pass filter) is preserved. In this figure, the Quartz-Tungsten lamp maximum intensity occurs between 1.1 and 1.3 eV.

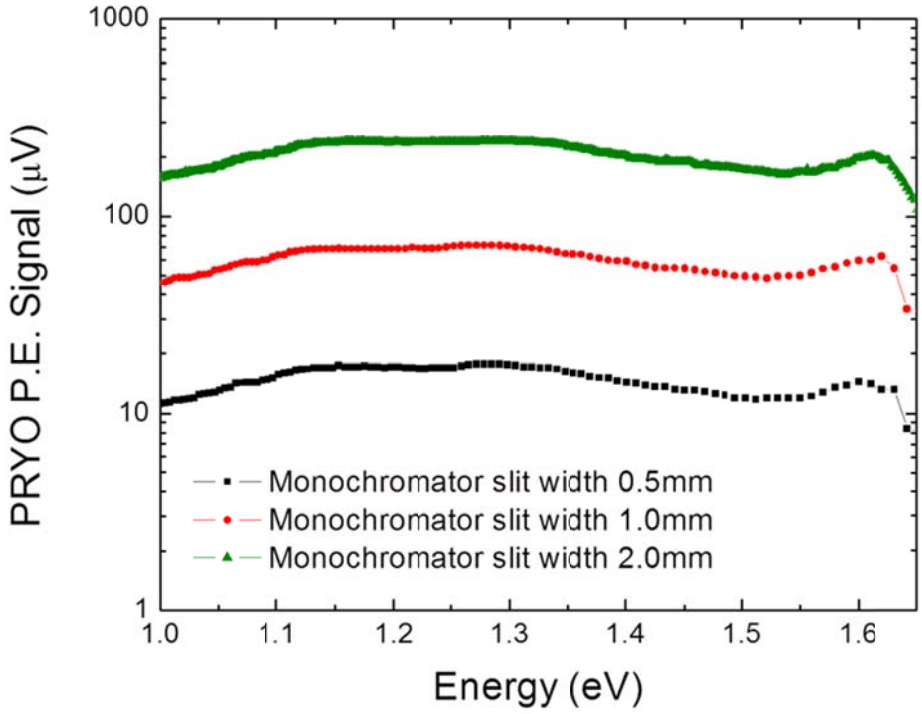

Figure 44 Photon flux measurements using different slits widths of 0.5mm, 1.0mm, and 2.0mm.

Presented in **Figure 45** are SPV measurements using different slits widths on the same region of the same high resistivity Cd(Zn)Te sample. It is important to observe how the spectral resolution of the instrument depends to a large extent on the slits used for acquisition of the spectra. Using a slit width of 0.25-0.50mm yields good results in terms of maintaining high photon fluxes while providing good spectral resolution. Further decreasing this slit width to 0.1mm does not substantially improve the measured energy resolution. Indeed, the traps measured using a 1.5mm slit with were nearly 0.7-1.0eV lower in energy than the traps measured using a 0.5mm slit width. Indeed, referring to **Table 3**, the differences in spectra resolution may justify such disagreement.

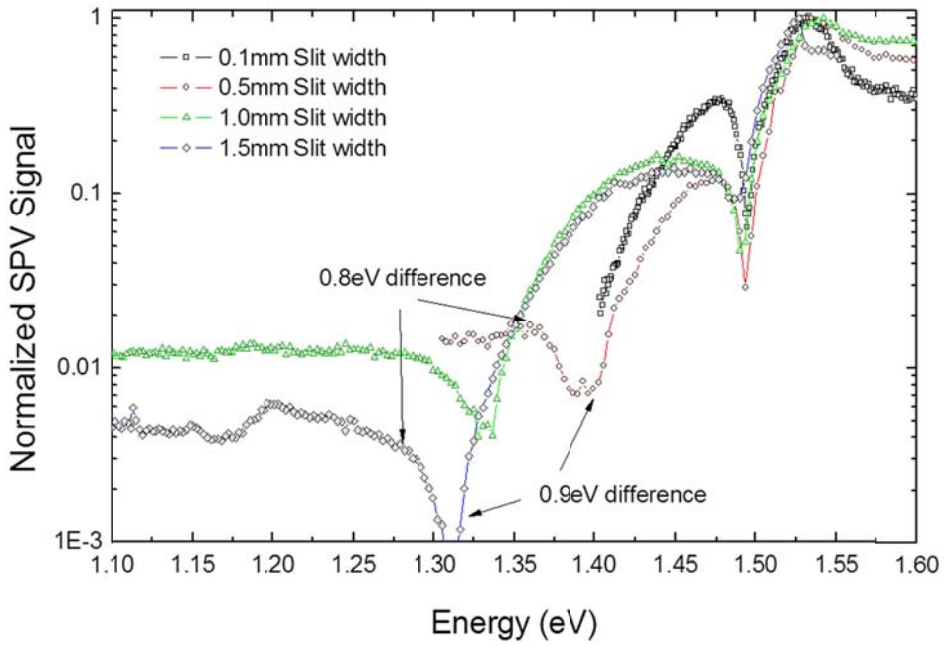

Figure 45 Dependence of the SPV signal in Cd(Zn)Te on the slits width of the monochromator

It is important to note that a peak at the bandgap energy near 1.6eV is observed, instead of a ´´knee´´ which has been observed by other researchers (14). For this work, the bandgap energy could be determined by the peak intensity which correlates to peak absorption, rather than changes in the slope. The reason for the decrease in intensity in super-bandgap excitation is related to the increase in the absorption coefficient for wavelengths with energy $\lambda \geq E_g$. Absorption at the surface produces electron-hole pairs, which undergo rapid surface recombination. As a result, they are not swept into the bulk, the net carrier concentration at the surface decreases, and the SPV signal decays, forming what appears to be a peak.

4.3.2 Energy Dispersive X-ray Spectroscopy

The physical principles guiding EDS spectroscopy are presented in **Figure 46**. This technique relies upon (1) the excitation and ejection of core electrons of the atom and the creation of a hole (2) the relaxation of electrons at higher energy levels to fill that hole and (3) the emission of a characteristic X-ray whose energy is equal to the energy difference between the two states. The detection and classification of these X-rays determines the elemental surface composition.

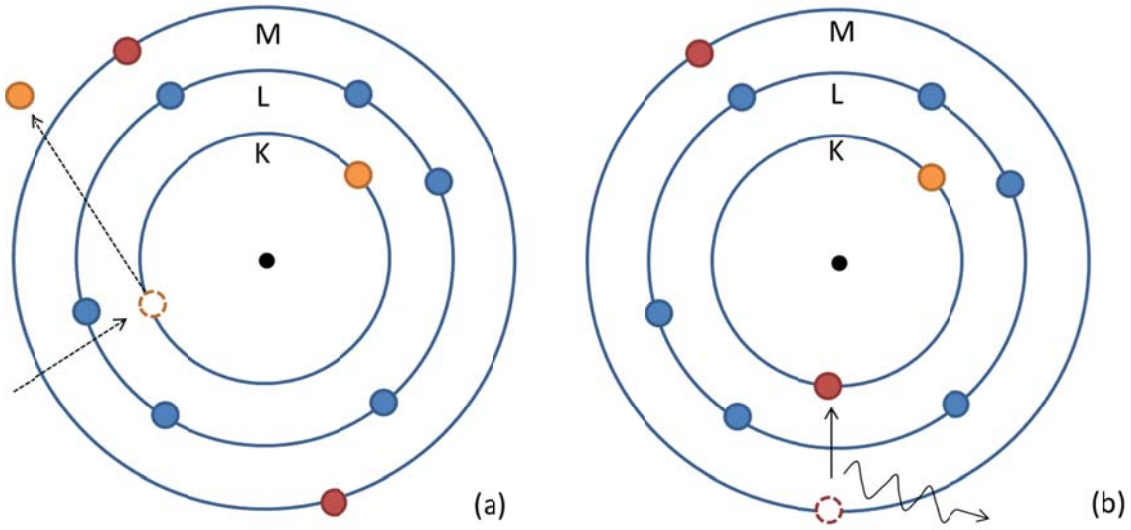

Figure 46 (a) core electron is excited to energetic state by incident electron beam (b) relaxation of higher energy electron produces characteristic x-ray associated with element. Measurement of these characteristic x-ray energies is used for the determination of the material composition.

Indeed, the most useful property of these characteristic x-rays is the variation of their energy with atomic number. This relationship may be expressed using Moseley's law, presented in **Equation 19**, where E is the energy of the x-ray, c_1 and c_2 are constants for a given line type (i.e. K, L, M), and Z is the atomic number. This equation may also be derived from the Bohr model of the atom which followed later.

Equation 19

$$E_{x-ray} = (c_1 \cdot (Z - c_2)^2) \cdot h$$

For example for main K-α line, these values are 2.47×10^{15} and 1 for c_1 and c_2 respectively. For the L-α line these values take 4.57×10^{14} and 7.4 respectively. Taking into account the atomic number of an element, the X-ray energy for each line may be determined.

Presented in **Table 4** are the characteristic energies calculated using **Equation 19** for several of the materials which have been used in this investigation. Databases providing the energies associated with charactistic X-rays emitted all of the elements by may be found elsewhere (15).

Table 4 Characteristic K-line X-rays energies for various materials investigated in this work.

Material	Z	K-X-ray (keV)	L-X-ray (keV)
Boron	5	0.163	-
Nitrogen	7	0.367	-
Oxygen	8	0.500	-
Aluminum	13	1.470	-
Zinc	30	8.58	0.965
Cadmium	48	23.017	3.114
Tellurium	42	26.56	3.758
Gold	79	62.138	9.089

A Scanning Electron Microscope (SEM) Hitachi S-3000N, coupled to an energy dispersive X-ray (EDS) analyzer by Oxford Instruments, INCAx-sight model was used for characterization of the compositional surface and bulk properties. The components of the electron beam which are used for excitation are presented in Section 4.2.2. The EDS system itself, used for measurement of the characteristic X-rays, is presented below in **Figure 47**. This system consists of (i) a set of permanent magnets which deflect stray electrons from entering the detector and degrading the signal (ii) a low pass filter fabricated from Beryllium or a polymer material placed between the vacuum system and the detector crystal (iii) a detector crystal based on either Si or HpGe which remains application specific (iv) a field effect transistor for pulse processing and amplification and (v) cryostat which is used for cryogenic cooling of the semiconductor crystal.

One of the principle advantages of the EDS are that this technique may be used with a wide range of materials whose properties may vary substantially. Presented in **Figure 48** are examples of EDS spectra taken for conductive materials such as elemental Cadmium, semi-insulating materials such as Cd(Zn)Te, and insulating materials such as Boron Nitride. For the insulating materials, it is necessary to deposit a thin film of Au on the surface, which allows focusing on the surface using secondary electrons. Comparing these values with the characteristic energies presented in **Table 4** shows good agreement between the experimental and theoretical predictions.

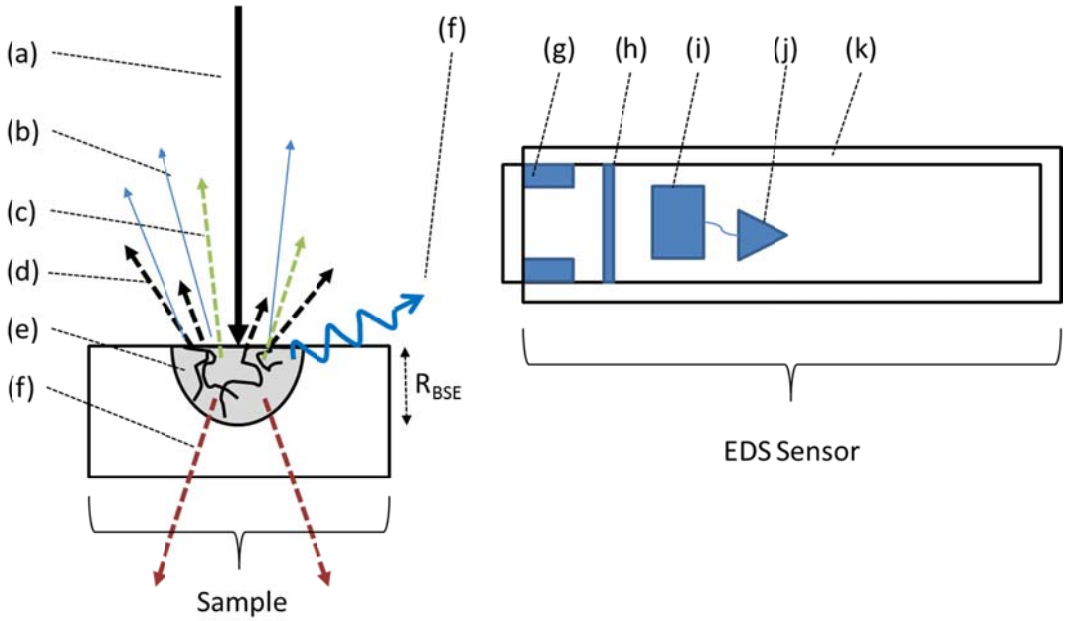

Figure 47 Experimental geometry for EDS. (a) Electron beam impinging on sample surface produces (b) luminescent photons, (c) back scattered electrons, (d) secondary electrons throughout the interaction depth, (e) denoted as R_{BSE}. Inelastically scatteed electrons also produced. The chararacteristic x-rays (f) reach the EDS sensor. Fixed magnets (g) and a low pass filter (h) prevent charged electrons and low energy bremsstrahlung from entering sensor and interacting with the detector crystal (i). (j) FET connected to the anode ofd detector crystal for signal amplification. (k) Cryostat housing.

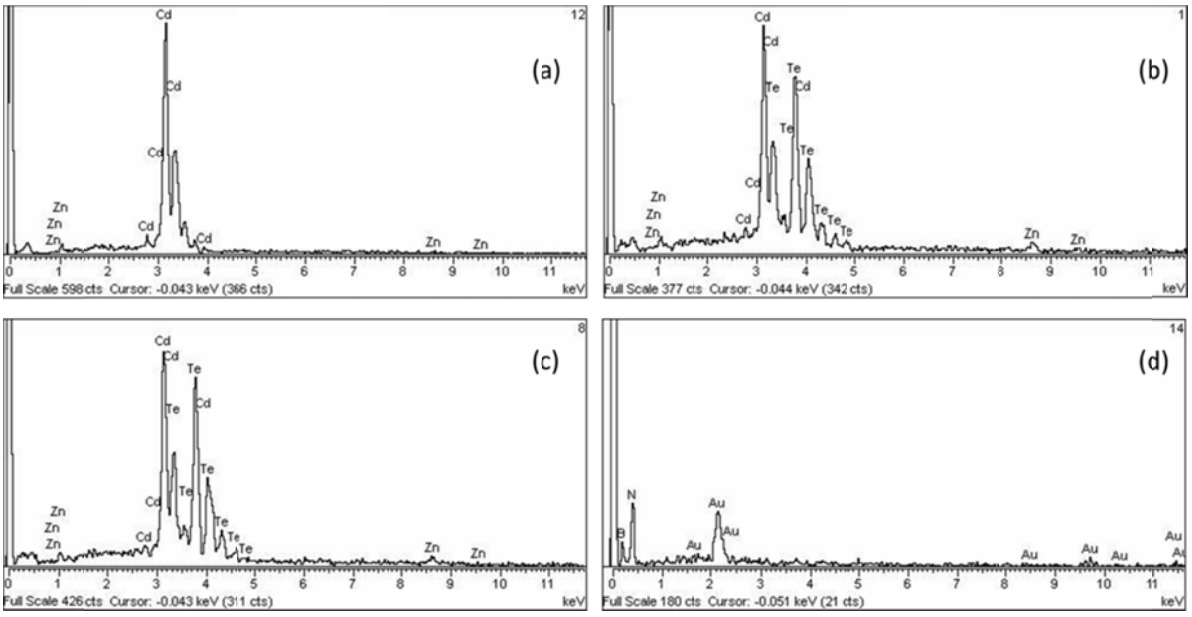

Figure 48 EDS measurements of (a) elemental Cd (b) & (c) Cd(Zn)Te surfaces and (d) boron nitride.

4.3.3 Rutherford Backscattering Spectroscopy

Rutherford Backscattering Spectroscopy (RBS) is an experimental technique used for the determination the kinds of elements present in a sample, the stoichiometry, and their distribution as a function of depth. This method ultimately rests upon the set of experiments carried out by Lord Ernest Rutherford who studied the scattering of alpha particles through gold films in 1911. These experiments provided the first experimental evidence for the presence of a nucleus, as the positive charge of this nucleus produced backscattering of incident alpha particles, indicating a strong elastic Coulomb interaction.

A diagram of this experimental method is presented in **Figure 49**. A typical RBS system is composed of an ion source, a linear accelerator for accelerating ions to high energies, and a detector which is used for measuring the energies of the backscattered ions. A Van der Graff linear accelerator was used bringing the He^{2+} to 2.0MeV.

Usually, a solid state silicon detector is used for determination of the energy of backscattered particles. The ion source used in this work is an energetic He^{2+} ions accelerated to 2MeV, however heavier ions may also be accelerated to higher energies to improve the resolving power of the technique i.e. 8 MeV Li^{3+} ions. Indeed, due to the similarity of the densities and mass numbers of Cd and Te, higher energies may be used for improving the separation of the scattered particles. The detector used in these investigations was located at a scattering angle of $\theta = 165^{o}$

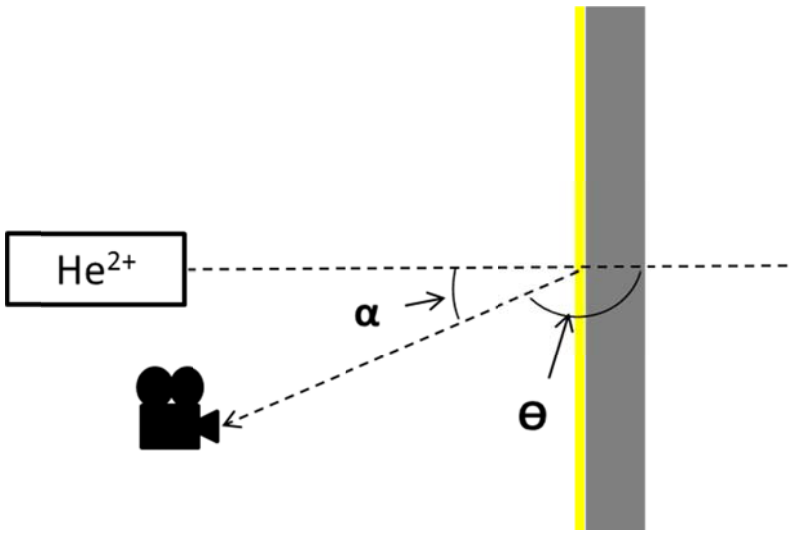

Figure 49 Experimental arrangement for RBS measurement consisting of an accelerated ion source at some angle α normal to the surface. The ions are backscattered at an angle of β to the normal, an detected by the Si detector. The angle Θ is referred to as the scattering angle.

The energy loss of the scattered ions is sensitive to the number of atomic layers crossed by the beam, and independent of their spacing. Indeed, the energy relation of a backscattered ion with energy E_1 mass M_1 is described using **Equation 20**, where energy E_0 represents the incident energy before the scattering event.

Equation 20 $$\boldsymbol{E_0 = E_1 \cdot K}$$

The kinematic factor k, may be represented taking into account the mass of the incident material M_2, the scattering angle Θ, using **Equation 21** (16). Taking into account $M_2 > M_1$, an average atomic mass of 119, the scattering angle of 165º, this kinematic factor comes to k ~ 0.88307.

Equation 21 $$\boldsymbol{K = \frac{M_1^2}{(M_1+M_2)^2} \cdot \left\{ cos(\theta) + \left[\left(\frac{M_2}{M_1}\right)^2 - sin^2(\theta) \right]^{1/2} \right\}^2}$$

Indeed, for materials such as CdTe which have similar atomic masses, the energy separation of the backscattered particles is given by **Equation 22**. The factor $\boldsymbol{\Delta M_2}$ for Cd and Te is 15.2, $\boldsymbol{E_0}$ is 2 MeV, and $\boldsymbol{dK/dM_2}$ may be calculated using Equation 21 for both Cd and Te (~0.08). To improve energy separation, heavier incident ions may be used (16).

Equation 22 $$\boldsymbol{\Delta E_1 = E_0 \frac{dK}{dM_2} \Delta M_2}$$

In general, it may be summarized that at high angles of incidence the depth resolution at the surface also improves, while the depth probed decreases by the same factor. Also, the mass resolution of the RBS decreases with the square of the mass analyzed. This means that mass separation is very good for low masses, and poor for high masses

RBS alone is not sufficient to determine layer composition and thicknesses. The RBS technique is sensitive to areal density with units of at-cm^{-2} or g-cm^2. Therefore, it is required to know the density of the various layers to calculate their thicknesses i.e. gold, Cd(Zn)Te, as well

as Te_2O_3. Presented below in **Table 5** are the densities of the materials which have been investigated by RBS in this work.

Table 5 Densities of Materials investigated by RBS

Material	Density ($g\text{-}cm^{-3}$)	Density ($atoms\text{-}cm^{-3}$)
$Cd_{0.9}Zn_{0.1}Te$	5.65	1.45×10^{22}
Au	19.2	5.84×10^{22}
TeO_2	5.67	2.15×10^{22}

The measurements carried out in this work, the experimental data were analyzed with the IBA Data-Furnace NDF v9.3_f and the theoretical aspects of this software are presented in (17). Presented below in **Figure 50** is one example of a RBS profile which is used for determining the thickness of TeO2 at the Au-Cd(Zn)Te interface.

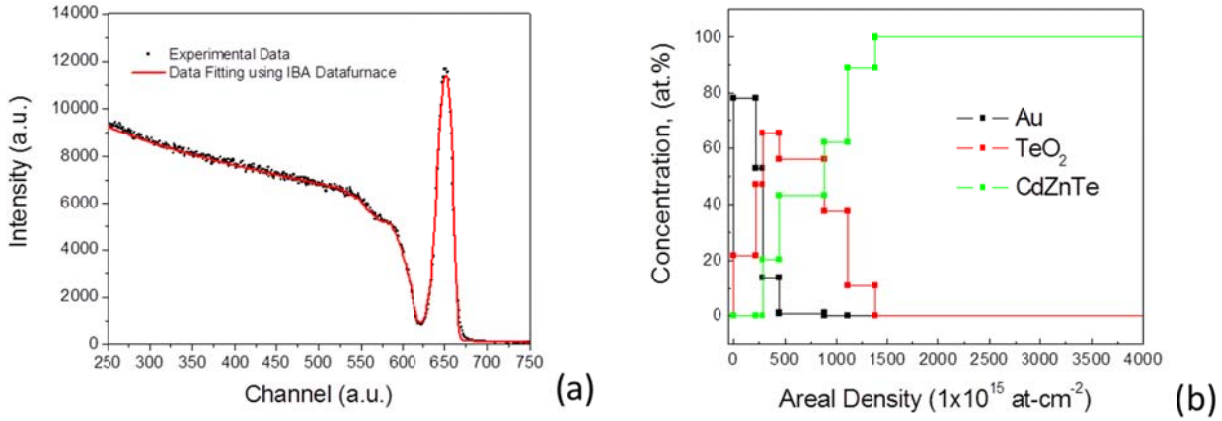

Figure 50 (a) Experimentally measured data and fitting provided by IBA Datafurnace NDF v.9.3 and (b) Typical RBS profile of Au-Cd(Zn)Te interface showing the presence of a TeO_2 interfacial layer.

Taking into account the densities of the materials, the thickness of the Au layer is near 100nm, while the thickness of the TeO_2 layer is measured to be near 29-35nm in thickness. Presented in **Equation 23** is an example of one such calculation.

Equation 23

$$\delta_{Au} = \frac{(218 \cdot 10^{15})}{(5.84 \cdot 10^{22})} \sim 3.7 \cdot 10^{-5}\ cm \sim 40nm$$

$$\delta_{TeO_2} = \frac{(1380 \cdot 10^{15})}{(2.15 \cdot 10^{22})} \sim 6.4 \cdot 10^{-5}\ cm \sim 64nm$$

4.3.4 Inductively coupled plasma mass spectroscopy

For the determination of compositional properties and trace impurities, ion couple plasma mass spectroscopy or ICP-MS is a powerful technique which has been implemented extensively throughout this investigation. This technique relies upon the coupling of inductively produced plasma to a mass spectrometer for analysis of the ions produced through the injection of material into the plasma.

The sample introduction system consists of a peristaltic pumping apparatus coupled to a spray nebulizer and chamber. While there are many configurations of both the nebulizer and spray chamber available, the basic operation is (i) to create a fine mist of very small droplets and (ii) to introduce these droplets into the ICP torch and (iii) to eliminate larger droplets which may cause problems in the analysis.

When these fine droplets pass into the ICP-torch, the atoms are completely ionized by the plasma source. For the production of plasma, Argon gas is commonly used in conjunction with a helically shaped electrode. When a time dependent electrical current is passed through the helical electrode, it produces a time dependent magnetic field, which in turn induces an electrical current in the Argon gas. These currents lead to the formation of the plasma, which reaches temperatures as high as 6,000K. Indeed, the sample matrix containing the elements to be analyzed undergoes phase change from a liquid droplet, to a solid, eventually to a gas. As the atoms travel through the plasma torch, they eventually gain enough energy to lose an electron, become singly ionized, and exhibit a positive charge.

For these singly charged ions to enter the quadropole, a special interface is used for linking the ICP-torch, which operates under ambient pressures, to the mass spectrometer, which operates under a high vacuum system (1 x 10^{-6} Torr). This is a fairly sophisticated and proprietary system which allows the ions produced in the previous step, to pass into the ion lens region and the subsequent quadropole spectrometer. This region is composed of skimmer or sampler cones, which exhibit an orifice normally about 1mm in diameter which allows the ion beam to pass into the high vacuum system.

The quadropole filters the ions according to their mass such that only atoms with the desired mass may impinge upon the detector. The quadropole sets voltages and RF frequencies which allow ions with a given mass-to-charge ratio to remain stable as they pass through the quadropole on to the detector. Indeed, the diploe moment is zero when the ion is placed at the center of the quadropole. By changing the settings of the quadropole, different mass-to-charge ratios may be examined, allowing for spectroscopic analysis. Presented below in **Figure 51** is a schematic of the type of ICP-MS system which has been used in this work.

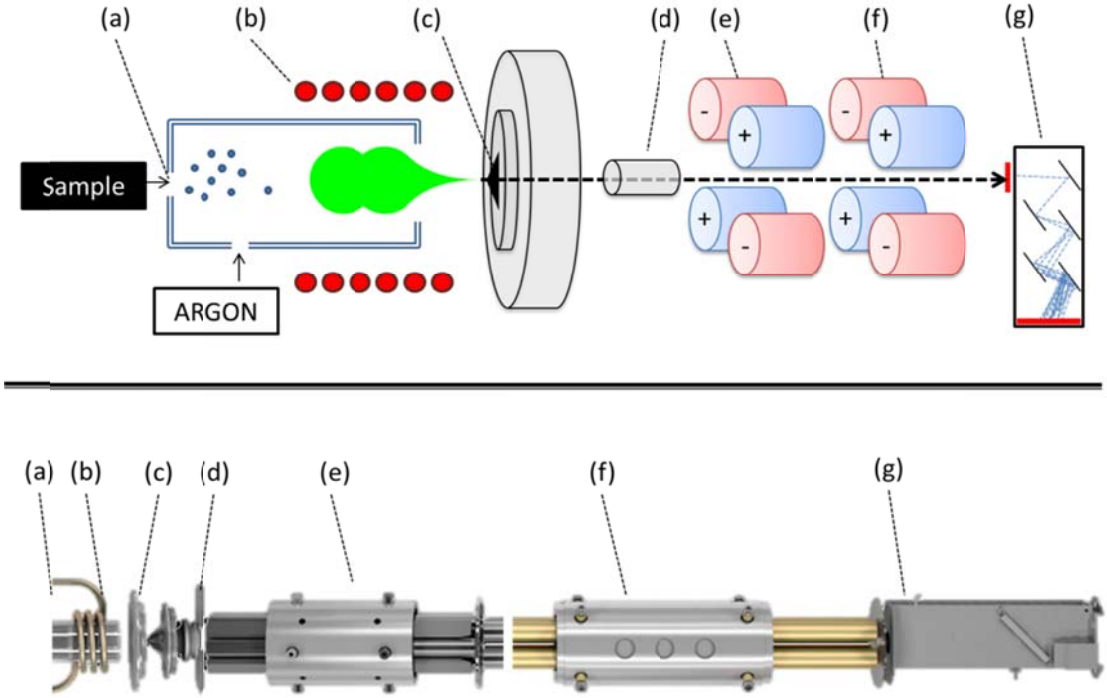

Figure 51 ICP-MS system composed of (a) nebulizer, (b) ICP-Torch, (c) skimmer/sampler cones, (d) ion lens, (e) universal cell (f) quadropole mass filter (g) dynode.

An ELAN-6000 equipment was used for ICP-MS measurements. Since Cd(Zn)Te is a material insoluble in water, a process of dilution is used. Thus is done by dissolving the sample in HCl:HNO_3 (commonly referred to *Aqua Regia*) in a ratio of 3:1.

$10HNO_3 + 12ZnTe \rightarrow 12ZnO + 6Te_2O_3 + 5H_2 + 5N_2$

$10HNO_3 + 12CdTe \rightarrow 12CdO + 6Te_2O_3 + 5H_2 + 5N_2$

These polar oxides readily dissolve in water. Using approximately 3 μg of Cd(Zn)Te, 1 mL of aqua regia for digestion, and 2 mL of water, the solution is warmed to 80^{o} to complete the dissolution. A micropipette is used for measuring volumes while analytical scale accurate to 0.00001g is used for measuring masses. The ICP-MS equipment is maintained inside of a class 100K cleanroom environment, at a temperature of 20^{o}C, with a HEPA filtration system used to provide positive overpressure.

It is necessary to take into account several important experimental considerations. First, for elements with lower atomic masses, the Argon plasma at 6,000K does not supply the energy required to remove a single electron to form an ion. As a result, Carbon, Oxygen, Boron, and lighter elements all go undetected by this technique. Furthermore, one a consequence of using the Aqua Regia as the dilution matrix is that Nitrogen and Chlorine are undetectable.

It is also important to take into account interferences which may occur between elements. Interferences in ICP-MS are caused when ions generated from the plasma, the sample, or a combination of the two carry a mass-to-charge ratio that is identical to that of the analyte ion. For example stable molecules such as O_2 may form through a collision and reaction process, and will subsequently register in the spectrometer as having a total mass of 16 + 16 = 32. As a result, this molecule will be registered as Sulfur which also has an atomic mass of 32. It is important to take these interferences into account during measurement to eliminate sources of measurement error.

4.3.5 Glow Discharge Mass Spectroscopy

Glow discharge Mass Spectroscopy (GDMS) is an experimental technique free from the constraints of using a matrix for material dissolution and atomization. Consequently this method is ideal for analysis of trace elements in high purity materials, only requiring a small sample volume of homogenous material. Moreover, GDMS can provide elemental analysis of the entire periodic table (except Hydrogen) from sub-ppb to part per trillion (ppt) detection limits.

This technique makes use of argon plasma to sputter the surface of the sample (hence the name glow discharge). Typically, voltages between 600-1000V are used to accelerate the Argon ions. Once the surface atoms are liberated from the sample, they are subsequently ionized in the argon plasma and extracted from the chamber. Thus, the atomization of the material is achieved without the use of any matrix, which could possibly contaminate the source. The extracted ions

are then separated using a mass spectrometer and detected using an electron multiplier or dynode configuration which has been previously discussed. Presented in **Figure 52** is an illustration of this method.

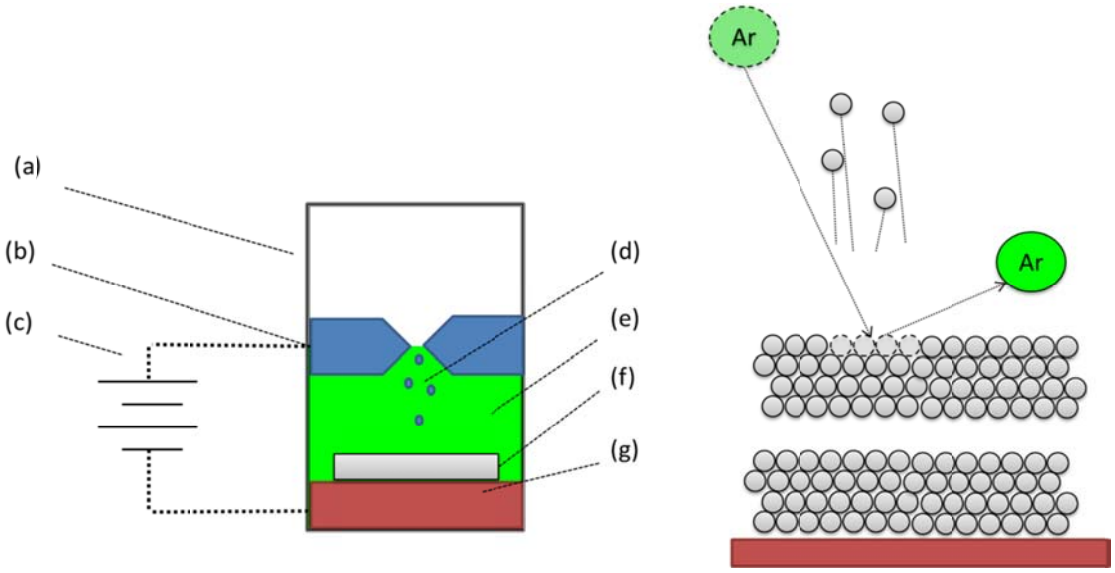

Figure 52 Experimental schematic for GDMS measurements consisting of (a) high vacuum chamber, (b) anode for acceleration of Argon ions, (c) accelerating voltage, (d) sputtered surface ions, (e) argon plasma, (f) sample, and (g) cathode.

Glow Discharge Mass Spectrometry is a micro-sampling technique requiring a solid sample and, as such, the results are subject to the homogeneity of that portion of the sample sputtered into the ionization volume. As there are very few reference materials available for the purity metals and semiconductor materials, the only practical quality control samples are in-house control standards (The standards used in this work are those developed by the National Research Council of Canada).

In this thesis investigation GDMS has been used for the analysis of Cd(Zn)Te purity. This method is necessary for analyzing impurities introduced by the process such as Carbon, Nitrogen, and Boron that are not detectable by methods such as ICP-MS due to the dissolution reagent used (see previous section). For these measurements, it was necessary to cut samples to a dimension of 2.3mm x 2.3mm x 20mm. A typical sample prepared for these measurements is presented in **Figure 53**. This is the ideal sample geometry for the GDMS analysis equipment. Immediately prior to analysis, the samples are chemically pre-cleaned in a 5% bromine in

methanol solution. This step removes surface contamination that may exist from the cutting process or packaging/shipping of the sample.

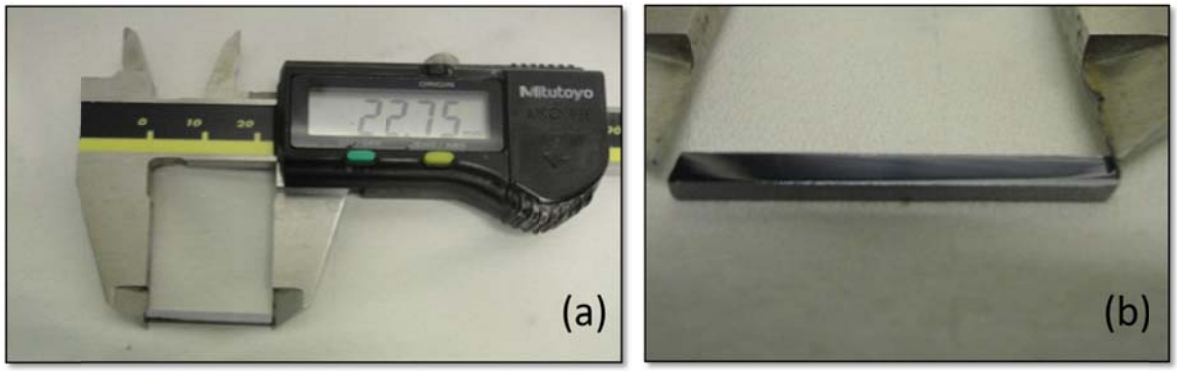

Figure 53 (a) Typical CZT polished bar used for GDMS measurements (b) close up of polished surface.

4.3.6 Photo-Induced Current Transient Spectroscopy

Photo Induced Transient Spectroscopy is an experimental technique which has been implemented extensively throughout this thesis for the investigation of deep centers and defects in semi-insulating Cd(Zn)Te. Moreover, the application of PICTS theory for the calculation of the activation energy, apparent cross section, and concentration of deep centers present in the material grown in this investigation has been a crucial part of this thesis. For this reason, not only the experimental aspect of the technique is presented, but the theory which has been implemented for calculation of the aforementioned parameters.

It is important to comment that this technique has been developed over the past several decades specifically for the analysis of the electronic properties of semi-insulating materials. Specifically, as an alternative to capacitance probe and DLTS techniques, PICTS is well suited for the analysis of high resistivity materials, such as those which have been used in this work.

4.3.6.1 Experimental Measurement Considerations

The experimental apparatus used for carrying out the PICTS measurements is presented in **Figure 54**. The experimental arrangement consisted of an aluminum sample holder within a cryostat cooled to liquid nitrogen temperatures. A heating element and thermocouple were embedded in the housing such that the temperature of the sample could be controlled using a Lakeshore DRC-91C temperature controller. Pulsed optical excitation was achieved using a HP-8003A Pulse Generator in conjunction with 644nm and 890 nm LEDs. Using this arrangement, pulses on the order of 10 – 20 μs and a period of 300 – 500 μs could be used to probe the sample.

The current transient induced by the optical pulsing was measured and recording using a LeCroy 9631Dual 300 MHz 2.5 Gs/s Oscilloscope in conjunction with a SULA Technologies Correlator. Custom developed software was used for generating the differential current transient plots as a function of temperature, and saving to comma separated values (*.csv) format.

Each sample investigated in this work was prepared using the methods presented in Chapter 4, Section 3. Specifically, each electrode surface was polished using 1 μm diamond slurry and subsequently chemically etched using 2% Bromine Methanol. Gold contacts with a thickness near 90 nm were deposited using the electroless method. The lateral edges of the samples were mechanically polished using 3 μm Alumina Oxide, a technique which has proven to reduce leakage current in planar detectors.

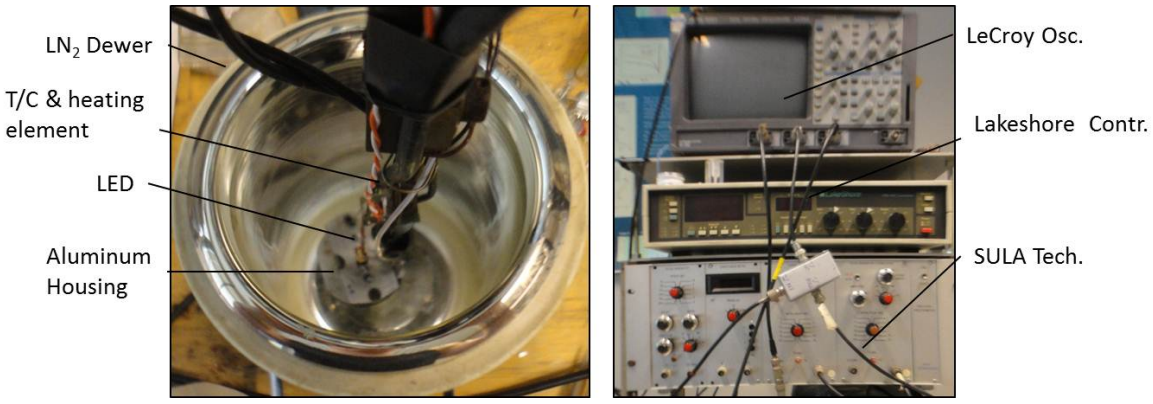

Figure 54 Left: Experimental sample holder with cryogenic cooling chamber. Right: (From top to bottom) LeCroy 9631Dual 300 MHz 2.5 Gs/s Oscilloscope, Lakeshore DRC-91C temperature controller, SULA Technologies Correlators.

From an experimental point of view there are several challenges to achieving useful measurement data. First, it is important that the samples have low leakage current such that the signal to noise ratio of the transient current is sufficiently high. It is important to keep in mind the PICTS method was developed specifically for application to high resistivity materials. Second, the quality of the contacts as a source of noise must also be considered. Fluctuations in the LED photon flux as a function of current must be taken into account for normalization of absorbed intensity. For this reason, the photon flux of the 640 nm LED used has been measured to be 1 x 10^{16} photons / second.

Presented in **Figure 55** is the geometry used for making experimental measurements. During the measurement, it is also important that the temperature remains stable and there is no temperature gradient across the sample. This latter consideration becomes of a challenge for larger area samples. Therefore, for these larger samples a sandwich configuration mounting block configuration has been used with thermally conductive paste for homogenizing the temperature across the sample. The sample is mounted and fixed vertically beneath the opening in the Aluminum housing. The light from the LED enters through this opening. The copper slabs were used for increasing the uniformity of the temperature across the sample to eliminate temperature gradients across the sample.

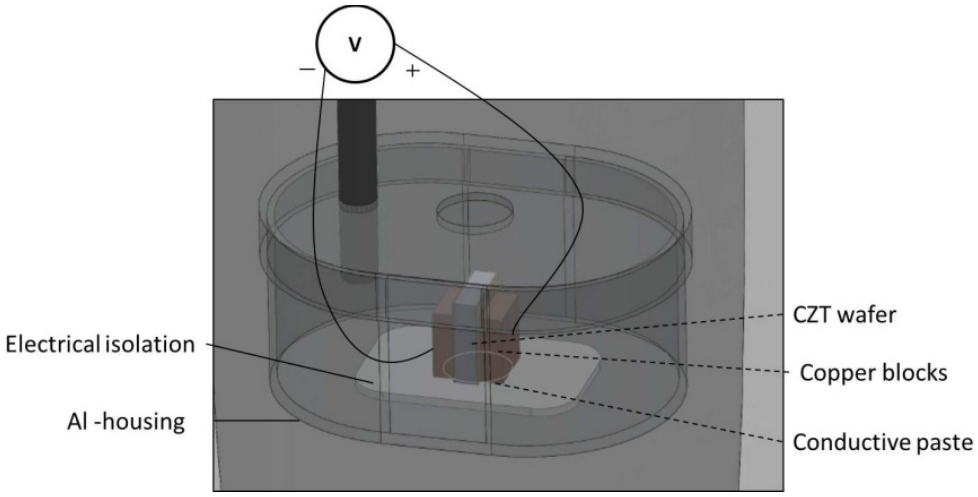

Figure 55 Sample mounting geometry used for PICTS measurements.

To understand the results obtained using this technique, it is important to first understand the nature of the phenomena being measured. In the PICTS measurement, carriers are generated within the semiconductor using a pulsed light (in this case an LED), which enters the aluminum housing directly above the sample shown in **Figure 55**. The energy of the pulsed light is typically near or just below the band-gap energy of the semiconductor. In the present study LEDs which emit 644nm and 890nm wavelength light were used. This assures high and uniform absorption of light by the crystal.

The photo-generated carriers become trapped by active defects within the material up until a saturation limit. It is also useful to point out that for high resistivity materials, re-trapping is negligible. When the light pulse is switched off, the photo-generated electrons are then

thermally emitted. In the presence of an external electric field, the slow thermal release of electrons will give rise to a measureable transient current.

Presented schematically in **Figure 56** is the relation between (i) the optical pulse, (ii) the photo-saturation, and (iii) the transient decay of current. This figure illustrates the current measured as a function of time for a device under electrical bias, which is photo-excited by an externally pulsed LED. Point ´´A´´ corresponds to a single optical pulse generating photo-current within the material. There is a sharp increase in current up to Point ´´B´´ where trapping begins to take place. Trapping continues until a saturation current is reached, $i(0)_L$. Between points C and D, the light pulse is switched off and the photo-generated carriers undergo rapid recombination. Between points D and E, the slow decay of current is of principal interest for PICTS measurements. It is important to consider that the time between each optical pulse is long enough to allow the system to return to equilibrium, and that the length of each light pulse is sufficiently long to completely fill the traps. It is important to point out that the PICTS method is sensitive only to majority carriers in the material. For all of the materials studied here, the majority carrier is n-type.

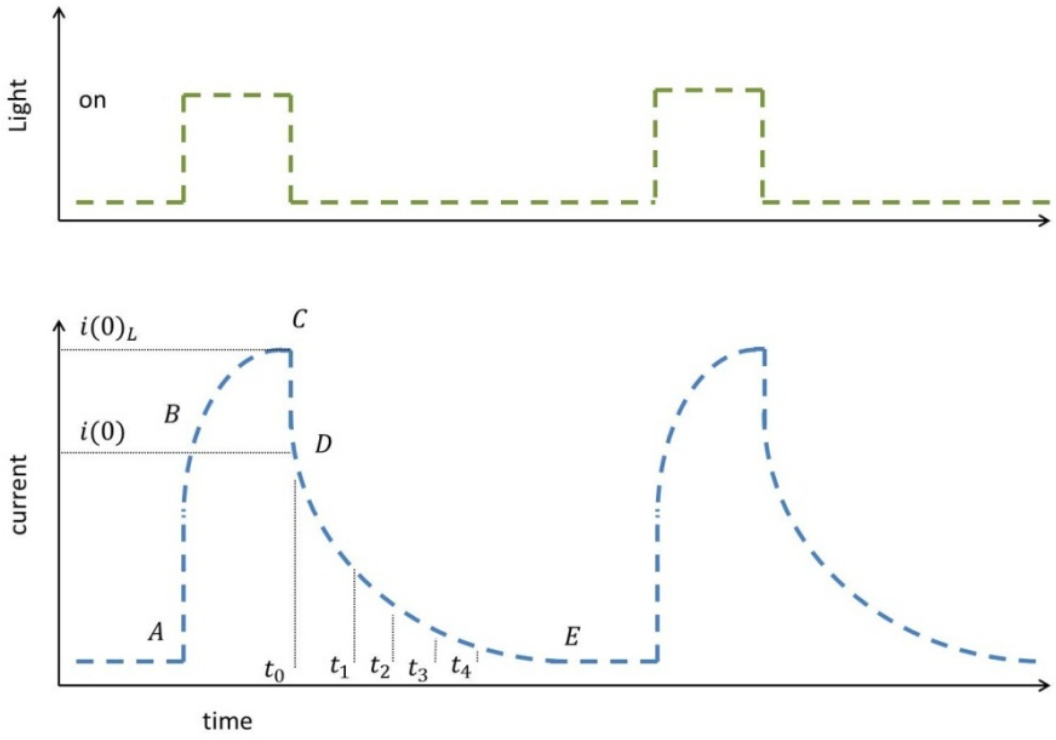

Figure 56 Top: Pulsed light, Middle, Photo Induced Current.

4.3.6.2 Trap Energy and Cross Section Determination

The decaying current transient, $\boldsymbol{I(t)}$, may be expressed analytically using Equation **24**, where $\boldsymbol{q}$ is electron charge, $\boldsymbol{E}$ is the electric field, $\boldsymbol{\mu_e}$ is the electron mobility, $\boldsymbol{\tau_e}$ is the electron lifetime, and $\boldsymbol{n_t(0)}$ is the saturation density of trapped electrons. The parameter $\boldsymbol{A}$ takes into account electron charge, mobility, applied bias, device geometry, and the lifetime of the carriers.

Equation 24

$$\begin{aligned} \boldsymbol{I(t)} &= \boldsymbol{q \cdot E \cdot \mu \cdot \tau \cdot n_t(0) \cdot e_n \cdot exp(-e_n \cdot t)}\ ) \\ &= \boldsymbol{A \cdot e_n \cdot exp(-e_n \cdot t} \end{aligned}$$

These electron and hole emission rates are a thermally mediated process and may be described using **Equation 25**, where $\boldsymbol{\sigma_n}$[1] is the electron or hole capture cross-section, $\boldsymbol{N_c}$ the density of states for Cd(Zn)Te, $\boldsymbol{v_n} = (\boldsymbol{k \cdot T/m_e})^{\mathbf{1/2}}$ the thermal velocity, $\boldsymbol{k}$ is the Boltzmann constant, $\boldsymbol{T_{max}}$ is the temperature at which the transient reaches a local maxima, and $\boldsymbol{E_t}$ is the trap ionization energy. The effective mass $\boldsymbol{m_e}$ of electrons in Cd(Zn)Te is taken to be $\boldsymbol{0.14 \cdot m_0}$ (18).

Equation 25

$$\boldsymbol{e_n = N_c \cdot v_n \cdot \sigma_n \cdot T_{max}^2 \cdot exp\left(-\frac{E_t}{kT_{max}}\right)}$$

By measuring the current transient as a function of temperature, the electron/hole emission rates will reach a maximum whose temperature depends on the ionization energy $\boldsymbol{E_t}$ of the trap. By measuring this position at which the emission rate is at a maximum, or $\boldsymbol{T_{max}}$, the emission rate may be determined experimentally. It is this experimental measurement which provides for the simultaneous measurement of trap energy and cross section.

The double gate PICTS method (which is the differential method used here) consists of reading the transient current at two different times after the optical pulse, and plotting the differential measurement $i(t_1) - i(t_2)$. By choosing two delay times t_1 and t_2 such that $t_2 \gg t_1$, the change in current, $\boldsymbol{\Delta i(t)}$, may be represented using Equation **26**. This result follows

[1] The capture cross section, $\boldsymbol{\sigma_n}$, represents an effective area such that the probability that an electron will undergo a transition inside of this boundary is 1 and the probability outside the boundary is zero. Therefore the cross section represents the spatial volume into which electrons or holes may become trapped by the defect.

directly from the representation of the transient current as an exponential decay of a thermally mediated process.

Equation 26

$$\boldsymbol{\Delta i(t) = A \cdot e_n \cdot [exp(-e_n \cdot t_1) - exp(-e_n \cdot t_n)]}$$

For a given delay time, t_1, the trap with ionization energy $\boldsymbol{E_t}$ and emission rate $\boldsymbol{e_n}$ will reach a maximum specifically when $\boldsymbol{e_n = 1/t_1}$. This relationship is demonstrated graphically in **Figure 57** using **Equation 26** for $t_1 = 50\,ms,\ 20\,ms, 10\,ms, \& 1ms$. With respect to each delay time, the maxima occur when $e_n = 20, 50, 100, \& 200$ respectively. It is also important to point out that using shorter delay times results in higher current transient measurements because the system is further from equilibrium. For longer delay times, however, the photo-generated current have already decayed to a large extent, and the differential current is substantially lower.

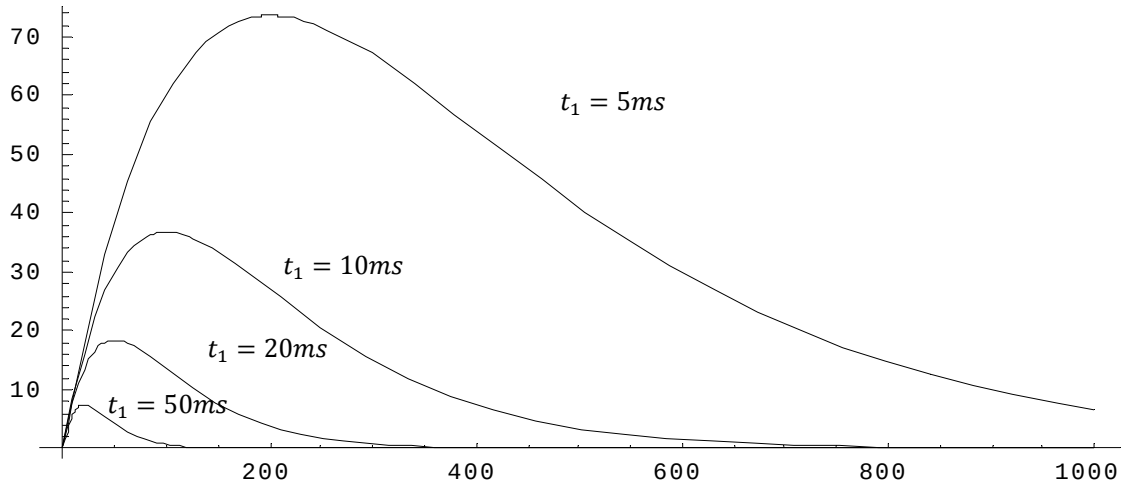

Figure 57 Plot of equation 3 with $\boldsymbol{t_1 = 50,\ 20, 10, \& 5ms}$ $\boldsymbol{t_n = 100ms}$. For $\boldsymbol{t_1 = 10ms}$ the maxima occurs at $\boldsymbol{e_n = 100s^{-1}}$.

Equation 27 was used to derive the relation between the delay tine (controlled by the SULA Correlator) and the emission rate of electrons, where $\boldsymbol{t_i}$ is the delay time, measured from Point D in **Figure 56**. The value 1.95 is a constant associated with the SULA correlator measurement hardware. Presented in **Table 6** are experimental values derived for the emission rate, $\boldsymbol{t_1}$, and $\boldsymbol{t_2}$ associated with different emission rates.

Equation 27 $$e_n = \frac{1}{(t_i^{-1} * 1.95)}$$

Table 6 Experimental values for the emission rate, t_1, and t_2 associated with each ID used.

ID	e_n	t_1	t_2
100	5.1	1.191×10^{-1}	2.978×10^{-1}
50	10.3	5.956×10^{-2}	1.489×10^{-1}
20	25.6	2.382×10^{-2}	5.956×10^{-2}
10	51.3	1.191×10^{-2}	2.978×10^{-2}
5	102.6	5.956×10^{-3}	1.489×10^{-2}
2	256.4	2.382×10^{-3}	5.956×10^{-3}
1	512.8	1.191×10^{-3}	2.978×10^{-3}
0.5	1025.6	5.956×10^{-4}	1.489×10^{-3}
0.2	2564.1	2.382×10^{-4}	5.956×10^{-4}
0.1	5128.2	1.191×10^{-4}	2.978×10^{-4}
0.05	10256.4	5.956×10^{-5}	1.489×10^{-4}

The emission rate, also referred to as ID, has a large impact on the PICTS spectra which is obtained. Shown in **Figure 58** is a PICTS spectra obtained for a high resistivity Cd(Zn)Te test device, biased at 20 V and using a 640 nm LED with a pulse width of 20ms and a period of 500ms. The right hand axis corresponds to the measured value of $i(0)_L$ and the dotted orange line corresponds to how this parameter increases with temperature. The solid lines correspond to the measured current transient, using different delay times, in this case 2, 5, 10, and 20 μs. As may be seen, for higher e_n values, the differential current transient diminishes. This is consistent with **Equation 26**.

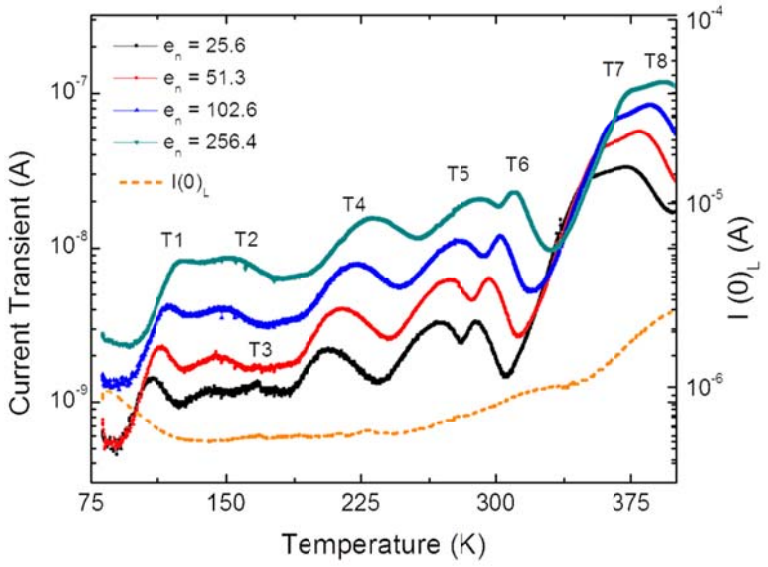

Figure 58 PICTS Spectra of Cd(Zn)Te sample obtained using four different delay times, and the experimentally observed traps.

After identifying the local maxima at $\boldsymbol{T_{max}}$ associated with each trap for each delay time, an Ahrennius plot is constructed to determine the energy of the traps involved. This is determined by plotting 1000/T vs. T^2/e_n, using the experimentally determined values of $\boldsymbol{T_{max}}$ and $\boldsymbol{e_n}$. $\boldsymbol{T_{max}}$ corresponds to the experimentally measured temperature at which the emission rate reaches a local maxima, while $\boldsymbol{e_n}$ is calculated using **Equation 27**. Each data point for each of the traps may then be fit using Equation 28. Thus, the carrier cross section $\boldsymbol{\sigma_n}$ and the trap ionization energy $\boldsymbol{E_t}$ may be determined in this way.

Equation 28
$$\boldsymbol{e_n/T^2 = [\sigma_n * \gamma * exp(E_t/k \cdot T_{max})]^{-1}}$$

The value 2.4×10^{20} is a normalized value which takes into account the temperature dependence of the emission rate following **Equation 29**.

Equation 29
$$\boldsymbol{\gamma = (N_c \cdot v_n)/T^2 = constant}$$

Where the density of states in the conduction band and the thermal velocity of the electrons may be expressed using **Equation 30**

Equation 30

$$N_c = 2\left(\frac{m_0 \cdot k \cdot T}{\pi^2 \hbar^2}\right)^{3/2}$$
$$v_n = (k \cdot T/m_e)^{1/2}$$

4.3.6.3 Trap Concentration Determination

The double gate PICTS method consists of reading the transient current at two different delay times, and plotting $i(t_1) - i(t_2)$. It is important that the delay times satisfy the requirement $t_2 > 4 \cdot t_1$ so that $e_n(T_{max}) \sim t_2$. This condition makes it possible to determine the height of the double gate peak using **Equation 31** (19).

Equation 31

$$\Delta i(T_{max}) = q \cdot E \cdot \mu \cdot \tau \cdot n_t(0) \,/\, 2.718 \cdot t_1$$

Using the normalized double gate spectrum, it is possible to evaluate the concentration of electron and hole traps present in the material. The normalized transient, $i_{norm}(t)$, takes the form of **Equation 32** where d^* is the thickness of the photo-exited layer, $\beta(\lambda)$ the quantum efficiency, I_a the light energy absorbed by the sample, and λ the wavelength of light used (19).

Equation 32

$$i_{norm}(t) = \frac{\Delta i(t)}{i_L(0)} = \frac{\mu \cdot \tau}{\mu_0 \tau_0} \cdot \frac{d^*}{\beta(\lambda) \cdot I_a} \cdot \frac{h \cdot c}{\lambda} \cdot \frac{N_t}{e_n} \cdot \exp(-e_n \cdot t)$$

A practical form of the PICTS equation, and the one used here for determining trap concentration can be expressed following (20). In **Equation 33** , the concentration of defects N_t will be equal to n_0 if a high enough optical excitation is applied to reach saturation (19). Using **Equation 34**, it is then possible to measure the concentration of defects

Equation 33

$$i_{norm}(t) = \frac{\Delta i(t)}{i_L(0)} = \frac{n_0}{\varphi_0 \cdot \alpha} \cdot e_n \cdot [\exp(-e_n \cdot t_1) - \exp(-e_n \cdot t_2)]$$

Equation 34

$$n_o = N_t = \frac{\Delta i(t)}{i_L(0)} \cdot \frac{\varphi_0 \cdot \alpha}{e_n \cdot [\exp(-e_n \cdot t_1) - \exp(-e_n \cdot t_2)]}$$

For the 640nm wavelength LED, the absorption coefficient has been reported 1.2034×10^4 cm^{-1} and the reflection coefficient is reported to be 0.2504. For 880nm an absorption coefficient of 5.5×10^3 cm^{-1} and a reflection coefficient of 0.2292 have been reported. These values are for non-polarized light at normal incidence. The parameter $i_n(t) = i(t)/i_L(0)$ is determined experimentally from the normalized PICTS spectra, and is presented in **Figure 59**. From this experimental data it is possible to extract the value for $i_n(t)$ measured for each trap by calculating $i(t)/i_L(0)$ at T_{max}. The photon flux of the LED used in these experiments has been determined experimentally to be 1.02×10^{16} $\text{photons/cm}^2\cdot\text{s}$.

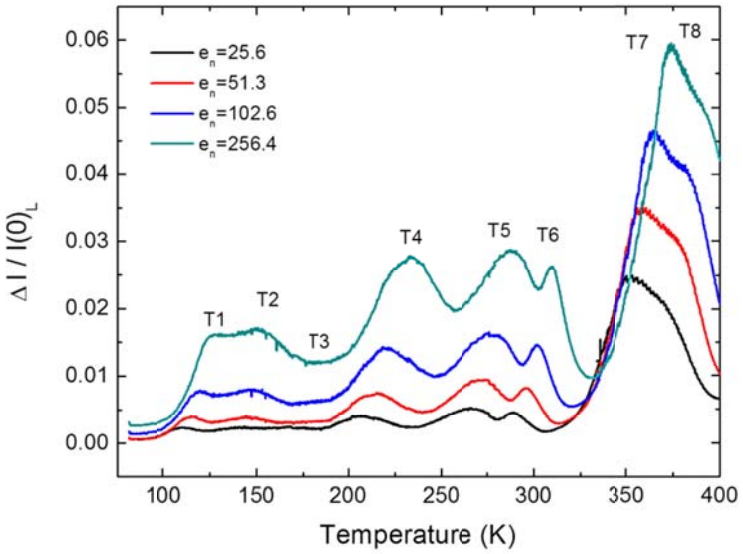

Figure 59 PICTS plot of $\boldsymbol{i(t)/i_L(0)}$ as a function of temperature for the same crystal presented in **Figure 58**

4.4 Electrical Measurements

4.4.1 Contactless Resistivity Mapping

The Contactless Resistivity Mapping or COREMA instrument measures the exponential decay of charge induced by a dielectric polarization of the material. Samples are placed into the system as a dielectric substance and resistivity is evaluated by measuring a time dependent charge transient observed after application of a voltage step between the two electrodes. The exponential time dependence of the charge Q(t) allows one to measure the relaxation constant τ as well as the charges Q(0), Q(∞). The terms $\boldsymbol{\varepsilon_0}$ and $\boldsymbol{\varepsilon}$ represent the permittivity of free space

and the dielectric constant of Cd(Zn)Te (10.9). With the dielectric constant of Cd(Zn)Te, and using Equation 35, one obtains the resistivity of the material. The measurement range of this instrument is $10^5 - 10^{12}$ Ω-cm.

Equation 35 $$\boldsymbol{\rho = \tau \cdot Q(0)/(\varepsilon_0 \cdot \varepsilon \cdot Q(\infty))}$$

The capacitive probe of the COREMA consists of a metal rod about 1mm in diameter, surrounded by a guard electrode. The probe is brought to within 50-100 μm of the wafer surface and a voltage step is applied, and the decay of charge is measured. Lateral displacement of the probe provides mapping and topography capability. Presented in **Figure 60** is the effective circuit diagram of the COREMA and the basic configuration. It is important to comment that for 50mm wafers, a high degree of parallelism was required for achieving this mapping capability.

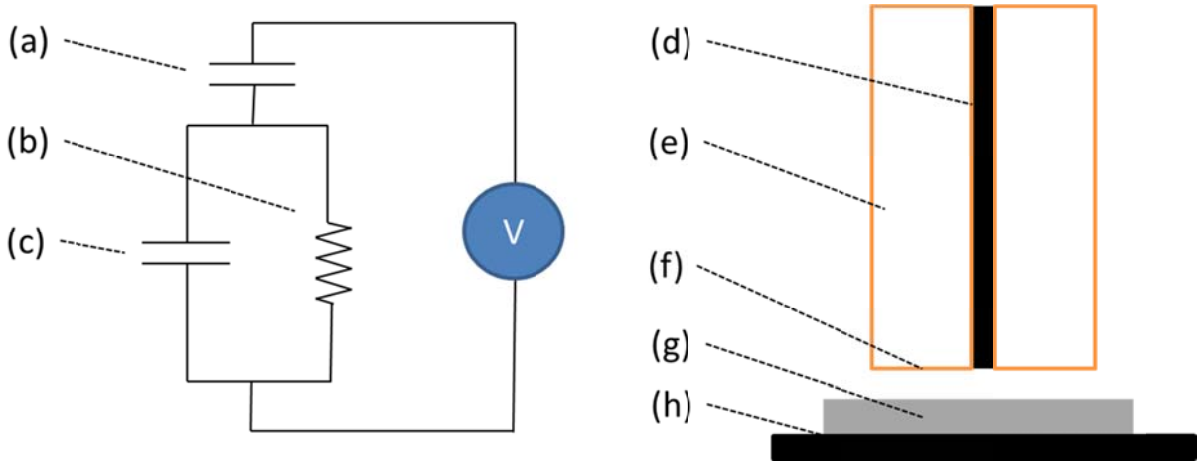

Figure 60 Circuit diagram of COREMA (a) capacitance of probe material (b) and (c) capacitance and resistivity of semiconductor, (d) COREMA probe, (e) guard ring, (f) air gap between probe and wafer, (g) semi-insulating wafer, (h) backside electrode.

The COREMA system is shown below in **Figure 61** with the system open (left) and the system closed (right). The system is closed during measurement to prevent free carrier absorption and excitation which decreases the resistivity of the material due to photoconductivity.

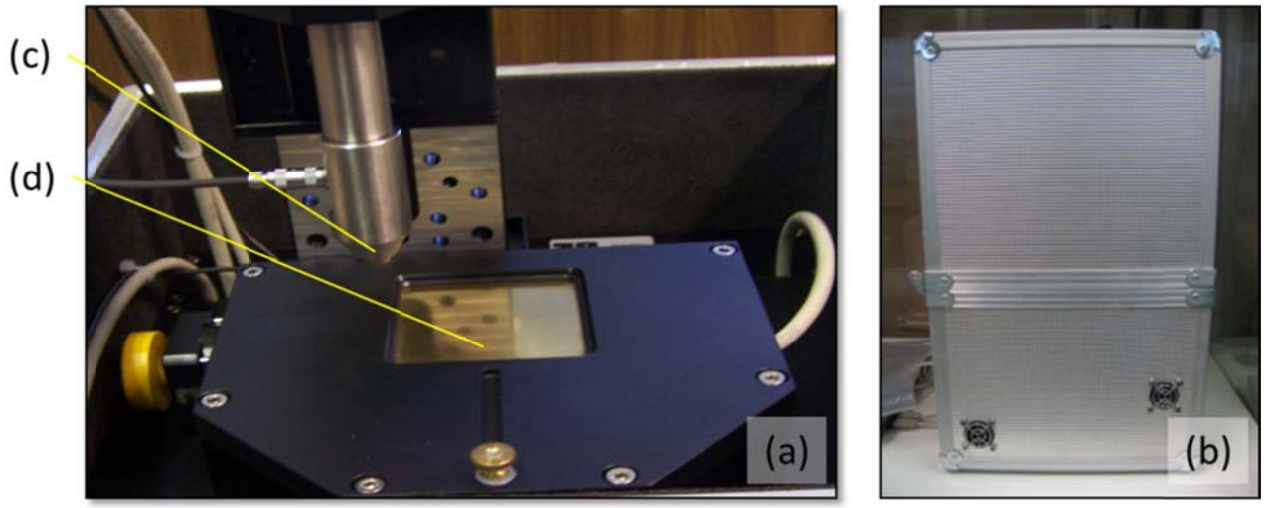

Figure 61 COREMA system at CGL for non-contact measurement (a) open system, (b) system closed, (c) measurement probe, (d) sample stage/backside electrode.

4.4.2 Current-Voltage

Current voltage (I-V) characteristics were measured using a Kiethley 2400 automated I-V module, shown below in **Figure 62**. These measurements were used for testing detector performance, comparing the effects of different surface treatments on detector resistivity, and measuring temporal effects of radiation devices. Also presented in **Figure 62** are the components which were designed and built for contacting planar devices used in this work. This small part was comprised of an anode plate, a cantilever-type cathode for contacting the device, and electrical isolation components. The system is also closed during measurement to prevent free carrier absorption and excitation which increases carrier concentration and decreases the resistivity of the material due to photoconductivity.

Samples were biased between +200 and -200 volts, and bulk resistivity was measured following **Equation 36**, where A is detector area, ρ is the sample resistance determined from I-V curve $\frac{\Delta V}{\Delta I} = \rho$, and δ is the detector thickness.

Equation 36

$$\boldsymbol{\Omega . cm = [A \cdot \rho]/\delta}$$

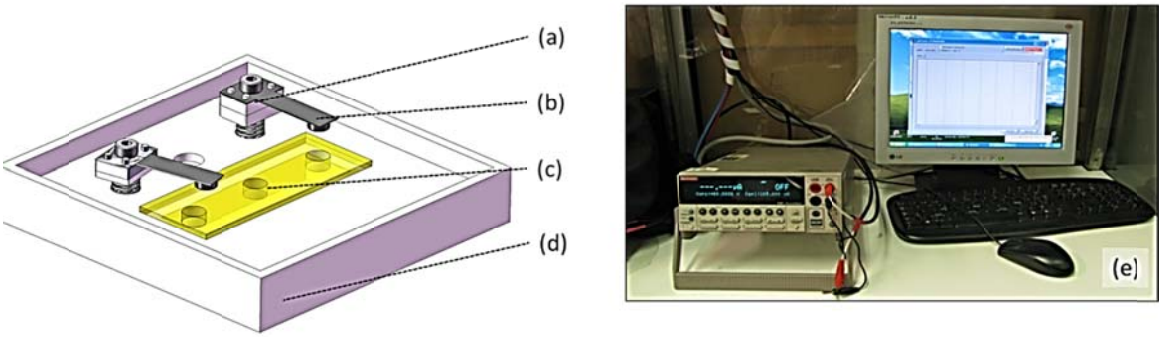

Figure 62 Sample mounting fixture used for I-V measurements comprised of (a) ceramic isolation, (b) gold coated cantilever (cathode), (c) gold coated plate (anode), (d) Teflon isolation, (e) Kiethley 2400 I-V module used for current voltage measurements.

4.4.3 Hot Probe Measurement

In order to establish the carrier type of the material grown in this thesis, the ´´hot-probe´´ technique was used for characterization of wafers harvested from each of the growths. The "hot-probe" technique provides a quick method to distinguish between n-type and p-type semiconductors using only basic experimental implementations.

Due to the high resistive nature of the Cd(Zn)Te studied in this work, it was necessary to use a high impedance electrometer for measurement of the current induced by the probe (Kiethley Electrometer Model 6517). This current was on the order of Pico amperes. A small resistance heater was attached to a tungsten tipped probe, which was positioned on the top semiconductor surface and served as the hot probe in the experiment. The bottom side of the sample was connected to a ´´cold probe´´. The hot probe is connected to the positive terminal and the cold probe is connected to the negative terminal of the electrometer.

When the hot probe is in contact with the semiconductor surface, the carriers within the semiconductor move from the hot probe towards the cold probe. The temperature applied at the surface causes a change in the conduction band energy relative to the Fermi level of the semiconductor. The effective density of states of the semiconductor changes following **Equation 37** for the conduction band and **Equation 38** for the Valence band. It is also important to note that the Fermi Energy does not vary throughout the semiconductor, but remains constant.

Equation 37
$$N_C = \left(\frac{2\pi \cdot m_{de} \cdot k \cdot T}{h^2}\right)^{3/2} M_c$$

Equation 38
$$N_V = \left(\frac{2\pi \cdot m_{dh} \cdot k \cdot T}{h^2}\right)^{3/2} M_c$$

The density of states in the conduction band at 300K is ~6.6 x 10^{17} cm^{-3}, but increases slightly to ~7.3 x 10^{17} cm^{-3} when the temperature is increased by only 20K. The density of states in the valence band is ~1.18 x 10^{19} but increase to ~1.3 x 10^{19} with increasing temperature by 20K. This higher density of states in the CB of n-type material corresponds to a local increase in the electron density surrounding the hot probe. This in turn produces an electric field between the hot probe and the cold probe. Using the high resistivity electrometer, the drift current produced by the electric field is measured. This electric field causes the electrons to flow from the high temperature region (high electron density) to the low temperature region (low electron density). When applying the probes to n-type material one obtains a positive current reading on the meter, while for p-type material the situation is reverse and a negative current is measured.

Presented in **Figure 63** is the 3D model of the hot probe system developed for implementation in the Crystal Growth Laboratory in Madrid. This configuration allows for measuring in planar configuration wherein the hot probe is on top and the cold probe is on bottom. This design also permits the possibility to measure with both hot and cold probes on the top surface. The pins of each electrode are connected to a Kiethley 6517 electrometer and the hot probe is connected to a small resistance heating element. Raising the temperature of the semiconductor surface by 20º was found to be sufficient for generating a measureable signal in the high resistivity elements studied. Additional features of the design include a Kiethley 6517 electrometer, a 5W heating power supply, and a ceramic resistive element.

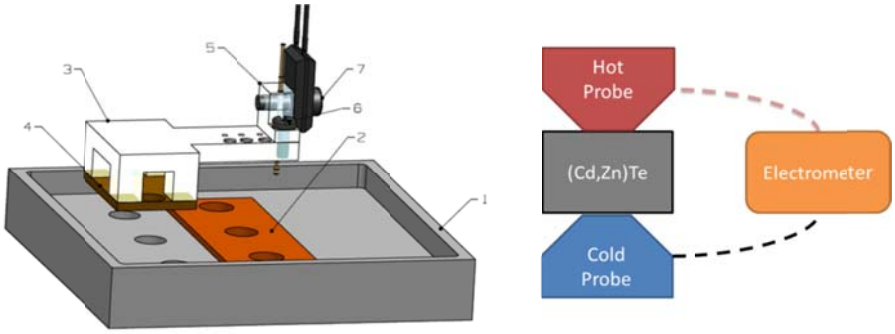

Figure 63 Left: 3D model of hot probe developed in CGL lab: (1) Teflon isolation (2) gold plated electrode (3) acrylic cantilever (4) magnetic mounting plate (5) resistance heating mount (6) retractable probe (7) resistance heater. Right: Hot probe measurement schematic.

4.5 Other Methods

4.5.1 Surface Profilometry

Surface profilometry relies upon the use of a piezoelectric material used to convert mechanical displacement of a scanning stylus into an analog signal. Indeed, in certain materials more than others, a significant amount of charge accumulates as a result of stress introduced into the sample, referred to as piezoelectricity. The surface profilometer can measure small surface variations as a function of position due to the interaction of the piezoelectric stylus and surface roughness of the material.

In contact profilometry, the piezoelectric stylus is moved laterally while in contact with a surface for a specified distance and with a specified contact force applied. A typical profilometer can measure small vertical features ranging in height from 10 nanometers to 1 millimeter. This instrument has been used for the analysis of carbon films, ceramic crucible materials, as well as semiconductor surface roughness.

A Dektak surface profilometer shown below in **Figure 64** was used for analysis of surface morphology. Typical scan parameters used in this work were 2mm in length using a stylus force of approximately 25mg.

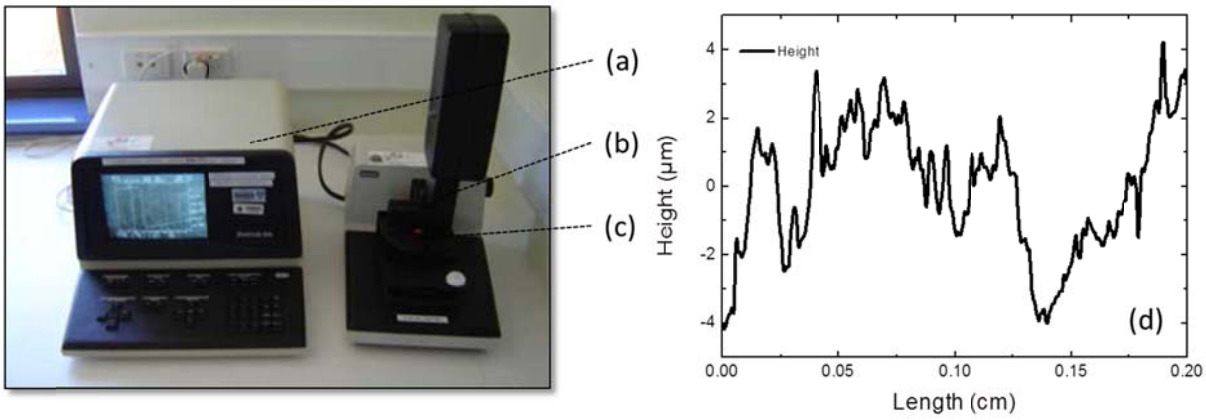

Figure 64 Profilometer used for measuring surface roughness of crucible with (a) control system (b) stylus head and (c) sample stage, and (d) typical profilometer line scan.

5 CHAPTER SUMMARY

In conclusion, this chapter summarizes (i) the experimental technology which have been developed for the synthesis and growth of Cd(Zn)Te compound semiconductors (ii) the methods used for carrying out gamma ray spectroscopy and (iii) the experimental and theoretical techniques which have been implemented in this investigation. Indeed, the furnaces which have been designed and built during this thesis for crystal growth as well as carbon coating have been presented. The calibration of noise in the detector spectroscopy was also presented to demonstrate a system which exhibits low noise for the spectroscopic gamma measurements which are presented in Chapter 4. Finally, the theoretical aspects which have been used in this work are presented for several characterization techniques which have been used.

6 BIBLIOGRAPHY

1. **E. Raiskin, J.F. Butler.** 1987, IEEE Trans. Nucl. Sci., Vols. NS-35, p. 81.
2. XCOM Database. *NIST.* [Online] National Institute of Standards and Technology. http://physics.nist.gov/PhysRefData/Xcom/html/xcom1.html.
3. **AppNano.** Technical Specification Sheet Probe Model DD-ACTA.
4. *Kelvin probe force microscopy and its application.* **W. Melitz, J. Shen, A. Kummel, S. Lee.** 2011, Surf. Sci. Reports, Vol. 66, pp. 1-27.
5. *Evidence for Surface States on Semiconductors from Change in Contact Potential on Illumination.* **Brattain, W.H.** 1947, Phys. Rev., Vol. 72, p. 345.
6. *Physical Theory of Semiconductor Surfaces.* **C.G.B. Garrett, W.H. Brattain,.** 1955, Phys. Rev., Vol. 99, p. 376.
7. *Surface Properties of Germanium.* **W.H. Brattain, J. Bardeen.** 1953, Bell System Tech. J., Vol. 32, p. 1.
8. *Surface Photovoltage Spectroscopy—A New Approach to the Study of High-Gap Semiconductor Surfaces.* **H.C. Gatos, J. Lagowski.** 1973, J. Vac. Sci. Technol., Vol. 10, p. 130.
9. **Lueth, H.** 1975, Appl. Phys., Vol. 8, p. 1.
10. *Surface studies by modulation spectroscopy.* **G. Heiland, W. Moench.** 1973, Surf. Sci., Vol. 37, p. 30.
11. *Alloy composition and electronic structure of CdZnTe by surface photovoltage spectroscopy.* **J. Yang, Y. Zidon, Y. Shapira.** 2, 2002, J. Appl. Phys., Vol. 91, p. 703.
12. *A comparison of techniques for nondestructive composition measurements in CZT substrates.* **S. P. Tobin, J. P. Tower, P. W. Norton, D. Chandler-Horowitz, P. M. Amirtharaj, V. C. Lopes, W. M. Duncan, A. J. Syllaios, C. K. Ard and N. C. Giles,.** 5, J. Electron. Mater., Vol. 24, p. 697.
13. *Surface photovoltage spectroscopy analyses of CZT.* **D. Cavalcoli, B. Fraboni, A. Cavallini.** 2008, J. App. Phys., Vol. 103, p. 043713.
14. *Alloy composition and electronic structure of CZT by surface photovoltage spectroscopy.* **J. Yang, Y. Zidon, Y. Shapira.** 2, 2002, J. Appl. Phys., Vol. 91.
15. **Instrumentation, Center for Synchotron Radiation Research and.** Periodic Table. [Online] Illinois Institute of Technology. [Cited: January 16, 2012.] http://www.csrri.iit.edu/periodic-table.html.
16. *Rutherford Backscattering (RBS).* **Mayer, M.** Trieste : s.n., 2003. Workshop on Nuclear Data for Science and Technology: Materials Analysis. pp. 59-80.
17. *Appl. Phys. Lett.* **N.P. Barradas, C. Jeynes, R.P. Webb,.** 1997, Simulated annealing analysis of Rutherford backscattering data, Vol. 71, p. 291.
18. *Compensation and trapping in CZT radiation detectors studied by TEES, TSC, and I-V measurements.* **E. Y. Lee, R. B. James, R. W. Olsen, H. Hermon.** 6, 1999, J. Electronic. Mater., Vol. 28.
19. **M. Tapiero, N. Jalloun, J.P Zielinger, S.El Hamad, C. Noguet.** 8, 1988, J. Appl. Phys. , Vol. 64 .
20. *Real defect concentration measurements of nuclear detectormaterials by the combination of PICTS and SCLC methods.* **M. Ayoub, M. Hage-Ali, J.M. Koebel, R. Regal, C. Rit, F. Klotz, A. Zumbiehli, P. Siffert.** 2001, Mater. Sci. & Eng., Vol. B83, pp. 173-179.
21. **Amptek.** Charge Sensitive Preamplifer. [Online] Amptek. [Cited: January 22, 2012.] http://www.amptek.com/a250.html.

Chapter III

Synthesis and Crystal Growth of Cd(Zn)Te

This page intentionally left blank

Chapter III Content

1 CHAPTER III INTRODUCTION

This chapter presents original results which have been produced during this thesis related with the material synthesis and crystal growth of Cd(Zn)Te. This chapter is divided into six sections, each related with a distinct aspect of crystal growth.

At the start of this investigation, appropriate protocol for the homogenization and subsequent crystal growth faced certain challenges with respect to reproducibility and obtaining complete homogenization of the starting materials. These problems were associated with (1) accurate determination of the temperature inside the furnace (2) the growth temperature, as well as (3) the temperature used for material homogenization.

Section 1 of this chapter presents the experimental results pertinent to the material homogenization phase, and how this phase of material synthesis impacts the optical, electrical, and compositional properties of the as-grown crystals. In this section we observe the reaction between Cd and Te, the effects of superheating on the melt, and we present a physical model describing the observed phenomenon.

Section 2 presents results obtained through the development of novel crucible materials for crystal growth. In nearly all of the crystals grown in this work, pBN crucibles have been used. One disadvantage of pBN crucibles, however, has to do with the crucible material interacting with the melt during the growth cycle. This observed interaction between the walls of the pBN crucible and that of the Cd(Zn)Te melt prompted the development of a vacuum carbon coating system for applying a carbon coating to pBN crucibles. In order for a new crucible technology to be successfully introduced for the fabrication of Cd(Zn)Te based nuclear imaging detectors, it is important this new technology at least preserves or improves the material quality. For this reason, it was also important to demonstrate that high quality material could be harvested from Cd(Zn)Te ingots grown using carbon coated pBN Crucibles (hereafter referred to as cc-pBN crucibles).

Sections 3 and 4 of this chapter are related with the development of crystal growth protocol using dynamic temperature gradients. In this work, methods to reduce the thermo-mechanical stress imparted into the crystal are implemented. Specifically, crystals have been grown under dynamic temperature gradients to minimize the temperature gradient

across the ingot, while maintaining relatively higher temperature gradients at the Solid Liquid Interface (SLI). In Section 3, how this adjustment affects bulk resistivity and photoconductivity is presented. In Section 4, we investigate test devices harvested from the ingot along the axial direction, and studied in terms of their optical and electrical properties to investigate (1) how these temperature adjustments may lead to variations in material properties and (2) how this variation may affect test device performance.

Section 5 is related with scaling the technology which has been developed for 25mm Cd(Zn)Te ingots, to larger 50mm diameter ingots. Indeed, state of the art gamma radiation detectors based on Cd(Zn)Te require large volumes of uniform and mono-crystalline material. Obtaining large volumes of single crystal materials requires control over a number of crystal growth parameters. The solid-liquid interface shape is an important parameter which is strongly dependent upon the balance between axial and radial heat flow. Indeed, this balance may be controlled to some degree by the ampoule geometry. Furnace materials and geometries which are used to modify the thermal environment to facilitate the crystal growth process are presented. Specifically, the implementation of a Silicon Carbide (SiC) ampoule support pedestal in conjunction with the pBN crucible geometry lead to an increase in the axial heat flow, a decrease in radial heat flow, and improved temperature gradients at the crucible tip

Finally, in Section 6 is discussed the development of a 2-D model based on the experimental geometry which has been designed in this thesis. A great deal of progress has been made over the last decade in not only in crystal growth but simulation of the growth process as well. This chapter is focused on the development of this model, and its application to Cd(Zn)Te growth.

This page intentionally left blank.

2 MATERIAL SYNTHESIS AND MELT HOMOGENIZATION

Section Contents

2.1 Introduction

At the start of this investigation, appropriate protocol for the homogenization and subsequent crystal growth faced certain challenges with respect to reproducibility and obtaining complete homogenization of the starting materials. These problems were associated with (1) accurate determination of the temperature inside the furnace (2) the growth temperature, as well as (3) the temperature used for material homogenization. Presented in **Figure 1** are some of the early ingots which were grown that suffered from incomplete homogenization. Indeed, large volumes of second phase inclusions, voids, and many other crystallographic defects are present.

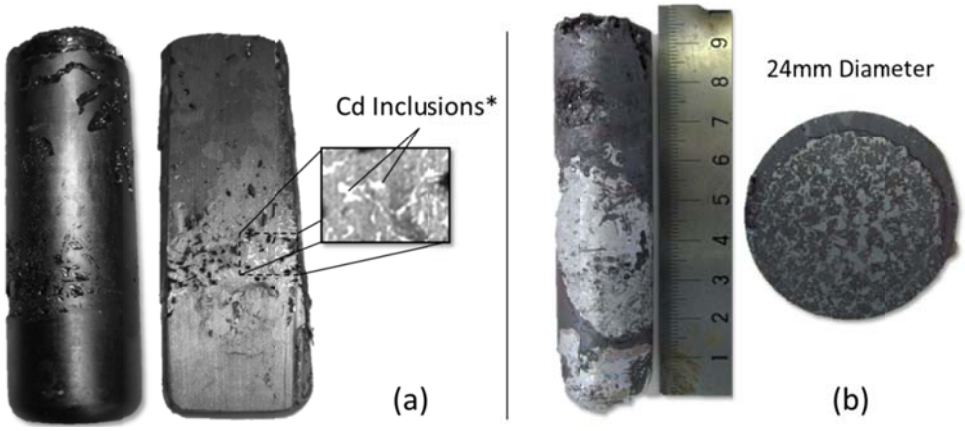

Figure 1 Difficulties in homogenization of raw elements at the start of this investigation. (a) Voids and large Cd-inclusions present in material (b) very poor homogenization results in large non-uniformities.

In order to develop a reproducible process for the synthesis and growth of Cd(Zn)Te from starting elemental compounds, it was necessary to investigate independently the material synthesis and melt homogenization phases.

In general, there are two strategies for material synthesis and homogenization of Cd(Zn)Te. The first method is referred to as ex-situ synthesis or compounding. Using this method, raw materials are charged into an ampoule, sealed, and set into some homogenization algorithm such as a rocking furnace, accelerated crucible rotation, or vibrational stirring. After a certain period of homogenization has elapsed, the melt is cooled and the reacted Cd(Zn)Te alloy is removed. This starting material may then be loaded into a second ampoule to be used for subsequent crystal growth.

Ex-situ synthesis of CdTe single crystals has been presented as far back as the 1970s (1). The THM method is now used quite regularly for material synthesis and

homogenization. The advantages of this ex-situ THM synthesis technique include the capacity for synthesizing large quantities of Cd(Zn)Te without the high temperatures and pressures associated with directional solidification methods, and without the detrimental effects of Zinc segregation (2).

A second method referred to as in-situ compounding, refers to a process wherein the same ampoule is used for material synthesis, homogenization, as well as crystal growth. Therefore, material synthesis and crystal growth can essentially be divided into three different and somewhat dynamic phases. The first phase, which is the focus of this chapter, is the melt homogenization phase. The crystal growth phase is the subject of the following sections of this chapter.

A discussion of the fundamental aspects related with material synthesis of CdTe is presented by Triboulet (3). For example, one important parameter is the starting material shape, size, and the geometry of the crucible used. Another is the method used for physically mixing of the elements, whether it is via rocking furnace, accelerated crucible rotation, melt-oscillating temperature methods, or vibrational methods. For example thermo-mechanical methods for improving melt uniformity have been proposed using oscillating temperatures to cyclically melt and solidify the charge (4). Furthermore, Cd(Zn)Te homogenization has also been achieved using lower temperatures as high as 1160ºC in conjunction with a rocking furnace to mechanically break apart clusters in the melt (5). In general, there exist many parameters and many different methods that have been implemented towards achieving this end. Some of these parameters are listed below in **Table 1** in which those parameters used in this work are also presented.

Material synthesis, homogenization, and crystal growth of detector grade Cd(Zn)Te using in-situ approaches have been demonstrated using carbon coated quartz ampoules and by heating the melt to only 20º-40º above the melting point of Cd(Zn)Te (6) (7) (8). It was not clear whether the experimental conditions used for quartz ampoules would necessarily apply for pBN crucibles, which is the crucible material of choice used in this thesis investigation. The objective of this study is the development of a reliable homogenization protocol for improving the uniformity of synthesized materials.

Table 1 Small set of possible parameters used in the growth and synthesis of Cd(Zn)Te

Parameters	Possibilities	Ref.	Used in Investigation
Growth Technique	• High pressure Bridgman	(9)	Vertical Gradient Freeze
	• Travelling Heater Method	(10)	
	• Bridgman	(6)	
	• Vertical Gradient Freeze	(11)	
	• Physical Vapor Transport	(12)	
Furnace Position	• Horizontal	(13)	Vertical
	• Vertical	(14)	
	• Tilted	(15)	
Melt Homogenization Technique	• Accelerated crucible rotation	(7)	Superheating of melt
	• Furnace rocking	(5)	
	• Oscillating temperature methods	(4)	
	• Superheating of melt	(11)	
Ampoule & Crucible	• Carbon coated quartz	(8)	Carbon coated quartz Pyrolytic Boron Nitride
	• Pyrolytic Boron Nitride (pBN)	(16)	
	• Graphite	(17)	
	• De-wetted growth (no crucible)	(18)	
Atmosphere	• Vacuum	(15)	Vacuum
	• B_2O_3 encapsulated melt	(19)	
Ingot Weight	• Variable		200g 750g
Dopant	• Chlorine	(20)	Indium
	• Vanadium	(21)	
	• Indium	(14)	
	• Germanium	(8)	
	• Lead	(22)	
	• Bismuth	(23)	

2.2 Experimental Approach

The approach adopted here for in-situ homogenization includes (i) Preparation of the starting elemental materials, (ii) Choice of melt stoichiometry, (iii) Charging of the material within the crucible/ampoule, and (iv) Insertion of the material into the VGF furnace for reaction and synthesis. Some of the more important experimental considerations which have been taken into account are summarized here.

2.2.1 Preparation of Starting Materials

As has been previously discussed, the size, shape, geometry, and stoichiometry of the starting material play an important role in the homogenization process. Both the 6N- and 7N-pure elemental Cd, Zn, and Te were used in this investigation. For the 7N starting materials, the material was received in the desired size and shape, packaged in Argon, and no cleaning procedure was necessary. For the 6N material, the starting materials were in large chunk or ingot form, and required physical cutting to reduce their size.

Presented below in **Figure 2** are examples of the 6N elements used in this investigation. The tellurium ingot exhibits a reflective metallic surface, is very brittle and therefore quite easy to break into smaller fragments. The Te came in pieces as large as 7cm, but it was not difficult to reduce these chunks to a size less than 10mm in diameter.

Cadmium, however, is a ductile and hard material, exhibiting a dull matte surface finish. Strong cutting tools were necessary to reduce the size of these chunks to a smaller size i.e. < 10mm. These stainless steel cutting tools also posed to be a strong source of contamination including Fe, C, Cr, Mg, V, as well as other metallic impurities used for the alloying of steel. The Zinc used was 5N in quality and was purchased in small shots which were less than 5mm in diameter and 2mm in thickness.

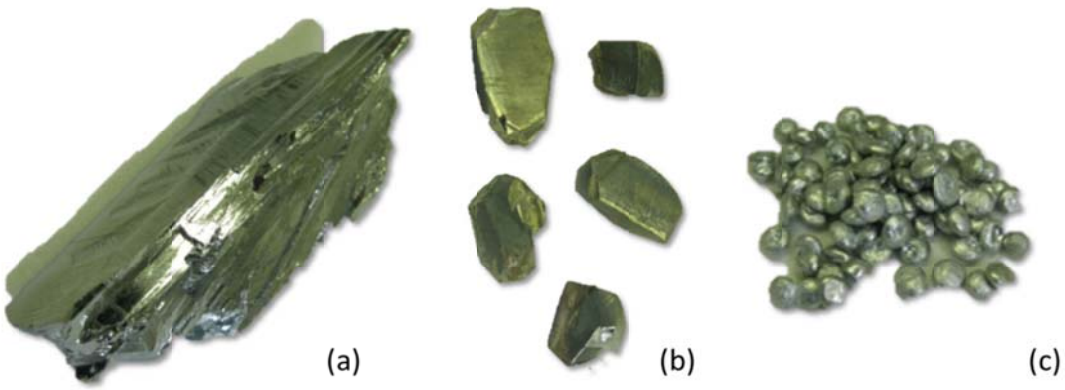

Figure 2 (a) Large ingot of 6N Tellurium, approx. 8cm in length. (b) 6N Cadmium, approx. 3-4cm in diameter. (c) 6N Zinc pellets 5mm in diameter.

The mechanical cutting and handling of material is a potential source of contamination, as the impurities imparted by the surfaces of the cutting tools degrade the electrical and

transport properties of the synthesized material. Therefore, this surface contamination must be eliminated before the material may be used for synthesis. Indeed, a substantial amount of the surface layer must be removed using chemical etching methods to remove the impurities which have penetrated deep into the surface.

Figure 3 presents the experimental setup which has been used for cleaning of the Cd and Te surfaces after cutting. The experimental procedure used for cleaning Cd and Te was (i) manual cutting of the chunks into smaller pieces, (ii) degreasing in strong solvents, (iii) acid cleaning, (iv) rinsing in18MΩ deionized water, (v) solvent rinsing in trichloroethylene and Methanol, and (vi) drying using Acetone.

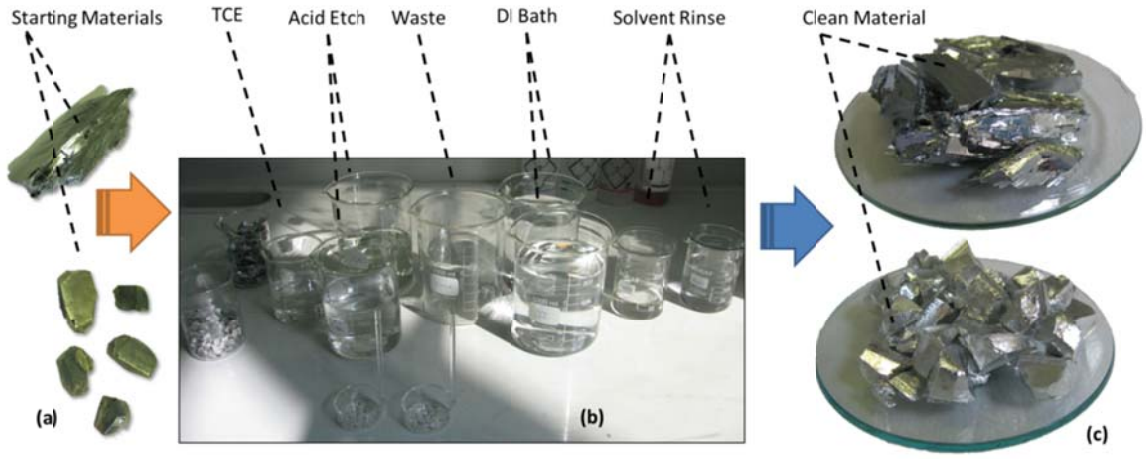

Figure 3 (a) Large chunks reduced into smaller pieces (b) degreasing and acid cleaning procedure (c) material after cleaning procedure.

A dilute HCl solution was used for etching Tellurium fragments while a strong 15% HNO_3 in CH_3CH_3OH solution was used for etching Cadmium. This percentage was increased from 4% as reported by (1) to 15% in order to increase stock removal of material and achieve higher removal rates to eliminate deeply penetrating contamination faster.

Presented in **Figure 4** is elemental Cd after manually cutting the large chunks to smaller shot sizes, as well as after chemical etching using 4% and 15% HNO_3 in ethanol. The surface after etching with 15% appears more reflective with less visible damage imparted by the cutting edge.

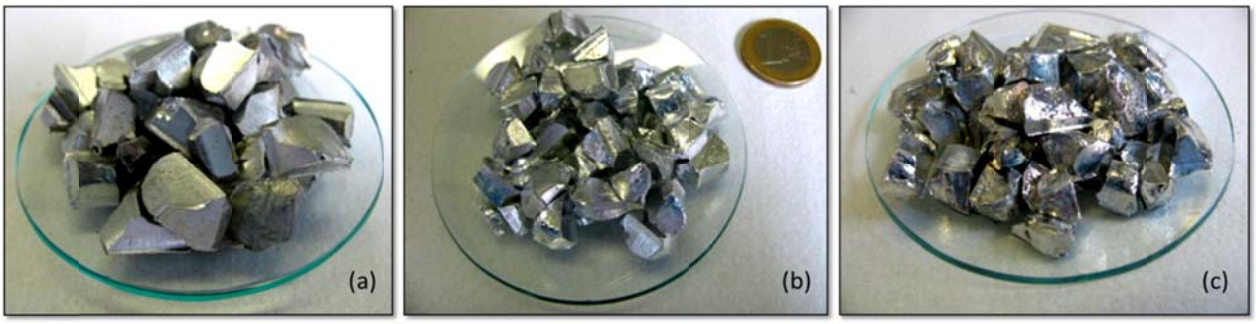

Figure 4 (a) Elemental cadmium after manual cutting. (b) Cadmium after etching using 4% HNO_3 in ethanol, (b) Cadmium after etching using 15% HNO_3 in ethanol.

2.2.2 Establishing Stoichiometric Control

Control over the stoichiometry of the melt is probably one of the most important requirements for the growth of high resistivity Cd(Zn)Te. Therefore, it was important to first set forth the desired stoichiometry at the start of the investigation, based on the phase diagram of Cd(Zn)Te.

The phase diagram of a given semiconductor, and in this case the phase diagram of Cd(Zn)Te, is a representation of the chemical equilibrium between the components in the system. More specifically, the phase diagram describes the interdependence of the composition (x), pressure (P) and temperature (T) for any ´x´, ´P´ and ´T´ of a system. It is important, therefore, to have precise knowledge of the solid, liquid and gas existence regions with respect to temperature ´T´, pressure ´P´ and composition ´x´ if one is to work with this material, especially in a crystal growth capacity. In the following paragraphs are summarized some of the more important considerations which have been implemented in this work.

The P-T projection shown below in **Figure 5**, and adapted from (24), shows the variation in overpressure associated with increasing Te-content in the melt for both Cd- and Te_2 species. As may be seen with increasing Te content (ranging from 50.005 to 50.025), the Cd overpressure decreases by nearly an order of magnitude, while the Te_2 overpressure increases by nearly double. While there are several Te-species present in the vapor phase, for the temperature range of interest these species are negligible and the Te_2 represents the most dominant species (25). Zinc is not presented here as under Te-rich melts, the contribution of P(Zn) is less than < 1mm Hg.

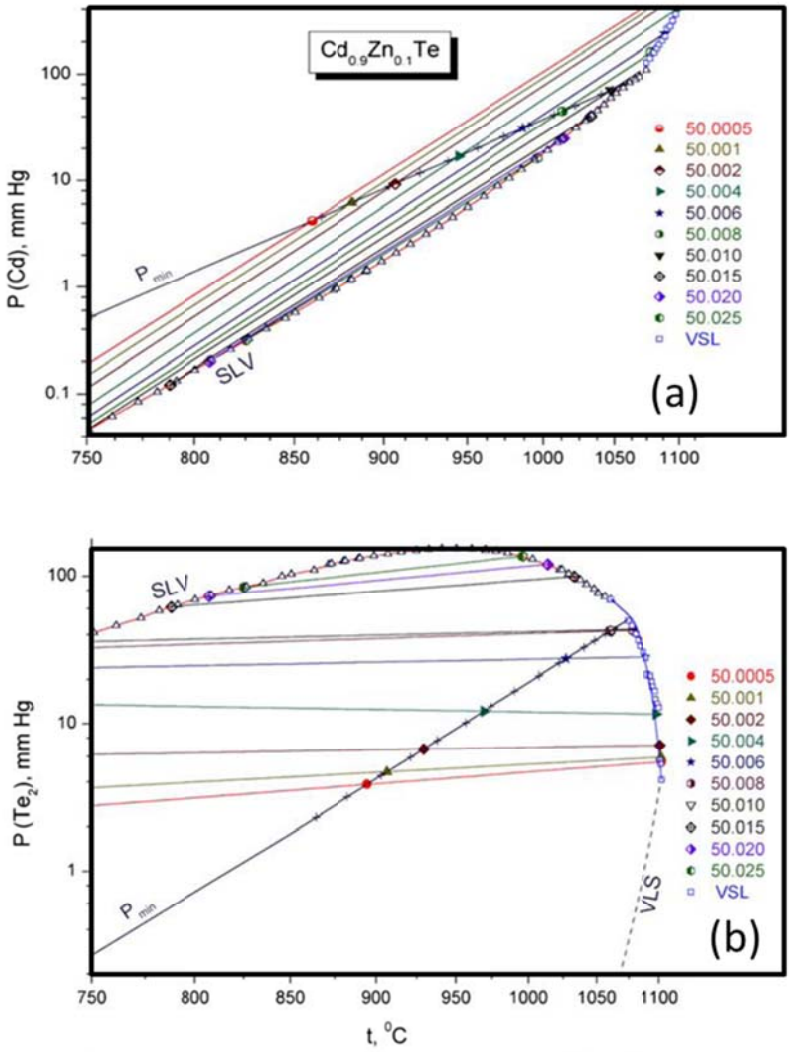

Figure 5 P-T phase diagram for (a) Cd and (b) Te_2 species taken from (24).

From the P-x phase diagram presented in **Figure 6**, taken from (24), experimental results for the ternary Cd-Zn-Te phase diagram are presented at fixed temperatures. These experimental results provide important information regarding the relationship between Cd, Zn, and Te vapors in equilibrium with solid Cd(Zn)Te, at a given temperature. It is important to note that for Te-rich melts, the vapor pressure is dominated by Te-species, while under Cd-rich melts, the vapor pressure is dominated by Cd species. Also, the minimum system pressure is realized under slightly Te-rich conditions.

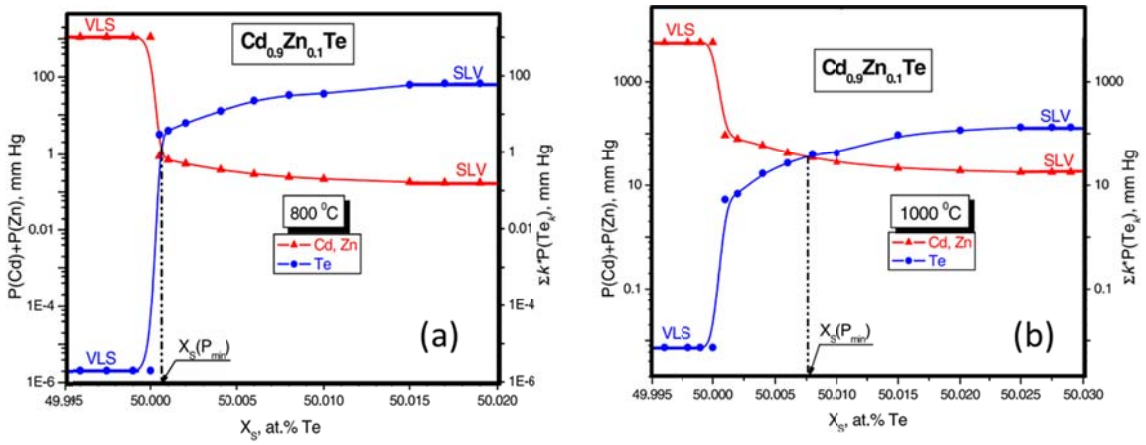

Figure 6 The P-x diagram for $Cd_{0.9}Zn_{0.1}Te$ at (a) 800ºC and (b) 1000^{O}C taken from (24). The vapor pressure is dominated by Cd & Zinc species for Cd-rich melts and by the Te species for Te-rich melts.

From the T-x projection shown below in **Figure 7**, also adapted from (24), it is observed that Cd(Zn)Te melt-solidification does not occur under congruent conditions. Indeed, the liquidus line displays a hyperbolic shape near the melting point. Some very practical information obtained from this data is that the maximum deviation from stoichiometry occurs on the Te-rich side of the solidus-liquidus, with a maximum solid solubility of Tellurium occurring at approximately 860º C (50.05% or $4x10^{18}$ at-cm^{-3}). A very important consequence of this retrograde solubility is the Te precipitation which occurs at temperatures below the melting point, during the crystal cooling phase (See Chapter 1, Section 2).

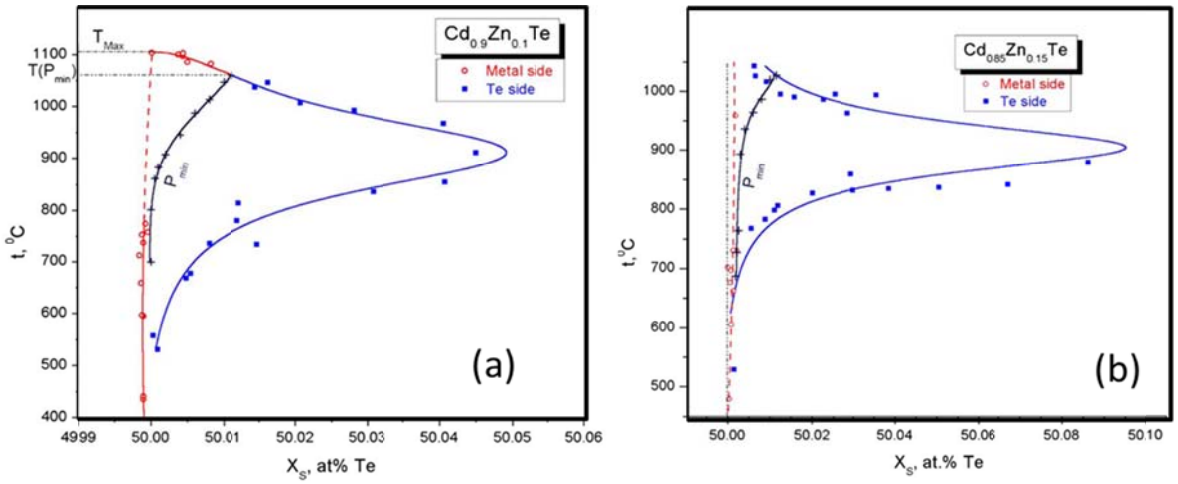

Figure 7 T-x phase diagram for $Cd_{0.90}Zn_{0.10}Te$ and $Cd_{0.85}Zn_{0.15}Te$, illustrating the effect of increased zinc concentration on the retrograde solubility of Te. Taken from (24).

Based on the preceding P-T-x diagrams, the desired melt stoichiometry was selected to be slightly Te-rich. Crystal growth under these conditions would provide minimum internal pressure reducing the probabilities of ampoule rupture. This was an important factor due to the use of superheating as the desired method of homogenization (as opposed to furnace rocking).

In order to achieve these considerations experimentally, control over the stoichiometry of the charge is paramount. Due to the difficulties with cutting and weighing Cd, this material was weighed first with some idea of the approximate quantity necessary for a boule with a given mass. In addition to the stoichiometric quantity required, an extra amount of Cadmium was used to compensate for material loss arising from the equilibrium overpressure of Cd at high temperatures. This Cd excess was calculated using **Equation 1**, where $\boldsymbol{P}$ is system pressure measured in Pascals, $\boldsymbol{V}$ is the volume of the ampoule measured in m^3, $\boldsymbol{n_{Cd,gp}}$ is the number of moles of Cd in the gas phase, $\boldsymbol{R}$ is the ideal gas constant, and $\boldsymbol{T}$ is the system temperature measured in Kelvin. The total system pressure was approximated by using experimental data at 1000° C reported in (24). The ampoule volume could be calculated exactly from its CAD geometry.

Equation 1
$$\boldsymbol{P_{Cd} \cdot V_{ampoule} = n_{Cd,gp} \cdot R \cdot T}$$

From this calculation, the quantity of material that will exist in the vapor phase can be calculated. This weight is then <u>*subtracted*</u> from the total weight of Cd which has been measured. To be clear, this value is subtracted because the Cd existing in the gas phase is not a component of the melt. Using this reduced value for the Cd the required quantity of Tellurium to obtain a stoichiometric charge may be determined using **Equation 2**, where $\boldsymbol{n_{Te}}$ represents the moles of Tellurium required for a stoichiometric charge.

Equation 2
$$\boldsymbol{(n_{Cd\,total} - n_{Cd,gp}) + n_{Zn} = n_{Te}}$$

The stoichiometry of the Cd(Zn)Te charge was chosen to be slightly Tellurium rich in order minimize system pressure, following the previous line of discussion. The

stoichiometry which minimized pressure within the ampoule at high temperature (1273^{o}K) was 49.005 : 50.007 Cd/Zn : Te (see **Figure 6**(b)). Therefore, from the stoichiometric point, the required quantity of Te could be calculated using **Equation 3**.

Equation 3

$$n_{Te} = (n_{Cd} + n_{Zn}) \cdot \frac{50.007}{50}$$

Presented in **Figure 8** is the process view for charging the crucible/ampoule with the Cd, Zn, and Te materials. The sizes of the charges grown in this work were between of 180-220 g for the 25 mm ingots, and 750 g for the 50mm diameter ingots. The elemental material was loaded in order from bottom of the ampoule to top: Tellurium, Zinc, and Cadmium. The ampoules were sealed in vacuum at 1x10^{-6} Torr using Mini-task Varian Turbo-molecular pump and were doped with 1-3ppm of Indium to achieve electrical compensation. The loading of material and doping were carried out inside an Argon purged glove-box prior to vacuum sealing of the ampoule and subsequent loading into the VGF furnace.

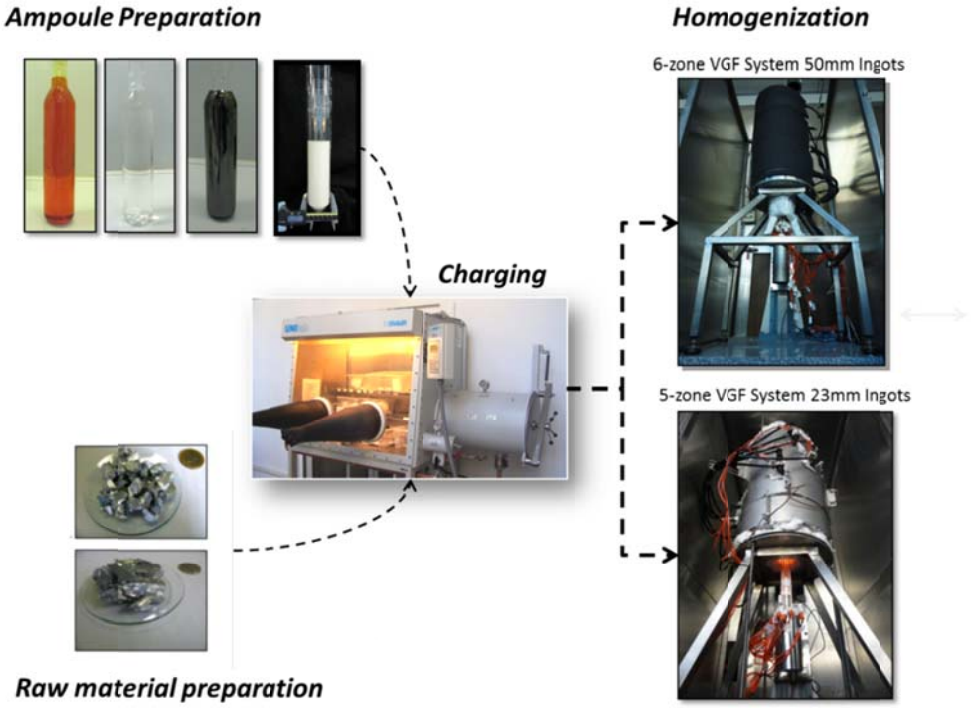

Figure 8 Flow-diagram for material synthesis. The raw material is loaded into the crucible/ampoule using an argon purged glove-box to minimize environmental sources of contamination. Once the ampoule is loaded with the Cd(Zn)Te, the ampoule is vacuum sealed and placed inside the VGF furnace.

Presented in **Figure 9** is a typical thermal ramp which is used for material synthesis. This temperature ramp is divided into three stages, as already has been mentioned. These stages are (i) melt homogenization, (ii) crystal growth, and (iii) crystal cooling. The temperatures and times spent at each stage in fact have a great impact on the crystals electrical, structural, and optical properties.

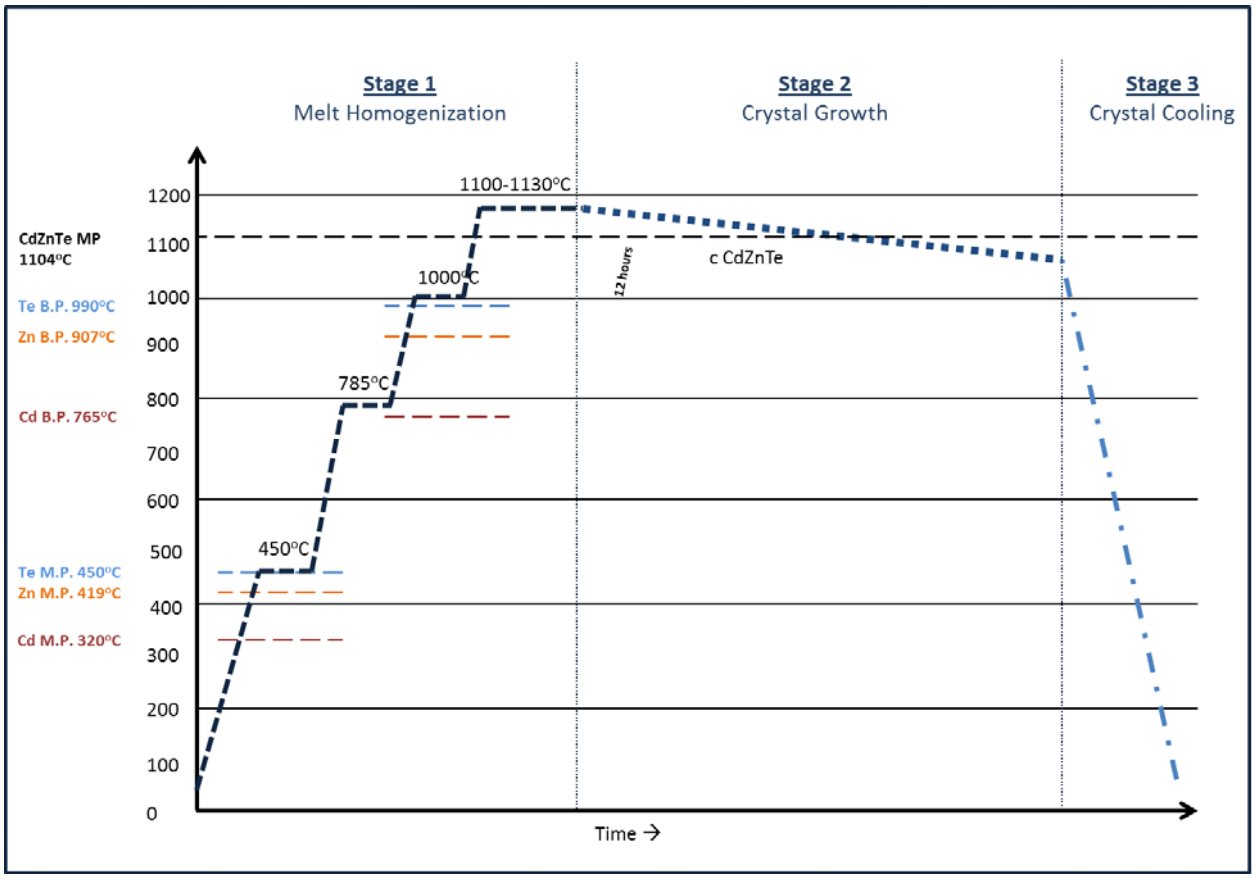

Figure 9 Typical thermal cycle for the material synthesis, crystal growth, annealing and cooling. The melting points (MP) and boiling points (BP) of Cd, Zn, and Te are indicated using dotted lines.

Presented in **Figure 10** is the experimental pedestal used in this work for measuring the temperature along the axis of the ingot. Thermocouples were placed along the exterior of the quartz crucible, every 1.5 cm up to 9 cm. Additionally, 1 thermocouple was placed 1 cm below the tip of the quartz crucible. See Chapter 2, Section 1.2 for additional details regarding this experimental configuration.

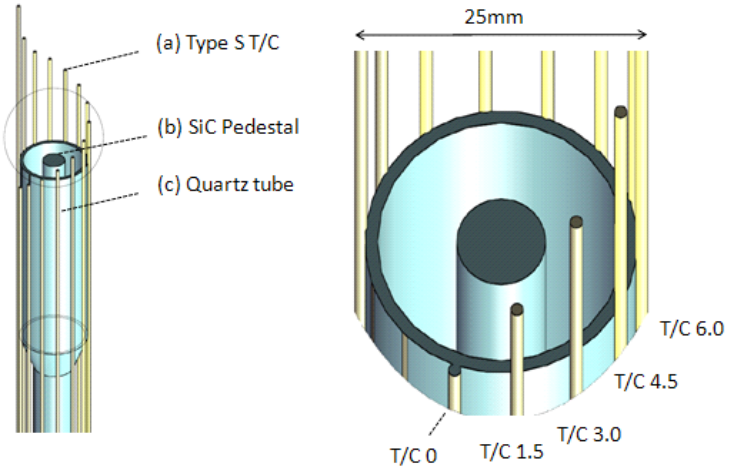

Figure 10 Furnace pedestal used for detecting exothermic reactions and measuring the temperature adjacent to the crucible, along the axial direction.

Material synthesis and homogenization may be divided into two phases. The first phase of Cd(Zn)Te synthesis is reaction between Cd and Te, which has been reported near 450º C, above the melting points of both. As already mentioned, the crucible was filled with Te, Cd, and Zn in the order of their melting points. Using this approach, the molten Cd melts first and covers the surface of the Te pieces.

The exothermic behavior of Cd(Zn)Te synthesis is observed during this phase and is described using **Equation 4**. The exothermic heat of fusion of Cd with Te has been reported to be $\Delta H = 1.81\ x\ 10^5\ J/kg$ (26). This is an important value, and was taken into account to ensure a properly controlled and safe crystal growth process. For the 25mm ingots, which weighed between 160 and 200 g, this energy produced is between 33 kJ and 42 kJ while for the 50mm ingots, this energy increases to near 160 kJ. Taking into account the heat capacities of the materials (see section 7.2 page 290 of this chapter), the change in temperature associated with the exothermic reaction of 1kg of Cd(Zn)Te may be calculated using **Equation 5**.

Equation 4 $$\boldsymbol{Cd(s) + Te(s) = CdTe(s) + \Delta H}$$

Equation 5 $$\boldsymbol{\Delta T = \Delta H / C_p = 688^o K}$$

The investigation carried out in this chapter was not only to study each stage of the homogenization phase in detail, but to study how changes made to the thermal ramping cycle influenced resultant material quality. In total, four different temperature set points were investigated to observe thermodynamic changes taking place within the ampoule. Those temperature set-points, and the experimental motivation is presented in **Table 2**

Table 2 Temperature set points and experimental motivation for homogenization experiments.

Temperature Set-points	Experimental Motivation
450°C	• Set point above melting point of Cd, Zn, Te • Observe exothermic reaction
785°C	• Set point above boiling point of Cd • Observe exothermic reactions associated with un-reacted Cd/Te
<1100°C	• Set point above boiling point of Cd, Zn, and Te • Observe exothermic reactions associated with un-reacted Cd/Te
1130°C	• Set point above boiling point of Cd(Zn)Te • Observe changes in ingot homogeneity

2.3 Results

The results are presented here for each stage of homogenization. The results regarding the exothermic reaction with between Cd and Te near 450 ºC are first presented. Some comments are provided to explain the release of exothermic heat at temperatures below the melting point of Cd(Zn)Te. And finally, the experimental results with respect to melt homogenization, and how these factors affect second phase inclusions, composition, and material homogeneity are discussed, taking into account their importance with respect to radiation detection applications.

2.3.1 Stage 1: Thermodynamic Processes at 450° C

The first temperature ramp investigated was to 450°C, recognized as the temperature at which the reaction of Cadmium with Tellurium takes place to form CdTe. It is important to note that this temperature is above the melting point of all three elements (Te ~ 450° C, Zn ~ 419° C, Cd ~320° C). In order to observe the reaction dynamics, the Cd(Zn)Te charge was brought to a temperature just below the reaction temperature, and slowly ramped through the range of interest. This was done to observe at precisely which temperature the

reaction would occur. With circumferentially arranged thermocouples arranged along the axis of growth, it was possible to see the change in temperature as the chemical reaction takes place. The first ramp to 450°C is shown below in **Figure 11**. The thermocouple position refers to the circumferential geometry, adjacent to the ampoule wall, which is presented in **Figure 10**.

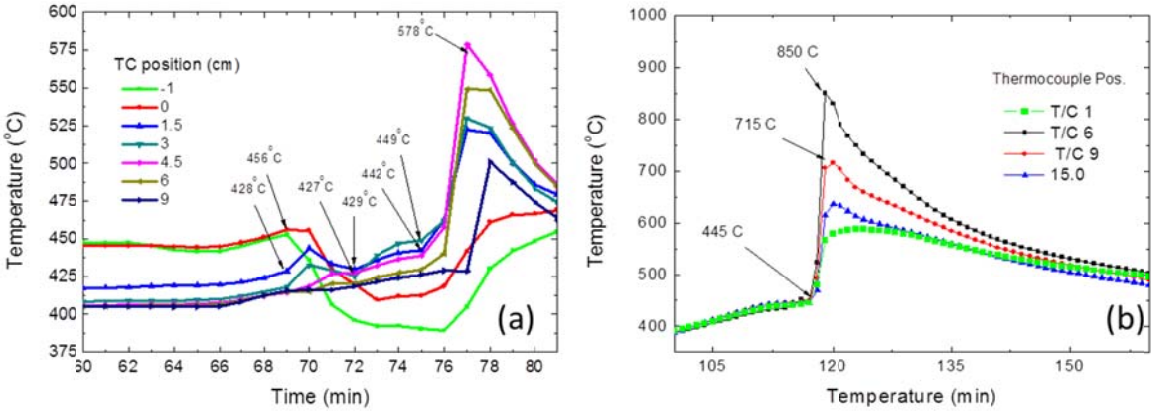

Figure 11 (a) Exothermic peaks for 200g, 25mm Cd(Zn)Te Ingot which is in-situ compounded (b) Exothermic peaks for 1 kg 50mm diameter in-situ compounded Cd(Zn)Te.

The expected change in temperature, using Equation 5 for both 0.2kg and 0.75kg charges is presented in Table 3. In general, the change in temperature produced by the exothermic reaction is in agreement with the expected values. The small discrepancy between the observed ΔT and the calculated ΔT may be attributed to the following experimental factors:

1. The thermocouple sampling rate too slow to detect the peak maximum
2. Thermocouple position along axis is placed away from radiating body.
3. The chemical reaction does not reach completion.
4. The entire chemical reaction is not instantaneous, but occurs over several minutes allowing the dissipation of heat.

Indeed, for the larger 50mm charge, the disagreement between expected and observed values increases to near 20%, likely due to a summation of these factors.

Table 3 Expected and observed changes in temperature associated with Cd-Te exothermic reaction

Cd(Zn)Te Mass (kg)	Expected ΔT (°K)	Observed ΔT (°K)
0.2	138	129
0.75	516	405

The change in the axial temperature profile throughout the duration of the Cd-Te exothermic reaction is illustrated in **Figure 12** and **Figure 13** for the 25 mm and 50mm Cd(Zn)Te ingots respectively. Before the reaction occurs (t=40 for 25mm ingot, t=117 for 50mm ingot), the temperature profile across the ingot is nearly constant, with a slightly higher temperature at the tip (axial position=0) than across the body. In fact, the temperature gradient is negative in this case.

As the temperature approaches 450º C, the temperature inside the ampoule increases suddenly from 450º C to nearly 580º C for the 25mm ingot. For the 50mm ingot, the temperature increases to nearly 850º C. It is important to note that immediately after the reaction takes place (t = 75, t=117), the axial gradient becomes substantially convex with the hottest spot in the furnace being slightly higher than the center of the ingot. The position of each ingot, with respect to the thermocouple measurements is shown above each of the thermocouple measurement data.

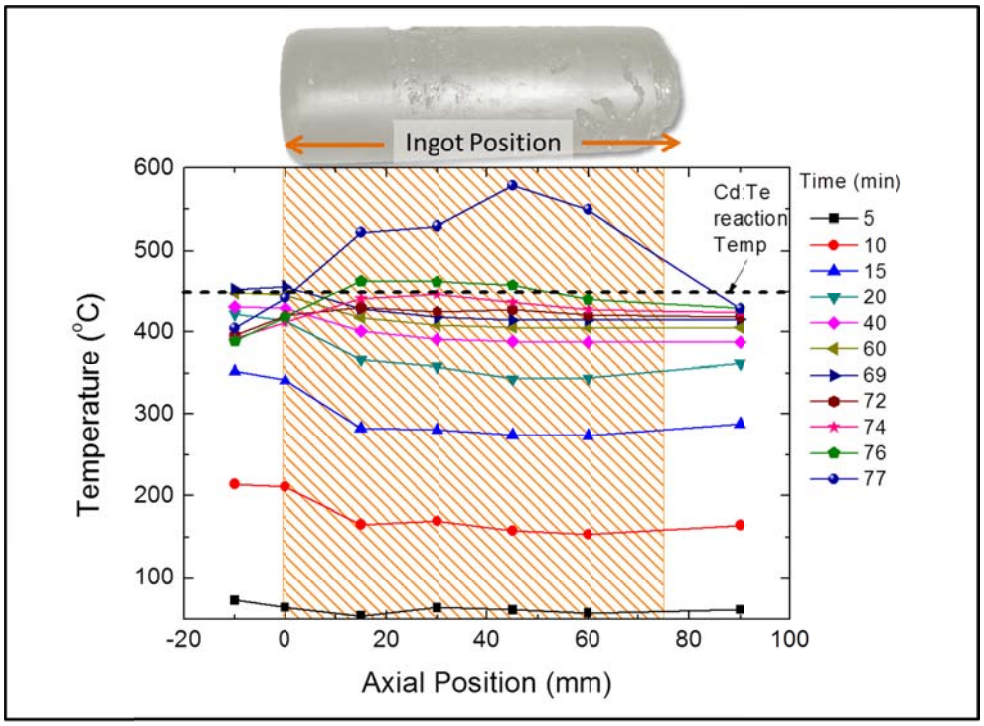

Figure 12 The axial temperature profile across 25mm Cd(Zn)Te ingot during Cd:Te reaction at 450ºC

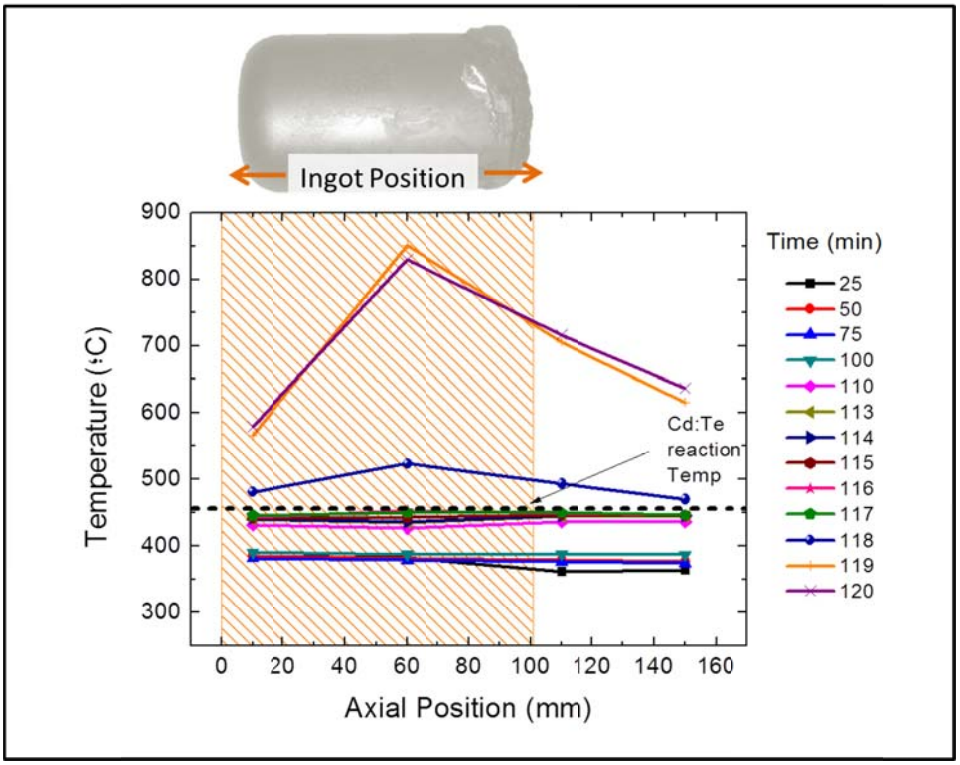

Figure 13 The axial temperature profile across 50mm Cd(Zn)Te ingot during Cd:Te reaction at 450ºC

2.3.2 Stage 2: Temperature ramp to 785° C

The temperature set point of 785º C was investigated because it is above the boiling point of Cd. It was of interest to observe if there were any exothermic reactions associated with un-reacted Cd/Te at this stage. The ampoule was brought to this temperature, and maintained for three days, however no significant thermodynamic behavior was observed in the thermocouple data.

2.3.3 Stage 3: Temperature ramp to 1100° C

The third temperature profile investigated was the temperature ramp from 800º C to 1100º C, which was above the boiling points of Cd, Zn, and Te but still below the melting point of Cd(Zn)Te. In some cases small exothermic reactions could be observed to take place. These reactions were detected as temperature spikes in the T/C data, and may be associated with the fusion of unreacted Cd and Te at these elevated temperatures.

This phenomenon is presented in **Figure 14** for one of the 25mm ingots investigated. Indeed, from the temperature spikes observed by the thermocouples, it is possible to estimate the quantity of material reacting by the change in temperature following Equation 5. For the temperature spike 1, the change in temperature of 3º C corresponds to a mass of roughly 4grams of reacted Cd(Zn)Te. For the temperature spike 2, the change in temperature of 23ºC corresponds to a mass of nearly 30grams of Cd(Zn)Te. Indeed, the starting size of the material can play a large role in determining the high temperature dynamics. These small exothermic reactions are attributed to the use of small diameter Te and Cd particles.

This exothermic behavior may be explained in **Figure 15**. When the Cd and Te undergo fusion at 450ºC, elemental Cd may passivate the surface of a Te droplet through the formation of a CdTe crust surrounding the Te droplet. For a large enough Te particle, this passivation layer will prevent the Te inside from reacting with the Cd in the melt. As a consequence, the melt will become slightly Cd-rich for a high enough concentration of un-reacted Te-particles. Moreover, the crust which encapsulated the Te droplet may be stable up to 1100ºC, which is near the melting point of CdTe. Once the melting point of CdTe is reached, this passivated crust will also melt, allowing the encapsulated Te to react with either the Cd vapor or with the Cd-rich melt. As a result of the subsequent exothermic

reaction, a temperature spike may be observed as the Te is released into the melt and undergoes the reaction with Cd to form molten CdTe.

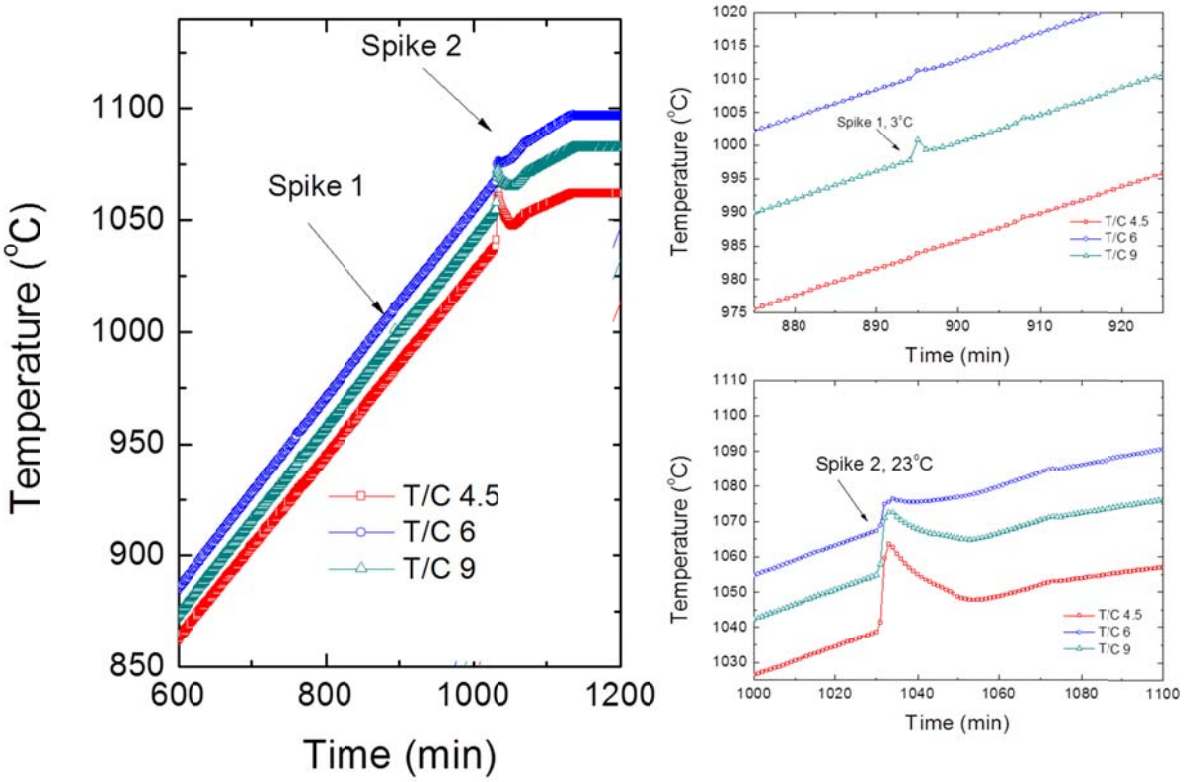

Figure 14 Temperature spikes in Cd(Zn)Te associated with the melting of CdTe crust from Te particles and allowing encapsulated Te to react with free Cd atoms.

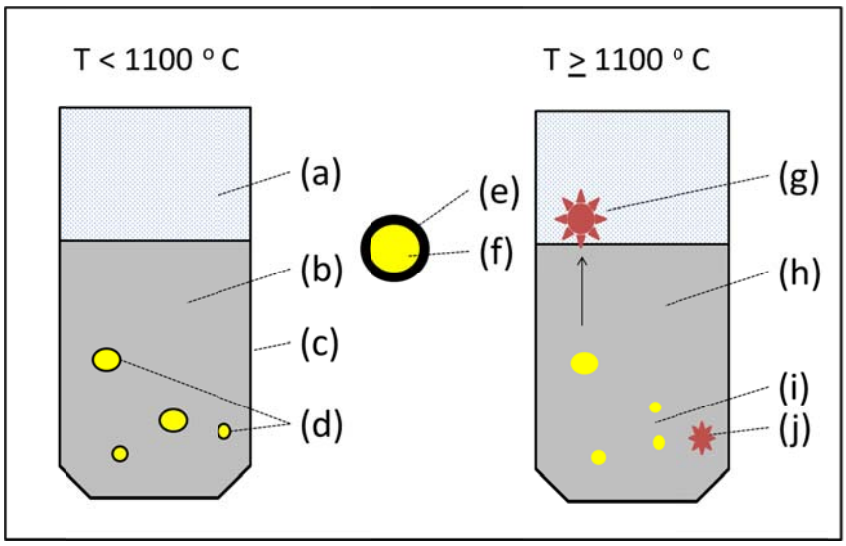

Figure 15 (a) Cd Vapor (b) Cd-rich melt (c) crucible (d) CdTe passivated Te particles (e) CdTe (f) Tellurium (g) Exothermic reaction of Te-particle with Cd vapor (h) Cd-rich melt (i) separation of Te particles to smaller particles (j) free Te-particles reacting with Cd-rich melt.

2.3.4 Stage 4: Temperature ramp to 1100-1130ºC

Probably the most important phase of material synthesis involves the homogenization of the molten Cd(Zn)Te material. This remains a key stage in achieving material with good optical and electrical properties. One of the principal objectives of this phase is the breaking apart Te-inclusions in the melt using temperatures well above the melting point of Cd(Zn)Te.

The quartz ampoule constrains the operating temperature to below 1160º C (which is the softening point of quartz). For short periods of time, however, it is possible to ramp the temperature of the melt to higher temperatures and achieve improved homogenization of the elements without pressing the limits of the quartz vessel.

Presented in **Figure 16** are two different types of thermal ramps used in this investigation. In the Type-1 homogenization ramp, the temperature at the tip of the crucible is taken to the melting point of Cd(Zn)Te. In the Type-2 homogenization ramp, this temperature at the tip of the crucible is increased to +30ºC of the melting point of Cd(Zn)Te (note however T/C 3 and 4.5 are at 1160ºC, near the softening point of quartz). This higher temperature is intended to push the reaction further, and break apart secondary phases present in the melt. It is important to comment that the T/C used for measuring the superheating temperature was T/C 1, placed near the tip of the ingot. This was intended to provide results which are comparable with existing conventions presented throughout the literature (see P. Rudolph (27)). However, the large temperature difference between T/C 0 and T/C 3 is notable, and is likely the result of the high temperature gradient induced by the SiC pedestal which has been used.

For the Type-1 homogenization profile (referred to as H1-profile), the furnace set points were raised such that the T/C located at the tip of the crucible would reach a temperature near 1104ºC. This convention is consistent with that reported by Rudolph with respect to superheating of the melt (28). However, it is interesting to also observe from this thermocouple data that the temperature across the melt is 30º C higher than the temperature at the tip. Regardless, using the conventions proposed by Rudolph for measuring the superheating, the furnace was then allowed to come to thermal equilibrium over the course of 72 hours, to provide sufficient time for the melt to become homogenous.

For the Type-2 homogenization profile (referred to H2-profile), the furnace set points are raised by nearly 30º such that the T/C 0, located at the tip of the ingot, would reach a temperature of 1130ºC. Again, the temperature across the melt is 30º C higher with respect to the temperature measured at the tip. But using the same experimental arrangement, the furnace was allowed to reach equilibrium over the course of 72 hours.

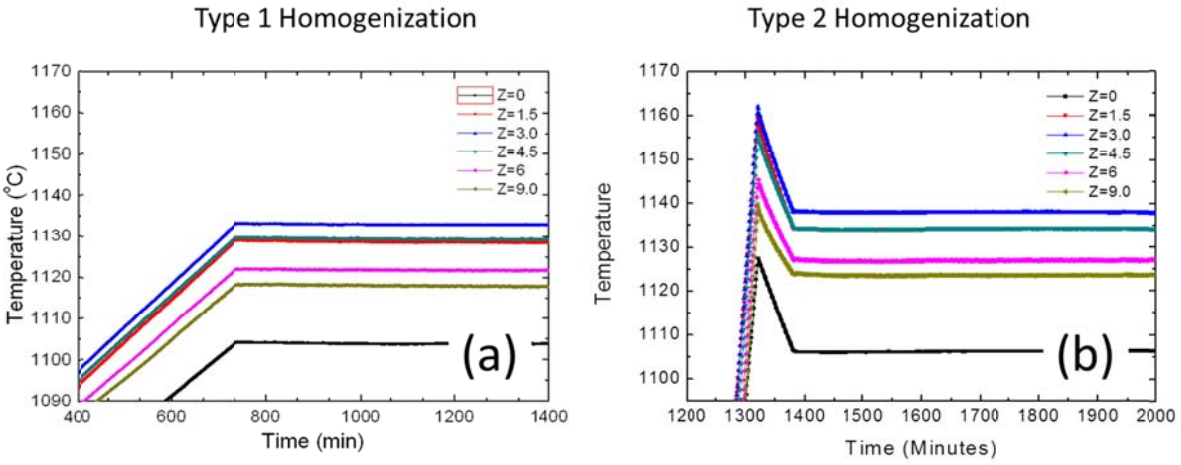

Figure 16 Temperature profile H1 and H2 for superheating the melt by (a) 0ºC and (b) 30ºC respectively.

The Type-1 homogenization profile was applied to using both carbon coated quartz (cc-Quartz) and pBN crucibles to observe the differences. As will be shown below, the Type I homogenization was not suitable for the crystals grown using pBN crucibles. For this reason, the Type-2 homogenization protocol was developed. The results for each protocol are discussed here.

2.3.4.1 *Type-1 Homogenization using cc-quartz Ampoule*

Using the Type-1 homogenization temperature ramp, in conjunction with carbon coated quartz ampoules (whose development is discussed in Chapter 2), material homogenization has been carried out using 7N pure Cd, Zn, and Te starting elements.

Taking into account only the surface of the as grown ingot, presented in **Figure 17**, it appears that the starting elements have fully reacted to form Cd(Zn)Te (compared with the ingots presented in the following paragraphs). After slicing of the wafer along the axial direction, it was observed that the material has indeed reacted, without the formation of voids, large secondary inclusions, or other related defects. The ingot grown using the cc-Quartz ampoule is shown in **Figure 17**. The resistivity of the ingot however was below 1 ×

10^7 Ω-cm, and was therefore not useful for detector applications. It is possible that the low resistivity may be associated with impurities diffusing into ingot from the cc-Quartz ampoule.

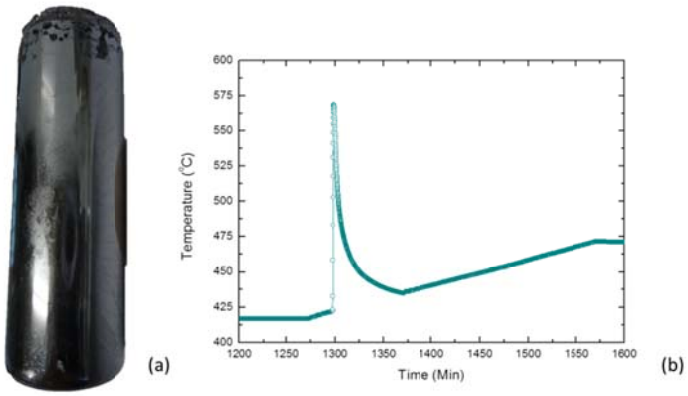

Figure 17 (a) as grown Cd(Zn)Te ingot using Type-1 homogenization in conjunction with carbon coated quartz ampoule (b) exothermic heat of fusion released during material synthesis.

2.3.4.2 *Type-1 Homogenization using pBN Crucibles*

The same temperature ramp was applied to crystals gown using pBN crucibles (instead of cc-Quartz). Presented in **Figure 18** are three ingots which have undergone the same crystal growth and cooling ramps as that which has been applied to the ingot shown in **Figure 17**.

Indeed, these three Cd(Zn)Te ingots were grown using the Type-1 Homogenization (H1) protocol, following the profile in **Figure 16(a)**. One of these ingots were grown using pre-synthesized 7N Cd(Zn)Te (Ingot H1A) while two of the Ingots were grown using 7N Cd, Zn, and Te starting elements (Ingot H1B, H1C).

The metallic material on the outer diameter of the first ingot has been verified by EDS measurements to be unreacted elemental tellurium. The data from these measurements is also presented below in **Figure 18**. The ingots H1A grown using pre-compounded materials did not exhibit secondary phases of unreacted Te on the surface, likely because the reaction had previously been carried out.

Also of importance, and presented in **Figure 19**, are the tail of the ingots, or the last to freeze region which has been obtained using the Type-1 homogenization protocol. This tail region is highly polycrystalline, and exhibits a conical shape present to varying degrees in all three ingots, regardless of starting material composition. This polycrystalline region of

the ingot, exhibits high void content and is obviously detrimental to the yield of the material.

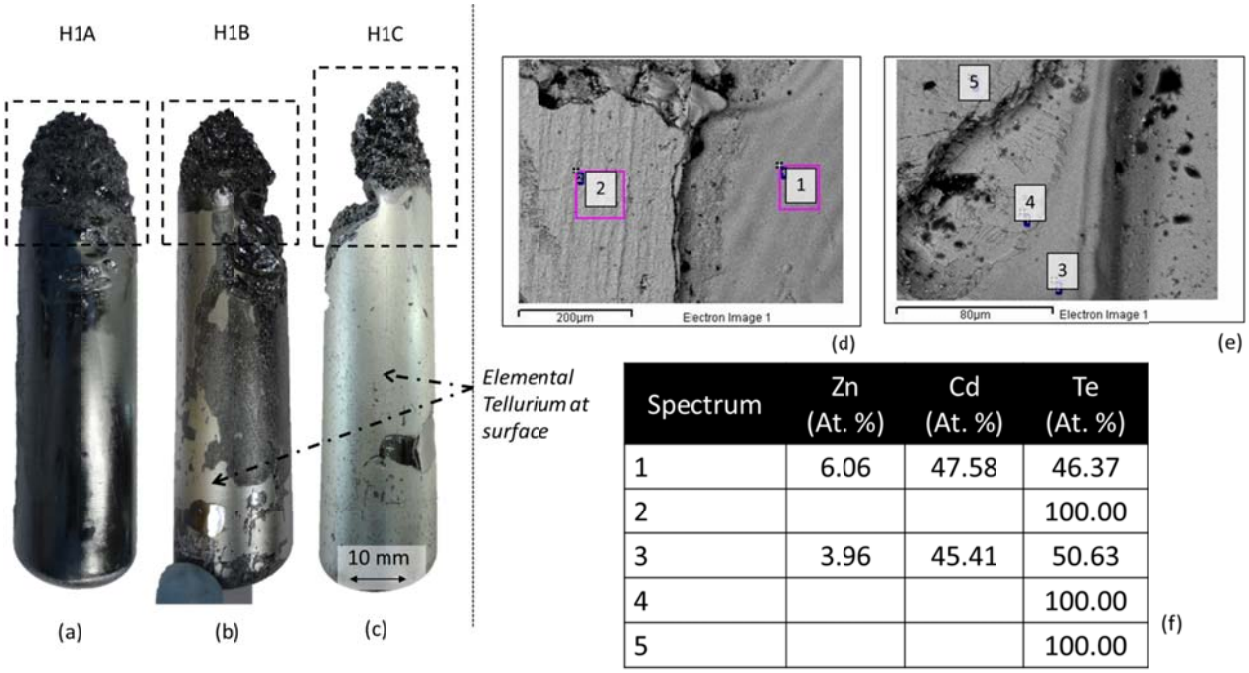

Spectrum	Zn (At. %)	Cd (At. %)	Te (At. %)
1	6.06	47.58	46.37
2			100.00
3	3.96	45.41	50.63
4			100.00
5			100.00

(f)

Figure 18 Ingots (a) H1A, (b) H1B, and (c) H1C grown using Type-1 Homogenization Protocol. (d)-(f) EDS measurements of surface of the ingots showing presence of Te at the surface of H1B and H1C

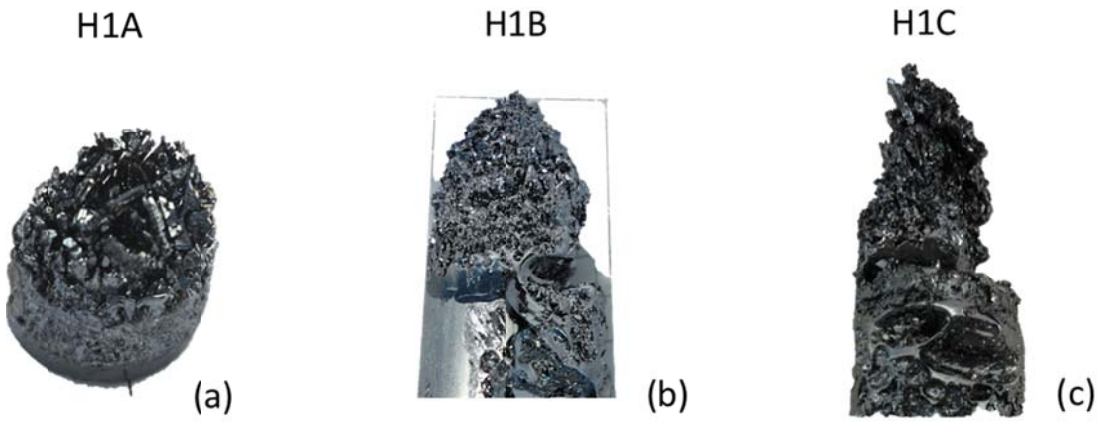

Figure 19 Close up image of last to freeze tail regions of (a) H1A (b) H1B and (c) H1C illustrating the poor crystalline quality of the material

2.3.4.3 *Type-2 Homogenization using pBN Crucibles*

To overcome the poor homogenization of material which was obtained from the H1 homogenization procedure, it was necessary to modify the recipe. One possible experimental modification towards achieving this end was to increase the homogenization temperature, to break apart associated particles in the melt.

Three Cd(Zn)Te ingots were grown using the modified Type-2 Homogenization (H2) protocol, and are presented in **Figure 20**. All three of these ingots were grown using 7N elemental starting materials. Using the elemental Cd, Zn, and Te, each ingot was synthesized in-situ using the H2 protocol following the profile in **Figure 16**(b). These ingots, each of which have been grown from 7N pure starting elements, (i) do not exhibit secondary phases of elemental Te on the surface and (ii) the tail of the ingots does not exhibit a polycrystalline high void content cap. Strictly based on these macroscopic features of the ingots, the Type-2 homogenization protocol appears to have had some positive effects on the as-grown crystals.

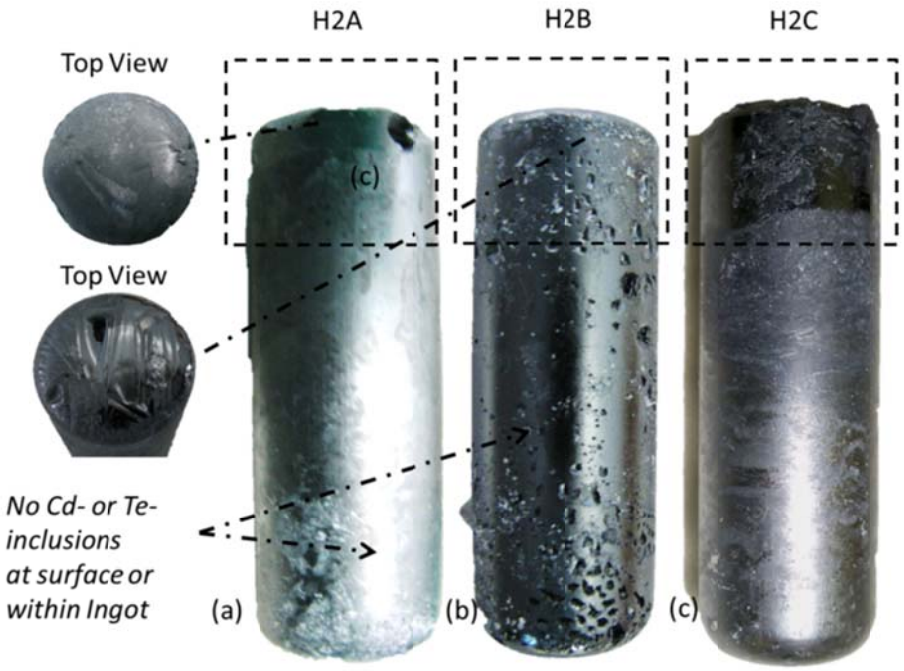

Figure 20 Ingots H2A, H2B, and H2C grown using Type-2 Homogenization Protocol

It is also important to comment here that these same differences between the H1 and H2 homogenization profiles were also observed in the 50mm diameter ingots grown in this work (the 50mm ingot growth is discussed in more detail in Section 2 on page 261 of this chapter). The 50mm ingot grown using H1 homogenization, referred to here as H1.50mm, exhibited a similar conical polycrystalline region at the tail end of the ingot, as may be seen in **Figure 21**(a).

To eliminate this non-uniformity, one ingot was grown using the H2 homogenization protocol and is presented in **Figure 21**(b). This ingot, referred to as H2A.50mm was raised

to a superheating temperature of 1130ºC for 15 minutes, following the Type-2 axial profile. In fact, for the smaller 25mm diameter ingots, 15 minutes proved sufficient to eliminate the polycrystalline cap. However, for the 50mm ingot, the volume of this conical poly-crystal region was only reduced.

While increasing the temperature to 1130º appeared to reduce this feature, it was not sufficient. Therefore, a second ingot, referred to as H2B.50mm was grown using similar protocol, except the melt was held at a temperature of 1130ºC for a duration of 5 hours. As may be seen in **Figure 21**(c), this polycrystalline region has been to a large extent confined to a small thin cap. This reduction in size of the polycrystalline cap has increased substantially the yield of the material. In fact for the 50mm ingots, the amount of material associated with this conical region, and other polycrystalline material not shown constitutes nearly 40% of the mass of the ingot. This value has been reduced to less than 10% through the implementation of this homogenization protocol.

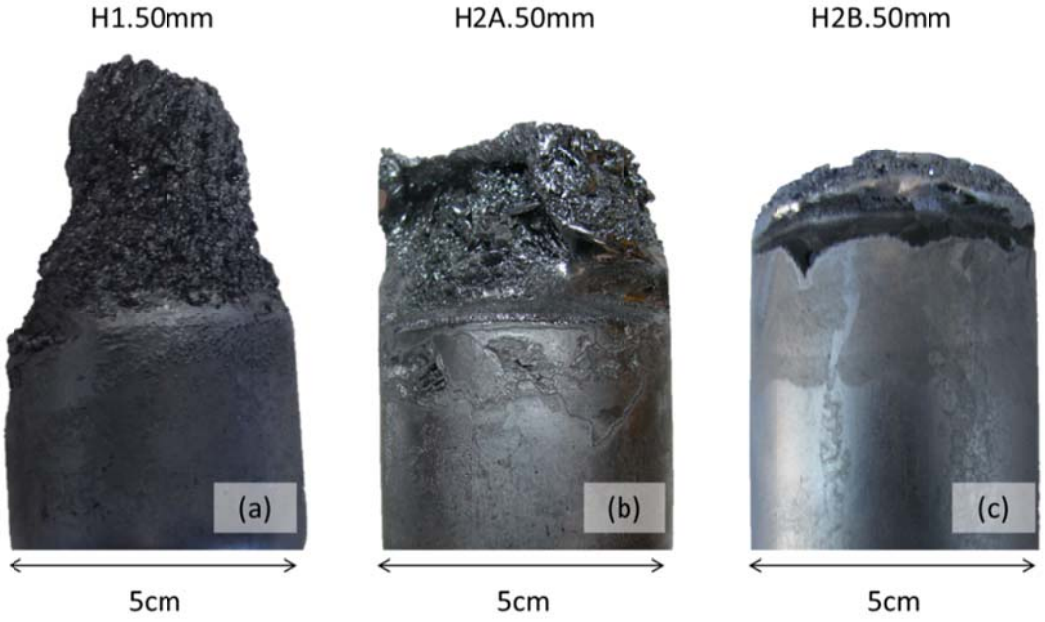

Figure 21 5cm diameter Cd(Zn)Te ingots grown using (1) Type-1 homogenization (b) Type 2 homogenization, 15min. and (c) Type 2 homogenization, 5 hours.

2.3.5 Physical Model

The formation of the polycrystalline cap may be attributed to the type of axial temperature profile which has been used throughout the growth cycle. As may be seen in **Figure 16**(b), the tip and the tail are at lower temperatures (T/C 0 and T/C 9 respectively)

than the temperature at the center of the ingot (T/C 3). In fact, the uppermost wall of the quartz ampoule is located in Zone 3 of the furnace, which is held at 1000ºC throughout the growth cycle. It is therefore proposed that radiative heat transfer between the surface of the melt and the wall of the Quartz ampoule is responsible for this phenomenon.

Presented in **Figure 22** are results from numerical simulations of 50mm Cd(Zn)Te ingots which may help explain this behavior. From these simulations we observe that before the halfway point of the growth cycle, the isotherm across the melt surface is below the melting point of Cd(Zn)Te. This occurrence supports the hypothesis that nucleation may occur at the melt surface, effectively producing two distinct crystallization fronts. This nucleation and subsequent outward growth from the center of the melt also helps explain the conical shape of the tail. The development of the 2D model used for numerical simulations is presented in greater detail in Section 7 of this chapter.

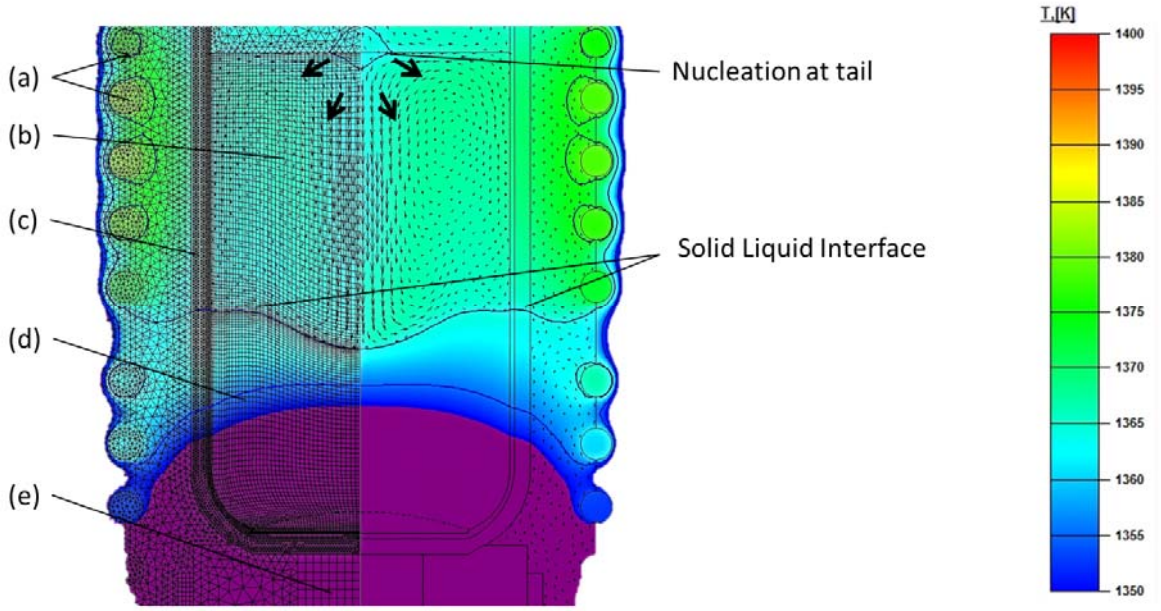

Figure 22 2D isotherms delineating the solid liquid interface of the melt. (a) Kanthal furnace element (b) Cd(Zn)Te melt, (c) pBN crucible & Quartz ampoule, (d) Cd(Zn)Te solid, (e) SiC pedestal.

A schematic representation of these changes in material phases throughout the homogenization and growth cycle is presented in **Figure 23**. Indeed, it is not necessary that this nucleation is a single crystal, but may actually be composed of many solid particles. The similarity in density of CdTe(s) and CdTe(l) makes it possible that the nucleated CdTe(s) particles could become trapped in the surface boundary layer, possibly due to

lower convection near the melt surface (29) (30). These particles would continue to grow together as the temperature in the furnace is lowered following the growth cycle. These particles would remain floating on top of the melt throughout the duration of the growth cycle forming a polycrystalline cap.

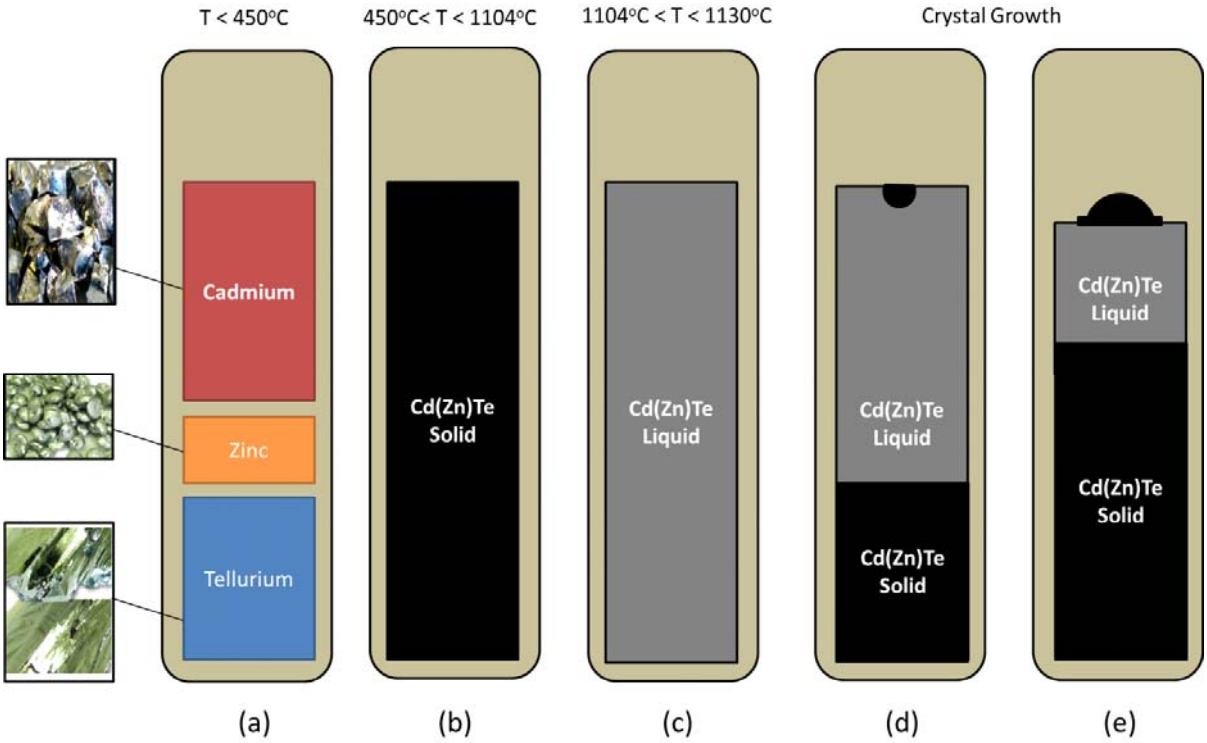

Figure 23 Changes in material phases throughout the homogenization cycle (a) starting elements Cd(s), Te(s), and Zn(s) undergo exothermic reaction at (b) 450ºC to form Cd(Zn)Te(s) which remains solid to temperatures (c) 1104ºC above the melting point of Cd(Zn)Te. (d) At some point during the growth cycle, nucleation occurs at the top surface of the melt and (e) continues to grow forming a poly-crystalline cap.

The fact that this phenomenon does not occur in the Type-2 homogenization is also interesting. This may be explained by taking into account the amount of supercooling required for nucleation to occur in superheated melts. Presented below in Figure 24 are experimental results presented by P. Rudolph (28), illustrating the relationship between superheating and supercooling of the melt. For small values of superheating, as is the case of the H1 homogenization, only a small degree of supercooling is required for nucleation to occur. For values of superheating +30ºC, as is the case for H2 homogenization, larger values of supercooling of the melt are required for nucleation to occur. As a result, in the H2 homogenization, this degree of supercooling near the melt surface is not reached. Therefore, by increasing the homogenization temperature, it is possible to completely

eliminate this solid Cd(Zn)Te layer from forming on the free surface of the melt. Indeed, increasing the homogenization temperature by 30ºC appears to be sufficient to achieve this.

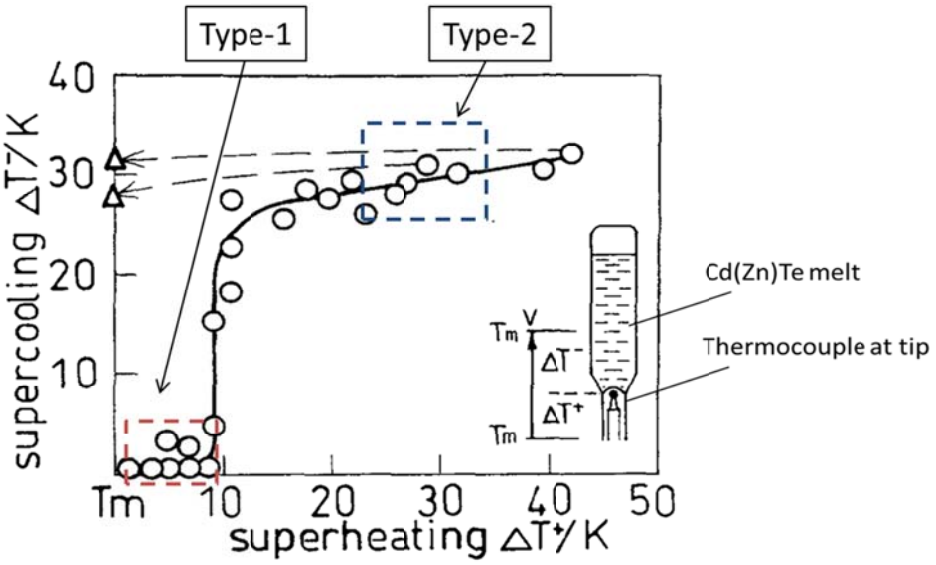

Figure 24 Results adapted from P. Rudolph (28) illustrating experimental results for the effect of superheating and constitutional supercooling of the melt in CdTe.

2.3.6 Second Phase Inclusions

While the macroscopic properties of the crystals provides useful information with respect to the general dynamics of growth, the optical properties of the as-grown crystals play a major role in their performance as radiation devices, such as their CCE. Therefore, it was necessary to probe the optical characteristics of Cd(Zn)Te to determine how the melt-homogenization dynamics effects the formation of secondary phases such as Te-inclusions

Presented in **Figure 25** are transmission microscopy images of Cd(Zn)Te wafers harvested from the same regions of two different ingots (see ingots H1B and H2B in **Figure 18**). It seems plausible that if the ingot has been characterized to have large concentrations of Te on the surface, then a similar result may be found in the bulk, a consequence of an incomplete reaction between Cd and Te.

These secondary metallic phases act as scattering centers for IR light passing through the sample. As a result, they appear as black opaque spots in transmission. From these images it is clear that not only is there a substantial quantity of unreacted Te on the surface of the ingot, but also within the bulk of the material. Such large inclusions of Te in the Cd(Zn)Te matrix has a very strong impact on detector properties.

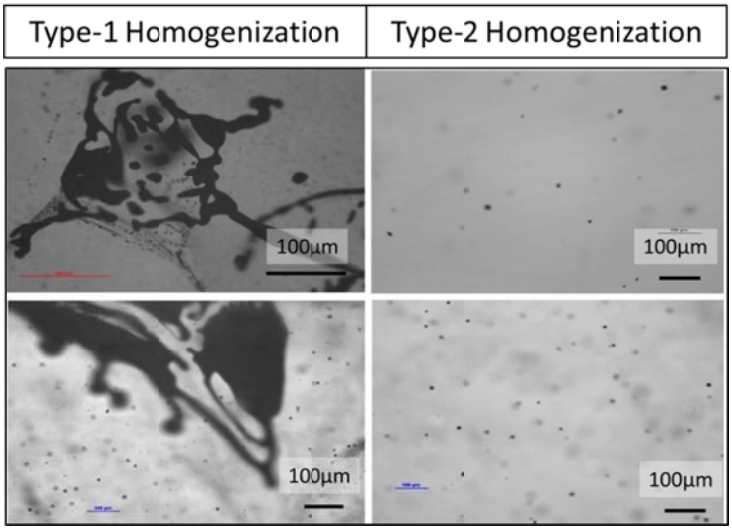

Figure 25 IR transmission microscopy of Cd(Zn)Te ingot grown using elemental Cd, Zn, and Te using (left column) Type-1 homogenization protocol and (Right Column) Type-2 homogenization protocol

The dispersion of these defects throughout a detector volume may be better understood using optical microscopy mapping techniques. The IR transmission mappings for two wafers presented in **Figure 26** demonstrates well the problems with incomplete material homogenization. Such a high density of large inclusions results in large scattering centers, dislocations, poor charge mobility, low resistivity, and ultimately the material is not suitable for detector applications. It is important to point out that this result was only obtained for using pure elemental starting materials. Pre-compounded Cd(Zn)Te the problems associated with such large inclusion present in high density was not encountered.

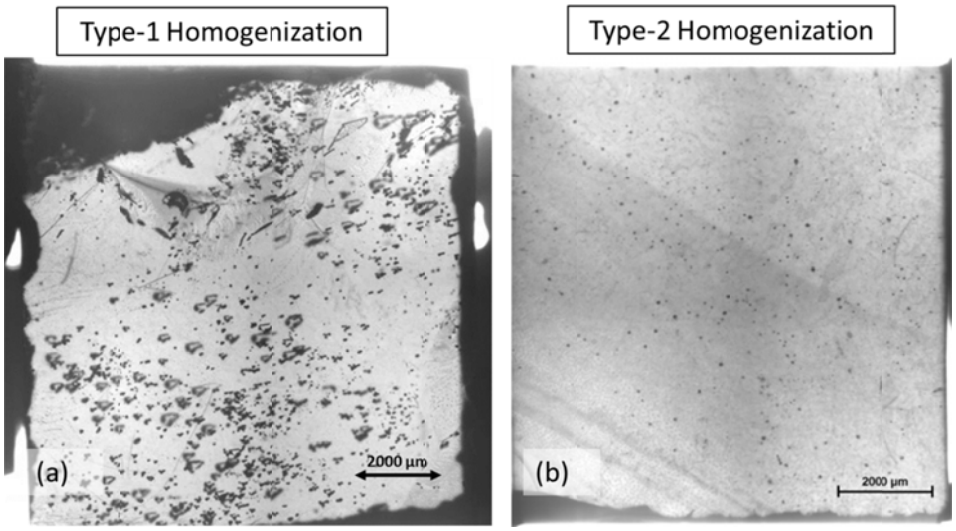

Figure 26 IR Transmission of 10mm x 10mm Cd(Zn)Te wafers. (a) Type-1 Homogenization (b) Type-2 Homogenization

2.3.7 Material Composition

The axial composition of Zinc using Type-1 Homogenization and Type-2 Homogenization profiles has been characterized for ingots grown using carbon coated quartz (cc-Quartz) ampoules, as well as pBN crucibles. From the data presented in **Figure 27**, the Zinc segregation coefficient has been calculated to be 1.34 < k <1.37, using **Equation 6** and based on this experimental data. In fact, the effect of superheating did not have a substantial impact on the Zinc Segregation, as was expected.

Equation 6 $$C_s = k \cdot C_o(1-g)^{k-1}$$

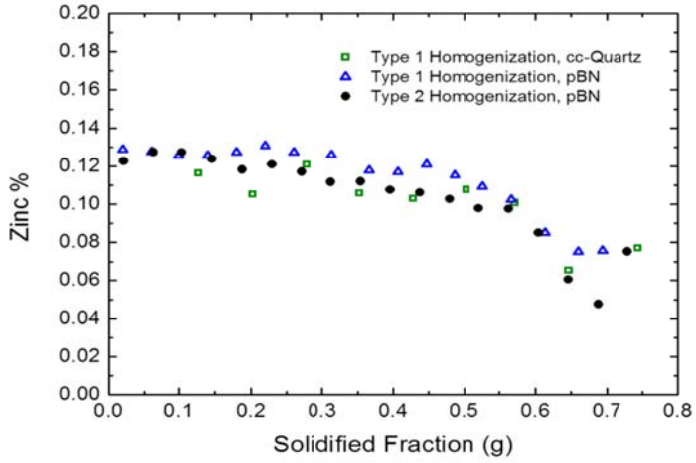

Figure 27 ICP-MS data for ingots grown using Type 1 and Type 2 Homogenization.

It was also of interest to assess the composition in terms of the molar ratio of the cation species (Cd and Zn) to the anion species (Te). ICP-MS data presenting the changes in molar content of Cd and Zn with respect to the Te anions is shown in **Figure 28**. It is important to first note that in each of the growths, each of the ingots exhibit Cd-rich composition. For ingots H1B and H1C, this is expected due to the excess Te which has been identified on the surface of the ingot using EDS spectroscopy. In the case of H2A, the slightly Cd-rich content may be associated with Te-loss in the vapor phase during the growth cycle. As a result, each of the crystals exhibit n-type conductivity as has been determined by the hot probe technique.

It is also important to note that the ingots grown using the H1 homogenization protocol exhibited larger fluctuations in content than did the ingots grown using the H2 homogenization protocol. These fluctuations in Te or Cd content correspond changes in carrier concentration and in general, changes in the electrical properties of the detector crystals. We attribute these fluctuations to a non-uniform melt composition, possibly associated with the incomplete melting of Cd(Zn)Te as previously discussed. Indeed, the elemental Te layer present on the surface of the as-grown ingot is possibly associated with such strong fluctuations.

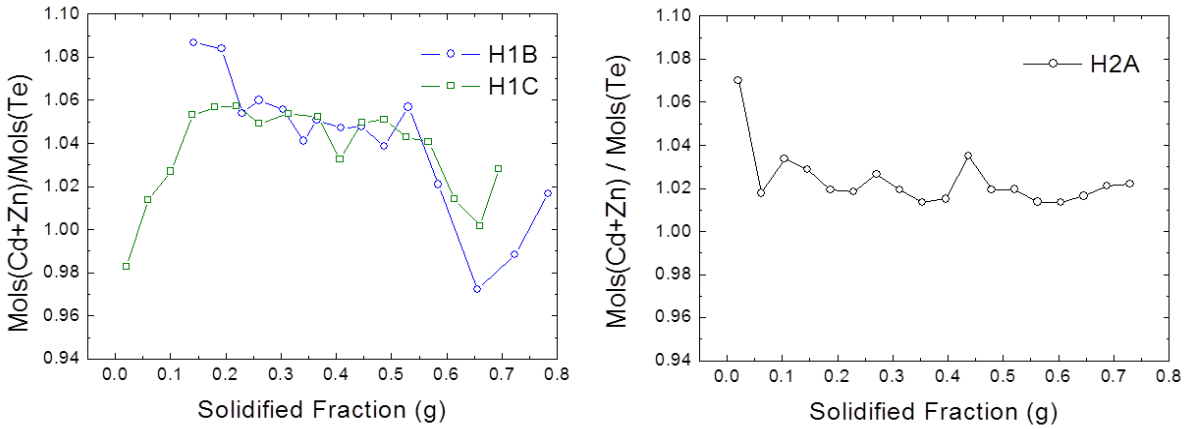

Figure 28 Composition of ingots grown using Type-and Type-2 homogenization (H2A).

2.3.8 Melt Homogenization and Gamma Spectroscopy

The most important figure of merit is that material grown under these conditions may be used for gamma-ray spectroscopy. Therefore, it was necessary that material harvested from the homogenized ingots be harvested and fabricated into Cd(Zn)Te detectors. Presented in **Figure 29** are the gamma spectra obtained for ingots grown using Type-2 in-situ compounding techniques. Indeed, many comparable detectors have been harvested from ingots grown using these methods. The devices presented only serve as a representative sample. A more complete discussion regarding detector fabrication, testing, and characterization is reserved for Chapter 4.

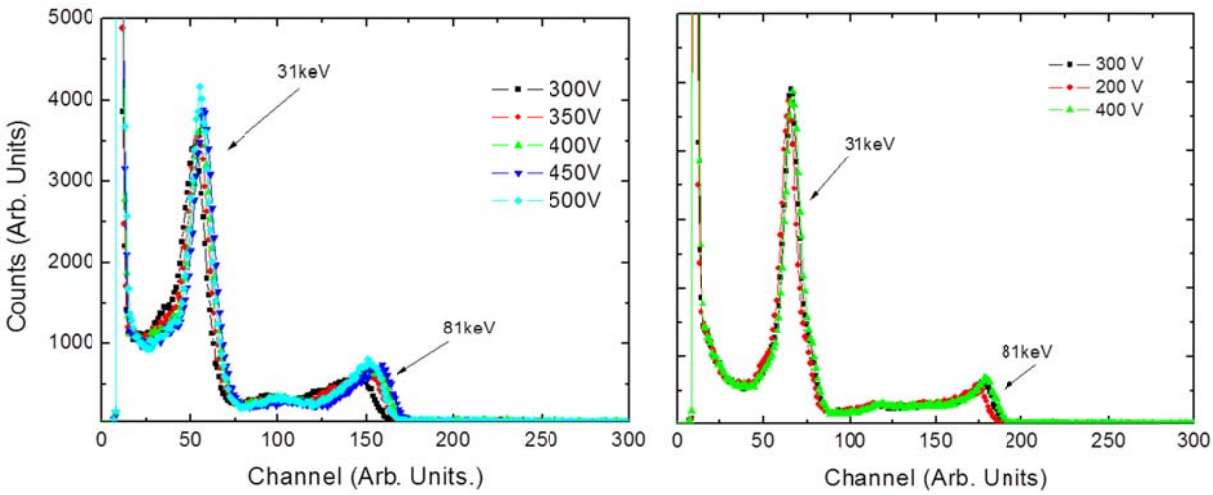

Figure 29 Gamma responses of detectors harvested grown using Type-2 homogenization methods described.

2.4 Conclusions and Future Work

With respect to the development of in-situ homogenization protocol, the conclusions may be summarized as follows:

1) The thermal behavior of the Cd(Zn)Te system has been studied near 450ºC and the reaction temperature has been measured directly.
2) This exothermic reaction has the effect of increasing the temperature by several hundreds of degrees, consistent with predictions. Moreover, the central region of the ingot reaches the highest temperature during the reaction.
3) Below the melting point of Cd(Zn)Te exothermic reactions have been observed. This has been associated with passivated Te-clusters being liberated into the melt as the passivating layer becomes molten. The liberated Te cluster is then free to react with Cd. The size of these particles are estimated to be no larger than 1 millimeter in diameter
4) Results from the numerical model which has been developed for Cd(Zn)Te growth suggest this poly-crystal cap may be associated with nucleation occurring at the melt surface.

5) It was observed that the Type-2 superheating of the melt by 30ºC was sufficient to (i) improve material homogeneity, (ii) prevent nucleation from occurring at the melt surface, and (iii) increase overall yield.
6) Infrared transmission measurements have been used to demonstrate how this superheating has reduced the size and density of secondary phases within the Cd(Zn)Te matrix.
7) Detector material has been harvested from Cd(Zn)Te ingots synthesized from 7N Cd, Zn, and Te pure elements. The gamma spectra exhibit substantially better FWHM than those obtained using pre-compounded Cd(Zn)Te. This result may be associated with the higher material purity of the starting elements, introducing lower levels of impurities and charge trapping centers.

Based on these results, several new avenues for further investigation have been opened. For example, it is interesting to investigate the effects of using higher temperatures for superheating of the melt. In addition to the material synthesis, homogenization, and crystal growth which have been presented here, it will also be useful to study the ingot cooling stage, in which the ingot is brought from the growth temperature near 1100ºC to room temperature. Indeed, a consequence of the retrograde solubility of Te in Cd(Zn)Te means that this cooling algorithm will have substantial influence on the precipitation which occurs. Moreover, for non-uniform distribution of Zinc, this will lead to non-uniformities in the precipitation following from the results presented in **Figure 7**.

This page intentionally left blank.

3 NOVEL CRUCIBLE MATERIALS FOR CRYSTAL GROWTH

Section Contents

3.1 Introduction

In the Bridgman and Vertical Gradient Freeze (VGF) techniques, it is common to use a sealed quartz ampoule for material synthesis and crystal growth of Cd(Zn)Te. However, to maintain the purity of the starting materials, it is important to prevent interaction between the quartz ampoule and the Cd(Zn)Te melt. One method commonly used is to deposit a layer of carbon on the quartz surface. The carbon layer is typically quite thin, on the order of microns. There is some doubt, however, whether or not this carbon layer effectively blocks quartz impurities from diffusing into the ingot. Other disadvantages include thermal stresses and interface curvature derived from using a quartz ampoule (31) (32).

A second approach is to use a high purity crucible, and to seal the crucible within the quartz vessel, such as pyrolytic boron nitride (pBN). One of the most commonly cited advantages of using pBN is the anisotropic thermal conductivity of the material. This is a result asymmetric hexagonal crystal structure of pBN, with the preferred direction of growth parallel to the c-axis (33). That pBN crucibles are grown on graphite mandrels imply a c-axis normal to the crucible wall. The thermal anisotropy is a result of low thermal conductivity along the c-axis direction (2 W/m) and higher thermal conductivity perpendicular to the c-axis (60 W /m). As a result, radial heat flow is suppressed, being perpendicular to the c-axis.

There are several other important advantages as well. High purity material can be achieved using pBN crucibles, a consequence of the Chemical Vapor Deposition (CVD) process and its material purity inputs. A comparison of crucible materials for InP has shown that the lowest residual contaminations have been obtained using pBN (34). It was also demonstrated for Cd(Zn)Te that pBN crucibles led to the production of ingots with both lower impurities and lower etch pit density compared with carbon coated quartz (35). Work has been carried out on boron nitride (BN) films which show the wetting angle between CdTe and BN is substantially larger than for quartz, carbon coated quartz, and other materials (36) (37). This lower wetting angle leads to less stress induced by the melt-wall interaction. Finally, simulations describing the implementation of pBN as a crucible for Cd(Zn)Te further illustrate the beneficial properties of pBN (29) (38) (39).

One disadvantage of pBN crucibles has to do with the crucible material interacting with the melt during the growth cycle. It has been presented for III-V materials that the

texture of a pBN crucible can have an influence on crystal growth and that the crucible does interact with the melt from cycle to cycle as observed by particulates in the as grown crystal (40). However, exactly how and if this affects the actual material quality has not yet been determined.

This observed interaction between the walls of the pBN crucible and that of the Cd(Zn)Te melt led to the development of a vacuum carbon coating system for applying a carbon coating to pBN crucibles. In order for a new crucible technology to be successfully introduced for the fabrication of Cd(Zn)Te based nuclear imaging detectors, it is important this new technology at least preserves or improves the material quality. For this reason, it was also important to demonstrate that high quality material could be harvested from Cd(Zn)Te ingots grown using carbon coated pBN Crucibles (hereafter referred to as cc-pBN crucibles).

In this work, results for vacuum carbon coating technology applied to pBN crucibles is presented. The compositional and detector properties of the material demonstrate this crucible technology may possess some positive attributes.

3.2 Experimental and Characterization Methods

Cd(Zn)Te crystals of 25mm diameter were grown by the Vertical Gradient Freeze (VGF) method using a 5-zone furnace. A typical thermal profile for a crystal growth run of Cd(Zn)Te is presented in Section 1 of this Chapter. For these growths, it is important to point out that Type-1 homogenization protocol was used, as the Type-2 homogenization protocol had not yet been developed. What is important to note, however, is that a majority of the profile is at temperatures as high as 1130º C, or higher. Moreover, a typical crystal growth cycle may last as long as 200 hours.

For deposition of carbon films, a vacuum carbon coating system was used for carrying out the pyrolysis of Acetone at 1000ºC. Surface roughness of pBN and carbon coated pBN crucibles have been investigated with a Dektak IIA surface profilometer using 2mm scan lengths with a stylus force of 25mg. The morphology of the carbon films was investigated using secondary electron images from a Scanning Electron Microscope (SEM) Hitachi S-3000N, coupled to an energy dispersive X-ray (EDS) analyzer by Oxford Instruments, INCAx-sight model.

From each of the ingots grown using cc-pBN, material was harvested to fabricate test devices. The electronic properties of the Cd(Zn)Te test devices harvested from the ingot were investigated using a Kiethley 6517 electrometer. Carrier type of the devices has been determined using the hot probe method. The fabrication of planar test devices used in this work follows the methods presented by (41).

The ingot composition has been determined using quantitative ICP-MS measurements and using Glow Discharge Mass Spectroscopy (GDMS). Glow Discharge Mass Spectroscopy has been implemented for the analysis of Cd(Zn)Te purity using both pBN and using cc-pBN, and compared with their starting purity.

3.3 Results

3.3.1 Boron Nitride / Cd(Zn)Te Melt Interaction

Using pBN crucibles for the growth of Cd(Zn)Te, we have observed that the crucible does in fact interact with the Cd(Zn)Te melt. Small fragments of material have been extracted from the tip of the ingot, as well as from the lateral sides of as grown ingots. The composition of these particulates was confirmed to contain Boron and Nitrogen by the low energy Kα characteristic X-rays detected near 0.163 and 0.367 keV respectively. One example is shown in **Figure 30**. The Au present in the spectra has been deposited on the sample prior to analysis, and does not represent Au in the Cd(Zn)Te sample.

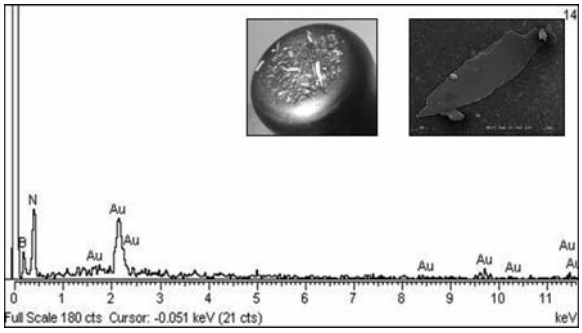

Figure 30 Boron Nitride particulate embedded in Cd(Zn)Te tip, extracted and characterized using EDS. Inset: Boron Nitride flake.

3.3.2 Carbon Coating of pBN Crucibles

As already mentioned, due to the high cost of pBN crucibles, methods to increase their longevity is valuable for reducing recurring costs. This work has been carried out with the

objectives to (i) minimize melt-crucible chemical interactions (ii) increase the longevity of the pBN crucible (iii) maintain process purity.

It was not possible to measure the interior surface properties of pBN and cc-pBN crucibles non-destructively. Therefore, a set of new pBN crucibles were used for surface characterization to establish a base case in terms of morphology and surface roughness. A cc-pBN crucible was also fabricated only for characterization of the surface morphology after carbon deposition.

To demonstrate the effects of thermal cycling on the crucibles, multiple crystal growth cycles were carried out using the same crucibles to simulate how the crystal growth conditions affected pBN and cc-pBN crucibles.

Presented in **Figure 31** are images of a new pBN crucible, a pBN crucible after several growth cycles, and a pBN crucible which has undergone carbon coating treatment using the vacuum carbon coating system and methods described above. The physical dimensions of the crucibles used in this work are 25mm diameter x 150mm length x 0.5mm wall thickness.

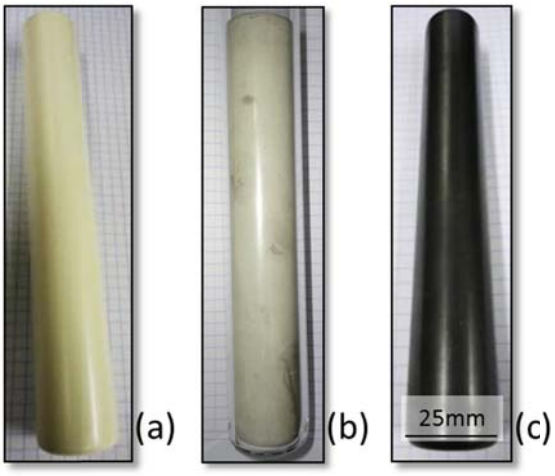

Figure 31 (a) New pBN crucible (b) pBN after crystal growth cycle (c) pBN crucible after carbon coating.

Profilometry measurements of brand new and used pBN crucibles are presented in **Figure 32(a)**. It is important to mention that used pBN crucibles are those which have been used for more than 600hrs at elevated temperatures between 1130-1160^{o}C, for three or more crystal growth cycles.

Not only the surface roughness increases with use, but the difference of the peak-to-valley (P-V) also increases substantially. This increase in the P-V may be associated with BN material actually being removed from the crucible wall through some interaction with the melt. For the new pBN crucibles, the P-V value was lower than 2 μm for most of the range of the profiles measured, and the larger 4 μm peaks are only tens of microns in width. The P-V value measured for pBN crucibles after crystal growth cycling increases substantially with peaks as high as 10 μm and on the order of hundreds of microns in width.

Profilometry measurements of both new and used cc-pBN crucibles are presented in **Figure 32**. The cc-pBN crucibles were not as strongly affected after repeated growth cycles as the uncoated pBN. It is proposed therefore that the interfacial carbon layer may act as a barrier at high temperatures preventing the pBN from interacting with the melt, and therefore preserving the original morphology of the crucible.

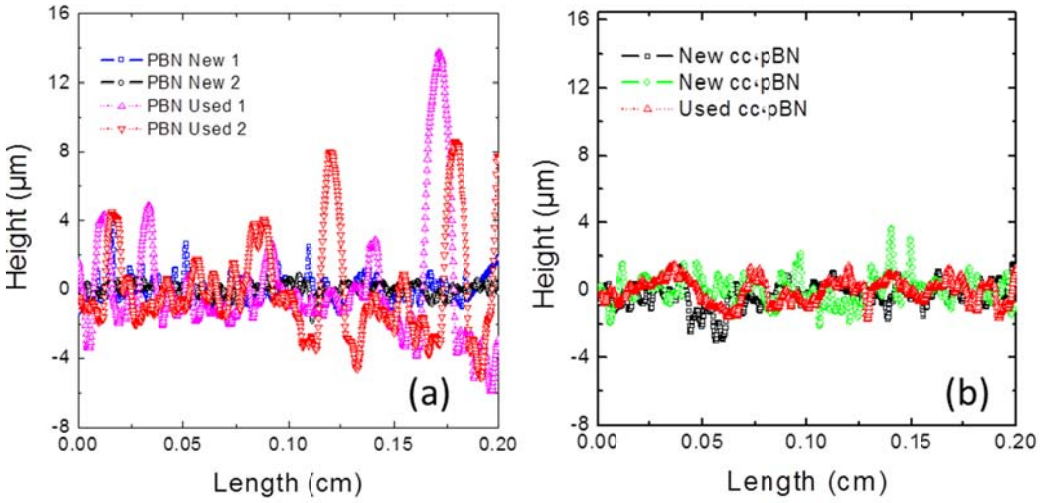

Figure 32 (a) Profilometry of new and used pBN crucibles. (b) Profilometry of new and used cc-pBN crucibles.

Corroborating data has been obtained using the SEM. Using the SEM, it is more feasible to image the surface of the pBN and cc-pBN crucible surface both before and after thermal cycling. This surface information provides a more intuitive image of the crucible surface, with the capability to see changes in morphology more clearly.

Presented in **Figure 33** are SEM images of new pBN and cc-pBN crucibles which have not yet been used for crystal growth. The new cc-pBN crucible appears slightly smoother

than the new pBN crucible. This may have to do with the deposited carbon filling the gaps in the pBN surface as the carbon layer is grown. In any case, the roughness of the pBN and cc-pBN are quite similar.

Presented in **Figure 34** is the surface morphology for pBN and cc-pBN after several crystal growths cycles. For the pBN crucible, the surface morphology appears to have changed dramatically after several growths. This may be associated with interactions between the pBN crucible and the melt. It may also be associated with the removal of the ingot from the crucible causing significant scratching at the surface due to sticking.

It is important to note that the width of the peaks and valleys are one the same order of magnitude as those measured using the Dektak profilometer. After being used for several crystal growths, the roughness of the cc-pBN does appear to have increased, but not as substantially as the pBN crucible.

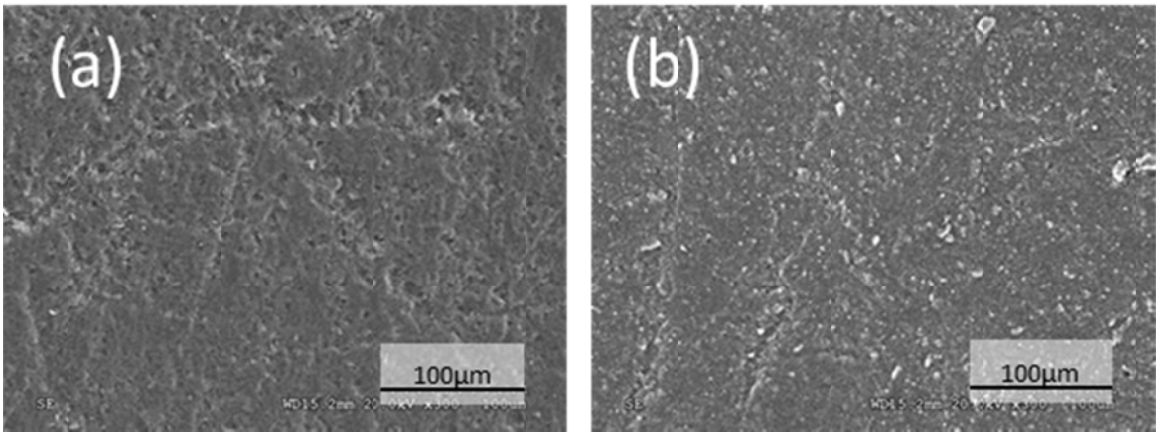

Figure 33 Surface morphology of (a) new pBN and (b) cc-pBN crucible measured using SEM.

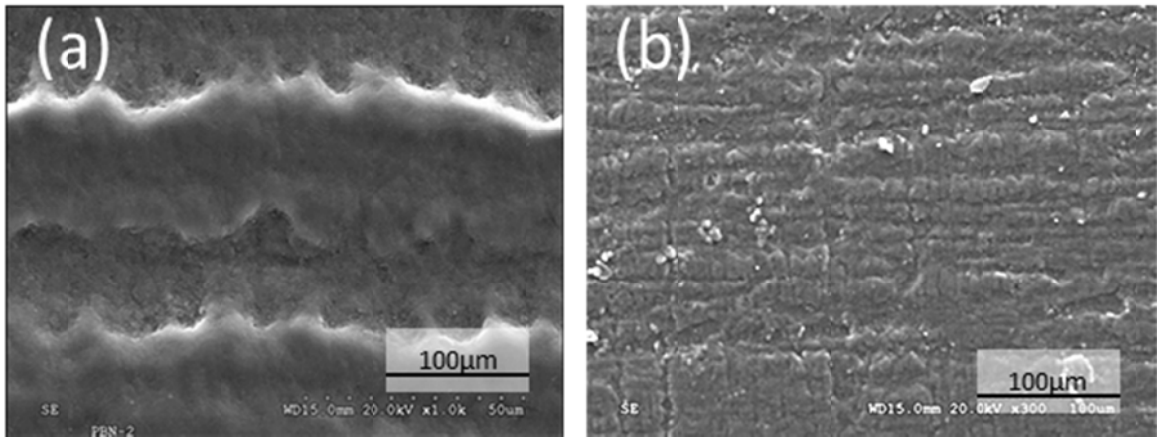

Figure 34 Surface morphology of (a) used pBN and (b) used cc-pBN crucibles measured using SEM.

3.3.3 Ingot Surface Characterization

It was also important to include how the surface morphology of the crucible affected the morphology of the as grown Cd(Zn)Te ingot. Therefore, SEM measurements of Cd(Zn)Te ingots grown using cc-pBN, and pBN crucibles are presented in **Figure 35**. For comparison, SEM measurements of Cd(Zn)Te ingots grown using carbon coated Quartz (cc-Quartz) are also shown.

The most striking observation is that the high roughness of the pBN crucible has a substantial influence on the roughness of the crystal grown using pBN. In fact the surface morphologies appear quite similar under the same magnifications. Many Cd(Zn)Te ingots have been grown using pBN crucibles in this work, and all ingots have similar non-reflective rough surface morphologies.

The cc-pBN crucible, however, is similar in roughness to the pBN crucible, and as such it may be expected that the roughness of the as-grown ingot should be similar. However, despite this similarity in roughness, Cd(Zn)Te crystals grown using the cc-pBN crucible produce ingots with reflective surfaces, and with surfaces more similar to ingots grown using carbon coated quartz ampoules, than to pBN crucibles. For comparison, the surface of a Cd(Zn)Te ingot grown using carbon coated quartz is also presented.

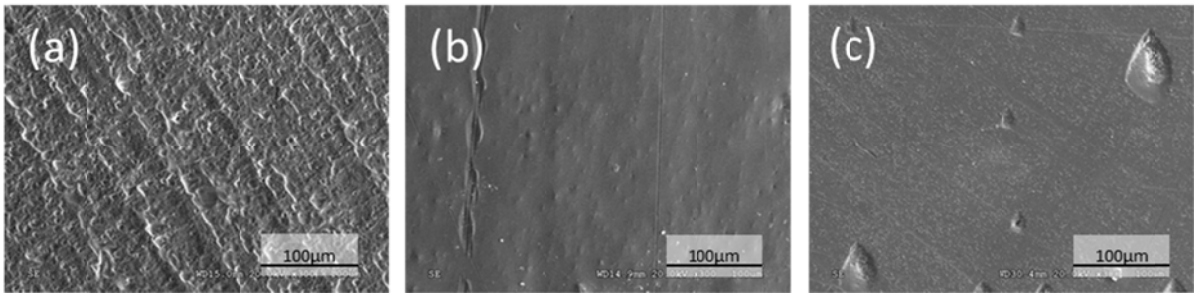

Figure 35 Ingot surface grown using (a) pBN, (b) cc-pBN, and (c) cc-Quartz.

In the case of cc-quartz, the reflective surface finish of the ingot is a direct consequence of the low surface roughness of the quartz ampoule and the corresponding low surface roughness of the carbon coating applied to the quartz ampoule i.e. the as-grown ingot conforms to the surface roughness of the vessel in which it is contained. This is the same case for the Cd(Zn)Te grown in the pBN crucible, albeit the surface roughness of the ingot exhibits a higher degree of roughness.

A relation between the as-grown ingot surface roughness and detached growth has been observed by others using pBN crucibles (42). The high surface roughness of the ingot is associated with attached growth, while a reflective surface is with detached growth. Furthermore, it has been put forth that higher levels of surface roughness of the crucible leads to improved de-wetted conditions, a consequence of the higher wetting angle of the crucible (43).

Presented in **Figure 36** are three possible wetting conditions which may occur between a liquid and solid surface. The contact angle is constructed by the angle between the tangent of the liquid droplet and the contact surface.

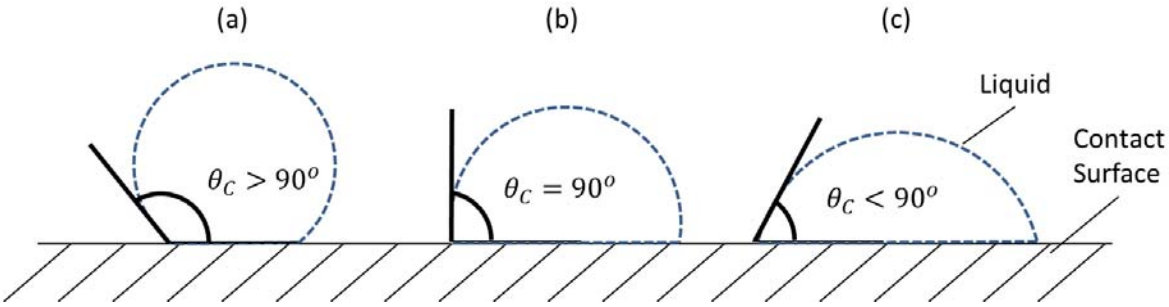

Figure 36 (a) Large contact angle (b) contact angle = 90°, and (c) small contact angle

Liquids which exhibit lower contact angles conform to a greater extent to the morphology of the contact surface. Indeed, the surface of the Cd(Zn)Te ingot grown using cc-quartz also has similar roughness to that of the carbon layer (See Chapter 2, Section 1.3 for more information on the carbon layer morphology). In the case of the pBN crucible, the surface morphology of the ingot is comparable to that of the crucible, and we attribute this to a relatively lower contact angle.

In the case of cc-pBN, the high roughness of the crucible was not imparted into the surface of the ingot. This indicates the contact angle of the Cd(Zn)Te melt with the cc-pBN crucible may be relatively larger than that obtained using the pBN crucible alone. It is possible that this interaction may be associated with the carbon layer changing the contact angle at the surface, however further investigation of the surface wetting phenomenon using cc-pBN is required.

3.3.4 GDMS Measurements

Due to the nature and high purity of the elements used in the synthesis of high resistivity Cd(Zn)Te, there are many potential sources of contamination. It is of paramount importance, therefore, that the number of material processing stages is kept to a minimum, and that appropriate material handling protocol is adapted. Environmental sources of contamination include impurities present not only in the air, but on the surfaces of the laboratory components such as tables, bench tops, computers, etc. Common impurities present even in clean room environments include Na, Al, Mg, Si, and S.

The diffusion of chemical species within the quartz matrix becomes significant at temperatures reaching 1,000°C or more. Such impurities include sodium, lithium, calcium, and potassium. Typical trace elements for HSQ 300 Quartz glass are presented in **Table 4**.

Other experimental related impurities may originate from a number of sources, including the processes performed in the clean room, the clean room personnel, the cleaning agents, and the ventilation system and general air quality. Additionally, contamination with iron and chromium can be expected if stainless steel tools come in violent contact with the charge material.

Table 4 Trace impurities for different Quartz tubes measured in ppm (44)

Grade	Al	Ca	Cr	Cu	Fe	K	Li	Mg	Mn	Na	Ti	Zr
CFQ 099	15	0.8	<0.05	<0.1	0.4	0.8	1.2	0.1	0.1	0.9	1.5	0.8
HSQ 100	15	0.5	<0.05	<0.05	0.1	0.4	0.6	0.05	<0.05	0.3	1.1	0.7
HSQ 300	**15**	**0.5**	**<0.05**	**<0.05**	**0.1**	**0.4**	**0.6**	**0.05**	**<0.05**	**0.3**	**1.1**	**0.7**
HSQ 700	15	0.5	<0.05	<0.05	0.1	0.1	0.05	0.05	<0.05	0.3	1.1	0.7

The terminology for Cd(Zn)Te 7N quality is determined by the maximum quantity of impurities lower than 100PPB normally excluding C, O, and N. By comparing the 7N as received material with as grown high resistivity material, it is possible to observe how the experimental conditions affect impurity levels in the as grown material. In total, trace impurities of 55 elements have been investigated in as grown ingots, as well as in the starting material. Only those elements which exhibit larger concentrations than the starting 7N material are presented.

Table 5 GDMS Data for Cd(Zn)Te ingots grown under same conditions using a carbon coated quartz, pBN, and carbon coated pBN growth vessels.

	cc-SiO_2	pBN	Cc-pBN	CZT
Li	**<2**	**26**	**6**	**<10**
Be	**<2**	**<2**	**<2**	**<4**
B	**<4**	**30**	**<3**	**<6**
C	**190**	**150**	**200**	**390**
N	**40**	**65**	**8**	**10**
O	**190**	**65**	**2200**	**430**
F	<7	<10	<5	<6
Na	**27**	**18**	**45**	**<4**
Mg	**51**	**14**	**64**	**28**
Al	**28**	**<2**	**620**	**<2**
Si	<2	<2	10	5
P	**<2**	**28**	**<2**	**<3**
S	**170**	**350**	**29**	**15**
Cl	**190**	**2000**	**1200**	**<4**
K	<50	<50	<15	<30
Ca	<15	<20	180	<25
Sc	<1	<1	<1	<2
Ti	<0.4	<0.5	<0.8	<0.6
V	<0.3	<0.3	<0.4	<0.5
Cr	4	14	13	<3
Mn	<10	<10	<10	<10
Fe	**<5**	**<5**	**74**	**<5**
Co	<0.6	<0.7	<0.7	<1
Ni	<3	<3	<4	<5
Cu	<18	<20	<30	<25
Ga	<4	<5	<5	<5
Ge	<16	<35	<30	<45
As	<65	<35	<40	<50
Se	<35	<55	<15	<10
Rb	<0.4	<0.4	<0.4	<0.6
Sr	<0.3	<0.3	<0.3	<0.5
Y	<0.2	<0.3	<0.3	<0.4
Zr	<0.4	<0.5	<0.5	<0.7
Nb	<2	<3	<5	<0.5
Mo	<1	<3	<3	<2
Ag	40	<40	<100	<110
In	**1000**	**5000**	**1800**	**<100**
Sn	<30	<40	<65	<60
Sb	<35	<35	<55	<50
I	<480	<500	<540	<420
Cs	<4	<6	<7	<6
Ba	<3	<100	<12	<0.9
La	<0.3	<9	<12	<0.2
Ce	<3	<95	<9	<0.8
Hf	<7	<7	<30	<17
W	<3	<3	<6	<5
Pt	<4	<5	<6	<14
Au	<5	<5	<5	<5
Hg	<4	<4	<4	<6
Tl	<1	<1	<1	<2
Pb	<1	<1	<1	<2
Bi	<0.6	<0.8	<0.8	<1
Th	<1	<1	<2	<2
U	<2	<2	<3	<3

From the results presented in **Table 5**, several observations may be made. The relatively high concentrations of Indium present in the as grown Cd(Zn)Te compared with the In levels in the as-received bulk Cd(Zn)Te is a result of intentional doping of the crystal with donor impurities to achieve electrical neutrality. The In content of the crystals is discussed in greater detail in the following paragraphs regarding ICP-MS measurements.

Comparing the crystals grown using carbon coated crucibles (cc-pBN and cc-Quartz) and uncoated crucibles materials (pBN crucible=, the effects of the carbon coating may also be observed. For the ingots grown using cc-pBN and cc-Quartz the Boron and Nitrogen levels were consistent with impurity levels found in the starting materials. For the ingot grown using a pBN crucible, the incorporated B and N were slightly higher than expected. However, the concentration of carbon incorporated was higher for the cc-Quartz and the cc-pBN compared with the ingot grown using pBN.

The high chlorine content observed in the cc-pBN and pBN grown ingots may be associated with the cleaning procedure which uses a reagent containing HCL. The cc-quartz ampoule also undergoes this cleaning, but is later exposed to high temperatures for the carbon deposition process, so residual contamination may be removed as the carbon layer is deposited. Slightly higher levels of trace amounts of

iron and chromium may be associated with the stainless steel tools which are used within the glove box for charging the crucible. Other impurities such as Al, Mg, Na, P, and S may come from material handling and environmental conditions.

3.3.5 Material Segregation

The axial composition of the ingot was characterized using ICP-MS to measure axial Zinc concentration. Results are presented below in **Figure 37**. Using the Scheil Equation represented in , the segregation coefficient has been calculated to be between 1.3 and 1.5. C_o is the initial concentration of Zinc, C_s is the concentration of Zinc in the solid, k is the segregation coefficient, and g is the solidified fraction. The values obtained for k are consistent to the commonly reported values found in literature (45).

Equation 7 $$\boldsymbol{C_s = k \cdot C_o(1-g)^{k-1}}$$

The variation in the axial concentration of Zinc may be divided into three regions, as is presented in **Figure 37**. In Region I, the segregation coefficient in this super-cooled region is close to 1, and reflects the bulk concentration of the melt i.e. 10%. This affect has been studied by, and is illustrated by the closely spaced iso-concentration contours in the first to freeze region of the ingot (46).

Of the three as-grown ingots, only cc-pBN 1 demonstrated this effect strongly. That this behavior was not observed in cc-pBN 2 and cc-pBN 3 is attributed to the use of a SiC pedestal which increases the axial gradient, bounds the super-cooled region to a smaller volume, and increases the extraction of latent heat at the onset of nucleation (38) (39). Poor contact between the SiC pedestal and the cc-pBN crucible for cc-pBN 1 may have influenced these results. In general, the influence of the pBN crucible in conjunction with a SiC pedestal appears to reduce the supercooling of the melt. This is further evidenced by detectors harvested from the first to freeze region of the ingot.

In Region II of the crystal, the segregation of Zinc follows fairly closely the Scheil equation. However, in Region III, the concentration of Zinc falls fairly quickly in each of the ingots studied. This may be related with changes in melt convection arising from a reduction of the melt zone and thermal end effects.

With respect to Indium concentration, the calculation of the segregation coefficient using was not possible. For each ingot, the concentration profile may be divided into two regions, with Region I $0 < g < 0.6$, and Region II $g > 0.6$.

With respect to Indium, the concentration profile may be divided into two regions, with Region I $0 < g < 0.6$, and Region II $g > 0.6$. In the first region, between 5×10^{15} - 1.2×10^{16} at/cm^3 of In is accepted into the lattice. This appears somewhat independent of the starting concentration of In, as may be seen by comparing cc-pBN 1, 2, and 3 each containing different doping levels between 1.5 and 2.4×10^{16} at/cm^3. Furthermore, as the solidified fraction increases, the concentration of In in the melt continues to grow as the intended doping level is higher than the Indium which is incorporated into the matrix. However, between g = 0.5 and g= 0.6, there is a sharp increase in the concentration of In incorporated into the Cd(Zn)Te matrix, which prevents the calculation of a segregation coefficient using **Equation 7**.

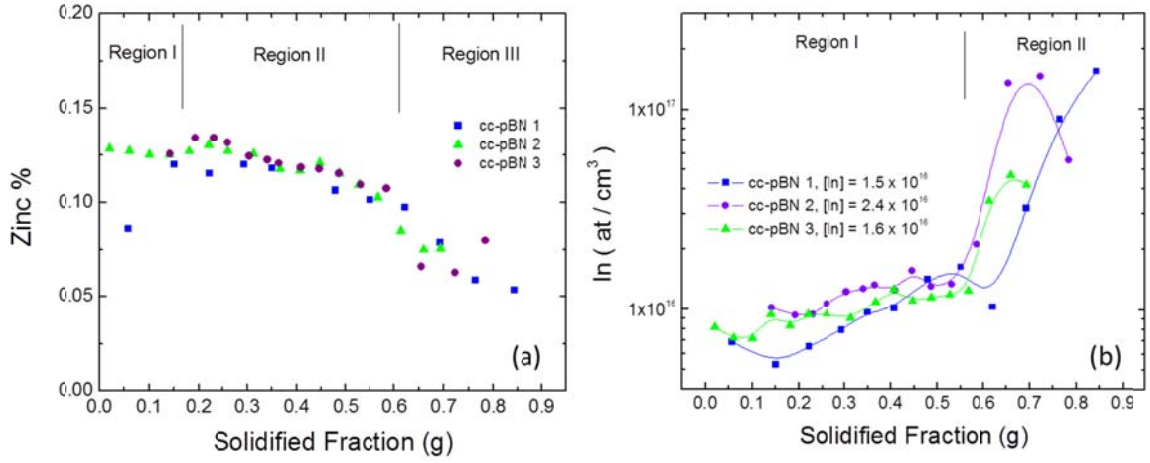

Figure 37 Axial segregation of (a) Zinc and (b) Indium in crystals grown using cc-pBN Crucible

One possible explanation for this irregular behavior may be attributed to solid state diffusion of In at the end of the ingot diffusing back into the solidified charge through solid state diffusion. The diffusion equation is derived from Fick´s Law, which relates diffusive flux to its concentration. Taking into account the diffusion coefficient for Indium in the Cd(Zn)Te matrix, which has been determined by two independent investigators, this explanation faces some difficulty. The diffusion coefficient for Indium as presented in **Equation 8**.

Equation 8 $$D_{In} = 3.29 \times 10^{-4} \cdot exp(-1.10eV/kT) \quad (47)$$

Equation 9 $$D_{In} = 3.22 \times 10^{-4} \cdot exp(-1.13eV/kT) \quad (48)$$

Indeed, taking into account these values the characteristic diffusion length, ***d***, of Indium may be calculated using Equation 10 , where D_{In} is the diffusion coefficient at a certain temperature, and *t*, represents the amount of time at this temperature. Taking into account (i) the length of the growth cycle at temperatures near 1100ºC and (ii) the crystal cooling cycle (the ingot is cooled in 10 hour durations from 1000°C, 800°C, 500°C, and 300°) the characteristic diffusion length bay be calculated using **Equation 10**. This characteristic length is only on the order of 0.1mm, and is not sufficient to explain this behavior which occurs over a length of 2 cm.

Equation 10 $$d = \sqrt{2 \cdot D_{In} \cdot t}$$

A more plausible explanation of these experimental results may be found by considering that each crystal was grown using Type-1 homogenization profiles, discussed in Section 2 of this chapter. Specifically, the second nucleation event which is claimed to occur at the melt surface during the growth cycle may produce indium segregation from the tail end of the ingot. Indeed, after the second nucleation event occurs, there will be Indium segregation from both the top and bottom ends of the ingot arising from two propagating solid liquid interfaces (see **Figure 23** on page 203).

For a segregation coefficient lower than 1, as is the case of Indium, the maximum In content will not be found at the ends of the ingot, but somewhere in the center. As may be seen in Figure 37b, such a local maximum is observed. Therefore, it is possible that this phenomenon may be explained using this physical description. It will be of future interest to compare these results with In segregation in ingots grown using Type-2 homogenization where the second nucleation at the melt surface does not occur due to the imposed superheating condition.

3.3.6 Gamma Response

The gamma response of test devices harvested from each ingot grown using cc-pBN crucible is presented in Figure 38. These Cd(Zn)Te test devices exhibit good performance, having a FWHM of between 5-12 % at 81keV. The spectra presented are for the devices biased between 2000 - 3000V / cm. Such high electric fields provide improved charge collection efficiency of the device. These are representative samples of several devices which have been harvested from each ingot. The difference in peak locations is a consequence of different gain settings used during the measurement of each device, according to its resistivity.

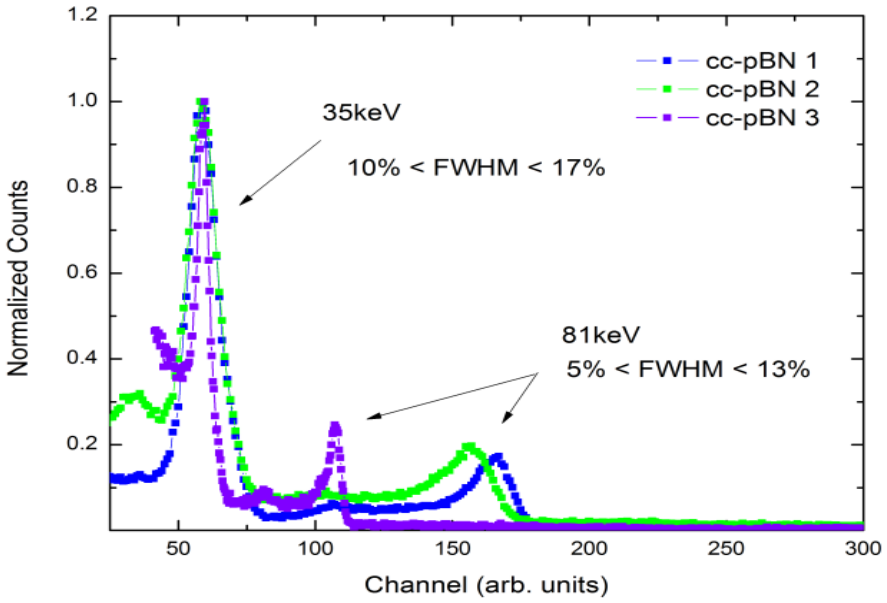

Figure 38 Gamma response measurements using ^{133}Ba radioactive source for test devices harvested from crystals grown using cc-pBN crucible

3.4 Conclusions and Future Work

In summary, high quality material Cd(Zn)Te has been harvested from all regions of the ingot, from the tip to the tail, effectively demonstrating the advantages of cc-pBN crucible technology used for crystal growth of Cd(Zn)Te. The summary of this investigation are as follows:

1) A vacuum carbon coating system has been designed, assembled, tested, and successfully implemented for carbon coating of pBN crucible materials. To the extent of the Authors knowledge, this is the first time carbon coating has been applied to pBN crucibles.
2) Results indicate this technology may be implemented for increasing the longevity of pBN crucible through reducing melt-crucible interactions.
3) A second advantage of the carbon coating system is that the method may be reapplied, so it may be possible to re-deposit another carbon layer after a certain number of growth cycles.
4) Despite the high roughness of the crucible, a reflective surface of the Cd(Zn)Te ingot has been obtained using the cc-pBN crucible. This indicates the properties of the carbon layer may effectively increase the wetting angle of the Cd(Zn)Te-Carbon-PBN interface. As a result, it is possible that the stress imparted by the crucible wall may be reduced through the implementation of carbon coating.
5) Ingots grown using cc-pBN and cc-Quartz exhibited lower concentration of B and N incorporated into the matrix, as was expected. Cleaning of pBN crucibles using acid reagents such as HCL appear to leave residual contamination which could influence the compensation mechanism in Cd(Zn)Te.
6) Indium content and segregation may be influenced by the Type-1 homogenization protocol discussed in Section 2 of this chapter.
7) Detectors grown using cc-pBN crucible and harvested along the axis of growth exhibit high resistivity and good functionality as room temperature gamma ray detectors, indicating that the cc-pBN technology preserves, if not improves the resultant material quality of the process.

Based on these experimental results, further investigation into the wetting properties of the cc-pBN crucible is warranted. Indeed, the ability to decrease crucible wetting may have play a large role in reducing dislocations induced by the crucible wall into the crystal during the growth cycle.

4 Development Of Crystal Growth Part 1: Effect of Dynamic Temperature Adjustments on Resistivity and Photoconductivity

Section Contents

4.1 Introduction

Crystal growth of Cd(Zn)Te remains an experimental challenge for achieving large volumes of single grain high resistivity material useful for high energy spectroscopy applications. Moreover, the large number of experimental considerations necessary for establishing reproducible results makes scientific progress in crystal growth slow and time consuming.

One of the most important parameters relating to crystal growth of Cd(Zn)Te is the temperature gradient applied at the solid-liquid interface throughout the growth cycle. Indeed, it has been known for some time that crystal growth of Cd(Zn)Te is preferable under low temperature gradients to reduce dislocation densities associated with the low stacking fault energy of CdTe (49). This is one of the factors which prohibit liquid encapsulated Czochralski method from being implemented in Cd(Zn)Te (50). The thermo-mechanical stress imparted by the applied temperature gradient at the solid liquid interface may be obtained through second order differentiation of the axial temperature profile, as is presented in **Equation 11** (28).

Equation 11

$$\frac{d^2T}{dz^2} = -4\frac{G_t^2}{(T_h - T_c)} tanh\left(\frac{2 \cdot G_t}{(T_h - T_c)}(z - z_t)\right) cosh^{-2}\left(\frac{2 \cdot G_t}{(T_h - T_c)}(z - z_t)\right)$$

In this case, a simplified hyperbolic tangent function has been used for describing a furnace which consists of two temperature zones. The terms T_h and T_c are the temperatures of the hot and cold zones of the furnace, G_t is the temperature gradient at the turning point z_t between the two zones. The reader is referred to (28) for additional details. The thermo-mechanical stress function illustrates that (i) fluctuations in the temperature gradient cause fluctuations in the thermo-mechanical stress at the solid liquid interface and (ii) decreasing the temperature gradient, G_t, reduces the growth induced stress.

In the VGF method, which has been used extensively throughout this thesis investigation, changes in the gradient as a function of axial position also produce non-uniformities in the crystal growth velocity. This may be observed using **Equation 12**, which relates the crystal growth velocity, v, to the temperature gradient, ∇T, by the cooling rate of the VGF furnace, ΔT. In the standard approach to the VGF method, a single cooling

rate is used throughout the growth cycle. As a result, a furnace cooling rate of 0.25 °C-hr^{-1} will imply a crystal growth rate of 0.025 cm-hr^{-1} and 0.05 cm-hr^{-1} for temperature gradients of 10 °C-cm^{-1} and 5° °C-cm^{-1} respectively.

Equation 12 $$\boldsymbol{v_{Growth\ velocity} = \Delta T_{Cooling\ Rate\ VGF} \ / \ \nabla T_{Axial\ Gradient}}$$

Finally, the temperature gradient at the solid-liquid interface also plays a role in the general growth dynamics described by **Equation 13**, which is referred to as the heat equation. From this equation, the growth velocity, $\boldsymbol{v}$, is determined by latent heat of fusion, $\boldsymbol{\Delta H}$, and density, $\boldsymbol{\rho}$, of the compound, as well as the thermal conductivity of the solid/liquid phase, $\boldsymbol{\lambda_{s,l}}$, and the temperature gradient across the solid/liquid bodies, $\boldsymbol{T_{s,l}}$. Changes in the crystal growth velocity are disrupted by changes in mass solidification and latent heat release induced by axial variation in the temperature gradient. It has been shown by that the maximum thermally balanced growth rate (i.e. heat extracted > generation of latent heat) occurs for growth rates less than 1 mm/hour, at temperature gradients less than 10 °C/hour (28).

Equation 13 $$\boldsymbol{v \leq \frac{1}{\Delta H \cdot \rho}\left(\lambda_s \frac{dT_s}{dz} - \lambda_l \frac{dT_l}{dz}\right)}$$

In the present investigation, it is demonstrated that by controlling the temperature set points of each zone in 5-zone furnace, the axial temperature gradient could be controlled through dynamic adjustments made throughout the growth cycle. This adjustment of the temperature gradient is intended to keep the shape of the crystallization front stable, by keeping the temperature gradient at the interface uniform. It is important to note that this approach has been applied to several crystals, and is now being implemented routinely on both 25mm and 50mm ingots. A detailed study of the electrical properties of two representative crystals grown with and without the dynamic adjustment of temperature gradient will be presented in this first section. The next section of this chapter will further discuss the electrical and optical properties of Cd(Zn)Te radiation devices grown using this technique.

4.2 Results and Discussion

4.2.1 Dynamic Temperature Gradients

The crystals grown without and with dynamic temperature adjustments will be referred to as crystal No.1 and crystal No. 2 respectively. During the growth of crystal No.1 the VGF furnace cooling rate was kept constant, with no dynamic changes made to the furnaces throughout the growth cycle. As a result of the decreasing temperature gradient along the axial direction, the growth velocity also decreases with the increase of the solidified fraction, following from **Equation 12**.

Experimental conditions which exhibit non-uniform growth rates are known to not be optimal for crystal growth and normally result in deterioration of crystal quality. This is often connected with fluctuations in the resistivity and charge collection efficiency of fabricated detectors arising from compositional inhomogeneity and growth related defects.

The temperature gradients for each of the crystals, derived from the differential measurements of adjacent thermocouples, are presented in Table 6 (see **Figure 10** page 189 for experimental pedestal description). As can be seen, the application of the dynamic temperature adjustments has led to more uniform temperature gradients across the entire length of the ingots (the term *g* in this table represents solidified fraction of the ingot). The stabilization of the temperature gradient at the SLI through adjustments made to the set point of the hot zones is demonstrated for crystal No.2 in **Figure 39**.

Table 6 The thermal gradients applied to the grown Cd(Zn)Te ingots.

Solidified Fraction	**No.1(111009) Fixed Cooling Rate**	**No2 (120709) Dynamic Furnace Adjustments**
	ºK / cm	ºK / cm
Tip (0)	17	10
g = 0-0.25	7	17
g = 0.25-0.50	8	7
g = 0.50-0.75	2.5	8-10
g = 0.75-1.00	N/A	10

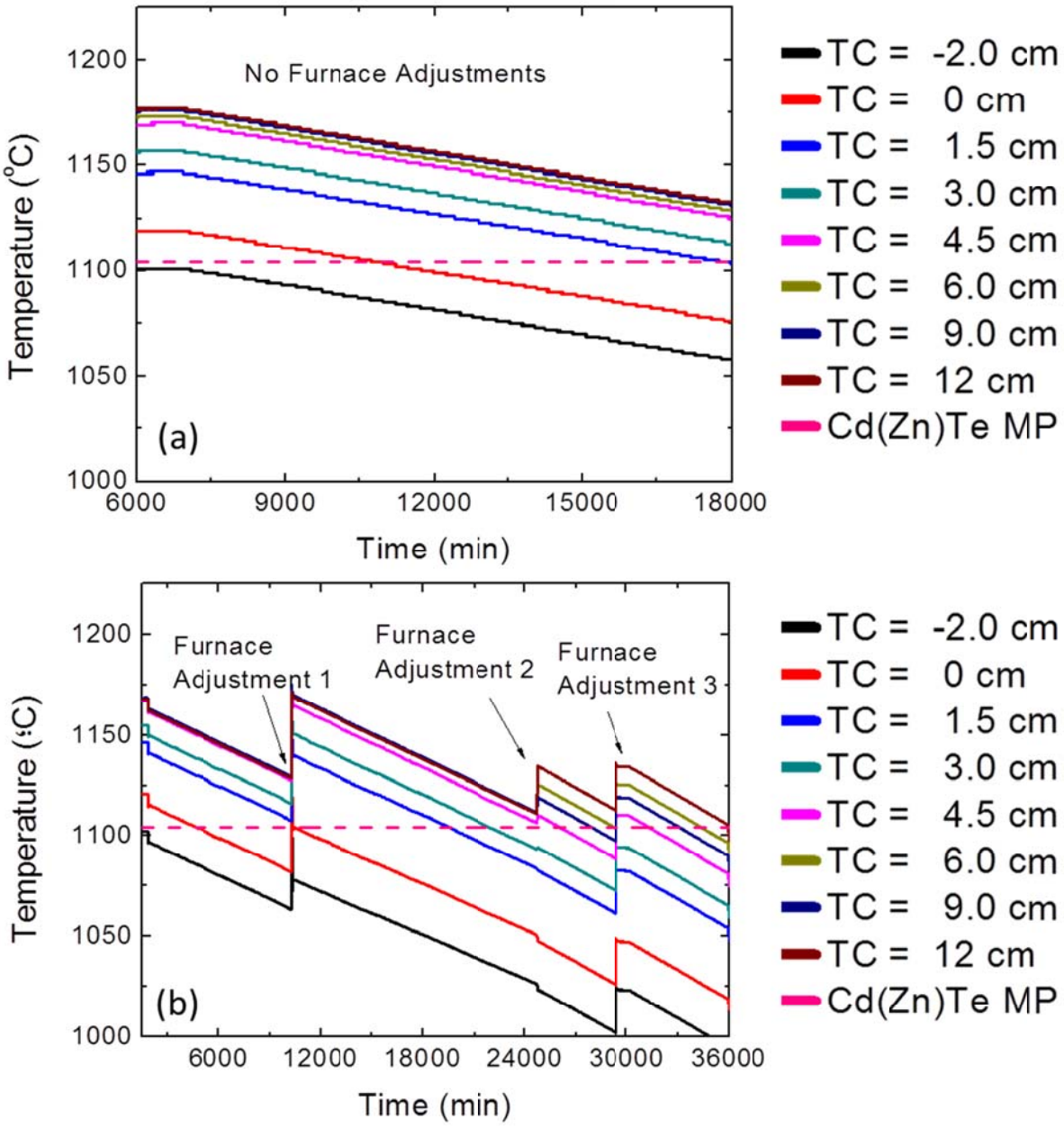

Figure 39 Measured temperatures along the axis of growing crystals for (a) Ingot No. 1 with no furnace adjustments made and (b) Ingot No.2 with furnace adjustment made throughout the growth cycle to control the applied temperature gradient.

By increasing the temperature of one of the zones of the VGF furnace, the temperature gradient across the ingot will also be increased. These furnace adjustments in fact melt back a small part of the crystal, a result of increasing the temperature in one of the upper zones. However after this adjustment, the growth continues with the same cooling rate. This

small melt-back procedure applied to crystal No.2 has not only improved the crystal quality at the tip of the ingot (compared with ingot No.1 which has voids and bubbles), but also the grain size throughout the rest of the ingot. A comparison of the two ingots is presented in **Figure 40**.

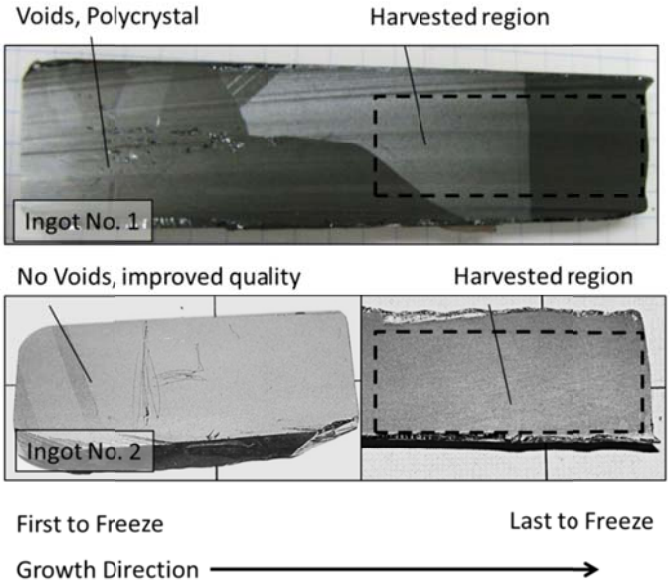

Figure 40 Crystal quality of crystal No.1 (no adjustment of temperature gradient) and crystal No.2 (temperature gradient adjusted throughout growth cycle).

4.2.2 Photoconductivity & Resistivity

Resistivity and photoconductivity maps were measured using a contactless method on a COREMA commercial setup. For contactless photoconductivity IR light emitting diodes were used with maximum peak intensity at 830nm. The area of the contactless probe is $1mm^2$ and its minimal mapping step is 0.1mm. More details regarding the photocurrent technique are presented elsewhere (51). The resistivity maps without illumination were measured in a contactless regime at room temperature. The measured maps for crystals No1 and 2 are presented in **Figure 41**. As may be seen, crystal No. 2 exhibits higher resistivity over a larger volume of the crystal. Indeed, the electrical resistivity is an important parameter which determines the dark current of devices fabricated using Ohmic contacts.

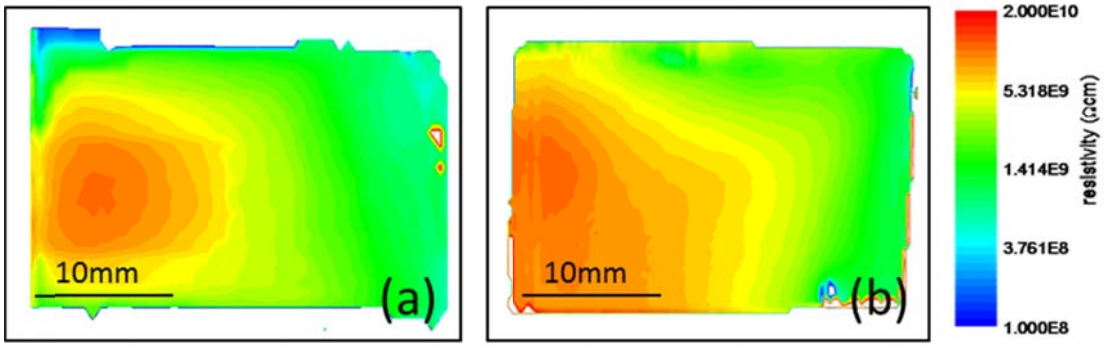

Figure 41 Contactless resistivity map measured in the Cd(Zn)Te crystal No1 (a) and No.2 crystal (b)

Presented in **Figure 42** are resistivity profiles along the growth axis of both crystal No. 1 and No. 2, which have been extracted from the 2-D resistivity maps. The modification of the temperature profiles used with crystal No. 2 has produced a shift of the resistivity maximum towards the end of the ingot. As a result, a larger volume of the crystal is potentially useful for detector fabrication. The characteristic feature of the profiles is that resistivity goes through maximum located in the central parts of the ingots and this maximum is shifting towards the end of crystals with increasing average resistivity depending on the Zn content. Therefore, the adopted modification of the growth process was also from this point of view beneficial.

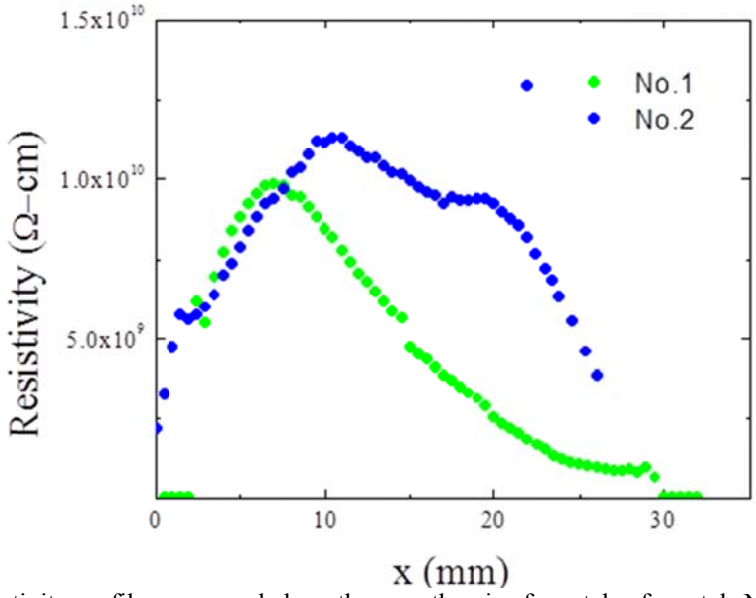

Figure 42 Resistivity profiles measured along the growth axis of crystals of crystals No. 1 and No. 2

A second key parameter used to characterize the charge collection efficiency of semi-insulating material is the mobility-lifetime product. Photoconductivity is directly linked to the mobility-lifetime product through the modified form of the Hecht relation (51). The

possibility to predict distribution of charge collection by photocurrent mapping was presented in (52). In order to characterize maps of charge collection efficiency of the studied wafers, we performed measurements of photoconductivity by contactless method. A comparison of the photoconductivity maps for crystals No.1 and No.2 are presented in **Figure 43**.

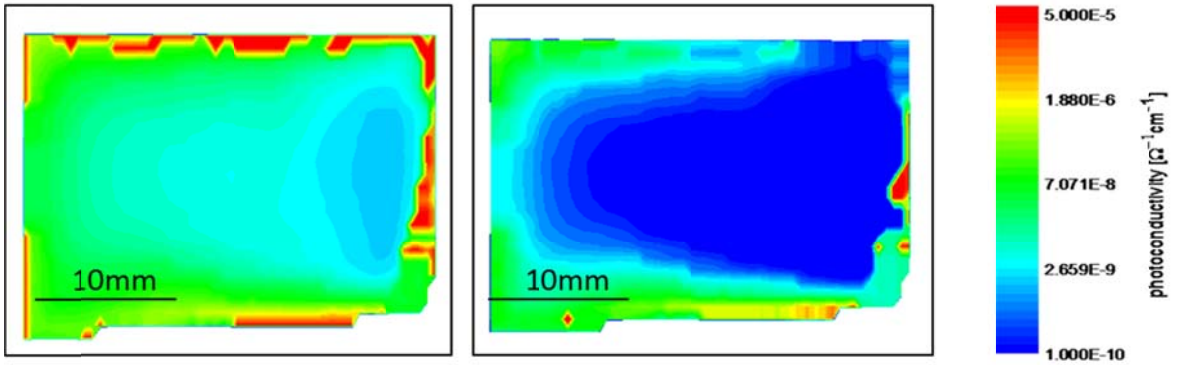

Figure 43 Photoconductivity map obtained by the contactless method on the Cd(Zn)Te crystal No.1 (left) and crystal No. 2 (right)

A comparison of the photoconductivity profiles measured along the growth axis of both samples is presented in **Figure 44**. Several differences among the profiles can be seen. The photoconductivity profile of crystal No. 1 has a wavy character which may be attributed to instabilities during the growth. Indeed for crystal No. 1 the temperature gradients near the last to freeze region of the ingot were relatively low, as is presented in **Table 6**. Not only are the temperature gradients lower, but the gradual change in the axial temperature gradient represents a corresponding change in growth velocity described above using **Equation 12**. This instability in the growth interface is further supported by **Figure 40**, wherein the crystalline quality near the first to freeze region is poly-crystal and exhibits voids, and only moderate size grains are evident.

The photoconductivity profile of crystal No.2 is quite stable, however, and decreasing towards the end of the ingot. This may be related with the improved temperature gradients at the solid liquid interface, leading to a more stable growth velocity. The absolute value of the signal for crystal No. 2 is smaller than in case of the crystal No.1.

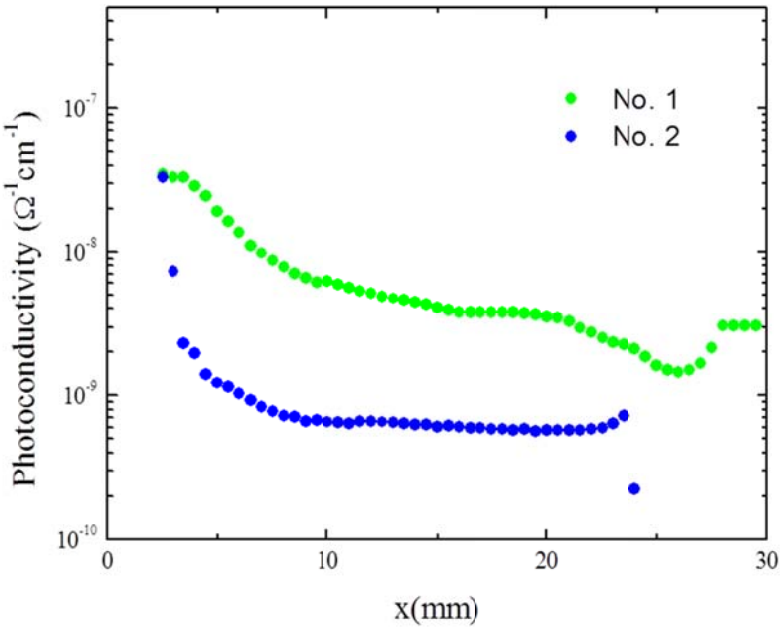

Figure 44 Profiles of photoconductivity measured along the growth axis of crystals No. 1 and No.2.

In order to increase our understanding of factors affecting photoconductivity the resistivity and photoconductivity profiles presented are compared in **Figure 45** for crystal No.1 and No. 2. For both crystals, anti-correlation between the resistivity and photoconductivity is clearly seen in the beginning of the slice (representing the middle of the ingot). After reaching a maximum, the resistivity is correlated with changes in the photoconductivity nearly to the end of crystal.

This behavior can be qualitatively explained by a model presented in (10) and (19). The change of resistivity results in a corresponding shift of the Fermi level. If there is a deep level near the Fermi level position, this shift changes its occupation. This will influence trapping and recombination fluxes connected with this level. Comparison of axial profiles of resistivity and photoconductivity for crystal No.2 is presented in **Figure 45**(b).

The observed anti-correlation between resistivity and photoconductivity observed in beginning of the ingot can be explained by a decreased electron occupation of the deep level with increasing resistivity caused by shift of the Fermi level towards the mid-gap. Decreased occupation results in increased electron trapping and recombination. This mechanism further decreases the photoconductivity when both the photoconductivity and resistivity become correlated. Here the Fermi level continues to shift relatively to the deep

near mid-gap level decreasing its equilibrium occupation and increasing its trapping capacity. The same behavior is also observed in case of crystal No.2.

The mechanism driving this behavior was proposed and described in (53), however, only anti-correlation of resistivity and photoconductivity was observed in the studied CdTe:In crystal. The transition from anti-correlation to correlation of both quantities near the theoretical maximum of resistivity experimentally observed in the current contribution represents to our opinion an important argument fo the validity of the model.

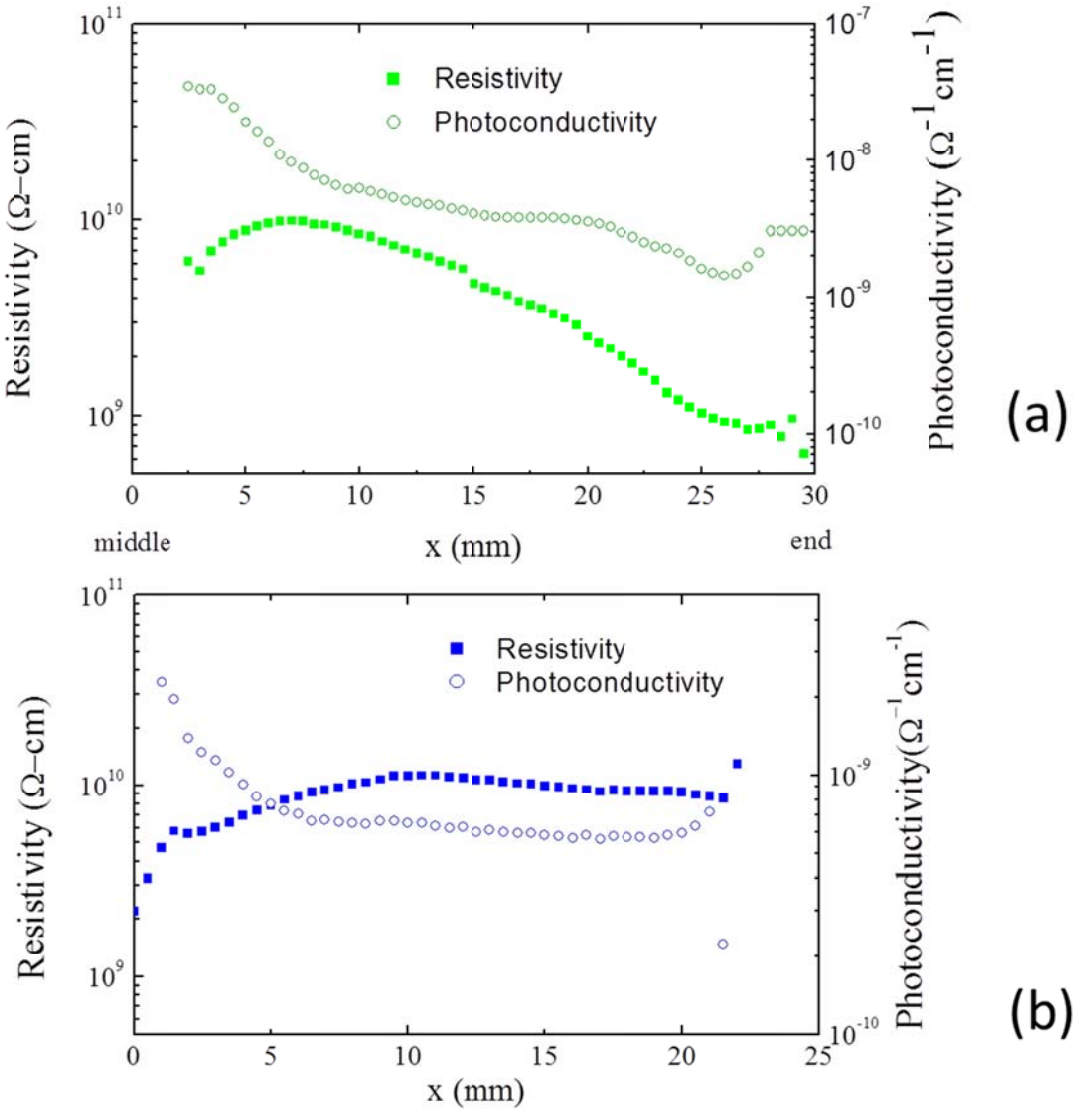

Figure 45 Resistivity and photoconductivity profiles of (a) crystal No.1 and (b) crystal No. 2

Indeed, in the following section of this chapter, experimental results of devices harvested from crystal grown under similar conditions to crystal No. 2 exhibit such axial variation. Towards the tail end of the ingot, there is a decrease in deep donors associated with V_{Cd} and an increase in the formation of A-center complexes (see **Figure 56** on page 254).

4.2.3 Bulk Composition

Profiles of the Zn and In content of crystals No.1 and No.2 are shown in **Figure 46**(a) and b to illustrate their similarities and differences. From **Figure 41** it is apparent that the values of resistivity differ in both crystals. This may be explained in part by the different Zn contents of the two crystals: The measured difference in resistivity is similar to the difference which would arise from the bandgap associated with the Zinc content (factor of 1.3).

It is also important to take into account the axial variation in the Indium content. Indium acts as a donor in Cd(Zn)Te to compensate the formation of ionized cadmium vacancies (acceptors) through the formation of A-center complexes. Therefore, the slightly higher Indium content in crystal No. 2 may also explain the higher resistivity which has been measured. The bulk resistivity depends to a large extent of the position of the Fermi Level near the mid-gap. As can be seen in **Figure 46**(b) the doping level in Ingot No. 2 is higher by nearly a factor of 2 for the tail end of the ingot. This is consistent with the resistivity of crystal No. 2 being higher by a factor of 2 for the same region of the crystal.

The concentration and size of inclusions have been measured using infrared transmission microscopy. A summary of the diameter and densities of various Cd(Zn)Te samples measured along the growth direction are presented in **Figure 47**. The average size of inclusions in crystal No. 1 was 7 μm, and the average density was 4.2×10^4 cm^{-2}; in crystal No. 2 the average size was 8 μm, and the average square density was 4.6×10^4 cm^{-2}. Therefore, neither the size nor density of inclusions appeared to be significantly affected by adjusting the temperature gradient during crystal growth.

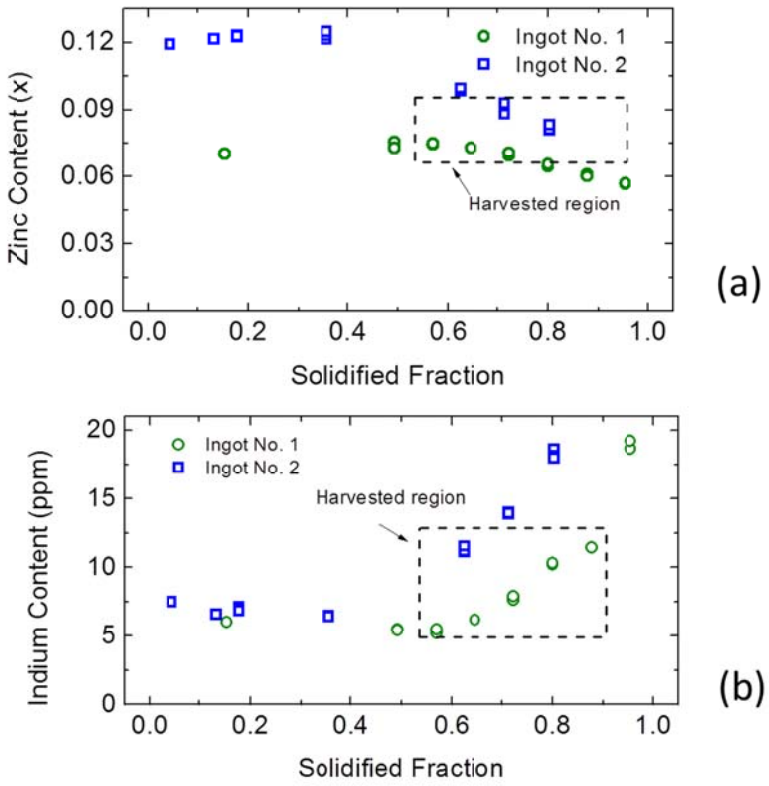

Figure 46 (a) Zn profiles in the studied part of crystal No.1 and No. 2. (b) Axial profiles of In for crystal No. 1 and No. 2.

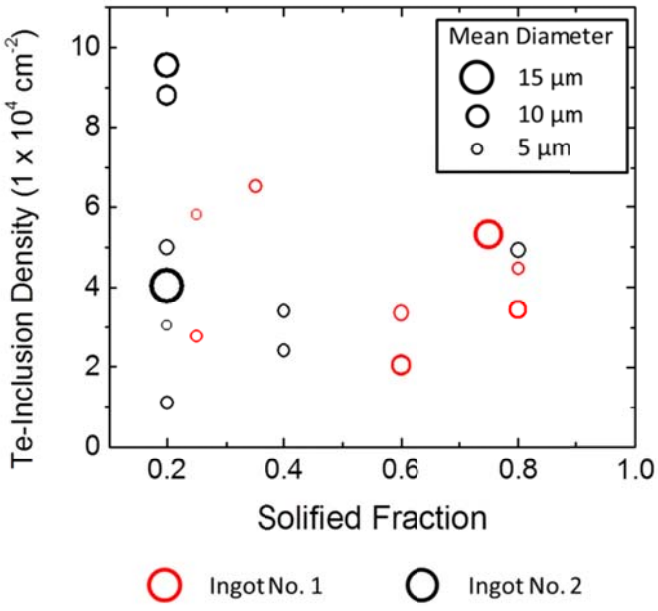

Figure 47 Te inclusion density and size distribution as a function of solidified fraction for ingots No. 1 and No. 2.

4.2.4 Low temperature photoluminescence

Photoluminescence measurements were obtained using a monochromator coupled with Si- and InSb-detectors in the spectral range (0.45–1.8) eV at a temperature of 4.2 K in a He cryostat. Samples were excited with a He–Ne laser at a power of 15 mW. The resulting spectra were corrected with respect to the sensitivity of the detectors.

The photoluminescence (4.2K) spectra of crystal No.2 measured in the middle and at the end of the ingot are presented in **Figure 48**. It is apparent, that the PL intensity of the mid-gap level with a maximum at ~0.8eV increases near the end of the crystal. This may be explained by a change in the occupation factor the level corresponding to the shift of the Fermi level discussed above, and is likely related with increases in the Indium content near the tail end of the crystal. The Indium content in the tail is also likely responsible for the A-center complex, located near 1.45eV, becoming the dominant feature in the PL spectra taken from the tail of the ingot. The A-center is related with VCd and donor complexes. These results are further corroborated by PICTS measurements of crystals grown using similar conditions and doping levels.

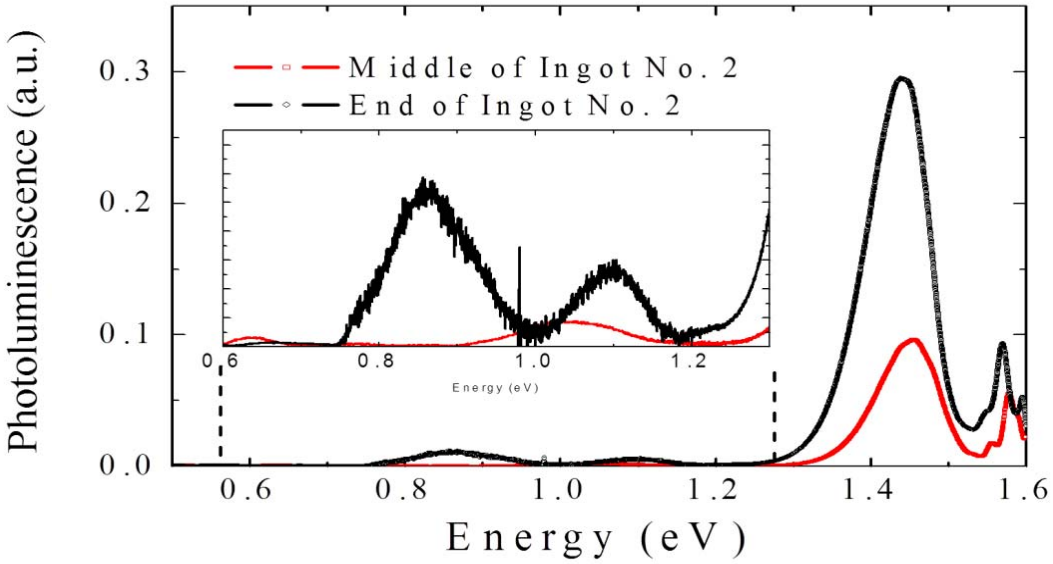

Figure 48 Photoluminescence spectra measured with the Si detector along the crystal length in two different positions at 4.5K

The photoluminescence (4.2K) spectra of crystal No.2 measured in the middle and at the end of the ingot are presented in Figure 46. It is apparent, that the PL intensity of the mid-gap level with a maximum at ~0.8eV increases near the end of the crystal. This may be explained by a change in the occupation corresponding to the shift of the Fermi level discussed above, and is likely related with the increasing Indium content near the tail end of the crystal. The Indium content in the tail is also likely responsible for the A-center complex, located near 1.45eV, becoming a dominant feature in the PL spectra taken from the tail of the ingot. The A-center is related to complexes between a V_{Cd} and electron donors such as Indium. These results are further corroborated by PICTS measurements of crystals grown using similar conditions and doping levels.

When the mid-gap level occupation decreases due to a change of the Fermi level position, transitions of electrons from conduction band to the level become more probable resulting in an increase in photoluminescence intensity. Correlation of resistivity and photoconductivity profiles with photoluminescence supports the supposition that the key factor limiting charge collection efficiency may be the changing of equilibrium occupation of the mid-gap level. Indeed, this mid gap level is influenced by Zinc content, doping level content, as well as the crystal growth conditions. This relationship between the resistivity, Zn content, and the Fermi Energy is presented graphically in **Figure 49**. For increasing concentrations of Zinc comes the potential for increasing resistivity material. However this maximum resistivity for each Zinc iso-concentration contour ultimately depends on the position of the Fermi level. In the present case, it depends on the position of the Fermi level with respect to the mid-gap state.

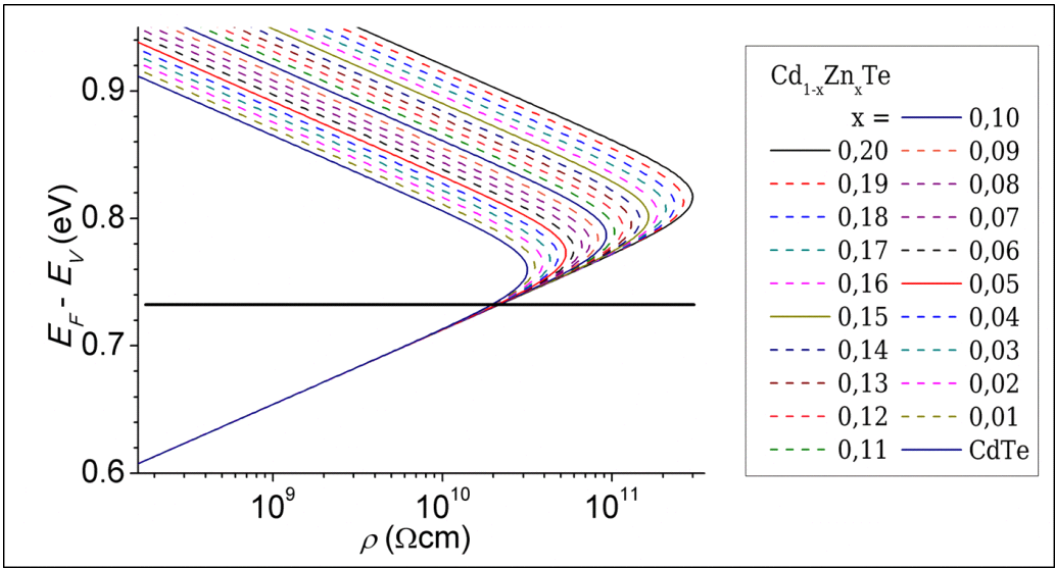

Figure 49 Relationship between the resistivity, Zn content, and the Fermi Energy.

4.2.5 Physical Model

The measured resistivity and photoconductivity profiles can be qualitatively explained by a following model, which is depicted in **Figure 50**.

1) The increase in the electrical resistivity results in a corresponding shift of the Fermi level.
2) The occupation of deep levels close to the middle of the bandgap will also change, and as a result will influence trapping and recombination rates connected with this level.

The observed anti-correlation between resistivity and photoconductivity observed in the first part of the ingot can be explained by a decreased electron occupation of the deep level with increasing resistivity caused by shift of the Fermi level towards the mid-gap. Decreased occupation of this deep level results in an increased electron trapping and recombination. As such the photoconductivity will decrease.

This mechanism further decreases the photoconductivity when both the photoconductivity and resistivity become correlated. Here the Fermi level continues to shift towards the near mid-gap level, decreasing its equilibrium occupation and increasing its trapping capacity (52).

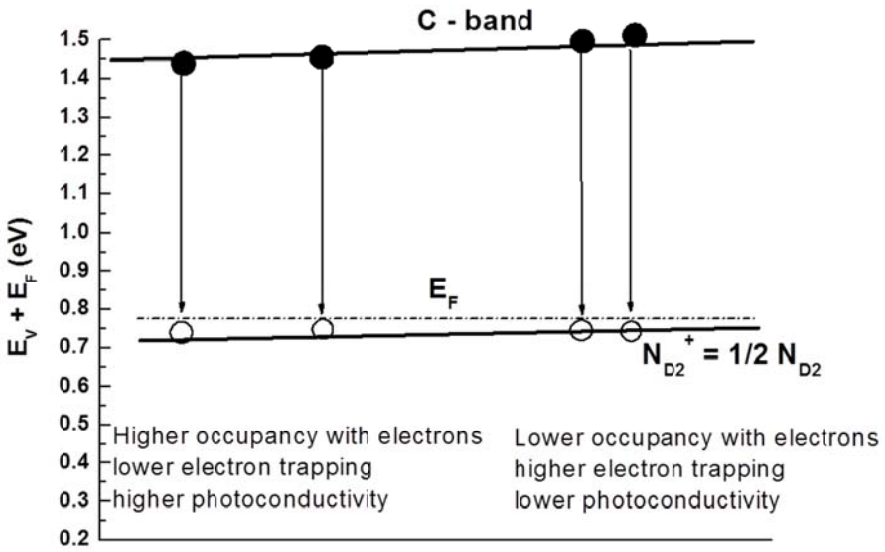

Figure 50 Graphical representation of trapping in Cd(Zn)Te

Real differences in the gamma spectra have are demonstrated for devices harvested from Ingots No. 1 and No. 2 in **Figure 51**. Each device was biased through a range of voltages in an effort to select optimal voltage which produces the best spectra. The two best spectra for each device are presented for comparison.

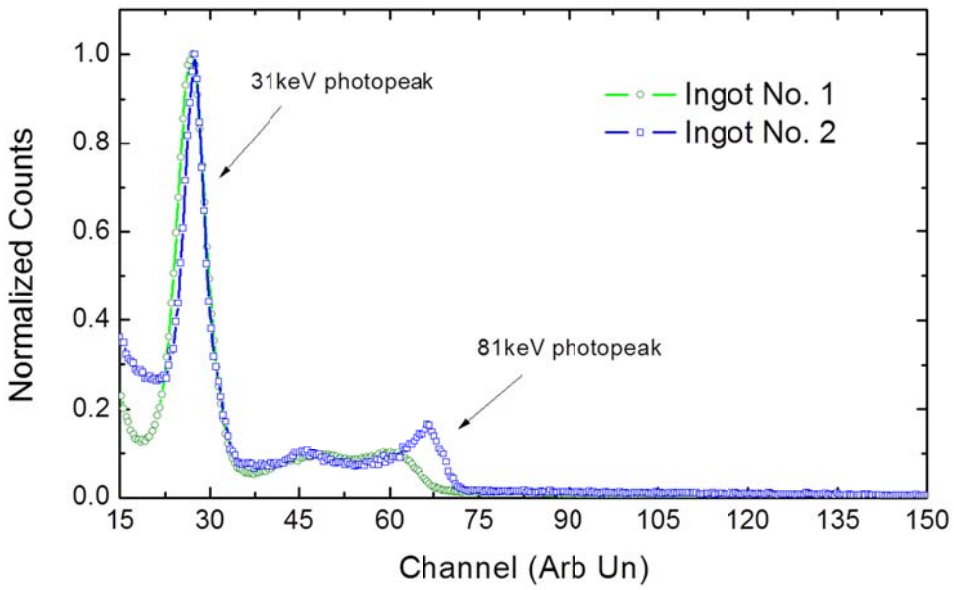

Figure 51 Gamma spectra obtained for devices harvested from Ingot No. 1 and Ingot No. 2.

From these normalized spectra a few observations may be made. First, the noise threshold at the low energies for each of the devices is similar, which is directly related to the resistivity of the device. Of greater importance, however, are the FWHM of the photo-peaks, especially that of the 81keV photo-peak. Broadening of the photo-peak is a consequence of a lower mobility lifetime product, and as a consequence a lower charge collection efficiency of the device. Based on the results already presented, this may be related with increased charge trapping within the device.

The conclusion that the dynamic adjustment of the furnace during the growth cycle improves the material quality is further supported.

4.3 Conclusions and Future Work

The results from this investigation may be summarized as follows:

1) The dynamic adjustments of the temperature gradient results in melting back of the crystal during growth. This small melt-back procedure appears to improve the yield by shifting of resistivity maximum towards the crystal center.
2) Measurement of photocurrent in mapping regime and mapping of the resistivity revealed, anti-correlation of these parameters in the beginning and central parts of the ingots and their correlation at ingot ends. This fact may be explained by a slight shifting of the pinned Fermi level in the vicinity of the deep level energy.
3) The effect of the dynamic temperature adjustment appears to be beneficial, not only in terms of the electrical properties, but also in terms of the structural properties, as is evidenced by the increased grain sizes.
4) This approach is now being implemented routinely in the crystal growth of Cd(Zn)Te, with ingots exhibiting similar characteristics. Of principle importance is that this dynamic in-situ adjustment does not degrade the material quality, but serves to increase the yield of material which may be harvested.

This page intentionally left blank.

5 Development of Crystal Growth Part 2: Dynamic Temperature Gradients Effects on Crystalline Defects

Section Contents

5.1 Introduction

There are several challenges to producing detector grade material based on Cd(Zn)Te, which includes material synthesis, growth of electrically compensated crystals, as well as the extraction of high resistivity material suitable for device applications. Principle among these is the choice of the growth method use for material synthesis and crystal growth.

One of the challenges towards producing large volumes of compensated material using the Vertical Gradient Freeze (VGF) method is the axial and radial variation in material homogeneity. One source of variation arises from non-uniform temperature distribution along the axial growth direction. Indeed, the axial temperature profile and its influence on growth velocity and thermo-mechanical stress are discussed in Section 4.1 on page 228 of this chapter.

Another source affecting material homogeneity in Cd(Zn)Te has to do with the non-uniform distribution of Zinc and Indium throughout the crystal matrix. For Cd(Zn)Te, the segregation coefficient of Zn has been reported near 1.35, which corresponds to a difference of nearly 5% Zinc between the tip and the tail (54). A discussion of how zinc segregation affects mechanical strain in Cd(Zn)Te is presented in (55), and describes how changes in the concentration of Zinc leads to misfit strain in the crystal. Very briefly, with increasing Zinc content, there is a decreasing lattice parameter. As a result, near the tail end of the ingot where the Zinc content is lowest, there will be a dilation coefficient associated with the expansion of material. This dilation of the material induces strain and dislocations into the crystal lattice.

In fact, strain is one of the more important factors in the crystal growth of Cd(Zn)Te because of the low critically resolved sheer stress (CRSS) value for this material (49). Sources of strain may be attributed to factors including variation of Zn composition along the growth axis, melt-crucible interactions, as well as the temperature gradients applied at the SLI. While it is not possible to control Zinc segregation, and the choices of crucible materials is limited, there is some flexibility in the choice of temperature profile applied throughout the growth cycle. In general it is helpful to take into account the following experimental considerations:

- What temperature gradient is applied at the solid-liquid interface?
- What is the temperature difference applied across the entire ingot length?

With respect to the first point, it has been previously shown that increasing the temperature gradient has the effect of increasing the thermo-mechanical stress at the solid-liquid interface. Taking into account the volume coefficients of thermal expansion for CdTe and ZnTe ($\beta_{CdTe} = 1.5\times 10^{-5}$ K^{-1} and $\beta_{ZnTe} = 2.9\times 10^{-5}$ K^{-1} (56) (57)) it can be shown that using a thermal gradient of 10º C/cm will induce close to 2.5 MPa of strain into the lattice. Indeed, this value is on the same order of magnitude as the CRSS for Cd(Zn)Te (54). Therefore, it is of interest to maintain temperature gradients near the solid liquid interface at or below this value of 10º C/cm.

With respect to the second point, it is of practical importance to consider that using global temperature gradients on the order of 10 ºC/cm leads to a difference in temperature between the tip and tail of the ingot up to 100ºC (for an ingot 10cm in length). Taking into account the melting point of Cd(Zn)Te is near 1100ºC and the softening point of quartz is near 1160º, these types of temperature gradients should not be applied for extended durations such as those required by crystal growth (200+ hours).

In this section, methods to reduce the thermo-mechanical stress imparted into the crystal have been implemented using dynamic temperature gradients to minimize the temperature gradient across the ingot, while maintaining relatively uniform temperature gradients at the Solid Liquid Interface (SLI). How this dynamic adjustment affects bulk resistivity and photoconductivity has been investigated in the preceding section of this chapter for two typical crystals. In this study, we investigate test devices harvested from a Cd(Zn)Te ingot along the axial direction, and studied in terms of its optical and electrical properties. The objective of this investigation is to study how these temperature adjustments (i) lead to variations in material properties and (ii) affect the concentrations and types of deep levels present in the test devices.

5.2 Experimental Methods

Using dynamic temperature gradients in a 5 zone furnace which have been presented in the previous section, high resistivity 25 mm Cd(Zn)Te ingots have been grown using Cd(Zn)Te supplied by 5N+. These ingots were doped using indium to achieve electrical compensation between 2-3ppm. The melt was superheated at following Type 1

Homogenization o break apart Te-Inclusions and improve material homogenization following the experimental data provided by (58). It is important to comment that at this point of investigation, the Type-2 Homogenization program had not yet been developed (see Section 2.3.4 on page 196).

The axial composition of the as grown 25mm ingots have been characterized using Ion Coupled Plasma Mass Spectroscopy (ICP-MS) in order to obtain information relevant to Zinc and Indium segregation using a Elan 6000 Perkin Elmer Sciex.

Cd(Zn)Te devices have been harvested from a single Cd(Zn)Te ingot to evaluate how the electrical and optical properties of the devices change as a function of their axial position in the as grown ingot. The ingot was sliced perpendicular to the growth direction into a single slab nearly 3 mm in thickness, as shown in **Figure 52**. From this slab small single crystals were harvested, polished, and electrodes were deposited to fabricate small test devices following the protocol described in Chapter IV, Section 3 & 4 (59). The area of each test device was ranging from 5x5 to 8x8 mm^2.

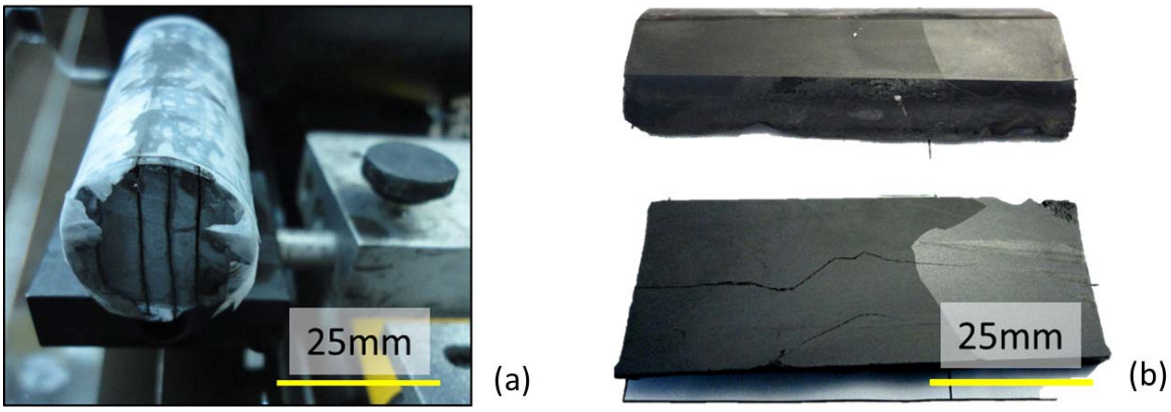

Figure 52 Cd(Zn)Te ingot slicing (a) parallel to growth direction and (b) longitudinal cross sections of the Cd(Zn)Te ingot.

For the PICTS measurements, a Lakeshore DRC-91C temperature controller was used for controlling the sample temperature. Pulsed optical excitation was achieved using a HP-8003A Pulse Generator. Using this arrangement, 20 μs pulses with a period of 300 – 500 μs could be used to probe the sample. The current transient induced by the optical pulsing was measured and recorded using a LeCroy 9631Dual 300 MHz 2.5 Gs /s Oscilloscope in

conjunction with SULA Technologies Correlators. Custom developed software was used for generating the differential current transient plots as a function of temperature. Further reading on the technological approach to PICTS is more fully presented in in Section 3.3 of Chapter 2, as well as in (60) (61) (62).

5.3 Results & Discussion

5.3.1 Application of Dynamic Temperature Gradients

The axial temperature profile was modified through an adjustment in the hot zone in order to increase the temperature gradient at certain points in the growth cycle. These periodic temperature adjustments in the hot zone of the VGF furnace are aimed at increasing the temperature gradient locally around the SLI as it travels upwards along the growth direction. Presented in **Figure 39**(b) on page 231 is one example of the dynamic temperature profile in which the thermal gradients are periodically increased by adjusting (increasing) the temperature of the hot zone. The temperature measurements have been obtained using thermocouples (T/C) distributed along the axial direction (See Chapter 2, Section 1, or **Figure 10** on page 189 of this chapter). The beneficial effects of similar furnace adjustments on the photoconductivity and resistivity of as grown Cd(Zn)Te crystals has been presented in the preceding section (63).

By dynamically adjusting the temperature gradient with the propagation of the solid liquid interface, it was possible to minimize the thermal stress applied throughout the growth cycle, while maintaining a constant temperature gradient at the growth interface. In this sense, this approach departs somewhat from traditional VGF growth methods where the crystal growth consists of controlled cooling of the furnace elements without the dynamic adjustment of temperature gradients.

5.3.2 Material Composition

Before presenting the electrical and optical properties of the devices, the axial composition of the ingot was first characterized to determine both Zinc and Indium content. The segregation of Zinc and Indium plays an important role in crystals grown using directional solidification methods such as the VGF technique. Material was extracted from the as grown ingot along the axis of growth for analysis of Zinc and Indium content. Presented below in **Figure 53** is the axial distribution of Zinc and Indium, which has been measured using Inductively Coupled Plasma Mass Spectroscopy (ICP-MS).

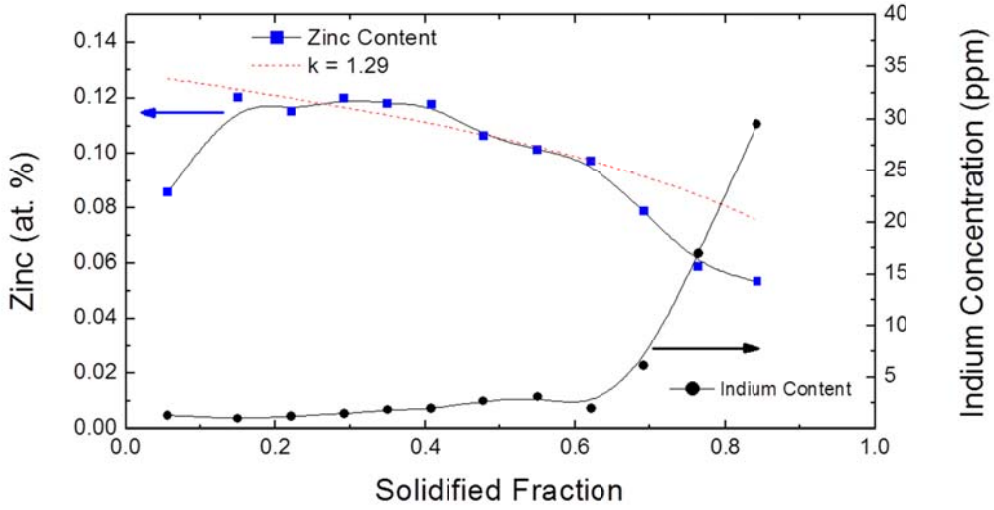

Figure 53 ICP-MS data obtained for axial segregation of Zinc and for Indium

The variation in the axial concentration of Zinc may be divided into three regions. For the fraction of solidified material, g < 0.1, the segregation coefficient is close to 1, and reflects the bulk concentration of the melt i.e. 10%. This is a consequence of the rapid growth at the onset of nucleation, such that the steady state assumptions of the Scheil equation do not apply. This behavior has also been demonstrated using numerical simulations taking into account Zinc diffusivity (46).

Between g= 0.2 and g = 0.6, the segregation of Zinc follows fairly closely the Scheil equation. After g=0.6, however, the concentration of Zinc falls fairly quickly. This may be related with changes in melt convection arising from a reduction of the melt zone and thermal end effects. Overall, there is a difference of more than 6% between the tip and tail.

With respect to indium concentration, the calculation of the segregation coefficient using the Scheil equation was not possible. For g < 0.5, between 5 x 10^{15} at/cm^3 1 x 10^{16} at/cm^3 of In is accepted into the lattice. This particular growth was intentionally doped with 1.5 x 10^{16} at/cm^3 of Indium, which implies that as the solidified fraction increases, the concentration of In also increases. Between g = 0.5 and g= 0.6, there was a sharp increase in the concentration of In incorporated into the Cd(Zn)Te matrix. A possible explanation of this behavior is presented in Section 3.3.5 on page 222 of this Chapter. What is important to note is that there is substantial variation in both the concentrations of zinc and indium throughout the as grown ingot. Indeed, variations in the material composition presents a real challenges to obtaining material with uniform electrical and optical properties.

5.3.3 Electrical Characterization

Test devices were harvested from the Cd(Zn)Te ingot parallel to the growth direction. The large crystal slabs shown in **Figure 52** were cut into wafers, mechanically polished, chemically etched using 2% bromine methanol, and electrodes were deposited using the gold electroless method. The lateral edges of the devices were finished following the protocol outlined in (59). Each test devices was first characterized using Current-Voltage (I-V) measurement and the hot probe technique to determine material resistivity and carrier type respectively. Presented below in **Figure 54** are I-V characteristics for devices harvested along the growth axis, as well as the devices. The dark spot on each of the electrodes represents a wax mark which was used for differentiating the two electrodes, which exhibit asymmetric characteristics.

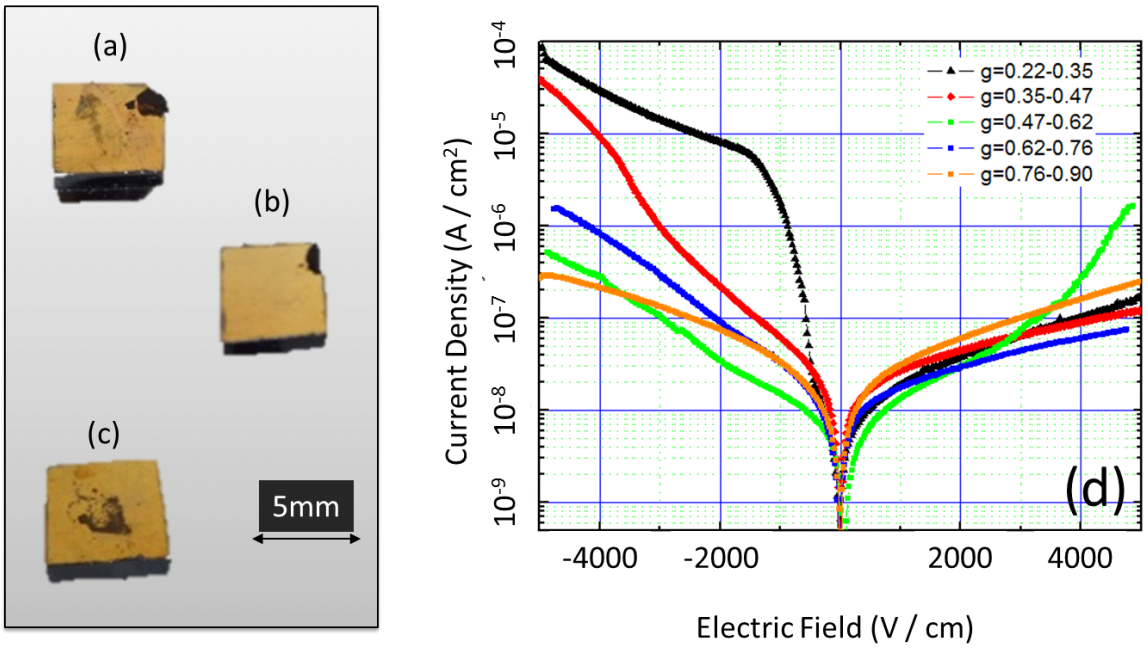

Figure 54 Test devices (a) g=0.22-0.35, (b) g=0.47-0.62, and (c) g=0.76-0.90. (d) I-V characteristics presented for samples harvested along the axis of crystal growth for different % solidified fraction values (g).

These devices are named according to their position in terms of % solidified fraction or ´´g´´. From these I-V characteristics, it is clear that all devices exhibited high resistivity and low leakage current, required for spectroscopy applications. For example, the test devices under an electric field 2000V/cm exhibited leakage current near 2 - 5x 10^{-8} A / cm^2,

which is a reasonable number for detector applications. However it is also clear from the asymmetry of the I-V characteristics that the leakage current of the device depends to a large extent on which electrode is used as the cathode. What is important to note, is the decreasing asymmetry observed with increasing In content. Indeed, for all the devices harvested, there is a monotonic decrease in the asymmetry of the I-V plot.

A summary of the compositional and electrical properties of the Cd(Zn)Te test devices are presented in **Table 7**. Here the Zinc and Indium concentration are shown for each detector, as is the carrier type and resistivity. The resistivity was calculated using Ohm´s law, in the Ohmic region of the I-V plot. For decreasing Zinc content, the resistivity actually appears to increase, which runs contrary to typical expectations.

Table 7 Compositional and Electronic Properties of detector based on Cd(Zn)Te grown using cc-pBN

Solidified Fraction	*Zinc % (Avg.)*	*Indium (Avg. ppm)*	*Resistivity* (Ω-cm)	*Carrier type*
0.22-0.35	12	1.5	4.7×10^{10}	Type n
0.35-0.47	11	2.5	5.5×10^{10}	Type n
0.47-0.62	10	3	7.3×10^{10}	Type n
0.62-0.76	8	10	3.4×10^{10}	Type n
0.76-0.90	6	20	8.3×10^{10}	Type n

5.3.4 PICTS Measurements

To explain the changes in the asymmetry of the test device I-V characteristics, Photo-Induced Current Spectroscopy (PICTS) measurements of two devices harvested from g = 0.22-0.35 and g= 0.76-0.79 have been investigated (see **Figure 37** and Table 7). Indeed, it was of interest to investigate how the deep levels may be influenced by the variation in material properties induced by the crystal growth process. The difference in Zinc content (6%) and Indium content (18ppm) was substantial.

The PICTS spectra and the corresponding Arrhenius plot for each test device are presented in Figure 55. The traps are identified by their position in the Arrhenius plot and may therefore be correlated as the traps are active in the same temperature and with similar emission rates. The levels have been named following the conventions used by A. Castaldini *et. al.* (64).

All of the observed levels A, B, C, F, H, and I have been studied and previously identified in Cd(Zn)Te. The A-family levels with energies between 0.1-0.2eV are identified with the V_{Cd}-impurity complex and are associated with the transition between the A-center complex and the Valence band (64) (45). Trap B has been related with V_{Te} among other complexes (64). Trap C has been related with C, Au, and Cu introducing electronic levels in the band gap. It has been proposed that Trap F has been related with Zinc as it has been observed in $Cd_{0.8}Zn_{0.2}T$ and not in CdTe (64) (45). Trap H should be the deep center, responsible for pinning of the Fermi level. Trap I, located near 1.0-1.1eV has been attributed to Te related defects, such as the ionized V_{Te}^{+}, and has been found to behave as a dominant mid-gap trap in CdTe: Cl, behaving as an electron trap. For more information on these defects in Cd(Zn)Te the reader is referred to (64) (65) (66) (67) (14) (68) (69) (70) (71).

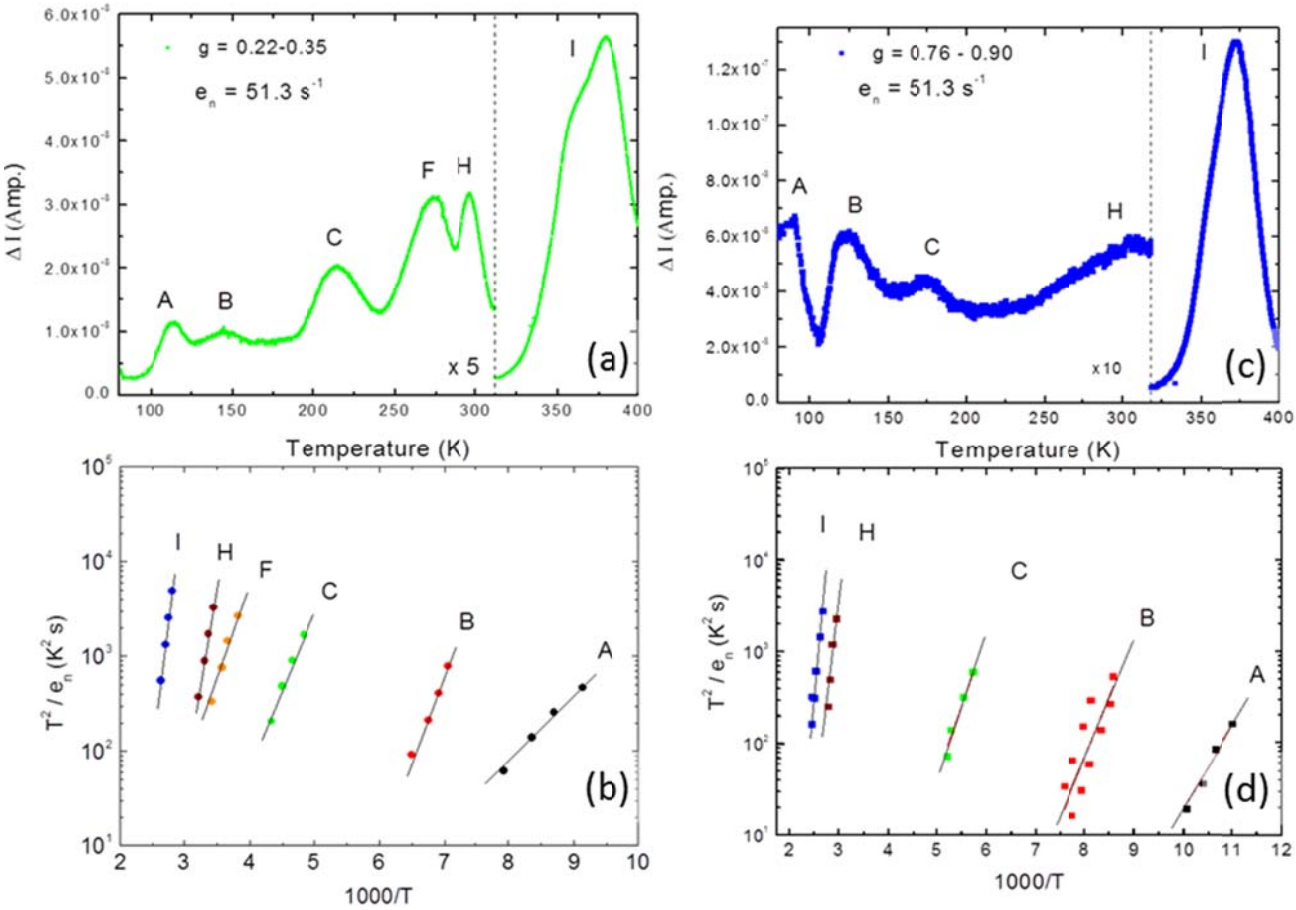

Figure 55 Top: (a) Gated PICTS Spectrum of device harvested from g = 0.22-0.35 (b) Arrhenius plot for devices harvested from g = 0.22-0.35 (c) gated PICTS Spectra of devices harvested from g= 0.76 - 0.90. (d) Arrhenius plot for device harvested from and g= 76 - 0.90.

With the exception of Trap F, the two devices exhibited similar trap energies and capture cross sections. Of particular importance, however, are the relative concentrations of defect levels present in the material, and how these might impact the devices electrical properties. Presented in **Figure 56** are the concentrations of each trap present in the test devices.

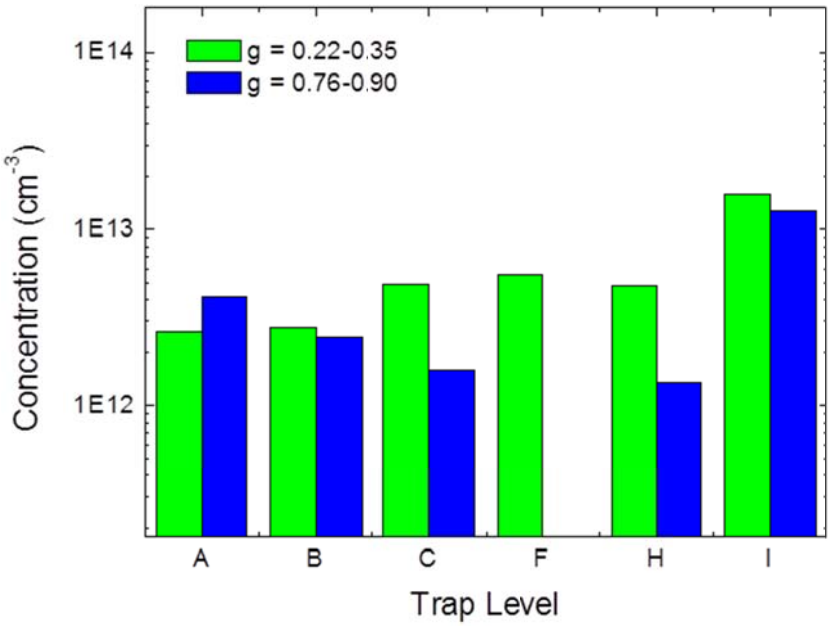

Figure 56 Trap concentrations for devices harvested from g = 0.22-0.35 and g= 76 - 0.90 (see **Figure 37**).

5.3.4.1 *Trap A and Trap H*

As may be seen from **Figure 56**, Trap A related defects are found in higher concentration in device g = 0.76-0.90, than for the device g = 0.22-0.35. Taking into account the ICP-MS results regarding In content, this difference may be associated with the relatively higher In content for device g=0.76-0.90 (20ppm) compared with test device g = 0.22-0.35 (1.5ppm). This higher concentration of Indium throughout the matrix means that there is the possibility for more A-centers to be formed. As a result, the observed concentration of these complexes increases through the formation of A-centers following **Equation 14**. This aspect of electrical compensation is presented in more detail in Section 2.8.3 of Chapter 1.

Equation 14

$$In_{Cd}^{+1} + \left[In_{Cd}^{+1} \cdot V_{Cd}^{-2}\right]^{-1} = \left[2In_{Cd}^{+1} \cdot V_{Cd}^{-2}\right]^{0}$$

Also shown in Figure 56, the concentration of Trap H is higher in g = 0.22-0.35 than in g=0.76-0.90. This trap H has been related to doubly ionized V_{Cd}^{--}. Continuing with the line of reasoning presented in the previous paragraph, the higher concentration of Indium implies a higher propensity for the formation of A-centers. All things equal, there would be a corresponding decrease in the concentration of V_{cd}, and as a corollary this may explain the lower concentration of doubly ionized V_{Cd}^{--}.

This feature of electrical compensation also helps explain to some extent the variation in the I-V characteristics of the devices. The doubly ionized V_{Cd}^{--} acts as an electron donor in Cd(Zn)Te. Therefore for increasing concentrations of doubly ionized V_{Cd}^{--}, there would be a higher concentration of free carriers throughout the crystal and correspondingly the crystals would exhibit higher leakage current. This subject of asymmetry in Cd(Zn)Te based radiation devices is discussed in greater detail in Chapter 4, Section 7.

Presented in **Figure 57** is a representation of this possible explanation. In material which exhibits low indium content, there will be a higher V_{Cd} concentration which may also lead to a higher V_{Cd}^{--} concentration. During crystal cooling, there is retrograde solubility and Te_i diffuse to available lattice sites, occupying anti-sites and forming Te_{Cd} point defects. When higher doping levels of Indium are used (c-d), the Indium neutralizes the ionized cadmium vacancy forming an A-center complex. This structure may block the Te_i from occupying an anti-site.

5.3.4.2 *Trap B and Trap I*

A diagram illustrating a possible explanation of this behavior is presented in **Figure 57**. Traps B and I have been related with impurities on Cd sites, V_{Te} and the ionized V_{Te+} defects respectively (67) (64). The concentration of Traps B and I were both lower in device g = 0.76-0.90 than in device g = 0.22-0.35.

As has already been put forth, a lower Indium content in the first to freeze region may result in a higher concentration of V_{Cd}^{--} sites for Te interstitials, T_i, to diffuse and form Te anti-sites, Te_{Cd} i.e. a Te occupying a Cd lattice site. This phenomenon is due to the high mobility of the T_i (72) as well as the retrograde solubility of Te in Cd(Zn)Te (see **Figure 7** on page 185). Indeed, with increasing Zinc content comes increasing solubility of Te in the Cd(Zn)Te matrix, which would lead to an increase in the T_i point defects.

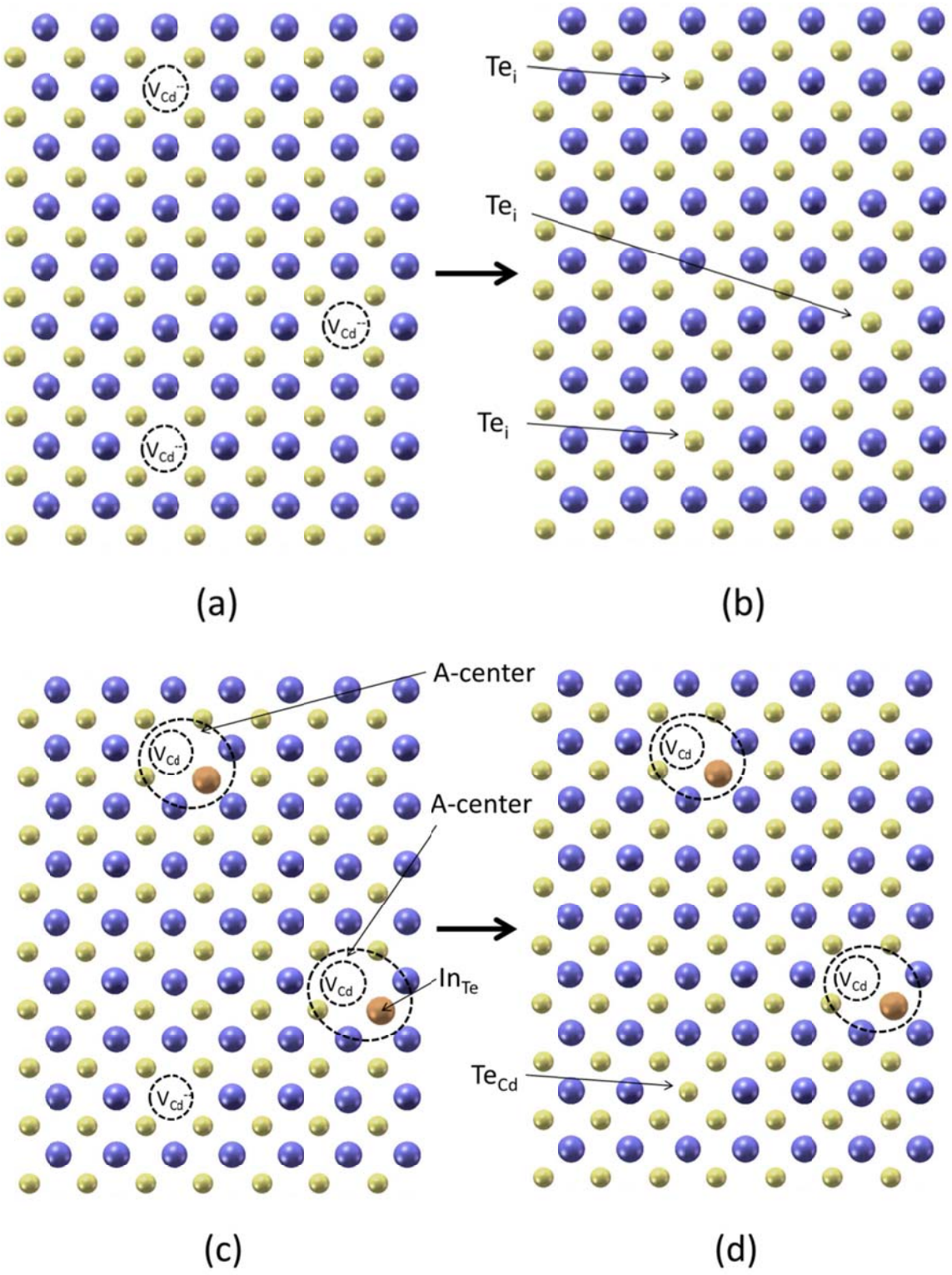

Figure 57 In the case of low indium content, (a) there will be a higher concentration of ionized cadmium vacancies, (b) to which Te-interstitials may diffuse at high temperatures. In the case of higher indium content (c) the indium form an A-center with V_{Cd}, preventing the Te-interstitial from diffusing into and occupying the lattice point.

These Te_{Cd} point defects may also act as nucleation sites for precipitation which occurs during the cooling phase of crystal growth, a result of the retrograde solubility of Te in Cd(Zn)Te. As a larger number of these sites are available for the nucleation of Te-precipitates, there would be a correspondingly larger concentration of V_{Te} sites after the Te has precipitated out of the Cd(Zn)Te matrix. Thus it is consistent that we would find a higher concentration of these point defects with lower indium content.

Near the end of the ingot, the higher concentration of indium may result in a lower number of ionized V_{Cd}^{--} to which the Te_i may diffuse. This might be due to the observations that (i) the V_{Cd} may form an A-center complex with In_{Te} atom and (ii) the lower concentration of Zn in the tail corresponds to a lower concentration of Te_i. As a result the concentration of V_{Te} will be lower, as the Indium atoms occupy these lattice sites, and there should be a corresponding lower density of second phase Te-particles. Typical distributions of second phase Te-particles found in test devices g = 0.22-0.35, g=0.47-0.62, g= 0.62-0.76, g= 0.76-0.90 are presented in **Figure 58** which are consistent with this explanation. Larger inclusions are found in higher density for devices g=0.22-0.35, whereas lower densities of smaller inclusions are found near the tail of the ingot for g=0.76-0.90. This type of behavior was also observed in 50mm ingots (comparing **Figure 64** and **Figure 65** on page 273)

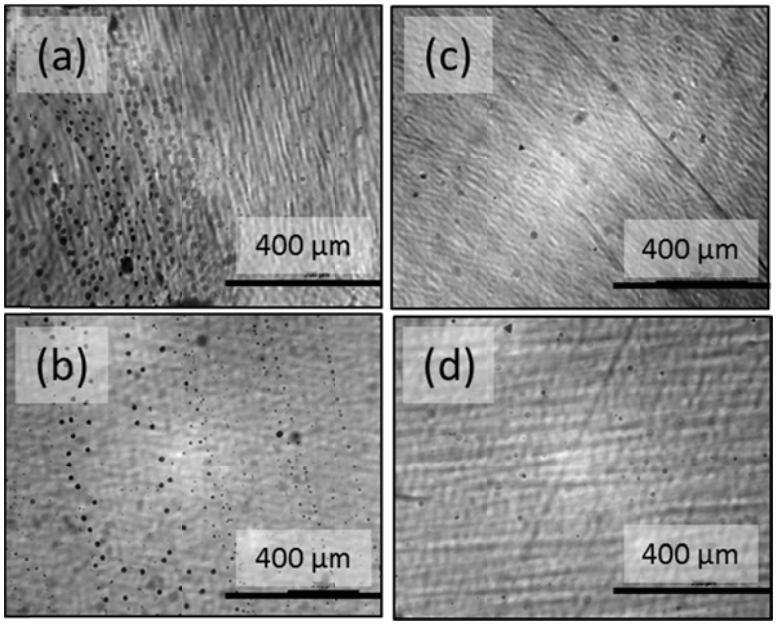

Figure 58 Te inclusions in devices (a) g = 0.22-0.35, (b) g=0.47-0.62, (c) g= 0.62-0.76, and (d) g= 0.76-0.90.

5.3.4.3 *Trap C and Trap F*

The differences in concentration observed in Trap C is not well understood, but may be related to the relative concentration and segregation of impurities between the two regions.

A somewhat remarkable difference observed between the two devices was that the device g=0.76-0.90 did not exhibit a Trap F while the device g=0.22-0.35 did. As previously mentioned, this trap has been related with Zinc content as it has been observed in $Cd_{0.8}Zn_{0.2}T$ but not in CdTe (64). As may be seen from **Table 7**, the Zinc content has been measured to be 12 % for the device g=0.22-0.35 and near 5-6% for the device g=0.76-0.90. The possibility exists that increasing the concentration of Zinc would lead to increasing concentrations of this Zinc-related Trap. Indeed, higher zinc content has been shown to increase stress throughout the crystal lattice, a consequence of the changing lattice parameter. For relatively lower Zinc content, the concentration of this defect may become too small to be detected by the instrumentation which has been implemented

A summary of the trap activation energy, capture cross section, and concentration for the two devices studied is presented in **Table 8**. The deep levels present in the as grown material are typical levels which have been previously reported on for detector grade Cd(Zn)Te. Moreover, the concentration of these deep levels is consistent with those reported for Bridgman and VGF growth of Cd(Zn)Te. The dynamic temperature adjustments appear to maintain the quality of the as grown crystals. The changes in the concentration of deep levels identified in Cd(Zn)Te have been related to variation in the composition of the as grown ingot. The error associated with the second digit of the concentration N_t was estimated to be at least 10%, and the measurement error for the apparent cross section is estimated to be nearly an order of magnitude.

5.3.5 Gamma Response

The devices used in this study have exhibited substantial differences in their compositional, electronic, and optical characteristics. In order to investigate how these differences affect the performance in radiation detection applications, the gamma response of each device presented in **Figure 54** has been measured. All measurements were made using the planar device geometry with the anode of the detector connected to the FET and pre-amplifier.

Presented in **Figure 59** are the 35keV and 81keV Photo-peak response of Cd(Zn)Te devices to ^{133}Ba. The FWHM of the 35keV peak was measured to be between 15-20% while the FWHM for the 81keV peak was measured near 12% for all devices. For most of the devices which exhibited a Zinc % near 10%, an electric field of 2500 V / cm could be achieved. However, for the device with lower Zinc content, a maximum electric field of only 1800 V / cm was used.

Table 8 Trap activation energy, apparent capture cross section, and concentration for devices harvested from cc-pBN ingot and studied using PICTS

Device	Level	E_a (eV)	σ (cm^{-2})	Conc. (cm^{-3})
A	A	0.15	9×10^{-17}	2.6×10^{12}
	B	0.28	5×10^{-11}	2.7×10^{12}
	C	0.36	1×10^{-15}	4.9×10^{12}
	F	0.61	5×10^{-13}	5.5×10^{12}
	H	0.73	7×10^{-12}	5.8×10^{12}
	I	1.07	3×10^{-9}	1.6×10^{13}
B	A	0.2	9×10^{-15}	4.2×10^{12}
	B	0.3	4×10^{-15}	2.4×10^{12}
	C	0.36	2×10^{-13}	1.6×10^{12}
	H	0.72	3×10^{-12}	1.3×10^{12}
	I	0.85	2×10^{-12}	1.3×10^{13}

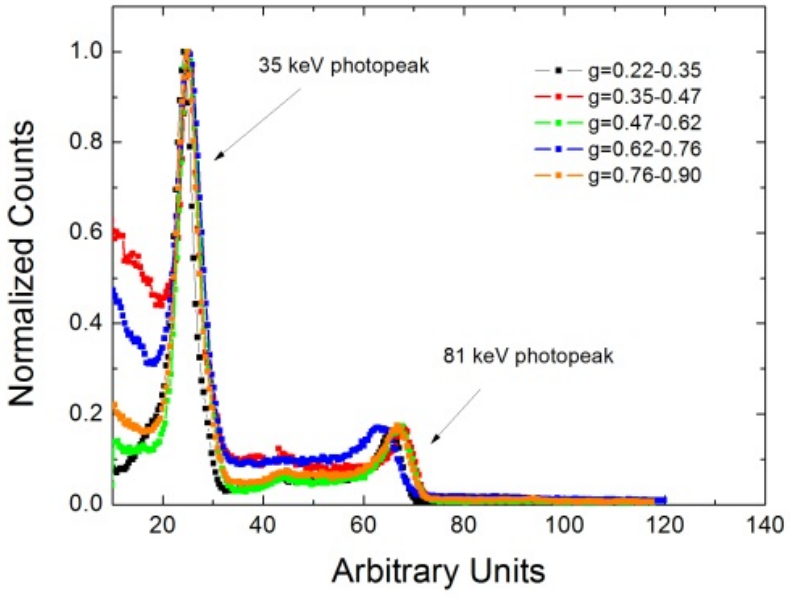

Figure 59 35keV and 81keV Photo-peak response of Cd(Zn)Te devices to ^{133}Ba.

These results indicate that the dynamic temperature adjustments do not have a negative impact on the crystal growth for device applications. Moreover, despite the seemingly large differences in electronic I-V, compositional, and optical properties of the devices, the performance of the devices tested did not exhibit as large a variation.

5.4 Conclusions and Future Work

One of the benefits of the VGF growth method is the ability to dynamically adjust the temperature gradients. It is important to point out that the dynamic temperature adjustments maintain the quality of the as grown crystals, without introducing new point defects or related levels as has been observed elsewhere. In fact, the beneficial effects of these furnace adjustments on the photoconductivity and resistivity of as grown Cd(Zn)Te crystals has been reported in the preceding section (and also published (63)) and these results are corroborated here.

To the Authors best knowledge, this is the first time such dynamic changes in the axial temperature profile have been reported for Cd(Zn)Te. These dynamic temperature gradients do not appear to affect strongly mass segregation of either Zn nor In. In fact, there is a large variation in the material properties of a single ingot grown by the VGF

method, not only in the bulk composition but also in the electrical and optical characteristics, the distribution of second phase inclusions, and also concentration and types of traps present in the material. These features all appear to be strongly influenced by mass segregation of Zinc and Indium. Despite such large differences in the electrical compositional properties the test device performance was similar in terms of device FWHM.

Further investigation which is warranted by these results will include the investigation of Defect Level F, and its relation with Zinc content. In addition, it is of interest to investigate the Etch Pit Density associated with dislocations in the crystal structure. Indeed, how these dynamic temperature adjustments affect dislocations in the as-grown material remains a topic of great interest.

This page intentionally left blank.

6 SCALING OF CRYSTAL GROWTH TECHNOLOGY TO 50MM

Section Contents

This page intentionally left blank.

6.1 Introduction

The objective of this thesis investigation was the development of crystals for the COCAE camera. For the development of the COCAE instrument, which is presented in Section 1.3 of Chapter 1, it was necessary the development of a larger crystal growth capacity in order to meet the requirements of the Compton Camera. Specifically, this camera required ten parallel planar layers placed 2 cm apart made of pixilated 2 mm thick Cd(Zn)Te crystals occupying an area of 4 cm 4 cm. Therefore, large volumes of uniform material were required for detector crystals.

This problem is illustrated in **Figure 60** showing the maximum diameter of the crystal, and the size of the detector required by the COCAE camera. For the 25mm ingots, the diameter was insufficient to harvest detector crystals from radial slices, and therefore must be cut longitudinally as may be seen in either **Figure 40** on page 232 or **Figure 52** on page 248. Indeed a substantial amount of material was supplied in this form. The disadvantage of this is the large variation in Zinc and Indium content resulting in substantial changes to the electrical resistivity. One example of how this variation in composition (see **Figure 53** page 250) leads to substantial variation in the electrical properties may be seen in **Figure 41** on page 233.

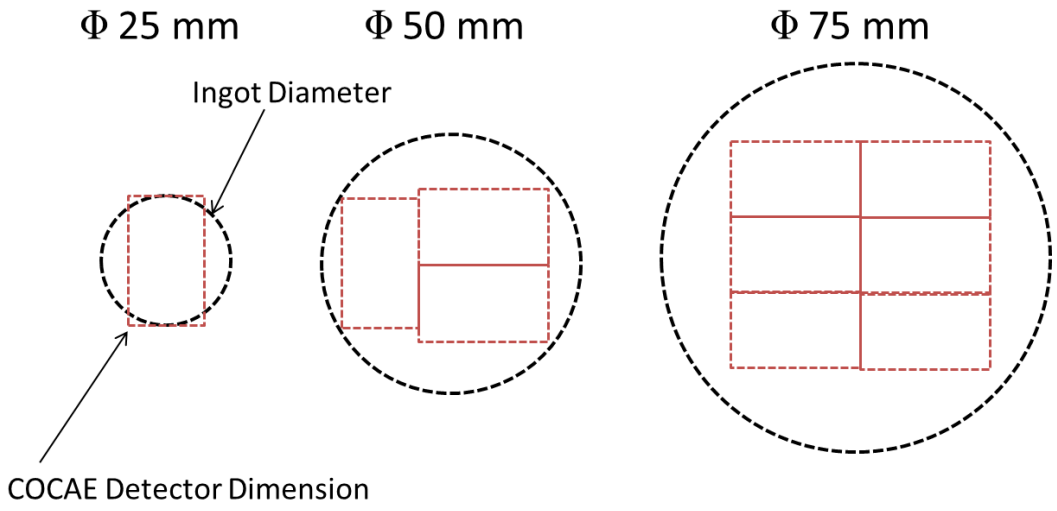

Figure 60 The diameter of Cd(Zn)Te ingots compared with the detector crystal required by the COCAE camera. From a 50mm diameter ingot, three detector crystals could be harvested from each wafer. Increasing the diameter of the crystal to 75mm further increases this number to six.

Taking into account (i) the poor axial homogeneity of the crystals with respect to Zinc and Indium segregation (ii) the size of crystals with uniform properties required by the COCAE project i.e. 15mm x 25mm x 2mm and (iii) the costs associated with crystal growth, it was decided to scale the crystal growth capacity in CGL to permit larger diameter crystal growth. This scaling in technology required the development of the following processes/technologies

1) Design, construction, testing of new VGF furnace
2) Ampoule and crucible design and preparation
3) Material synthesis and melt homogenization
4) Crystal growth
5) Ingot slicing
6) 50mm wafer polishing
7) Wafer level electrode patterning

Points 1 and 2 are discussed in Chapter 2, Section 1 in which the experimental methods which have been applied throughout this thesis are presented. Point 3, In-situ homogenization, is discussed briefly in section 2.3.5 of this chapter, with respect to the improvements we have made in melt homogenization of 50mm diameter, 750g ingots. The processes related with ingot slicing, wafer polishing, and electrode patterning are further discussed in Chapter 4, related with the preparation of detector surfaces for device fabrication

The focus of this section is the crystal growth phase which has been developed at CGL using the Vertical Gradient Freeze method. Indeed, it is worthwhile reminding the reader of the wide range of competing technologies used for bulk crystal growth of Cd(Zn)Te. These methods include, but are not limited to Horizontal and Vertical Bridgman (20) (8) (19) (16) (27), Vertical Gradient Freeze (11) (14), High Pressure Bridgman (73), Electro-dynamic Gradient Freeze (74), Travelling Heater Method (75) (76), Vapor Phase Transport (12) (77), Solid State Recrystallization (78), De-wetted Crystal Growth (18), as well as several other modified furnace geometries and experimental arrangements (1) (79) (23).

In addition to this, the experimental geometries, the types of refractory materials used, and the crystal growth programs vary substantially between investigators using the same experimental arrangement.

6.2 Importance of Furnace Pedestal

To demonstrate some of the variation in experimental geometries used even for the same growth method, examples of different furnace pedestal materials and crucible materials which have been implemented for the crystal growth of Cd(Zn)Te are presented in **Figure 61**. Indeed, not only the furnace pedestal geometry used by each investigator is markedly different, but the crucible material used for housing the molten Cd(Zn)Te material also changes.

Figure 61(a) shows a furnace pedestal constructed from a conical graphite core, with an embedded thermocouple which has been used by T. Rule (57). Furthermore, a conical tipped carbon coated quartz ampoule (not shown) was used for containing the melt. Note that the shape of the conical pedestal was designed to conform to the shape of the ampoule itself. Despite these considerations, the crystals which have been harvested using this pedestal geometry exhibited a high void content in the first to freeze region of the crystal (see **Figure 62**(d) below).

A novel pedestal was also proposed by (31), was designed for sensing changes in impedance associated with (i) melting of Cd(Zn)Te and (ii) nucleation from the melt. The CAD representation of this pedestal is presented in **Figure 61**(b). The sensing coils were located near the tip of the ampoule wall, while concentric alumina rods were used for physically supporting the crucible weight. In this case, a pBN liner was inserted into the quartz ampoule for containing the Cd(Zn)Te melt.

The sophisticated design of this pedestal demonstrates to some degree the importance of this particular component. This furnace pedestal was developed for monitoring the solid liquid interface and melt temperature at the tip of the crucible and to avoid unstable solidification at the onset of growth. This was achieved by ensuring that the charge was completely molten at its tip, without incurring large superheats elsewhere in the melt. As a result, large degrees of undercooling were avoided during the melt solidification phase of growth. While the quality of the crucible tip is still polycrystalline, there was a substantial

improvement in the undercooled region, which appeared smaller in volume. **Figure 62**(f) shows on example of the polycrystalline cap present in a Cd(Zn)Te ingot grown using this pedestal

Also presented in **Figure 61**(c), is the geometry which has been adapted by (17) for Cd(Zn)Te growth. In this geometry, the furnace pedestal has been altogether removed, while a graphite crucible was used for containing the molten Cd(Zn)Te. From these three examples which are only related with the Bridgman growth technique, a small sense of the broad range of experimental techniques applied to Cd(Zn)Te may be observed.

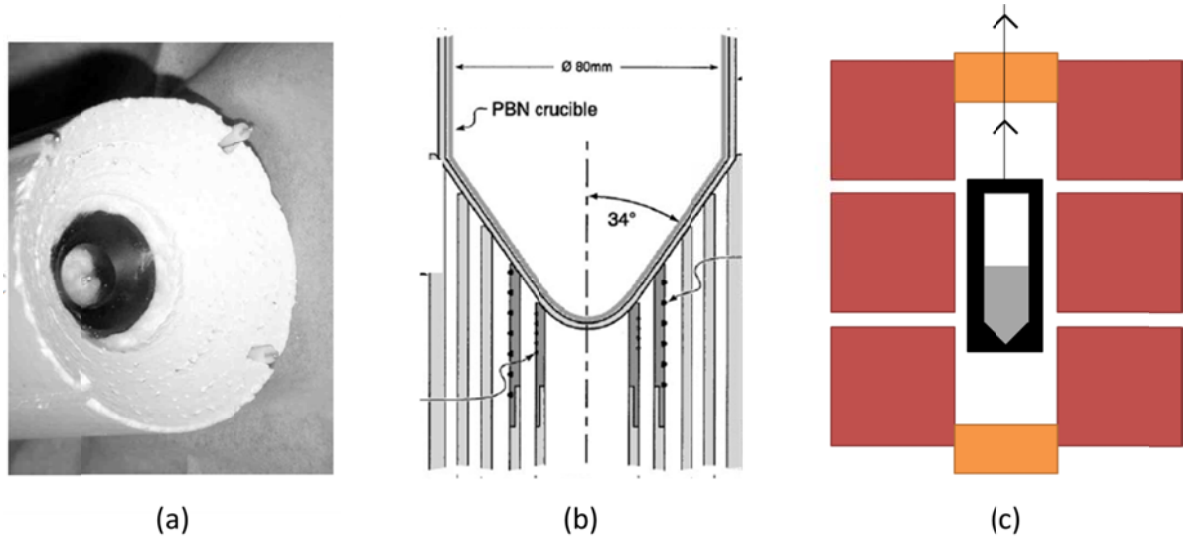

Figure 61 (a) results obtained by (57) using carbon coated quartz ampoule with a graphite pedestal (b) results obtained by (31) using an insulating alumina pedestal in conjunction with pBN crucible. (c) geometry adapted by (17) using a graphite crucible and no furnace pedestal.

To demonstrate one of the problems associated with crystal growth of Cd(Zn)Te, longitudinal cross sections of the tips of Cd(Zn)Te ingots grown using a variety of techniques is presented in **Figure 62**. These crystals have been grown by the Bridgman method (a,b,c,f), electro-dynamic gradient freeze method (d) , modified Bridgman method (e), and high pressure Bridgman method (g). As may be seen, each of the crystals exhibit either or both (i) polycrystalline tips with numerous grain boundaries and (ii) high void content. In general, each of the techniques which have been applied, suffer from similar crystallographic defects. Indeed, such large macroscopic defects degrade the quality and reduce the yield of material which may be used for detector applications.

The purpose of this investigation is the development and implementation of a furnace pedestal with integral thermocouples which may be used for (i) controlling growth dynamics (ii) to reduce the effects of undercooling, and (iii) and to improve the quality of the first to freeze region of the crystal. The experimental geometries and materials used in this work are based on extensive numerical studies (80) (81) (82) (30) (83) (84), in which the materials used to modify the thermal environment to facilitate the crystal growth process are presented. Specifically, the implementation of a Silicon Carbide (SiC) ampoule support pedestal in conjunction with the conical pBN crucible geometry has the following experimental benefits:

1. The SiC pedestal acts as a cold-finger and is designed to (i) increase the axial heat flow and (ii) increase the temperature gradient at the crucible tip.
2. The anisotropic thermal properties of the pBN crucible decrease radial heat flow in order to suppress interface deflection through radial heat losses.
3. The conical shape of the crucible is intended to focus the axial heat flux vectors inwards, which should lead to a convex solid liquid interface.

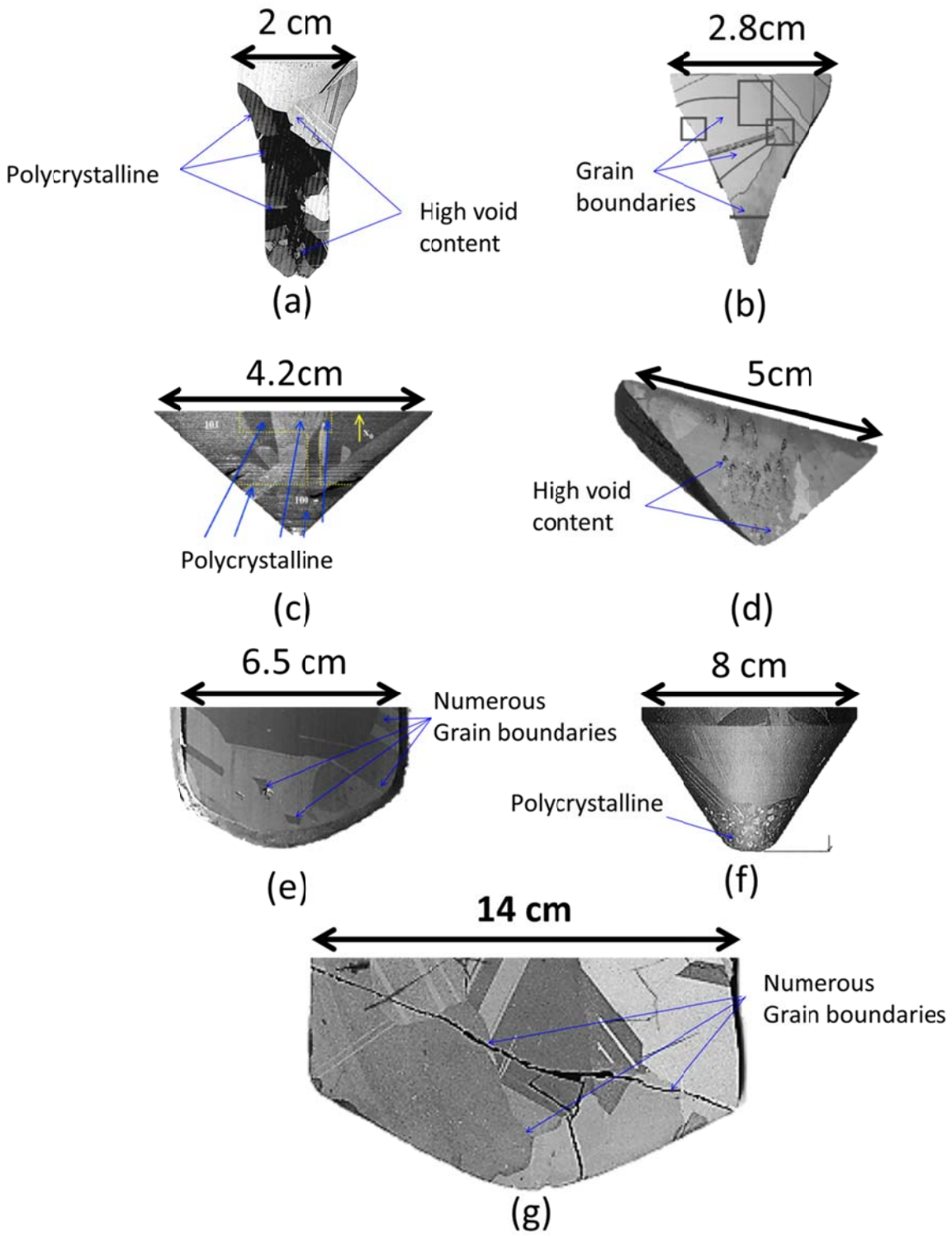

Figure 62 Cd(Zn)Te tips grown by various investigators. Cd(Zn)Te grown by (a) **ref**. (85) (b) **ref**. (86) (c) **ref**. (87) (d) **ref.** (88)(e) **ref**. (89) (f) **ref**. (90) (g) **ref**. (9)

6.3 Experimental Furnace Pedestal

50mm diameter, 750g Cd(Zn)Te crystals were grown by the Vertical Gradient Freeze (VGF) method using a 6-zone furnace which has been designed and built during this investigation. A novel crystal growth pedestal was developed in this work to provide for in-situ measurements of temperature gradients, while also serving to increase the axial temperature gradient near the first to freeze region of the crystal.

The detailed furnace and pedestal geometry are presented below in Figure 63. Thermocouples were placed circumferentially along the axial direction to measure temperature gradients along the ingot throughout the growth cycle. The region referred to as the Conical-Cylindrical transition, labeled as (f), is also presented here as this region of the growth cycle exhibits interesting characteristics which are discussed below.

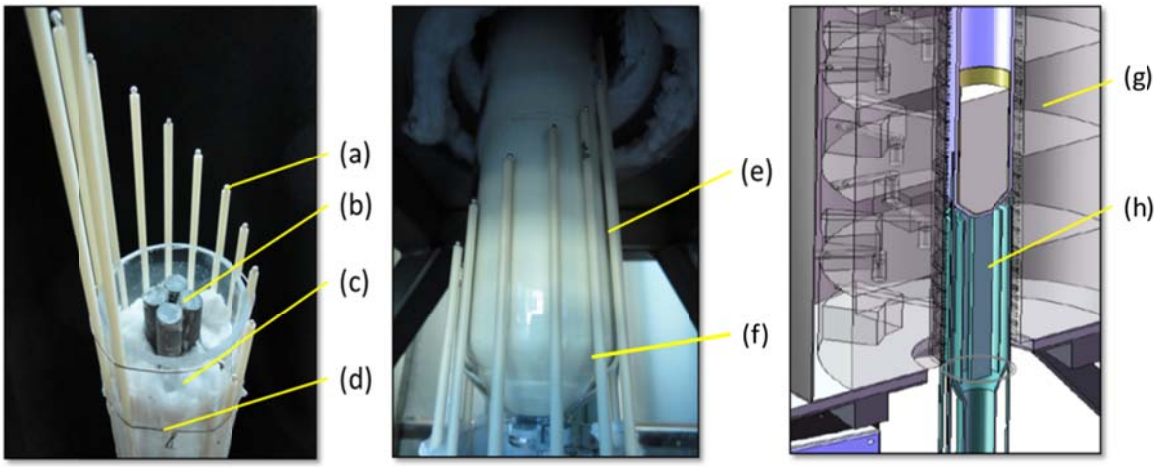

Figure 63 Furnace pedestal used for measuring temperature gradients throughout the growth process. (a) Type S thermocouple, (b) sintered SiC pedestal (c) Quartz support (d) Kanthal wire (e) pBN crucible & Quartz ampoule placed onto pedestal (f) conical cylindrical transition (g) Cd(Zn)Te ingot positioned between Zone 2 and Zone 3 of furnace and resting on (h) SiC furnace pedestal.

All ingots were grown using a pyrolytic Boron Nitride (pBN) crucible in this work. The pBN crucible was immediately loaded with 7N pure Cd(Zn)Te obtained from 5N+. The concentration of Indium used for each experiment ranged between 1-3ppm. Ingots 1, 2, and 3 were all grown under the same conditions to demonstrate reproducibility of the experimental results. The growth geometry of Ingot 4 was carried out without contact between the pBN crucible and SiC pedestal for comparison.

Bulk resistivity was measured using the Contactless Resistivity Mapping (COREMA) system. Devices used in this work have been contacted with Au using the electroless method. Further details regarding detector preparation and measurement may be found in (41) (91) (92) as well as Chapter 4 of this thesis.

6.4 Results & Discussion

6.4.1 As Grown 50mm Ingot Growth

The four Cd(Zn)Te ingots grown in this work are presented below in **Figure 64**. Using a 5 zone Vertical Gradient Freeze (VGF) furnace, 50mm Cd(Zn)Te was grown following the experimental design modeled by (80) - (84). The melt was homogenization using H1 homogenization for Ingots 1, 3 and 4. The H2 homogenization protocol has been used for the synthesis of Ingot 2. Crystals were grown under low temperature gradients between 5 and 10 ^{o}C-cm^{-1}. This choice of temperature gradients was intended to reduce the thermo-mechanical stress imparted at the solid liquid interface.

Figure 64 50mm diameter Cd(Zn)Te ingots were grown in contact with the SiC pedestal (Ingots 1- 3) and with no SiC pedestal (Ingot 4)

While the last to freeze tail end of each ingot exhibited some variation in structure and void content, this phenomenon is explained in more detail in Section 2.3.5 page 201. The current discourse is related with the effects of the SiC pedestal and pBN crucible geometry on the characteristics of the First to Freeze region of the crystal.

As is illustrated in **Figure 64**, a SiC pedestal was not used for crystal growth of Ingot 4, and this requires some explanation. Indeed, it was important to demonstrate what influence, if any, the SiC pedestal plays in improving grain structure of the as-grown crystals. For this reason, Ingots 1, 2, and 3 were grown with the pBN crucible in direct contact with the SiC pedestal. For Ingot 3, however, the pBN crucible was displaced by 3cm from the SiC pedestal, as shown in **Figure 65**. Using the experimental geometry, the benefits of the SiC pedestal are removed from the experiment, while all other considerations remain equal. The difference in the electrical and structural properties of the ingot may therefore be attributed to the influence of the SiC pedestal.

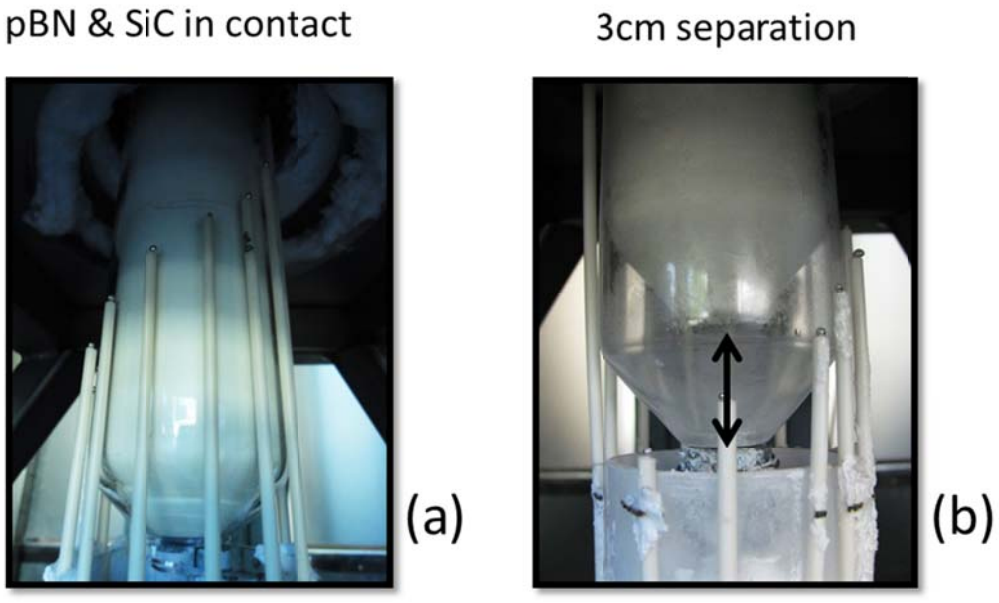

Figure 65 (a) Pedestal geometry used for growth of Ingots 1,2 and 3 (b) Pedestal geometry used for growth of Ingot 4, with the pBN crucible displaced by 3cm

6.4.2 Grain Structure Evolution

Each Ingot was sliced into circular wafers, perpendicular to the growth direction. These cross sections permit the analysis of how the crystal grain structure evolves along the

growth direction. To demonstrate the uniformity and continuity of the grain structure (or lack thereof), transverse cross sectional analysis of the as grown ingots are presented here.

For Ingot 1, only two grains are present at the first to freeze region and after 1 cm of growth (**Figure 66**a,b). It is remarkable that these first to freeze regions are often characterized as polycrystalline in nature with voids and other detrimental macroscopic defects (see **Figure 62**). From this first crystal however, the tip is only comprised of two large grains, nearly 1cm in thickness.

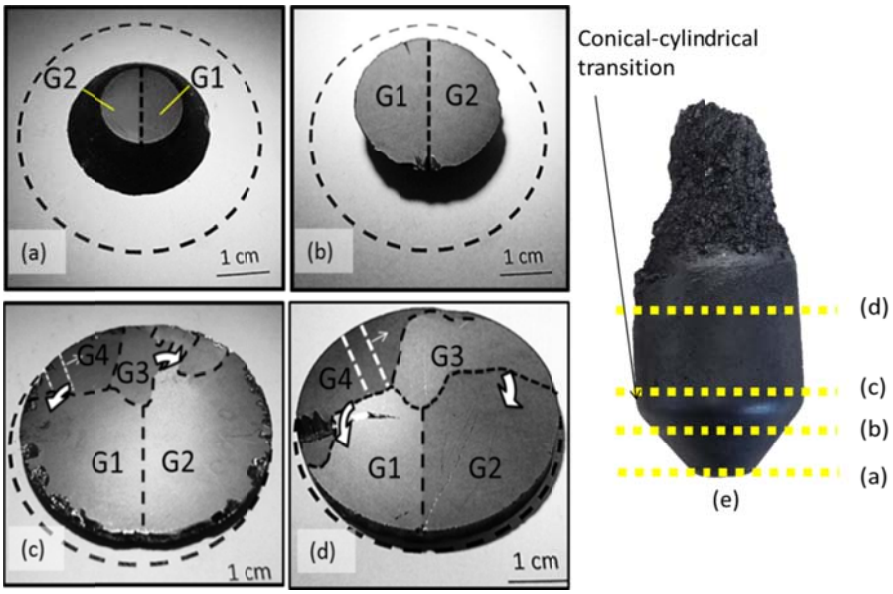

Figure 66 Evolution of grain structure in Ingot 1 at (a): First to Freeze tip, (b): After 1 cm of growth, (c): just before conical-cylindrical transition, (d): Near last to freeze region of ingot (e) yellow dotted lines delineate region from which wafers are harvested

Near the transition between the conical and cylindrical region of the pBN crucible however, new grains nucleate and grow inwards as shown in **Figure 66**c. The same grains which were present at the start of growth are also present here (G1 and G2), but with new grains growing inward from the crucible wall (G3 and G4). These new grains continue to increase in area following the growth direction, as shown in **Figure 66**(d). However, no additional grains are observed in any of the wafers harvested from this ingot after this conical-cylindrical transition.

Similar behavior is also observed for Ingots 2 and 3. For Ingot 2, only two grains are present at the start of growth (G1 and G2). Again it is observed that near the conical-cylindrical transition, a new grain nucleates at the crucible wall and grow inwards toward the center (G3). However, for wafers harvested from regions after the conical-cylindrical transition, no significant new grains are observed, while Grains 2 and 3 slowly increase in area with respect to Grain 1.

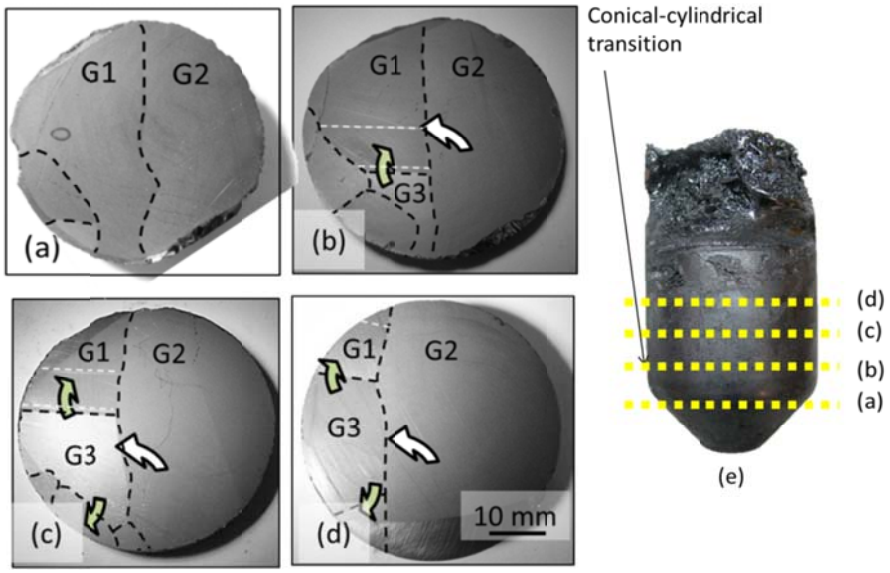

Figure 67 Evolution of grain structure in Ingot 2 at (a): just before Conical-cylindrical transition, (b): At conical-cylindrical transition (c): After conical-cylindrical transition, (d): Near last to freeze region of ingot.

Finally, for Ingot 3, the same type of behavior is observed. A longitudinal cross section of the ingot tip, in this case parallel to the growth direction, is presented in **Figure 68(**a) for Ingot 3. The new grain introduced near the conical-cylindrical transition (**Figure 68**(b)) rapidly grows inward toward the centerline of the growth axis.

Transverse cross sections of wafers along the growth axis further corroborate that, consistent with the other as grown ingots, after the conical-cylindrical transition no new grains are introduced (**Figure 68(**c) & (d)). As may be seen from these images, the wafers which have been harvested exhibit large apparently single grain structure, albeit with twins oriented vertically throughout the ingot, parallel to the growth axis.

What is important to point out in each of these growths, with respect to grain structure, are the following points

1. Each ingot tip exhibited only 1 or 2 grains, free of voids
2. 1-2 new grains appear near the conical-cylindrical transition of the crucible.
3. Of these grains, there existed continuous columnar growth of each grain.

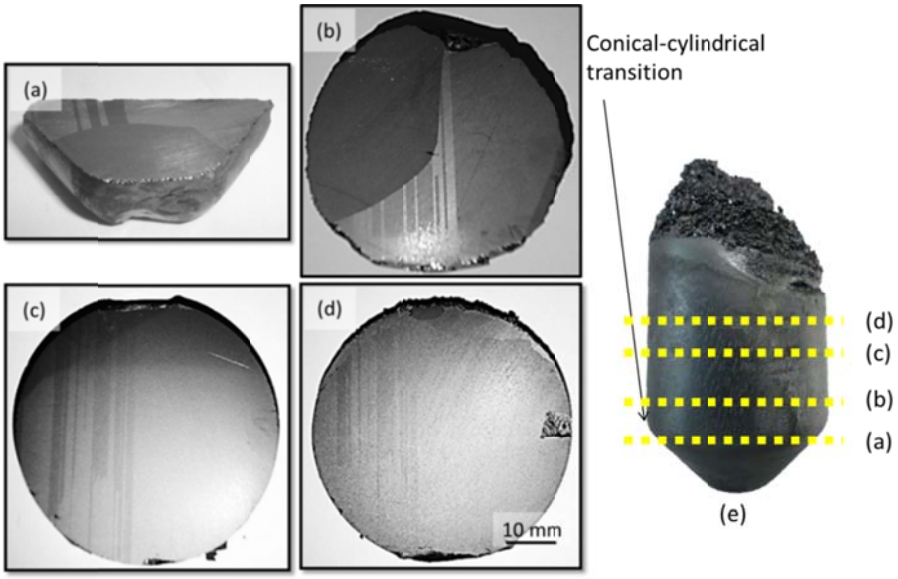

Figure 68 Evolution of grain structure in Ingot 3 at (a): First to Freeze tip parallel to growth direction, (b): just before conical-cylindrical transition (c): After conical-cylindrical transition, (d): Near last to freeze region of ingot.

Ingot 4 has been grown with the tip of the pBN crucible separated from the SiC pedestal by 3 cm. This growth was carried out to investigate the relative importance of crucible – pedestal contact on the as grown crystal quality. Presented in **Figure 69** are four wafers which have been harvested from this Ingot, along the growth axis. It is immediately apparent the grain size is much smaller and does not exhibit the same continuity from wafer to wafer as was observed in the other growths as there is nucleation of new grain structures throughout the entire growth.

This difference in grain structure is one of the first principal differences observed between the ingots grown in contact with the SiC pedestal and this ingot where the contact with the SiC pedestal has been removed. Specifically, in the First to Freeze region of Ingots 1, 2, and 3 only one or two grains have been observed. The first to freeze region of Ingot 4 exhibits more than 8 of these grains. Moreover, the continuous columnar growth of

these grains was not evident either, as each wafer exhibits a markedly unique grain structure pattern, indicative of very small grain volumes.

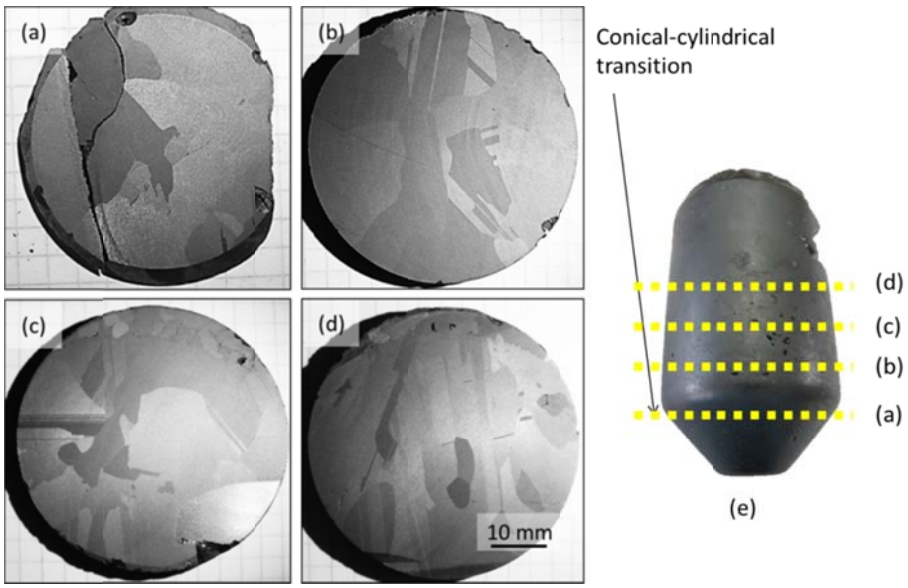

Figure 69 Evolution of grain structure in Ingot 4 at (a): Just before conical-cylindrical transition, (b): Just after conical-cylindrical transition (c): After conical-cylindrical transition, (d): Near last to freeze region of ingot.

6.4.3 Melt Convection near Conical-Cylindrical Transition

Based on these experimental observations, it is necessary to try to explain (i) the nucleation event occurring near the conical cylindrical transition of the pBN crucible and (ii) the difference in the grain structure observed for ingots grown with and without the SiC pedestal.

For Ingots 1-3, conditions leading to the nucleation of new grains near the conical-cylindrical transition (see **Figure 66(**c), **Figure 67(**a), and **Figure 68**(b)) in the pBN crucible may be attributed to heat transfer properties of the furnace and refractory materials geometry. Since the furnace geometries and materials are based on an existing numerical model, simulation results are expected to be applicable to the observed experimental phenomena. In particular, changes in the melt convection and heat flux near the conical-cylindrical transition of the pBN crucible are expected to be responsible for the change in grain structure observed in this region.

Presented in **Figure 70** are data adapted from (29) (39) based on the experimental model which has been used here. From this figure it may be seen that at the start of growth, there is a convective cell in the melt just in front of the interface (Cell 1), flowing clockwise, downwards along the wall and upwards along the center axis. Directly above convective Cell 1, there is a second convective cell, or Cell 2, which exhibits counter clockwise convection. Finally, at the surface of the melt, there is a convective cell, or Cell 3, which exhibits clockwise convection. The relative convection intensity is relayed by the streamlines whose values are reported in **Figure 70**.

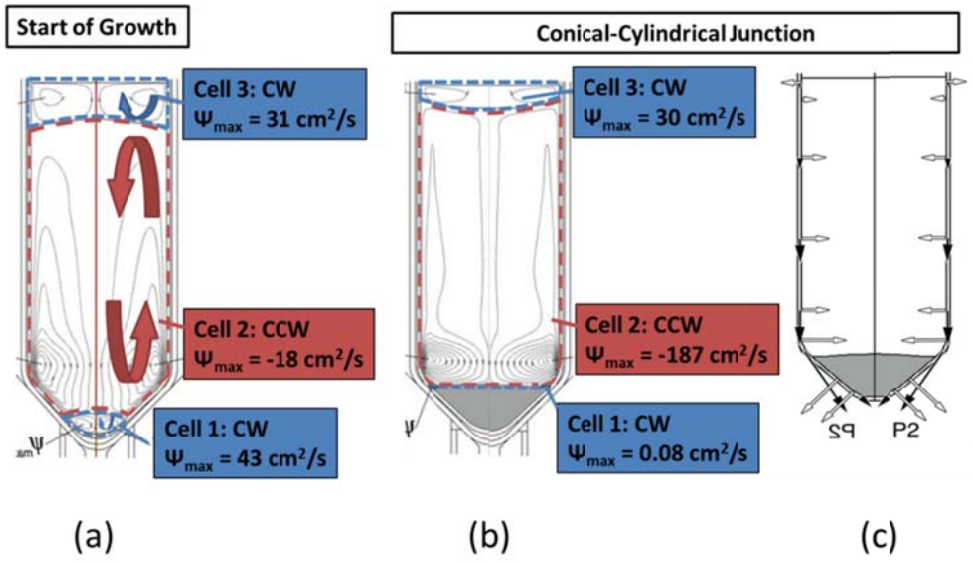

Figure 70 Melt convection characteristics (a) at the start of growth (b) at the cylindrical conical interface (c) heat flux characteristic. Heat flow represented in logarithmic terms with respect to heat flux. (29) (39)

As growth continues along thru the conical region, the convection intensity of Cell 1 decays substantially, eventually coming almost to a complete stop out as the interface reaches the conical-cylindrical transition. This reduced convective intensity of the melt will result in a thicker thermal boundary layer (δ), as the convection velocity (v_c) is reduced, according to **Equation 15**. The parameter α is the thermal diffusivity of the melt and R is the crucible radius.

Equation 15 $$\boldsymbol{\delta = \sqrt{\alpha \cdot R / v_c}}$$

A thicker boundary layer will lead to a decrease in the thermal gradient across the melt in front of the SLI following **Equation 16** where ΔT is the temperature difference across the boundary layer, and G is the gradient across the melt

Equation 16 $$\boldsymbol{G = \Delta T / \delta}$$

It is reasonable to suppose that a decrease in the temperature gradient as the solid-liquid interface approaches the conical-cylindrical transition will increase the thickness of the layer of undercooled liquid ahead of the SLI. Indeed, taking into account the stagnant undercooled liquid of Cell 1 directly above the solid liquid interface, it is possible that conditions may exist for nucleation of new grains.

After passing this conical-cylindrical transition region however, the flow ahead of the SLI is replaced by another convective cell flowing counter-clockwise, or upwards at the wall and downwards at the center axis (Cell 2). The convection in this cell is orders of magnitude more intense, and could serve to (1) suppress the thermal boundary layer by (2) increasing the thermal gradient to (3) reduce the thickness of the undercooled melt in front of the SLI. For this reason, it seems probable that we do not observe additional grains forming after the conical-cylindrical transition (see **Figure 66**(d), **Figure 67**(d), and **Figure 68**(d)).

6.4.4 Heat Flux near Conical-Cylindrical Transition

Aside from melt convection, the unique anisotropic properties of the pBN crucible could also play a role in the formation of new grains at the conical-cylindrical interface. The pBN crucible has high thermal conductivity parallel to the crucible wall (a-b axis 60 $W\text{-}m^{-1}K^{-1}$) and a low thermal conductivity perpendicular to the wall (c-axis 2 $W\text{-}m^{-1}K^{-1}$). This encourages heat flux down the crucible axis, while suppressing radial heat losses normal to the wall surface.

As the initial solidification occurs at the tip of the conical region, the pBN and SiC thermal conductivity focuses the heat flux such that it is extracted axially down through the SiC pedestal. This leads to the formation of a convex interface initially, as the solid liquid interface is normal to the axial heat flux vectors

As the solidification front approaches the conical-cylindrical transition, the SiC pedestal has less influence on determining the SLI shape. Additionally, more latent heat is generated due to an increase in cross sectional area of the conical region. Taking into

account (i) reduced axial heat extraction through the SiC pedestal and (ii) increased latent heat production, an inevitable increase in radial heat losses has the effect of reducing interface convexity. In addition, this behavior will be more influential in the vicinity of the crucible walls, as solidification proceeds. Finally, when the SLI actually reaches the conical-cylindrical transition, the contact angle between the SLI and the crucible wall suddenly changes, exacerbating the aforementioned effects on radial heat losses (82) (30).

6.4.5 Observation and Measurement of Nucleation Events

Using the SiC pedestal in conjunction with the pBN crucible, the onset of crystal growth at the tip should be characterized by a higher axial temperature gradient and higher axial heat flux. Indeed, the first-to-freeze (FF) region does not appear to be polycrystalline or exhibiting high void content, as has been observed by other investigators using different pedestal geometries for the bulk growth of Cd(Zn)Te (see **Figure 62**).

Ingot 4, grown without the SiC pedestal, exhibits a polycrystalline grain structure at the ingot tip, indicating a difference in the kinetics driving the initial nucleation processes. Evidence to support this presumption has been observed experimentally, and is presented in **Figure 71**(a). Specifically, we may observe the exothermic release of latent heat associated with nucleation for ingots grown with and without the SiC pedestal.

Using thermocouples which have been placed at the first to freeze tip of the pBN crucible, temperature fluctuations associated with nucleation and crystal growth may be readily detected. The first case presented is for the Ingot 4, which has been grown with the SiC pedestal removed.

In Region I of **Figure 71**(a), the temperature of the melt is cooling at the same rate as the furnace (0.3^{o} C/ hr). In Region IIa, near t = 1215-1280, the slope of the temperature ramp flattens and no longer coincides with the programmed temperature ramp of the furnace. This flattening observed may be a result of the latent heat of solidification, effectively slowing the temperature ramp in the melt.

A pulse of latent heat is detected in Region IIb near t=1280. It is important to note that this occurs at a 1097.5 ^{o}C, a temperature nearly 7 ^{o}C below the melting point of Cd(Zn)Te. Over the course of 2.5 hours, the heat is slowly dissipated until the temperature ramp returns to its previous rate in Region III.

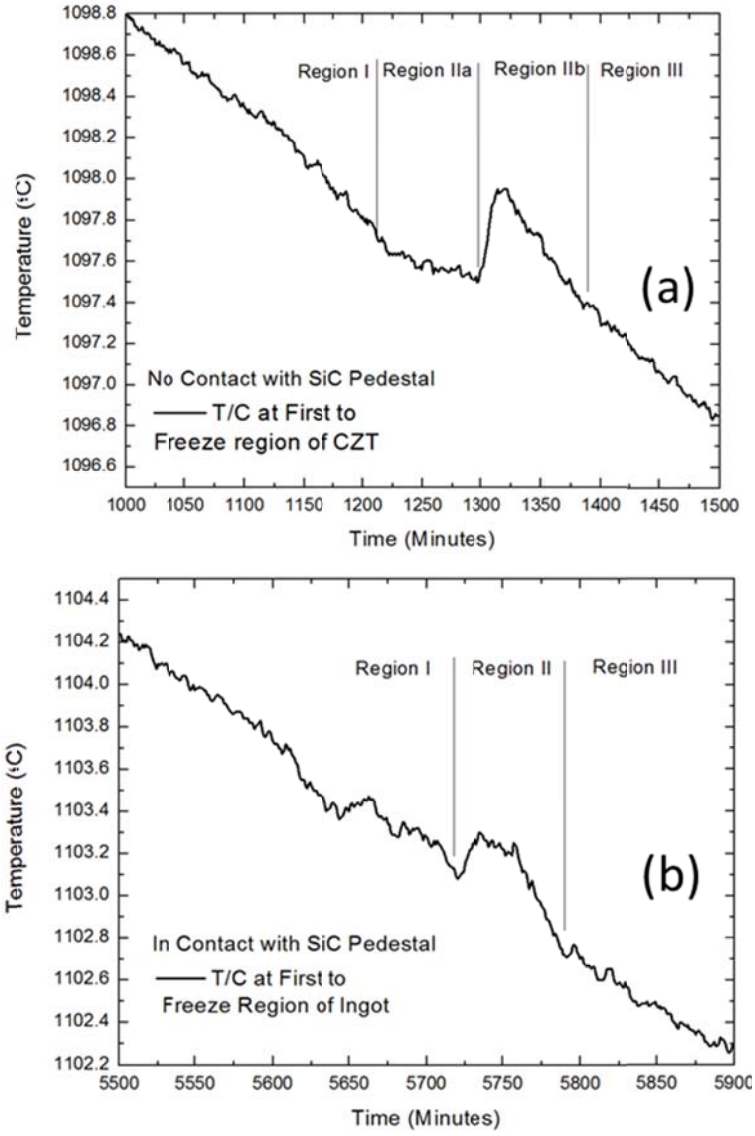

Figure 71 Temperature measured at first to freeze region of ingot for Cd(Zn)Te ingot grown (a) with tip of pBN crucible in contact SiC pedestal (b) and not in contact with SiC pedestal.

This case is compared with Ingot 2, for which a SiC pedestal has been used. Again, in Region I the melt is being cooled at the same rate as the furnace (0.3^{o} C/hr). In Region II, there is an exothermic heat pulse detected by the thermocouples placed near the first to freeze tip. In this case however, this event occurs near 1103.1^{o} C, nearly 1^{o} C below the melting point of Cd(Zn)Te. The dissipation of heat takes place over an interval of 1.15 hr until the temperature ramp returns to its previous rate in Region III. A summary of these experimental observations is presented in Table 9

Table 9 Effects of SiC pedestal on Crystal Growth dynamics measured *in-situ*

Observation	No Contact with SiC Pedestal	Contact with SiC Pedestal
Temperature Spike Associated with Nucleation	0.45 ^{o}C	0.15 ^{o}C
Nucleation Temperature	1097.5 ^{o}C	1103.1 ^{o}C
Heat dissipation time	2.25 hrs	1.15 hrs
Axial ∇T at FF	2.5 ^{o}C/cm	3.5 ^{o}C/cm

The experimental measurements of the temperature gradient near the tip for each growth are also presented in **Table 9**, consistent with the prediction that using the SiC pedestal results in a higher temperature gradient. It is important to mention that the distance between the circumferentially arranged T/Cs and the tip may have influenced the measurement. The actual temperature gradient at the tip is likely to be even higher than we have measured, as the effects of the SiC pedestal will become more influential (see section 7.5 on page 303).

This increased temperature gradient at the First to Freeze tip bounds the super-cooled region of the melt to a smaller volume. As a result, spurious grain formation is suppressed at the onset of nucleation. All of these measurements seem to be tied to the fact that the axial heat extraction will be less efficient in the absence of the SiC pedestal, and will require a higher undercooling of the melt to drive the growth.

Different grain structures are also clearly observed in both cases with and without the SiC pedestal. Columnar grains are observed in the case of a SiC pedestal, with relatively large surface area perpendicular to the growth direction, extending vertically through large volumes of the solid. In the case where the SiC pedestal has been removed, much smaller grains are present, with shorter characteristic lengths both parallel and normal to the direction of growth.

Constitutional supercooling is caused by the presence of a liquid layer in front of the interface that is below the local liquidus temperature. Assuming that Zinc, being the most abundant impurity, controls constitutional supercooling, the CdTe-ZnTe phase diagram gives a liquidus slope of m= 198 K/molfrac $m = 198K/molfrac$ (93) a partition coefficient

of $k = C_s/C_l$=1.35$k = C_s/C_l = 1.35$, and a diffusion coefficient of $D = 1 \times 10^{-4}$ cm^2/s (94). The molar zinc concentration present is $C_\infty = 0.1C_\infty = 0.10$. In order for constitutional supercooling to be avoided, **Equation 17** must be satisfied, where *V* is the interface growth velocity and *G* is the melt temperature gradient in front of the (95).

Equation 17 $$\boldsymbol{G/V > [m \cdot C_\infty \cdot (k - 1)] \,/\, [k \cdot D]}$$

Evaluating the right hand side of this expression gives a value of nearly 14 K-hr/cm^2. Evaluating the left hand side with the measured temperature gradients and growth velocities, the smallest values obtained are about 250 K-hr/cm^2, which are more than sufficient to prevent constitutional supercooling. Therefore, the small irregular grains may not be caused by constitutional supercooling near the propagating SLI. Several possible explanations for the difference in grain structure will be explored in the future, including possible heterogeneous nucleation effects.

Overall, the use of the silicon carbide pedestal seems to lower the undercooling necessary to drive the growth of Cd(Zn)Te. As a result, the first to freeze tip exhibits improved crystalline quality, without the presence of voids or polycrystalline caps.

6.4.6 Wafer Characterization

Of principal importance for detector applications are the electrical and optical properties of the bulk materials. Specifically, it is important to obtain high resistivity materials, with low concentrations and sizes of inclusions and precipitates. The leakage current in a device acts as a source of noise during the spectroscopy measurements, while the second phase inclusions act as scattering centers of the charge induced by the high energy radiation.

Bulk resistivity mappings of wafers harvested from each ingot are presented in **Figure 72**. These wafers represent the typical measurements which have been obtained on several wafers from the same ingot. For Ingots 1 and 2, the bulk resistivity measured for a 5mm thick 50mm diameter wafer exhibited resistivity values between $2\text{-}3\times10^9$ Ω-cm uniformly across the entire wafer surface. This mapping presented in **Figure 72** corresponds to the wafer presented in **Figure 66**(c). In general for this ingot, there was no correspondence

between the new grains and changes in resistivity. Moreover, each wafer harvested from this ingot exhibited resistivity higher than 1×10^9 Ω-cm over 85% of the surface.

For Ingot 3, the location of the twins did correspond to lower resistivity in each wafer. This is attributed to the higher density of Te-inclusions found within the twinned structures (see discussion below). However, the entire wafer also exhibited resistivity higher than 1×10^9 Ω-cm. The sample for Ingot 3 corresponds to the wafer presented in **Figure 68**(c). In general however, wafers with similar or even better resistivity maps have been harvested along the entire length of each of the Ingots 1-3.

For Ingot 4, the bulk resistivity of each wafers was lower than the other three ingots, though still near 1×10^9 Ω-cm over a substantial range. This behavior is attributed to the higher density of smaller grains present in these wafers and the corresponding non-uniform distribution of second phase inclusions throughout the matrix (see **Figure 73**). Indeed, the influence of grain boundaries on the electrical properties and CCE of Cd(Zn)Te detectors has been investigated by (9).

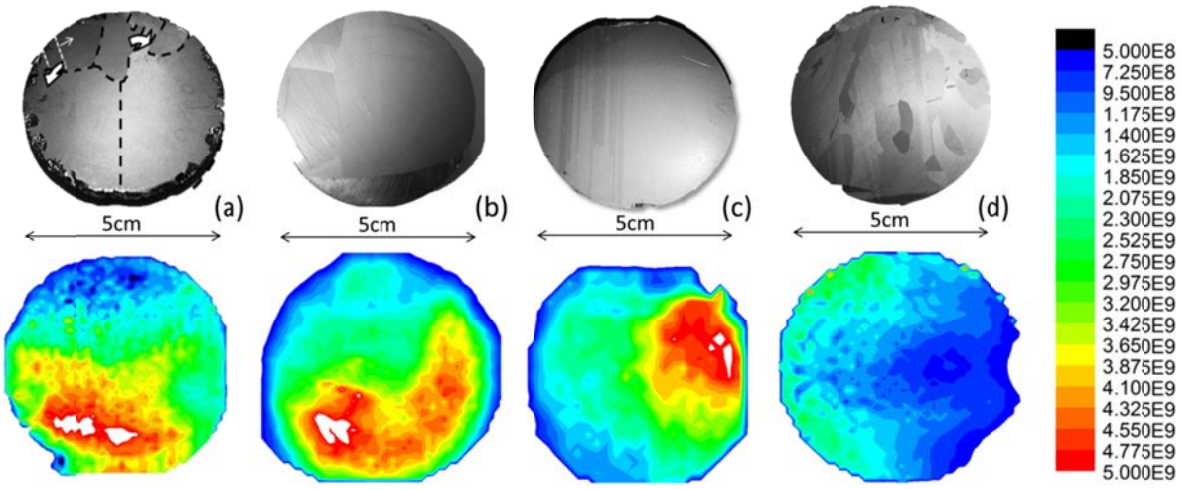

Figure 72 (a) – (c) Grain structure and bulk resistivity of Cd(Zn)Te wafers grown using modified VGF method with SiC pedestal. (d) Cd(Zn)Te grown using same growth recipe, but without SiC pedestal.

Second phase inclusions have been investigated using optical transmission techniques to elucidate the distribution of Te-inclusions in ingots grown with and without a SiC pedestal. Presented in **Figure 73** are x-y optical transmission mappings of Cd(Zn)Te wafers which are presented in **Figure 68**(d) and **Figure 69**(d). The Te-inclusions act as scattering centers for the IR light, and are detected as small dark spots in the microscope.

By comparing **Figure 73**(a) with the resistivity mapping of Ingot 3 in **Figure 72**(c), regions which exhibit higher densities of Te-inclusions result in a lower bulk resistivity. The Te-inclusions are found in higher densities within the twins present in each waver and these areas of the wafer correspond to lower resistivity. It is important to note that it is not the twins which are attributed to the lowering of the resistivity, but the higher density of second phase inclusions. Such behavior has also been reported elsewhere, and is consistent with the results presented here (9) (96) (97). Similar uniform distributions of Te-inclusions have also been observed in Ingots 1 & 2.

With respect to Ingot 4, the poor grain structure resulting from the change in furnace geometry results in very non-homogenous distribution of second phase inclusions, as can be clearly seen in **Figure 73**(b). We attribute the non-uniform capture of these second phase particles to an unstable growth interface arising from poor axial heat flow, as well as to the high number of grain boundaries present within the wafer, to which the Inclusions may diffuse. Indeed, the grains of the crystal may be observed to some extent by the Te-inclusions. Such non-uniformity is detrimental to (i) reproducibility of devices harvested from the same wafer and (ii) the CCE of harvested detectors.

To demonstrate the real benefits of the SiC pedestal, however, it was necessary to show real improvement in terms of functioning devices harvested from the FF tip of the ingot. In fact, the FF region of the Cd(Zn)Te has normally been associated with low quality material due to the lower temperature gradients, an unstable growth interface, and uncontrolled growth dynamics, as may be seen in **Figure 62**.

Therefore the FF region of Ingot 1 (pictured in **Figure 66**(a) and (b)), was directly fabricated into a planar device. Presented in **Figure 74** is the procedure used for creating this test device. Presented in **Figure 75** is the gamma response of the device using ^{133}Ba radioactive source. The inset is a photo of the actual detector which has a thickness of 10 mm. For a region of the ingot which is normally polycrystalline, this result demonstrates the benefit of using a SiC pedestal. The latent heat is more efficiently extracted, and the super-cooled region is confined to a smaller volume. As a result, material which is of sufficient quality may be harvested for device applications. It is important to note that this result has been reproduced and samples harvested from the First to Freeze region of several

25mm Cd(Zn)Te Ingots have also been fabricated into planar test devices which exhibit good spectroscopic performance.

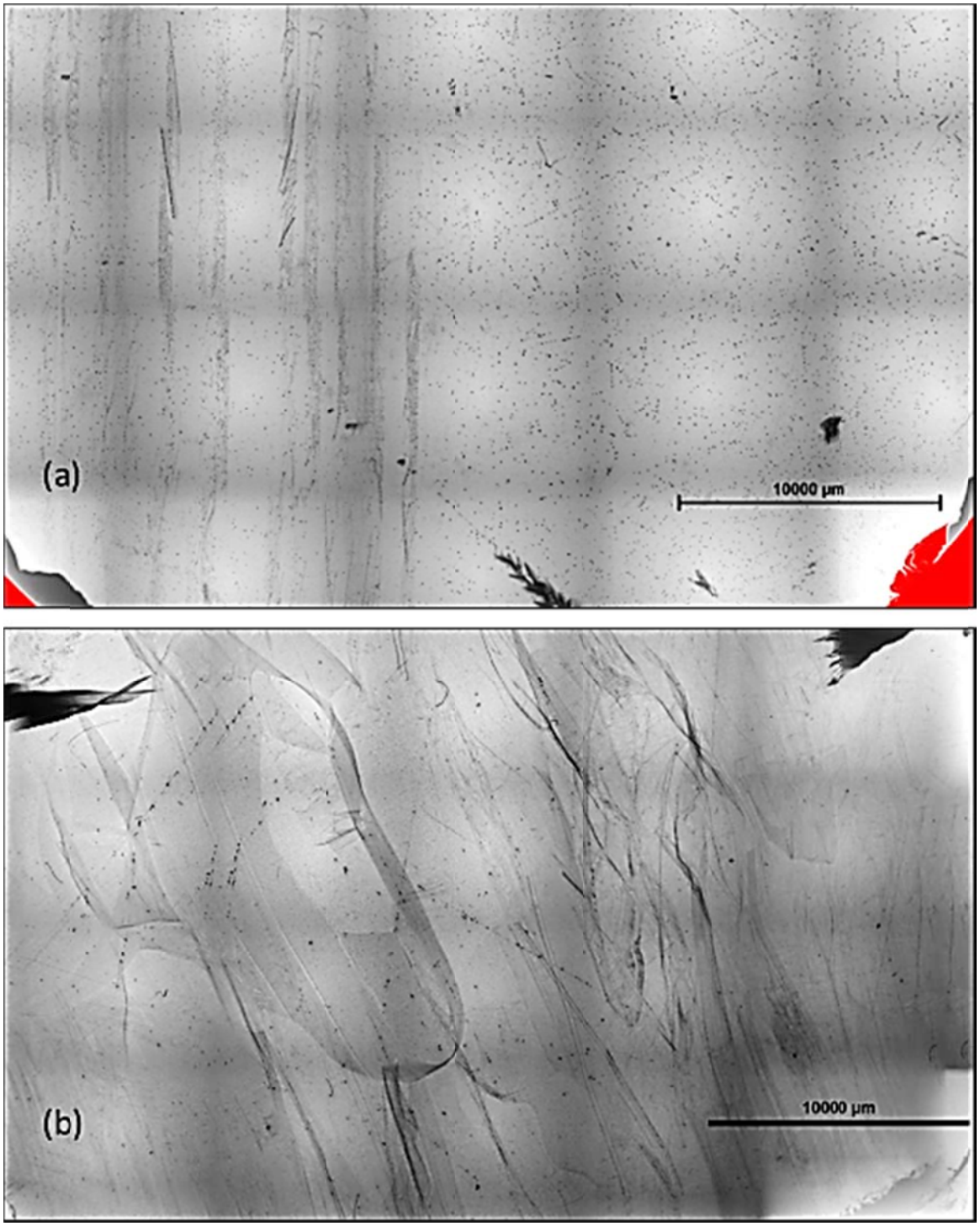

Figure 73 Te precipitate map of second phase inclusions in Ingot 3D grown using with the pBN in contact with the SiC pedestal (Left) and Ingot 4D in which contact between the pBN crucible and the SiC pedestal has been removed (Right).

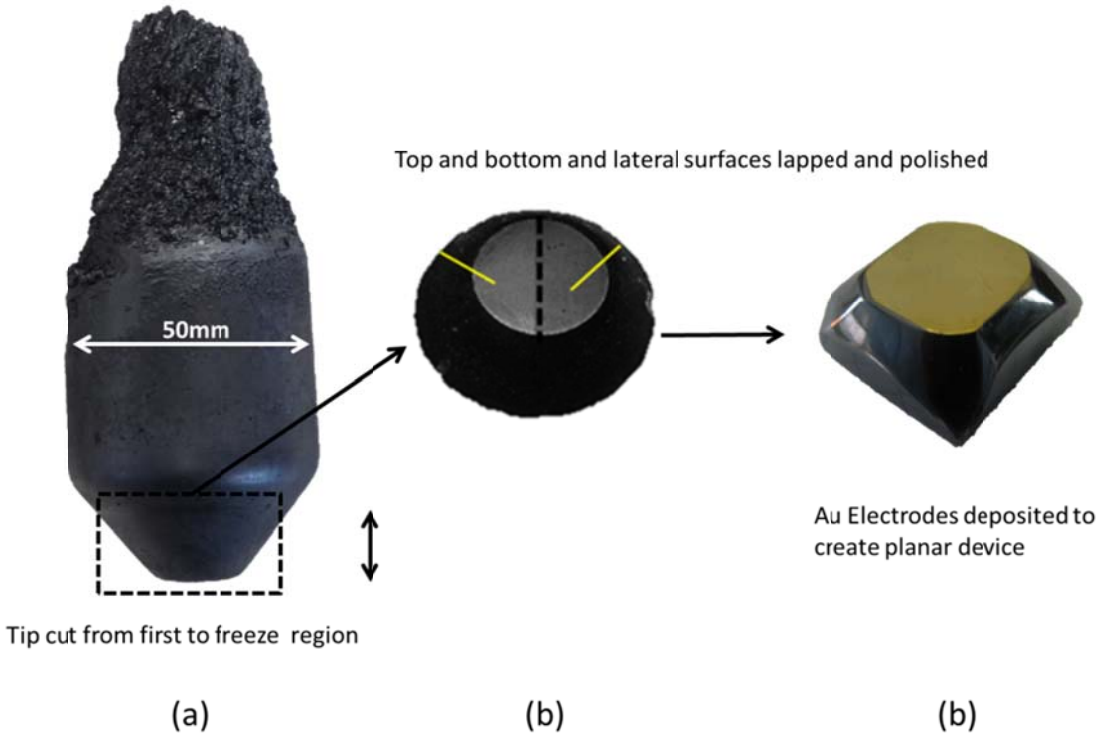

Figure 74 Gamma response of device harvested from first to freeze region of 50mm ingot.

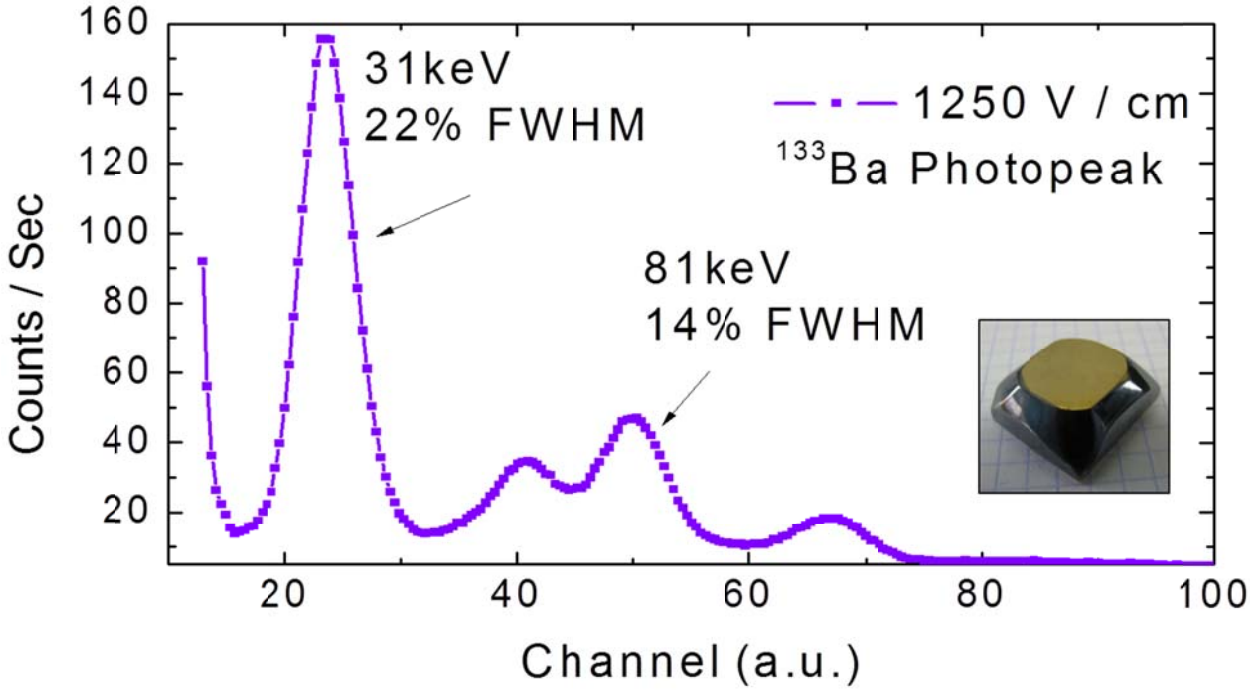

Figure 75 Spectral response to ^{133}Ba of planar device fabricated from tip of Ingot 1.

6.5 Conclusions and Future Work

Based on the experimental work, the capacity to grow larger quantities of bulk single crystal high resistivity Cd(Zn)Te has been demonstrated. Indeed, comparing the resistivity of this material with that of state of the art material (discussed in Section 1 of Chapter 4), the resistivity clearly comparable for spectroscopy applications. From this investigation, the conclusions are summarized as follows:

1. Cd(Zn)Te has been grown implementing a furnace geometry designed specifically for improving the thermal environment during crystal growth (80)- (83). As a result, relatively large crystal grains and volumes have been obtained for 50mm ingots.
2. The benefit of using this thermal geometry has been demonstrated by comparing Cd(Zn)Te ingots grown with and without the SiC pedestal.
3. Gamma spectra are presented for planar devices which have been harvested from the First to Freeze regions which are most influence by the effects of the SiC pedestal.
4. The results demonstrate the benefit of using a pedestal with sufficiently high thermal conductivity which extracts the latent heat of solidification at the very beginning of the crystal growth cycle.
5. One disadvantage of this geometry however is associated with the conical-cylindrical transition of the pBN geometry. This region of the growth promotes the nucleation of new grains from the crucible wall which grow inward. This feature been attributed to the increased radial heat losses at the side walls and very low intensity convection in the melt for the convection cell immediately above the SLI.

Based on these results, additional new opportunities for investigation are proposed. These include:

1. The development of a flat bottom pBN crucible without the cylindrical conical transition

2. Implementation of Cd-overpressure control using Zone 6 of the VGF furnace.

3. Implementation of a retractable, cylindrical (hollow) SiC pedestal to improve cold-finger thermodynamics. This feature is discussed in greater detail in the following section.

7 DEVELOPMENT OF HEAT TRANSPORT MODEL

Section Contents

7.1 Introduction

Progress has been made over the last decade in not only in crystal growth but the development of numerical approaches for engendering a deeper understanding of the growth process. From the simulation point of view, several different claims have been presented for optimizing the thermal conditions in an effort to modify crystal growth kinetics. Indeed, simulations have demonstrated that the solid-liquid interface is strongly dependent upon the balance between axial and radial heat flow, and that this balance can be controlled by the ampoule geometry (80).

As a first step towards this end, a model has been developed in conjunction with Andreas Black based on CAD model of the 6-zone VGF furnace which is presented in Chapter 2. The development of this model has required investigation into the thermodynamic material properties of Cd(Zn)Te, as well as the other furnace refractory materials used in our geometry. Based on the CAD model and these material properties, preliminary simulation results are also presented in this chapter as a first step towards developing a predictive model for Cd(Zn)Te growth.

We first present the thermodynamic properties of Cd(Zn)Te, followed by a description of the CAD model and mesh which has been generated for this geometry. We conclude with two studies which have been carried out related with (i) thermocouple placement within the furnace as well as (ii) observed changes in melt convection associated with modification of the furnace pedestal geometry, which has been proposed in this thesis.

7.2 Thermodynamic Material Properties of Cd(Zn)Te

7.2.1 Heat of Fusion

The heat of fusion, or latent heat of solidification, is one important parameter for developing an understanding of crystal growth dynamics. Indeed, the gradual change from the liquid-phase to the solid-phase and the corresponding release of latent heat has a strong influence on the profile of the solid liquid interface (SLI). As solidification continues and the solid phase grows, the thermodynamic parameters such as thermal conductivity and heat capacity become increasingly important. Indeed, the latent heat generated at the propagating SLI must be efficiently extracted through the solid phase before the

solidification front may advance. How this heat is removed from the interface plays a strong role in determining the crystal growth process.

Experimental determination of these thermodynamic properties of semiconductor materials such as CdTe and ZnTe requires the implementation of specialized calorimeter devices. In general, II - VI compounds exhibit high dissociation pressures at elevated temperatures (98), which results in error in determining their heat contents. As one example, departure from stoichiometry due to the preferential evaporation of Cd would produce a melting temperature below the actual melting temperature of the binary compound CdTe. Examples of how this experimental error is taken into account are presented elsewhere (99). Due to the experimental challenges associated with carrying out such fundamental measurements, there exist few sources available in the literature with such important information.

The value for the heat of fusion parameter for both CdTe and ZnTe at their melting points have been experimentally determined by (100) (101) (102) (103) (104) and are presented in **Figure 76**. Increasing Zinc content results in an increase in the latent heat released throughout the solidification. Due to the miscibility of CdTe and ZnTe at all temperatures, a value of 1.98×10^5 J-kg^{-1} (47.6 kj-mol^{-1}) was chosen as an appropriate value for the heat of fusion by using the weighted values provided by Yamaguchi (26).

7.2.2 Heat Capacity

A specialized drop calorimeter is used for the determination of a materials heat capacity at high temperatures. This is measured by bringing the material into thermal equilibrium at high temperature, and subsequently dropping the material into a calorimeter to measure the heat content of the material.

The temperature dependence of the high-temperature heat content data may be expressed using algebraic parameters following the method outline by (105). This method provides the ability to fit heat content data using algebraic equations for smoothing of experimental data and for correlation between low temperature and high temperature data sets. The general algebraic expression used for the fitting is expressed using **Equation 18**. The experimental data for CdTe and ZnTe has been fit setting the parameters C = 0 and E = 0.

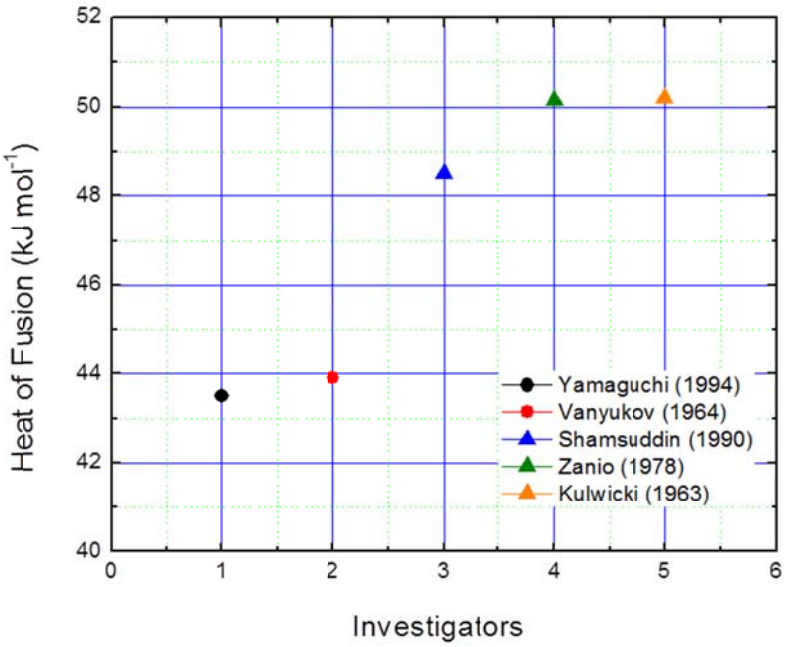

Material	Heat of Fusion J-kg^{-1}	Heat of Fusion kJ-mol^{-1}	Ref.
CdTe	1.81×10^5	43.5	Yamaguchi (1994)
CdTe	1.82×10^5	43.9	Vanyukov (1964)
CdTe	2.02×10^5	48.5	Shamsuddin (1990)
CdTe	2.09×10^5	50.16	Zanio (1978)
CdTe	2.09×10^5	50.2	Kulwicki (1963)
ZnTe	3.38×10^5	81.12	Yamaguchi (1994)

Figure 76 Top: Heat of Fusion of CdTe measured by different groups (100) (100) (101) (102) (103) (26). Bottom: Heat of Fusion for CdTe and ZnTe compounds

Equation 18 $$\Delta H_T - \Delta H_{298.15} = A \cdot T + B \cdot T^2 + C \cdot T^3 + D \cdot T^{-1} + E \cdot T^{1/2} + I$$

Determination of heat capacitance from the heat content is achieved using Equation 18 in conjunction with the Shomate function presented in **Equation 19** (105). The Shomate function is used for the determination of the B and D coefficients, while A and I are

determined from the boundary conditions at 298.15 K for $C_p - C_{298.15} = 0$ and $\Delta H_T - \Delta H_{298.15} = 0$ respectively.

Equation 19 $$\mathbf{S.F.} \equiv \mathbf{T}[(\boldsymbol{H_t - H_{298.15}}) - \boldsymbol{C_{p,298.15}} \cdot \frac{(\boldsymbol{T-298.15})}{(\boldsymbol{T-298.15})^2} \equiv \boldsymbol{B \cdot T} + \frac{\boldsymbol{D}}{\boldsymbol{(298.15)^2}}$$

The temperature dependence of the heat capacity may be represented by differentiation of Equation 18 with respect to temperature, as is presented below in Equation 20. The A and B parameters which have been determined thus provide the necessary information with respect to the temperature dependence of the heat capacity. The values for each parameter have been obtained from (26) for CdTe(s), ZnTe(s) and CdTe(l).

Equation 20 $$\boldsymbol{C_p = A + 2B \cdot T - D \cdot T^{-2}}$$

In a paper on the Hg-Cd-Zn-Te phase diagram, Yu. And Breberick (104) use an equation provided by (106) to extrapolate heat capacity for CdTe from room temperature up to near 1100°C. For ZnTe, they use an equation provided by (107) for extrapolation of heat capacity to high temperatures. Yamaguchi (26) and more recently Pavlova (108) have argued that these heat capacities for CdTe are too high based on the experimental work originally presented by (109).

Presented in **Figure 77** is the comparison of CdTe and ZnTe heat capacities extrapolated to high temperatures using results from several authors including the original results of Breberick (104) as well as their more recently revised values (110) taking into the comments by (26) (108). It is important to comment that in this work, it is presumed that these properties do not change substantially between the solid and liquid phases, following similar conventions as those outlined in (57).

The derived heat capacitance data for $Cd_{0.9}Zn_{0.1}Te$ used in this work is presented in **Figure 77** . This value has been computed as a weighted average of the CdTe and ZnTe heat capacity data sets. This is permissible due to the miscibility of ZnTe and CdTe binary compounds and their thermal properties. The most notable impact of ZnTe incorporation into the CdTe matrix in this case is the small increase in the heat capacity of the material.

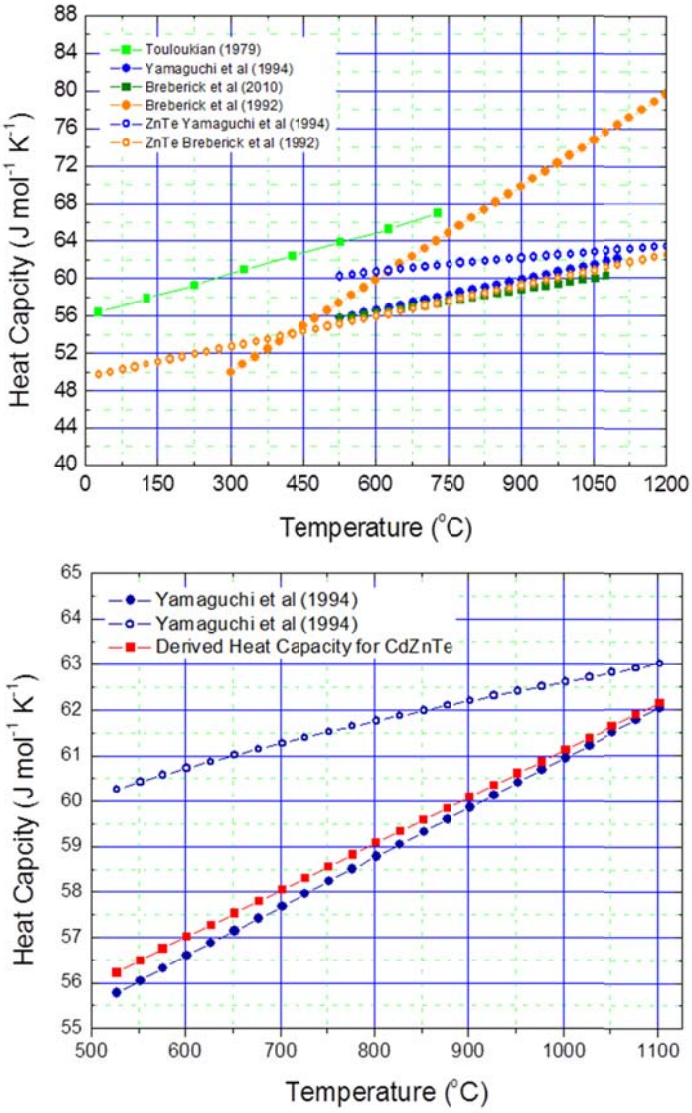

Figure 77 Top: Heat Capacity for CdTe adapted from (104) (26) (110) and ZnTe adapted from (57). Bottom: Derived Heat capacity of $Cd_{0.9}Zn_{0.1}Te$ used in this work.

7.2.3 Thermal Diffusivity

For the determination of thermal conductivity from heat capacitance, it is also necessary to take into account the thermal diffusivity of the material. This parameter describes how quickly heat may be conducted through a material relative to its heat capacitance. This parameter is normally measured using a flash method in which a short

energy pulse is injected at one end of the sample while the temperature change is measured at the opposite end.

The thermal diffusivity parameter was obtained following the laser-flash measurement for both CdTe and $Cd_{0.96}Zn_{0.04}Te$, carried out by (111). The experimental data is presented below in **Figure 78**. The purpose of this measurement was to establish the ratio of the thermal conductivity between the liquid and solid for modeling of the interface shape. By taking the ratio of the thermal diffusivity near 1090°C and after 1100°C the thermal conductivity ratio was determined to be near 1.15 for CdTe. The effect of introducing a larger ZnTe content into the CdTe matrix is reduced thermal diffusivity of the material, and a higher melting point past 1100°C. Furthermore, the ratio of thermal $\lambda_{Liquid}/\ \lambda_{Solid}$ conductivity for the alloy $Cd_{0.96}Zn_{0.04}Te$ decreases slightly to 1.11. It is suspected that increasing the ZnTe content would likely lead to a lower thermal diffusivity parameter, but this was not taken into account in the model which has been developed.

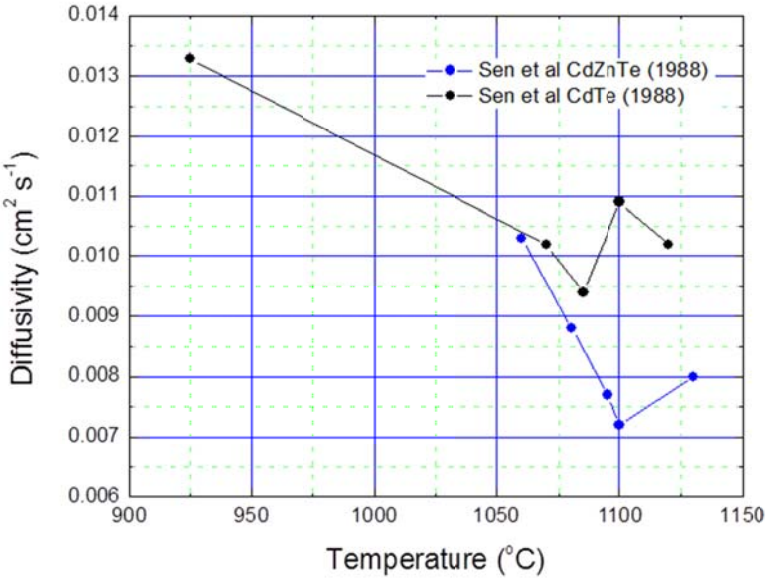

Figure 78 Laser-flash measurement for both CdTe and $Cd_{0.96}Zn_{0.04}Te$, carried out by (111).

7.2.4 Thermal Conductivity

The thermal conductivity (k) may be related to thermal diffusivity (α) by taking into account the density (ρ) and heat capacitance of a material (C_p) following **Equation 21**. The

thermal conductivity is fundamental for modeling heat flux through a solid, following directly from the heat equation.

In the work presented by (57) the thermal conductivity of Cd(Zn)Te is determined, taking into account the values provided for the thermal diffusivity of $7.5 \pm 2.5 \times 10^{-7}$ m^2/s, heat capacity of 72 J $mol^{-1}K^{-1}$, and using a density of 5650 kg-m^{-3}. The thermal conductivity of the solid λ_{Solid} calculated is 1.3 W-$m^{-1}K^{-1}$. The corresponding value of λ_{Liquid} is determined using the ratio $\lambda_{Liquid}/\lambda_{Solid}$ of 1.25.

It is important to re-evaluate this parameter taking into account more recent developments. Based on the derived heat capacity for $Cd_{0.9}Zn_{0.1}Te$ presented in **Figure 77**, the heat capacity ranges from 56 J-$mol^{-1}K^{-1}$ at 600°C to near 60 J-$mol^{-1}K^{-1}$ at 1100°C. For the temperatures of interest near the melting point of Cd(Zn)Te, the thermal conductivity in the solid then becomes 1.05 W-$m^{-1}K^{-1}$. This is the value used in this work for $Cd_{0.9}Zn_{0.1}Te$. It is likely however that the diffusivity of Cd(Zn)Te may be lower due to the higher zinc content.

Equation 21 $$\boldsymbol{\alpha = k/(\rho \cdot C_p) \rightarrow \; k = \rho \cdot C_p \cdot \alpha}$$

7.2.5 Cd(Zn)Te Melting Point,

The melting point of Cd(Zn)Te is of fundamental importance to the crystal growth process. To establish appropriate growth conditions such as thermal gradients, homogenization temperatures, and crystal growth rates it is fundamental to first have the melting point for subsequent growth operations. This is a very important number because throughout literature, it is very common to confuse superheating temperatures with growth temperatures, as the distinction between the two is not well maintained throughout the literature.

The melting point of CdTe has been estimated by Yamaguchi to be 1100 ± 3 °C (26), which is higher than other reported values for CdTe. Guskov reports for $Cd_{0.9}Zn_{0.1}Te$ a melting occurs near 1104ºC (112). In addition the nucleation process in the homogeneous melt is reported to initiate at 1380 ± 1K (1107ºC) and solidification is claimed to complete at 1364±1K (1091ºC) (58). Other techniques have also been investigated to determine the melting point of Cd(Zn)Te, such as those used by H.N.G. Wadley with similar results

(113). In general the melting point of $Cd_{0.9}Zn_{0.1}Te$ is likely to be higher than that of CdTe, falling between 1104 - 1107°C.

7.2.6 Kinematic Viscosity & Density

Shcherbak *et al*. investigates viscosity as a function of temperature $\eta(T)$, and reports the changes in the slope of $\eta(T)$ at 1385±1K (1112ºC) and 1394±1K (1121ºC) which indicate a cluster dissolving mechanism (58). Heating and cooling curves intersect at 1399±1K (1126ºC) and it was concluded that the heated liquid becomes homogeneous at this temperature. Indeed the viscosity as a function of temperature tends to increase which departs from the Arrhenius-like exponential decay which most liquids exhibit i.e. higher temperature corresponds to a lower viscosity. In fact, it is important to comment that these results run contrary to the values presented by Glazov *et al*. (56) for CdTe in 1969. It is interesting to note however, that T. Rule uses a high limit of 11,300 mPa-s (2×10^{-3} m^2/s) to examine the impact of neglecting fluid flow (57). The value used by Rule including fluid flow was between 1.1-4.5 mPa-s.

A comparison of the results published by Shcherbak *et al*. (58) and by Glazov *et al*. (56) are presented in **Figure 79** to demonstrate the differences between the two data sets. The viscosity of the Cd(Zn)Te melt used in this work is 8 mPa-s based of the recent experimental results provided by Schcherbak *et al*.

7.2.7 Density and Thermal Expansion

Temperature dependent density measurements from Glazov (56) were used in this work. The density of the liquid and solid phase Cd(Zn)Te is estimated using the known densities of CdTe (5.86 g-cm^{-3}) and ZnTe (5.65 g-cm^{-3}) to approximate the alloy density. The difference between the solid and liquid phase densities has been observed to be very small. The volume coefficients of thermal expansion for CdTe and ZnTe are $\beta_{CdTe} = 1.5\times 10^{-5}$ K^{-1} and $\beta_{ZnTe} = 2.9\times 10^{-5}$ K^{-1} respectively (56) (57).

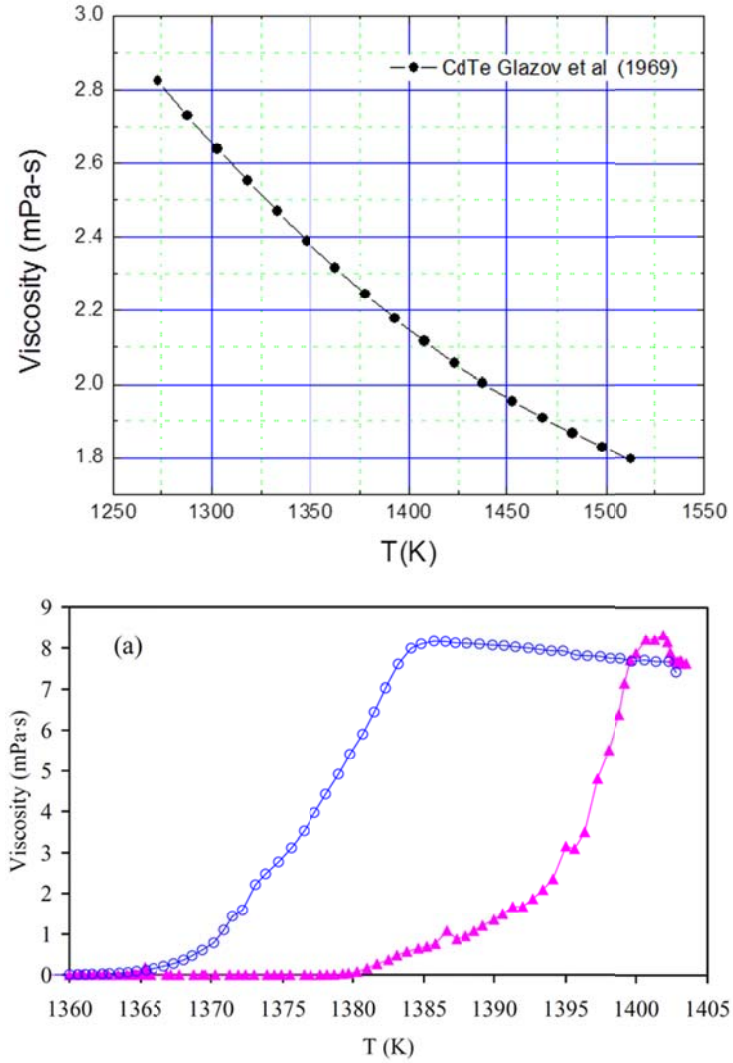

Figure 79 Top: Viscosity of CdTe following an Arrhenius-like decay following (56) Bottom: Viscosity of Cd(Zn)Te melt during the heating phase (▲) and the cooling phase (°) determined by (58)

7.2.8 Thermal Radiation

Following from the Stefan-Boltzmann law presented in **Equation 22**, the power emitted from the surface of a black body is directly proportional to the its absolute temperature. The parameter j* is the power radiated per unit area, T is the absolute temperature, and σ is the Stefan-Boltzmann constant. This fourth order dependence of heat transfer on radiation necessitates that the emissivity's of the surfaces of each material are accounted for.

Equation 22 $$j^* = \sigma \cdot T^4$$

Presented below in **Figure 80** is the power irradiated from an ideal blackbody (emissivity 1.0), using Plank´s law of radiation and three different temperatures. For absolute temperatures approaching the melting point of Cd(Zn)Te, the wavelength associated with the blackbody´s peak intensity output is near 3-4 µm. Indeed, a majority of the light is emitted with a wavelength longer than 2 µm.

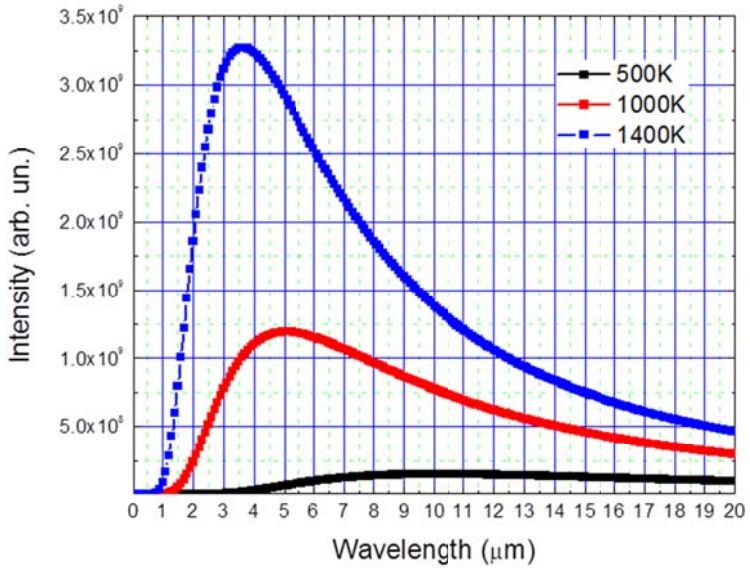

Figure 80 Power irradiated from an ideal blackbody using Plank´s law of radiation for three different temperatures

For the mid to far IR band of interest, the reflectivity of Cd(Zn)Te is close to 0.21 (114). Taking this parameter in account, the transmittance of Cd(Zn)Te may be calculated using **Equation 23** where R is the reflectivity while α in this case is the absorption coefficient and is considered as negligible. From this relationship between reflectivity and transmission, the amount of light actually reflected by the crystal is near 14%. Following similar conventions proposed by (57), the material is expected to be transparent to thermal radiation longer than 2µm, internal radiation was neglected. Choosing a reflectance value between 0.2-0.3 yields an emissivity of between 0.7 and 0.8 for the Cd(Zn)Te solid.

Equation 23

$$T = \frac{(1-R)^2 \cdot e^{-\alpha x}}{1-R^2 \cdot e^{-\alpha x}} = \frac{0.6241}{0.9559} \approx 65\%$$

It is anticipated that the optical properties of the Cd(Zn)Te melt will not differ greatly from the solid near the melting temperature. This is somewhat justified taking into account that the electrical properties of molten CdTe are similar to those in the solid phase i.e. that the electrical conductivity continues to increase with temperature (56) (115).

7.3 Other Material Properties

It was also necessary to include the thermal properties of the refractory compounds which would be incorporated into the 2-D model. These refractory components were used for determination of temperature fields inside the furnace, and therefore only the material properties which are required by the heat equation were necessary i.e. thermal diffusivity, thermal conductivity, and heat capacity. Emissivity of these materials was also included for the radiation transport model.

The properties used in this work are presented below in

Table 10. It is important to note the relatively high thermal conductivity of Quartz with respect to pBN and Cd(Zn)Te which illustrates the limiting factor affecting heat transport is the low thermal conductivity of the Cd(Zn)Te solid. The low density and high heat capacity of the alumina wool makes this material appropriate for thermal insulation applications. The high thermal conductivity of SiC is one of the reasons this material was chosen as a suitable high temperature refractory for the furnace pedestal.

Table 10 Properties of Cd(Zn)Te and refractory materials used in the development of the 2-D heat-transport model

Material	Therm. Cond. $W\ m^{-1}\ K^{-1}$	Heat Cap. $J\text{-}kg^{-1}\ K^{-1}$	Heat of Fusion $J\text{-}kg^{-1}$	Therm. Exp. K^{-1}	Therm. Diff. $m^2\text{-}s^{-1}$	Emiss.	Melting Point ^oC	Den. $kg\text{-}m^{-3}$	Kin. Vis. $m^2\ s^{-1}$
Quartz	2.93	1150	N/A	N/A	1×10^{-6}	0.5	N/A	2200	N/A
Alumina Refractory	0.31	1047	N/A	N/A	3×10^{-6}	0.6	N/A	96	N/A
Cd(Zn)Te (liquid)	1.16	263.8	1.98×10^{5}	N/A	8×10^{-7}	0.8-0.7	N/A	5650	1.4×10^{-6}
Cd(Zn)Te (solid)	1.05	263.8	1.98×10^{5}	1.5×10^{-5}	7.2×10^{-7}	0.8-0.7	1104-1107	5650	N/A
Sintered SiC	62	750	N/A	N/A	2.7×10^{-5}	0.7	N/A	3100	N/A
Kanthal Coils	13	460	N/A	N/A	3.9×10^{-6}	0.7	N/A	7250	N/A
pBN-a **pBN-c**	0.63 0.03	2092	N/A	N/A	1.4×10^{-7} 5.4×10^{-9}	0.5	N/A	2210	N/A

7.4 Model Development

7.4.1 CAD Design and Mesh Refinement

Based upon the 3D CAD model of the VGF furnace, a 2D layout was developed using the CGSim software. From this 2D CAD layout which was generated, a meshing algorithm was applied to each distinct structure of the furnace. Presented in **Figure 81** is the resulting mesh which has been developed, based on the 3D furnace model. The upper most part of the furnace is closed with a thick alumina blanket (a). The quartz crucible which has been filled with Cd(Zn)Te material was placed inside the VGF furnace on top of the SiC pedestal (e). The SiC pedestal was supported by a quartz support structure (f), which has been filled with refractory alumina wool. The bottom of the furnace is closed with a thick layer of alumina wool (g).

During preliminary trials, there were high residuals found in the lateral edges of the ampoule and pBN crucible. Therefore, a higher mesh refinement was used around crucible wall, which was only 1 mm thick (i) and (j). This mesh refinement basically consisted of decreasing the area of each cell to provide a higher density of cells. A higher mesh refinement was also used around Zone 2 of the VGF furnace, a region in which the most dynamic behavior is expected to take place during crystal growth cycle. The difference in the mesh structures may be observed in **Figure 81**.

Mesh refinement near the growth interfaces is an important consideration which must be carefully studied in order to capture the transient behavior near the interfaces of the defined materials. These include the solid/solid interface, solid-liquid interface of the Cd(Zn)Te melt, and liquid-gas interface.

An unstructured mesh was used for all of the furnace components, with the exception of the Cd(Zn)Te solid and Cd(Zn)Te melt bodies. For these bodies a rectangular structured mesh was used for improved interface tracking purposes.

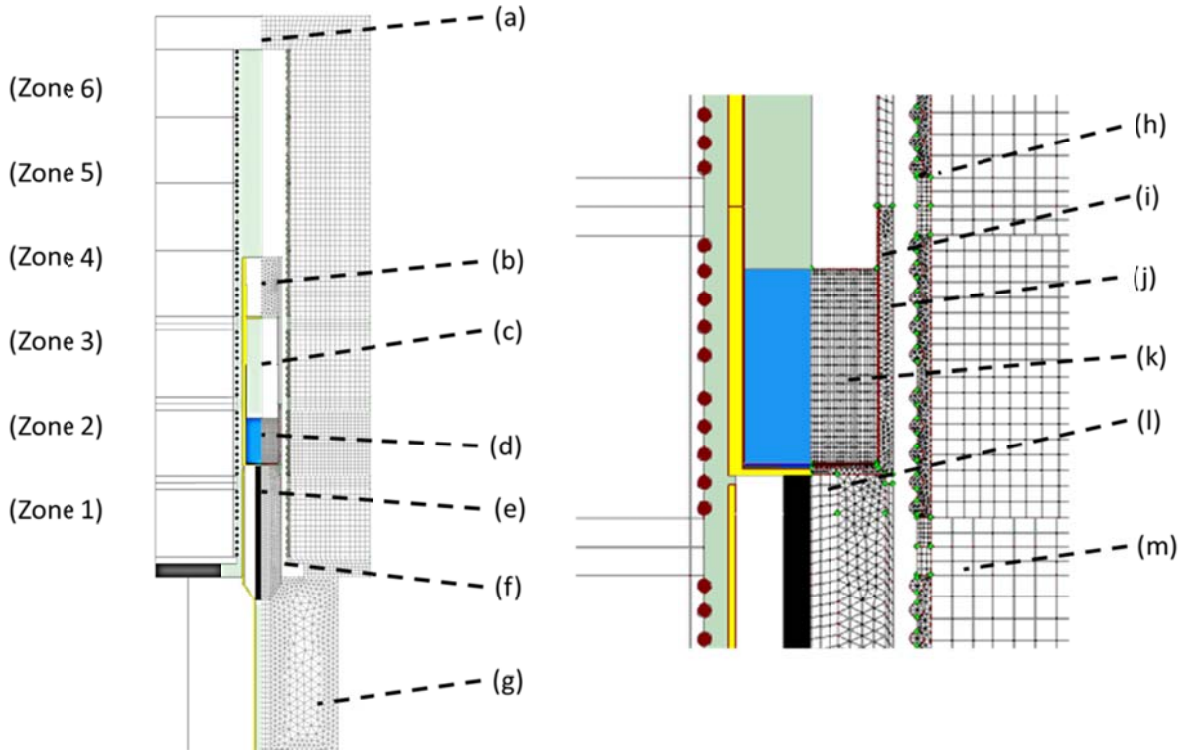

Figure 81 Left: Mesh structure of 6-zone VGF furnace (a) upper insulation (b) alumina insulation (c) ampoule free space (d) Cd(Zn)Te melt (e) SiC pedestal (f) Quartz support structure (g) lower insulation. Right: Close up of crucible geometry (h) adiabatic interfacial zone between furnace elements (i) quartz ampoule wall (j) pBN liner (k) Cd(Zn)Te melt (l) SiC pedestal (m) furnace element.

7.4.2 Governing Equations

To calculate natural convective flow in the Cd(Zn)Te melt, the *FlowModule* of the CGSIM package was used. This package has been designed for the use of steady state flow of incompressible fluids, as well as for tracking the crystallization front or solid liquid interface.

The Navier-Stokes equations are used within the CGSIM solver using no-slip boundary conditions to calculate fluid flow. Arising from the application of Newton´s second law to fluids, the Navier-Stokes equation relates the changes in momentum of a fluid to both the internal and external forces acting on the fluid. The left hand side of the equation **Equation 24** describes changes in momentum associated with unsteady acceleration of the fluid $(\delta v/\delta t)$ as well as convective acceleration of the fluid $(v \cdot \nabla v)$. This second term related with convective acceleration is a time-independent quantity and is a spatial effect (not a temporal effect). The right hand side of the equation relates these changes in

momentum to changes in the pressure gradient $(-\nabla p)$ stress fields $(\mu\nabla^2 v)$ and other body forces (f).

Equation 24 $$\boldsymbol{\rho \cdot \left(\frac{\delta v}{\delta t} + v \cdot \nabla v\right) = -\nabla p + \mu \nabla^2 v + f}$$

In addition, the heat equation has been used for solving for temperature fields inside the furnace geometry. This equation is derived from the coupling of the conservation of energy and Fourier´s law which states that the flow rate of heat through a surface is proportional to the negative temperature gradient across that surface following **Equation 25**, where *k* is the thermal conductivity, *q* is the heat flux, and T is the temperature.

Equation 25 $$\boldsymbol{q = k \cdot \nabla T}$$

The heat equation is given by **Equation 26**, where α the thermal diffusivity of the material, and q is represents heat introduced by some external source i.e. fusion. These second order time dependent partial differential equations may be readily solved using computation methods, which rely upon separation constants, as well as known boundary conditions, and initial conditions.

Equation 26 $$\boldsymbol{dT/dt = \alpha \cdot \nabla^2 T + q}$$

7.5 Simulation Studies

7.5.1 Study 1: Thermocouple Shading

One of the more important and fundamental challenges to the crystal growth process is controlling the temperature profile within each zone of the furnace. In fact, it was observed that the control set-point for the furnace and the actual temperature measured within the furnace disagreed by more than 20ºC for both VGF furnaces investigated in this work. Moreover, this result was not observed on only a single growth using a special conditions but in every growth carried out in this work. Such a large discrepancy between the real temperatures measured *in-situ* and the programmed temperature profile sent to the *ex-situ*

control is remarkable. In fact this degree of error would have a devastating impact on the crystal growth if not well controlled. Presented in **Figure 82** is one example of such discrepancy. The temperature set-point for the furnace was set to 1096°C for Zone 2 of the VGF furnace. However, thermocouples placed inside Zone 2 and distributed along the axis in 1cm intervals demonstrate that the temperature can be up to 26°C higher than the actual set-point.

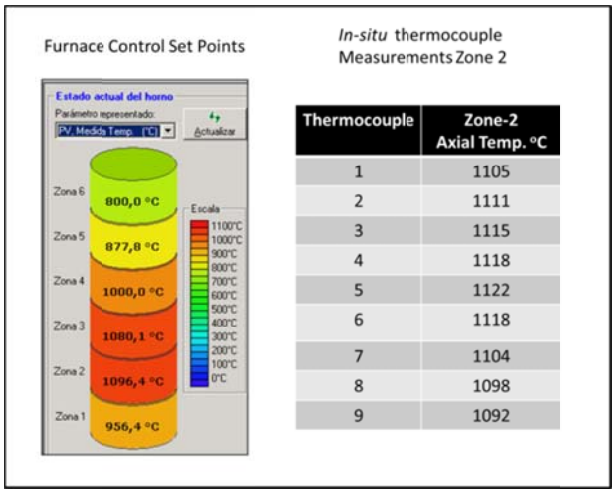

Thermocouple	Zone-2 Axial Temp. °C
1	1105
2	1111
3	1115
4	1118
5	1122
6	1118
7	1104
8	1098
9	1092

Figure 82 Left) Programmed furnace temperatures and Right: actual temperatures measured within the furnace Zone 2 along the axial direction.

Physical explanations for this divergent behavior were not easily forthcoming and the development of a 2D model was crucial to explain this experimental disagreement. One idea proposed to account for this behavior was that the physical location of the control-thermocouple used for measuring the furnace set point may play a strong role in determining the furnace temperature profile. The experimental procedure was to move the position of this control-thermocouple from its original location in the center of the furnace (Case I) and observe its effects on the temperature profile. The control-thermocouple has been displaced 5mm inwards in the radial or x-direction (Case II). This geometry is illustrated below in **Figure 83** for Case I and Case II taking into account an empty furnace geometry. Moreover, only Zone 2 of the 6-zone furnace is analyzed here because (a) it is the most important zone in terms of crystal growth and (b) similar behavior was observed for the other zones.

In general, it is important to first observe that both the axial and radial temperature profiles exhibited similar behavior. Starting from the bottom of the furnace element and moving upward following the z-axis, the axial temperature profile first increases until it reaches a relative maximum, and then begins to decrease after reaching the center point. The radial temperature profile may be characterized as being hottest near the heating coil surfaces, and decreasing towards the centerline of the furnace element. The temperature gradient immediately outside of the hot zone is on the order of 100^{o} C/cm due to the lower thermal conductivity of the refractory components of the furnace element used for insulation.

Each zone of the VGF furnace consisted of a heating element with 10 heating coils which are shown in the geometry, and are labeled as C1-C10. It is important to notice from the geometry that each coil is actually embedded in the furnace refractory. This detail was incorporated into the model to coincide with the physical geometry of the furnaces used. As a result, one half of the coil is exposed to vacuum/air while the other is embedded in the low thermal conductivity insulation. This inter-coil distance being filled with refractory material results in a higher temperature gradient between each coil. This is clearly demonstrated by the relative temperature minima occurring periodically between each of the coil elements on the ID of the furnace wall.

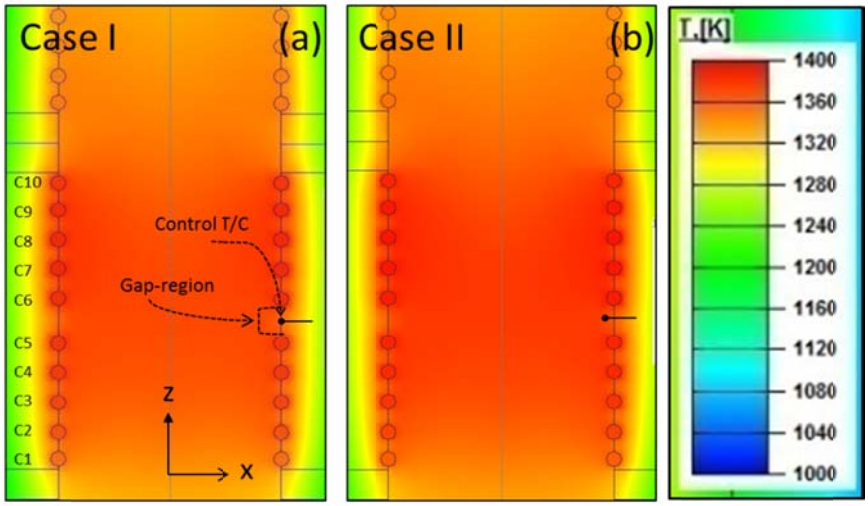

Figure 83 (a) Case I with thermocouple in middle of heating element (b) Case II with thermocouple moved inward by 5 mm.

In the center of the heating element, the gap between the coils C5 and C6 is larger than the gaps between each of the other heating coils. The purpose of this gap is to provide sufficient space for a thermocouple to pass through the coils and into the furnace hot zone. However, due to the increased inter-coil distance, this region is under a substantially higher gradient. The position of the control-thermocouple within this gap region is also presented to illustrate the differences in each case.

Presented below in **Figure 84** is magnification of this gap-region between the C5-C6 heating coils. Again, the lower thermal conductivity of the refractory insulation and the larger inter-coil distance results in a higher temperature gradient, and as a result the read-out temperature of the control-thermocouple will be quite sensitive to its horizontal position.

In Case I, there is substantial difference between the temperature measured by the thermo-couple and the measured temperature within the furnace.

In Case II, displacement of the control-thermocouple 5 mm inwards has the effect of increasing the temperature inside the furnace. This may be explained by observing how the high-gradient region extends into the furnace. Even though the control thermocouple is placed further into the hot-zone, the temperature may be lower in this small volume due to the distance between coil 5 and coil 6. This behavior is referred to here as thermocouple shading and is an important characteristic from the furnace design perspective and must be taken into account for accurate positioning of the thermocouple.

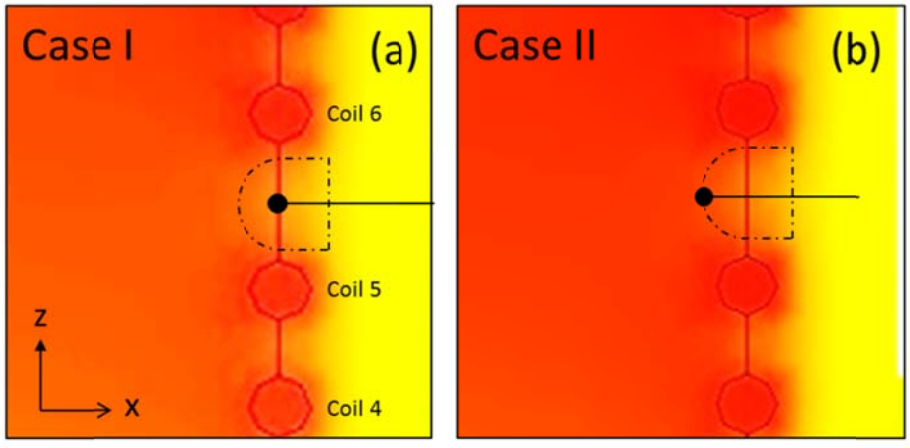

Figure 84 (a) Case I with thermocouple in middle of heating element (b) Case II with thermocouple moved inward by 5 mm.

Presented in **Figure 85** are similar results obtained for when the Cd(Zn)Te charge is placed within the furnace. Indeed, these results clearly indicate that (1) the low thermal conductivity material filling the inter-coil distances significantly lowers the temperature measured by the control thermocouple (2) placement of the set-point control thermocouple within the furnace has a strong impact on the actual temperatures inside the hot-zone of the furnace and (3) to obtain good agreement between experimental and simulated temperatures, correct placement of the thermocouple is crucial in both the physical furnace as well as the computational model.

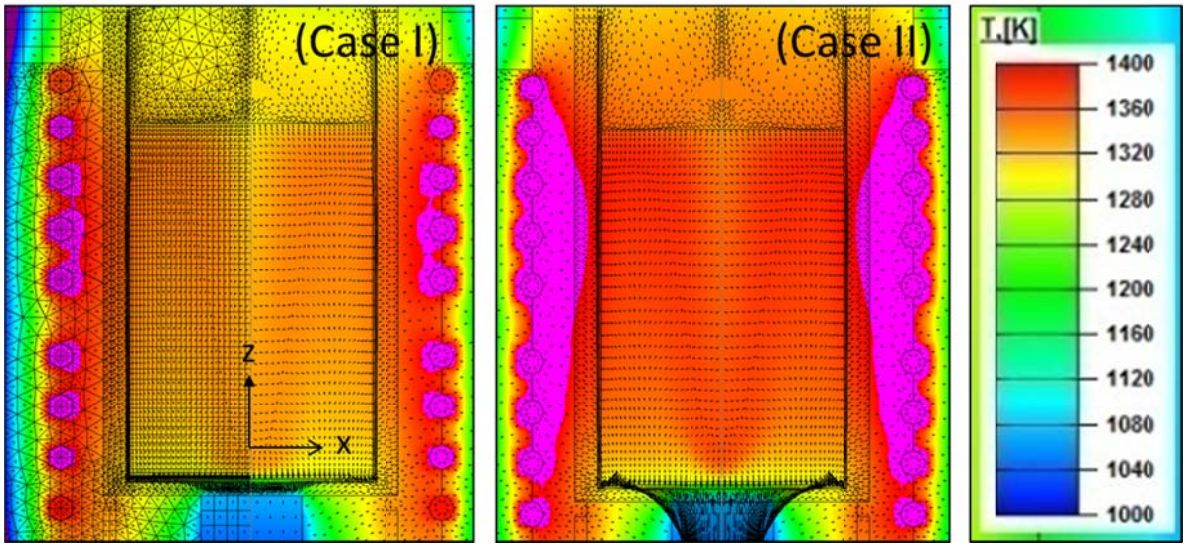

Figure 85 (a) Case I with thermocouple in middle of heating element (b) Case II with thermocouple moved inward by 5 mm.

7.5.2 Study 2: Crucible Geometry Effect on Melt Flow Characteristics

This conical pBN geometry has been proposed to increase in the axial heat flow, decrease in radial heat flow, and improve the temperature gradients at the crucible tip As can be seen in **Figure 86**, using a conical tipped crucible leads to the production of three convective cells, two rotating clockwise and one rotating counter-clockwise. Furthermore, this geometry produces a high temperature gradient at the tip, evidenced by the close-spacing of the isotherms.

The goal of this second study was to investigate how the melt flow characteristics change through the modification of the crucible geometry from a conical tipped crucible

proposed by (80) (81) (82) (30) (83) (84), to a flat bottom crucible which has been proposed based on the experimental conclusions presented in Section 6.5.

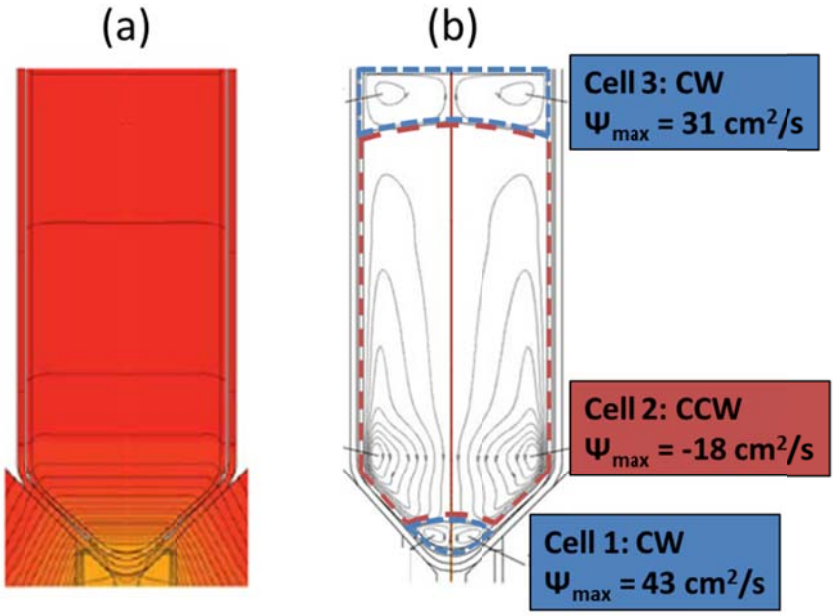

Figure 86 (a) Isotherms and (b) the convective cells and convection intensity using a conical shaped pBN crucible

When this geometry is changed for a flat bottom crucible, clear differences between the crucible geometry quickly emerge. First, only a single strong convective cell is observed. The convection cell in the center of the crucible is relatively strong (see **Figure 87**), and is pushing warm molten Cd(Zn)Te from the center of the charge down toward the SLI. This results in flattening of the thermal boundary layer near the center of the interface. It is important to point out that because the SiC pedestal creates a large vertical thermal gradient in the melt. However a compressed boundary layer leads to a higher temperature gradient.

In summary, changing the geometry of the crucible has a large effect on the natural convection within the melt. It has been observed that the conical shape of the pBN crucible may have deleterious effects on the grain structure near the conical-cylindrical transition. For these reasons, the effect of changing the crucible geometry has been studied in terms of melt convection. The flat bottom crucible does not exhibit the 3-cell convection structure,

but exhibits a single convection cell. This type of convection may be beneficial for improving material homogenization, however further investigation of the furnace pedestal is proposed to suppress the observed deflection of the SLI by the single intense convective cell pushing the hot molten Cd(Zn)Te down toward the center of the interface.

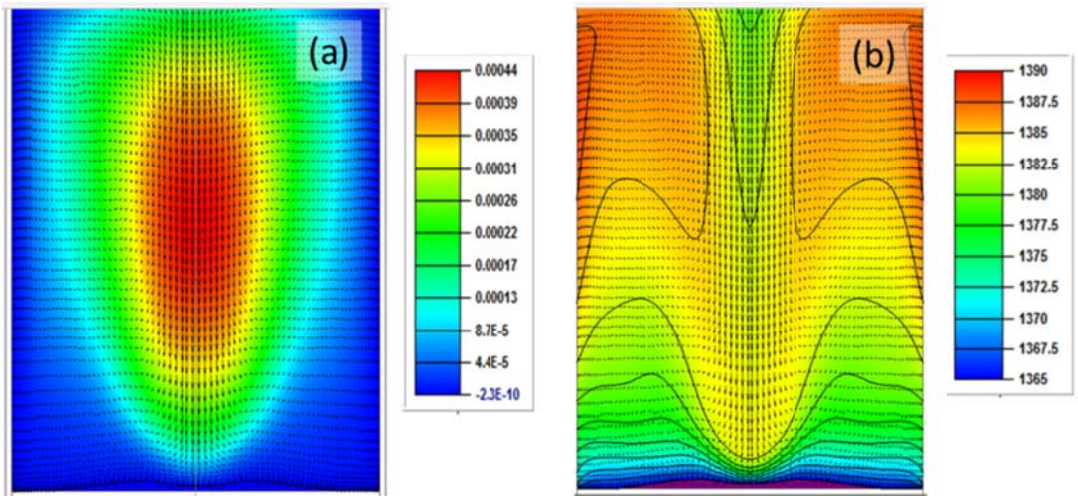

Figure 87 (a) Convective cells and convection intensity using a conical shaped crucible. (b) Convective cell and intensity using a flat bottom crucible (units in m^2/s)

7.5.3 Study 3: Crucible Pedestal Effects

Analysis of the thermal properties of the crucible pedestal and its effect on convection in the melt is important for designing a thermal environment suited to the growth of Cd(Zn)Te. In order to understand the relationship between the thermal convection in the melt induced by the pedestal support, two different materials were investigated as possible candidates for a pedestal support structure: Quartz and Silicon Carbide (SiC). Both materials are high-temperature refractories compatible suitable for supporting the weight of the crucible. The major difference between the two materials is the large difference in their thermal conductivities, heat capacities, and in general their ability to extract heat throughout the growth cycle.

As may be seen in **Figure 89**, using the same temperature set-points in the furnace, the resulting temperature distribution inside the melt is markedly different for both the quartz and SiC pedestal. In the case of the quartz pedestal, the temperature of the melt is nearly 10 ºK higher for the same x-y position than the temperature distribution obtained using the SiC

pedestal. Indeed, using the quartz pedestal, a temperature of 1110ºC (1383 ºK) is obtained at the first to freeze region, whereas a temperature of 1100ºC (1273ºK) is obtained using a SiC pedestal. Furthermore, the temperature distribution throughout the melt is clearly more homogenous than the temperature distribution obtained using the SiC pedestal. More than 75% of the molten Cd(Zn)Te is at a temperature above 1110ºC, whereas for the SiC pedestal, the temperature throughout the melt increases and decreases between 1373 ºC and 1381ºC, but never reaching as high temperatures achieved using the quartz pedestal.

It is interesting to observe that the quartz pedestal, or in general materials with relatively higher thermal conductivity may be more useful in the homogenization phase of material synthesis in that they better ensure that the charge is completely molten at the tip, without incurring large superheats elsewhere in the melt. Correspondingly, large degrees of under-coolings can be avoided during subsequent solidification. Indeed, under-cooling of the melt can be prevented by using low thermal gradients at the tip, which was achieved experimentally using an insulating pedestal. This experimental result has also been obtained elsewhere in the development of a novel pedestal (31). While the quality of the crucible tip is still polycrystalline, the undercooled region appears smaller in volume as a result.

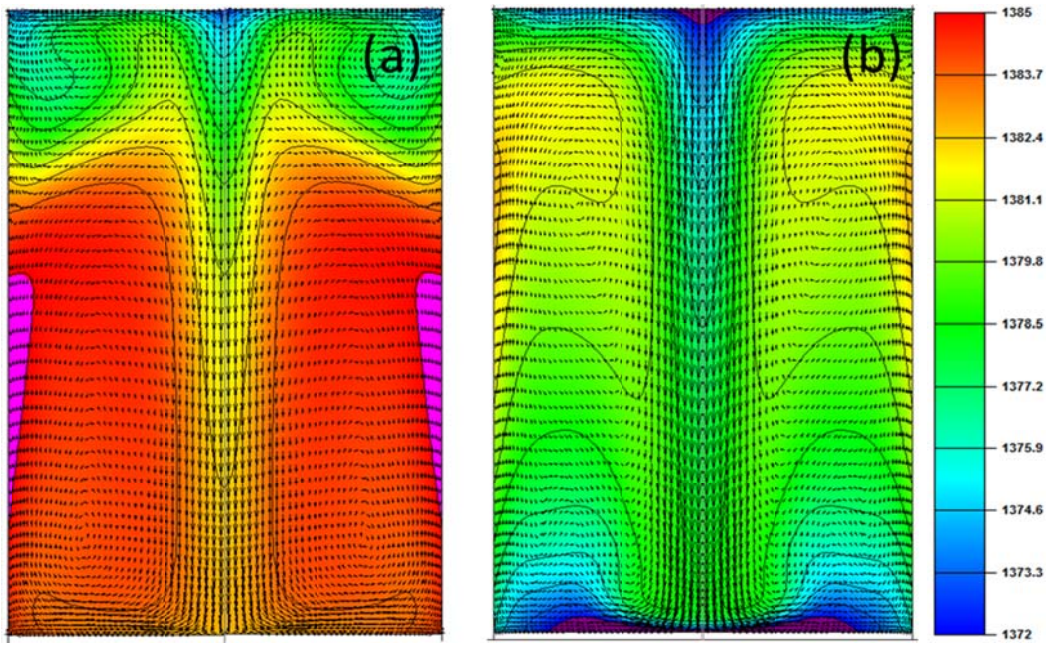

Figure 88 Iso-therm profile of Cd(Zn)Te melt obtained using a flat bottom pBN crucible in conjunction with (a) quartz pedestal support and (b) SiC pedestal support.

With respect to melt convection, there is substantially lower melt convection observed using the Quartz rather than the SiC pedestal geometry as is presented in **Figure 89**. This result is a direct consequence of the lower temperature gradient imposed by the Quartz pedestal compared to the SiC pedestal. According to **Equation 15**, this reduced convective intensity will result in a thicker thermal boundary layer (δ), as the convection velocity (v_c) is reduce. The term α is the thermal diffusivity of the melt and R is the crucible radius. Due to the lower intensity of the melt convection, and the homogenous temperature distribution throughout the melt, a second convection cell near the upper surface of the forms as Marangoni forces start to become more influential.

Equation 27 $$\delta \sim \sqrt{\alpha \cdot R / v_c}\delta$$

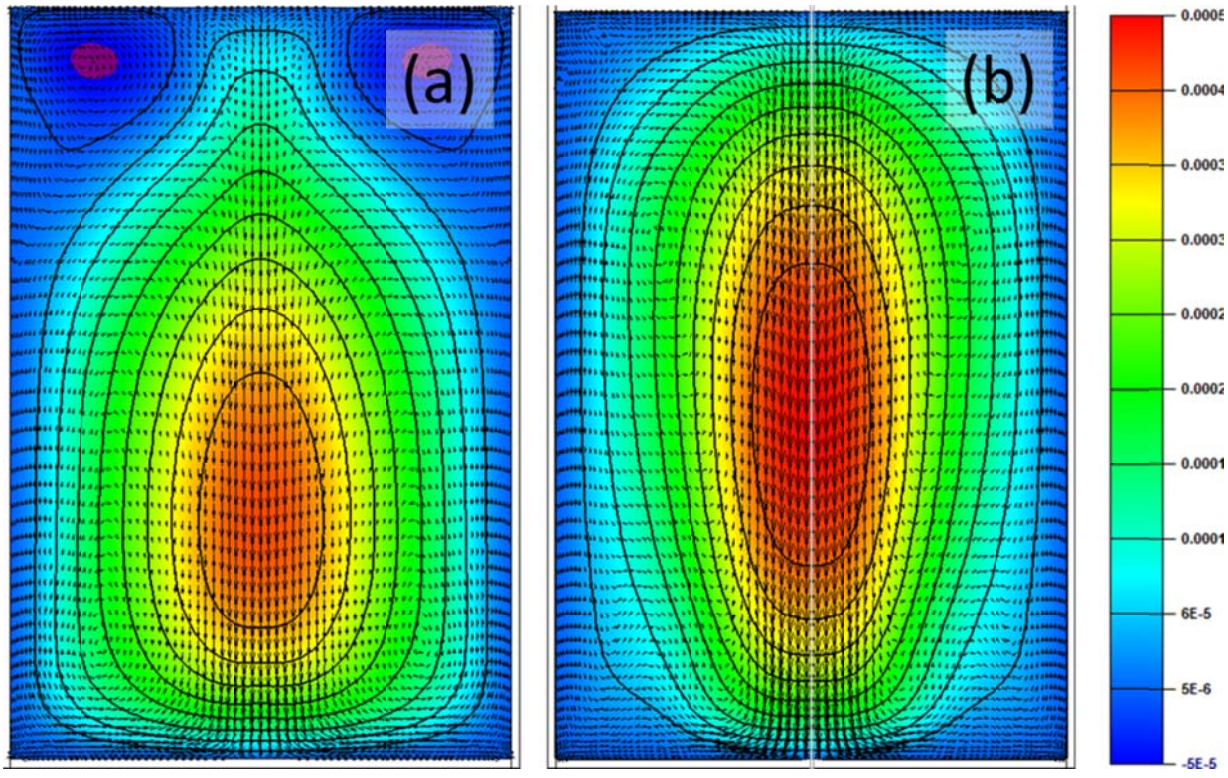

Figure 89 Convection of Cd(Zn)Te melt obtained using a flat bottom pBN crucible in conjunction with (a) quartz pedestal support and (b) SiC pedestal support.

With respect to homogenization and superheating for breaking apart a structured melt, a material with low thermal conductivity is more desirable. This is because the heat extracted by the pedestal effectively lowers the *in-situ* temperature of the melt by several degrees. This cooling of the may prevent that the charge is completely molten at the tip, or may require substantially higher temperatures to complete material homogenization.

However, in the case of crystal growth where the directional solidification releases a corresponding quantity of latent heat, this lower thermal conductivity is undesirable. The less intense convection will produce a thicker boundary layer which will lead to a decrease in the thermal gradient across the melt directly in front of the SLI following **Equation 16**. The term ΔT is the temperature difference across the boundary layer.

Equation 28 $$G = \Delta T \ / \ \delta$$

Finally it is important to observe that in the case of the SiC pedestal, the intensity and of melt flow is directed towards the center of the crucible, a consequence of the higher thermal conductivity of the pedestal material and convergence of the heat flux vectors. This strong convective cell pushing the hot liquid from the center down towards the interface has the effect of inhibiting growth near the center as may be seen in **Figure 90**. Indeed, the interface shape at the onset of crystal growth is irregular with two 'humps' located off-center. It is possible that through changing the geometry of the SiC pedestal, this interface deflection may be suppressed, however requires further investigation.

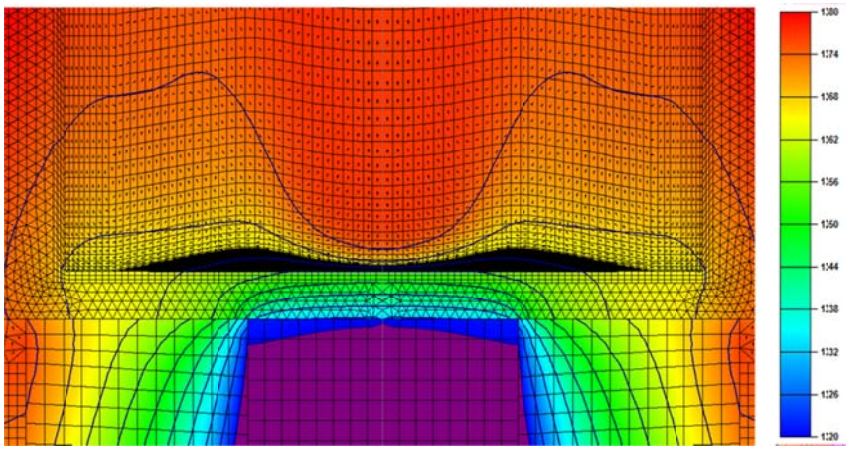

Figure 90 Convection of Cd(Zn)Te melt obtained using a flat bottom pBN crucible in conjunction with a SiC pedestal support.

7.6 Conclusions and Future Work

In conclusion, an investigation of the material properties of Cd(Zn)Te has been completed. A 2-D model for the simulation of crystal growth applied towards Cd(Zn)Te has been developed. Preliminary studies using this model have given insight into the position of the thermocouples inside the furnace, as well as the role played by the SiC pedestal during the growth cycle.

To develop flow characteristics which are more beneficial to the formation of a stable, smooth, and convex solid liquid interface, it is necessary to study the effects of changing the geometry of the the SiC pedestal. Indeed even changing the shape of the pedestal from rod-like to cylindrical is of interest in order to deflect the high intensity melt convection from suppressing growth near the center. The objective will be to improve the SLI shape through the study of different pedestal materials and geometries and their effects on melt convection.

Three general geometries are depicted below in **Figure 91** for (a) cylindrical SiC pedestal geometries, (b) increasing the diameter of the rod-like SiC pedestal, and (c) increasing the diameter of the cylindrical SiC pedestal geometry. Each of these geometries are designed to deflect the intensity of the hot molten Cd(Zn)Te away from the interface, facilitating a planar or slightly convex growth interface. This design will also take into account the afore-mentioned study regarding the dis-engagement and re-engagement of the pedestal for homogenization. These components will be fully developed in 3-D and will be integrated into the design of the VGF system.

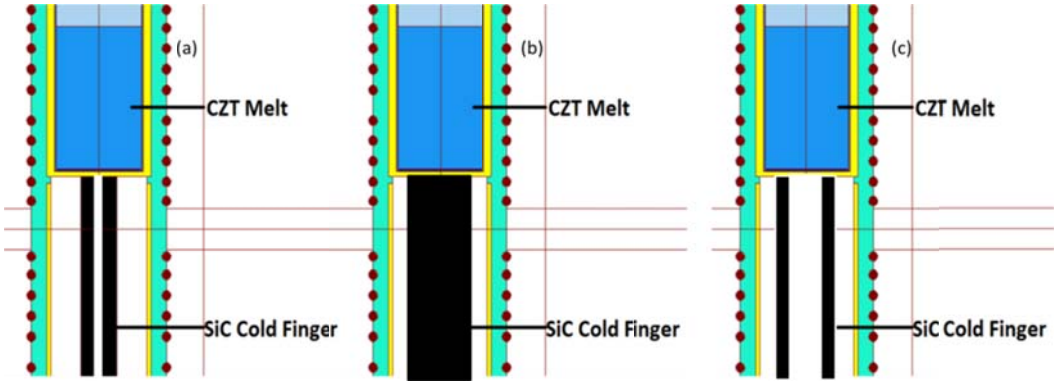

Figure 91(a) VGF furnace with CZT charge and tube-like SiC cold finger (engaged) (b) increasing diameter of SiC pedestal and (c) tube like SiC pedestal with larger diameter.

8 CHAPTER CONCLUSIONS AND FUTURE WORK

In summary, a great deal of effort has been put forth for improving the crystal growth capabilities at the Crystal Growth Laboratory. The process of melt homogenization and synthesis, crystal growth, and the development of a numerical model have all been critical to developing the knowledgebase necessary for crystal growth.

1) Results from the numerical model which has been developed for Cd(Zn)Te growth suggest the poly-crystal observed at the tail end of many ingots cap is likely associated with nucleation occurring at the melt surface. It was observed that superheating of the melt by 30ºC was sufficient to (i) improve material homogeneity, (ii) prevent nucleation from occurring at the melt surface, and (iii) increase overall yield. Infrared transmission measurements have been used to demonstrate how this superheating has reduced the size and density of secondary phases within the Cd(Zn)Te matrix.

2) A vacuum carbon coating system has been used for carbon coating of pBN crucible materials. To the extent of the Authors knowledge, this is the first time carbon coating has been applied to pBN crucibles. Results indicate this technology may be implemented for increasing the longevity of pBN crucible through reducing melt-crucible interactions. A second advantage of the carbon coating system is that the method may be reapplied, so it may be possible to re-deposit another carbon layer after a certain number of growth cycles. Detectors grown using cc-pBN crucible and harvested along the axis of growth exhibit high resistivity and good functionality as room temperature gamma ray detectors, indicating that the cc-pBN technology preserves, if not improves the resultant material quality of the process.

3) The dynamic adjustments of the temperature gradient results in melting back of the crystal during growth. This small melt-back procedure appears to improve the yield by shifting of resistivity maximum towards the crystal center. Measurement of photocurrent in mapping regime and mapping of the resistivity revealed, anti-correlation of these parameters in the beginning and central parts of the ingots and their

correlation at ingot ends. This fact may be explained by a slight shifting of the pinned Fermi level in the vicinity of the deep level energy. The effect of the dynamic temperature adjustment appears to be beneficial, not only in terms of the electrical properties, but also in terms of the structural properties, as is evidenced by the increased grain sizes.

4) Using all of this developed technology, Cd(Zn)Te has been grown implementing a furnace geometry designed specifically for improving the thermal environment during crystal growth (80)- (83). As a result, relatively large crystal grains and volumes have been obtained for 50mm ingots. The benefit of using this thermal geometry has been demonstrated by comparing Cd(Zn)Te ingots grown with and without the SiC pedestal. Gamma spectra are presented for planar devices which have been harvested from the First to Freeze regions which are most influence by the effects of the SiC pedestal. The results demonstrate the benefit of using a pedestal with sufficiently high thermal conductivity which extracts the latent heat of solidification at the very beginning of the crystal growth cycle.

5) A 2-D model for the simulation of crystal growth applied towards Cd(Zn)Te has been developed. Preliminary studies using this model have given insight into the position of the thermocouples inside the furnace, as well as the role played by the SiC pedestal during the growth cycle, as well as nucleation which may occur at the melt surface.

9 BIBLIOGRAPHY

1. *Growth of High Purity CdTe Single Crystals by Vertical Zone Melting.* **R. Triboulet, Y. Marfaing.** 1973, J. Electrochem. Soc. Sol. Stat. Sci. and Tech., Vol. 120, p. 1260.
2. *Traveling Heater Method Preparation and Composition Analysisof CdTe Ingots.* **N. Audet, V.N. Guskov, J.H. Greenberg.** 2005, J. Elec. Mater., Vol. 34, p. 687.
3. *Fundamentals of the CdTe Synthesis.* **Triboulet, R.** 2004, J. of Alloys and Compounds, Vol. 371, pp. 67-71.
4. *Modified Growth of CZT Single Crystas.* **S. Zhu, B. Zhao, Q. Li, F. Yu, S. Shao, X. Zhu.** 2000, J. Crystal Growth, Vol. 208, pp. 264-268.
5. *Growth of CZT Crystals by Bridgman Technique with Controlled Overpressures of Cd.* **C. Su, S. Lehoczky.**
6. *Crystal Growth and Characterization of Detector Grade CZT Crystals.* **M. Fiederle, A. Fauler, Z. Zwerger.** 2007, IEEE Trans. on Nucl. Sci., Vol. 54, p. 769.
7. *Correlation between Ingot Diameter and Crystal Properties of CZT Grown by the Modified Bridgman Method.* **G. Yang, W. Jie, T. Want, G. Li, L. Li, H. Hua.** 2007, Crystal Growth and Design, Vol. 7, pp. 435-438.
8. *Characterization of CdTe Crystals Grown by the Bridgman Method.* **M. Fiederle, A. Fauler, V. Babenstov, J. Franc, J. Konrath, M. Webel, J. Ludwig, K.W. Benz.** 2003, Nuc. Inst. and Meth. in Phys. Res. A, Vol. 509, pp. 70-75.
9. *Growth and properties of semi-insulating CdZnTe for radiation detector applications.* **C. Szeles, M. C. Driver.** San Diego : s.n., 1998. SPIE Conference on Hard X-ray and Gamma-Ray Detector Physics and Applications. Vols. 3446, 1.
10. *Characterization of large cadmium zinc telluride crystals grown by traveling heater method",.* **H.Chen, S.A.Awadalla, K.Iniewski, P.H.Lu, F.Harris, J.Mackenzie, T.Hasanen, H.Chen, R.Redden, G.Bindley, I.Kuvvetli, C. Budtz-Jorgensen, P.Luke, M.Amman, J.S.Lee, A.E.Bolotnikov, G.S.Camarda, Y.Cui, A.Hossain, R.B.James.** 1, 2008, J.Appl.Phys., Vol. 103, p. 014903.
11. *Characterization of 100 mm Diameter CZT Single Crystals Grown by the Vertical Gradient Freeze Technique.* **T. Asahi, O. Oda, Y. Taniguchi, A. Koyama.** 1995, J. Crystal Growth, Vol. 149, pp. 23-29.
12. *Vapor-Phase Growth of Bulk Crystals of Cadmium Telluride and Cadmium Zinc Telluride on GaAs Seed.* **J. T. Mullins, B. J. Cantwell, A. Basu, Q. Jiang, A. Choubey, A.W. Brinkman, and B.K. Tanner.** 2008, J. Electron. Mater., Vol. 37, p. 1460.
13. *Understanding horizontal Bridgman shelf growth of cadmium telluride and cadmium zinc telluride. I. Heat and momentum transfer.* **K. Edwards, J.J. Derby.** 1-2, 1997, J. Crystal Growth, Vol. 179, pp. 120-132.
14. *Defect Structure of High Resistive CdTe:In Prepared by Vertical Gradient Freeze.* **J. Franc, V. Babensotv, M. Fiederle, E. Belas, R. Grill, K. W. Benz, P. Hoeschl.** 3, 2004, IEEE Trans. Nucl. Sci., Vol. 51.
15. *Modified Bridgman Growth of CdTe crystals.* **E. Sacudeo, P. Rudolph, E. Dieguez.** 2008, J. Crystal Growth, Vol. 310, pp. 2067-2071.

16. *Improvements in Production of CZT Crystals Grown by the Bridgman Method.* **H.L. Glass, A.J. Socha, C.L. Parfeniuk, D.W. Bakken.** 1998, J. Crystal Growth, Vol. 184/185, pp. 1035-1038.
17. *Improvement in crystalline quality of CdZnTe crystals grown in graphite crucible.* **A. Garg, M. Srivastava, R.C. Narula, R.K. Bagai, V. Kumar.** 2004, J. Crystal Growth, Vol. 260, pp. 148-158.
18. *Dewetting application to CdTe single crystal growth on earth.* **N. Chevalier, P. Dusserre, J. Garandet, T. Duffar.** 2004, J. Crystal Growth, Vol. 261, pp. 590-594.
19. *Boron Oxide Encapsulated Vertical Bridgman Grown CdZnTe Crystals as X-Ray Detector Material.* **A.Zappettini, M.Zha, L.Marchini, D.Calestani, R.Mosca, E.Gombia, L.Zanotti, M.Zanichelli, M.Pavesi, N.Auricchio, E.Caroli.** 4, IEEE Trans. Nucl. Sci., Vol. 56, p. 1.
20. *Growth of high resistivity CdTe and (Cd,Zn)Te crystals.* **M. Fiederle, V. Babentsov, J. Franc, A. Fauler, J.P. Konrath.** 2003, Cryst. Res. Technol., Vol. 38, p. 588.
21. *State of the art and prospects of photorefractive CdTe.* **Y. Marfaing.** 1999, J. Crystal Growth, Vol. 197, p. 707.
22. *Electrical properties and X-ray spectrum of semi-insulating CZT:Pb crystals.* **J.H. Won, K.H. Kim, S.H. Cho, J.H. Suh, J.K. Hong, S.U. Kim.** 2008, Nuc. Instr. Meth. Phys. Res. A, Vol. 586, pp. 211-214.
23. **V. Carcelen, N. Vijayana, E. Dieguez, A. Zappettini, M. Zha, L. Sylla, A. Fauler, M. Fiederle.** 11, 2008, J. Optoelectron. Adv. M, Vol. 10, pp. 3135 – 3140.
24. *Vapor pressure scanning of non-stoichiometry in Cd0.9Zn0.1Te and Cd0.85Zn0.15Te.* **Guskov, V.N. and Greenberg, J. H.** 2006, Journal of Crystal Growth, Vol. 289, pp. 552-558.
25. *CdT I: Solidus Curve and Composition-Temperature-Tellurium Partial Pressure Data for Te-rich CdTe(s) from Optical Density Measurements.* **R. Fang, R.F. Brebrick.** 4, 1996, J. Phys. Chem. Sol., Vol. 57, pp. 443-450.
26. *Measurements of High Temperature Heat Content of the II-VI and IV-VI (II:Zn, Cd IV:Sn, Pb VI:Se, Te) Compounds.* **K. Yamaguchi, K. Kameda, Y. Takeda, K. Itagaki.** 2, 1994, Mater. Trans. JIM, Vol. 35, p. 118.
27. *Basic problems of vertical Bridgman growth of CdTe.* **P. Rudolph, M. Mühlberg.** 1993, Mater. Sci. & Eng. B, Vol. 16, p. 8.
28. *Fundamental Studies on Bridgman Growth of CdTe.* **Rudolph, P.** 1994, Prog. Crystal Growth and Charact., Vol. 29, pp. 275-381.
29. *Challenges, Modeling the Crystal Growth of Cadmium Zinc Telluride: Accomplishments and Future.* **J.J. Derby, D. Gasperino, N. Zhang, and A. Yeckel.** 05, 2009, Mater. Res. Soc. Symp. Proc., Vol. 1164.
30. *Computational Models for Crystal Growth of Radiation Detector Materials: Growth of CZT by the EDG Method.* **J.J. Derby, and D. Gasperino.** O5, 2005, Mater. Res. Soc. Symp. Proc., Vol. 1038.
31. *In situ studies of Cd1−xZnxTe nucleation and crystal growth.* **B. W. Choi, H.N.G. Wadley.** 1-4, 2000, J. Crystal Growth, Vol. 208, p. 219.
32. *Crystalline and chemical quality of CdTe and Cd1-xZnxTe grown by the Bridgman method in low temperature gradients.* **M. Muehlberg, P. Rudolph, C. Genzel, B. Wermke, U. Becker.** 1-4, 1990, J. Crystal Growth, Vol. 101, p. 275.

33. *Characterization of pyrolytic boron nitride for semiconductor materials processing.* **Moore, A.W.** 1, 1990, J. Crystal Growth, Vol. 106, p. 6.
34. *Characterization of InP grown by LEC using glassy carbon, silica, and pBN crucibles.* **C. Oliveira, M.M.G. de Carvalho,C.A.C. Mendonca, C.R. Miskys, G.M. Guadalupi, M. Battagliarin, M. Bueno.** 4, 1998, J. Crystal Growth, Vol. 186, pp. 487-493.
35. *Control of Defects in the Production of CdZnTe Crystal by the Bridgman Method.* **H. L. Glass, A. J. Socha, D. W. Bakken, V. M. Speziale, J. P. Flint.** 1998, Mat. Res. Soc. Symp. Proc., Vol. 487.
36. *Boron Nitride Coating of Fused Silica Ampoulles for Semiconductor Crystal Growth.* **R. Shetty, W. R. Wilcox.** 1, 1995, J. Crystal Growth, Vol. 153, pp. 97-102.
37. *Influence of Ampoulle Coatings on CdTe Solidification.* **R. Shetty, W. R. Wilcox, L. L. Regel.** 3-4, 1995, Vol. 153, pp. 103-109.
38. *Computational Models for Crystal Growth of Radiation Detector Materials: Growth of CZT by the EDG Method.* **J.J. Derby, D. Gasperino.** O5, 2005, Mater. Res. Soc. Symp. Proc., Vol. 1038.
39. *On Crucible Effects During the Growth of CdZnTe in an Electrodynamic Gradient Freeze Furnace.* **D. Gasperino, M, Bliss, K. Jones, K. Lynn, J.J.Derby.** 8, 2009, J. Crystal Growth, Vol. 311, pp. 2327–2335.
40. *Influence of pyrolytic boron nitride crucibles on GaAs crystal growth process and crystal properties.* **L. Fischer, U. Lambert, G. Nagel, H. Riifer, E. Tomzig.** 3, 1995, J. Crystal Growth, Vol. 153, pp. 90-96.
41. *Study of the Effects of Edge Morphology on Detector Performance by Leakage Current and Cathodoluminescence.* **J. Crocco, H. Bensalah, Q. Zheng, F. Dierre, P. Hidalgo, J. Carrascal, O. Vela, J. Piqueras, E. Dieguez.** 4, IEEE Trans. Nucl. Sci., Vol. 58, pp. 1935-1941.
42. *Bridgman growth of detached GeSi crystals.* **M.P. Volz, M. Schweizer, N. Kaiser, S.D. Cobb, L. Vujisic, S. Motakef, F. R. Szofran.** 2002, J. Crystal Growtn, Vols. 237-239, pp. 1844-1848.
43. *Crucible de-wetting during bridgman growth of semiconductors in microgravity.* **T. Duffar, I. Paret-Harter, P. Dusserre.** 1-2, 1990, J. Crystal Growth, Vol. 100, p. 171.
44. **Quartz, Heraus.** Quartz Glass Tubes. *Heraeus Quartz Glass.* [Online] www.base-materials.heraeus-quarzglas.com.
45. *CdTe and CdZnTe for nuclear detectors: facts and fictions.* **P. Fougeres, P. Siffert, M. Hageali, J. M. Koebel, R. Regal.** 1, 1999, Nucl. Instr. Meth. Phys. Res. A, Vol. 428, pp. 38-44.
46. *Modeling the vertical Bridgman growth of cadmium zinc telluride II. Transient Analysis of Zinc Segregation.* **S. Kuppurao, S. Brandon, J.J. Derby.** 1995, J. Crystal Growth, Vol. 155, pp. 103-111.
47. *Indium dopant behaviour in CdTe single crystals.* **P. Fochuk, O. Panchuk, P. Feychuk, L. Shcherbak, A. Savitskyi, O. Parfenyuk, M. Ilashchuk, M. Hage-Ali, P. Siffert.** 2001, Nuc. Inst. Meth. Phys. Res. A, Vol. 458, pp. 104-112.
48. *The Solubility and Diffusivity of In in CdTe.* **E. Watson, D. Shaw.** 3, 1983, J. Phys. C, Vol. 16, p. 515.
49. *The Origins of Twinning in CdTe.* **A.W. Vere, S. Cole, D.J. Wililams.** 3, 1983, J. Elec. Mater., Vol. 12, p. 551.

50. *Czochralski Growth of CdTe and CdMnTe from Liquid Encapsulated Melts.* **H.M. Hobgood, B.W. Swanson, R.N. Thomas.** 1987, J. Crystal Growth, Vol. 85, pp. 510-520.
51. *Characterization of Bulk and Surface Transport Mechanisms by Means of the Photocurrent Technique.* **M.Zanichelli, M.Pavesi, A.Zappettini, L. Marchini, N.Auricchio, E. Caroli, and M. Manfredi.** 6, 2009, IEEE Trans. Nuc. Sci., Vol. 56, pp. 3591-3596.
52. *Photoconductivity mapping of semi-insulating CdTe",.* **J.Kubát, J.Franc, V.Dědič, E.Belas, P.Moravec, V.Babentsov, P.Höschl, R,Grill.** 4, 2011, IEEE Trans. Nucl. Sci. , Vol. 58, pp. 1953-1957.
53. *Compensation and carrier trapping in indium-doped CdTe, Contributions from an important near-mid-gap donor.* **V. Babentsov, J. Franc, R. James,.** 2009, Appl. Phys. Lett., Vol. 95, p. 052102.
54. **Triboulet., R.** [ed.] H.J. Scheel and T. Fukuda. *Crystal Growth Technology.* s.l. : Wiley,, (2003), p. 373.
55. *Fundamentals of the CdTe and CdZnTe bulk growth.* **Triboulet, R.** 5, 2005, Phys. Stat. Sol. (c), Vol. 2, pp. 1556-1565.
56. **V.M. Glazov, S.N. Chizhevskaya, and N.N. Glagoleva.** *Liquid Semiconductors.* New York : Plenum, 1969.
57. **Rule, T. D.** *Experimental Validation Of (Cd,Zn)Te Growth Model.* Washington State University. 2002.
58. *Structure rearrangement of the Cd1−xZnxTe (0 < x < 0.1) melts.* **L. Shcherbak, P. Feychuk, Yu. Plevachuk, Ch. Dong,.** 2004, Journal of Alloys and Compounds, pp. 186-190.
59. *Study of the Effects of Edge Morphology on Detector Performance by Leakage Current and Cathodoluminescence.* **J. Crocco, et. al.** 2011, IEEE. Trans. on Nucl. Sci., Vol. In Press.
60. *Photoinduced current transient spectroscopy in high-resistivity bulk materials: Instrumentation and methodology.* **M. Tapiero, N. Benjelloun, J.P Zielinger, S. El Hamd, C. Noguet.** 1988, J. Appl. Phys., Vol. 64, p. 4006.
61. *Photo-induced current transient spectroscopic study of the traps in CdTe.* **Mathew, X.** 2003, Solar Energy Mater. and Solar Cells, Vol. 76, pp. 225-242.
62. *Real defect concentration measurements of nuclear detectormaterials by the combination of PICTS and SCLC methods.* **M. Ayoub, M. Hage-Ali, J.M. Koebel, R. Regal, C. Rit, F. Klotz, A. Zumbiehli, P. Siffert.** 2001, Mater. Sci. & Eng., Vol. B83, pp. 173-179.
63. *Comprehensive Study of Semi-Insulated Cd1-xZnxTe Grown by the Bridgman Method.* **J.V. Babenstov, J. Franc, J. Zazvorka, E. Dieguez, J. Crocco, M.V. Sochinskyi, R.B.James.** In Press.
64. *Deep Energy Levels in CdTe and CdZnTe.* **A. Castaldini, A. Cavallini, and B. Fraboni, P. Fernandez, J. Piqueras.** 4, 1998, J. Appl. Phys., Vol. 83, p. 4.
65. *Cathodoluminescence and photoinduced current transient spectroscopy studies of defects in Cd0.8Zn0.2Te.* **A. Castaldini, A. Cavallini, B. Fraboni, L. Polenta, P. Fernandez, J. Piqueras.** 11, 1996, Phys. Rev. B, Vol. 54, p. 7622.

66. *Properties of CdZnTe crystals grown by High Pressure Bridgman.* **A. Drighil, R. Adhiri, C. Sribi, M. Mousstad, K. Cherkaoui, G. Marrakchi, A. Zerrai, M. Zazoui.** 1, 1999, M. J. Cond. Matter, Vol. 2.
67. *CdTe and CdZnTe for nuclear detectors: facts and fictions.* **P. Fougeres, P. Siffert, M. Hageali, J. M. Koebel, R. Regal.** 1999, Nucl. Instr. Meth. Phys. Res. A, Vol. 428, pp. 38-44.
68. *Effects of copper in high resistivity CdTe.* **B. Biglari, M. Samimi, M. Hage-Ali, J.M. Koebel, P. Siffert.** 4, 1988, J. Crystal Growth, Vol. 89, pp. 428-434.
69. *Detailed characterization of deep centers in CdTe: Photoionization and thermal ionization properties.* **T. Takebe, J. Sarie, H. Matsunami.** 1, 1982, J. Appl. Phys., Vol. 53, p. 457.
70. *Defective states induced in CdTe and CdZnTe detectors by high and low energy neutron irradiation.* **A. Cavallini, B. Fraboni, W. Dusi, M. Zanarini.** 5, 2003, J. Appl. Phys., Vol. 94.
71. *Point defects in CdZnTe Crystals Grown by Different Techniques.* **R, Gul, A. Bolotnikov, H. K. Kim, R. Rodriguez, K. Keeter, Z. Li, G. Gu, R. B. James.** 3, 2011, J. Electron. Mater., Vol. 40, p. 274.
72. *Theory of Te Precipitation and Related Effects in CdTe Crystals.* **R.D.S. Yadava, R.K. Bagai, W.N. Borle.** 10, 1992, J. Electron. Mater., Vol. 21.
73. *Advances in the High-pressure Crystal Growth Technology of Semi-insulating CdZnTe for Radiation Detector Applications.* **C. Szeles, S. Cameron, J. Ndap, M. Reed.** San Diego : s.n., 2003. SPIE Conference on Hard X-Ray, Gamma-Ray and Neutron Detector Physics V.
74. *Development of the High-Pressure Electro-Dynamic Gradient.* **C. Szeles, et. al.** 6, 2004, J. Electron. Mater., Vol. 33, p. 742.
75. *Characterization of detector-grade CdZnTe crystals grown by the Travelling Heater method.* **S.A. Awadalla, et al.** 2010, J. Crystal Growth, Vol. 312 , pp. 507-513.
76. *Spectral Response of THM Grown CdZnTe Crystals.* **H. Chen, et al.** 3, 2008, IEEE Trans. Nucl. Sci, Vol. 55.
77. *Crystal growth of large-diameter bulk CdTe on GaAs wafer seed plates.* **J.T. Mullins, B.J. Cantwell, A. Basu, Q. Jiang, A. Choubey, A.W. Brinkman.** 7-9, 2008, J. Crystal Growth, Vol. 310, pp. 2058-2061.
78. *Seed-free growth of (1 1 1) oriented CdTe and CdZnTe crystals by solid-state recrystallization.* **S. Hassani, A. Lusson, A. Tromson-Carli, R. Triboulet.** 2003, J. Crystal Growth, Vol. 249, pp. 121-127.
79. *Full encapsulated CdZnTe crystals by the vertical Bridgman method.* **M. Zha, A. Zappettini, D. Calestani, L. Marchini, L. Zanotti, C. Paorici.** 7-9, 2008, J. Crystal Growth, Vol. 310, p. 2072.
80. *Designing thermal environments to promote convex interface shapes during the vertical Bridgman growth of cadmium zinc telluride.* **S. Kuppurao, J. J. Derby.** 3-4, 1997, J. Crys.l Grwth., Vol. 172, pp. 350-360.
81. *D. Gasperino, M. Bliss, K. Jones, K. Lynn, J. Derby.* **Furnace, On crucible effects during the growth of Cadmium Zinc Telluride in an EDG.** 2009, J. Crystal Growth, Vol. 311, pp. 2327-2335.

82. *Challenges, Modeling the Crystal Growth of Cadmium Zinc Telluride: Accomplishments and Future.* **J.J. Derby, D. Gasperino, N. Zhang, and A. Yeckel.** 2009, Mater. Res. Soc. Symp. Proc., Vol. 1164.
83. *Modeling the vertical Bridgman growth of cadmium zinc Telluride.* **S. Kuppurao, S. Brandon, J. Derby.** 1995, Journal of Crystal Growth , Vol. 155, pp. 93-102.
84. *D. Gasperino, M. Bliss, K. Jones, K. Lynn, J. Derby.* **Furnace, On crucible effects during the growth of Cadmium Zinc Telluride in an EDG.** 2009, J. Crystal Growth, Vol. 311, pp. 2327-2335.
85. *The Correlation Between Superheating and Supercooling in CdTe melts during unseeded Bridgman Growth.* **M. Muhlberg, P. Rudolph, M. Laasch, E. Tesser.** 1993, J. Crystal Growth, Vol. 128, pp. 571-575.
86. *Crystal Growth and Characterization of Detector Grade CZT.* **M. Fiederle, A. Fauler, A. Zwerger.** 4, 2007, IEEE Trans. Nucl. Sci., Vol. 54.
87. *Electron Backscatter Diffraction Analysis of a CZT Growth Tip from a VGF furnace.* **S.K. Sundaram, C.H. Henager, D.J. Edwards, A.L. Schemer-Kohrn, M. Bliss, B.R. Riley.** 2010, J. Crystal Growth, Vol. In press.
88. *CZT Growth.* **Rule, T.**
89. *Study of Different Cool Down Schemes During the Crystal Growth of Detector Grade CdZnTe.* **S. Swain, K. Jones, A. Datta, K. Lynn.** 5, 2011, IEEE Trans. Nucl. Sci. , Vol. 58, p. 2341.
90. *In situ studies of CdZnTe Nucleation and crystlal growth.* **B. W. Choi, H. N. G. Wadley.** 2000, J. Crystal Growth, Vol. 208, pp. 219-230.
91. *Influence of surface preparation on CdZnTe nuclear radiation detectors.* **Q. Zheng, F. Dierre, J. Crocco, V. Carcelen, H. Bensalah, J.L. Plaza, E. Dieguez.** 2011, App. Surf. Sci., Vol. 257, pp. 8742-8746.
92. *Comparison of radiation detector performance for different metal contacts on CdZnTe deposited by electroless deposition method.* **Q. Zheng, F. Dierre, M. Ayoub, J. Crocco, H. Bensalah, V. Corregidor, E. Alves, R. Fernandez-Ruiz, J. M. Perez, and E. Dieguez.** 11, 2011, Cryst. Res. Technol., Vol. 46, pp. 1131-1136.
93. *Phase Diagram of the Zn-Cd-Te Ternary System.* **J. Steininger, A. Jacques, F. Brebick.** 1970, J. Electrochem Soc , Vol. 117 , p. 1305.
94. *Decreasing lateral segregation in cadmium zinc telluride via ampoule tilting during vertical Bridgman growth.* **L. Lun, A. Yeckel, P. Daotidis, J. Derby.** 2006, J. Crystal Growth, Vol. 291, pp. 348-357.
95. *Kinetic Processes: Crystal Growth, Diffusion, and Phase Transition in Materials.* **Jackson, Kenneth. A.** Weinheim : WILEY-VCH Verlag GmbH & Co., 2000, p. 194. 3-527-30694-3.
96. *Study of impurity segregation,crystallinity,and detector performance of melt-grown cadmium zinc telluride crystals.* **M. Schieber, T.E. Schlesinger, R.B. James, H. Hermon, H. Yoon, M. Goorsky.** 2002, J. Crystal Growth, Vols. 237-239, pp. 2082-2090.
97. *GET PAPER.* **C. Szeles, E.E. Eissler.** 2998. MRS Symposium Proceedings. Vol. 3, p. 487.
98. **O. Knacke, O. Kubaschewski and K. Hesselmann.** *Thermochemical Properties of Inorganic Substances.* Berlin : Springer-Verlag, 1991.
99. **Yamaguchi:, K. Itagaki and K.** 1990, Thermochim. Acta, Vol. 163, p. 1.

100. **Zanio., K.** 1978, Semiconductors and Semimetals, Vol. 13.
101. **A. V. Vanyukov, A. A. Davydov and A. S. Tomson: Zh. Fiz.** 1964, Rus. J. Phys. Chem., Vol. 43, p. 2364.
102. **M. Shamsuddin, A. Nasar.** 1990, High Temp. Sci., Vol. 28, p. 245.
103. **Kulwicki, B. M.** *Ph. D. Dissertation.* Univ. of Michigan. Ann Arbor, Michigan : s.n., 1963.
104. *The Hg-Cd-Zn-Te phase diagram.* **T.C. Yu, R.F. Brebreck.** 5, 1992, J. of Phase Equilibria, Vol. 13.
105. **Shomate, C. H.** 1954, J. Phys. Chem, Vol. 58, p. 368.
106. *Thermodynamic Data for Inorganic Sulphides, Selenides and Tellurides.* **Mills., K. C.** s.l. : Butterworths, 1974. 040870537X / 0-408-70537-X.
107. *Thermochemical Properties of Inorganic Substances.* **I. Barin, O. Knacke, and O. Kubaschewski.** s.l. : Springer-Verlag, 1977.
108. *The heat capacity of CdTe and medium and high temperatures.* **L.M. Pavlova, A.S. Pashinkin, D.S. Gaev, A.S. Pak.** 6, 2006, High Temp., Vol. 44, p. 843.
109. *High temperature thermodynamic functions for refractory compounds.* **R. Mezaki, E.W. Tilleux, T.F. Jambois, J.L. Margrave.** Purdue University : s.n., 1965. Procs. Symp. Adv. in Thermophys. Proper. Ext. Temp. Press. p. 135.
110. *High Temperature Thermodynamic Data for CdTe(c).* **Brebrick, R. F.** 3, 2010, J. of Phase Equilib. and Diff., Vol. 31.
111. *Crystal growth of large-area single-crystal CdTe and CdZnTe by the computer-controlled vertical modified-Bridgman process.* **S. Sen, W. H. Konkel, S.J. Tighe, L.G. Bland, S.R. Sharma, and R.E. Taylor.** 4, 1990, J. Crystal Growth, Vol. 86.
112. *Vapour pressure investigation of CdZnTe.* **Guskov, V. N.** 2004, J. Alloys. Compounds, Vol. 371, p. 118.
113. *Eddy current determination of the electrical conductivity-temperature relation of Cdl_xZn xTe alloys.* **H.N.G. Wadley, B.W. Choi.** 1997, Journal of Crystal Growth, p. 323.
114. *The effects of Te precipitation on IR transmittance and crystalline quality of as-grown CdZnTe crystals.* **J. Zhu, X. Zhang, B. Li, J. Chu.** 1999, Infrared Phys Technology, Vol. 40, p. 411.
115. *High-temperature conductivity of solid and liquid CdTe.* **P. Hoschl, E. Belas, L. Turjanska, R. Grill, J. Franc, R. Fesh, P. Moravec.** 2000, J. Crystal Growth, Vol. 220, p. 444.

Chapter IV

Cd(Zn)Te Radiation Devices

This page intentionally left blank.

Chapter IV Content

1 INTRODUCTION

This chapter presents original results which have been produced during this thesis related with development of detectors based on Cd(Zn)Te. This chapter is divided into six sections, each related with a distinct aspect of detector development.

In the first section, state-of-the-art commercial detectors are characterized in terms of their electrical, optical, and detector characteristics. In addition, the defect structure of these devices is compared with those grown in this thesis investigation in order to highlight some important differences. These detectors were intended to serve as a reference for comparing the devices which have been developed in this thesis investigation.

In the second section of this chapter, the device fabrication protocol which has been developed over the course of this thesis investigation is presented. This includes wire-saw cutting, wafer lapping, polishing, chemical etching, as well as a novel surface cleaning procedure. These processes are necessary for preparing the surface of the detector material for subsequent metallization and electrode deposition.

In the third section, the type of surface treatment given to the lateral sides of a functioning detector is investigated, for the first time. Not only does the deformation of the Cd(Zn)Te surface by slicing and lapping impart dislocations into the material, but the extended depth of these defects could provide a larger volume of avenues for the surface leakage current to pass between anode and cathode and effectively degrade the signal to noise ratio of the detector. The lateral edges of the detector may act as a 'short circuit' under the correct circumstances. For this reason, special consideration to the treatment to the lateral sides is required, in order to identify practical methods for enhancing detector performance.

Section 4 of this chapter presents results from an investigation of the deep centers states induced by the lapping process. In order to study the deep centers present in Cd(Zn)Te devices and how these two treatments affect these energy levels, Photo Induced Current Transient Spectroscopy, or PICTS, has been used. PICTS is a technique whose technology has been developed over the past several decades for the analysis of the electronic properties in a number of semi-insulating materials

Section 5 presents results related with crystallographic twinning in Cd(Zn)Te. The objective of this investigation is to study the effects of twinning on the surface and bulk properties of Cd(Zn)Te. While the structural properties of twinning may have a negligible impact on the electrical properties of Cd(Zn)Te devices, these twins act as gettering planes, and also produce changes in the direction of the Cd-Te electric dipole. Furthermore, how the surface termination may affect surface states induced by the surface polarity is investigated.

Finally, in Section 6, an investigation into the asymmetric electrical I-V characteristics has been undertaken. This investigation has been carried out with three objectives, all oriented towards establishing reliable methods for the selection of the anode and cathode surfaces, independent of the crystallographic orientation. The objectives of this study are

1) to investigate how the asymmetry in I-V characteristics of Cd(Zn)Te devices is associated with the TeO_2 interfacial layer using RBS to study the structure at the Au-Cd(Zn)Te interface

2) Develop an understanding of how the concentration of traps in Cd(Zn)Te varies with the external bias polarity using PICTS to measure the energy and concentration of deep centers and

3) Propose non-destructive methods for selection of the anode and cathode which are not sensitive to crystallographic orientation i.e. chemical etching.

The results from each of these investigations represent the original work carried out during the course of this thesis for the development of radiation detectors based on Cd(Zn)Te.

This page intentionally left blank.

2 STATE OF THE ART: CHARACTERIZATION

Section Contents

2.1 Introduction

State of the art Cd(Zn)Te spectrometer devices were investigated in this work in order to establish a benchmark in terms of detector characteristics and performance. These detectors were intended to serve as a reference for comparing the devices which have been developed in this thesis investigation. It was necessary, therefore, to carry out characterization of the bulk electrical, optical, and structural properties of the commercial detectors.

The first characterization was that of the geometry of the detectors themselves. Presented in **Figure 1** are the commercial samples which have been studied in this work. Each sample exhibited two planar electrodes, but with one dark black spot on only one side. Furthermore, a red lacquer was applied, likely as a protective coating for lateral edges of each detector.

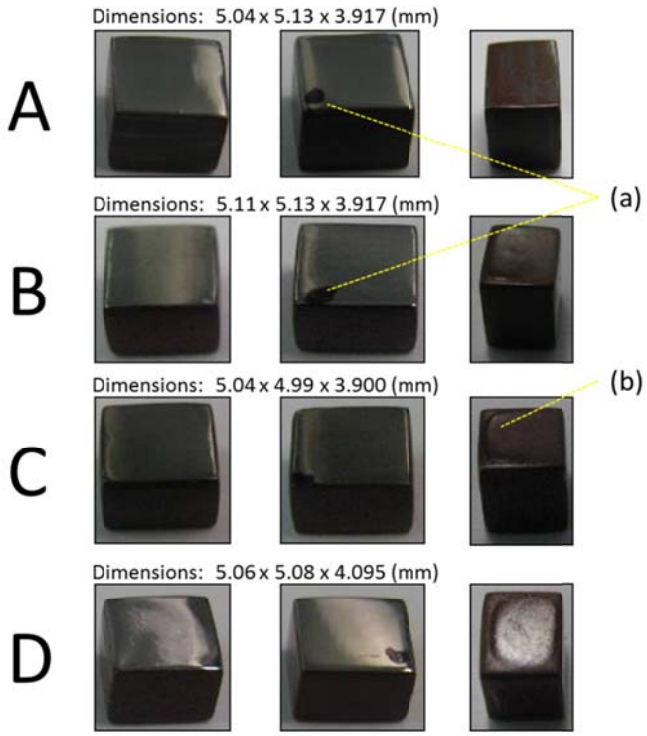

Figure 1 As-received samples Detectors A, B, C, and D. From Left to Right: Back side, Front side, lateral edges. (a) dark spot present on only one side of each detector (b) red-lacquer coating lateral edges of detectors.

2.2 Surface Measurements

Of these four detectors, Detectors A and B were selected for investigating the surface morphology of the devices, as well as the elemental composition of the electrode surface. The surface composition measurements were taken using an Energy Dispersive X-ray (EDS) detector coupled to a scanning electron microscope. From the surface morphology images of detectors A and B presented in **Figure 2**, the electrode surfaces appear smooth, with minimal scratching. Presented in

Table 1 are surface composition measurements which have been obtained using the EDS technique. From these measurements it is clear that Platinum electrodes were used for fabricating these planar spectrometers. Indeed, the type of metal used for electrodes deposition plays a strong role in affecting the electrical properties of the detector. Indeed, one of the challenges associated with achieving Ohmic contacts on wide bandgap materials are that the work functions of metals are usually not low enough to yield a low contact barrier.

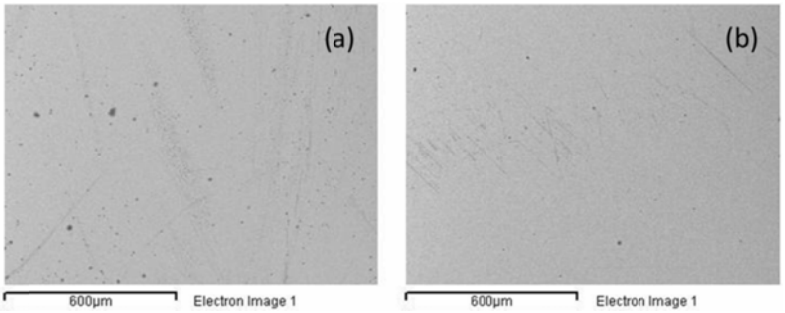

Figure 2 SEM measurements of commercial Cd(Zn)Te detectors (a) Detector A (b) Detector B.

Table 1 Surface composition of commercial Cd(Zn)Te detectors. All results are in atomic %.

	Zinc (at %)	Cadmium (at %)	Tellurium (at %)	Platinum (at %)
Detector A	4.89	31.27	32.96	30.89
Detector B	4.29	22.72	28.01	44.98

2.3 Electrical Characterization

The commercial detectors were characterized using the COREMA system to evaluate uniformity and magnitude of the samples′ bulk resistivity. Presented in **Figure 3** are the COREMA resistivity mappings which have been completed for each device. From these measurements, it is clear that all detectors exhibited bulk resistivity values between 1-4×10^9 Ω-cm.

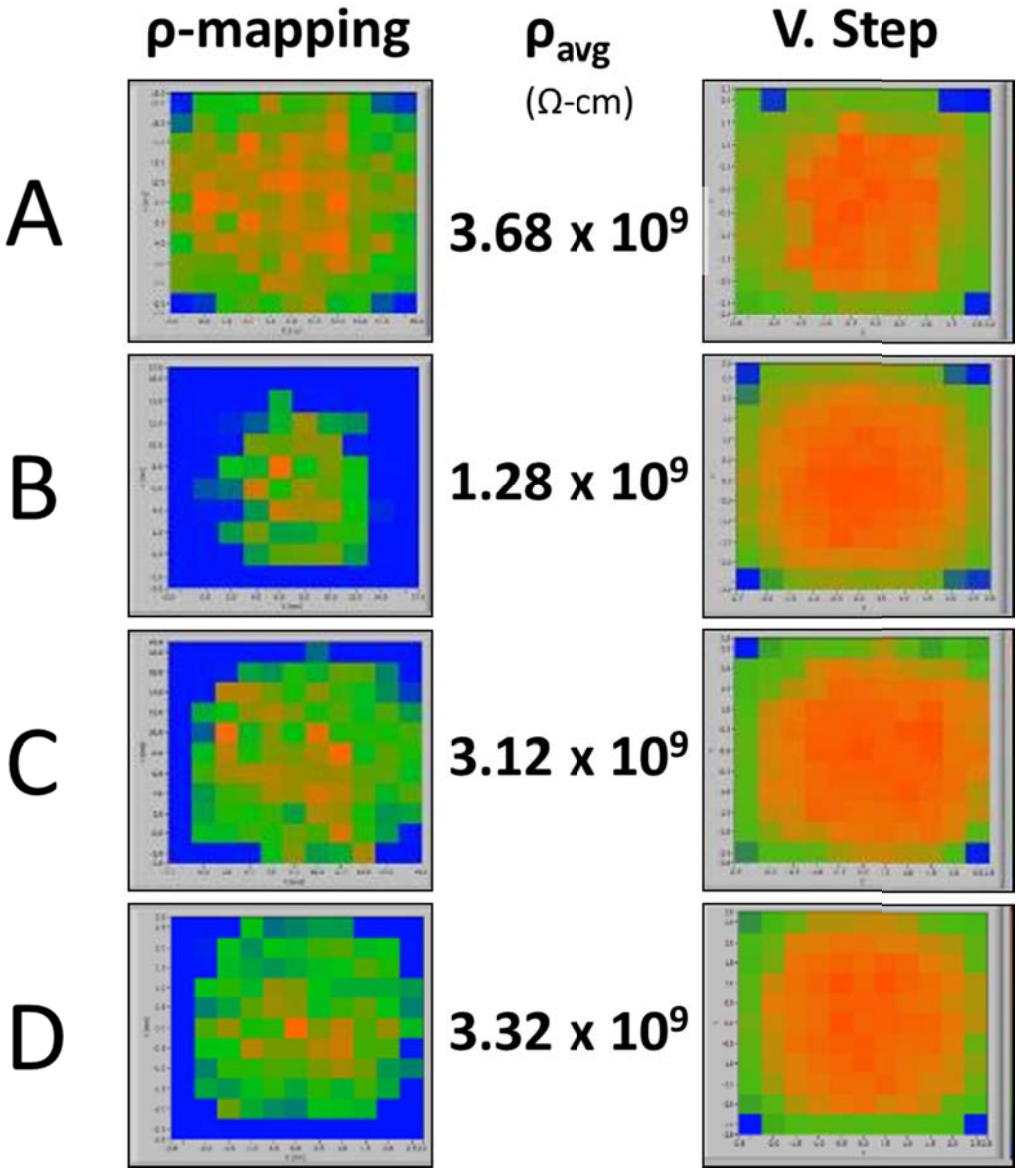

Figure 3 Left: COREMA resistivity mapping of Detectors A,B,C, and D Right: Voltage step applied to detector

Presented in **Figure 4** are the I-V characteristics for each commercial detector. Current - Voltage characteristics were measured using a computer-controlled Kiethley 2400 source meter to measure the detector leakage current under an external bias ranging from -200 V and +200 V. From these measurements, the I-V characteristics may be normalized in terms of current density and electrical field using the detector cross sectional area **A**, thickness **δ**, (see **Figure 1**), and by measuring the slope of the I-V characteristic using **Equation 1**.

Equation 1 $$\boldsymbol{\Omega = \frac{A}{\delta} \cdot \frac{I}{V}}$$

These characteristics exhibit a few interesting characteristics worth discussing. First of all, each detector exhibits Ohmic-type contacts, which are preferable for detector applications. Ohmic contacts are those which exhibit negligible contact resistance, such that the voltage drop across the semiconductor-metal contact region is negligible compared to the voltage applied across the device. For these reasons they are referred to as non-injecting or non-blocking as the current is nearly free to move across the metal-semiconductor junction under external bias.

This relationship describing the Ohmic behavior of the metal contacts be expressed using **Equation 2**, such that the exponent ***b*** describes the Ohmicity of the metal-semiconductor junction i.e. for ideal Ohmic contacts ***b*** = 1. With the exception of Device A which exhibited an exponent of 0.67, each of the other three devices B, C, and D each exhibited exponents very close to 1. The values obtained from the numerical fitting of experimental data are presented in **Table 2** on page 338.

Equation 2 $$\boldsymbol{I(V) = a \cdot V^{b}}$$

Secondly, the low leakage current and correspondingly high resistivity of the devices demonstrates that these devices may be suitable for gamma-ray spectroscopy applications. Specifically, the devices exhibit between 1-4 nA leakage current per 100 V/cm of applied electric field. However, it is interesting to note that the resistivity determined from the I-V characteristics is nearly an order of magnitude *higher* than that measured by the COREMA mapping system.

Indeed, this is a recurring phenomenon which has been observed across nearly all samples investigated throughout this investigation. One possible reason for this disagreement between the COREMA system and the I-V characteristics may be related with surface-state trapping of leakage current, which may reduce leakage current in the devices. This latter phenomenon associated with surface preparation is discussed in more depth in Section 7 on page 425 of this chapter.

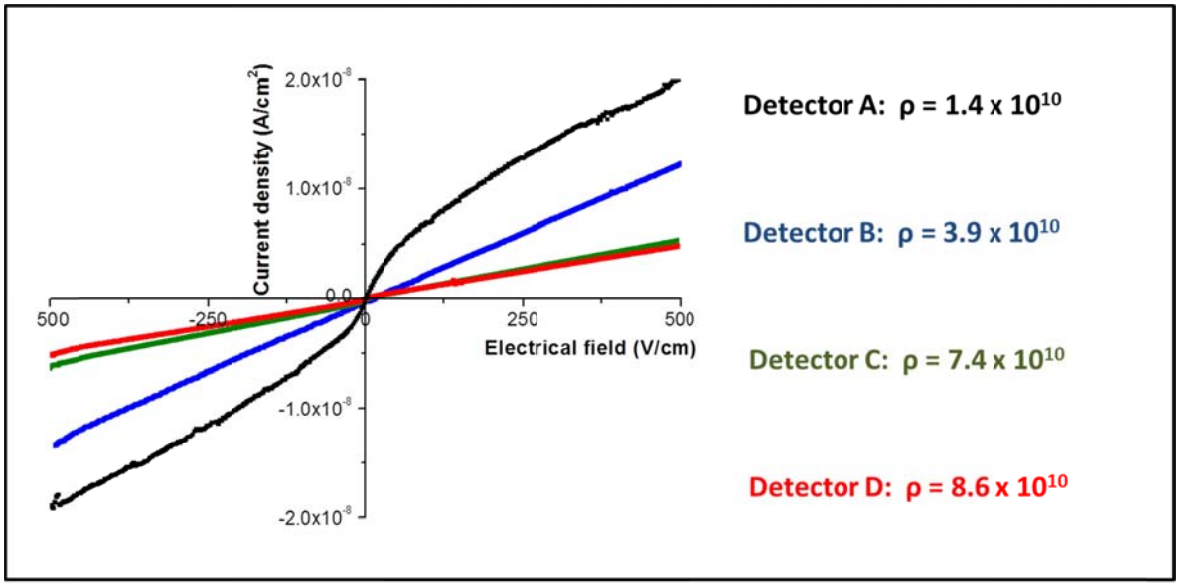

Figure 4 I-V characteristics for commercial samples

2.4 Infrared Microscope

The optical properties of the commercial detectors were analyzed using an Eclipse 90i Nikkon microscope using a DS-Qi1Mc camera for imaging. Presented in **Figure 5** are 5x, 10x, and 20x microscope images representative of the Te inclusions found within the samples. The 5x image shown below is of the near-surface of the sample analyzed. A thin 'dotted line' can be seen running across the sample surface. Although it may appear to be a scratch associated with the polishing process, a closer sub-surface examination reveals a plane of precipitates, very close in size (~7 micron diameter) and all aligned along a plane approximately 30^{o} normal to the surface. A white dotted line is drawn in **Figure 5**(a) to illustrate the direction of the inclusions. Faint dark shadows of these features can also be seen running parallel to this white marker in the

50x image. The 100x image shows the Te-inclusions halfway through the sample. The 200x image shown in **Figure 5**(c) well illustrates the triangular structure of the Te inclusions. Shown in **Figure 5**(d) are the Te-precipitates in the commercial samples, which are normally attributed to the retrograde solubility of Te in Cd(Zn)Te. These precipitates are between 0.5 and 2μm in diameter, are arranged in cellular structures, and are present in somewhat higher densities.

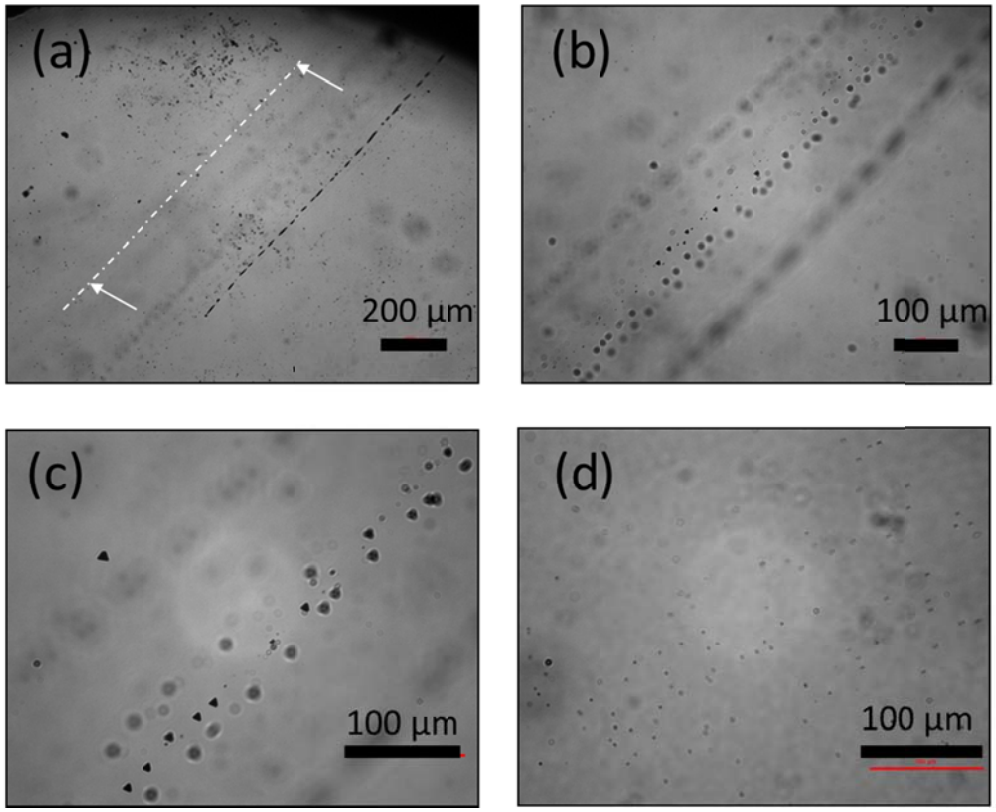

Figure 5 IR microscope images of Te Precipitates in commercial sample (a) 5x magnification (b) 10x magnification and (c) 20x magnification of Te-inclusions (d) 20x magnification of Te-precipitates

2.5 Electronic Defect Structure

One of the principle and most notable differences between the commercial detectors and the detectors grown in this thesis investigation is the electronic defect structure and the relative concentrations of defects present within the crystals.

To compare the commercial crystals with the crystals grown in this work, the bulk surfaces were polished, and characterized using Cathodoluminescence. This technique is a surface sensitive characterization technique which relies upon (1) excitation of surface and bulk states using an energetic beam of electrons, (2) the subsequent decay of these occupied surface states and the emission of photons in the optical region and (3) selection, detection, and amplification of the analog signal produced by these detected photons. Additional experimental details on this technique are presented in Section 3.2.2. Presented in **Figure 6** is the CL spectra of the commercial detectors A and B, as well as a typical CL spectra obtained for crystals grown using the methods discussed in Chapter 3 of this thesis. A summary of each of the defect levels present in each of the crystals is presented here.

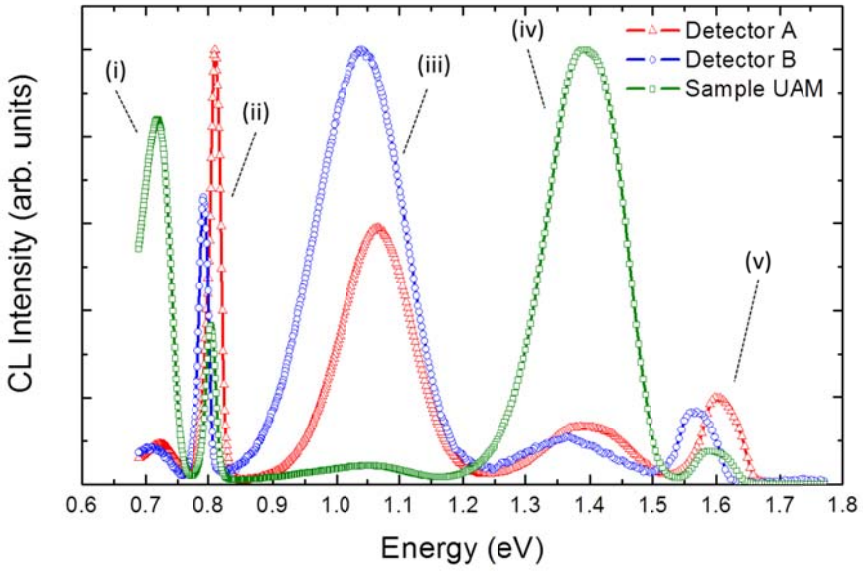

Figure 6 CL spectra obtained under high excitation conditions of commercial detectors and typical UAM device. The labeled defect bands may be associated with (i) Trap H (ii) Trap H1 (iii) Trap I (iv) Trap A (v) the bandgap of the material.

The peak emission near 1.6eV represents band to band transitions and permits the measurement of the bandgap of the material. From this bandgap parameter, the Zinc content of each device may be estimated (see **Table 2**, Section 3.3.1 of Chapter 2). As may be derived using the approach outlined in Chapter 2, Detector A exhibits a Zinc content near 16%, Detector

B exhibits a Zinc content between 9-10%, while the crystal grown by UAM exhibits a Zinc content near 13%.

The broad band centered about 1.4 eV may be related with surface damage or trace impurities, but in general has been attributed to family of crystalline point defects generally referred to as the A-center family (1) (2) (3) (4) (5), or Trap A. This family of point defects have been associated with cadmium vacancies forming complexes with metallic donor impurities such as [V_{Cd}, In_{Te}], but have also been attributed to impurities on Cd sites (6). The transition occurs with the valance band, thus exhibiting acceptor character, such that the activation energy of this defect may be described $E_a = E_v + 0.16$. As may be seen from the CL spectra, the peak emission associated with this band is much more intense in the UAM crystals than in the commercial devices investigated. Indeed, this higher intensity in the CL spectra corresponds to a higher luminescence and thus may indicate a higher concentration of these complexes. We attribute these differences in concentrations to the growth method which has been used for material synthesis (discussed in more detail below).

The wide band centered about 1.05 eV has been attributed to ionized V_{Te}^{+} and is referred to as Trap I following the naming convention proposed by (1). For the UAM grown samples, the concentration of this defect is relatively lower than the commercial detectors.

The narrow trap centered about 0.8 eV may be the trap referred to as Trap H1, which has been identified as a mid-gap donor level associated with Cl induced deep level in CdTe (1). This energy level is observed to be more intense for the commercial samples, which may suggest higher doping levels and the use of Cl as a dopant for achieving electrical compensation. This quite possibly may explain the lower intensity of this particular trap, as In has been used for achieving electrical compensation in the case of the UAM grown crystals. GDMS measurements of UAM grown crystals has also indicated the presence of Cl in low concentrations, which we attribute to the crucible cleaning procedure (see Chapter 3, Section 3).

The last defect observed in the CL spectra is centered about 0.7 eV and is likely the deep center responsible for pinning of the Fermi level. This defect has been attributed to an acceptor complex associated with the native defect V_{Cd} and a donor impurity, and has been termed Trap H throughout the literature (1). As the concentration of Trap A is more intense in the UAM grown devices than in the commercial crystals (i.e. related with V_{Cd}), it is consistent that this band will

also exhibit a higher luminescence. Furthermore, this level has been detected in the case of CdTe: In (7), which supports the strong luminescence in the UAM grown crystals, which have been doped using In to achieve electrical compensation.

CL Spectra have also been recorded under low excitation conditions to account for radiative centers with different lifetimes. Usually by low excitation, the luminescence intensity of defects with low lifetime increases compared to defects with very high lifetimes. This is also referred to as de-focused CL excitation, as the focal point of the CL beam is located just below the sample surface. As a result, a lower flux of electrons reach the surface, which results in lower excitation of surface states.

As may be seen from **Figure 7**, the dominant traps in the CL spectra are quite different for the commercial samples, and the samples grown in this thesis investigation. Indeed, in the case of the UAM grown crystals, the dominant features in the CL spectra are associated with the A-band (Trap A) and the ionized cadmium vacancies (Trap H) and with ionized tellurium vacancies in the case of the commercial detectors.

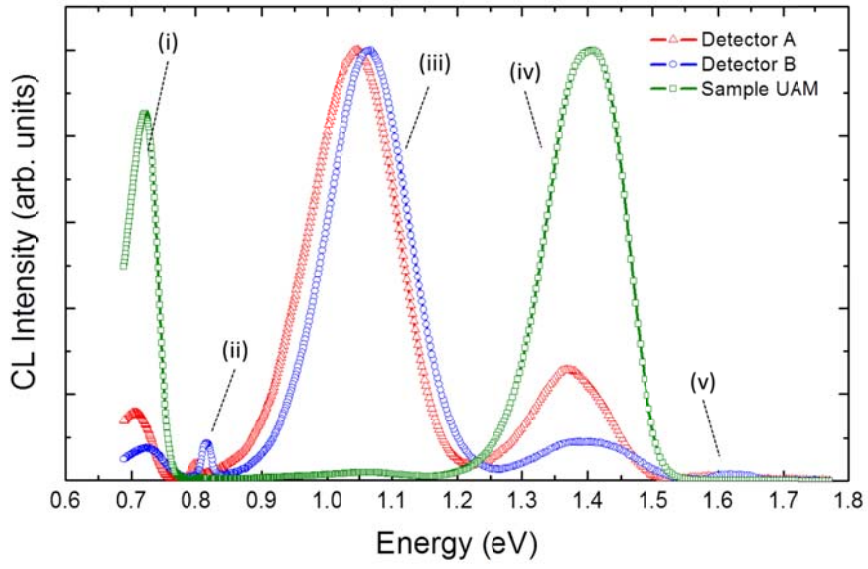

Figure 7 CL spectra obtained under low excitation conditions of commercial detectors and typical UAM device. The labeled defect bands may be associated with (i) Trap H (ii) Trap H1 (iii) Trap I (iv) Trap A (v) the bandgap of the material.

These differences in the CL spectra may possibly be explained through (i) the choice of dopant used for achieving electrical compensation and (ii) the growth technique used. Specifically, the crystals grown in this thesis investigation were done so using the VGF method, using In as a dopant for achieving electrical compensation. More importantly, no system for controlling the Cd-overpressure has been employed, which appears to result in a higher concentration of defects associated with cadmium vacancies. Indeed, the commercial crystals have been grown using the high-pressure Bridgman method in which a large overpressure is applied to reduce the concentration of cadmium vacancies. Therefore, it seems plausible that these defects associated with cadmium vacancies may be suppressed. The fact that the Trap H1 is also observed in the UAM crystals, may be attributed to residual trace impurities arising from the crucible cleaning using Aqua Regia. This has been demonstrated by GDMS measurements presented in Section 3 of Chapter 3.

2.6 Spectroscopic Performance

Spectroscopic gamma ray measurements were carried out on the commercial detectors A, B, and D. Using a Barium radioactive source, the 35KeV and 81KeV photon response was measured. The samples were biased at 1000V-cm as well as 1500V-cm, but the difference between the photo response was negligible using this experimental setup. For Detector A and B biased at 1000V/cm, a FWHM of 3.1%, 1.62%,was obtained for the 81keV photo-peak, as may be seen below in **Figure 8**. These measurements clearly demonstrate the high spectral resolution of commercially available devices. A summary of the compositional, electrical, and spectroscopic properties of these detectors is presented in **Table 2**.

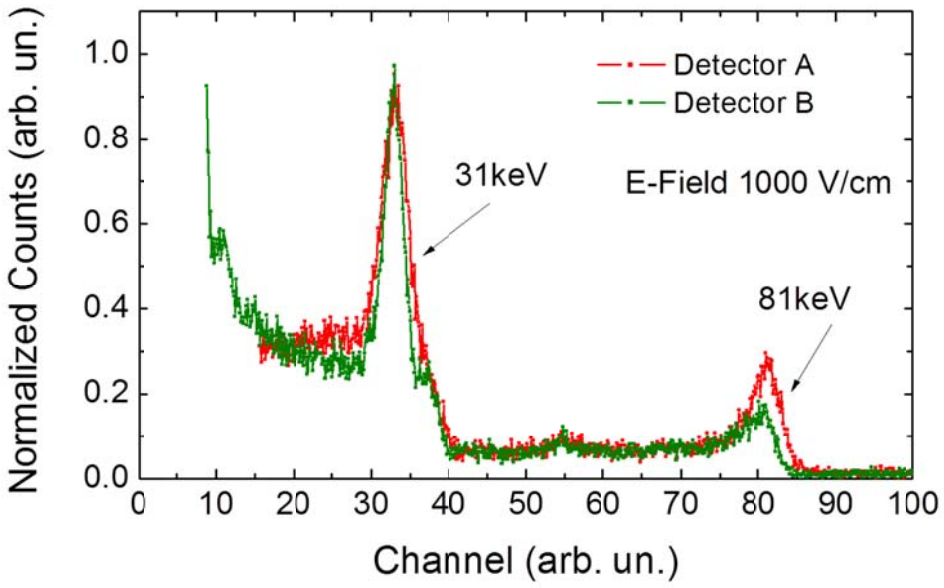

Figure 8 Spectroscopic performance of commercial Cd(Zn)Te Detectors A,B, and D using a ^{133}Ba radioactive source.

Table 2 Summary of compositional, electrical, and spectroscopic performance of Cd(Zn)Te radiation devices

ID	Dimensions (L x W x H) mm	Electrode Material	COREMA (Ω·cm)	I-V (Ω·cm)	Contact Ohmicity	FWHM @ 35KeV	FWHM @ 81KeV
A	5.04 x 5.13 x 3.917	Pt	$1.28 \cdot 10^9$	$8,9.10^9$	0.46	10.79	3.11
B	5.11 x 5.13 x 3.917	Pt	$3.12 \cdot 10^9$	$6,2.10^{10}$	1.02	7.35	1.62
C	5.04 x 4.99 x 3.900	Pt	$3.32 \cdot 10^9$	$3,3.10^{10}$	0.99	N/A	N/A
D	5.06 x 5.08 x 4.095	Pt	$3.32 \cdot 10^9$	$6,9.10^{10}$	0.99	N/A	N/A

2.7 Conclusions

The compositional, electrical, and spectroscopic properties of commercial Cd(Zn)Te devices, which have been grown by the high pressure Bridgman method have been presented. The conclusions may be summarized as follows:

1. State of the art spectrometers have been characterized in terms of the optical, electrical, and compositional properties.
2. Resistivity measurements of detectors exhibit low leakage current and exhibit Ohmic contacts.
3. CL measurements of the bulk material demonstrate the defect structure of these materials, which is substantially different than the materials grown by UAM.
4. Based on the CL measurements of commercial detectors, the defect structure of these materials may indicate a suppression of the formation of V_{Cd}. Indeed, this may be associated with the growth technique (High Pressure Bridgman) in which a high overpressure is used to prevent Cd loss and the formation of vacancies.
5. These detectors biased at 1000V/cm, exhibited a FWHM between 2% and 3% for the 81keV photo-peak of ^{133}Ba.

This page intentionally left blank.

3 DEVICE FABRICATION AND SURFACE PREPARATION

Section Contents

3.1 Introduction

Preparation of Cd(Zn)Te based detectors for x-ray and gamma ray applications involves the implementation of several classical semiconductor processes such as wire saw cutting, wafer lapping, chemical and/or mechanical polishing, and chemical etching. These processes are necessary for the extraction and preparation of detector material suitable for metallization and electrode deposition. The preparation of Cd(Zn)Te is normally carried out in stages, each designed with distinct objectives, procedures, and figures of merit. These stages may be divided into the following groups, each with altogether different aims and procedures.

- Ingot Slicing
- Wafer Lapping
- Mechanical Polishing
- Chemical Polishing
- Chemical Etching
- Surface Cleaning
- Electrode Deposition & Patterning

As was briefly mentioned in Chapter 3, increasing the diameter of crystal growth necessitated the development of complimentary processes in order to efficiently extract material from the as-grown ingot, and prepare this extracted material into functioning detectors. Indeed, the development of ingot slicing technology, wafer lapping and polishing protocol, and the deposition of electrodes is non-trivial and required substantial investigation.

Presented below in **Figure 9** is a generalized process flow, which has been developed during this thesis investigation for 50 mm diameter ingot. Indeed, each of the processing steps illustrated above required substantial investigation for achieving uniform and reproducible results. It is important to also comment that the processes presented here remain valid for the smaller ingot and wafer processing as well. The end result of this investigation is presented here, with the protocol which has been developed presented in sequential order.

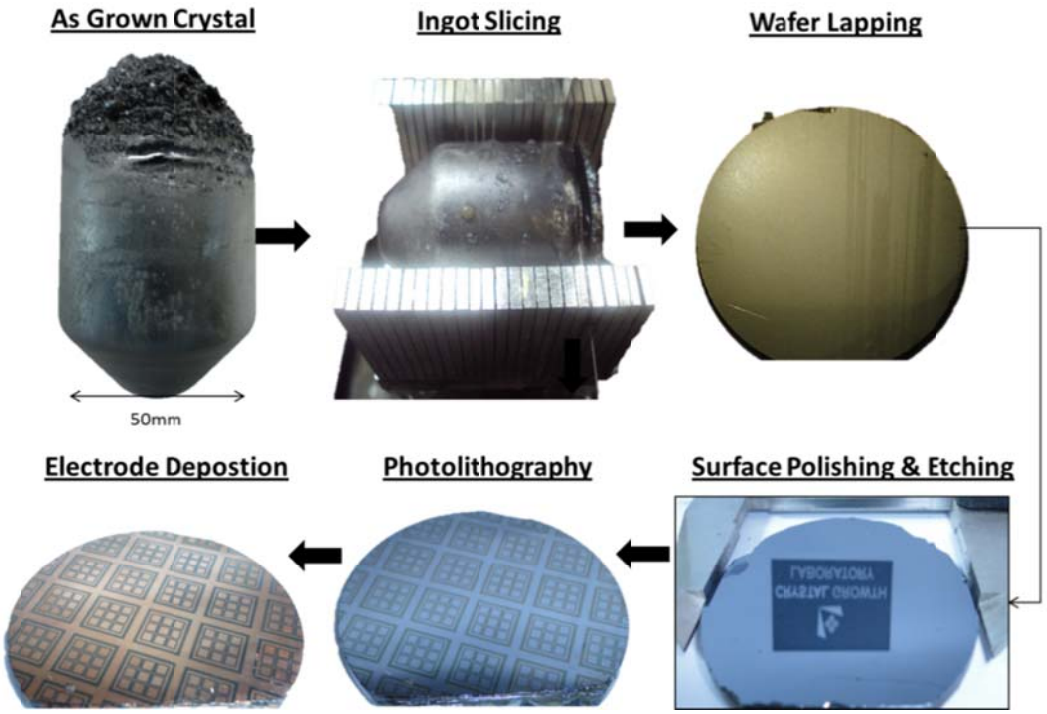

Figure 9 Process flow for harvesting Cd(Zn)Te material from 50 mm ingots grown in this work.

3.2 Sample Preparation Equipment

The experimental equipment used for or ingot slicing and surface preparation of wafers includes a Well´s diamond wire saw,e saw, a Logitech Lapping and Polishing PM4 a Logitech CP3000 system for chemical poll polishing. These systems, shown below in represent some of the more important equipmt equipment implemented in this work for Cd(Zn)Te samples for electrode deposition. tion.

The surface of each wafer after being sli being sliced from the ingot exhibits a high and roughness, a result of the coarse wire a se wire and large grit size of the diamond used for slicing. To reduce this roughness oughness and to eliminate the sub-surface with thus process, wafer lapping and polishnd polishing protocol have been developed PM5 system and CP3000 polishing systems systems. The PM5 system was used in precision lapping jig for controlling the wafng the wafer down pressure and material presented in **Figure 11**, mounted on the PM5M5 lapping system.

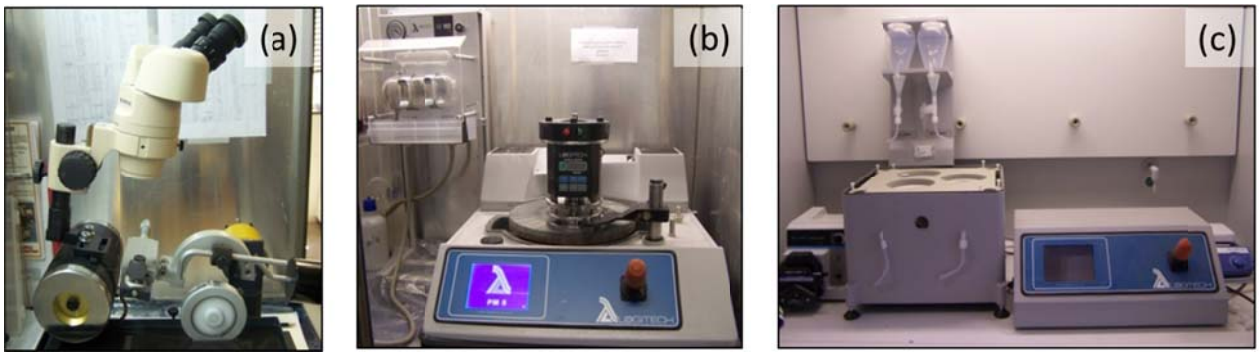

Figure 10 Wafer processing equipment at CGL: (a) Wells diamond wire saw for ingot and wafer slicing, (b) Logitech PM5 Lapping and Polishing system, (c) Logitech CP3000 Chemical Polishing System.

Using the CP3000 polishing equipment, a recirculating slurry system was implemented for the surface preparation of Cd(Zn)Te wafers. The system, presented in **Figure 12**, consisted of (i) the CP3000 chemical polishing system, (ii) a peristaltic pump used for slurry delivery, and (iii) a holding tank from which the fresh slurry was pumped, and to which the used slurry was deposited.

The implementation of a slurry recycling system was partly motivated by the high cost of the diamond slurry used for final surface preparation and the high slurry flow rates required to achieve substrate hydroplaning conditions. Indeed, for polishing a 50 mm Cd(Zn)Te wafer using the 1 μm diamond slurry with a typical delivery rate between 50-100 mL-min^{-1}, for 20-40 minutes would require 2-4L of slurry, which could cost more than 400 €. The implementation of this system for Cd(Zn)Te has allowed for the same slurry to be used for more than a 6 month period, providing significant cost savings while maintaining procedural integrity.

5.3 Ingot Slicing Protocol

Boule slicing is the first post crystal-growth step towards producing a The two primary boule slicing technologies are wire-saw boule slicing and ID-saw The ID-saw slicing technique was considered to be the baseline slicing method by silicon industry as far back as 1978 (8). ID saws were themselves initially used germanium and silicon semiconductor materials, but have also been applied to new Briefly, the ID saw uses an inner diameter, diamond tipped, nickel bonded cutting mechanically grind material away.

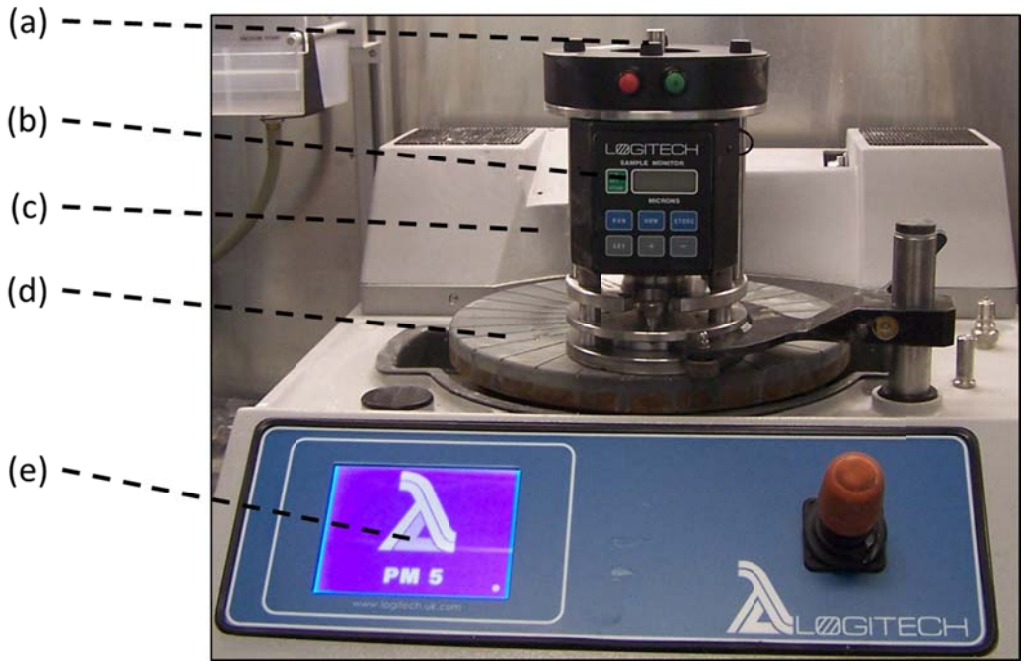

Figure 11 Precision PM5 Logitech lapping jig used for lapping and polishing of Cd(Zn)Te. (a) Vacuum connection, (b) material removal display, (c) Logitech jig, (d) grooved glass plate, (e) control interface.

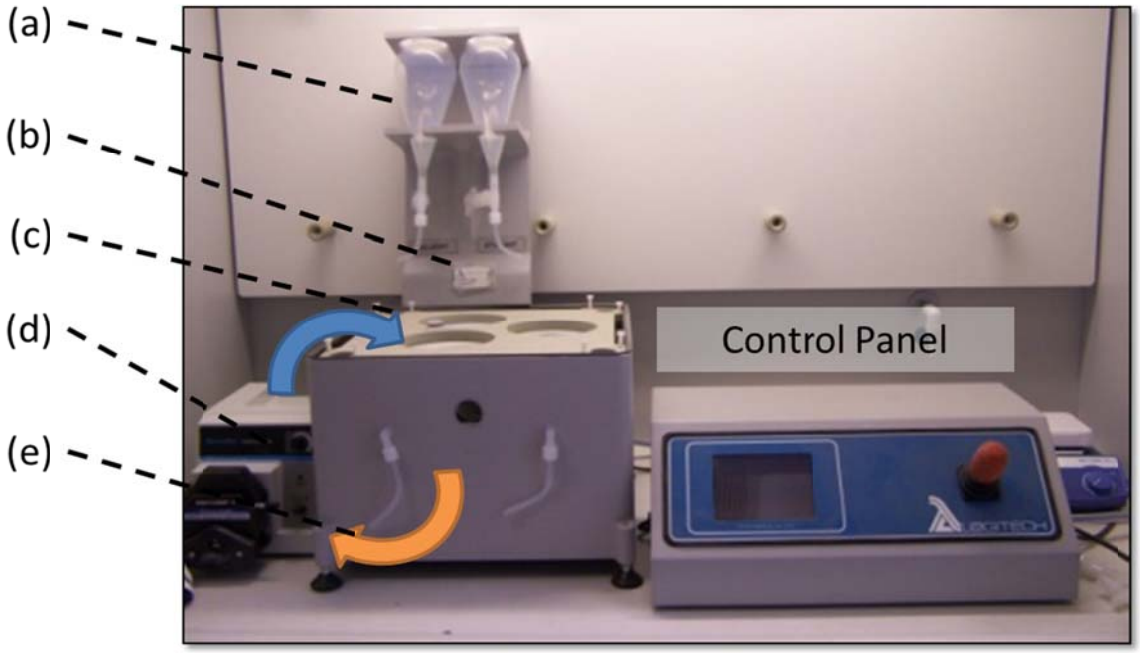

Figure 12 Logitech CP3000 polishing system polishing (a) chemical slurry containers, (b) dispensing nozzle, (c) sample deck /slurry dispensing port, (d) peristaltic pump, (e) slurry return line.

Due to the intrinsic brittleness and fragility of Cd(Zn)Te, the wire saw technique was adapted for slicing of Cd(Zn)Te ingots. In order to scale the crystal growth technology to 50 mm, it was also necessary to scale the ingot slicing capacity to slice 50 mm diameter ingots. One of the problems associated with using a wire saw for cutting Cd(Zn)Te is the elastic bowing and deflection of the wire during the cutting. As a result, wafers may exhibit a large degree of tapering and thickness variation if the correct measures are not taken. Indeed, wire deflection throughout the cutting process results in regions which exhibit very high thickness variation. In some cases, the stresses caused by this deflection cause the wafer to break. As a result, a large amount of bulk material needs to be removed in order to fully remove the damage imparted by the saw. In order to overcome this problem, a wire guide which throughout the duration of the cutting process was developed. In this way, is significantly reduced as was the total thickness variation of the wafers. Presented in **Figure 13** is the **1st prototype** of the wire guide cutting system which has been developed toward this end. This system is comprised of (50) 2.5mm thick Aluminum bars, 60mm in height, and with a spacing of 300 μm between each bar which permits the diamond wire to pass through. By mounting the 50 mm diameter Cd(Zn)Te ingot inside this fixture, 5mm thick wafers could be sliced from the ingot.

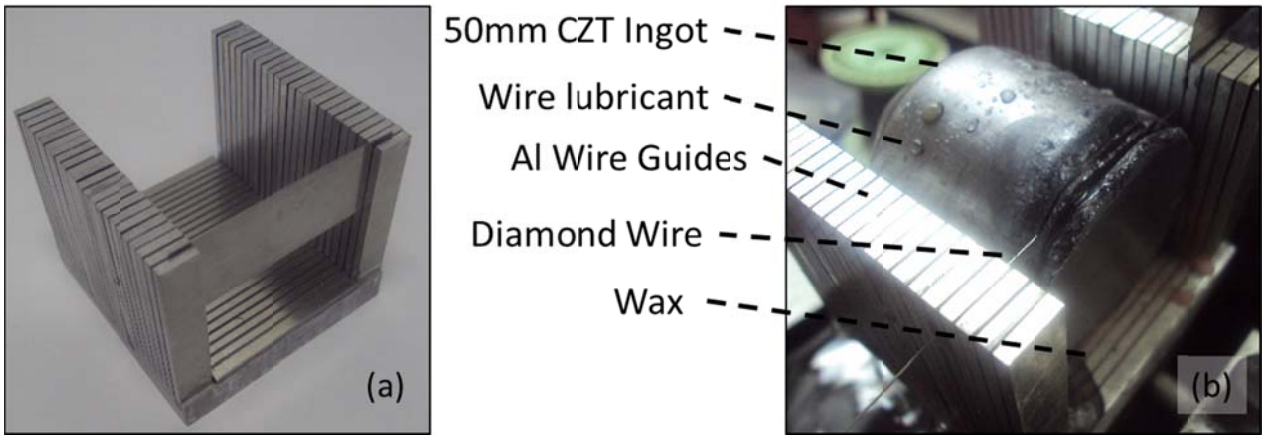

Figure 13 (a) Prototype wire guide developed in this work for decreasing TTV of Cd(Zn)Te wafers cut using diamond wire. (b) Cd(Zn)Te Ingot being cut using the diamond wire with wire guide.

The aluminum bars substantially decreased the wafer bowing. Indeed, it was harvest entire wafers from the ingot using this fixture. However, a more encountered using this system may be seen in **Figure 14**. During the cutting cycle, the diamond wire travels into the aluminum bars several millimeters due to deflection of the wire by the work-piece (i.e. the Cd(Zn)Te ingot). In these cases, the wire saw had to be stopped and the wire reset into place before the cutting could be resumed. The reason for this poor performance is associated with the low hardness value of aluminum compared with the diamond impregnated wire. Presented in **Figure 15** are two 50 mm wafers harvested using this fixture. From this photo, it is clear that the wire has imparted substantial damage into the wafers as a result of lateral deflection and wire bowing.

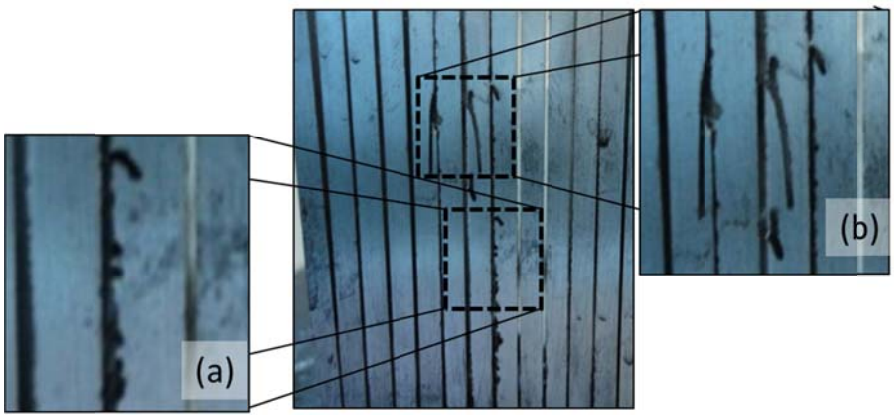

Figure 14 Damage imparted by diamond wire into the aluminum wire guide. (a) surface roughening of the aluminum (b) diamond wire cuts deeply into the aluminum guide.

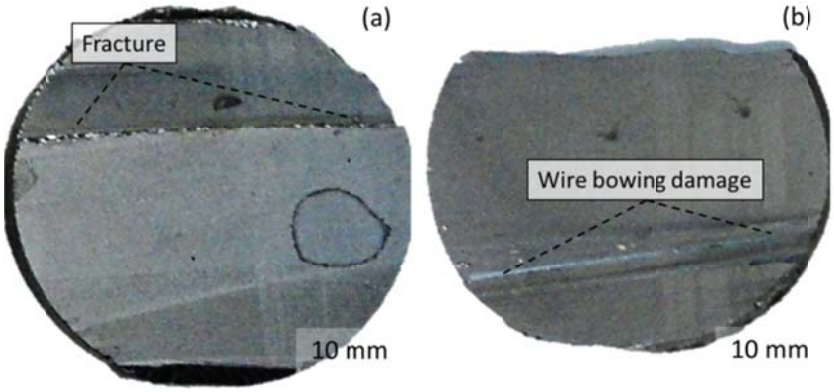

Figure 15 Cd(Zn)Te 50 mm wafers after wafer slicing exhibit large variations in total thickness variation due to the wire saw bending and travelling (a) in some cases the wafer breaks under the lateral stresses of the wire (b) while in other cases the lateral travel creates a local depression into the wafer surface.

To improve the quality of cutting using the diamond wire saw, a **2nd-prototype** wire guide was designed and implemented for cutting Cd(Zn)Te 50 mm ingots, and is presented in **Figure Figure 16**. In this case, the lateral bars were fabricated using a high hardness ceramic (Alsint ceramic(Alsint 99.7), in place of the aluminum. The thickness of the alumina bars were were increased from 2.5 mm in the previous design, to 3.0mm in the new design. This second second prototype has greatly facilitated the slicing of 50 mm diameter ingots investigated investigted throughout this work.

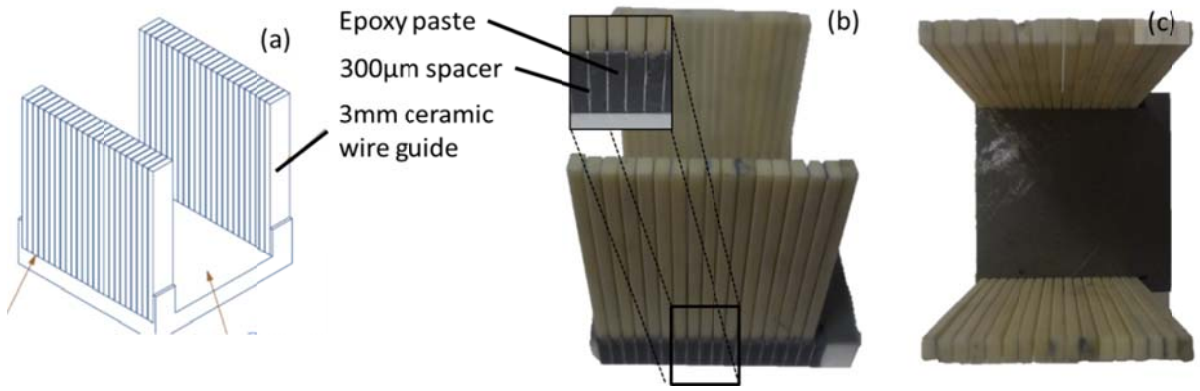

Figure 16 Second prototype design of wire guide for cutting 50 mm Cd(Zn)Te ingots. Instead of aluminum in this case, ceramic bars with a high hardness value were used for slicing the ingots.

3.4 Wafer Lapping

Mechanical lapping refers to the use of a rigid work surface in conjunction with rolling abrasive to produce flat surfaces. Wafer lapping is a commonly used free abrasive machining (FAM) technique in the semiconductor industry and has been implemented to control wafer flatnesthickness, total thickness variation (TTV), and bow. The flatness is the deviation of the top surce of the wafer, relative to the backside reference plane. The total thickness variation is expressed as the maximum deviation of thickness across the wafer surface. These concepts are presented in **Figure 17** where the TTV is determined by taking the difference of δ_1 and δ_2, while

δ_2, while the flatness of the wafer is determined by the deviation, θ, respect to the backside of the wafer.

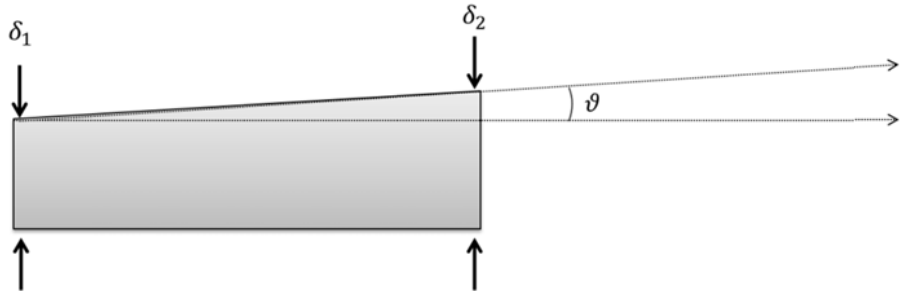

Figure 17 Wafer flatness and TTV

The objective of this technique is to (i) create planar surfaces (ii) with minimal sub-surface damage, and (iii) to establish a uniform surface finish from which to initiate wafer polishing. It was found that slurry composition, lapping platen RPM, lapping plate surface roughness, and wafer down pressure all played major roles in resultant wafer morphology and material removal rates. This was especially true for scaling this process for 50 mm diameter wafers. The parameters used in this work are listed in **Table 3**.

Table 3 Lapping parameters used for 50 mm Cd(Zn)Te wafers

Parameter	Used in this investigation
Slurry composition	10% by weight
Lapping plate RPM	40
Pressure	<15 kPa
Abrasive	9 µm / 3µm Al_2O_3
Platen	Cast Iron / Glass
Duration	< 20 minutes

As one example, the roughness of the lapping plate itself was observed to play a role with respect to the resultant surface morphology of the wafer. Presented in **Figure 18** is a Cd(Zn)Te wafer lapped using a lapping plate which has been conditioned using a 30 µm abrasive (a) and a 3

μm abrasive (b). The high roughness of the lapping plate induced by the larger diameter abrasive is subsequently imparted into the wafer, having a catastrophic effect.

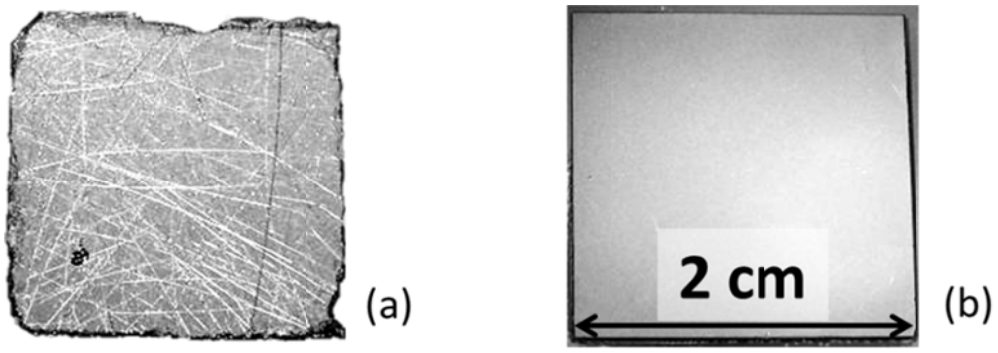

Figure 18 Cd(Zn)Te Wafers lapped under identical conditions with the only difference being the roughness of the lapping plate. (a) lapping plate conditioned using 30 μm abrasive (b) lapping plate conditioned using 3 μm abrasive

As previously mentioned, it was established through this work that the "roughness" of the lapping plate and the curvature of the lapping plate contributed significantly to the resultant wafer surface morphology. Therefore, for a given platen material to be suitable for Cd(Zn)Te, the platen itself must be conditioned to achieve a work surface as smooth as or smoother than the desired surface for the Cd(Zn)Te surface. Essentially, each lapping platen must also be itself ´´lapped´´ to achieve reproducible results lapping Cd(Zn)Te.

The mechanism that illustrates Preston's equation is indicated in **Equation 3** and shows how material is removed faster depending on the velocity of the lapping plate. Guided by Preston's Equation, the lapping plate can be made either concave or convex. In **Equation 3**, k is a material specific constant, P is the applied pressure, and v is the velocity of the plate with respect to a stationary sample. Since the angular velocity of a rotating platen depends on the position of the sample with respect to the radius of the platen, higher removal rates are expected at larger distances from the center. This aspect of the platen gives rise to concave and convex samples

Equation 3 $\text{Material Removal Rate} = k \times P \times v$

To control the curvature of the lapping plate a test block of the same material is placed on the plate in the same manner as the polishing jig. Since the test block is in direct contact with the

plate, it will acquire a shape that "mates" with the lapping plate (as they both remove material from one another's surfaces).

If the center of the test block is placed near the edge of the lapping plate, then the greater velocity near the outer-diameter (OD) will insure that more material is removed from the center of the test block than the edge of the test block. Therefore a concave test block will result. However, if the center of the test block is placed towards the inner diameter (ID) of the lapping plate, the OD velocity will insure that more material is removed from the edges of the test block than from the center of the test block. Therefore, a convex test block will result.

A precision Logitech Lapping & Polishing jig, shown in **Figure 11**, was used to control the wafer thickness during the mechanical lapping and polishing stages and to establish material removal rates for each lapping operation. Using this jig, the real-time thickness of the sample could be monitored and the quantity of material removal rate recorded with each sample.

3.4.1 Lapping Protocol

After the harvesting Cd(Zn)Te wafer from the ingot using the diamond wire saw, samples were first lapped using a 9μm Al_2O_3 abrasive powder, followed by a subsequent lapping operation using a 3 μm Al_2O_3 powder. Scanning Electron Microscope surface scans of wafers lapped using 9μm and 3 μm Al_2O_3 are presented in **Figure 19**. These two lapping stages remove damage and irregularities imparted by the diamond wire saw during ingot slicing (see **Figure 15**). The lapped surfaces exhibit a non-specular/non-reflective surface finishes, with somewhat large surface roughness.

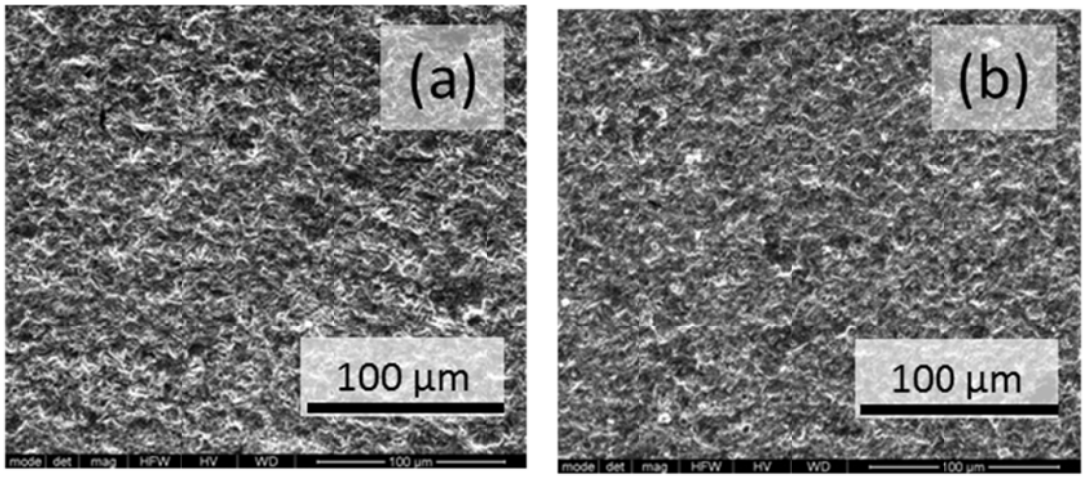

Figure 19 SEM surface analysis of Cd(Zn)Te after subsequent Lapping and CMP operations. (a) After lapping with 9µm Alumina, (b) After lapping with 3µm Alumina

Presented in **Figure 20** is the material removal rate which has been established for the lapping process, as well as a typical 50 mm wafer after lapping. The lapping process using 9 µm Al_2O_3 could produce removal rates as high as 25 µm / min. Therefore, this step could be used for achieving large stock removal of material after the diamond wire slicing process. In many cases, it was necessary to remove as much as 300 – 400µm of material from each side of the wafer.

The 3 µm Al_2O_3 lapping step was used for eliminating the sub-surface damage imparted by the 9 µm Al_2O_3 abrasive. Indeed, lower removal rates on the order of 10-15 µm/min could be achieved. Using pressures exceeding 15 kPa frequently led to catastrophic failure of the part, and therefore was avoided. Using these processes, a wafer flatness of 10 µm/cm could be achieved regularly. Indeed, this parallelism was an important aspect for measurements such as COREMA resistivity mapping which require uniform flatness over large areas.

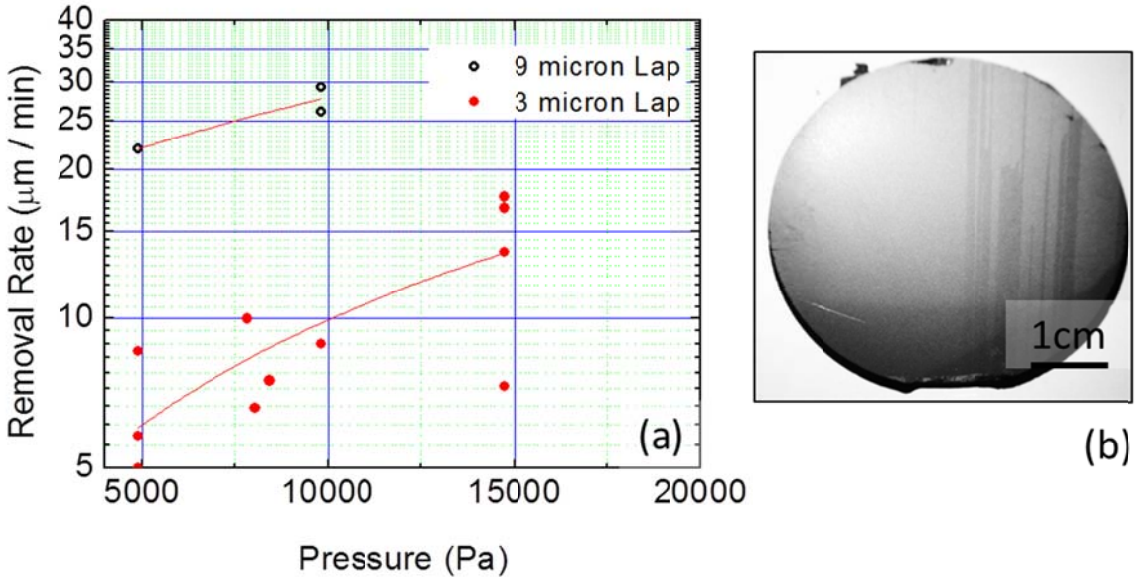

Figure 20 (a) Material removal rates using different abrasives and pressures. (b) Typical surface finish of a lapped 50 mm Cd(Zn)Te wafer.

3.5 Mechanical Surface Polishing

The process of mechanical polishing involves the abrasion of material from the surface by using soft polishing cloths and abrasive slurries, in which the abrasive is, to some degree, fixed within the pores of the polishing pad. The net size of the exposed particle is reduced and the surfaces produced are reflective. In this aspect, mechanical polishing is differentiated from the previous lapping stage, for which the abrasives are free to roll across the lapping plate.

Furthermore, mechanical polishing differs from the previous lapping stage in its principal aim. While the lapping process does remove a significant degree of the damage layer induced by the wire saw, the principle aim of lapping is to obtain planar samples which exhibit a high degree of parallelism between opposing surfaces. The objective of the polishing process is to reduce the amorphous layer and sub-surface damage layer imparted by the mechanical cutting and lapping process.

Presented in **Figure 21** is a schematic representation of the damage layer, $\boldsymbol{\delta}$, induced by saw cutting, lapping, and polishing. Yoon *et al* has studied the effects of saw-cutting, lapping, and polishing on the sub-surface disorder of Cd(Zn)Te using High Resolution X-ray Diffraction (HRXRD) (9). Indeed, these results have shown how the damage layer may be reduced through the implementation of the correct lapping and polishing protocol. The extended thickness of this damage layer may be estimated to be three times the diameter of the abrasive used, such that using a 3 μm abrasive would require a 9 μm surface layer be removed by the polishing process.

Therefore, the surface polishing is normally carried out in sequential steps, with decreasing abrasive grit sizes to achieve this end. There have been several different processes reported for Cd(Zn)Te using diamond grinding wheels (10), alumina oxide (11) (12), or magnesium oxide based slurries with abrasive sizes varying between 0.5-3 μm suspended in DI water. Still others have implemented processes using colloidal SiO_2 nanoparticles (13) to achieve the desired surface finish. In this work, different abrasive sizes have been tested to identify a linear protocol which may be used for the preparation of Cd(Zn)Te radiation device electrode surfaces.

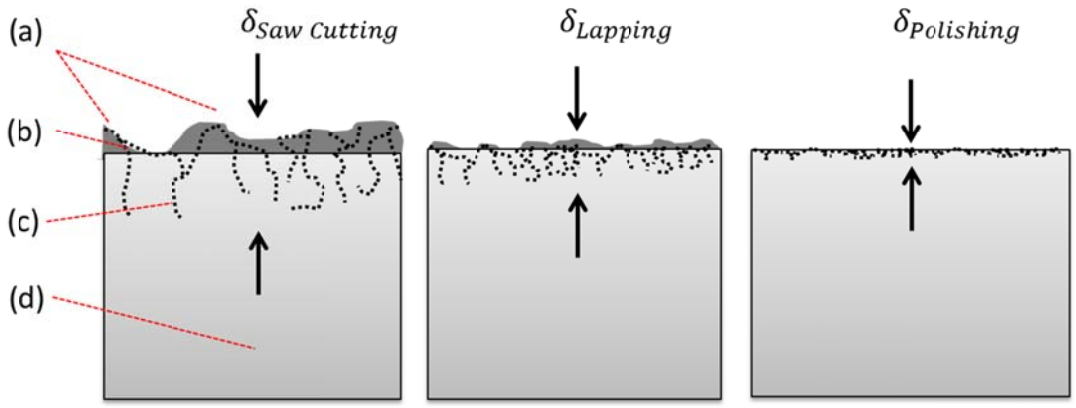

Figure 21 (a) topological roughness of surface, (b) amorphous layer, (c) subsurface damage and dislocations, (d) bulk.

3.5.1 Polishing Protocol

The results presented here represent the methodology used for fabricating detectors discussed throughout this entire thesis investigation. After the 3 μm Al_2O_3 lapping step, 50 mm Cd(Zn)Te wafers were polished using a 3 μm Al_2O_3 for 20-30 min. The time necessary to achieve a uniform surface finish depended to a large extent on (i) the parallelism of the wafer and (ii) the uniformity of the surface after the lapping step. After this rough polishing operation, the wafers were subsequently polished using a 1 μm diamond slurry to further reduce the surface damage layer and reduce the surface roughness.

Presented in **Figure 22** are the material removal rates obtained using the 3 μm Al_2O_3 and 1 μm diamond abrasive powders. Indeed, 20 minutes of polishing using 3μm Al_2O_3 under a 20 kPa pressure will remove a surface layer nearly 18-20μm in thickness. This is more than sufficient to eliminate the lapping damage. The subsequent polishing step using 1 μm diamond, despite the low material removal rate, is quite effective for reducing surface roughness. Also presented in **Figure 22**(b) is a typical 50 mm wafer after this mechanical polishing step.

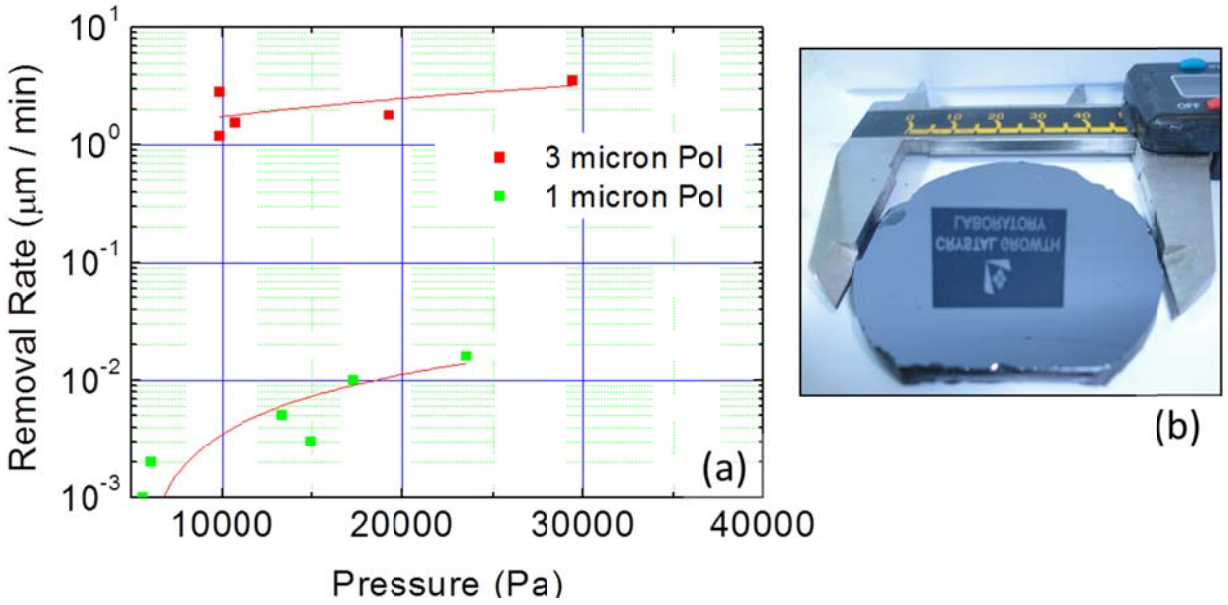

Figure 22 (a) Material Removal rates for Cd(Zn)Te wafers polished using different abrasives and pressures. (b) Typical 50 mm sample after polishing exhibits a uniform reflective surface with low surface roughness.

AFM measurements for typical Cd(Zn)Te surfaces polished using 3 µm Al_2O_3 are presented in **Figure 23** and **Figure 24**. The surface roughness after this step operation is on the order of 10-30 nm, as measured by the AFM. However, it is also important to note the peak to valley depth of the scratches as deep as 15 nm and particulates as large as 120 nm present on the surface (see **Figure 24)**.

The image of the probe area is included for the 3 µm Al_2O_3 polishing procedure, in **Figure 25**. This is done to illustrate the relative uniformity of the polishing operation over larger areas. It is clear that after this rough polishing step, there still remain large scratches present on the surface which require removal. Indeed, the effect of such surface defects has been shown to influence the charge collection efficiency of radiation devices (14), acting as recombination centers.

The surfaces polished using the 1 µm diamond abrasive exhibit uniform surface morphology, and low roughness. Typical AFM surface scans representative of this polishing step are presented in **Figure 26** and **Figure 27**, which exhibit surface roughness between 2-4 nm. This polishing operation produces a uniform surface finish across the entire wafer, while also decreasing the Peak to Valley by a factor of 3 (see **Figure 27**).

3.6 Chemical Polishing

Chemical polishing of Cd(Zn)Te remains an experimental challenge for the preparation of pristine surfaces. There only a small set of papers which discuss the principles of chemical polishing with respect to Cd(Zn)Te, including the paper by Singh *et al.*, which outlines the optimization of several physical parameters for $Cd_{0.96}Zn_{0.04}Te$ used to meet the demands for thin film growth by Molecular Beam Epitaxy (15). P. Morovec *et al.* presents the effects of load, chemical slurry concentration, bromine concentration, and pad type on material removal rates (12). Still other results have demonstrated that using weaker oxidants based on iodine with lower redox potential value, compared with bromine, the surface may be more stable with time, and with a surface roughness comparable to that obtained using bromine based slurries (16).

After the 1μm mechanical polishing step, the samples have been chemically polished for 60 minutes using the chemical polishing solution proposed by Singh *et al*. in conjunction with the CP3000 system. Typical surfaces polished using this chemical polishing solution are presented in **Figure 29** and **Figure 31**. It is important to comment that this step was only carried out on samples up to 2cm x 2cm in area, and only for special investigations. In general chemical etching has been the preferred method for post-polishing surface preparation.

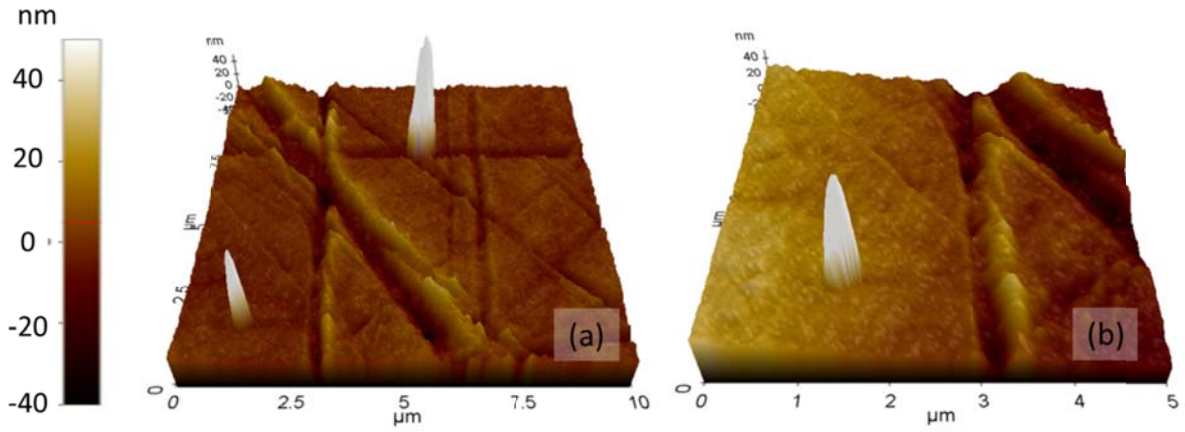

Figure 23 (a) 10 µm x 10 µm and (b) 5 µm x 5 µm AFM measurements of Cd(Zn)Te surface after polishing using 3 µm Al_2O_3.

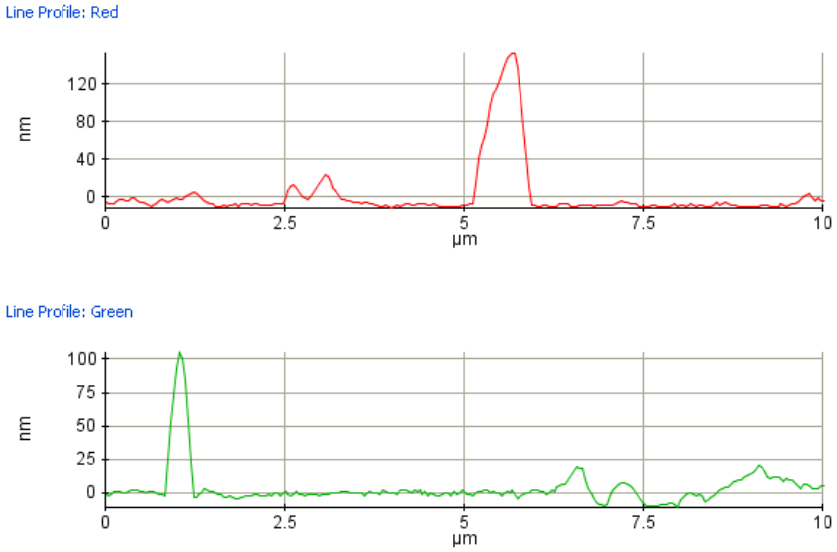

Figure 24 Line scan of surface of 10 µm x 10 µm after polishing using 3 µm Al_2O_3.

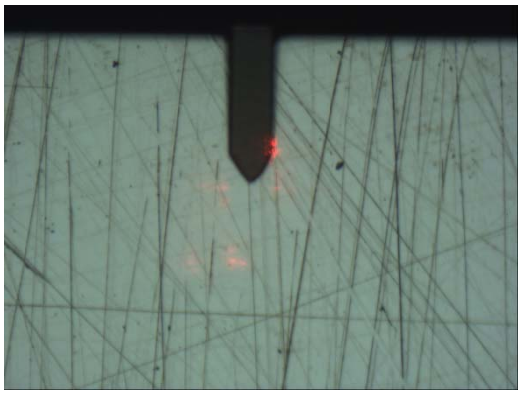

Figure 25 Optical microscope image of probe area of Cd(Zn)Te surface after 3 µm Al_2O_3 polishing

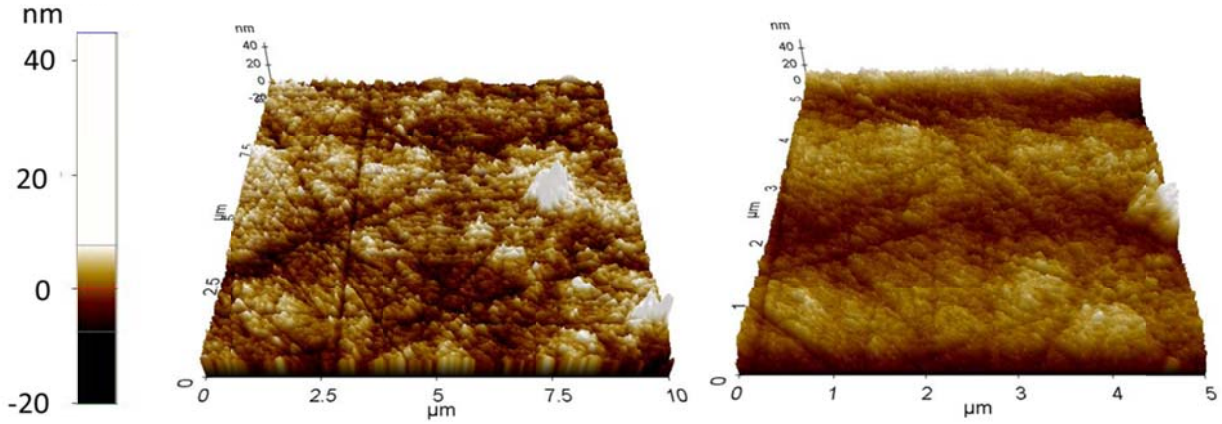

Figure 26 (a) 10 µm x 10 µm and (b) 5 µm x 5 µm AFM measurements of Cd(Zn)Te surface after polishing using 1 µm diamond.

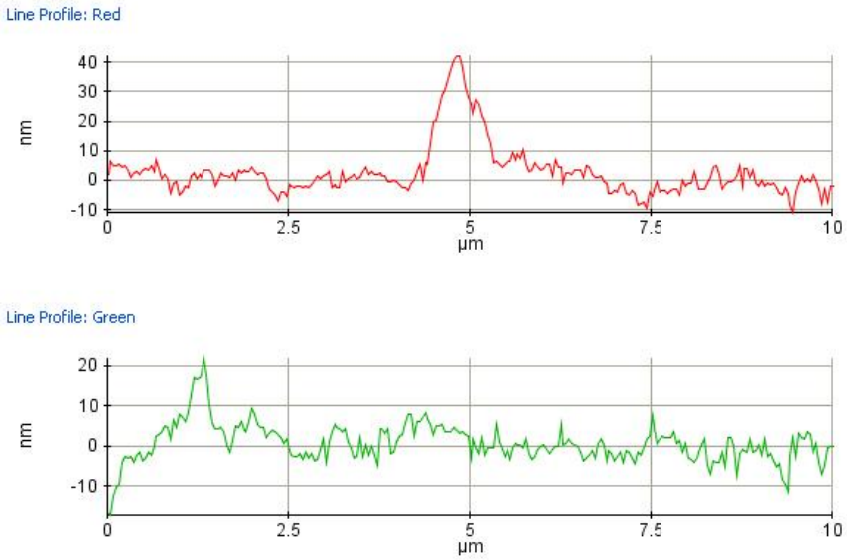

Figure 27 Line scan of surface of 10 µm x 10 µm after polishing using 1 µm diamond.

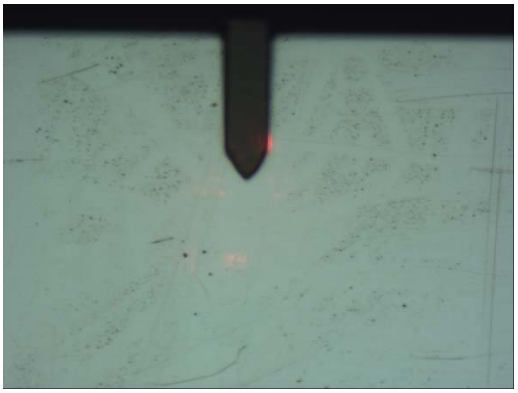

Figure 28 Optical microscope image of probe area of Cd(Zn)Te surface after 1 µm diamond polishing

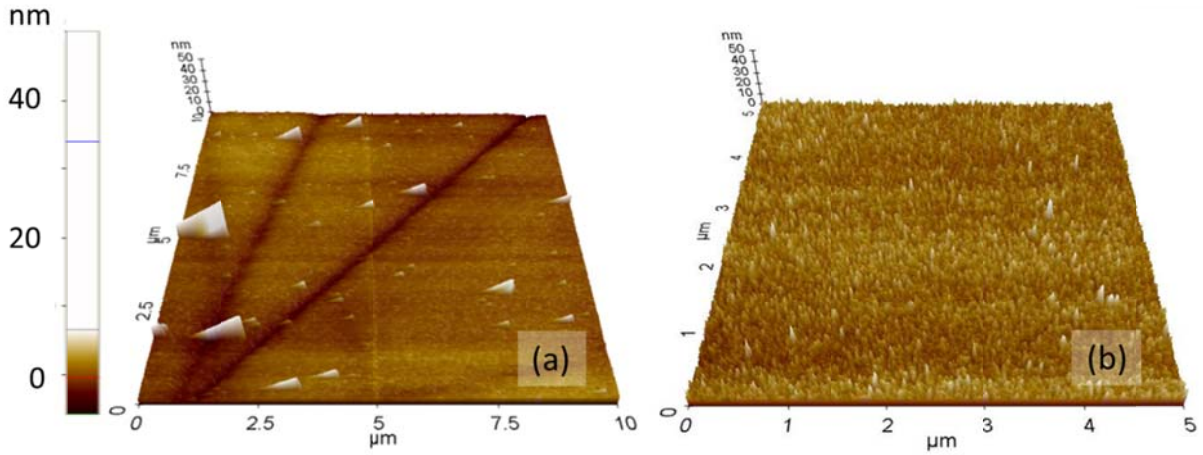

Figure 29 10 µm x 10 µm and 5 µm x 5 µm AFM measurements of Cd(Zn)Te surface after chemical polishing.

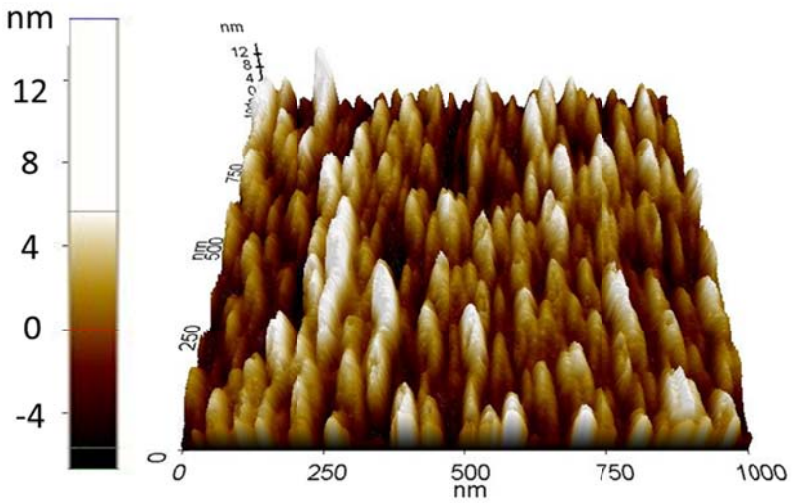

Figure 30 10 µm x 10 µm and 5 µm x 5 µm AFM measurements of Cd(Zn)Te surface after chemical polishing.

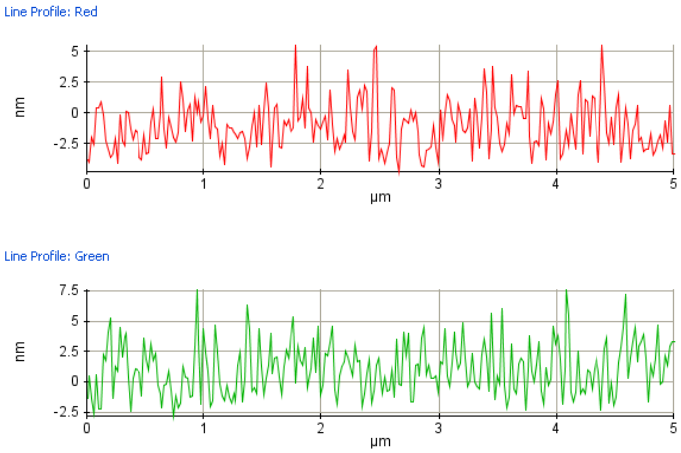

Figure 31 Line scan of surface of 10 µm x 10 µm after chemical polishing.

3.7 Chemical Etching

To eliminate the small damage layer created by the mechanical polishing process, chemical etching of the surface has been extensively employed throughout this investigation. Indeed, a thin damage layer imparted by the abrasive polishing agents may produce electron trapping centers, reducing the performance of the detector. Therefore, a final chemical etching step has been introduced to remove the damage layer imparted by the mechanical polishing operations used in this investigation (17).

The HRXRD taken at CGL and presented in **Figure 32** further demonstrate the strong influence of the damage layer imparted by the mechanical lapping and polishing operations on the crystalline quality at the surface (see **Figure 21**). The same sample was treated using 3µm Al_2O_3 lapping, 1µm Al_2O_3 polishing, 1µm diamond polishing, and 2% bromine methanol etching. The surface showing the most intense XRD peak is obtained after chemical etching, where the measured full-width-at-half-maximum (FWHM) value of etching sample was 68", significantly more intense than any of the other surface treatments.

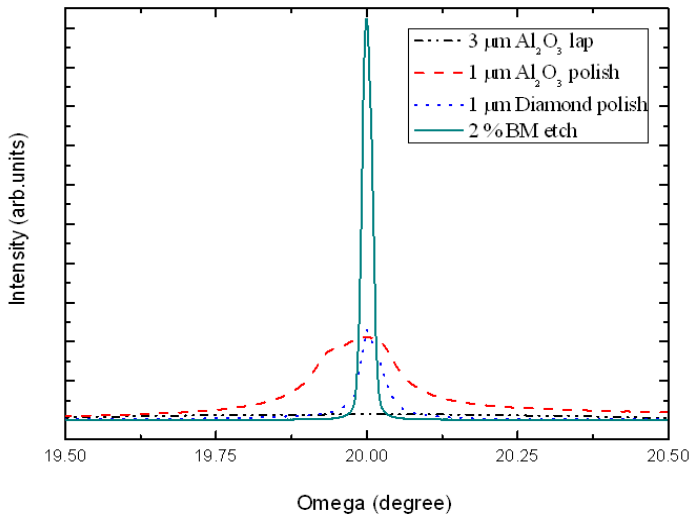

Figure 32 XRD peak of the same Cd(Zn)Te sample obtained after lapping, polishing, and chemical etching.

It has also been demonstrated how the roughness of the Cd(Zn)Te anode and cathode plays a role in reducing detector efficiency (18). Furthermore, the sensitivity of detector properties on

surface preparation have also been investigated using High Resolution X-ray Diffraction measurements of the surface by (9), and are in agreement with the measurements presented here.

Presented in **Figure 33** and **Figure 34** are the surface morphologies of the Cd(Zn)Te surface after chemical etching for 30 and 120 seconds respectively. It is important to observe that the micro-scratch defects from the previous polishing step have been removed to a large extent (see **Figure 23** and **Figure 26**), and the surface roughness has been reduced to less than 2nm. For longer durations of chemical etching greater than 2 min however, the surface roughness begins to increase, as may be seen from **Figure 35**.

Results presented in **Figure 35** demonstrate that the etching for 30sec and 2min produce surfaces whose stoichiometry is appropriate for electrode deposition. Indeed these surfaces exhibit low surface roughness and exhibit a higher concentration of Te at the surface, which is preferable for electrode deposition via the electroless method (19).

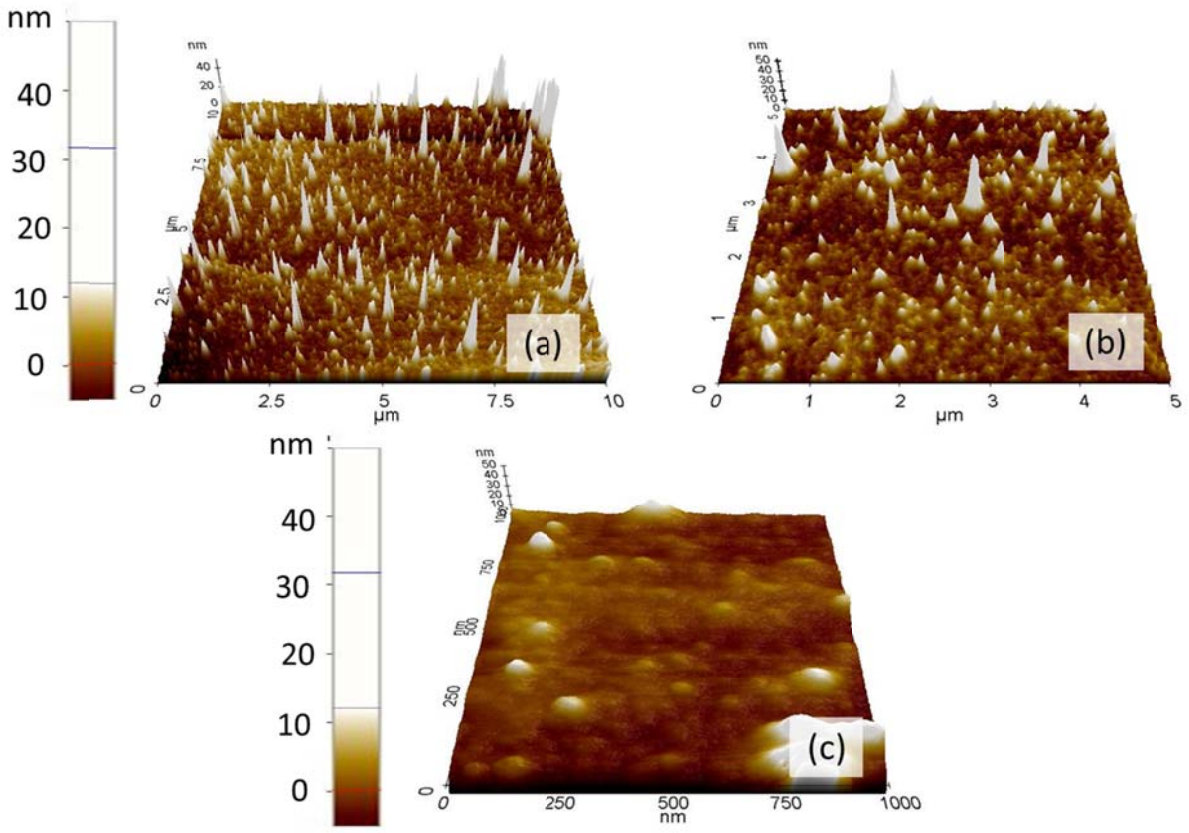

Figure 33 (a) 10 μm x 10 μm (b) 5 μm x 5 μm (c) 1 μm x 1 μm AFM measurements of Cd(Zn)Te surface after chemical etching using Bromine Methanol 30 seconds.

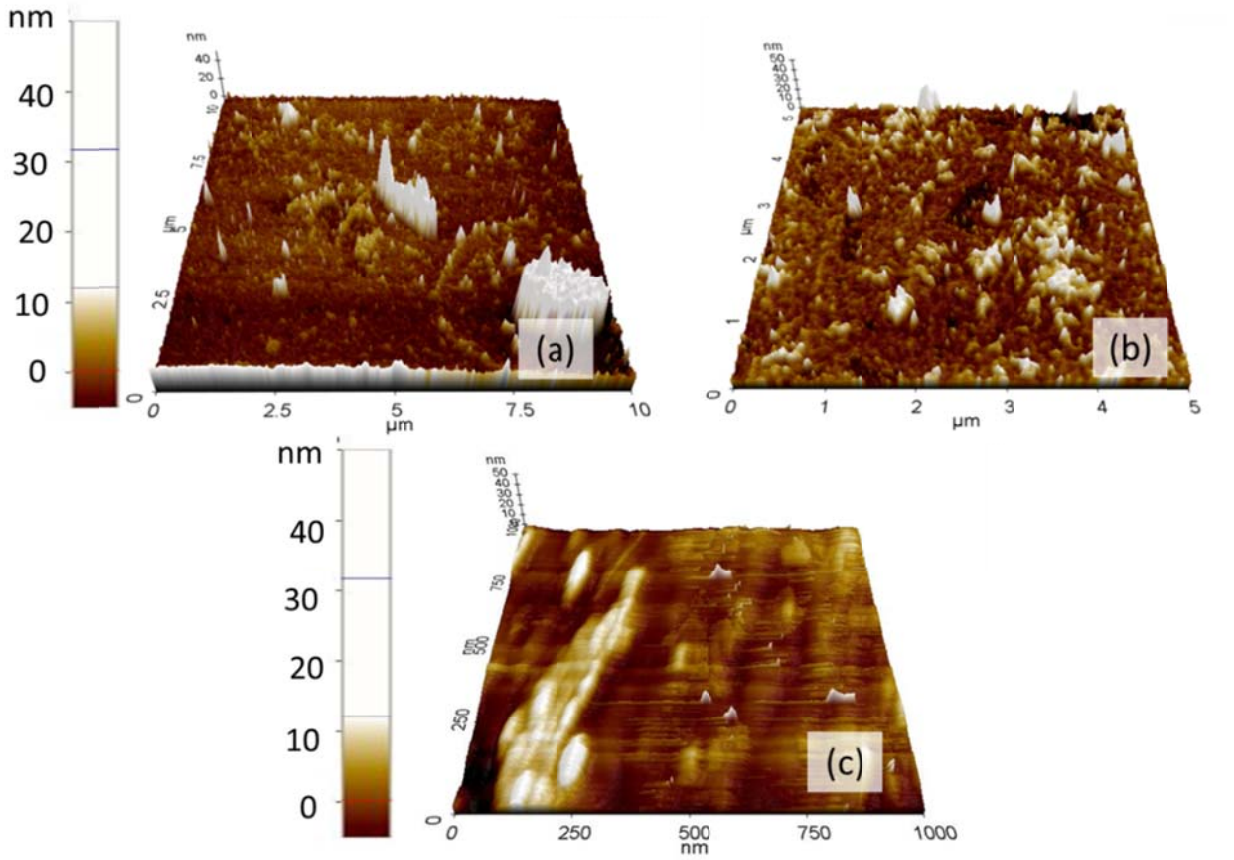

Figure 34 Top Left: 10 μm x 10 μm Top Right: 5 μm x 5 μm Bottom: 1 μm x 1 μm AFM measurements of Cd(Zn)Te surface after chemical etching using Bromine Methanol 120 seconds.

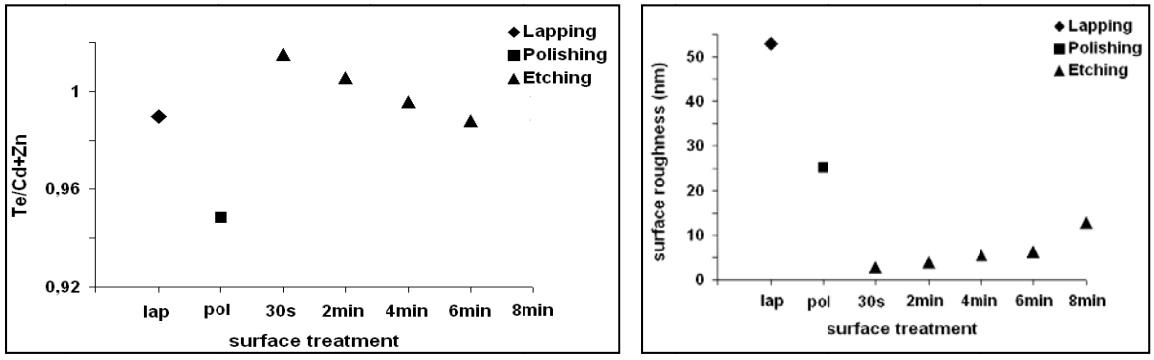

Figure 35 Left: Chemical composition from EDS and Right: surface roughness obtained after (i) lapping, (ii) polishing, and (iii) chemical etching for several durations.

3.8 Surface Cleaning

With respect to the surface processing of Cd(Zn)Te wafers, it was also necessary to investigate methods for removal of residual surface contamination, prior to electrode deposition. The use of abrasive slurries containing micron and sub-micron particulates results in these particles adhering directly to the work surface, or even in some cases using diamond slurries these abrasives have been observed to become embedded in the surface. In addition to this, the wax bonding of wafers to glass templates has also been identified as a potent source of surface contamination.

3.8.1 Capillary Force Templates (CFTs)

It was of interest to identify a method for polishing Cd(Zn)Te, not using wax based methods, to remove these sources of contamination. CFTs rely upon the surface tension of a liquid to hold the samples in place during the polishing operation. Shown in **Figure 36** is a schematic of the templates used in this work used with a 50mm wafer. The surface tension of the liquid between the felt pad and the wafer holds the wafer in place throughout the polishing process. The fiberglass cutout keeps the sample from sliding out of the pocket. In this way the wafer is secured in place. It is important to note that in this design, the tolerance for the dimensions of the plastic fixture should be very close to the dimensions of the wafer which sits within the pocket. If not, this small degree of lateral motion can cause substantial sample degradation.

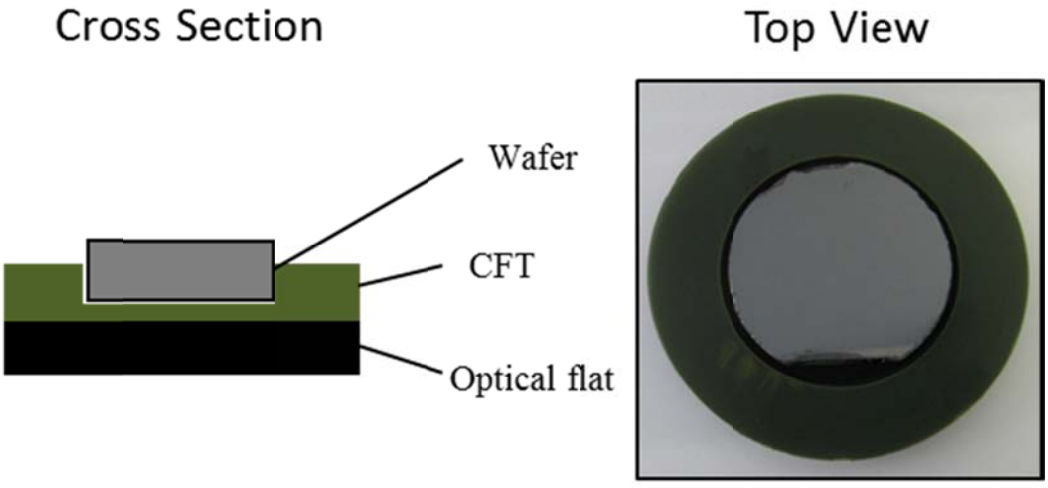

Figure 36 Left: Geometry for a capillary force template. Right: Surface tension of a liquid between the 50mm wafer and the felt pad keeps the sample inside the pocket.

For the standard template assemblies, there are two available choices of backing material that have been investigated: DF200 and WB20. The DF200 material is a buffed material which provides a tube like pore structure (nap) that absorbs particles and cushions their effect. This nap allows water tension to hold the wafer in place but still allows the wafer to rotate in the pocket, producing a flatter surface. The compressibility of this material is 15%. The WB20 material is an un-buffed material which offers an extremely strong wafer-to-mounting material bond. It has a smooth top layer that will hold the wafer when the wafer is pressed into the template. The wafer will not rotate in the pocket and the backside of the wafer is sealed against slurry. The compressibility of this material is less than 5%. The templates used in this work are of the DF200 type.

3.8.2 Surface contamination

Before presenting the efficiency of the CFTs with respect to polishing Cd(Zn)Te, it is important to present the challenges which have motivated their implementation. Indeed, many surfaces were characterized using EDS to determine if the particulates present on the surface could indeed be attributed to the polishing and cleaning processes. Presented below in **Figure 37** is a typical EDS spectrum for a polished sample, clearly showing the presence of Al_2O_3 abrasive particle on the surface. The inset image is the SEM surface image showing the particulates selected for this survey. From these measurements it can be seen that these abrasive particles remain on the surface even after cleaning using powerful solvents.

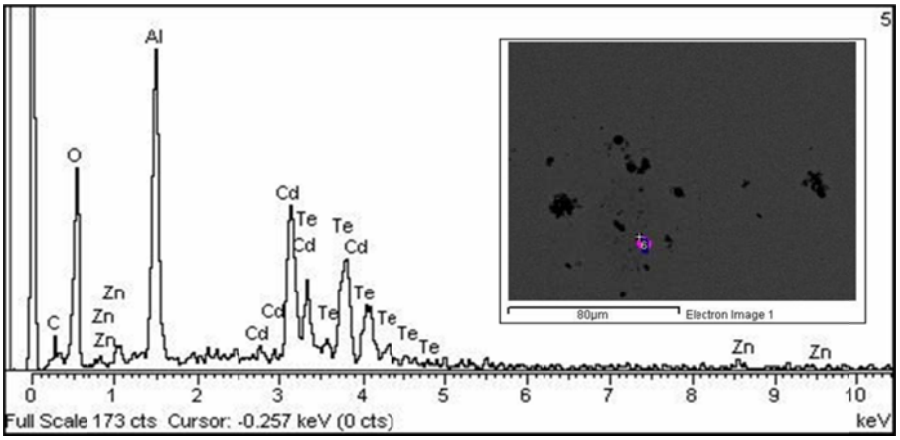

Figure 37 EDS Spectra of Cd(Zn)Te sample after polishing with 3 µm Al_2O_3. Strongly adhering aluminum oxide particulates remain present on the surface despite efforts to remove these abrasives with strong solvents.

Despite the useful quantitative data provided by EDS, it is not efficient to study surface cleaning methodology using this technique. This is partly due to the limited sample size, the limited sampling area, the possible sources of contamination which may be incurred due to sample handling, mounting and loading into the EDS vacuum system to name a few reasons. Instead, a quick method which can be used both at the microscopic level, as well as over much larger areas was necessary. The Brightfield (BF) and Darkfield (DF) microscopy modes were used to achieve this capability.

Samples were processed using the 3 μm Al_2O_3 and 1 μm diamond mechanical polishing protocol, as well as the chemical polishing protocol previously described. To demonstrate the effects of these processes on surface contamination, Brightfield (BF) and Darkfield (DF) images of the wafer surface immediately before and after each process to illustrate the differences. Furthermore, the surface was also characterized immediately following the wax-de-bonding stage to illustrate the effects of the wax removal process on the wafer surface condition. It was critical that these images were taken at the same time as the process to avoid environmental sources of contamination. The particles on each surface were then counted and sorted according to their diameter for comparison.

Presented in **Figure 38** are 50x magnifications of the Cd(Zn)Te samples after each respective surface treatment, for both BF and DF microscopy modes. Samples polished using a 3 μm Al_2O_3 abrasive, exhibited a surface roughness as high as 30 nm, as measured by the Atomic Force Microscope. As may be seen in **Figure 38**(a), the high surface roughness has made it difficult to extract surface particulate information from the sample in both BF and DF mode, as the surface exhibits a large degree of scattering. Though the surface particulates are clearly present on the surface, it is difficult to separate the particulates from the visible scratches on the surface for analysis.

Samples polished using a 1 μm diamond abrasive, however, exhibit a lower surface roughness between 2-5 nm, as measured by the Atomic Force Microscope. This procedure produces a uniform surface finish across the entire wafer, albeit with a high density of very fine scratches and also exhibits a significant density of foreign particles on the surface. As may be seen in **Figure 38**(b), these fine scratches are visible in the DF mode, while they are not visible in

the BF mode. Furthermore, due to the low roughness of the surface, the surface particulates may be differentiated from the background and counted.

After mechanical polishing using the diamond abrasive, the wafer was chemically polished for using the chemical polishing solution proposed by Singh *et al* (15). The surface immediately after chemical polishing was captured using the DF microscopy in order to demonstrate the pristine nature of the surface after chemical polishing. This may be seen by the absence of features in **Figure 38**(c). Indeed, the surface had to be scoured for any objects for which to focus. The particle counts for the DF images were practically null across the wafer surface as nearly **no** particulates were observed across the surface.

The same wafer was subsequently de-bonded from the wax carrier using standard wax removal solvents. The sample was dried and characterized again using DF microscopy. Presented in **Figure 38**(c) and (d) are 50x magnifications of the surface of polished Cd(Zn)Te after chemical polishing and wax de-bonding. The results demonstrate that the wax removal process can actually introduce a very large amount of surface contamination.

Presented below in in **Figure 39** are typical particle class counts for each above mentioned processes normalized for surface area. With respect to the 1μm diamond polishing process, it was observed that the particulates appear in concentrations larger than 200 mm^{-2} for particle class sizes between 2-3μm. These small particulates are associated with slurry residue adhering to the surface after the polishing operation and not being removed efficiently. For the larger diameter particles, their density falls quickly for increasing particle class, and is less than 10 mm^{-2} for particles larger than 10μm. These larger particles are likely associated with the slurry residue conglomerating into larger particulates as the surface dries.

Immediately after chemical polishing, the surface particle counts are practically null across all particle classes. However, after wafer de-bonding and the subsequent wax removal processes, the surface concentration of particulates increased orders of magnitude across nearly all particle classes This was evident especially for larger particle sizes up to 18μm.

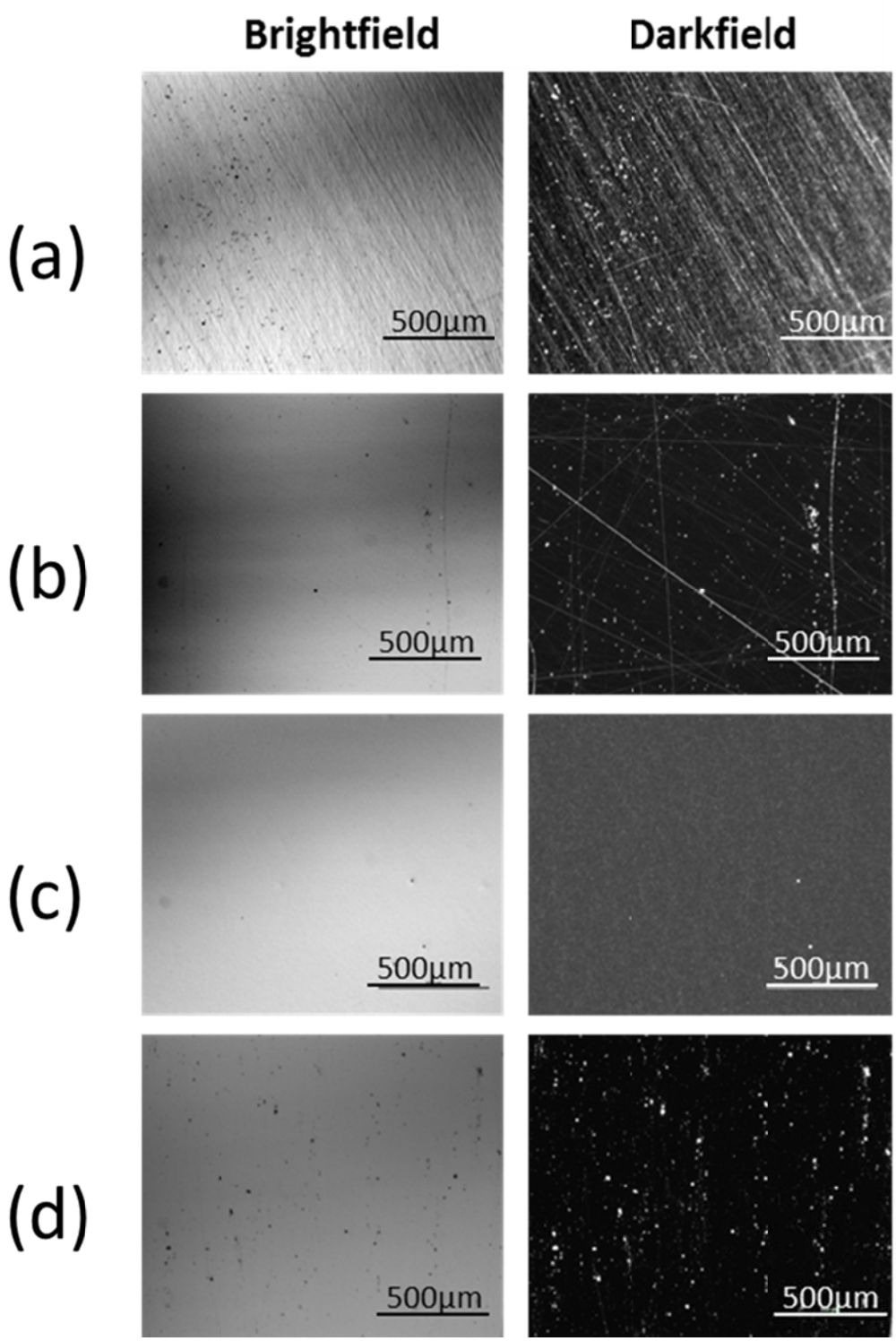

Figure 38 50x Optical microscope images of Cd(Zn)Te surfaces after (a) 3 µm Al_2O_3 polishing (b) 1 µm diamond polishing (c) chemical polishing (d) wax removal

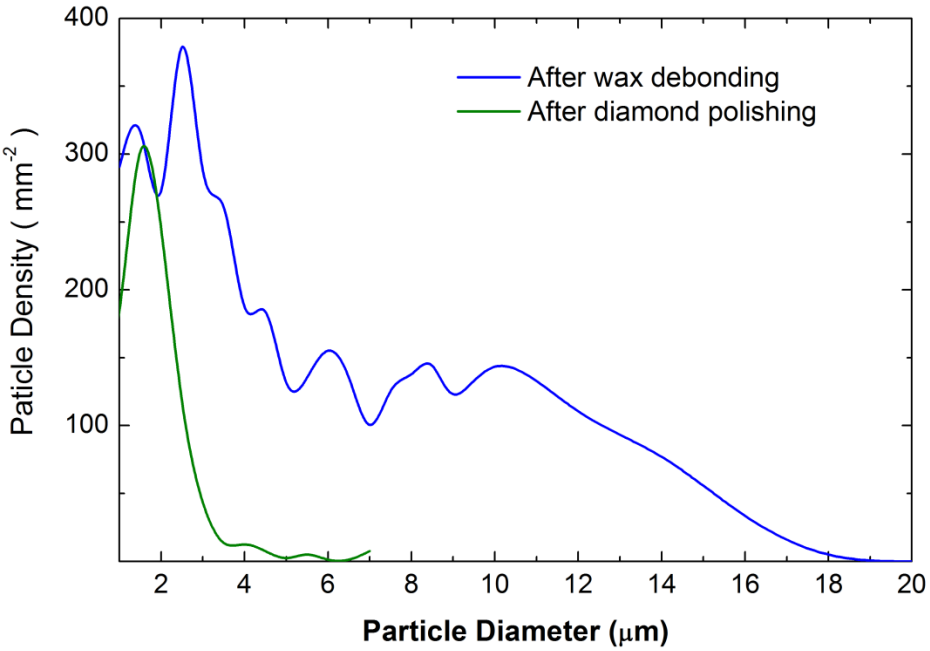

Figure 39 Surface particle density on polished Cd(Zn)Te after different surface treatments

Single microscope images of the surface provide a more macroscopic picture than the Atomic Force Microscope, but still exhibit substantial variation depending on where on the wafer surface the image is taken. This is in addition to all the statistical factors influencing particle adhesion to the surface. In fact, there are large non-uniformities in particulate concentration arising from how the surface is dried after the polishing operation as well. Therefore, an optical mapping of a 25mm x 12 mm Cd(Zn)Te sample is presented in **Figure 40**, to better represent these differences.

Figure 40(a) represents the surface after 1 μm diamond polishing. It is interesting to first note how the concentration of particulate matter is highest near the edges of the sample as may be seen by the high density of white dots. This segregation of particulate matter is related with the way in which the slurry is removed from the surface, and the surface is dried. When the surface is rinsed with a cleaning agent such as Isopropanol and dried using nitrogen, a large part of the particles adhering to the surface are removed by the solvent. The solvent however, transports these particulates away from the center to the edge. When the solvent dries, there is a deposit of abrasive particulates at the edge. In general, the particles are small in size, and are present in a relatively high density.

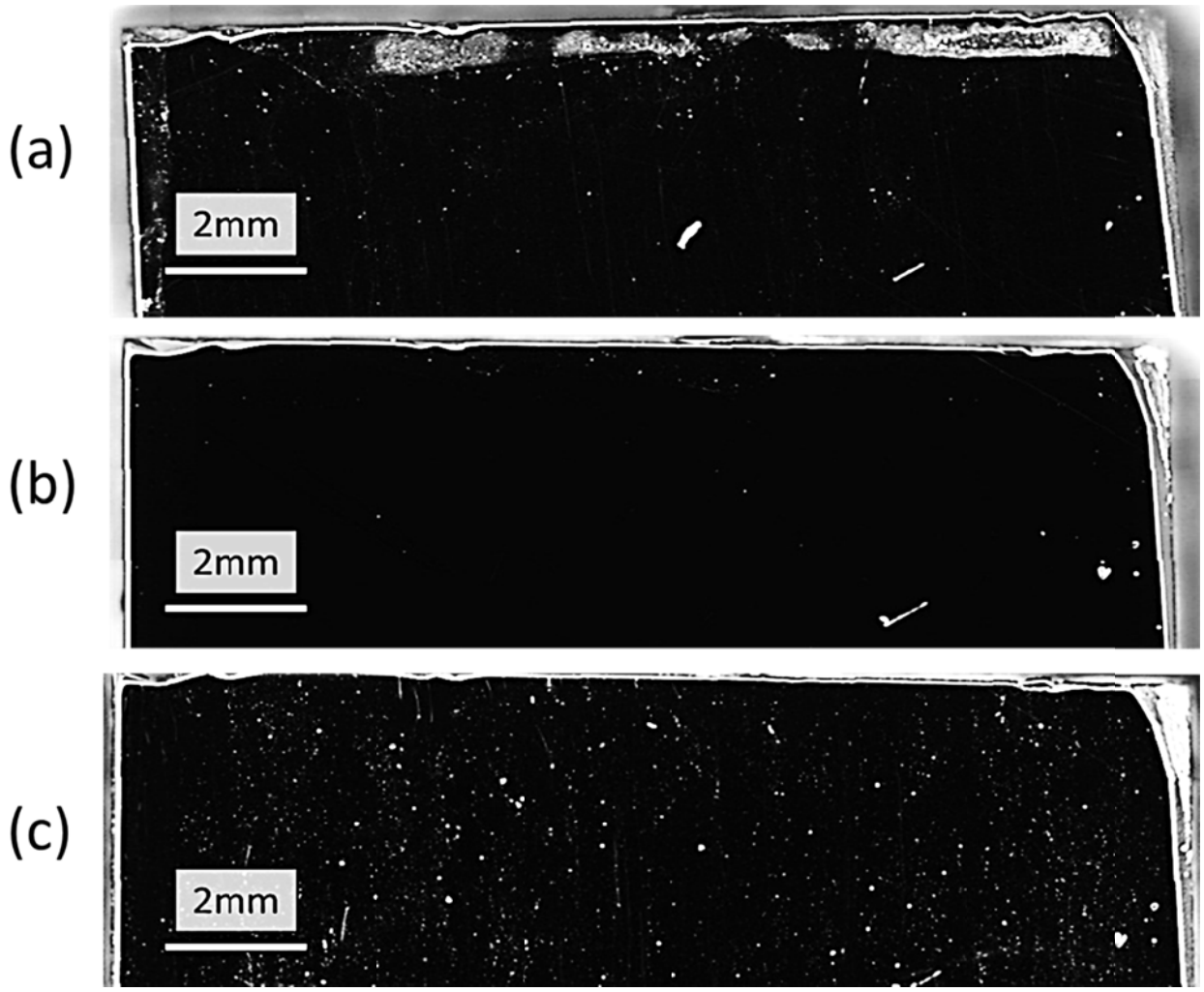

Figure 40 Darkfield optical mapping of Cd(Zn)Te surface after (a) 1 micron Diamond polishing (b), Chemical Polishing (c) and after de-bonding and wax removal (bottom).

The middle surface mapping Presented in **Figure 40**(b) is a mapping of the surface of the same wafer after chemical polishing. The small fine scratches have been removed from the surface, as have been a majority of the particulates introduced by the previous polishing operation. Near the edges of the wafer, there is a slightly higher density of particulates, but in general, the surface appears smooth and relatively clean of contamination. It is important to mention, that many of the smaller and larger dots which are observable in **Figure 40**(b) may not actually be particulates, but are features in morphology of the Cd(Zn)Te surface. These features may be associated with the second phase inclusions in the bulk of the material (see **Figure 5**(a) page 333).

Efforts to reduce the size and density of second phase inclusions in Cd(Zn)Te are therefore also important from the perspective of surface preparation. We have observed that for larger Te inclusions, between 20-30 μm, the impact on surface morphology is substantial. During the chemical polishing process, the Cd(Zn)Te surface reacts with the chemical slurry faster than the second phase Te-inclusion. As a result, the bulk material surrounding the inclusion is slowly removed until the inclusion is released from the Cd(Zn)Te matrix. This leaves behind a depression in the surface where the second phase inclusion had once occupied. This change is detected by the optical microscope in DF mode as light is scattered by this surface depression.

It is also very likely that larger inclusions (>20 μm) may deeply scratch the surface as they are released from the Cd(Zn)Te surface. This behavior has not been observed for mechanical polishing where the material removal is mechanical in nature and therefore indiscriminate between Cd(Zn)Te and Te inclusions. However this has been repeatedly observed for samples after chemical polishing which have large inclusions. The scratching can be so severe that the samples must be re-processed entirely. For smaller inclusions, less than 10 μm in diameter, this occurs less frequently.

Figure 40(c) is a mapping of the surface of the same Cd(Zn)Te wafer after the wax removal process. After the chemical polishing process, the wafer is removed from the wax fixture, cleaned, and rinsed. After this cleaning process, it becomes evident that the pristine surface has been compromised to a large degree. The surface exhibits very high densities of particulate matter distributed uniformly about the sample surface, and consistent with the particle counts presented in **Figure 39**: orders of magnitude higher densities of particulates, with quite large particulates present

These particulates are thought to be associated with wax from the backside of the wafer being removed by the solvent and transported to the front side of the surface of the wafer during the rinsing operations. In general, these small particulates are very difficult to remove. That this contamination is strongly adhering to the surface, and may be non-polar in nature, suggests that it may interfere strongly with the electrode deposition process.

3.8.3 Implementation of CFTs

In order to eliminate the wax-bonding procedure from the process, wafers were mounted rigidly using wax as well as the alternative capillary force templates (CFTs) in order to demonstrate the difference between the two methods. Presented in **Figure 41** is an example of a 10 mm x 10 mm Cd(Zn)Te sample polished using wax based methods and using a CFT. Because a de-bonding process is not necessary using the CFT approach, the pristine surface after chemical polishing is preserved.

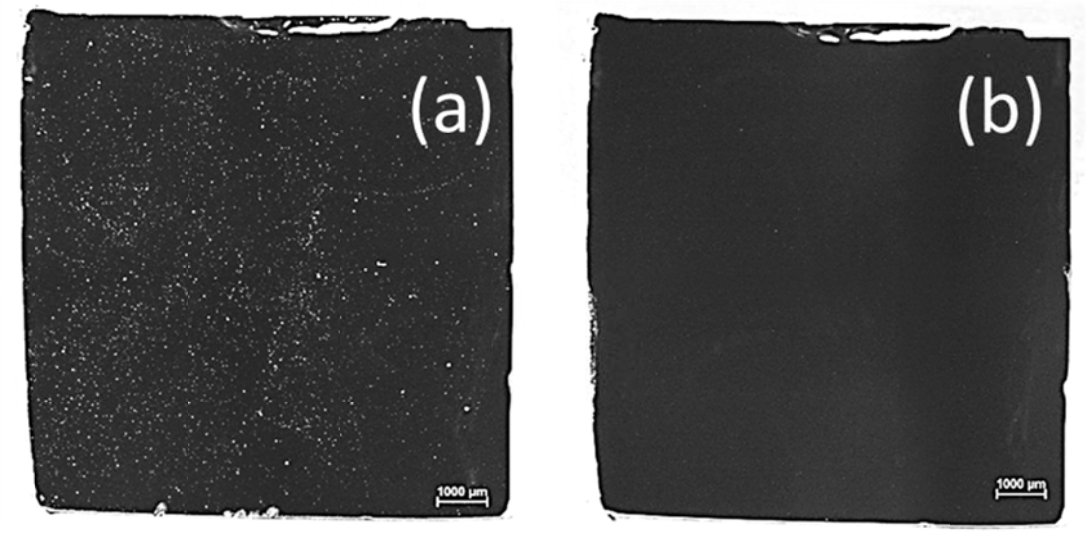

Figure 41 10mm x 10mm Cd(Zn)Te simple after chemical polishing and de-bonding using a wax mounting fixture (Top) and using a wax-less mounting fixture (bottom)

3.9 Electrode Deposition

In the preceding sections, the development of surface engineering protocols for processing Cd(Zn)Te crystals has been discussed in great detail. It is also important to include some description of the methodology used for contact deposition which has been applied in this work. For all detectors studied in this investigation, electrodes have been deposited primarily by the Au electroless method. This chemical method of deposition creates a strong chemical bond between the contact and the semiconductor when compared to physical deposition methods such as sputtering and evaporation. This technique also helps to reduce the formation of oxides at the interface metal/Cd(Zn)Te. (the Au-Cd(Zn)Te interface is discussed in more detail in Section 7).

Detectors fabricated with non-injecting quasi Ohmic contacts on fully depleted high resistivity material will exhibit linear current current-voltage characteristics. The leakage current is limited only by the bulk resistivity of the semiconductor. It is for this reason that gold is often chosen as the metallization contact.

Electrode deposition has been carried out using a solution consisting of 1 g $AuCl_3$ in 25mL water. The equation describing the chemical reaction between the chlorate solution and the Cd(Zn)Te surface may be described by **Equation 4**. The chloro-aurate anions react preferentially with the Cd on the surface of the sample leading to the formation of Au-Te and rejecting Cd^{2+} ions in the solution.

Equation 4
$$2 \cdot AuCl_4^- + 6 \cdot Cd(s) \rightarrow 2 \cdot Au(s) + 8 \cdot Cl^- + 3 \cdot Cd^2$$

A 15mm x 25mm sample which has undergone the electroless gold deposition process is shown in **Figure 42**. As may be seen from **Figure 42(**b), this experimental technique deposits Au on all exposed surfaces of the wafer. Therefore, an additional post-process step is required to remove the Au from the lateral edges to create planar devices. A discussion of this procedure is reserved for Section 4 of this chapter.

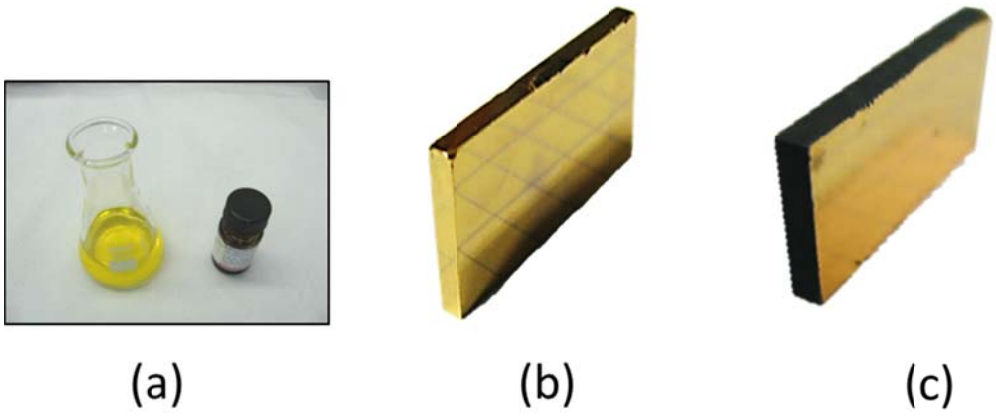

Figure 42 (a) Simple, low cost experimental arrangement required for Au electroless deposition: 25 mL DI water mixed with Gold Chloride, pH ~7 (b) 15mm x 25mm wafer after Au deposition, (c) 15mm x 25mm wafer after lateral edge treatment

SEM and EDS measurements of Cd(Zn)Te surfaces treated using the method are presented in below in **Figure 43**. The non-uniformity of the surface morphology is related with the etching procedure which has been discussed above. Indeed, the two circular shaped features in the morphology, highlighted in **Figure 43**(b), are associated to the non-uniform etching rate of the surface.

While Br_2 Methanol is effective at removing surface oxides and eliminating the damage layer imparted by the polishing process, non-uniformity of the etching process is a common phenomenon, and appears to create surface defects such as those shown below. To eliminate such features from the morphology, further development of the aforementioned chemical polishing protocol is needed. Indeed, comparing this typical surface with those of the commercial detectors shown in **Figure 2** on page 329 of this chapter, the difference is remarkable.

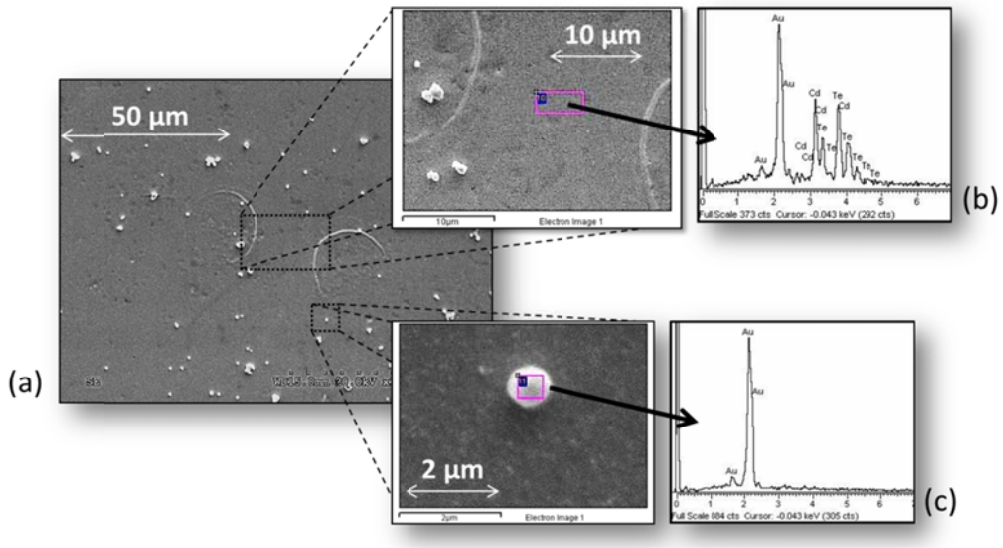

Figure 43 Left: SEM of surface of Cd(Zn)Te wafer after electroless process. Middle: High magnification of surface features. Right: EDX Spectra of features on surface demonstrating the presence of Cd, Te, and Au.

3.9.1 Photolithographic Methods

Although the development of pattered electrodes, and measurement of pixelated detectors was not the objective of this thesis investigation, the development of detectors with patterned

electrodes was investigated with some success. Indeed, the objective of this investigation was to develop a flexible and cost effective method for fabricating pixelated detectors at the laboratory level for characterization of the crystal spectroscopic properties.

This experimental work which has been carried out required the use of photolithographic methods and related infrastructure, and all work was carried out within an ISO-4 class cleanroom. To create the patterned electrodes, a 2-D CAD layout with the desired electrode geometry was designed and printed on a transparency. This transparency would serve as the mask for subsequent patterning. This mask geometry was placed above the sample and was exposed for a duration of 4 minutes. A Karl Suss MJB 3 Mask Aligner, as shown below in **Figure 44**, was used for this exposure. The exposed regions were subsequently removed using developer MF 319 manufactured by Rohm Haus.

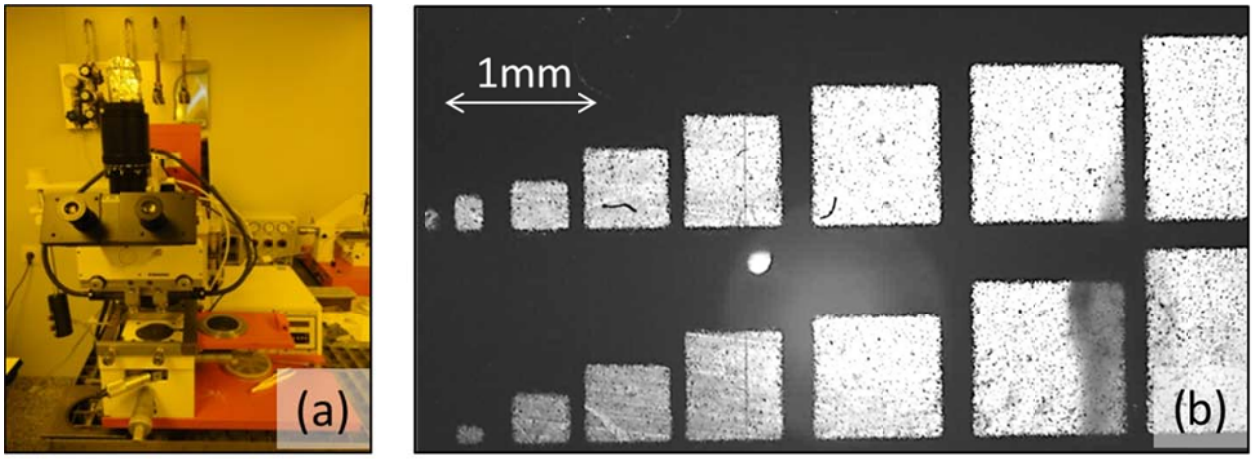

Figure 44 (a) Karl Suss MJB 3 Mask Aligner was used inside a ISO-4 Class Cleanroom at UAM Microelectronics Department. (b) Printed reproduction of 2-D CAD layout with various size square features.

This first study carried out using the Karl Suss mask aligner was intended to identify the lateral resolution achievable using photolithographic masks based on LaserJet printing technology. Indeed, the advantage of using a LaserJet printing technology for generating photolithography masks are (i) low cost of mask (ii) flexibility in mask design (iii) rapid prototyping. For the LaserJet printing, a Konika Minolta TA C350 PCL5c printer was used (600ppp). The as-printed transparency is presented in **Figure 44**(b). From this image, it is

evident that this reproduction begins to lose fidelity for feature sizes smaller than 100 x 100 μm. In some cases, the features do not even appear in the transparency. However, for features with dimensions 250 x 250 μm and larger, the reproduction appears of sufficient quality for laboratory purposes.

Patterned electrodes with the desired geometry were prepared using the 2-D CAD representation. This particular mask was designed for detectors 10 mm x 10 mm in size. The configuration of this pattern consists of an external guard ring circumventing each detector, for eliminating surface leakage current. A steering grid runs between each of the individual electrodes arranged in a 3 x 3 array. The size of each pixel is 1.5 mm x 1.5 mm square.

To prepare Cd(Zn)Te detectors for electrode patterning, the electrode surfaces were prepared using methods discussed in Sections 3.3-3.9. A Class 4 cleanroom facility was used for chemical etching and electrode patterning. Immediately after chemical etching using Br_2 methanol, the 50 mm wafers were spin-coated using 2 mL of S1813 G2 Photoresist to deposit a thin film of photoresist on the electrode surfaces. These wafers were spin-coated at a velocity of 2000 RPM for 20 seconds. The samples were immediately baked at 90ºC for 20 minutes to dry and harden the photoresist. Using these methods, a photoresist coating thickness of nearly 1 μm was expected.

After the photoresist hardens, the detector material is loaded onto the Karl Suss MJB 3 Mask Aligner for mask exposure. Each sample was exposed for 4 minutes, a time experimentally determined to be sufficient for the photolithographic process. The detectors were subsequently immersed in a developer bath, and thoroughly cleaned using deionized water. After this final photolithographic step, it was possible to see the photoresist pattern in order to ensure all of the preceding steps were carried out correctly. The patterned wafers are then immersed in an Au-electroless bath for contact deposition for 5 minutes. Presented in **Figure 45** are photos of typical 50 mm wafers after photolithographic patterning and gold deposition.

To determine the Au electrode geometry was consistent with the mask, optical microscopy methods were employed to evaluate the uniformity and quality of patterning and electrode deposition. Presented in **Figure 46**(a) and (b) is an optical mapping of one of the 50mm wafers which has been patterned using this geometry. As may be seen, the guard ring, steering grid, and

electrode are all represented as distinct entities. This was also confirmed using electrical measurements.

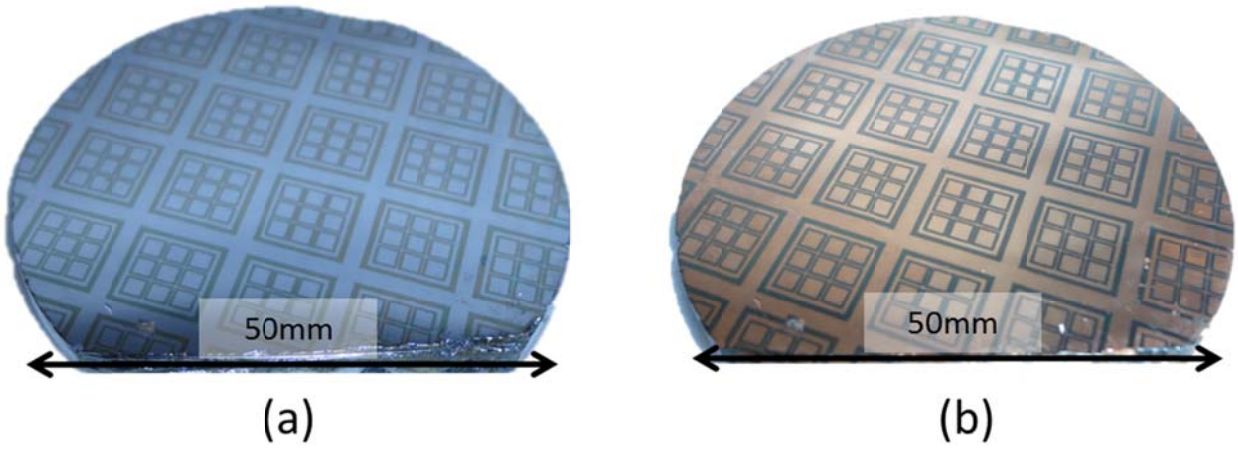

Figure 45: (a) 50 mm diameter Cd(Zn)Te wafer after photolithography. (b) 50mm wafer after gold deposition using the electroless method

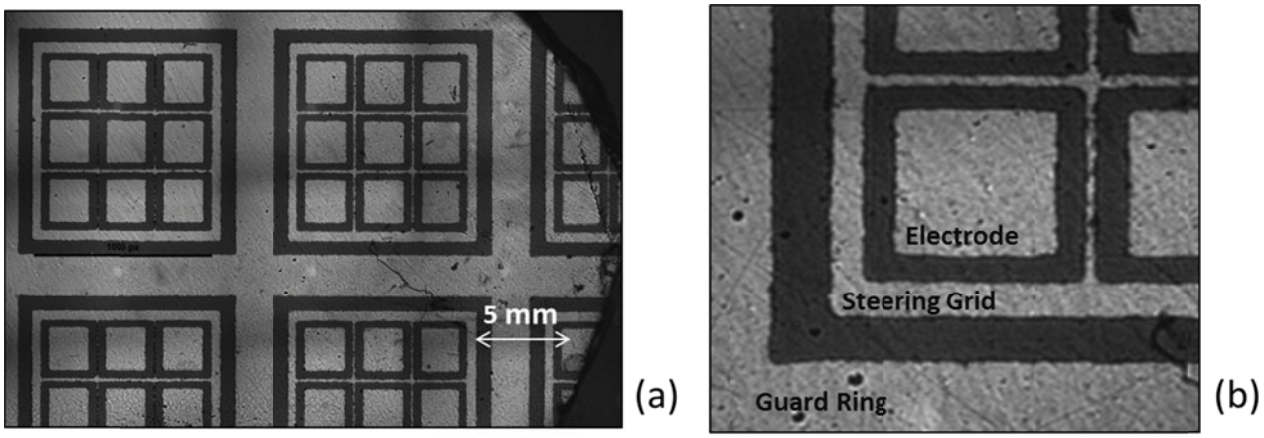

Figure 46 (a) Wafer patterning of 50 mm Cd(Zn)Te using LaserJet based photolithographic methods. (b) Detail electrode pattern with guard ring, steering grid, and individual pixel.

3.10 Conclusions

The work carried out in this investigation was focused on the development of protocol for processing of 50mm diameter ingots, and the production of radiation test devices. As a result,

several new processes have been developed and this technology has been scaled and implemented on 50 mm diameter wafers. We conclude the following

1. A diamond wire saw mounting fixtures has been designed and implemented for effectively cutting 50 mm Cd(Zn)Te ingots, reducing wafer bowing, TTV, and improving the yield of useful material.
2. A multi-stage lapping, mechanical polishing, and chemical etching process has been developed which produces surfaces with roughness < 2nm, and improving the near surface crystalline quality.
3. One of the major sources of surface contamination in the surface preparation of Cd(Zn)Te has been associated with the wax de-bonding process.
4. CFT templates have been implemented to successfully reduce surface contamination across all particle class sizes of polished wafers
5. Methods for deposition of Au electrodes have been developed for both planar and patterned electrode geometries, using a photolithographic approach and LaserJet printing technology.

Further work on following this line of investigation will include the further development of the chemical polishing protocol for 50mm diameter wafers, the development of wafer annealing to eliminate large inclusions which tend to scratch the wafer surface, as well as further investigation, development and testing of pixelated Cd(Zn)Te detectors.

This page intentionally left blank.

4 LATERAL SURFACE MORPHOLOGY OF DETECTORS AND TEMPORAL EFFECTS

Section Contents

4.1 Introduction

There are several challenges to producing detector grade material based on Cd(Zn)Te, one of which includes the mechanical engineering processes such as ingot slicing, wafer lapping and polishing, as has been discussed in the previous section, for preparation of the anode/cathode surfaces. H. Yoon et al describes how the effects of saw-cutting, lapping, polishing, and etching effect crystalline periodicity and sub-surface disorder in Cd(Zn)Te using High Resolution X-ray Diffraction (9). This sub-surface disorder is a result of the mechanical deformation of the surface and destruction of lattice periodicity.

While the effects of anode/cathode surface treatment on detector performance has been reported on by several groups (20) (21) (22) (23) (24), the surface treatment given to the lateral edges of Cd(Zn)Te devices has received little to no attention. As shown in **Figure 47**, the surface resistivity of these lateral edges can influence the overall resistivity of the detector. Indeed, the deformation of the Cd(Zn)Te surface throughout the mechanical slicing and lapping processes imparts extended dislocations into the sub-surface material (See **Figure 21** on page 354). If this damage layer is not removed as it is for the anode and cathode surfaces, these dislocations could provide a larger volume of avenues for the surface leakage current to pass between anode and cathode and effectively degrade the detector performance. For this reason, special consideration to the treatment to the lateral sides is necessary, in order to identify practical methods for enhancing detector performance.

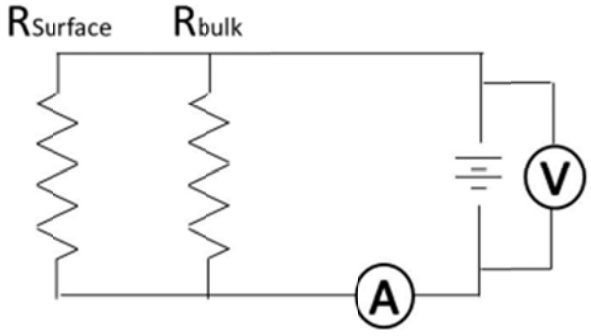

Figure 47 Simplified circuit diagram of a Cd(Zn)Te detector whose surface leakage current is limited by the surface resistivity.

In this section, the lapping and polishing processes which have been investigated in the previous section (see Sections 3.4-3.6) are implemented for modifying the morphology of the lateral edges of planar devices. The objectives of this study are to identify efficient and reproducible methods to (i) prepare bulk crystals for electrode deposition and (ii) reduce leakage current in planar devices.

4.2 Experimental

4.2.1 Material Synthesis and Sample Preparation

High resistivity Cd(Zn)Te ingots were grown by the VGF method for this study. The VGF system used in this work has 5 independently controlled heater zones used to create a dynamic temperature profile across the ingot. All three ingots, shown below in **Figure 48**, were grown using 7N Cd(Zn)Te material (5N+ Corp) loaded into a Boron Nitride (BN) crucible, and sealed within a quartz ampoule under a vacuum of 2e-6. The ingots were all doped with between 3-5ppm of Indium to achieve electrical compensation.

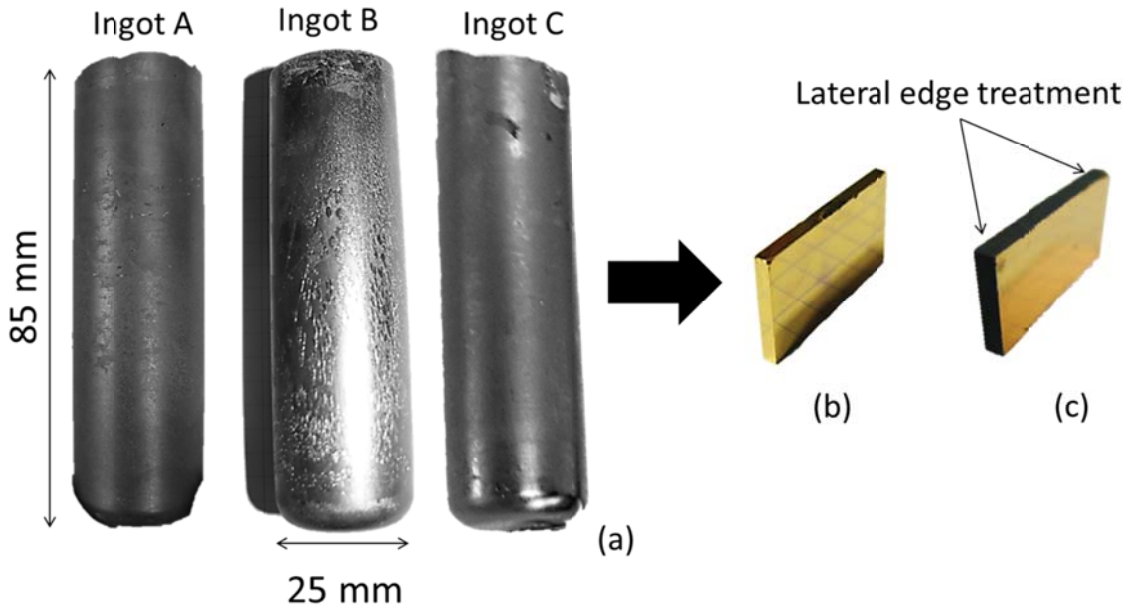

Figure 48 (a) Ingots A, B, and C used for harvesting devices studied in this work. One example of the 15mm x 25mm x 2mm Cd(Zn)Te crystals used in this study after (b) gold electroless process and (c) after lateral edge treatment

4.2.2 Processes Applied to Detector Fabrication

Wafers were sliced from the ingot using a diamond wire saw, and subsequently lapped and polished using a Logitech PM5 and CP3000 respectively. Detector material with dimensions of 8 mm x 8 mm x 1.5 mm and 15 mm x 25 mm x 2 mm were used in this work. Prior to metallization, samples were etched in 2% Bromine methanol for 30 seconds. Contacts were deposited using the gold electroless method. More detailed information regarding this technique has been reported elsewhere (25) and are described in the previous section.

After electrodes were deposited, the lateral edges of the detector were treated using lapping and polishing processes, as may be seen in **Figure 48**. It is important to comment that this lateral edge treatment was a necessary step to remove the gold from the electroless process. The effect of each subsequent surface processing step on leakage current and gamma response is presented in this work.

The abrasives used in this work for lapping and polishing the edges of the detectors include 9 μm Al_2O_3 and 3 μm Al_2O_3 distributed by Logitech, UK as well as 1 μm mono-crystalline diamond distributed by Eminess Technologies (U.S.). The chemical polishing solution used in this work is that reported by Singh *et al* consisting of Br_2 in ethylene glycol (15).

The lateral edge treatment applied to each detector included both lapping and polishing processes. Only the 9μm and 3μm Al_2O_3 abrasives were used for lapping the lateral edges of the detector. Hereafter, these processes will be referred to as *LEL-9* and *LEL-3*, which signifies **L**ateral **E**dge **L**apping using **9**μm Alumina.

For the mechanical polishing process, the 3μm Al_2O_3 and 1μm diamond abrasives were investigated. As already mentioned a 2% Br_2 in ethylene glycol solution was also used for the chemical polishing process. Hereafter, these processes will be referred to as *LEP-3*, *LEP-1*, and *LEP-CP* respectively. This naming scheme signifies **L**ateral **E**dge **P**olishing, using the respective polishing process of **3**μm Al_2O_3, **1**μm diamond, and **C**hemical **P**olishing.

4.2.3 Characterization Techniques and Methodology

Current-Voltage characteristics of detectors with planar contacts were measured using a Keithley 2400 source-meter, from which bulk resistivity could be determined for each detector after surface modification. The change in surface area of each detector as a result of the

lapping/polishing process was also taken into account when calculating current density. As the bulk resistivity of the material remains constant after each process, changes in I-V are attributed to changes in surface leakage current associated with the lateral edge treatment.

Bulk resistivity was measured using **Equation 5**, where $\boldsymbol{A}$ is detector area, ρ is the sample resistance determined from the I-V curve and δ is the detector thickness.

Equation 5 $$\boldsymbol{\Omega = (A \cdot \rho)/\delta}$$

Samples prepared for CL measurements were cut from the same region of Ingot 3. In total, five samples were prepared, one using each surface treatment: lapped using 9 & 3µm Al_2O_3 (*LEL-9* and *LEL-3*), polished using 3µm Al_2O_3, 1µm diamond, and chemically polished using the formulation proposed by Singh *et al* (*LEP-3*, *LEP-1*, *LEP-CP* respectively). Taking into account that each sample comes from the same region of the ingot, changes in the CL signal are attributed to changes imparted by the different surface treatments.

Secondary electron images and cathodoluminescence (CL) measurements of the lapped and polished Cd(Zn)Te surfaces were realized using an FEI-INSPECT and an Hitachi2500 Scanning Electron Microscope in conjunction with a R5509 Hamamatsu photomultiplier tube used for CL detection. For these measurements, the samples were cooled to a temperature of 90K, the electron beam under a 20kV potential difference was used, and all of the emission spectra were normalized to the maximum peak emission value.

Cd(Zn)Te detector performance was characterized using gamma spectroscopy measurements using a ^{133}Ba source, placed 3mm from the detector cathode. The pulse from the detector was amplified by a shaping amplifier with a shaping time of 1.5µs. The shaped signal was digitized and captured using an APTEC multichannel analyzer. The APTEC's control software finally records the data in comma separated values format. As the surface modification affects the surface leakage current, detector performance was measured in terms of the electronic noise introduced into the system i.e. energies lower than the 35keV peak of ^{133}Ba.

While the edges of each detector were subjected to each surface treatment, the cathode and anode of the detector were protected using a thin protective film of paraffin wax. This prevented

the cathode and anode from becoming damaged. By using this approach, the electrodes deposited on each detector were the same throughout the entire study, with no need to re-contact the detectors (which could possible introduce a large degree of error into the study of the gamma response).

To identify optimal working conditions, each detector was biased through a range of voltages to identify the best working voltage specific to each detector. The surface morphology study on detector performance was then carried out at this optimal voltage (though for some surface treatments, it was not possible to reach this working voltage).

4.3 Results & Discussion

The typical surface morphology of each treatment is presented in detail in the previous section (see Sections 3.4, 3.5, and 3.6). The LEL-9 and LEL-3 treatments exhibit very rough and are non-reflective surfaces. From the SEM images shown in **Figure 19** on page 351, the surfaces indeed do appear somewhat similar.

AFM measurements of the Cd(Zn)Te surfaces after polishing are presented on pages 357, 358, and 359 of this chapter. While the LEP-3 treatment produces a reflective finish, the surface contains a high density of relatively large scratches and exhibits RMS roughness >20nm. The LEP-1 and LEP-CP treatments both exhibit smoother surface morphology with lower scratch densities and depths.

Presented in **Figure 49** are typical I-V characteristics for one of the detectors used in this study, subjected to all of the treatments. The change in leakage current before and after each subsequent lapping and polishing operation was measured to observe the effects of surface preparation on the performance of planar detector geometry. The contacts and bulk resistivity have not changed and therefore the change in the I-V characteristics may be attributed to changes in surface leakage current. The axis is presented in logarithmic scale, necessary to illustrate the large differences between each surface treatment.

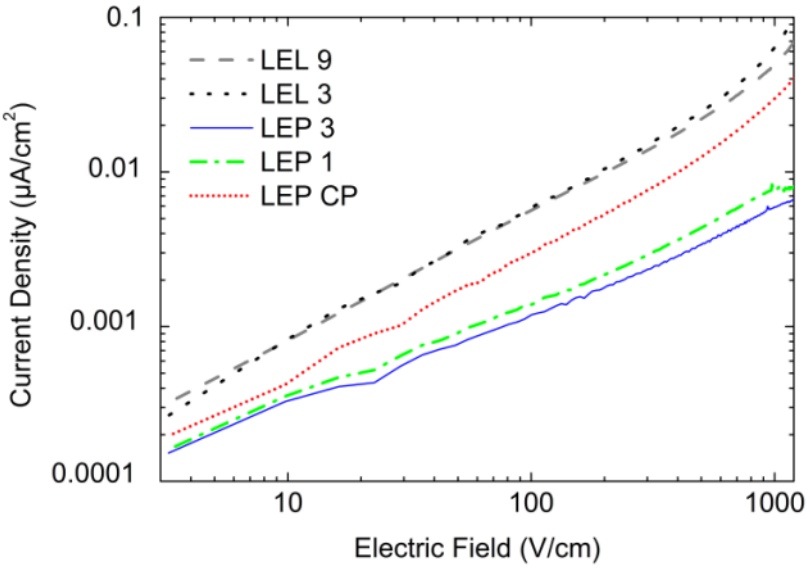

Figure 49 Typical I-V characteristics after modifying the lateral edges using different surface treatments.

After both the LEL-9 and LEL-3 treatment, the leakage current of each detector was higher than compared with the LEP-3 treatment. This is thought to be associated with the surface damage layer imparted by lapping creating dislocations and reducing the electrical resistivity of the surface layer.

A reduction in leakage current was obtained after polishing the lateral edges using the LEP-3 treatment, as may be seen in **Figure 49**. This treatment changes the edges from having a non-reflective matte surface to a mirror-like reflective finish. Leakage current for planar detectors having undergone LEP-3 treatment showed the best I-V characteristics of all edge treatments investigated.

After polishing the lateral edges of the detectors using the LEP-1 treatment, the lateral edges of the Cd(Zn)Te detector are substantially smoother. The removal rate of this polishing stage is much lower than previous steps, but the surface roughness is substantially reduced from >20nm for the LEP-3 treatment to < 5nm RMS roughness as measured by AFM. Despite this improved surface morphology, detectors having undergone LEP-1 treatment exhibited a slight increase in leakage current, as may be seen in **Figure 49**. This result was repeated on more than six different detectors harvested from different ingots to confirm the reproducibility of the result. In each case however, there was only a slight increase in leakage current.

Finally, the lateral edges of the planar test devices were chemically polished using a LEP-CP treatment. The cathode and anode of the devices were protected using a thin wax film, which could be removed afterwards using trichloroethylene. Detectors having undergone LEP-CP treatment exhibited higher leakage current, and showed some instability over a short period of 24hrs. The mechanical lapping and polishing treatments did not exhibit large changes over such short period of times, but an investigation of the temporal stability of these surfaces is discussed below (see page 393 of this section).

4.3.1 Surface Treatment Effects on Cathodoluminescence

Cathodoluminescence (CL) is a surface sensitive technique which provides a method to evaluate the dominant radiative trapping centers which exist within the bandgap of Cd(Zn)Te. It provides a method for identifying how different surface treatments can introduce different types of surface trapping levels, by the relative intensity of their radiative emissions. In general it may be observed that the luminescence of the surface increases with decreasing surface roughness. This is consistent with the removal of the surface damage layer imparted by polishing, and revealing the properties of the crystal, more close to that of the bulk.

Detectors having undergone *LEL-9* did not exhibit luminescence under both high and low excitation conditions. The absence of a luminescence peak in the sample lapped using the 9μm Al_2O_3 is attributed to non-radiative recombination of electrons being the dominant recombination mechanism.

The CL spectra measured for the sample after *LEL-3* did in fact exhibit a peak near 1.4eV, but only under low excitation conditions. The presence of this luminescent peak is attributed to a reduction in non-radiative recombination centers as a result of using a smaller abrasive particle which produces less surface damage, and reduces the non-radiative centers. Presented in **Figure 50** are the low excitation CL spectra taken for after each lapping treatment.

As the subsurface damage is removed through mechanical polishing using fine abrasives in conjunction with a porous felt pad, the non-radiative recombination centers are significantly reduced. This is related to an improvement in the crystal structure at the surface, and a reduction in the amorphous layer. This is further evidenced by XRD data presented in **Figure 32** (page

360). As a result, the luminescence produced by radiative centers arising from defects in the crystal structure may be more readily detected.

Presented in **Figure 50**(b) are the CL spectra for Cd(Zn)Te samples after *LEP-3*, *LEP-1*, and *LEP-CP* treatment. The CL spectra demonstrates the large dependence of the luminescence properties of Cd(Zn)Te with the surface preparation.

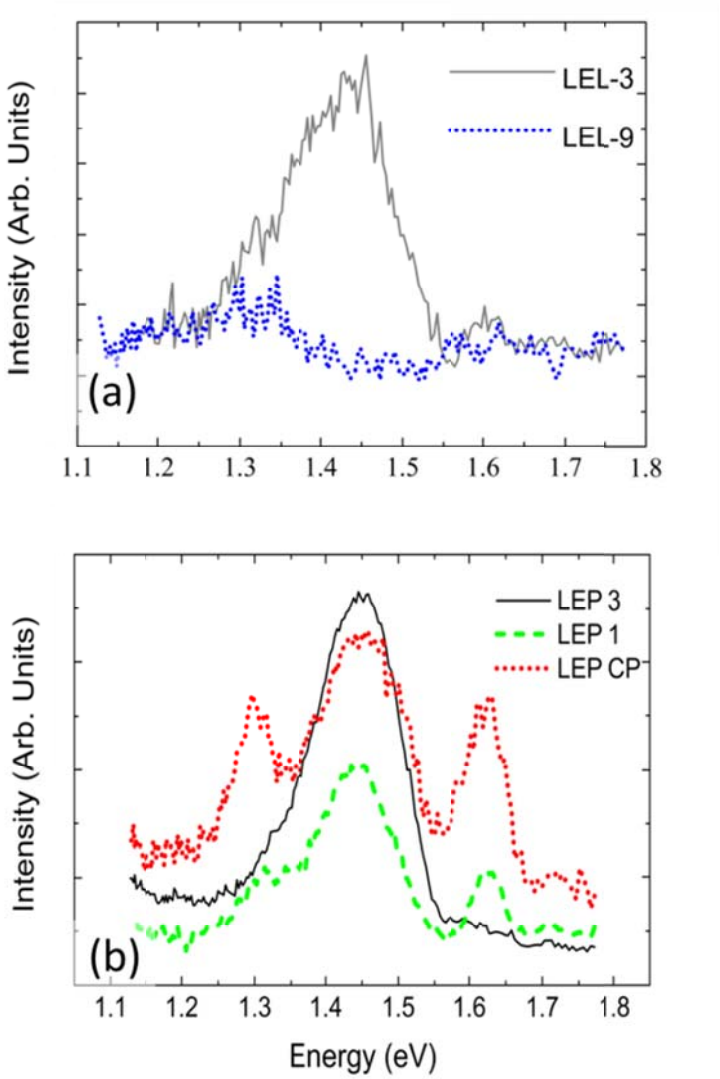

Figure 50 Left: CL intensity of Cd(Zn)Te surface after LEL-9 and LEL-3 treatment. Right: CL intensity of Cd(Zn)Te surface after LEP-3, LEP-1, and LEP-CP treatment.

When the detectors have been subjected to the *LEP-3* treatment, only a single and broad luminescence band located near 1.4-1.5eV is observed in the CL spectrum. It has been observed that after this treatment, the intensity of 1.4eV band is highest compared with the other situations.

Additional polishing of the detector edges using *LEP-1* treatment produces a lower surface roughness, a more uniform surface morphology, and removes to a large extent the surface damage layer imparted by polishing. Indeed, the concentration of surface related traps is reduced by the LEP-1 and LEP-CP treatment as additional luminescence peaks are resolved. The presence of these peaks suggests that the concentration of traps related with the 1.4eV peak are being reduced, while other radiative centers related with the bulk (i.e. near band gap emission centered at 1.6eV and 1.3 eV band related to impurities) may be identified.

Indeed, it has been observed that the concentration of the 1.4eV band plays a strong role in the measured leakage current of planar detectors. For surfaces which exhibited luminescence, the relation between detector resistivity and the peak intensity emission in the 1.4-1.5eV band are presented in **Figure 51**. These values have been determined by measuring the relative intensity, or Peak to Valley of the 1.4eV luminescent peak.

Superimposed upon the CL intensity data in **Figure 51** are also changes in resistivity as between each subsequent processing step (closed square, circle, and triangles). These data show a correlation between the relative intensity of the 1.4eV band and with changes in surface leakage current. We attribute these changes to polishing induced surface defects which increase surface trapping mechanisms, and decrease leakage current.

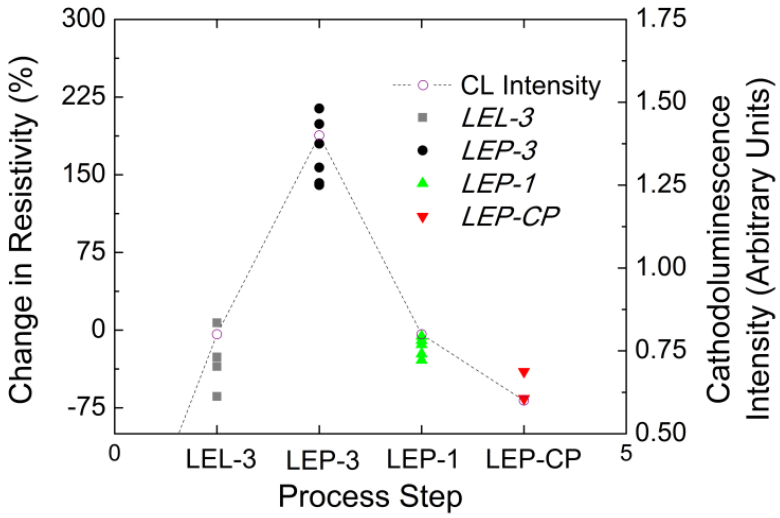

Figure 51 Correlation between the change in resistivity and the CL emission intensity at the 1.4eV band

In terms of electronic noise and improving the signal to noise ratio, the leakage current of a detector is a useful figure of merit for characterizing detector performance under operating conditions. Using the LEP-3 treatment as the treatment which provided the best performance of those treatments studied, changes in leakage current under bias may be represented using **Equation 6**.

Equation 6

$$\Delta I_V = \frac{I_i - I_{LEP-3}}{I_{LEP-3}}$$

where I_V is leakage current measured at a certain voltage (i.e. 500, 750, 1000), I_{LEP-3} is the leakage current measured for LEP-3 treatment, and I_i represents the leakage current from the other treatments at the same bias voltage (i.e. LEL-9, LEL-3, LEP-1, LEP-CP).

Presented below in **Table 4** are percentage increases in leakage current, and their standard deviation for the sample set with respect to the LEP-3 treatment. The number of samples investigated using each treatment are also presented. As is clearly demonstrated, the processes LEL-9, LEL-3, LEP-1, and LEP-CP all result in higher leakage currents with respect to the process LEP-3. Furthermore, increasing standard deviation with increased bias was observed in all of the detectors. This is due to non-linear increases in leakage current of the LEL-9, LEL-3, LEP-1, and LEP-CP with respect to LEP-3, as may also be seen in **Figure 49**

Table 4 Increases in leakage current as a function of bias voltage for LEL and LEP treatments compared with LEP-3

Treatment	**% Increase in Leakage Current**			
	500V/cm	750 V/cm	1000V/cm	# samples
LEL-9	338% σ = 1.50	389% σ = 2.16	424% σ = 3.29	4
LEL-3	223% σ = 1.49	221% σ = 1.56	228% σ = 1.82	13
LEP-1	49% σ = 0.57	55% σ = 0.46	60% σ = 0.49	7
LEP-CP	266% σ = 0.02	302% σ = 0.29	311% σ = 0.94	2

4.3.2 Gamma Ray Spectroscopy

The effect of these surface treatments on the gamma response of Cd(Zn)Te spectrometers is the most important figure of merit. Planar test devices were prepared using the methods described in the previous section using LEL-9, LEL-3, LEP-3, LEP-1, and LEP-CP treatments. The edges of these detectors were first polished using the *LEP-3* treatment as the starting point for this study, due to the improved I-V characteristics. The effects of surface morphology on the detector performance from this point were then studied.

The first observation was that after the *LEL-9* and *LEL-3* treatments, detectors could not reach the same operating voltage as was obtained using the *LEP-3* treatment. Instead, the voltage had to be reduced by up to 50% in some cases to obtain a gamma response. This is due to the increase in leakage current increasing the electronic noise present in the measurement system. In addition to this, the FWHM of the 35keV photo peak also increased substantially.

What is even more interesting is that the detector was operative at the reduced bias only for a short period of time. Indeed, for several detectors, the electronic noise would increase with time and would degrade the measured gamma spectra. In some cases this happened during a single recording measurement, in other cases it happened during a separate trial using the same detector under identical conditions.

Shown below in **Figure 52** is the gamma response of one of the detectors measured during a 2 hour period, after the LEL-9 treatment. The data collection was reset every thirty minutes to collect new data and observe how the detector changes with time. Also presented in this figure is the gamma response of the same detector after LEP-3 treatment illustrating the differences in the FWHM associated with these two processes.

After the *LEP-1* and *LEP-CP* treatment, using the Br_2 ethylene glycol solution, it has been demonstrated through *I-V* measurements that the detector leakage current increases as a result of these surface modifications. Presented below in **Figure 52** is the gamma ray response for a Cd(Zn)Te planar detector measured after the *LEP-3* treatment and after subsequent *LEP-1* and *LEP-CP* treatments. These results are in agreement with *I-V* measurements as the increase in dark current corresponds to a decrease in the signal to noise ratio. The large photo peak shown here is associated with the 31-35KeV emission line of ^{133}Ba. From this data it is clear that lower background noise in the detector is obtained after the *LEP-3* treatment. Additional polishing of

the edges results in increased dark current flowing between anode and cathode, which increases the RMS of the electronic noise.

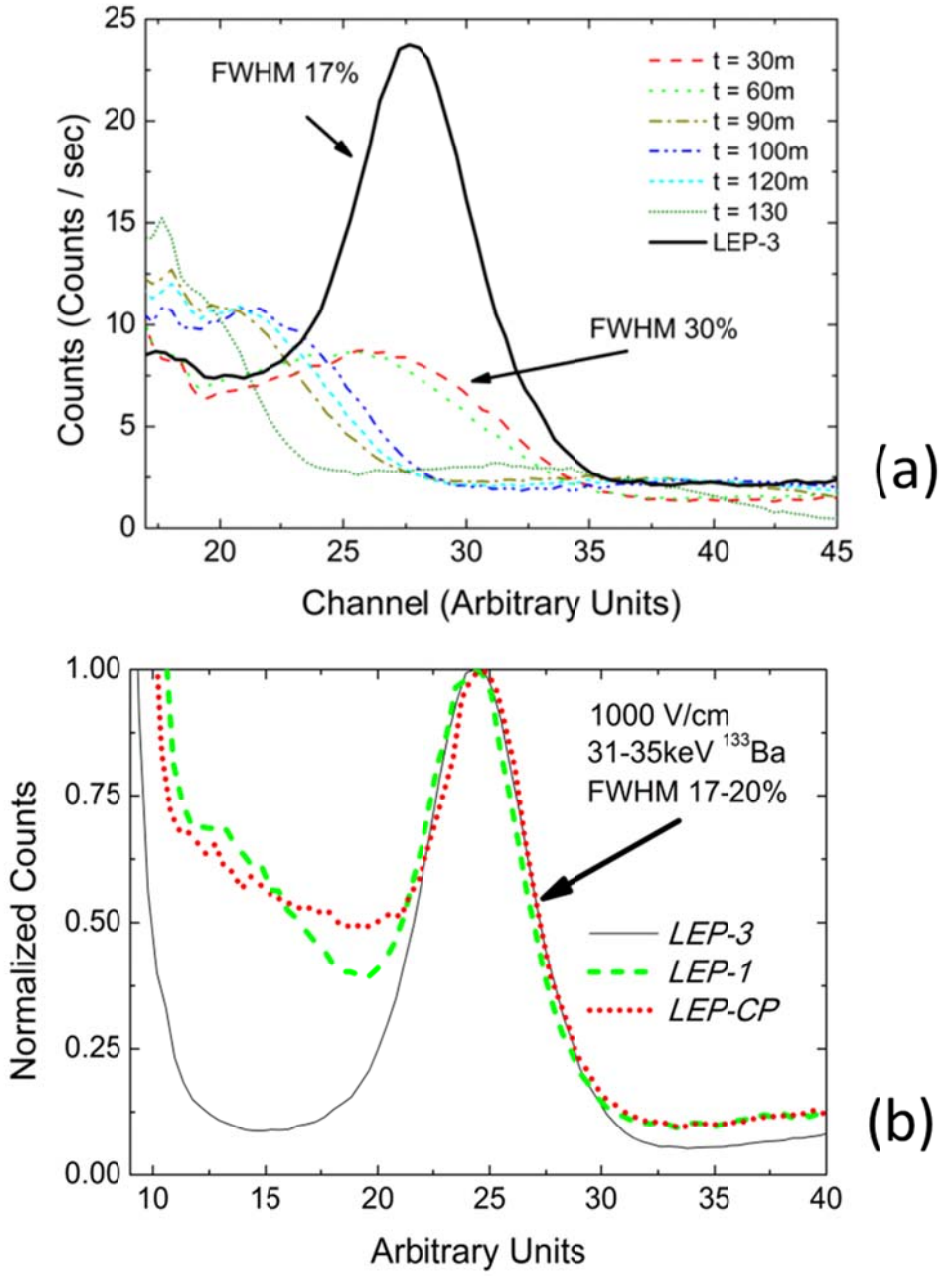

Figure 52 Left: Detector performance after LEL-9 was poor in terms of FWHM and also changed over the course of 2 hours compared with the same detector after LEP-3 treatment. Right: Gamma response of Cd(Zn)Te detector to ^{133}Ba after *LEP-3*, *LEP-1*, and *LEP-CP*, Br_2 in ethylene glycol.

For comparison commercially available spectrometer grade Cd(Zn)Te characterized under similar laboratory conditions exhibited FWHM values ranging from 4-10% for the 31-35keV photo peak of ^{133}Ba. These results have been presented in more detail in Section 2 on page 338 of this Chapter. Further improvements in FWHM to reach this level have required improvements in the crystal growth. However, the low energy tailing, associated with leakage current, is comparable or even better than that observed in the commercial detectors.

4.3.3 Temporal Stability of LEP-3 Treatment

All of the detectors whose lateral edges had been polished using 3 μm Al_2O_3 functioned at higher electric fields and did not show any signs of performance degradation during each measurement. This may be due to the elimination of non-radiative recombination centers after polishing, and an increase in the surface recombination velocity due to the LEP-3 surface treatment. Due to the detector failure after lapping *LEL-9* and *LEL-3* treatments, it was important to investigate if the detectors also had problems over longer periods of time, after the LEP-3 treatment has been applied.

To demonstrate this, the lateral edges of two Cd(Zn)Te detectors were polished using the *LEP-3* treatment, and the samples were biased for more than 10 hours. Presented in **Figure 53** is the gamma response for this detector after 10minutes as well as over the 10hour period, biased at 2500 V/cm. As may be seen, there is no temporal degradation over the course of the measurement.

In general, improved detector performance has been observed when the lateral edges exhibit a strong luminescent band near 1.4-1.5eV. When this luminescent emission is at its highest, it is more likely that electrons in the CB are becoming trapped and undergoing radiative emission of photons. This radiative decay of electrons at the surface corresponds to a decrease in surface leakage current between the anode and cathode. By decreasing the concentration of these recombination centers, less electrons can undergo this radiative recombination. As a result, dark current increases, and the noise observed in the detector increases as well.

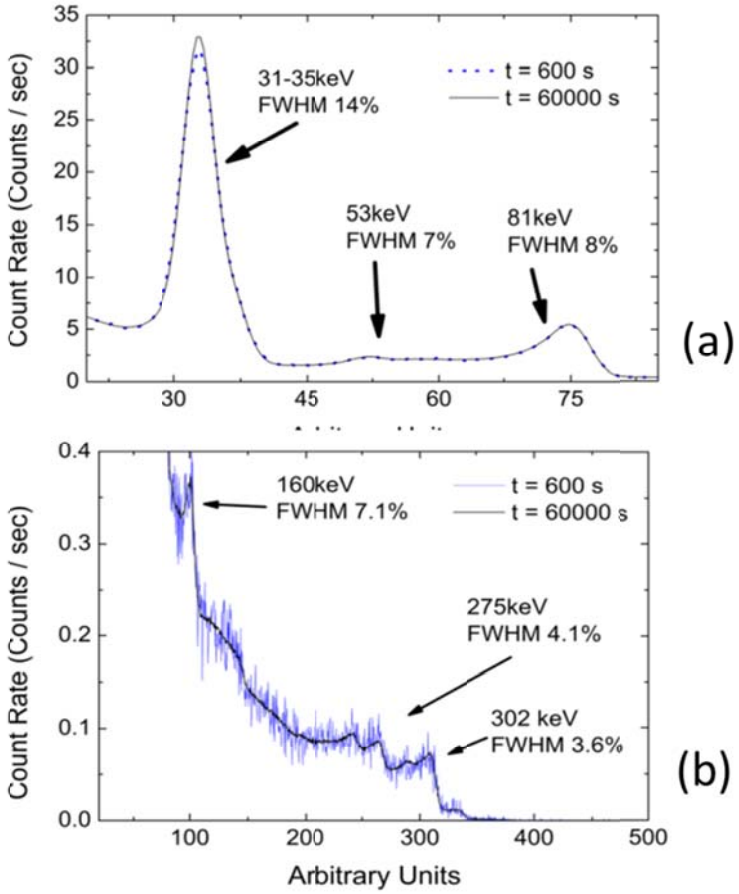

Figure 53 (a) Temporal gamma response of Cd(Zn)Te detector after *LEP-3* treatment. The detector was biased under 2000V-cm^{-1} for 10 hours. (b) Higher energy peaks detected after 10minutes and after 10 hours.

4.3.4 Work Function Measurements

To investigate and explain the small differences observed between the LEP-3 and LEP-1 processes, work function measurements of the Cd(Zn)Te surface have also been carried out. **Figure 54** illustrates the effect of polishing abrasives on the work function of the surface of Cd(Zn)Te. As may be seen, the effects of the scratches imparted by the polishing abrasive have the effect of decreasing the local surface potential. This lower surface potential may explain the higher surface resistivity observed in the LEP-3 samples. A more thorough investigation of this phenomenon is required, however, to develop a more complete understanding of how the surface properties are affected by surface treatments.

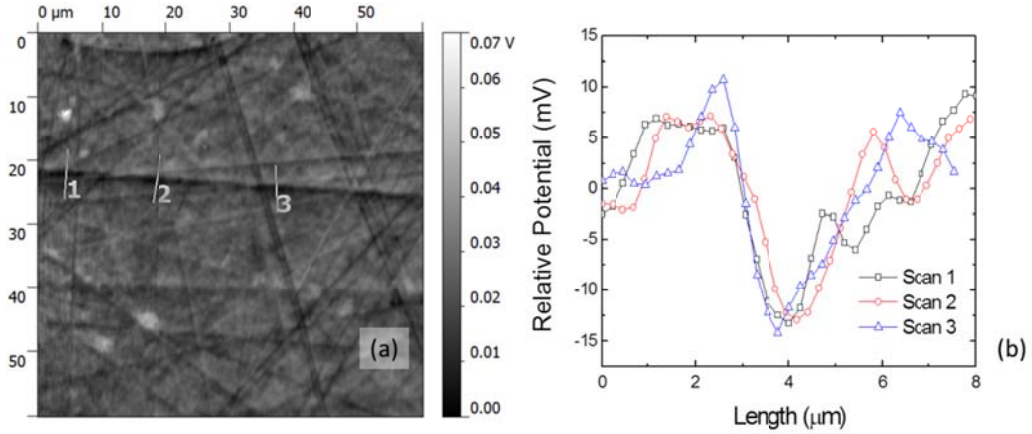

Figure 54 (a) KFPM of Cd(Zn)Te crystal surface after 3µm Alumina polishing (b) line scan of surface potential near scratches imparted by polishing abrasive.

4.3.5 Temporal Stability of LEP-3 Surfaces

To further investigate the temporal stability of this treatment on the surface leakage current of Cd(Zn)Te test devices, the samples were measured in October of 2009 and in July 2010 to demonstrate how the device leakage current had changes over 8 month period. Presented in **Figure 55** are two Cd(Zn)Te radiation devices which were investigated. During the 8 month period the surface leakage current does appear to increase in two of the devices.

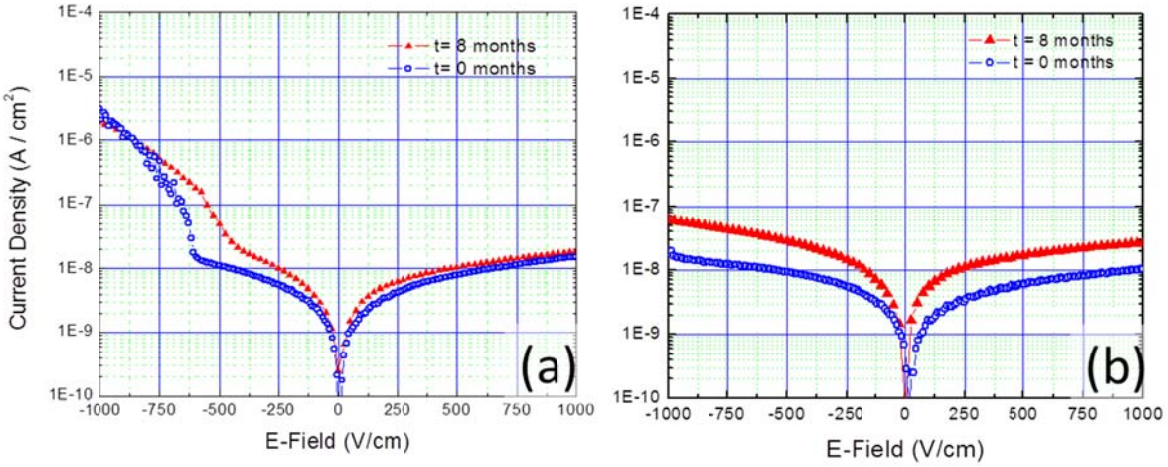

Figure 55 Changes in the electrical characteristics of devices treated using LEP-3 treatment. After 8 months, the leakage current does appear to slightly increase in some of the devices.

4.4 Conclusions

The results from this investigation may be summarized as follows:

1. Methods for improving the quality of planar detectors have been investigated. Specifically, the effect of lateral surface morphology on detector performance has been studied through the use of different lapping and polishing agents.
2. It has been demonstrated that polishing the edges of the planar detectors can help reduce leakage current by a factor of 200% compared with other methods, through the introduction of surface traps. These polishing induced traps possibly behave as recombination centers for surface travelling electrons, thus providing a mechanism for reducing leakage current.
3. A quick 2-stage protocol is proposed which can first use a 3 μm Alumina lapping step, followed by a 3 μm Alumina polishing step. Although the *LEP-1* and *LEP-CP* treatments provided improved surface morphology and lowered surface roughness, these results were not translated into lower leakage current at operating bias voltages. It was also been demonstrated that detectors prepared with lapped edges have a tendency to fail after period of time on the order of shorter than 1 hour and while operating at lower than optimal bias.
4. Through the use of CL a correlation between the 1.4-1.5eV luminescent band and reduced leakage current has been observed. Using this method, results obtained from *I-V* and Gamma ray measurements could be resolved.
5. The surfaces appear to be somewhat stable with time, however increases in leakage current have been observed over an 8 month temporal lapse. Possible chemical passivation mechanisms may be of interest for reducing this effect.
6. The low energy noise present in the devices treated using LEP-3 were comparable or better than the state of the art devices which have been investigated in this work.

Future work on this topic will include the development of passivation protocol to preserve the electrical characteristics of Cd(Zn)Te devices over longer period of times. Additional studies of interest include further studying the work function of the surface after different polishing treatments, different argon etching treatments, after passivation treatments, on oriented and non-oriented devices.

This page intentionally left blank.

5 Effect of Structural Defects in Cd(Zn)Te Detectors Investigated by PICTS

Section Contents

5.1 Introduction

In terms of electronic noise and improving the signal to noise ratio of the device, the leakage current of a detector is a useful figure of merit. In the previous section, we have investigated methods for improving the quality of planar detectors. Specifically, the effect of lateral surface morphology on detector performance has been studied through the use of different lapping and polishing agents (26).

As has been presented in the preceding section, detectors whose lateral edges were treated using a lapping procedure operated at a lower than optimal bias, exhibit significantly higher leakage current, and are unstable with time. Further study was deemed necessary to understand how the electronic properties of the lateral edges in Cd(Zn)Te devices are affected by the surface damage layer imparted by the manufacturing process.

The work presented here is intended to provide a physical explanation to the observed phenomena. Planar devices whose lateral edges have been treated using LEL-9 demonstrated the worst performance as spectrometers; while devices treated using LEP-3 exhibited the best performance of the treatments studied (see previous section). By comparing the two processes which exhibit the largest difference in terms of spectrometer performance (i.e. LEL-9 and LEP-3), the cause of device degradation may become evident.

In order to study the traps present in Cd(Zn)Te devices and how these two treatments affect these energy levels, special experimental techniques are necessary which allow for probing the electrical properties of materials with high electrical resistivity. Photo Induced Current Transient Spectroscopy, or PICTS, is a technique whose technology has been developed over the past several decades for the analysis of the electronic properties in a number of semi-insulating materials (27) (28) (29) (30) (31) (32). Specifically PICTS is well suited for the analysis of high resistivity materials, and may be used for determining the traps present within semi-insulating material. In the present case, this technique permits the investigation of structural defects imparted by surface processing.

5.2 Experimental Procedure

High resistivity Cd(Zn)Te ingots were grown by the VGF method for this study. Each sample investigated in this work was prepared using the methods previously described in Section

3, page 341 (26). Specifically, each electrode surface was polished using 1 μm diamond slurry and subsequently chemically etched using 2% Bromine Methanol. Gold contacts with a thickness near 60 nm were deposited using the electroless method.

Current Voltage (I-V) measurements of the planar devices was carried out using a Kiethley 6517 electrometer, while ^{133}Ba was used for characterizing the devices, and were measured at CIEMAT.

Two planar test devices, termed Device A and Device B, have been harvested from the same region of the same ingot. For the Device A, the lateral edges of the samples were first mechanically lapped using 9 μm Alumina Oxide, a technique which not only increases leakage current, but has been shown to degrade considerably the gamma response of the devices studied. This treatment is referred to hereafter as LEL-9 (Lateral Edge Lapping using 9μm Al_2O_3), using the same terminology from the preceding section of this Chapter.

For Device B, the lateral edges of the samples were mechanically polished using 3 μm Al_2O_3. This treatment is referred to hereafter as LEP-3 (Lateral Edge Polishing 3μm Al_2O_3). For comparison, Device A has also been treated using LEP-3 treatment.

PICTS measurements were carried out at the PHoS Laboratory of the University of Bologna, Italy. The experimental apparatus used for carrying out the PICTS consisted of an aluminum sample holder within a cryostat cooled to liquid nitrogen temperatures. The temperature of the sample was controlled using a Lakeshore DRC-91C controller. Pulsed optical excitation was achieved using a HP-8003A Pulse Generator

During the measurement, it is important that the temperature remains stable and there is no temperature gradient across the sample. Therefore, for these samples a sandwich configuration mounting block configuration has been adapted with thermally conductive paste for homogenizing the temperature across the simple. The sample is mounted and fixed vertically beneath the opening in the Aluminum housing. The light from the LED enters through the opening in the alumina housing and illuminates the exposed lateral side of the device. The lateral edges of the device were treated with different surface treatments, while the bias was applied to the planar electrodes. Presented in the Spectroscopic Methods section of Chapter 2 are additional details regarding the experimental configuration.

If it is assumed that the photocurrent is associated only with electrons, the current transient for the region of interest may be expressed using **Equation 7** (28) (33), where q is electron charge, E is the electric field, μ_e is the electron mobility, τ_e is the electron lifetime, and $n_t(0)$ is the saturation density of trapped electrons. This equation represents the current transient as a function of time with emission rate e_n. Using several emission rates and the gated form of the PICTS equation, the trap energy and carrier cross section may be determined. Further reading on the technological approach to PICTS is more fully presented in (28), and for CdTe and Cd(Zn)Te in (34) (33). In general, this equation illustrates the physical parameters involved in the transient current present in the sample after photo-excitation.

Equation 7 $$\boldsymbol{I(t) = q \cdot E \cdot \mu \cdot \tau \cdot n_t(0) \cdot e_n \cdot exp(-e_n \cdot t)}$$

5.3 Results & Discussion

To illustrate the differences between the surface treatments applied to each device in this study, it is important to recall the surface morphology which is imparted after lapping and polishing process. It has been shown that polishing surface treatments result is a subsequent reduction in the surface damage layer of the Cd(Zn)Te surface, as measured using XRD methods (23) (see also **Figure 32** page 360). Indeed the large difference in surface morphology is also evident from the SEM images presented in **Figure 19**, page 351. The surface after LEL-9 is non-reflective and highly amorphous while the surface after LEP-3 is more reflective and characterized by a high density of scratches imparted by the abrasive polishing process. Surface morphology measurements of LEP-3 treatment may be seen in **Figure 23**, page 357. Due to the roughness of the surface after LEL-9 treatment, it is not possible to measure the surface using the AFM technique.

After electrode deposition, the lateral edges of Device A were treated using LEL-9 surface treatment, which produces high surface roughness and imparts an amorphous damage layer into the surface. The lateral edges of Device B was treated using LEP-3 treatment which produces lower surface roughness (RMS of 30nm) and removes the damage layer imparted by the lapping

operation. By comparing the two test device, it is possible to observe the effects of the damage layer on the electrical properties of the test device.

5.3.1 PICTS Measurements

The PICTS spectra is presented in **Figure 56**. Differences in the PICTS spectra obtained using the 640 or 890nm LED for photo-excitation are clearly evident. First, the value of ΔI is consistently higher for the 890nm LED than for the 640nm LED, despite the output power of the 640nm LED being higher than the 880nm LED. Furthermore, local maxima are more clearly resolved using the 890nm LED than using the 640nm LED. We attribute these two differences in the spectra to the difference in penetration depth between the 890nm (below bandgap) and the 640nm (above bandgap) LED. The deeper penetration of the longer wavelength results in increased interaction with the electronic levels present in the bulk.

Each maxima measured in the spectra is associated with a deep levels present in the devices. From each PICTS spectra, an Arrhenius plots has been constructed to calculate trap levels and the carrier cross sections (see Chapter 2 Section 3.3.6 for theoretical details which have been used for this calculation). The Arrhenius plots for the traps detected in Device A and Device B are presented in **Figure 57**. The levels have been named following the conventions used by Castaldini *et al.* (1).

Also presented in **Figure 57**(c) are the calculated trap activation energies for devices treated with LEL-9 and LEP-3 treatment. The traps are identified by their position in the Arrhenius plot and may therefore be correlated if the traps are active in the same temperature and with similar emission rates. All but one of these trap have been previously identified in CdTe and Cd(Zn)Te. A brief description of these energy levels is first provided, with an elaboration of what we have termed the δ-defect, which is unique to this study.

The first trap was located at E_a = 0.1 – 0.2eV. This trap has been associated with the transition between the A-center complex and the Valence band, and is actually comprised of a family of centers related with impurities, possibly forming complexes with the V_{Cd}. The cross section for this defect has been reported to be between 1-3x10^{-16} cm^2 while the activation energy for this trap level has also been reported to range between 0.1 and 0.2eV (1) (2) (3) (4) (5).

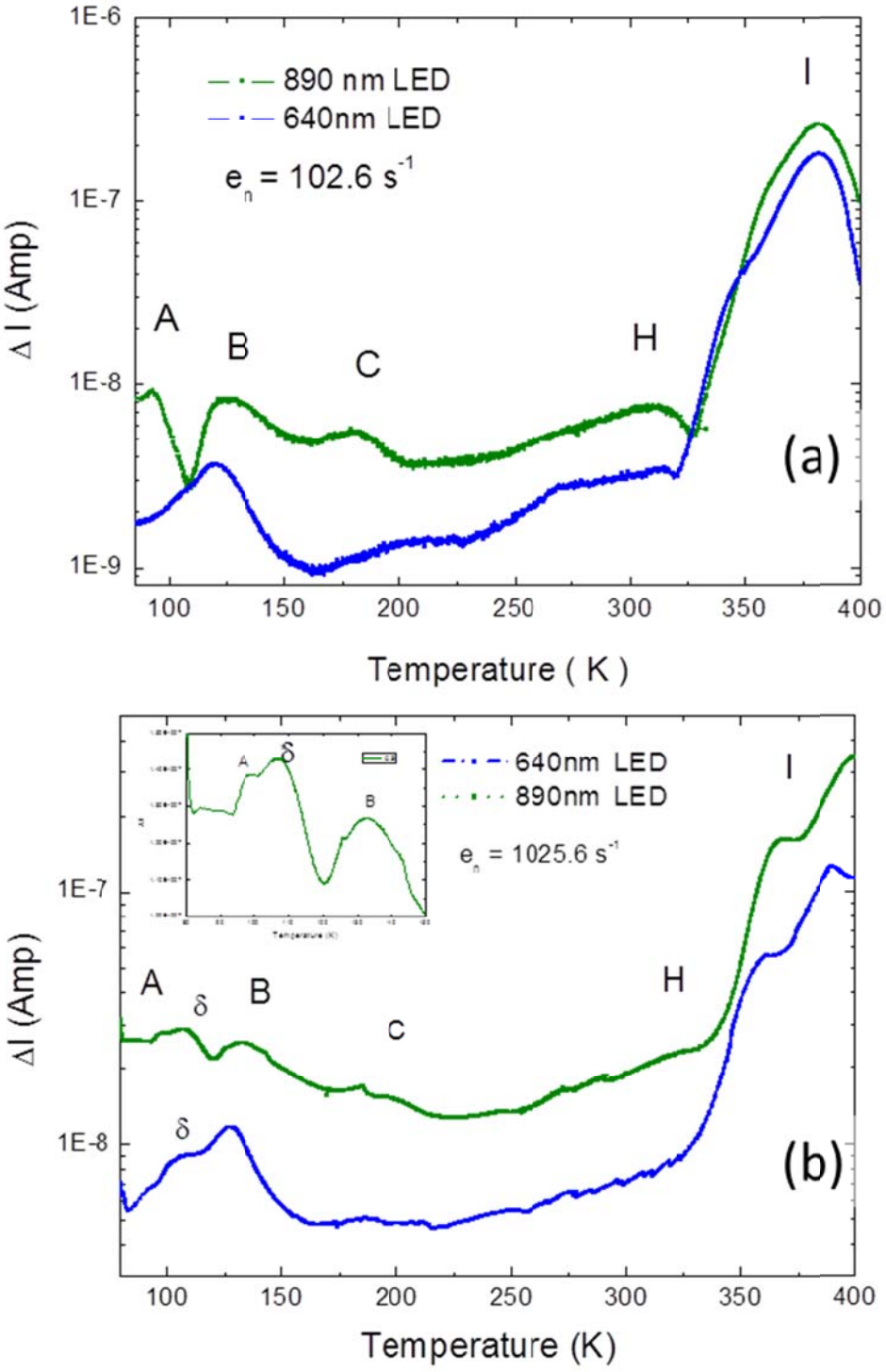

Figure 56 PICTS Spectra for each device treated using LEP-3 (a) and LEL-9 (b) treatment using a 644nm and 890nm LED. The Inset of the bottom PICTS spectra resolves the three levels A, δ, and B.

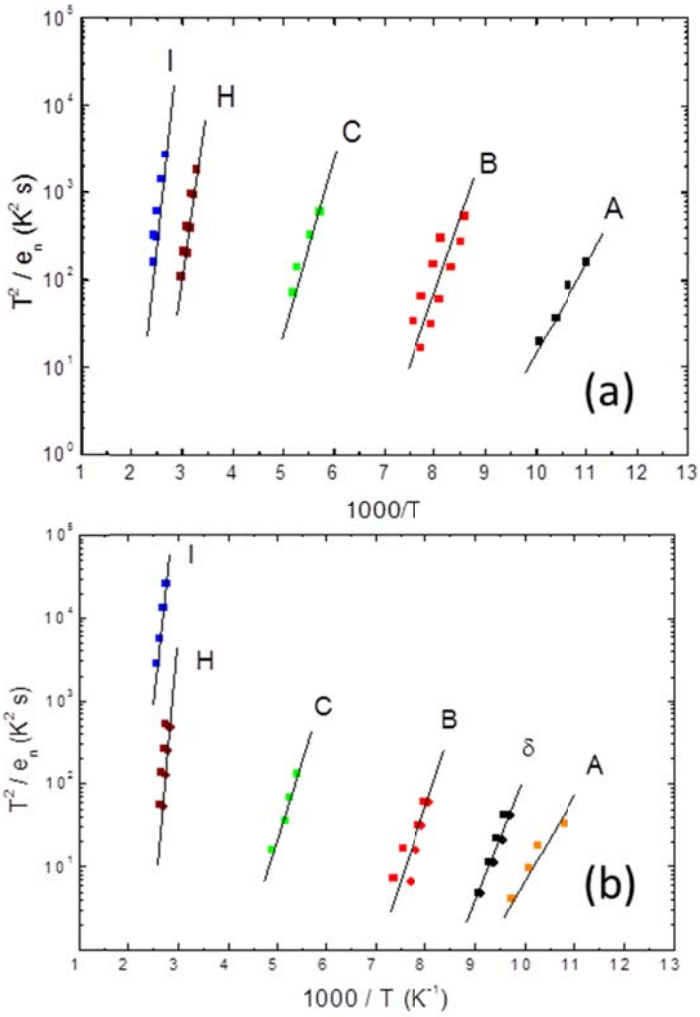

Device	Level	Energy (eV)
LEL-9	A	0.13
	B	0.29
	δ	0.38
	C	0.43
	H	0.85
	I	1.1
LEP-3	A	0.18
	B	0.26
	C	0.30
	H	0.80
	I	0.92

(c)

Figure 57 Arrhenius plot for the traps detected after (a) LEP-3 treatment and (b) LEL-9 treatment. (c) Energy levels for the traps in each device measured using PICTS

A deep level located E_a = 0.26 eV – 0.29 eV has also been observed in both devices, which has also been previously studied using PICTS for Cd(Zn)Te, termed Trap B. This trap may be related with Zinc or even possibly V_{Te} (1) (2) (5) (7).

The trap with E_a = 0.3 eV was observed in the sample which was treated using LEP-3. This energy level was also observed at E_a = 0.43eV using LEL-9 treatment. This energy and apparent cross section is consistent with reported values which exhibit similar positions in their Arrhenius plots and activation energies ranging from 0.32 eV to 0.41 eV (1) (2) (4) (5) (7). This deep level has been termed Trap C and may be related with C, Au, or Cu introducing electronic levels in this

regime, as well as V_{Zn} (35). GDMS measurements of this particular ingot have shown Carbon content on the order of 200ppb, a Cu the content less than 30ppb and Au less than 5ppb, making Carbon a more likely candidate.

The deep center, Trap H, likely responsible for pinning of the Fermi level (36), has been detected at E_a = 0.80eV for the device treated using LEP-3 and between 0.85eV for the device treated using LEL-9. These energy levels are consistent for those reported in literature (1) (2) (4) (5) (7). This defect has been attributed to the doubly ionized V_{Cd}^{--} and has been shown to undergo both radiative and and non-radiative electron capture (2) (37).

Trap I, the deep level near 1.0-1.1eV, has been attributed to Te related defects, such as the ionized V_{Te}^{+} (1), and has been found to behave as a dominant mid-gap trap in CdTe: Cl, behaving as an electron trap (38). This energy level has also observed in $Cd_{0.8}Zn_{0.2}Te$ (1) (2) (4) (5) (7) (39).

5.3.2 The δ-defect level

Of principal importance with respect to the current study presented here is the unique trap observed at E_a = 0.35 - 0.37eV in the device treated using LEL-9. This level was not observed in Device B after LEP-3 treatment, nor has this level been observed for other samples from the same ingot, which have also been investigated using PICTS (see Section 7 for further examples). Furthermore, this defect has been observed using both the 644nm LED as well as the 890nm LED as a prominent feature in the low temperature range of the spectra.

Considering that each test device was harvested from the same region of the same ingot, we attribute the difference in the PICTS spectra to the surface damage layer associated with the two types of surface processes applied to each device. Specifically, we attribute this δ-level to defects associated with the amorphous layer created by the LEL-9 surface treatment. Indeed a level with similar energy has already been attributed to structural defects and crystal stress (5), and these results provide further evidence to support this conclusion.

Mechanical lapping is known to impart substantial amount of damage into the surface, as has been demonstrated using similar lapping and polishing conditions (23). A physical explanation as to how the properties of the surface may influence the electronic properties of the detector is

proposed. Specifically, the introduction of a new surface state increases the dark current in the detector.

5.3.3 Electrical and Spectroscopic Properties

The I-V characteristics of Device B after LEL-9 and LEP-3 treatments are presented in **Figure 58**(a) for high biasing conditions. This increase in dark current associated with the LEL-0 treatment reduces the resistivity and also results in a substantially larger FWHM in the measured spectra of the device.

An example of this behavior is presented in **Figure 58**(b) for the Device A treated using both LEL-9 and LEP-3 treatments for comparison. The Device has been biased at 2000 V / cm for the collection of the ^{133}Ba spectra after LEP-3 treatment and LEL-9 treatment. The correspondingly higher leakage current after LEL-9 reduces the signal to noise ratio of the charge induced at the anode of the device. This is evidenced by higher background noise observed at the lower energies. After LEP-3 treatment the FWHM of the 31-35keV photo-peak of ^{133}Ba is near 17%, whereas after LEL-9 treatment for the same device this FWHM value broadens out to more than 30%.

These results are of technological interest, as the fabrication process of Cd(Zn)Te based devices rely upon traditional cutting, lapping, grinding, and polishing processes. If not effectively removed, these deep centers introduced by the mechanical deformation of the surface may limit the operability of the material. It is important to note that the LEP-3 treatment effectively eliminates the defects introduced by lapping, as has been demonstrated by PICTS measurements.

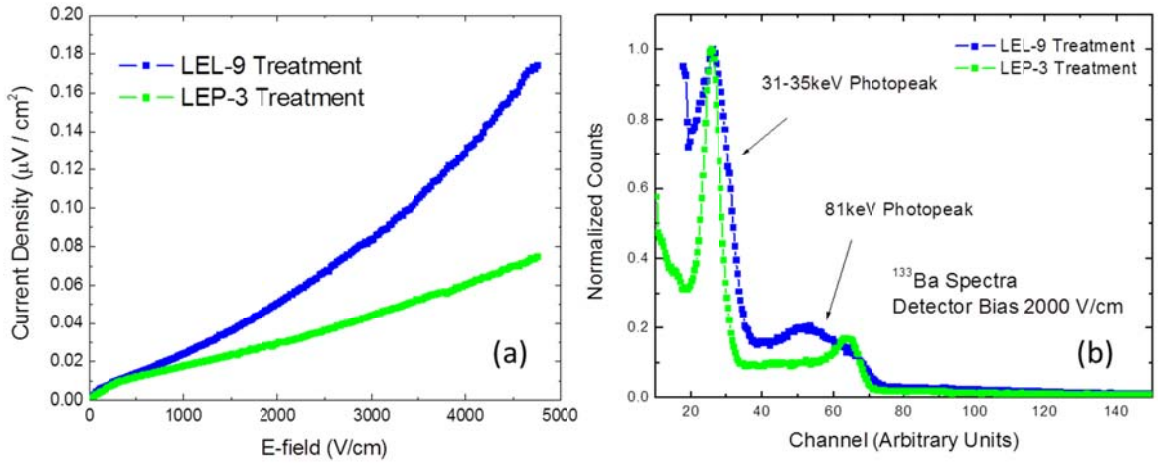

Figure 58 (a) Gamma ray spectroscopic measurements of Device A after LEL-9 and LEP-3 treatments. (b) I-V characteristics of Device A after LEL-9 and LEP-3 treatments.

5.4 Conclusions

1. To explain the effects of lateral surface treatment on device performance, two types of devices have been investigated using PICTS to study how their lateral surface morphology affects their electronic properties.
2. For each device, defects whose activation energies are very similar have been observed. Moreover, for traps A, B, C, H, I the activation energies are consistent with values reported in literature.
3. The most significant difference between LEL-9 and LEP-3 treatments has been observed in the appearance of a new deep level with E_a = 0.38eV, and which is attributed to the LEL-9 treatment inducing defects into the crystal.
4. That the LEL-9 treatment has a detrimental effect on device performance has been further demonstrated using I-V and gamma response measurements. The poor spectral performance of Cd(Zn)Te radiation devices treated using LEL-9 may be associated with the creation of this new defect.

6 TWINNING IN CD(ZN)TE

Section Contents

6.1 Introduction

Twinning in Cd(Zn)Te is an important crystallographic structure. Due to the crystallographic symmetry group of the Zinc Blende structure (F43m), twinning in Cd(Zn)Te may be expressed by (1) rotation of the of the lattice by 180º about the <111> orientation or (2) rotated 250.53° about the (011) plane (40) (41). Presented in Chapter 1 Section 2.6.5 is an example of twinning in Cd(Zn)Te such that the crystal lattice is rotated by 180º about the <111> orientation.

The objective of this investigation was to study how twinning of the surface and bulk properties of Cd(Zn)Te may influence radiation devices which exhibit twinning. Therefore wafers which exhibit twinning have been studied in terms of their electrical, optical, and structural properties.

Presented in **Figure 59** are the wafers which have been used for this study. The 50mm wafers discussed here were harvested from a between $0.20 < g < 0.50$ where g represents the solidified fraction of the ingot. All wafers exhibited high resistivity, and appeared to be single grain with twins oriented vertically throughout each wafer. A dotted line is used to differentiate the twinned region from the twin-free region for each wafer.

The axial composition of the ingot VGF122210 was first characterized using ICP-MS to measure Zinc content along the axial direction. Results are presented below in **Figure 60**. Using the Scheil Equation represented in **Equation 1**, the segregation coefficient has been calculated to be 1.23. C_0 is the initial concentration of zinc, C_s is the concentration of zinc in the solid, k is the segregation coefficient, and g is the solidified fraction. The values obtained for k are consistent to the commonly reported values found in literature (6).

Equation 1 $$C_s = k \bullet C_0 \bullet (1\text{-g})^{\text{k-1}}$$

COREMA measurements for the harvested wafers are presented in **Figure 61**. In general, all wafers harvested from the ingot exhibited resistivity higher than 1×10^9 Ω-cm across their entire surface. It is important to note that this is comparable to the resistivity of the much smaller commercial spectrometers which have been investigated in Section 1 of this chapter (see **Figure 3** page 330 of this chapter).

It is important to observe that the twinned regions corresponded to lower resistivity compared with the twin-free regions. The location of the twinning in each wafer was also the same, a result of the vertically orientated twin structure throughout the crystal. Line profiles of the bulk resistivity are presented in **Figure 62,** where the resistivity of the twinned region was measured 3-5 times lower than the twin-free regions.

It seems evident that this behavior may have significance with respect to the operation of detectors harvested from different regions of the crystal. Therefore, it was important to develop a deeper understanding of this phenomenon and how the twin structure may influence the electrical properties of Cd(Zn)Te devices. The wafers were first investigated using optical microscopy methods to identify possible sources of traps or defects within the bulk which may be affecting the electrical charge transport characteristics.

6.1.1 Twinning and Inclusions

Presented in **Figure 63** is an IR microscopy mapping of one of the 50 mm Cd(Zn)Te wafers shown above (g=0.2). From this image, it is apparent that the twinned region of the wafer contains a higher density of inclusions than the twin free region. Indeed, the spatial location of the twins is evident from the IR transmission, and they appear as dark bands in the mapping.

For the regions which have the lowest electrical resistivity (mid upper right of each wafer presented in **Figure 59**), Te-inclusion structures such as those presented in **Figure 66**(b) appear. These structures of closely packed Te particles appear oriented vertically and extend through the entire wafer from one side to the other. It is possible that the close proximity of these metallic particles may permit charge to pass between the polarized electrodes. This type of behavior has also been reported elsewhere, and is consistent with the results presented here (42) (43) (44).

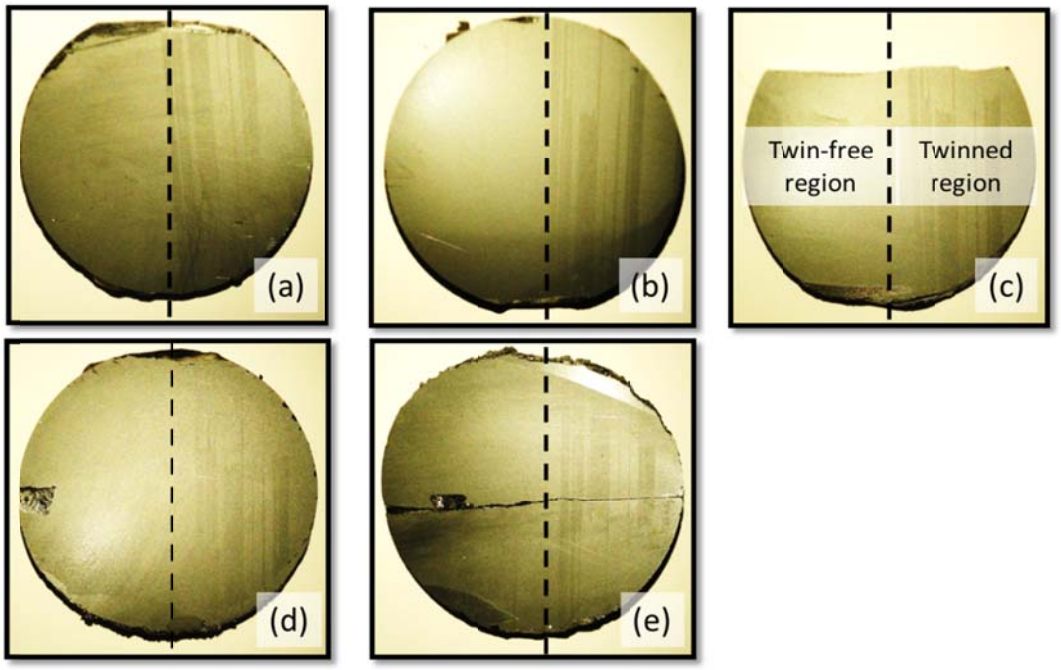

Figure 59 Wafers cross sections harvested following the growth direction from (a) g=0.20, (b) g=0.28 (c) g=0.38 (d) 0.43 (e) 0.5 of the as grown ingot. Each wafer is between 3 and 5mm in thickness and exhibits twinning normal to the wafer surface.

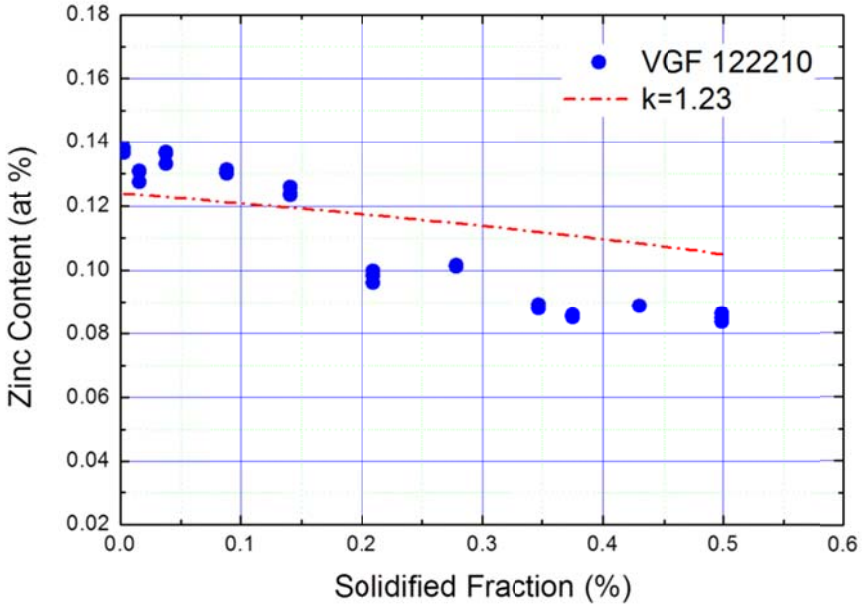

Figure 60 ICP-MS measurements of Zinc content as a function of solidified fraction for VGF122210

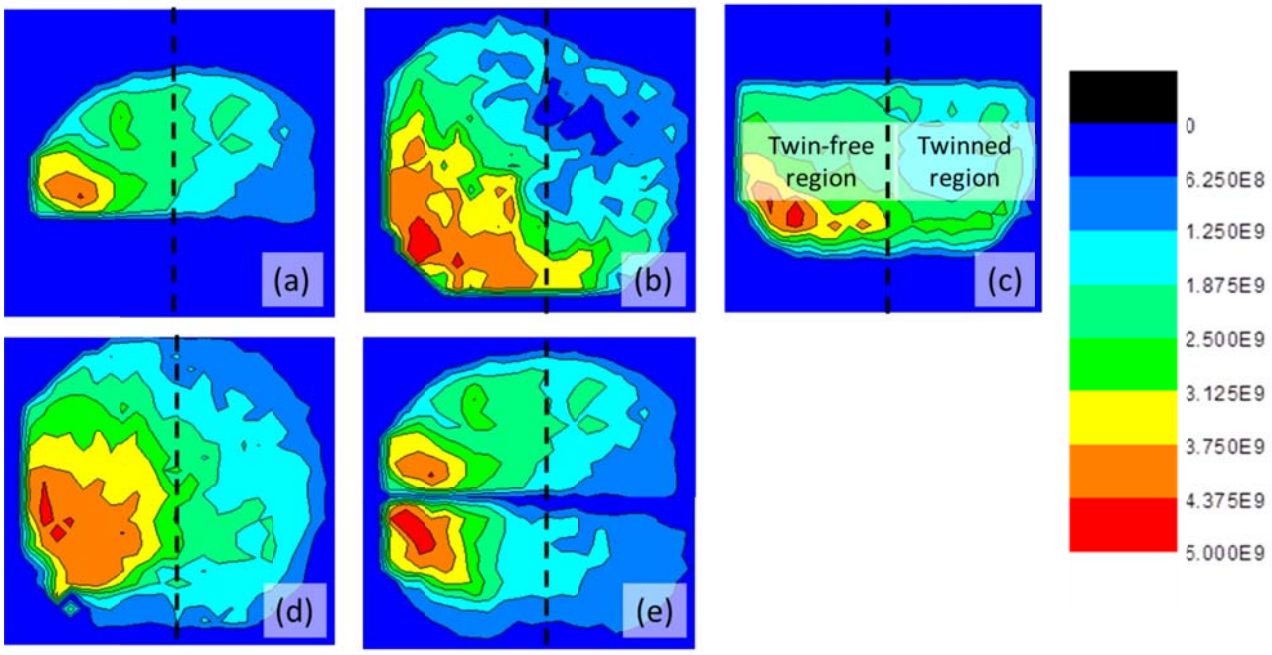

Figure 61 Bulk resistivity measurements of wafers cross sections from $0.2 < g < 0.6$ of the ingot. Each wafer is between 3 and 5mm in thickness.

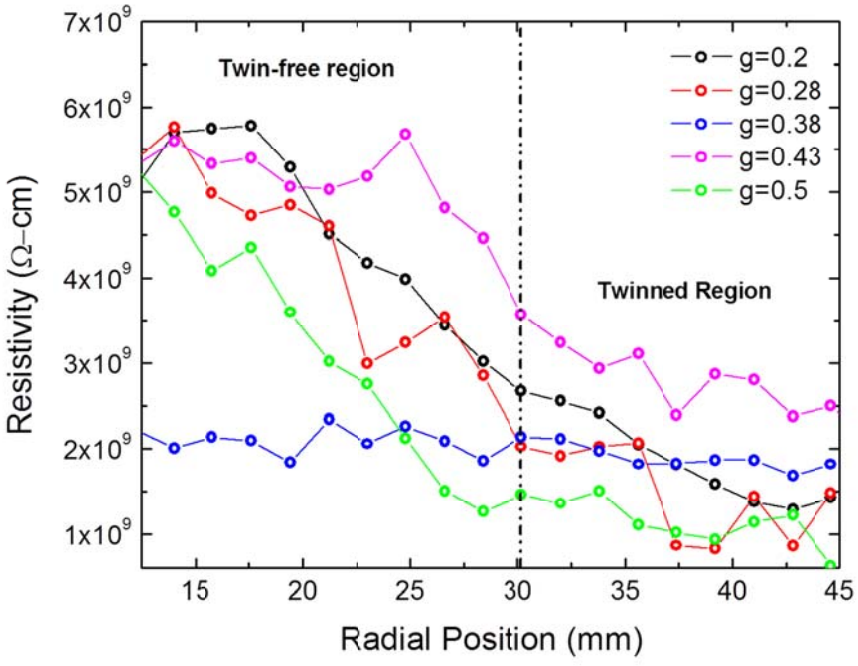

Figure 62 Horizontal centerline resistivity measured for wafers harvested from different axial locations. The resistivity is clearly higher in regions which do not exhibit twinning.

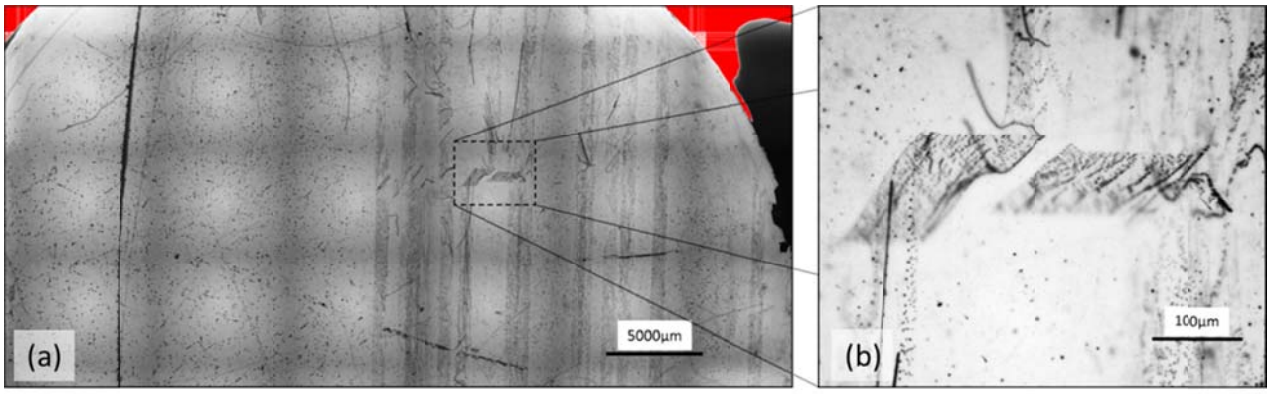

Figure 63 Typical transmission mapping of 5cm Cd(Zn)Te wafer grown using SiC pedestal with pBN crucible. The twins (right side of wafer) have higher concentrations of inclusions that does the bulk of the material. The large horizontal black lines are artifacts from the microscope slide used for mounting the wafer to the X-Y stage

For the twin-free region of the crystal, the inclusions appear larger in diameter, but are present in substantially lower densities. Indeed, for two isolated Te-inclusions distributed throughout the Cd(Zn)Te matrix, increasing the distance between these inclusions decreases the possibility that charge may be passed between the two structures, taking into account the high dielectric constant of the bulk Cd(Zn)Te matrix. As a result, the inclusions which are distributed throughout the Cd(Zn)Te matrix generally have less effect on the bulk electrical properties.

The inclusions which are segregated along the twin boundaries are much closer in proximity, and therefore have a larger influence on the bulk electrical properties. Indeed, this non-uniform distribution of Te-inclusions throughout the crystal even affect pixelated imaging systems, due to the non-uniformity in each pixel response arising from the spatial non-uniformity of the bulk.

In addition to the bulk properties, it was also of interest to investigate how the twin features, and their associated band of Te-inclusions may affect the Cd(Zn)Te surface properties. Again, from a device fabrication perspective, not only the electrical properties of the bulk are important for the development of gamma radiation devices, but the surface properties such as work function play a strong role in determining the rectifying behavior of the electrodes.

For optical probing of the surface states, the wafer harvested from g=0.38 was used. The IR microscopy mapping and the corresponding devices harvested from this wafer are presented in **Figure 64**. These test devices were harvested along the horizontal axis of the wafer, into wafers approximately 10 mm in length. Consistent with the previous results shown in **Figure 63**, the

twinned regions exhibit a higher density of more closely spaced Te-precipitates, whereas the twin-free regions exhibit larger diameter, but more isolated precipitates.

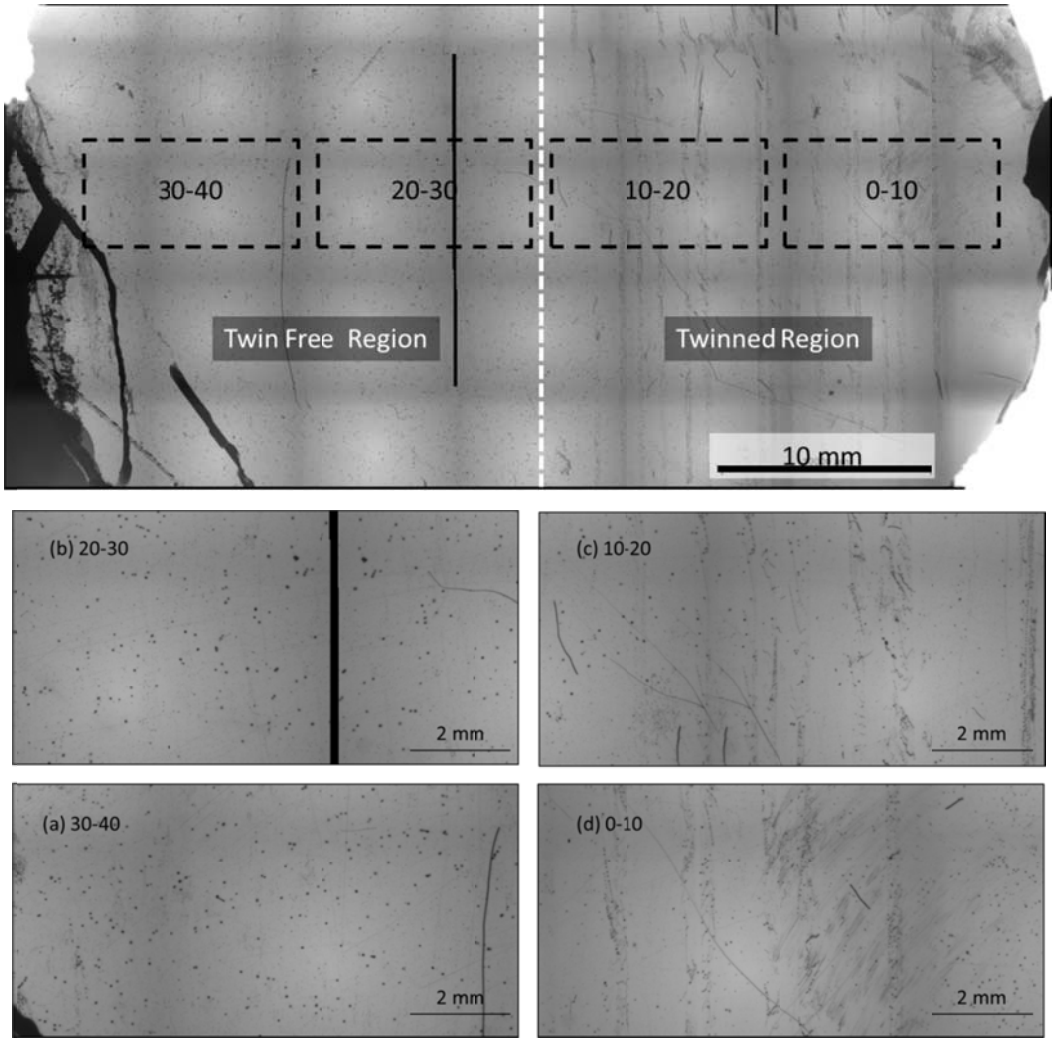

Figure 64 IR mapping of wafer harvested from g=0.38 of growth. Higher densities of smaller precipitates were observed along the twin boundaries.

6.1.2 I-V Characteristics of Twinned and Twin-free Devices

The I-V characteristics of samples 10-20 and 20-30 are presented in **Figure 65**. Based on the resistivity mapping reproduced in **Figure 65**(a) for the wafer harvested from g=0.38 of the crystal, the resistivity of test device 20-30 is expected to be higher than test device 10-20. However, after chemical etching and electrode deposition the measured resistivity as determined

from the I-V characteristics are substantially higher than those determined by COREMA. This phenomenon associated with the I-V determined resistivity being higher than the COREMA measured resistivity has also been observed with the commercial detectors studied in Section 1 of this chapter (see **Figure 3** and **Figure 4** on page 332). However, the leakage current in test device 10-20 is substantially lower than in 20-30, runs contrary to the COREMA measurements shown in **Figure 65**(a). We propose that this difference may be associated with the surface states of the crystal.

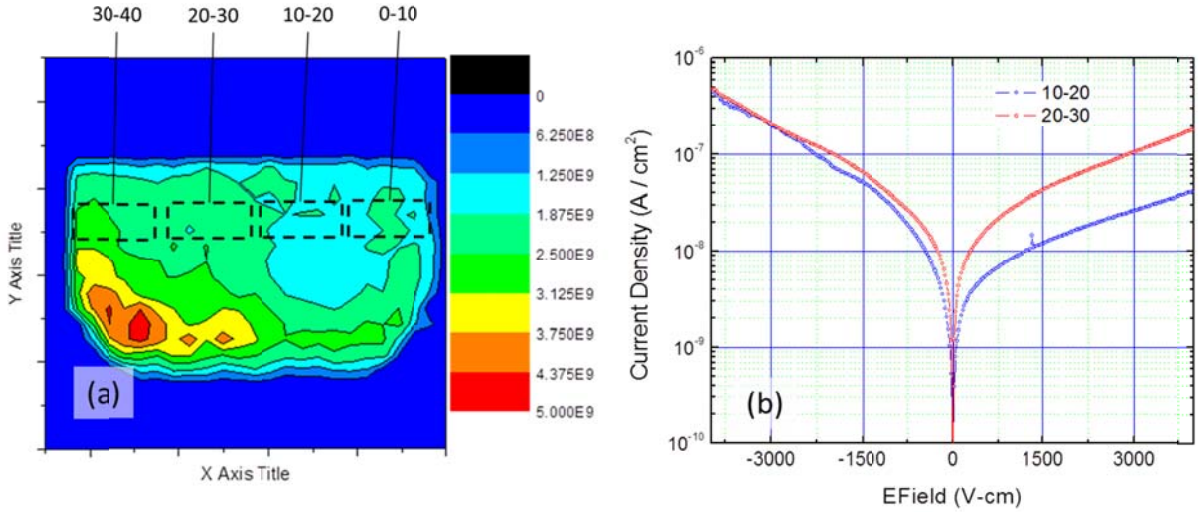

Figure 65 (a) COREMA mapping of Cd(Zn)Te wafer used for investigation (b) I-V measurements of devices 10-20 and 20-30 harvested from this wafer.

6.1.3 Effects of Twinning on Surface States

To better demonstrate this supposition, Cd(Zn)Te samples 10-20 and 20-30 were investigated using Surface Photo-voltage (SPV) spectroscopy to measure possible differences in their surface states which may give rise to changes in the I-V characteristics in the devices. As the wafers were harvested from the same region of the same wafer (see **Figure 61**), and as the surface processing protocol applied was identical for both wafers, changes in the SPV spectra may be attributed to changes at the surface, most probably induced by the twinning.

In the work presented here, the SPV technique is applied to bare Cd(Zn)Te wafers. Moreover, both faces of the crystals have been investigated using the SPV method, following an experimental arrangement presented in **Figure 66**. In order to remove Band-to-Band absorption,

sub-bandgap energies are used for excitation of gap states at the surface. As a result, carrier exchange between the gap states and valence and conduction bands induce changes in the surface voltage via optical transitions.

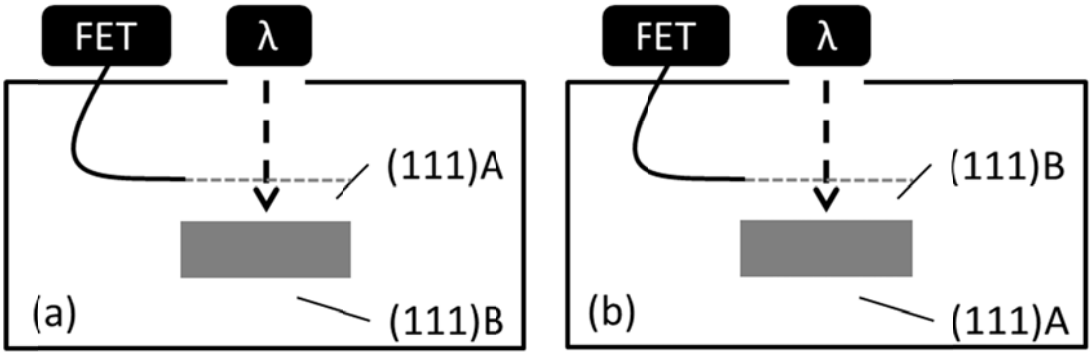

Figure 66 SPV measurements were taken of both sides of Cd(Zn)Te oriented wafers (a) measurement of A-face of crystal (b) measurement of B-face of crystal.

By definition, the energy band edge is lower with increasing surface potential, so that an increasing surface potential corresponds to downward-bent bands while decreasing surface potential corresponds to an upward shifting surface potential. Most semiconductor surfaces are depleted, which means that the bands of p-type semiconductors are bent downwards near the surface (higher surface potential with respect to bulk), whereas the bands of n-type semiconductors are bent upwards (lower surface potential with respect to bulk).

For n-type materials (such as those investigated here), positive changes in the measured SPV correspond to transitions with the conduction band which increase the surface potential, and negative changes in the SPV correspond to transitions between the valence band, which decrease the surface potential. These positive and negative changes in surface potential are illustrated in Chapter 2, Section 3.3.1 which discusses the theoretical aspect of SPV method.

The degree of band bending at the surface is influenced by the net charge distribution, and the resulting charge density at the surface of a semiconductor. These parameters differ from the charge distribution and potential of the bulk because the position of the ions will be different from their ideal Bravais lattice positions near the surface and the symmetry present in the bulk does not exist at the surface, as the periodic boundary condition is no longer satisfied.

Presented in **Figure 67**(a) and b are the SPV spectra obtained for both twinned and twin-free Cd(Zn)Te samples (Sample ID 10-20 and 20-30). The SPV spectra for both faces of the crystal containing twin features (10-20) are presented in **Figure 67**(a). For this sample, two donor levels were located near $E_C - 1.36eV$ and $E_C - 1.47eV$. For these traps, when the surface is illuminated with light whose energy $h\nu \geq E_c - E_t$, the electrons are excited into the conduction band, and swept into the space charge region (SCR) by the internal electric field. As a result, the SCR becomes less positive and we see a decrease in the SPV.

An acceptor trap located near $E_V + 1.41eV$ was also observed. Using a similar line of reasoning, excitation of electrons from the valence band using wavelengths $h\nu \geq E_t - E_V$ requires an additional charge from the SCR in order to reach equilibrium. As a result, the SCR becomes more positive with respect to the surface. **However, it is important to note that identical spectra were obtained for both faces of the crystal.**

For the region of the crystal with no twinning present, the SPV spectra shown in **Figure 67**(b) was quite different. A trap near E_c-*1.47eV* and E_c-*1.34eV* were observed, as was a acceptor site located at $E_V + 1.39eV$. In this respect the crystal exhibit similar characteristics as the crystal which exhibited twinning. However, when the opposite face of the crystal was measured, the spectra did not exhibit any of the trap states previously measured. The only prominent feature was the peak associated with band to band absorption i.e. the semiconductor bandgap.

It is crucial to recall that the SPV signal is proportional to the absorption of incident light by the crystal, and that this absorption is directly related to the concentration of defects present at the surface. From these measurements we observe, therefore, that the concentration of gap states depends to some degree on which crystal surface is measured. For the sample which exhibits twinning, this concentration of gap states present on each surface is similar. In the crystal which is free of twin features, the concentration is remarkably different. Using chemical etching methods for determining the (111)A and (111)B face of the oriented crystal, it is observed that the (111)A face (referred to as Side 1 of **Figure 67**(b)) exhibits a lower concentration of surface states than the (111)B surface. This is discussed in greater detail in the following paragraphs.

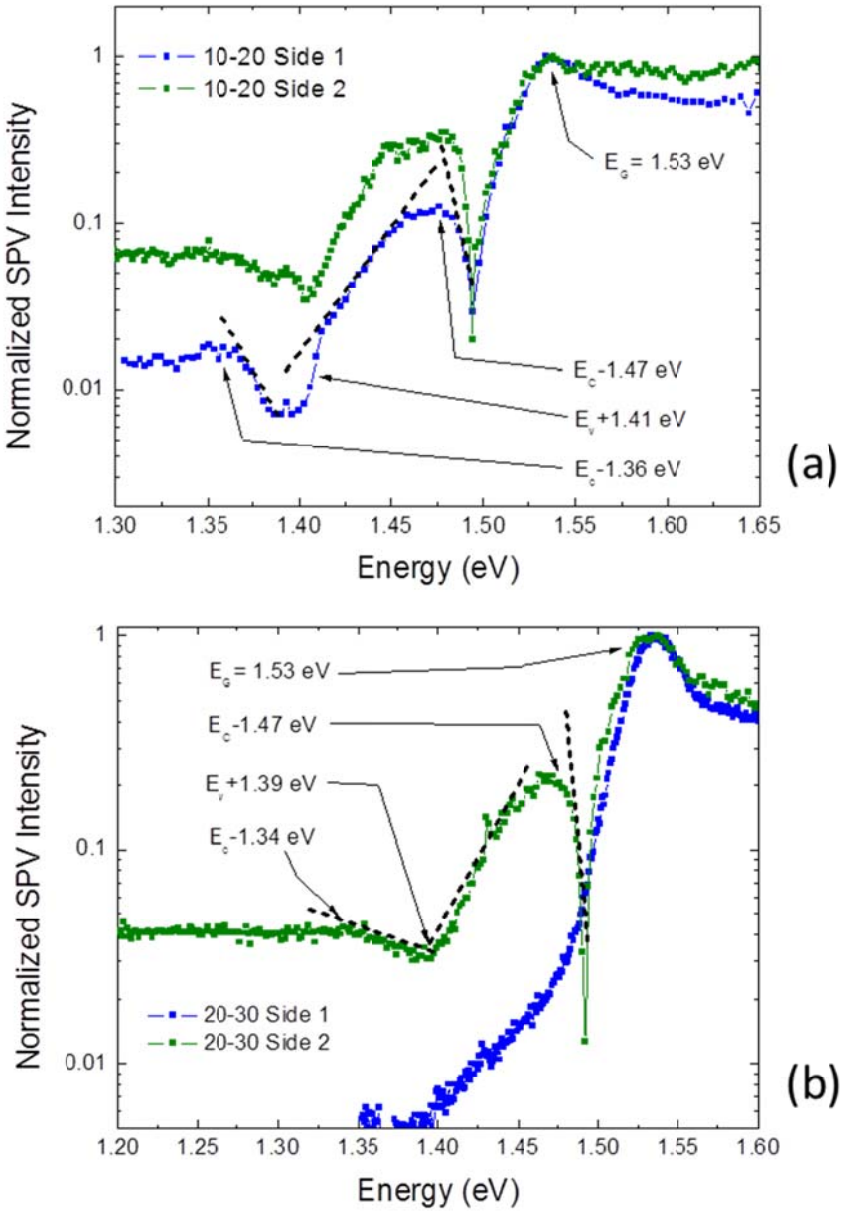

Figure 67 SPV measurements of Side 1 and Side 2 of wafer 10-20 and 20-30.

6.1.4 Effects of Twinning on Crystallographic Orientation

To understand this phenomenon, it is important to understand the properties of twins in Cd(Zn)Te and how these features may affect the surface states. The important difference observed between the two samples investigated using SPV methods was that for the sample

which exhibited twinning, both surfaces exhibited similar SPV spectra with the same types of traps present at the surface. The twin-free sample, however, did not exhibit this symmetry.

This behavior may be explained by considering (i) the structural changes induced by the twin (ii) the resultant change in the crystallographic orientation, and (iii) the corresponding surface termination. The twinning observed in these samples was the result of a rotation of the crystal by 180º about the (111) orientation. As a result, the twinned crystals have opposite surface terminations. This is illustrated in **Figure 68** where each crystal shares the same lattice points about the twin boundary. Due to the rotation by 180º, one surface terminates as (111)A while the adjacent crystal exhibits a (111)B surface termination.

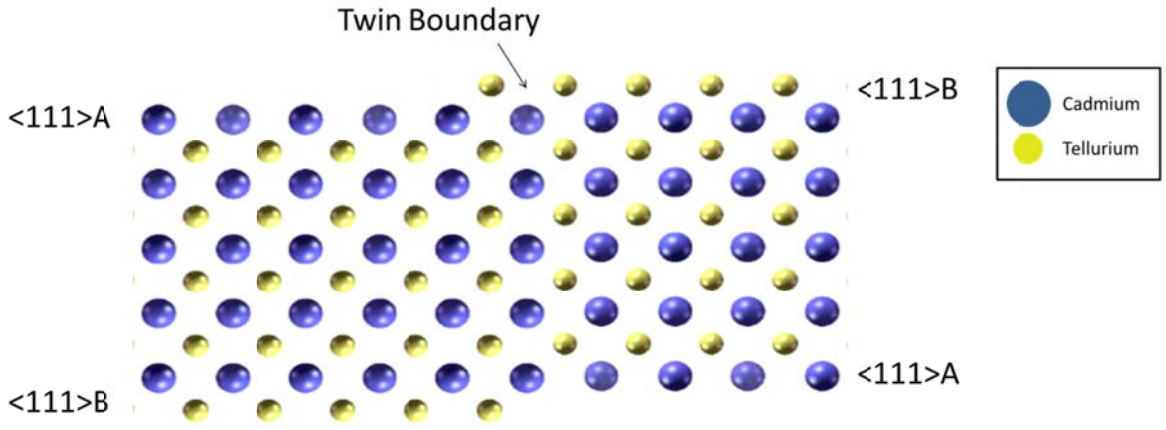

Figure 68 180º rotation of crystal orientation due to twinning results in adjacent surfaces having different surface terminations.

This behavior may also be demonstrated experimentally and is presented in **Figure 69**. Indeed, one of the wafers harvested from g=0.28 exhibits both a twin free region and a region with twins. After chemical etching using HNO_3:HF:CH_3COOH to determine the (111)A and (111) B face, the explanation becomes more clear. In the region with no twins, the sample orientation is uniform and either face of the crystal is strictly (111)A or (111)B. However, in the twinned region of the crystal, the surface termination is a mixture of (111)A and (111)B surface terminations.

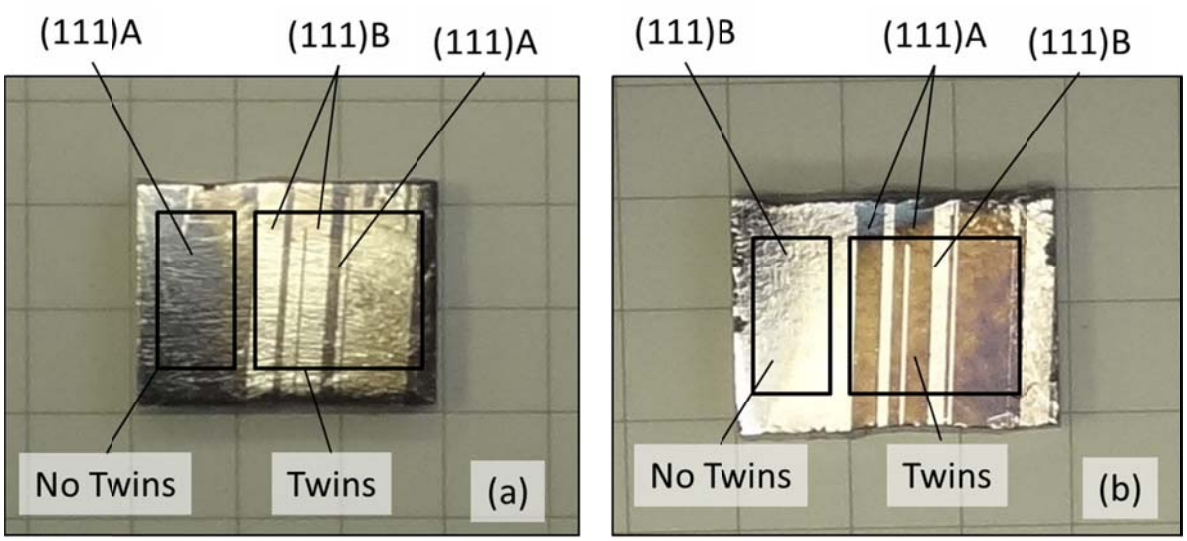

Figure 69 Twinned Cd(Zn)Te wafer after chemical etching using HNO_3:HF:CH_3COOH to determine the A-face and B-face of the (111) orientation. (a) the top surface of the twin free region is the (111)A surface, whereas the twinned region is rotated by 180º and exhibits (111)B termination. (b) the top surface of the twin free region is the (111)B surface, whereas the twinned region is rotated by 180º and exhibits (111)A termination.

For the sample which exhibits twining, each opposing surface exhibits both (111)A and (111)B surface terminations, as may be seen form the twinned region of **Figure 69**. Therefore, the defects associated with the (111)B surface termination may be seen in each SPV measurement of each surface. These particular defects associated with the (111)B face include deep centers such as cadmium vacancies and doubly ionized cadmium vacancies. For the twin-free surface, the opposing surfaces exhibits only either (111)A or (111)B. Therefore, the defects associated with the (111)B surface termination is only detected on a single surface.

6.1.5 Work Function of (111)A and (111)B

In addition to optical probing of the surface states, the work function of the Cd(Zn)Te surface near the twin features was investigated using Kelvin Force Probe Microscopy (KFPM). This was used to analyze local changes in the surface work function associated with the twin structure.

The KPFM technique is based on the AFM (Atomic Force Microscope), where the contact potential of the surface is measured by nulling the force caused by the voltage applied to the probe-sample system.

Changes in the density of surface states have been observed to be associated with structural and surface-termination related changes induced by the twin features. Indeed, the difference in the surface potential of the (111)A and (111)B surfaces has been measured to be as large as 30mV, as shown by the line profiles presented in **Figure 70**(c).

This difference may be ascribed to the polarity of the crystal. At the topmost (111)A surface, the stable atoms with one dangling bond are Cd, and Zn atoms, but those at the (111)B surface are Te atoms. Considering that the electronegativity of Cd and Zn is lower than that of Te, the s-orbitals of Cd move toward Te. As a result, there is a built-in electric field arising from the difference of electronegativity.

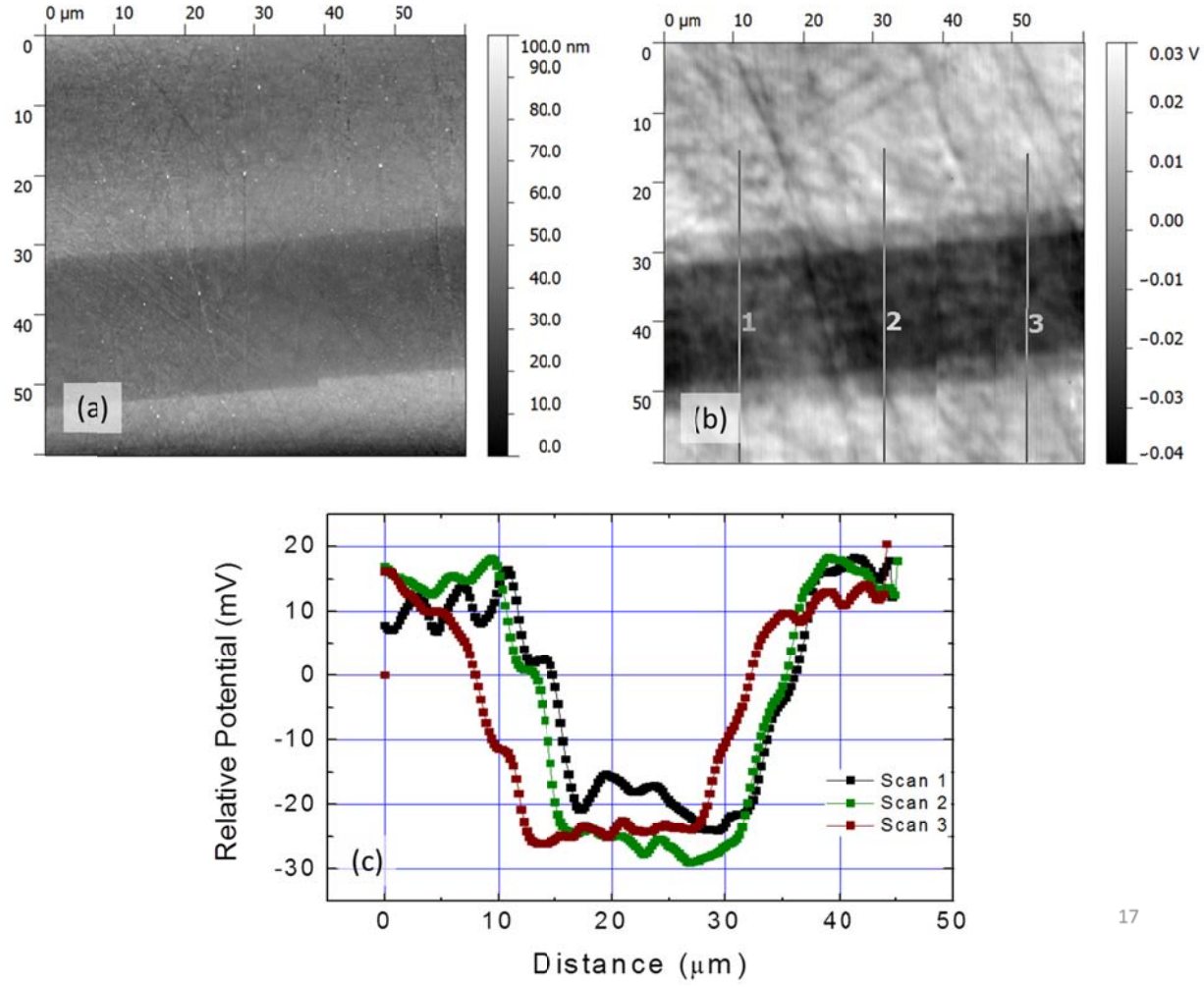

Figure 70 Work function measurements taken of a twin feature in Cd(Zn)Te (a) 60 x 60µm AFM scan (b) work function measurement of Cd(Zn)Te surface (c) line profiles showing the local decrease in the surface work function.

6.2 Cathodoluminescence of Twin and Twin Free Regions

Cathodoluminescence is a surface sensitive characterization technique used for studying the electrical and optical properties of materials. The method relies upon (1) excitation of surface and bulk states using an energetic beam of electrons, (2) the subsequent decay of these occupied surface states to and the emission of photons in the optical region and (3) selection, detection, and amplification of the analog signal produced by these captured photons.

Spectra have been recorded under different excitation conditions of the electron beam on the sample, to account for radiative centers with very different lifetimes. Usually by low excitation, the intensity of the bands associated to defects with low lifetime increase compared to bands associated to defects with a very high lifetime.

Twinned and twin free regions of the crystal were investigated using CL microscopy to determine the differences in the electronic structure of the surface states present in the two samples. Presented in **Figure 71** are the CL spectra for the twinned and twin free regions of the crystal. The variation in excitation conditions leads to important variations in the CL intensity. However, in general there is greater luminescence exhibited under both high excitation and low excitation conditions for the twin-free region.

The emission near 1.6eV represents band to band transitions and permits the measurement of the bandgap of the material. From this measured, the zinc concentration of the material may be determined. The bandgap near 1.59eV corresponds to a Zinc content near 14-15%. This measurement is in agreement with the zinc content determined by ICP-MS measurements (13%)

The broad band about 1.4 eV is related with surface damage, trace impurities, but in general is strongly related to the concentration of V_{Cd}. This band is generally referred to as the A-center and behaves as an Acceptor in Cd(Zn)Te. This cross section for this defect has been reported to be on the order between $1\text{-}3x10^{-16}$ cm^2. As may be seen from both of the presented CL spectra, the intensity of this band is higher in the twin free region of the sample than in the region which exhibits twinning. Indeed, this higher intensity corresponds to a higher concentration of these point defects.

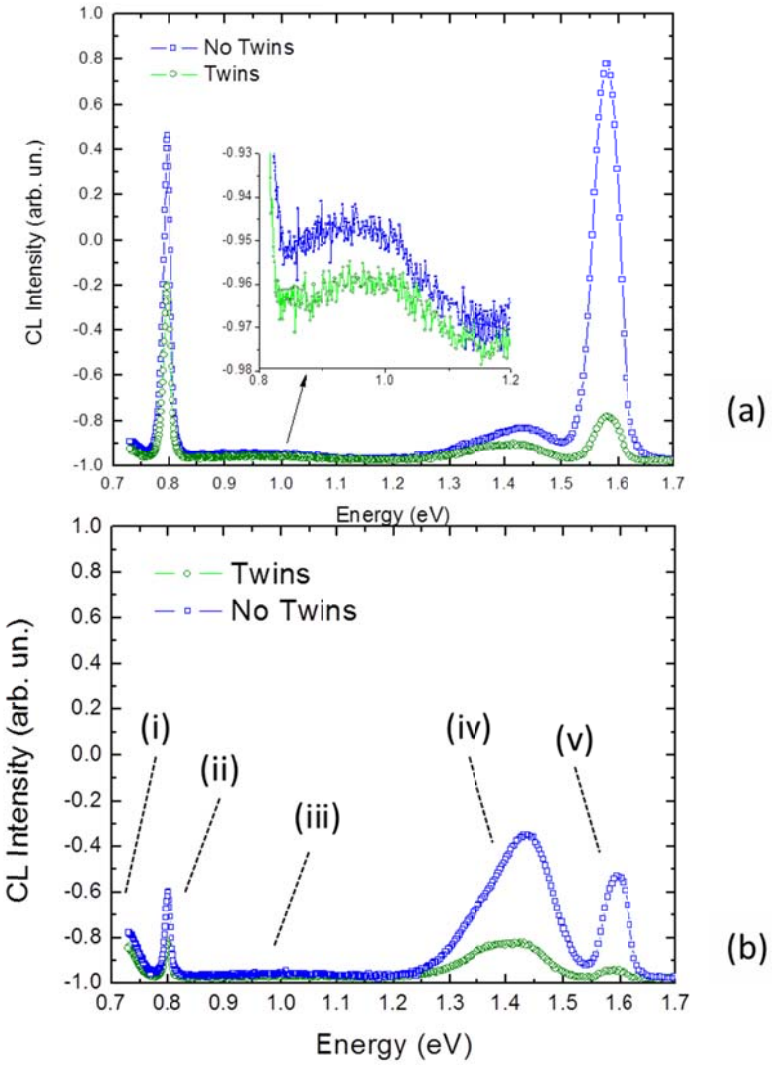

Figure 71 CL spectra of twin free region and samples which exhibit twinning for Cd(Zn)Te under high excitation (a) and low excitation (b) conditions. (i) Trap H associated with pinning of the Fermi level (ii) donor defect possibly associated with In in crystal (iii) donor defect possibly associated with ionized V_{Te} (iv) A-center, donor character (v) band to band transition.

The wide band between 1.0 eV has been related with ionized V_{Te}^{+} (1) and is referred to as Trap I throughout the literature (1). For these samples, which exhibit n-type character, the concentration of these defects is quite low in comparison to the other defects present in the material. These defects have been observed to behave as donors in Cd(Zn)Te, behaving as an electron trap in CdTe: Cl (38), and were also observed to be present in much higher concentrations in the commercial samples investigated (see **Figure 6**). The inset of **Figure 71**(a) shows this broad peak more clearly, under high excitation conditions. This energy level has also

observed in $Cd_{0.8}Zn_{0.2}Te$ with a carrier cross section on the order of $3x10^{-9}$ - $1x10^{-10}$ cm^{-2} (2) (4) (5) (7) (39).

The narrow trap located between 0.78-0.82eV has been attributed donor character, and may be associated with the indium or other metallic content present in the crystal, and has also been attributed to native defects in In doped CdTe (45). It is important to point out that the concentration of this defect was higher in the twin-free sample than in the sample which exhibited twinning. As a result, it is possible that this higher concentration of donor levels increases the leakage current in the twin free test device presented in **Figure 62** on page 414.

The last defect observed to be centered about 0.7eV under low excitation conditions is likely the deep center, responsible for pinning of the Fermi level (1) (2) (4) (5) (7). This defect, acceptor in character, has been attributed to the doubly ionized V_{Cd}^{--} and has been shown to undergo both radiative and non-radiative electron capture (2) (37).

6.3 Conclusion

Several wafers which exhibit twin features have been investigated in terms of their optical, electrical, and compositional properties. The conclusions of this section may be summarized as follows:

1. Twinning in Cd(Zn)Te has been investigated using IR microscopy, and the twinned regions of the wafer have been correlated with higher densities of closely spaced Te-precipitates. These second phase particles are likely responsible for the lower bulk resistivity in the region measured using the COREMA system.
2. The surface of the wafers have been investigated using SPV spectroscopy to investigate the surface states present in both twinned and twin-free regions of the crystals. Using this method, two acceptor states have been detected located at 1.47 eV and 1.36 eV below the CBM while a donor state situated 1.41 eV above the VBM has been detected. Furthermore, for the sample which exhibits twinning, the concentration of these defects appears relatively higher, as there is greater absorption at the surface.
3. Work function measurements using KPM have shown local decreases in surface potential associated the twin structure. A difference of 30mV has been measured between the (111)A and (111)B surfaces.

This page intentionally left blank.

7 INVESTIGATION OF ASYMMETRIES OF CD(ZN)TE DEVICES

Section Contents

7.1 Introduction

The operating mode of a planar Cd(Zn)Te device in its most basic form consists of two electrodes, one of which is biased under negative potential while the other which is typically connected to a charge sensitive pre-amplifier for signal amplification. It is also usually required that the detectors have sufficiently high resistivity such that the leakage current induced by the operating voltage is sufficiently low.

However, it is not enough to have material with high bulk resistivity. Surface preparation has a strong effect on the electronic properties of the device and is of paramount importance to achieve functioning and reproducible detectors. The effect of anode and cathode surface morphology on detector performance has been investigated by A. Hossain *et al.* (14). Furthermore the effects of using different chemical etchants for electrode surface preparation has been investigated by (46) Cd(Zn)Te. Finally, the effect of lateral edge morphology on device leakage current has been demonstrated by Crocco *et al.* (26) and is discussed in greater detail in Section 4 of this chapter.

Despite these recent advancements in preparing the surface of Cd(Zn)Te devices for detector applications, large asymmetries in the electronic properties of Cd(Zn)Te detectors are quite common. Indeed, we have observed differences in leakage current several orders in magnitude depending on which electrode of the planar configuration is used as the cathode. In fact, this phenomenon has been observed for both oriented as well as non-oriented crystals. Therefore an understanding of the material properties which contribute to this asymmetry is of paramount importance from a detector fabrication perspective.

For the development of patterned electrode geometries, correct selection of this surface is crucial. In the case of oriented crystals, it has been observed that the (111)A and (111)B surface terminations may have some influence on the electrical properties of the device. Shown below in **Figure 72** is the structure of (111) oriented Cd(Zn)Te, showing the alternating crystallographic planes of Cd(Zn) and Te atoms. Taking into account the unit cell of the crystal, the surface which will terminate in Te is referred to as the (111)B surface, and the surface which will terminate in Cd(Zn) is the (111)A surface.

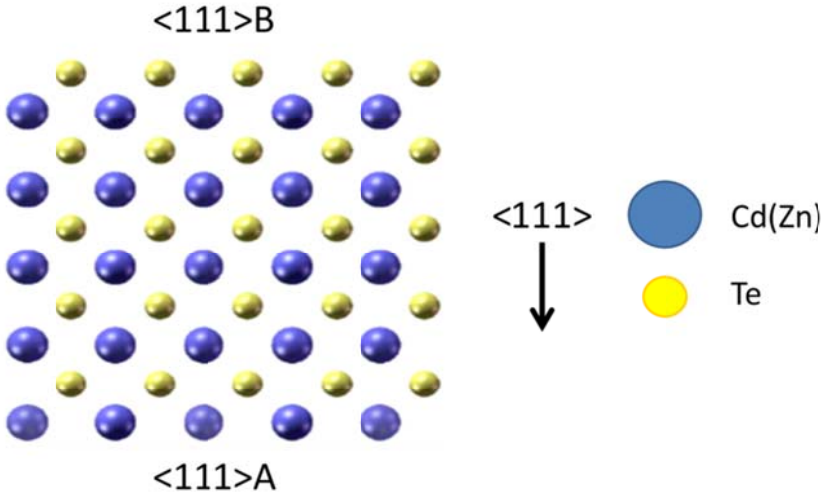

Figure 72 Atomic structure of (111) Cd(Zn)Te illustrating the (111)A and (111)B surface termination

Wright *et al.* demonstrate the existence of asymmetry in (111) oriented n-type devices. They provide a study which illustrates the effects of different chemical etchants used for surface preparation on device charge collection efficiency (21). One of the principal findings of their investigation was that surface processing conditions affect the surface recombination velocities *beneath* the electrodes, which in turn contribute to electron and hole collection efficiencies.

They conclude that defects at the surface lead to larger surface recombination rates for planar (111) oriented devices. Indeed they show that the gamma response of (111) oriented detectors depends to a large degree on which crystal surface is used as the cathode i.e. (111)A surface or (111)B surface. From this study, they conclude bromine Methanol etching of the anode/cathode prior to electrode deposition was observed to yield the lowest leakage current in the device. This choice of chemical etchant was also used in our work for the preparation of electrode surfaces presented in this section.

It is important to comment that in the study carried out by Wright. *et al.* (21), the lateral edges of the devices were not protected, passivated, nor was a guard ring geometry implemented for reducing surface leakage current. It is difficult to conjecture the role played by the oxidation of the lateral edges after using different chemical etchants, however it is known to increase leakage current in the device over time and leads to detector instabilities. For the devices investigated here, the lateral edges were treated following the protocol described in (26), or Section 4 of this chapter.

Wright *et al.* were not alone in their conjecture of the role played by the crystal orientation on device performance. These differences in device operability and resistivity have also been reported to depend on crystal orientation by other groups as well. In fact, this was observed to the extent that a gamma response could only be obtained when the cathode of the detector was on the Te-rich (111)B face (47). From the perspective of electrode patterning, the choice of the electrode surface is therefore of fundamental importance.

One possible explanation of this phenomenon may be associated with the observations by T. Takeuchi *et al.* (48) who have proposed that surface barriers at the B-face show recombination preferred processes for n-type (111) oriented materials. This result is evidenced by the Current-Voltage characteristics which show a higher electrical resistivity at the (111)B surface. However, they propose that the observed carrier transport on the B-face may be attributed to the presence of an interfacial tellurium oxide layer and provide experimental evidence that the top-most atoms of CdTe(111)A are predominantly Cd bonded to O, while the top most atoms of CdTe(111)B are Cd and Te atoms.

Other works have also demonstrated the how surface defects may affect the electrical characteristics of Cd(Zn)Te crystals. Using Ar sputtering technique to modifying the Cd:Te ratio at the A and B surfaces, changes in the electrical characteristics have been detected. It has been observed by Voss *et al.* that (i) the (211)B surface exhibits higher electrical resistivity than the (211)A surface, (ii) a reduction of leakage current may be achieved through argon bombardment of the surface and (iii) this change in leakage current may be attributed to plasma induced defect states (49).

Indeed, surface defects induced by Ar plasma have been shown to substantially modify the work function of the (111)B Cd(Zn)Te surface by as much as 0.8eV (50). Furthermore, this change is explained using a dipole model of the surface. In this model, bulk electrons become trapped in the damage layer near the surface, and may even undergo recombination. This trapping effectively increases the work function of the surface as it requires more energy for the electrons to reach the vacuum level. The as polished (111)A surface exhibits a higher work function than the (111)B surface, which is attributed to the lower electronegativity of the Cd(Zn) atoms with respect to Te.

A summary of the results obtained by different groups is presented in **Table 5**. From these results it may be seen that there is some agreement regarding the use of the (111)B face as the cathode for obtaining lower leakage current in devices. The only disagreement has been found in Ref. (21). However, the interpretation of the method used for the determination of the (111)A and (111)B is contrary to the original method reported by Brown for CdTe (51). Specifically, this etching method produces a reflective surface finish on the (111)B face while producing a dark surface finish on the (111)A face. The results reported by Wright *et al.* (21), however, state that the surface exhibiting a dull black coating was the (111)B face.

Table 5 Summary of results obtained by different groups for selection of the Anode and Cathode in Cd(Zn)Te radiation devices.

Ref.	Electrode material	Electrode surface which exhibits lower leakage current under reverse biased
(21)	Au	(111)A
(47)	Au	(111)B
(48)	Au	(111)B
(49)	Pt	(211)B

Overall, the selection of the Cd(Zn)Te surface used as the anode and cathode in planar or patterned device geometries plays a large role. However, not all devices harvested from Cd(Zn)Te ingots for radiation detection applications are oriented following the (111) or (211) directions. Therefore, using the chemical methods described above may not always be useful for determination of the A-face and B-face of un-oriented materials. More specifically, the surface state density of each face of the crystal will play a role in determining the electrical properties of the device. In fact, it has already been shown that the A and B surfaces of the (110) orientation exhibit higher surface sheet resistance than (111) surfaces. Therefore, non-contact or non-destructive methods which are sensitive to these surface states are of great interest in the selection of anode/cathode surfaces for electrode deposition.

This investigation presented here has been carried out with three objectives. Each objective is oriented towards establishing reliable methods for the selection of the anode and cathode

surfaces independent of the crystallographic orientation. The objectives of this study are the following:

- Investigate how the asymmetry in I-V characteristics of Cd(Zn)Te devices may be associated with the TeO_2 interfacial layer using RBS to study the structure at the Au-Cd(Zn)Te interface.

- Develop an understanding of how the concentration of the active traps in Cd(Zn)Te varies with the external bias polarity using PICTS.

- Propose non-destructive methods for selection of the anode and cathode which are independent of crystallographic orientation.

7.2 Experimental

Cd(Zn)Te surfaces have been prepared using the polishing methods described in (26) For Cd(Zn)Te devices studied in this work, the electroless Au deposition technique has been used for contact deposition. This process produces semi-transparent gold contact between 30-40nm thick. Further details regarding detector preparation and measurement may be found in (23) (52) (53) or in Section 3 of this chapter.

A chemical method for the determination of the A and B-face in CdTe has been reported (51), and has been implemented here. The technique consists of chemical etching of CdTe using a mixture of HF: HNO_3 : CH_3COOH in a ratio of 1:1:1. The chemical etching results in the (111)A face exhibiting a dark surface finish, while the (111)B face exhibits a reflective surface finish.

Because non-oriented test devices as well as oriented test devices have been investigated here, it was important that consistent terminology be applied to all samples. To do so, each electrode of the planar test devices has been designated as either S1 or S2. **This choice was made such that the electrode which exhibited lower leakage current under reverse bias would be referred to as the S2 electrode.** In this way the surface properties of oriented and non-oriented devices could be compared.

Presented in **Figure 73** is an illustration of how this geometry was applied for each of the measurements described below. Measurement of both S1 and S2 surfaces using complimentary techniques was intended to elucidate the differences which may exist between the two electrodes.

Photo-Induced Current Transient Spectroscopy (PICTS) measurements were used for measuring the energy, concentration, and apparent cross section of deep levels present in Cd(Zn)Te devices. Further reading on the theoretical and technological approach to PICTS or extracting defect energy, cross section, and concentration from the PICTS spectra is more fully presented in (28), and specifically for CdTe and Cd(Zn)Te in (34) (33). Further reading on the experimental methods and calculations used here are presented in Chapter 2, section 3.3.6.

Rutherford Backscattering (RBS) measurements have been carried out to study the symmetry of the Au-Cd(Zn)Te-Au contact structure, providing a comparison of the interfacial tellurium oxide layer thickness on both electrodes of the planar Cd(Zn)Te device. Experimental details for the RBS measurements are presented in Chapter 2, Section 3.3.3. The data were analyzed with the IBA Data Furnace NDF v9.3 f. (54).

To explain asymmetry arising from the metal-semiconductor interface, optical probing of the surface states using Surface Photo-voltage (SPV) spectroscopy was carried out (55) (56) (57). This technique provides the capability to measure the influence of surface trap states. In the work presented here, the SPV technique is applied to bare Cd(Zn)Te wafers as well as Cd(Zn)Te devices which have been contacted with semitransparent Au contacts. In order to probe sub-band, defect related electronic transitions, sub-bandgap energies are used for excitation of gap states. As a result, carrier exchange between the gap states and valence and conduction bands induce changes in the surface voltage via optical transitions.

For gamma ray spectroscopy, test devices were connected directly to a PCB board which contains the FET and the A250 charge sensitive pre-amplifier. The cathode of each detector was connected to high voltage, while the anode of the detector was connected using a short Pt wire to the input of the FET. The post-processor was connected to an MCA card and each spectrum was acquired using APTEC software in order to derive the FWHM of the photo-peaks. Both S1 and S2 surfaces were investigated as the cathode of the device.

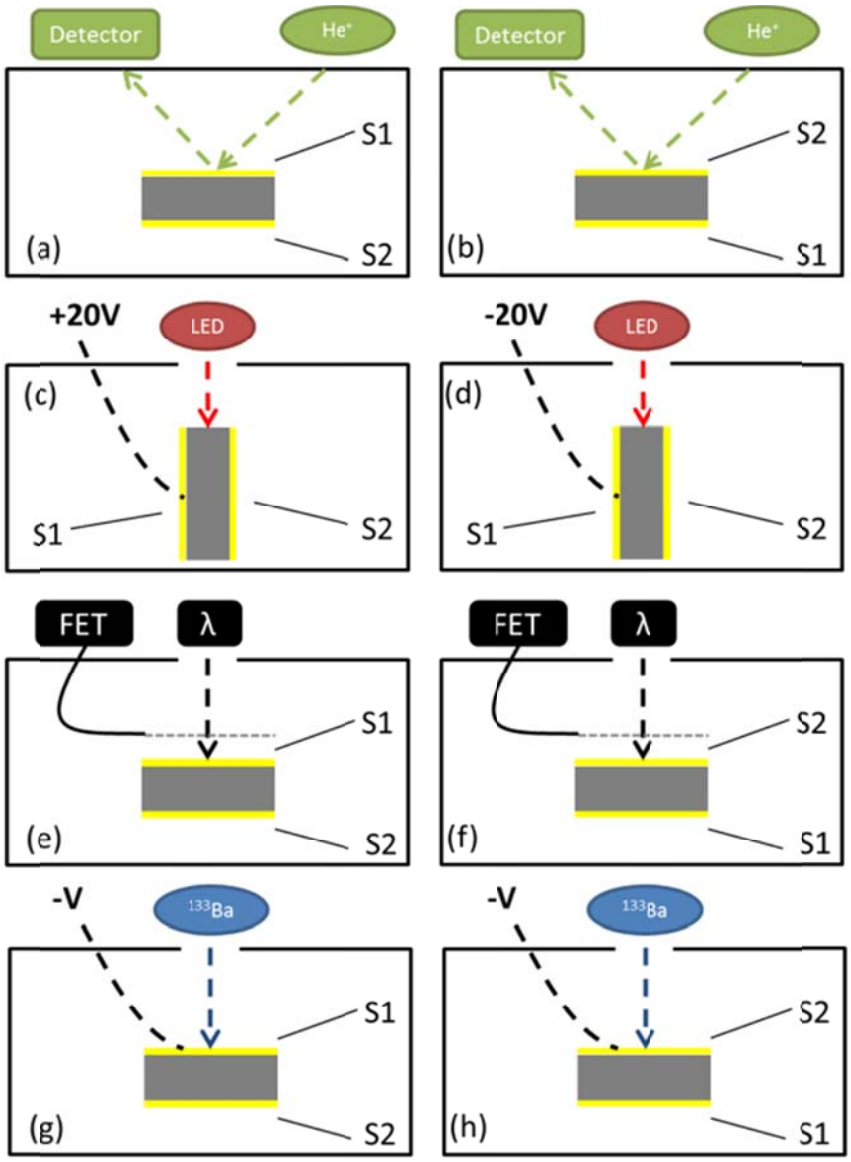

Figure 73 Geometry used for RBS (a)&(b) PICTS (c)&(d) SPS (e)&(f) and gamma radiation measurements (g)&(h) to study both S1 and S2 surfaces of Cd(Zn)Te devices.

7.3 Results & Discussion

7.3.1 RBS Measurements of Au-Cd(Zn)Te-Au structure

It has been proposed that the interfacial layer of tellurium oxide may be responsible for the asymmetry in the electrical characteristics observed in Cd(Zn)Te devices due to recombination events occurring at the Au-Cd(Zn)Te interface (48). For this reason it was important to

investigate the structure of the Au contacts of Cd(Zn)Te planar test devices which exhibit both asymmetric and symmetric I-V characteristics.

To demonstrate the level of asymmetry present within each device, the ratio of leakage current measured for each electrode under reverse bias is presented for an electric field intensity of 3000 V/cm. For the oriented crystals, the S1 and S2 electrodes correspond to the (111)A and (111)B surfaces of the crystal. For the non-oriented crystals the electrode which yields lower leakage current under reverse bias has been designated S2, while the opposing electrode is designated S1.

The I-V characteristics of the investigated devices are presented in **Figure 74** and the RBS results for each of these devices are summarized **Table 6**, where the devices have been ordered according to this asymmetry in their I-V characteristics. It is important to comment that a gamma response has been achieved in even the most asymmetric devices, however only when the correct electrode was selected as the cathode (see Section 7.6 page 443 for Device E).

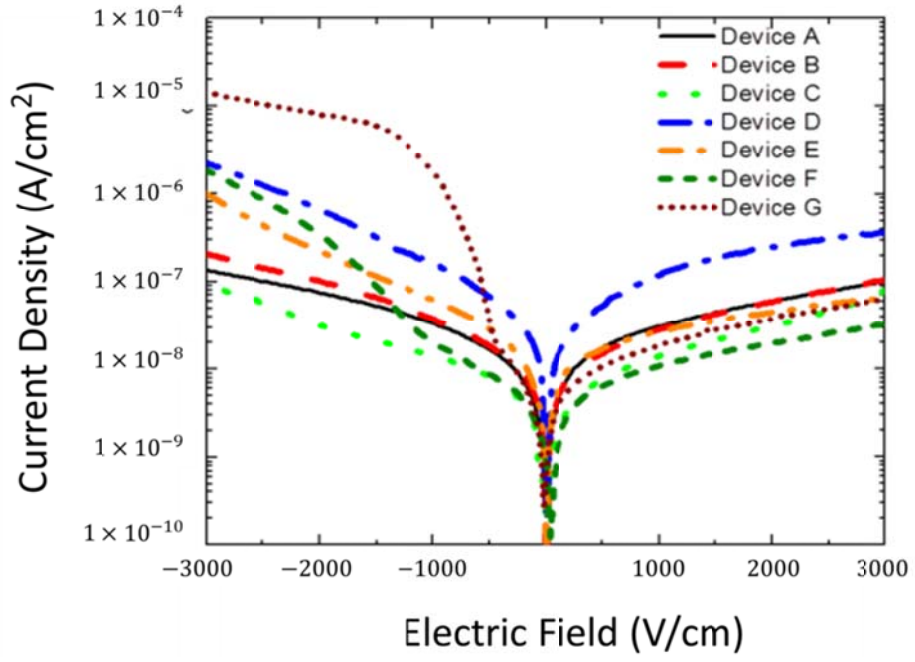

Figure 74 I-V characteristics of devices studied in this work.

It was observed from the RBS measurements that the thickness of the interfacial oxide does not strongly correlate with the measured leakage current associated with each individual test

device. For some test devices, the thickness of the oxide was much thicker on the S1 electrode than the S2 electrode. For other devices the relationship was reversed. Therefore the observed asymmetry in leakage current could not be correlated with the oxide layer present at the interface. Presented in **Figure 75** are typical RBS results for the Au-Te oxide-Cd(Zn)Te structure obtained for the Device G, which exhibited the most asymmetric I-V characteristics.

Table 6 RBS results of TeO_2 thickness for devices which exhibit asymmetric and symmetric I-V characteristics

ID	Electrode	Designation	TeO Layer Thickness	L.C. ratio @ 3000V / cm S2 : S1
Device A	S1	N/A	31 nm	1.25
	S2	N/A	34 nm	
Device B	S1	(111)A	-	1.33
	S2	(111)B	-	
Device C	S1	N/A	37 nm	1.38
	S2	N/A	40 nm	
Device D	S1	(111)A	36 nm	6
	S2	(111)B	29 nm	
Device E	S1	(111)A	14 nm	15.1
	S2	(111)B	58 nm	
Device F	S1	(111)A	41 nm	56.3
	S2	(111)B	38 nm	
Device G	S1	(111)A	22 nm	220.2
	S2	(111)B	14 nm	

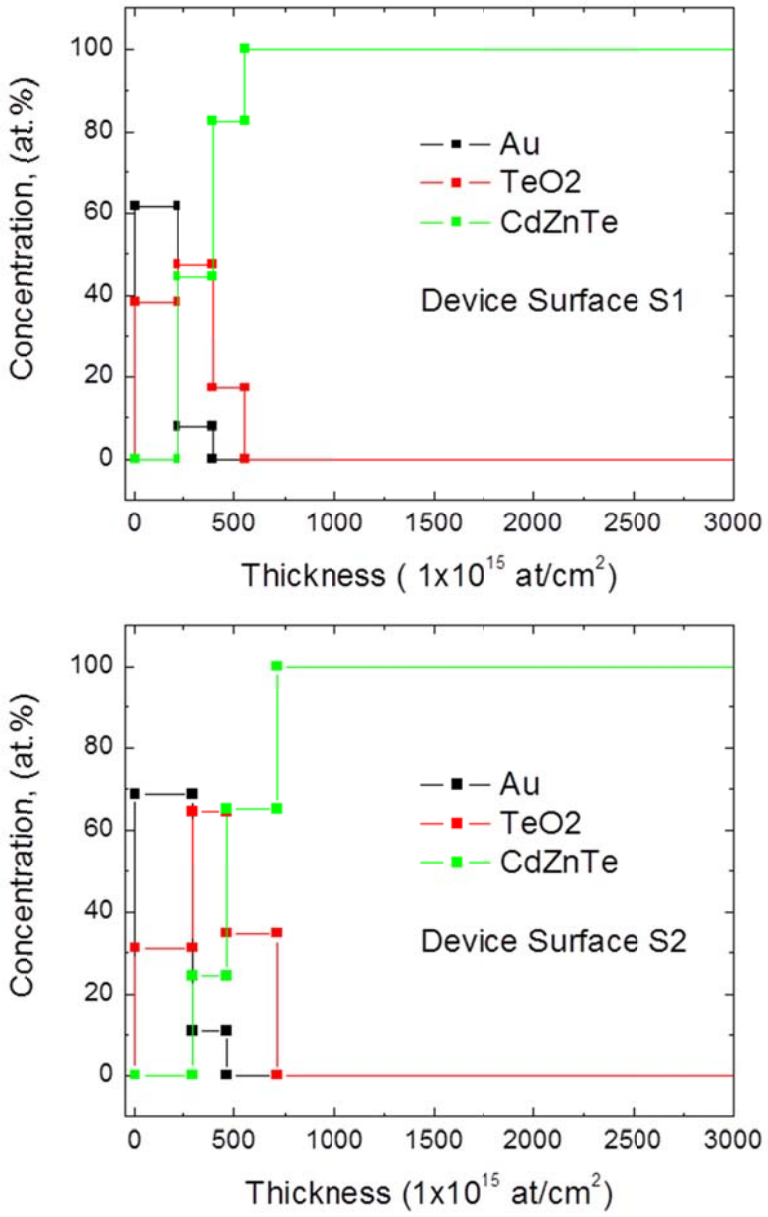

Figure 75 Simulated profile of Au and TeO_2 interfacial layer for S1 and S2 of Device E obtained from RBS measurements.

7.4 Active Deep Center and Device Polarization

To observe how the concentration of active deep levels present within the Cd(Zn)Te device depends upon the applied bias, a first PICTS spectrum was obtained by applying a bias of +20V to the S1 electrode and carrying out the PICTS measurement. The polarity of the bias was then reversed to -20V (using the same S1 electrode of the detector and maintaining the same

experimental configuration) and a second PICTS spectrum was recorded over the same temperature range (80K - 400K).

Planar test devices have been investigated using the PICTS method following the experimental arrangement presented in **Figure 73**(c) and (d). By changing the polarity of the bias, the photo-induced current will flow first toward the S1 electrode when the bias is positive, and then toward the S2 electrode when the bias is negative. Differences in the concentration of active deep centers associated with each electrode surface may then be observed.

Presented in **Figure 76** are the PICTS measurements, the Arrhenius plot, and the experimentally determined trap concentrations associated with each deep center identified for Devices A and B, which are also presented above in **Figure 74** and **Table 6**. When observing the differences between the two devices, it is important to note that Device A is a non-oriented sample whereas Device B is oriented along the (111).

From the PICTS spectra shown in **Figure 76**(a), it is possible to identify the local maximum associated with each deep level for a given emission rate. Presented in **Figure 76**(b) is the Arrhenius plot which has been constructed using several PICTS spectra to extract the trap energies and apparent cross sections of these deep centers. These traps have been named following the conventions used by A. Castaldini *et. al.* (1). All of the observed levels A, B, C, H, and I which have been found have been studied and previously identified in Cd(Zn)Te. It is important to note that there is good agreement of the energy level for both positive and negative biasing conditions. For more information on these defects in Cd(Zn)Te the reader is referred to (1) (2) (4) (5) (7) (35) (37) (38) (39).

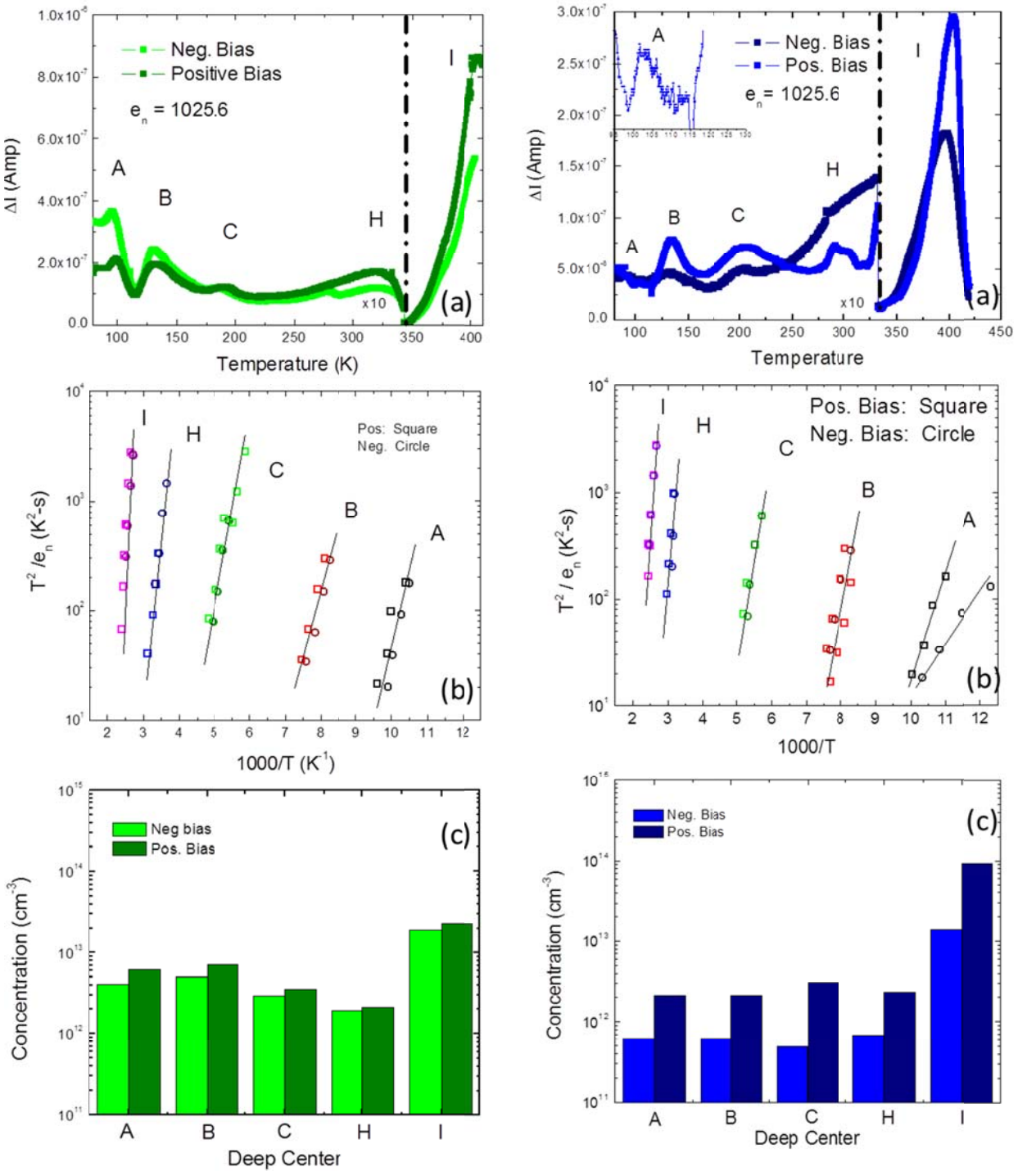

Figure 76 (a) PICTS Spectra for Cd(Zn)Te Device A (left) and Device B (right) under positive and negative biasing conditions, (b) Arrhenius plot for calculation of energies and apparent cross sections, and (c) experimentally determined concentration of deep centers in Cd(Zn)Te device

More importantly than the types of defects present in the Cd(Zn)Te, are their relative concentrations under positive and negative biasing conditions. Presented in **Table 7** are the active deep levels for both positive and negative biasing conditions of Device A and Device B. For Device A, the concentration of active energy levels did depend on the polarity of the bias. This concentration of active deep centers was observed to be higher under positive biasing conditions than under negative biasing conditions, and may be seen in **Figure 76**(c). Taking into account the S1 electrode was under bias, the higher activity of the deep centers corresponds to a lower leakage current within the device. For Traps A and B, positively biasing the device corresponds to a relative increase in the deep levels by up to 50% respectively. For traps C, H, and I, the increase in the measured concentration was slightly near 20%. We attribute this behavior to an increase in recombination processes.

The second sample investigated, Device B, was a (111) oriented device. As may be seen from **Figure 76**(c), there was an even more substantial increase in the concentration of active deep centers measured under positive biasing conditions. Furthermore, higher concentration of active deep centers would correspond to lower leakage current within the device (see **Figure 74**). For the deep centers A, B, and H, there was an increase in the relative concentration of active deep centers by >200%, while for the deep centers C and H, the increase in their concentration was by >500%.

Device B was an oriented device, and it is observed that using the (111)B as the cathode of a planar device leads to lower leakage current for the same biasing conditions imposed on the (111)A surface. The same behavior has been observed on other oriented Cd(Zn)Te devices as well. The behavior may be summarized as follows: when a reverse bias is applied to the (111)B electrode, this corresponds to a higher concentration of electrically active deep centers which may act as recombination centers and effectively lower the leakage current within the device.

More explicitly, when the S1 electrode was reverse biased, there was greater leakage current and a lower concentration of active deep centers. When the S1 electrode was forward biased, the concentration of active deep centers decreases.

Table 7 Activation energy and concentration for deep centers present in devices studied using positive and negative bias of electrode S1.

Device	Trap	Energy (eV)	Concentration (cm^{-3})	
		Pos.	Pos.	Neg.
Device A	A	0.15	6.2×10^{12}	4.1×10^{12}
	B	0.29	7.2×10^{12}	4.9×10^{12}
	C	0.35	3.6×10^{12}	2.9×10^{12}
	H	0.83	2.2×10^{12}	1.9×10^{12}
	I	0.91	2.3×10^{12}	1.8×10^{13}
Device B	A	0.18	2.1×10^{12}	6.1×10^{11}
	B	0.29	2.1×10^{12}	6.2×10^{11}
	C	0.36	3.1×10^{12}	4.9×10^{11}
	H	0.69	2.3×10^{12}	6.6×10^{11}
	I	0.97	9.3×10^{13}	1.38×10^{13}

7.5 SPV measurements

To demonstrate that the observed asymmetries may be attributed with the metal-semiconductor interface and not necessarily with the bulk material properties, optical probing of the surface states using SPV was carried out on several Cd(Zn)Te devices with and without electrical contacts following the arrangement presented in **Figure 73**(e) and (f). Measurements of the Surface Photo-Voltage (SPV) are presented for the S1 and S2 surface of Device B, which correspond to the (111)A and (111)B face of the crystal respectively. Other Cd(Zn)Te test devices have been studied as well, and each exhibit similar behavior as those investigated here.

The SPV spectra of S1 and S2 of Device B without Au contacts are presented in **Figure 77**. For the S1 surface, the SPV spectrum exhibits a peak near 1.53 eV which is related to the bandgap of the device and corresponds to a Zinc content of 4% following (58). The actual Zinc content of the device, using quantitative ICP-MS measurements, was determined to be 9-10%. This disagreement may be explained through red-shifting of the band gap energy by as much as 0.04 eV. Indeed, red shifting as much as 0.069eV has also been observed by (56), and has been attributed to oxidation of the surface.

More importantly with respect to the current discussion is that the SPV signal decays to zero for energies lower than the bandgap, to due to decreased absorption by the crystal of the incident light. For energies above the bandgap, surface recombination of electron-hole pairs begins to play an increasing role and the SPV begins to decay. For photons whose energy is greater than the bandgap, the absorption coefficient increases considerably and most photons are absorbed at the surface and are lost due to surface recombination mechanisms. This phenomenon gives rise to a peak instead of a plateau in the spectra, which has been observed by other investigators (59). Multiple locations on the same surface were measured to demonstrate the homogeneity of this behavior for the S1 surface.

The S2 surface of the wafer however exhibits a markedly different SPV spectrum. Indeed, it was possible to detect several sub-bandgap traps present at the Cd(Zn)Te surface. Two states located at 1.47 eV and 1.34 eV below the conduction band minimum (CBM) while a state situated 1.39 eV above the valence band minimum (VBM) have been detected. This may correspond to Trap A, which has been measured using the PICTS method. Finally, a state near E_V + 1.11 eV has also been detected (see **Table 7**).

Before describing the important differences between the two spectra, it is useful to compare these traps identified by the SPV method with those which have been observed by other investigators. Using correlative techniques including EDS and XPS in conjunction with SPV, results have been presented for gap states measured in n-type CdTe and $Cd_{0.094}Zn_{0.06}Te$. Specifically, a weak donor state at 1.42 eV above the valence band has been attributed to Cd atom displacement, and may correspond to the 1.39 eV state observed here (58) (60). A chemically induced surface state at 0.72eV below the CBM is attributed to chemical etching, is supported using XPS measurements, and is in agreement with reports that Br_2-CH_3OH etching depletes the

surface of Cadmium and Zinc, and enriches the surface in Te (58) (60). Indeed, this deep center may be responsible for increasing absorption for lower energies past 1.0 eV, however it is only observed in the S2 surface. In general, these surface traps have been related with depletion of the surface of Cd or with TeO_2 layer.

More generally, it is observed simply that for the S2 (or (111)B) surface of the crystal, the SPV signal does not decay but even increases out towards 1.0 eV and further. Indeed, absorption of incident light at the surface of Cd(Zn)Te is strongly dependent on which surface is measured.

For the S1 surface, the absorption decreases exponentially with increasing wavelength. This behavior suggests that the concentration of surface states is below the detection limit of the instrument. For the S2 surface however, this is not the case, and the deep surface states continue to absorb energies below the bandgap, resulting in a SPV signal which does not decay towards zero. **We may observe from these measurements, therefore, that the concentrations of surface states are asymmetrically present at the two surfaces.**

This absorption is associated with higher concentration of surface states which gives rise to the SPV signal (59) (58) (60). Indeed there is good evidence to support that these deep centers, which may act as an electron traps, are responsible for both (i) the sustained absorption of the crystal at longer wavelengths of incident light and (ii) the lower leakage current obtained when the (111)B surface is reverse biased.

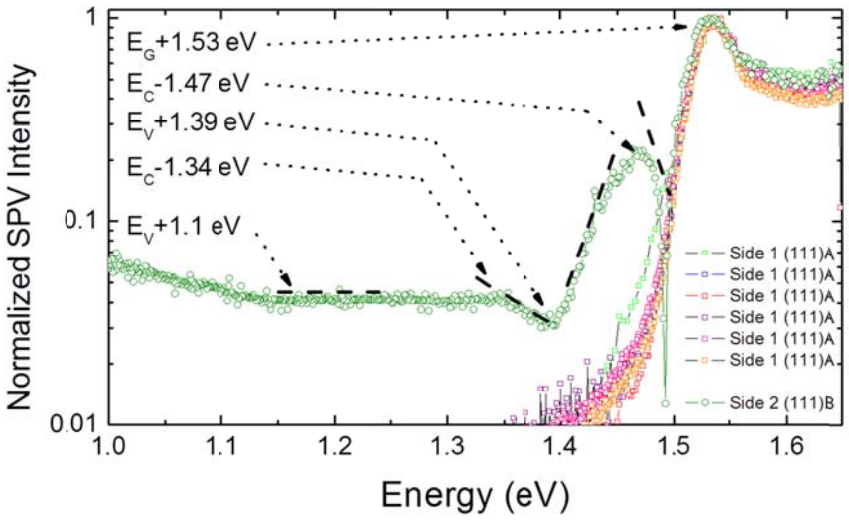

Figure 77 SPV measurements of Side 1 and Side 2 of Cd(Zn)Te Device B

7.5.1 Physical Model

To explain this behavior, it is important to note that the total amount of charge within each gap state must be supplied by the bulk. As a result the net carrier density near the surface will be different from the average bulk carrier density. This difference in carrier density between the bulk and the surface produces a Space Charge Region (SCR) in the crystal (57). Furthermore, the difference in the stoichiometry of the (111)A and (111)B surface will affect to a large extent the size of this space charge region, due to differences in carrier density at each surface.

The absorption by acceptor (or donor) surface states leads to the net surface state charge, $\boldsymbol{Q_{SS}}$, becoming less negative (more negative in the case of donors), as electrons are excited from the trap energy to the conduction band (or valence band to the trap in the case of donors), and subsequently swept into the bulk by the electric field at the surface. As a result, the SCR becomes less depleted (more depleted) and $\boldsymbol{Q_{SCR}}$ becomes less positive (more positive). Therefore, the surface potential decreases (increases), and it is this change which is observed by a change in the SPV and presented in the SPS spectra (57).

Essentially, when there is no absorption by the surface states, or when the concentration of surface states is too low, the incident light passes through the material without significantly affecting the magnitude of $\boldsymbol{Q_{SS}}$. This is observed with the S1 surface of the crystal and the SPV signal decays following the exponential dependence of the absorption coefficient of Cd(Zn)Te.

The higher concentrations of deep centers at the S2 (or (111)B) surface of the crystal has the effect of increasing the SPV signal due to increased absorption at longer wavelengths of light. This behavior observed in Device B is consistent with the PICTS measurements as well as the I-V measurements obtained for the same devices.

We have observed that this asymmetric distribution of active deep centers exists at the opposing surfaces of oriented and non-oriented Cd(Zn)Te devices. For the oriented samples, we attribute the carrier transport and recombination processes on the B-face to the presence of a higher concentration of deep centers possibly associated with Cd atom displacement, and not necessarily to a thicker tellurium oxide interfacial layer. This conclusion is supported by a lack of correlation between the TeO_2 thickness and the asymmetry in the I-V characteristics.

7.6 Spectroscopic Measurements of ^{133}Barium

From a device fabrication perspective, this difference in the active centers present at the surface can play a large role in the detector performance. Indeed, leakage current within the planar test devices has a strong impact on the resultant gamma ray spectra. For low electric field intensities, not only is the CCE poor but the signal induced at the anode of the device is too low to be extracted from the background noise. With increasing electric field intensity, comes improved CCE, higher induced currents with shorter transit and in general better separation and resolution of the photo-peaks.

For each of the devices, however, there was a critical electric field intensity such that incremental increases in the electric field would result in severe degradation of device performance i.e. contraction of the resolved spectrum and an exponential increase in electronic noise. Moreover, due to the asymmetric I-V characteristics, this critical point occurred at lower electric field intensities for the S1 electrode than for the S2 electrode. Or in the case of the oriented samples, using the (111)B surface as the cathode permitted higher operating voltages.

This typical asymmetric behavior in the gamma response spectra of planar test devices exposed to ^{133}Ba is presented in **Figure 78**(a). The test device presented here was measured using both S1 and S2 of the planar geometry as the cathode, following the geometry presented in **Figure 73**(g) and (h).

These spectroscopic measurements of ^{133}Ba show three different spectra recorded for a single Cd(Zn)Te test device, referred to here as Device E. Using S1 as the cathode (111)A, the maximum electric field which could be achieved was 1500 V/cm, whereas for S2 as the cathode (111)B, an electric field intensity as high has 7500 V/cm was achievable. This result clearly demonstrates the large difference existing at each surface.

The gamma response of the test device using each electrode as the cathode and applying an electric field of 1000 V/cm is presented in **Figure 78**(a) to show the gamma response of the device under similar operating conditions. Even under the same electric field intensities, there is substantial difference between the measured spectra.

Figure 78(b) illustrates the evolution of the 31keV and 81keV photo-peak FWHM of ^{133}Ba for the Cd(Zn)Te device with increasing electric field intensity, using both S1 and S2 as the cathode. It is important to emphasize the large differences in the FWHM observed for the same

electric field intensities applied within the same device, albeit across opposite electrodes. Using S1 as the cathode resulted in substantially lower electric field intensities and yielded substantially lower quality spectroscopic performance. Using S2 of the device, the FWHM for the 31keV and 81keV first go through a minimum near 3000 V-cm^{-1}, after which they increase due to increases in leakage current degrading the signal to noise ratio of the pulse height spectra.

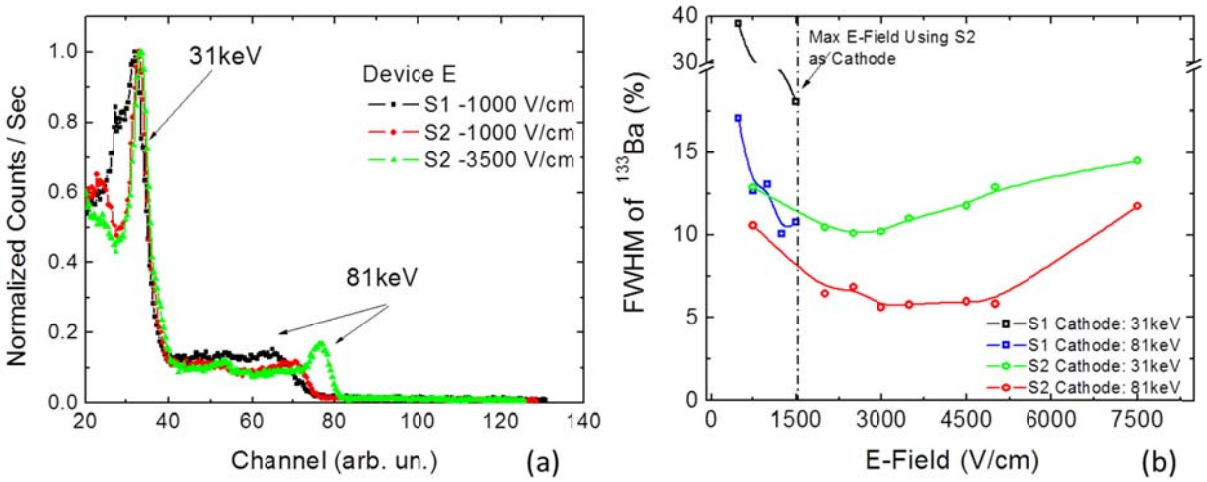

Figure 78 (a) Gamma response of each side of planar Cd(Zn)Te detectors exposed to 133Ba and (b) evolution of the 31keV and 81keV photo-peak of ^{133}Ba FWHM of Cd(Zn)Te Device E with electric field intensity, using S1 and S2 as the Cathode.

7.7 Conclusions and Future Work

In summary, substantially higher electric field intensities could be achieved depending on which electrode surface served as the cathode. For oriented crystals, this corresponded to the (111)B surface, which is referred to as S2 throughout this text. For un-oriented crystals, the surface which led to lower leakage current had to be experimentally determined through trial. Ultimately, this has led to the capacity to apply higher fields, which result in better charge collection efficiency, and better signal to noise ratio of the charge induced within the detector. This is typical behavior which has been observed in nearly all of the detectors investigated.

Several methods have been implemented to develop a better understanding of the nature of asymmetries in planar Cd(Zn)Te devices. The conclusions of this investigation are presented as follows:

1. Correlation between the interfacial TeO_2 thickness present at the Au-Cd(Zn)Te interface and the asymmetry of the planar test devices was not observed, using RBS and I-V measurements.
2. PICTS measurements in conjunction with I-V measurements provide evidence that the asymmetric electronic properties of Cd(Zn)Te devices arise from asymmetries in the concentration of active deep centers present within the device.
3. This behavior is attributed to a higher concentration of absorbing deep centers present at the surface, using the SPV spectroscopy technique.
4. It has been observed that detectors which exhibit A-face and B-face orientations normally exhibit stronger asymmetries in the I-V characteristics than do devices which do not exhibit A-face and B-face orientations, and has been demonstrated through spectroscopic measurements.
5. We therefore conclude that deep centers at the surface are responsible for the differences in device performance are consistent with reports found in literature. Based on these results study of more highly asymmetric samples is of interest and will be further investigated.
6. Finally, a new application for SPV Spectroscopy is proposed. Specifically, we propose the use of SPS for the determination of the anode/cathode surfaces of Cd(Zn)Te devices. Using this technique, the electrode surface which will yield lower leakage current when reverse biased may be determined using the methods described here. This is a non-destructive non-contact method which may be used before or after contacts deposition.

This page intentionally left blank

8 CONCLUSIONS AND FUTURE WORK

The development of technology and protocol for fabrication of radiation devices based on Cd(Zn)Te has been investigated in this chapter. Based on the studies which have been carried out used a number of radiation devices, the following conclusions summarize the results which have been obtained through this investigation.

State of the art Spectrometers have been characterized in terms of the optical, electrical, and compositional properties. These detectors biased at 1000V/cm, exhibited a FWHM between 1% and 3% for the 81keV photo-peak of ^{133}Ba. Moreover, CL measurements demonstrate the defect structure of these materials, which is substantially different than the materials grown by UAM. These measurements clearly demonstrate the high spectral resolution of commercially available devices.

For detector preparation several new protocols have been developed in this work. A diamond wire saw technology has been designed and implemented for effectively cutting 50 mm Cd(Zn)Te ingots. A multi-stage lapping, polishing, and chemical etching process has been developed in detail for preparing 50 mm Cd(Zn)Te wafer surfaces for electrode deposition with surface roughness less than 2nm. CFT templates, which do not use wax, have been implemented for cleaning the surface of polished wafers. A low cost photo lithographical approach has been implemented for fabrication of patterned electrode geometries.

The effect of lateral surface morphology on detector performance has been studied in Section 4, using different lapping and polishing agents. It has been found that polishing the lateral edges of the planar detectors can help reduce leakage current by a factor of 200% in most cases and improve the performance of planar detectors through the introduction of surface traps. These traps provide radiative recombination centers for surface travelling electrons.

To explain the effects of surface treatment on device performance, two types of devices have been investigated using PICTS to study how their lateral surface morphology affects their electronic properties. The most significant difference between LEL-9 and LEP-3 treatments has been observed in the appearance of a new deep level with E_a = 0.38eV, and which is attributed to structural defects imparted into the crystal by the lapping process.

The effects of crystallographic defects associated with twinning have been investigated in Section 6. Wafers which exhibit twin features have been investigated in terms of their optical, electrical, and compositional properties. The twin features have been investigated using IR microscopy, and the twinned regions of the wafer have been correlated with higher densities of closely spaced Te-precipitates. Difference in the SPV spectra of the (111)A and (111)B surfaces is attributed to a larger concentration of deep levels associated with the (111)B face. Work function measurements using KPM have shown local decreases in surface potential associated the twin structure.

Several methods have been implemented to develop a better understanding of the nature of asymmetries in the electronic properties of Cd(Zn)Te devices. From this work it is clear that the surface used as the cathode and anode determines to a large extent the performance of Cd(Zn)Te devices, and has been demonstrated through gamma ray spectroscopy measurements. We have observed that an asymmetric distribution of deep centers exists between the (111)A and (111)B surfaces of Cd(Zn)Te devices. Furthermore, we attribute the carrier transport and recombination processes on the B-face to the presence of a higher concentration of deep centers, and not to a thicker tellurium oxide interfacial layer

In addition, these investigations have opened the doors to additional investigations which require further study. Based on the CL measurements of commercial detectors, the defect structure of these materials illustrates a suppression of the formation of V_{Cd}. Indeed, this is likely associated with the growth technique (High Pressure Bridgman) in which a high overpressure is used to prevent Cd loss and the formation of vacancies. To reduce these kinds of defects, a method for overpressure control of Cadmium has been integrated in the design of the VGF-2 furnace. Further investigation of Cd over pressure control is of great interest for reducing these defects, as are ex-situ annealing methods.

While surfaces treated using the LEP-3 treatment appear to be somewhat stable with time, increases in leakage current have been observed over a longer 8 month temporal lapse. It is of interest the investigation of chemical passivation mechanisms for reducing this effect.

While the twinning in Cd(Zn)Te does appear to be related with the resistivity of the devices, further investigation is required to elucidate the relationship between the higher concentration of

second phase inclusions, the higher concentration of surface related traps at the (111)B face, and the differences in the surface potential of the two surface terminations.

Surface Photo voltage Spectroscopy is proposed as a non-destructive technique for determining the appropriate surface for anode/cathode selection. Further development of this technique at CGL is important to determine the electrode surface which will yield lower leakage current when reverse biased may be determined using the methods described here. This is a non-destructive non-contact method which may be used before or after electrode deposition. Moreover, we have demonstrated that very large differences in the SPV spectra can be observed depending on which surface is selected for measurement.

8.1 Conclusiones (Español)

De manera resumida se podría decir que se ha invertido una gran cantidad de esfuerzo en mejorar las capacidades de crecimiento del Laboratorio de Crecimiento de Cristales. El proceso de homogeneización de fusión y la síntesis, el propio crecimiento de cada lingote, y el desarrollo de un modelo numérico han sido fundamentales para alcanzar una mejor comprensión de los mecanismos que intervienen directamente en la síntesis de materiales cristalinos. El comportamiento térmico del sistema Cd (Zn) Te se ha estudiado en el entorno de los 450 ° C midiendo la temperatura de reacción directamente. Esta reacción de carácter exotérmico causa un aumento de la temperatura de varios centenares de grados, en consonancia con las predicciones. Los resultados del modelo numérico que ha sido desarrollado para el crecimiento de Cd (Zn) Te sugieren que esta etapa poli-cristal puede estar asociada con la nucleación que ocurre en la superficie del fundido. Se observó que un sobrecalentamiento de 30º C Tipo-2 de la masa fundida fue suficiente para (i) mejorar la homogeneidad de material, (ii) impedir que la nucleación ocurra en la superficie del fundido, y (iii) aumentar el rendimiento global.

Los crisoles PBN fueron recubiertos interiormente de carbono. Los resultados indican que esta tecnología se puede implementar para aumentar la longevidad de crisol de PBN a través de la reducción de las interacciones entre crisol y fundido. Una segunda ventaja del sistema de revestimiento de carbono es que el método se puede volver a aplicar, así que puede ser posible volver a depositar otra capa de carbono después de un cierto número de ciclos de crecimiento.

Los detectores obtenidos a partir de los crecimientos en los que se emplearon crisoles cc-PBN exhiben una elevada resistividad y buena funcionalidad como detectores de rayos gamma a temperatura ambiente, lo que indica que la tecnología CC-PBN conserva, si no mejora, la calidad del material resultante del proceso.

Una de las ventajas del método de crecimiento de VGF es la capacidad de ajustar dinámicamente los gradientes de temperatura. Es importante señalar que los ajustes de temperatura dinámicos mantienen la calidad de los cristales en bruto, sin introducir nuevos defectos puntuales o niveles relacionados como se ha observado en otros lugares. De hecho, los efectos beneficiosos de estos ajustes del horno en la fotoconductividad y la resistividad de como cultivadas Cd (Zn) los cristales de Te se ha informado en la sección anterior (y también publicado y estos resultados se corroboran aquí.

Para el mejor conocimiento de los autores, esta es la primera vez que se ha informado acerca de estos cambios dinámicos en el perfil de temperatura axial en crecimientos de Cd (Zn) Te. Estos gradientes de temperatura dinámicos parecen afectar a la segregación de Zn ni In. De hecho, hay una gran variación en las propiedades del material de un único lingote crecido por el método de VGF, no sólo en la composición global, sino también en las características eléctricas y ópticas, la distribución de las inclusiones de la segunda fase, y también de concentración y tipos de trampas presentes en el material. Estas características parecen estar fuertemente influenciadas por la segregación masiva de zinc e indio. A pesar de estas grandes diferencias en las propiedades eléctricas de la composición el rendimiento del dispositivo de prueba fue similar en términos de FWHM dispositivo.

Se desarrolló y aplicó un modelo 2-D para la simulación del crecimiento de los cristales Cd (Zn) Te. Los estudios preliminares utilizando este modelo han dado penetración en la posición de los termopares en el interior del horno, así como el papel desempeñado por el pedestal de SiC durante el ciclo de crecimiento, así como la nucleación que puede ocurrir en la superficie del fundido.

Igualmente se ha invertido gran esfuerzo en los detectores basados en Cd(Zn)Te. El desarrollo de la tecnología y el protocolo para la fabricación de dispositivos de radiación sobre la base de Cd (Zn) Te ha sido investigado en este capítulo. Basándose en los estudios que han sido

llevados a cabo utilizando varios dispositivos de radiación, las conclusiones siguientes resumen los resultados que se han obtenido a través de esta investigación.

El grado de calidad tecnológica se establece en términos de las propiedades ópticas, eléctricas, y de composición. Estos detectores sesgados en 1000V/cm, muestran una FWHM entre el 1% y 3% para el 81keV foto-pico de 133Ba. Además, las mediciones CL demostrar la estructura de defectos de estos materiales, que es sustancialmente diferente de los materiales cultivados por la UAM. Estas mediciones demuestran claramente la alta resolución espectral de los dispositivos comercialmente disponibles.

En este trabajo se han seguido diversos pasos para la preparación del detector. Se ha empleado y optimizado el proceso de corte por hilo diamantado para el corte de lingotes de 50 mm de Cd (Zn) Te. Se ha empleado lapeado de múltiples etapas, pulido y proceso de ataque químico para la preparación de obleas de Cd (Zn) Te con una rugosidad superfcial inferior a los 2nm. Plantillas CFT, que no utilizan cera, se han aplicado para la limpieza de la superficie de las obleas pulidas. Se empleó fotolitografía para el diseño de los electrodos.

El efecto de la morfología de la superficie lateral en el funcionamiento del detector ha sido estudiado en la Sección 4, utilizando diferentes condiciones de lapeado y agentes de pulido. Se ha encontrado que pulir los bordes laterales de los detectores planos puede ayudar a reducir la corriente de fuga en un factor de 200% en la mayoría de los casos y mejorar el rendimiento de los detectores planos mediante la introducción de trampas de superficie. Estas trampas proporcionan centros de recombinación de tipo radiativo.

Para explicar los efectos del tratamiento superficial sobre el rendimiento del dispositivo, dos tipos de dispositivos se han investigado utilizando PICT para estudiar cómo la morfología de la superficie lateral afecta a sus propiedades electrónicas. La diferencia más significativa entre LIE-9 y tratamientos LEP-3 se ha observado en la aparición de un nuevo nivel de profundidad con Ea = 0.38eV, y que se atribuye a defectos estructurales en el cristal itroducidos por el proceso de lapeado.

Los efectos de los defectos asociados con el maclado se han investigado en la Sección 6. Las obleas, que presentan características individuales han sido investigadas en cuanto a sus propiedades ópticas, eléctricas y de composición. Las características individuales se han investigado utilizando microscopía IR, y las regiones de macla de la oblea se han correlacionado

con mayores densidades de precipitados de Te débilmente separados. La diferencia en los espectros de la SPV de las superficies A(111) y B (111) se atribuye a una concentración mayor de niveles profundos asociados con la cara B(111). Los resultados obtenidos a partir de la técnica KPM han demostrado disminuciones locales en el valor del potencial de la superficie asociados a la estructura doble.

Varios métodos han sido implementados para desarrollar una mejor comprensión de la naturaleza de las asimetrías en las propiedades electrónicas de los dispositivos de Cd (Zn) Te. A partir de este trabajo, es evidente que la superficie utilizada como el cátodo y el ánodo determina en gran medida el rendimiento de los dispositivos de Cd (Zn) Te, y se ha demostrado a través de mediciones de espectroscopia de rayos gamma. Hemos observado que una distribución asimétrica de los centros de profundidad existe entre las superficies A(111) y B(111) de los dispositivos de Cd (Zn) Te . Además, se atribuyen el transporte portador y procesos de recombinación en la cara B a la presencia de una mayor concentración de centros profundos, y no a una gruesa capa de óxido de teluro interfacial

Además, estas investigaciones conducen a investigaciones adicionales que requerirían un mayor estudio. Basándose en las mediciones de CL de detectores comerciales, la estructura de defectos de estos materiales ilustra una supresión de la formación de VCD. En efecto, esto probablemente se asocie con la técnica de crecimiento (Bridgman de alta presión) en el que se usa una sobrepresión elevada para evitar la pérdida de Cd y la formación de vacantes. Para reducir este tipo de defectos, un método para el control de sobrepresión de cadmio se ha integrado en el diseño del horno de VGF-2. La investigación adicional de CD a través de control de la presión es de gran interés para la reducción de estos defectos, así como ex-situ los métodos de recocido.

Mientras que las superficies tratadas con el tratamiento LEP-3 parecen ser estables en el tiempo, el aumento de la corriente de fuga se han observado durante un largo lapso de 8 meses. Es de interés la investigación de los mecanismos de pasivación químicos para reducir este efecto.

Mientras que el maclado en Cd (Zn) Te parece estar relacionado con la resistividad de los dispositivos, se requiere una mayor investigación para dilucidar la relación entre la concentración más alta de inclusiones de segunda fase, la mayor concentración de trampas relacionadas con la superficie en la cara B(111), y las diferencias en el potencial superficial de las dos terminaciones superficiales.

La Espectroscopía de Fotovoltaje Superficial se propone como una técnica no destructiva, útil en la determinación de la superficie apropiada para ánodo / cátodo. Un mayor desarrollo de esta técnica en el CGL es importante para determinar la clase de superficie sobre la que se deposite el electrodo. Es un método no destructivo, de no contacto, que se puede utilizar antes o después de la deposición del electrodo. Además, hemos demostrado que se pueden observar grandes diferencias en los espectros de SPV dependiendo de la superficie que se selecciona para la medición

This page intentionally left blank.

9 BIBLIOGRAPHY

1. *Deep Energy Levels in CdTe and CdZnTe.* **A. Castaldini, A. Cavallini, and B. Fraboni, P. Fernandez, J. Piqueras.** 4, 1998, J. Appl. Phys., Vol. 83, p. 4.

2. *Cathodoluminescence and photoinduced current transient spectroscopy studies of defects in Cd0.8Zn0.2Te.* **A. Castaldini, A. Cavallini, B. Fraboni, L. Polenta, P. Fernandez, J. Piqueras.** 11, 1996, Phys. Rev. B, Vol. 54, p. 7622.

3. **A. Castaldini, A. Cavallini, and B. Fraboni.** 1998, J. Appl. Phys., Vol. 83, p. 4.

4. *Properties of CdZnTe crystals grown by High Pressure Bridgman.* **A. Drighil, R. Adhiri, C. Sribi, M. Mousstad, K. Cherkaoui, G. Marrakchi, A. Zerrai, M. Zazoui.** 1, 1999, M. J. Cond. Matter, Vol. 2.

5. *CdTe and CdZnTe for nuclear detectors: facts and fictions.* **P. Fougeres, P. Siffert, M. Hageali, J. M. Koebel, R. Regal.** 1999, Nucl. Instr. Meth. Phys. Res. A, Vol. 428, pp. 38-44.

6. —. **P. Fougeres, P. Siffert, M. Hageali, J. M. Koebel, R. Regal.** 1, 1999, Nucl. Instr. Meth. Phys. Res. A, Vol. 428, pp. 38-44.

7. *Defect Structure of High Resistive CdTe:In Prepared by Vertical Gradient Freeze.* **J. Franc, V. Babensotv, M. Fiederle, E. Belas, R. Grill, K. W. Benz, P. Hoeschl.** 3, 2004, IEEE Trans. Nucl. Sci., Vol. 51.

8. *Analysis of ID saw slicing of silicon for low cost solar cells.* **H. Yoo, R. Schwartz, P. Iles.** Washington D.C. : s.n., June 1978. 13th Photovoltaic Specialists Conference.

9. *Investigation of the Effects of Polishing and Etching on the Quality of Cd1-xZnxTe Using Spatial Mapping Techniques.* **H. Yoon, J.M. Van Scyoc, M.S. Goorsky.** 6, 1997, Journal of Electronic Materials, Vol. 26, p. 529.

10. *Surface and Subsurface Damages of CdZnTe Substrates Ground by Diamond Wheel.* **S. Gao, R.K. Lang, Y. Li, H. Gao.** 2011, Vol. 487, pp. 1-5.

11. *Effects of Surface Processing on the Performance of CdZnTe Radiation Detectors.* **Y. Cui, M. Groza, A. Burger, R.B. James.** 3, 2004, IEE Trans. on Nucl. Sci.. -, Vol. 51, pp. 1172-1175.

12. *Chemical polishing of CdZnTe substrates fabricated from crystals grown by the vertical-gradient freezing method.* **P. Moravec, P. Hoeschl, J. Franc, E.Belas, R. Fesh, R. Grill, P. Horodysky, P. Praus.** 6, 2006, J. Elec. Mat., Vol. 35, pp. 1206-1213.

13. *Chemical mechanical polishing and nanomechanics of semiconductor CdZnTe single crystals.* **Z. Zhang, H. Gao, W. Jie, D. Guo, R. Kang.** 2008, Semicnd. Sci. Technol., Vol. 23, p. 105023.

14. *Effects of Surface Processing on the Response of CZT Gamma Detectors: Studies with a Collimated Synchrotron X-Ray Beam.* **A. Hossain, A. E. Bolotnikov, G. S. Camarda, Y. Cui, S. Babalola, A. Burger, R. B. James.** 9, 2008, J. Electron. Mater., Vol. 37.

15. *Molecular Beam Epitaxy Growth of High-Quality HgCdTe LWIR Layers on Polished and Repolished CdZnTe Substrates.* **Singh, R., et al., et al.** 6, 2005, J. Electron. Mater., Vol. 34, pp. 885-890.

16. *Chemical Etching of CdTe in Aqueous Solutions of H2O2-HI-Citric Acid.* **al., Ivanitska V.G. et.** 8, 2007, J. Electron. Mater., Vol. 36, pp. 1021-1023.

17. *Influence of Surface Preparation on CdZnTe Nuclear Radiation Detectors.* **Q.Zheng, F. Dierre, J. Crocco, V. Carcelen, H. Bensalah, J.L. Plaza, E. Dieguez.** 2011, Appl. Surf. Sci., Vol. 257, pp. 8742-8746.

18. **A. Hossain, A.E. Bolotnicov, G. S. Camarada, Y. Cui, S. Babalola, A. Burger, and R.B. James.** 9, 2008, J. Electron. Mater,, Vol. Vol. 37 .

19. **H.Bensalah, J.L.Plaza, J.Crocco, Q.Zheng, V.Carcelen, A.Bensouici, E.Dieguez,.** J. Cryst. Growth, to be published.

20. *Effects of Surface Processing on the Response of CZT Gamma Detectors: Studies with a Collimated Synchrotron X-Ray Beam.* **A. Hossain, A.E. Bolotnicov, G. S. Camarada, Y. Cui, S. Babalola, A. Burger, and R.B. James.** 9, 2008, J. Electron. Mater., Vol. 37.

21. *Effects of Chemical Etching on (111) Oriented CdZnTe Nuclear Radiation Detectors.* **G. Wright, Y. Cui, N. Roy, C. Barnett, K. Reed, A. Burger, F. Lu, L. Li, R. B. James.** 5, 2002, IEEE Trans. Nucl. Sci., Vol. 49.

22. *Effect of surface preparation technique on the radiation detector radiation performance of CZT.* **M.C. Duff, D.B. Hunter, A. Burger, M. Groza, V. Buliga, D.R. Black.** 2008, App. Surf. Sci., Vol. 254, pp. 2889-2892.

23. *Influence of surface preparation on CdZnTe nuclear radiation detectors.* **Q. Zheng, F. Dierre, J. Crocco, V. Carcelen, H. Bensalah, J.L. Plaza, E. Dieguez.** 2011, App. Surf. Sci., Vol. 257, pp. 8742-8746.

24. *Effects of surface Processing on the performance of Cd1-xZnxTe radiation detectors.* **Y. Cui, M. Groza, A. Burger, and R. B. James.** 3, 2005, IEE Trans. on Nucl. Sci., Vols. 51. - pp. , pp. 1172-1175.

25. *Comparison of the Detector Performance for Different Metal Contacts on Cd(Zn)Te for Radiation Applications.* **Q. Zheng, F. Dierre, M. Ayoub, J. Crocco, H. Bensalah, V. Corregidor, E. Alves, R. Fernandez-Ruiz, J. M. Perez, E. Dieguez.** In Press.

26. *Study of the Effects of Edge Morphology on Detector Performance by Leakage Current and Cathodoluminescence.* **J. Crocco, H. Bensalah, Q. Zheng, F. Dierre, P. Hidalgo, J. Carrascal, O. Vela, J. Piqueras, E. Dieguez.** 4, IEEE Trans. Nucl. Sci., Vol. 58, pp. 1935-1941.

27. *Deep level spectroscopy in high-resistivity materials.* **Ch. Hurtes, M. Boulou, A. Mitonneau, D. Bois.** 12, 1978, Appl. Phys. Lett., Vol. 32, pp. 821-823.

28. *Photoinduced current transient spectroscopy in high-resistivity bulk materials: Instrumentation and methodology.* **M. Tapiero, N. Benjelloun, J.P Zielinger, S. El Hamd, C. Noguet.** 1988, J. Appl. Phys., Vol. 64, p. 4006.

29. **Kamihara, O. Yoshie and M.** 1983, Jpn. J. Appl. Phys, Vol. 22, p. 629.

30. *Transient photoconductivity measurements in semi-insulating GaAs I. An analog approach.* **R. E. Kremer, M. C. Arikan, J. C. Abele, J. S. Blakemore.** 6, 1987, J. Appl. Phys., Vol. 62.

31. *Investigation of deep levels in PbI2 by photoinduced current transient spectroscopy.* **J. P. Zielinger, B. Pohoryles, J. C. Bailand, J. G. Gross, A. Coret.** 2, 1985, J. Appl. Phys, Vol. 57, pp. 293-301.

32. *Characterization of deep levels in BiGeO by photoinduced current transient spectroscopy.* **N. Benjelloun, M. Tapiero, and J. P. Zielinger.** 8, 1968, J. Appl. Phys., Vol. 64, pp. 4013-4023.

33. *Real defect concentration measurements of nuclear detectormaterials by the combination of PICTS and SCLC methods.* **M. Ayoub, M. Hage-Ali, J.M. Koebel, R. Regal, C. Rit, F. Klotz, A. Zumbiehli, P. Siffert.** 2001, Mater. Sci. & Eng., Vol. B83, pp. 173-179.

34. *Photo-induced current transient spectroscopic study of the traps in CdTe.* **Mathew, X.** 2003, Solar Energy Mater. and Solar Cells, Vol. 76, pp. 225-242.

35. *Effects of copper in high resistivity CdTe.* **B. Biglari, M. Samimi, M. Hage-Ali, J.M. Koebel, P. Siffert.** 4, 1988, J. Crystal Growth, Vol. 89, pp. 428-434.

36. *Growth of high resistivity CdTe and (Cd,Zn)Te crystals.* **M. Fiederle, V. Babentsov, J. Franc, A. Fauler, J.P. Konrath.** 2003, Cryst. Res. Technol., Vol. 38, p. 588.

37. *Detailed characterization of deep centers in CdTe: Photoionization and thermal ionization properties.* **T. Takebe, J. Sarie, H. Matsunami.** 1, 1982, J. Appl. Phys., Vol. 53, p. 457.

38. *Defective states induced in CdTe and CdZnTe detectors by high and low energy neutron irradiation.* **A. Cavallini, B. Fraboni, W. Dusi, M. Zanarini.** 5, 2003, J. Appl. Phys., Vol. 94.

39. *Point defects in CdZnTe Crystals Grown by Different Techniques.* **R, Gul, A. Bolotnikov, H. K. Kim, R. Rodriguez, K. Keeter, Z. Li, G. Gu, R. B. James.** 3, 2011, J. Electron. Mater., Vol. 40, p. 274.

40. **K. Durose, G.J. Russell.** 1990, J. Cryst. Growth, Vol. 101, p. 246.

41. **K.F. Hulme, J.B. Mullin.** 1962, Solid State Electron, Vol. 5, p. 211.

42. *Growth and properties of semi-insulating CdZnTe for radiation detector applications.* **C. Szeles, M. C. Driver.** San Diego : s.n., 1998. SPIE Conference on Hard X-ray and Gamma-Ray Detector Physics and Applications. Vols. 3446, 1.

43. *Study of impurity segregation,crystallinity,and detector performance of melt-grown cadmium zinc telluride crystals.* **M. Schieber, T.E. Schlesinger, R.B. James, H. Hermon, H. Yoon, M. Goorsky.** 2002, J. Crystal Growth, Vols. 237-239, pp. 2082-2090.

44. *GET PAPER.* **C. Szeles, E.E. Eissler.** 2998. MRS Symposium Proceedings. Vol. 3, p. 487.

45. *Defect Structure of High Resistive CdTe:In Prepared by Vertical Gradient Freeze.* **J. Franc, V. Babensotv, M. Fiederle, E. Belas, R. Grill, K. W. Benz, P. Hoeschl.** 3, 2004, IEEE Trans. Nucl. Sci., Vol. 51, p. 1176.

46. *Low-temperature photoluminescence of detector grade Cd1−xZnxTe crystal treated by different chemical etchants.* **H. Chen, J. Tong, Z. Hu, D. T. Shi, G. H.Wu, K.-T. Chen, M. A. George,W. E. Collins, A. Burger, R. B. James, C. M. Stahle, and L. M. Bartlett,.** 1996, J. Appl. Phys, Vol. 80, p. 3509.

47. *Light-Induced Tellurium Enrichment on CdZnTe Crystal Detected by Raman Spectroscopy.* **S. Hawkins, E. Villa-Aleman, M. C. Duff, D. Hunter, A. Burger, M. Groza, V. Buliga, D. Black.** 9, 2008, J. Electron. Mater., Vol. 37.

48. *Surface barriers formation mechanisms of the chemically etched CdTe(111) polar surfaces and gold interfaces.* **T. Takeuchi, T. Kore-eda, A. Ebina.** 1996, Appl. Surf. Sci., Vol. 100/101, pp. 596-600.

49. *Surface current reduction in 211 oriented CdZnTe crystals by Ar bombardment.* **L. F. Voss, P. R. Beck, A. M. Conway, R. T. Graff, R. J. Nikolic, A. J. Nelson, S. A. Payne.** 2010, J. of Appl. Phys., Vol. 108, p. 014510.

50. *The Study of Work Function of CdZnTe with Different Surface States by Synchrotron Radiation Photoemission Spectroscopy.* **G. Zha, W. Jie, X. Bai, T. Wang, L. Fu, W. Zhang, J. Zhu, F. Xu.** 2009, J. Appl. Phys., Vol. 106, p. 053714.

51. *The absolute determination of CdTe crystal polarity.* **P.D. Brown, K. Durose, G.J. Russel, J. Woods.** 1-4, 1990, J. Crystal Growth, Vol. 101, p. 211.

52. *Comparison of radiation detector performance for different metal contacts on CdZnTe deposited by electroless deposition method.* **Q. Zheng, F. Dierre, M. Ayoub, J. Crocco, H. Bensalah, V. Corregidor, E. Alves, R. Fernandez-Ruiz, J. M. Perez, and E. Dieguez.** 11, 2011, Cryst. Res. Technol., Vol. 46, pp. 1131-1136.

53. *Detector surface preparation of CdZnTe for electrode patterning.* **J. Crocco, Q. Zheng, H. Bensalah, E. Deiguez.** Appl. Surf. Sci., Vol. In Press.

54. *Appl. Phys. Lett.* **N.P. Barradas, C. Jeynes, R.P. Webb,.** 1997, Simulated annealing analysis of Rutherford backscattering data, Vol. 71, p. 291.

55. *Determination of undoped CdTe(111) surface polarity by surface photovoltage spectrsocopy.* **L. Burstein, Y. Shapira, E. Moons, D. Cahen.** 1994, Appl. Surf. Sci., Vol. 74, p. 201.

56. *Surface photovoltage spectroscopy analyses of CZT.* **D. Cavalcoli, B. Fraboni, A. Cavallini.** 2008, J. App. Phys., Vol. 103, p. 043713.

57. *Surface photovoltage Phenomena: Theory, Experiment, and Applications.* **L. Kronik, Y. Shapira.** 1999, Surf. Sci. Rep., Vol. 37, pp. 1-206.

58. *Alloy composition and electronic structure of CZT by surface photovoltage spectroscopy.* **J. Yang, Y. Zidon, Y. Shapira.** 2, 2002, J. Appl. Phys., Vol. 91.

59. *Electrical activity of deep traps in high resistivity CdTe: Spectroscopic characterization.* **B. Fraboni, D. Cavalcoli, A. Cavallini, P. Fochuk.** 2009, J. Appl. Phys., Vol. 105, p. 073705.

60. *X-ray photoelectron spectroscopy and atomic force microscopy characterization of the effects of etching ZnxCd1−xTe surfaces* . **M.A. George, M. Azoulay, H.N. Jayatirtha, A. Burger, W.E. Collins, and E. Silberman.** 1993, Surf. Sci., Vol. 296, p. 231.

Appendix

This page intentionally left blank.

1 HEM/DSS SYSTEM DEVELOPMENT

1.1 Introduction

During the course of this thesis, the elaboration of a fairly sophisticated 30kW furnace for the growth of polycrystalline Si for was also developed. The design of the furnace was carried out to support efforts to increase the efficiency and crystalline quality of Si for photovoltaic applications.

Presented below in Figure 2 is a general cross section of the HEM/DSS system. The HEM/DSS system functionality was derived principally from the ability to have two linear translation systems incorporated into a single furnace. The first linear actuation system provided the capability to translate the lateral insulation in the vertical direction.

The HEM/DSS system consists of a stainless steel 316 double walled chamber, which provides the capability for integrated water-cooling of the chamber walls. The graphite hot-zone and insulating elements are contained within the chamber, while an external vacuum pumping station and gas purging system are used for controlling the overpressure within the chamber walls. A mezzanine support structure has been designed to not only support the substantial weight of the furnace and transformer elements, but to also provide access to the various components for service and maintenance. Presented in Figure 1 is a rendering of the final system design for the HEM/DSS furnace which has been developed in this thesis, illustrating the aforementioned key design elements.

The system is divided into several sub-systems for discussion. These sub-systems include (a) the LMS drive subsystem (or linear actuation sub-system 1) (b) water-cooled electrodes (c) the mezzanine structure (d) the hot-zone furnace elements (e) the crucible and crucible positioning elements (f) chamber open/close mechanism (or linear actuation sub-system 2) and (g) the vacuum pumping station.

1.2 Objectives of Investigation

The objectives of this research have been the development of a furnace which incorporates both the Heat Exchange Method (HEM) and Directional Solidification (DSS) functionalities. Some of the challenges associated with this undertaking include the design of a 30kW furnace with water cooled electrodes, selecting a system for gas and over pressure regulation and control, as well as the general chamber design and integration of moving furnace components.

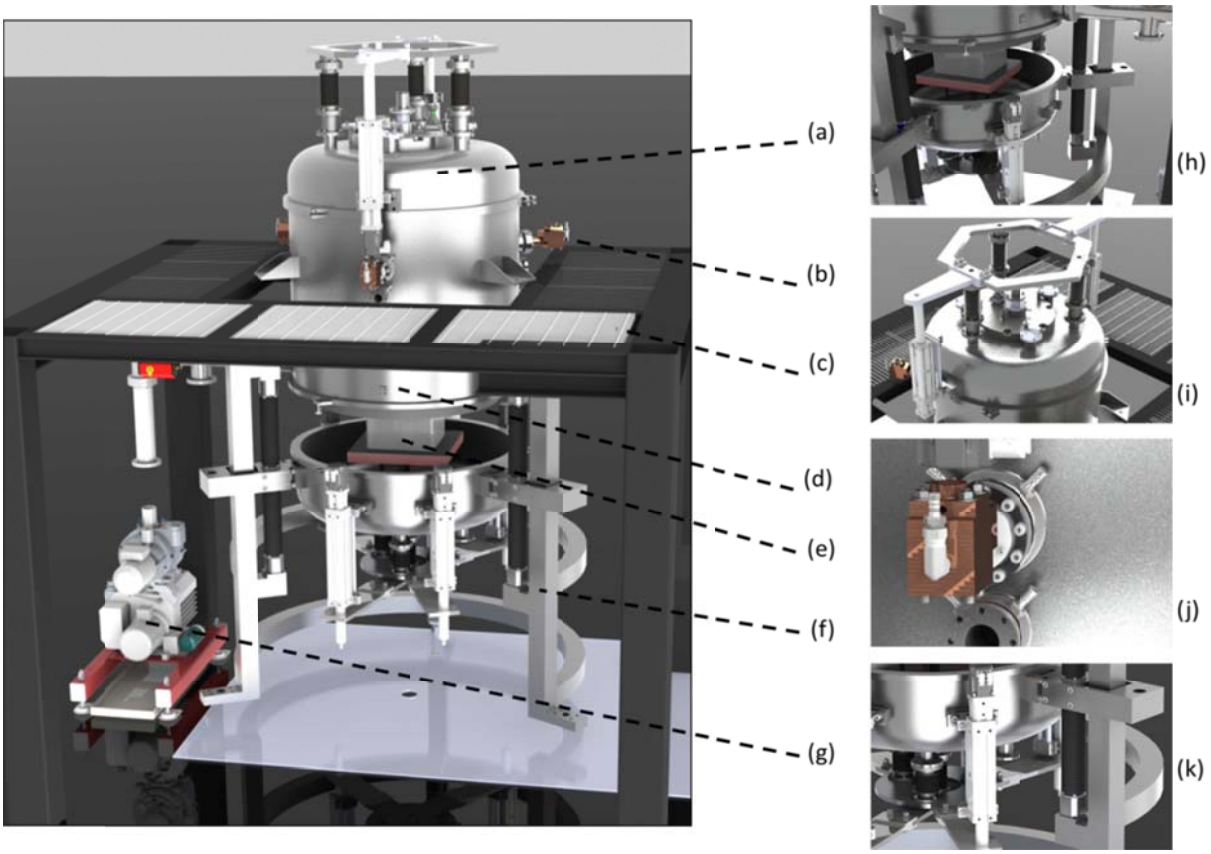

Figure 1 HEM/DSS key Sub-systems (a) LSM Drive Subsystem, (b) water-cooled electrodes, (c) the mezzanine structure, (d) the hot-zone furnace elements, (e) the crucible and crucible positioning elements, (f) chamber open/close mechanism, and (g) the vacuum pumping station, (h) close view of chamber opening, (i) view from top, (j) close view of electrode port, (k) view of lower linear actuation systems.

The challenge however, and the principle aim of this investigation, was the fusion of the HEM and DSS design elements. Presented in Figure 2 is a general cross sectional view of the system illustrating various key components of the design. The crucible is positioned on top of a large thermally conductive graphite block (DS block 1) and placed within the hot zone of the graphite heater. The lateral moving shield (LMS), is suspended from three support rods which are coupled via vacuum bellows to an external LMS displacement drive such that it may be displaced vertically. The LMS is highlighted in orange and blue for visibility. In addition to this, the molybdenum shaft entering from the bottom of the chamber is also coupled to external displacement drive using vacuum bellows. This molybdenum shaft provides the capability to position the DS block within the furnace.

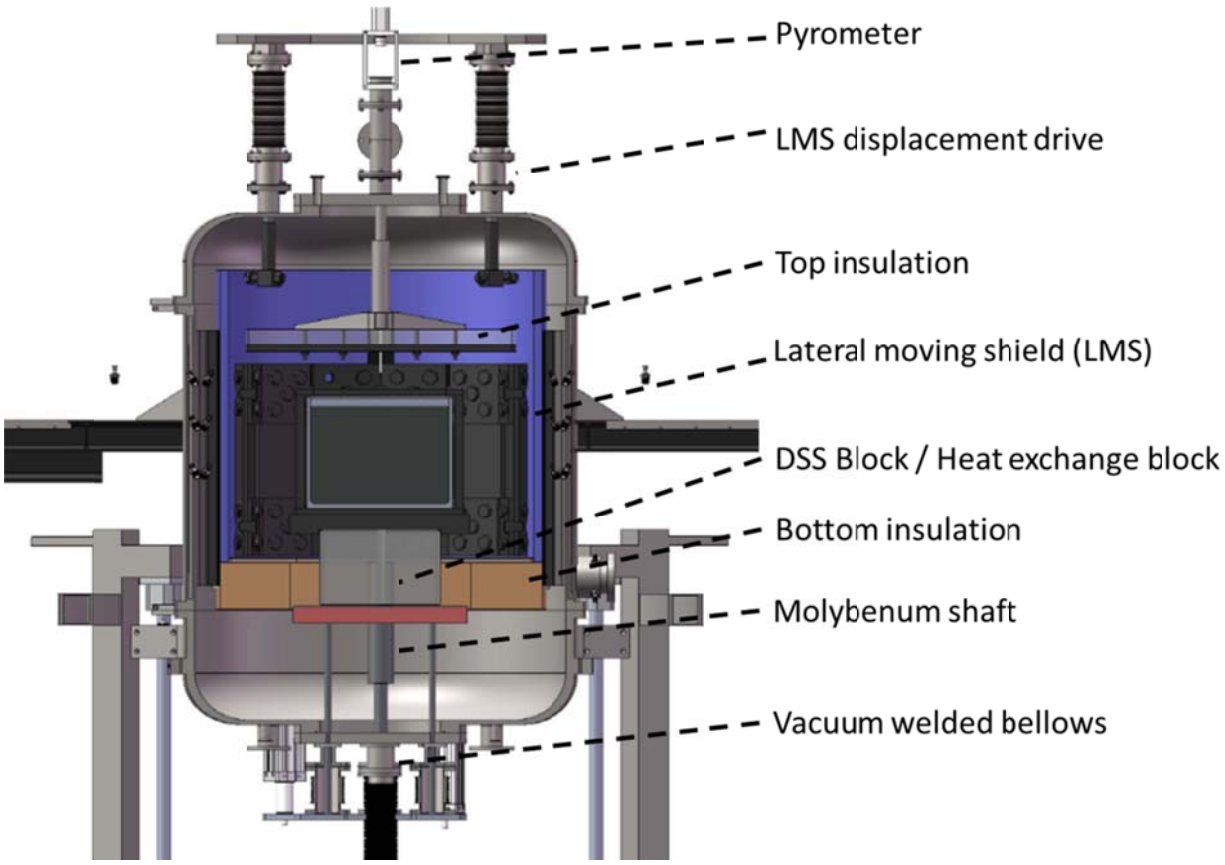

Figure 2 Cross sectional view of the HEM/DSS system illustrating various key components.

In the DSS modality, the DS block is fixed in place while the LMS (blue and orange) may be displaced vertically. When the LMS is raised, heat is radiated from the DS block to the water cooled walls of the chamber. As a result, the temperature of the DS block lowers, effectively increasing the temperature gradient at the bottom of the crucible. This temperature gradient is oriented vertically, and causes the silicon to solidify first at the bottom of the crucible. As the LMS continues to travel vertically, directional crystal growth continues. The DSS modality achieved using this design is presented in Figure 3. As the LMS displacement drive vertically actuates the shield, the view factor of the DS block with the water cooled chamber wall increases substantially. This is the driving principle behind crystal growth by DSS.

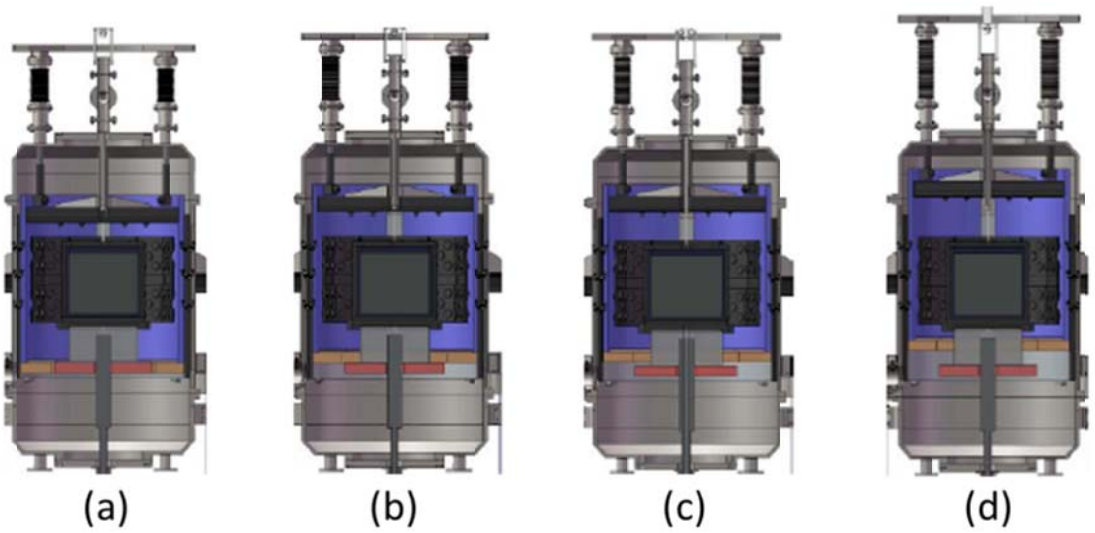

Figure 3 DSS modality of the furnace. The DS block is fixed in place, while the lateral insulation components (blue) and bottom insulation components (orange) are displaced vertically, leading to directional solidification.

It was also of interest to incorporate the principles behind the Heat Exchange Method (HEM) into the furnace design. The HEM modality is distinguished from the DSS modality in that it is not the lateral insulation which moves but the crucible. In this method, heat enters into the molten charge from the sides and is extracted by the heat exchange block situated beneath the crucible. As the heat exchange block is lowered from the center of the hot-zone down through an opening in the lower insulation, its temperature drops producing a temperature gradient. Crystal growth is achieved through a control algorithm designed to control the heat input by the furnace element and output by the heat exchange block. The HEM modality achieved using these design principles is presented in Figure 4. As may be seen, the heat exchange block is gradually lowered from its starting position in (a) to its final position displaced several centimeters from the hot zone in (d). The ability to reposition the crucible in the hot-zone for annealing is illustrated in (e).

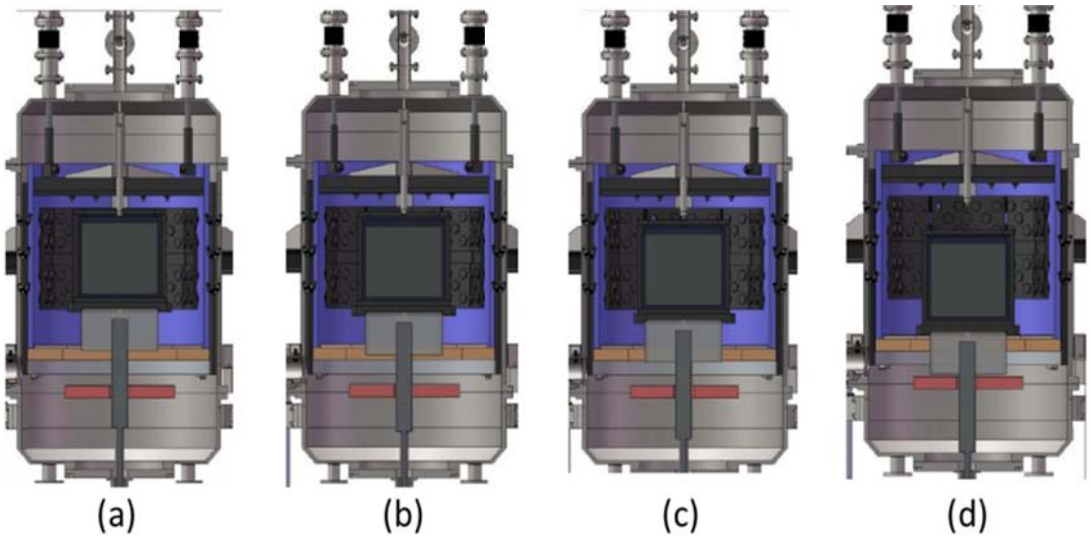

Figure 4 The heat exchange block is gradually lowered from its starting position in (a) to its final position displaced several centimeters from the hot zone in (d).

1.1 Subsystem 5-S-LA-CRUC

The heating elements, structural components of the double-walled chamber, the hot-zone insulating elements, and in general the entire HEM / DSS system was designed around the dimensions of the GEN1 crucible for the production of polycrystalline Si ingots 40kg to 60kg in size. Presented below in Figure 5 is the 3D model of the crucible and related components.

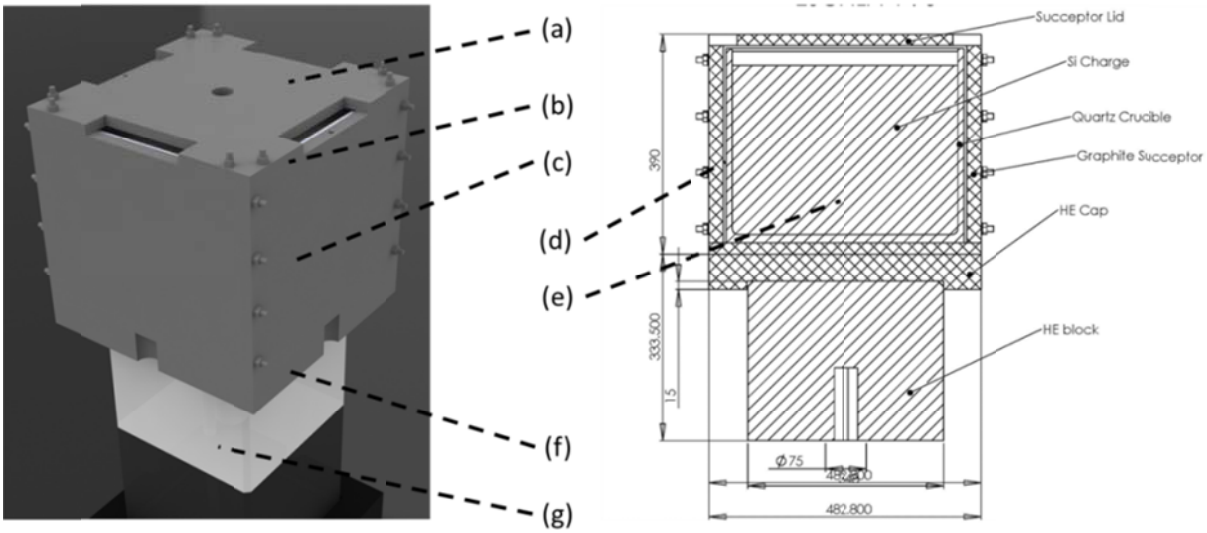

Figure 5 (a) Succeptor lid, (b) graphite screws, (c) graphite succeptor walls, (d) quartz crucible, (e) Silicon, (f) Zirconium plate, (g) heat exchange block.

As can be seen from above, the structure of the crucible has several layers. The SiN coated Quartz crucible (d) is filled with polycrystalline Si (e) and placed within a graphite succeptor structure (c). The graphite succeptor is used for providing rigid support to the Quartz crucible at such high growth temperatures. A graphite lid (a) is placed on top of the succeptor with a hole in the center and openings on the edges to provide the desired flow characteristics of argon gas over the molten Si surface. The graphite succeptor structure is closed using graphite screws and placed upon a Zirconium plate (f) which rests upon the Heat Exchange Block / DS block (g). An integral thermocouple (not shown) passes through the center of the heat exchange block to measure the temperature at the bottom of the graphite succeptor. This structure is placed upon a molybdenum rod for linear position as shown below in Figure 6.

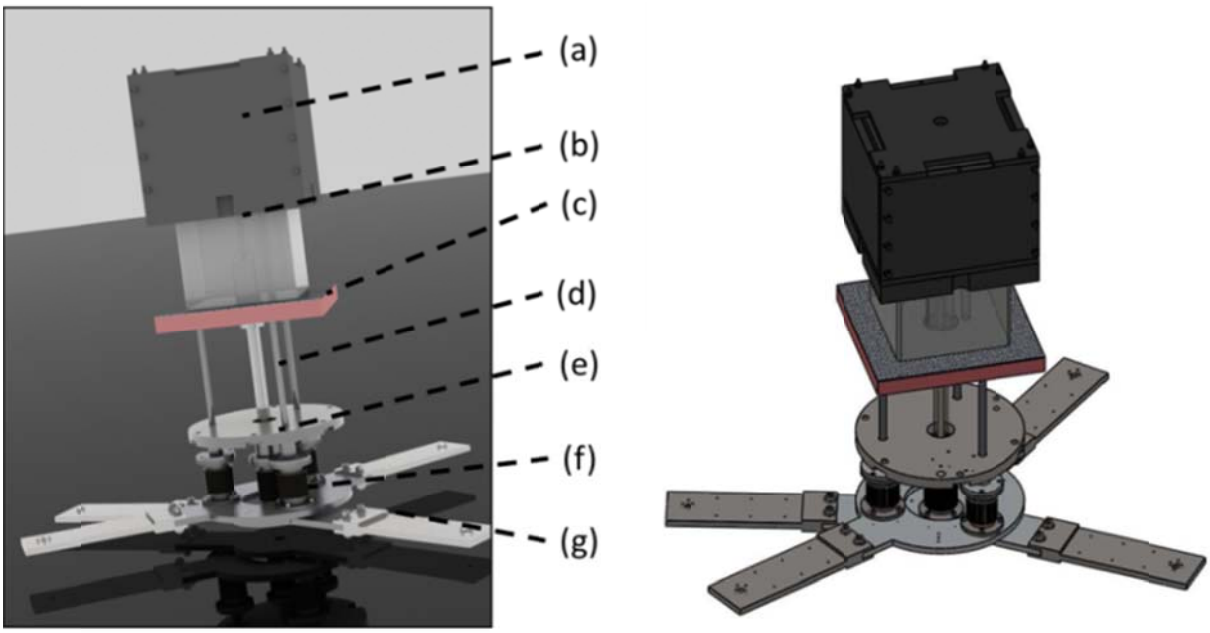

Figure 6 Left: (a) graphite succeptor, (b) Heat exchange block, (c) graphite insulation, (d) Molybdenum linear positioning shaft, (e) water cooled stainless steel plate, (f) stainless steel welded bellows, (g) linear positioning plate extensions.

Placing the crucible and succeptor structure (a) & (b) atop the molybdenum rod (d) provides the capability for position of the crucible within the hot zone. This is achieved

using welded stainless steel bellows pass through (f), which are fixed to the linear positioning plate extensions (g). This positioning system is what provides the HEM functionality allowing for the crucible to be slowly extracted from the hot-zone of the furnace.

1.2 Subsystem 6- Hot-Zone Graphite Elements

The hot-zone of the furnace immediately surrounding the Quartz crucible/succeptor structure consists of the graphite heating element for transferring heat into the molten Si and graphite insulation for reducing radial and axial heat losses in the system. The heating element which has been custom designed for this furnace has been fabricated from a graphite SGL CZ3 R6300, which has a resistivity of 20 μΩ·m and an electrical resistivity between phases of 0.050 Ω. A three phase 100kVA transformer has been selected with primary and secondary voltages of 400 V and 60 V respectively. Presented below in Figure 7 is the 3D CAD model developed for the HEM/DSS furnace and an image of an actual furnace element with similar dimensions.

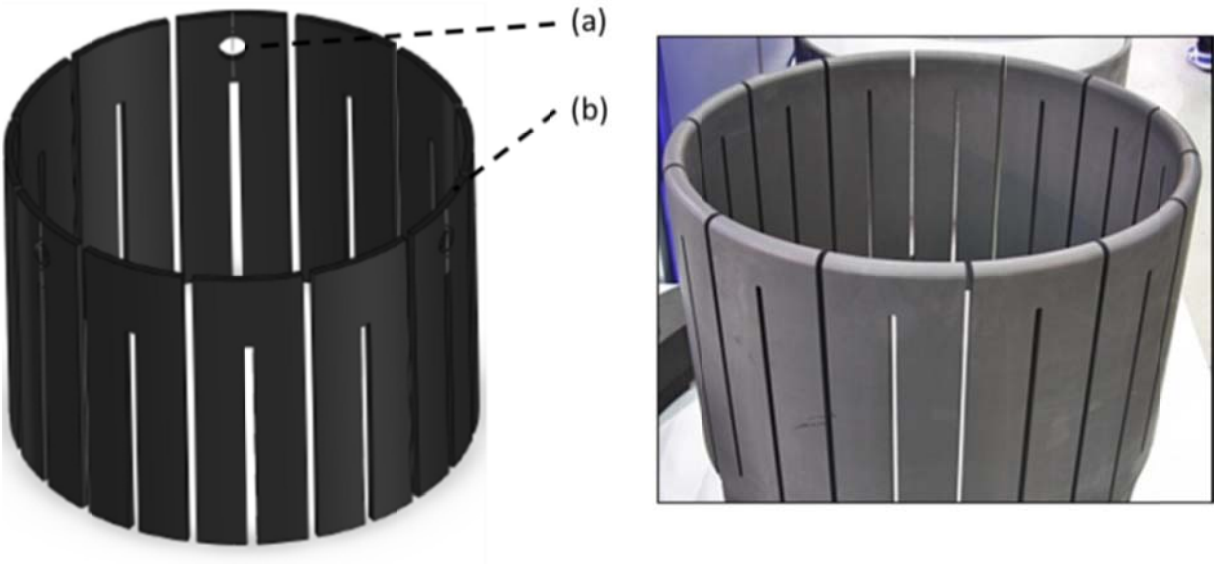

Figure 7 Left: CAD model of graphite heating element designed for the HEM/DSS System, (a) mounting holes for furnace electrodes, (b) conductive graphite panels, and (b) actual furnace element.

The insulation elements were designed as a closed insulating cylinder surrounding the graphite heating element, to reduce lateral and axial heat losses. These components

consisted of a special kind of low density composite graphite which exhibits substantially higher porosity and thermal conductivity. A comparison of the different material properties of the graphite components used for the heating element, insulation elements, and the heat exchange block are presented in Table 1.

Presented below in Figure 8 is the 3D CAD model of the furnace insulation elements used to form an insulating cylinder in the hot-zone. The upper insulation (b) is supported by a stainless steel brace (a) which is suspended from the upper chamber wall. The LMS (d) is capable of linear translation along the axial direction, and is supported by a circular graphite ring (c) which is also supported by three graphite-molybdenum composite rods which are suspended from the upper chamber wall. Inside of these furnace insulation elements is the previously described heating element (e). Finally, the bottom of the structure is closed with thick composite graphite discs and composite graphite plates (f & g)

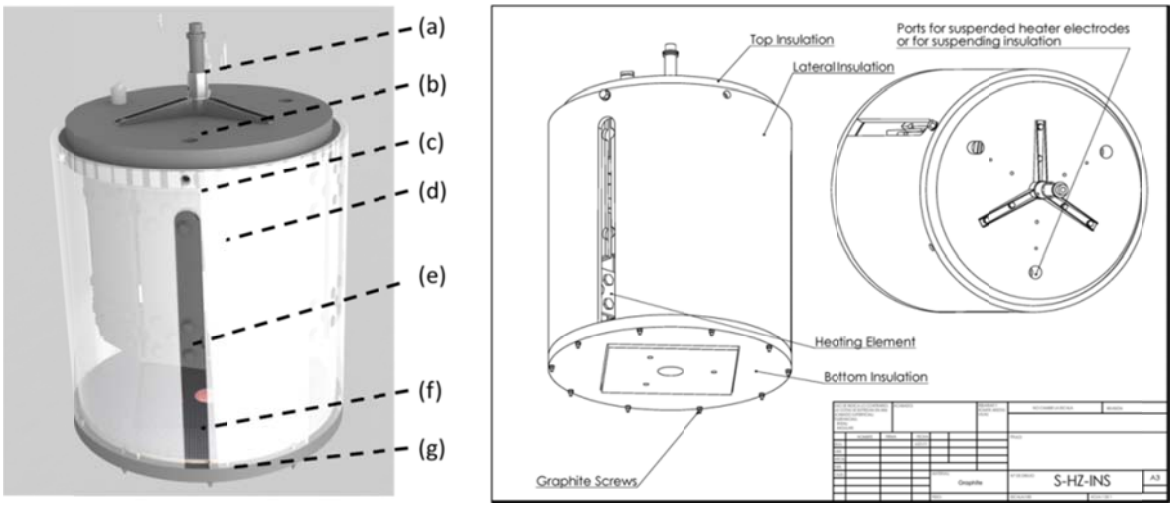

Figure 8 Left: (a) stainless steel brace, (b) upper insulation, (c) circular graphite ring, (d) LMS, (e) graphite heating element, (f) composite graphite plate, (g) thick graphite plate.

1.3 Chamber Central Section

The mechanical structure used for the HEM/DSS system consisted in total of 5 stainless steel double-walled water cooled chamber. The design of these five sections has gone through a large number of revisions throughout the entire design phase of the system. The final design has been built around chamber section 3 (e) which is bolted to the mezzanine structure for mechanical support (see Figure 15). The chamber section 2 is

actually part of a larger sub-assembly (see Figure 10) which is lowered as an assembled sub-system into the chamber section 2. Finally, the chamber is closed from the bottom against chamber sections 4 and 5 using the linear drive system presented in Figure 11. For simplicity, the top three sections of the furnace chamber are presented in Figure 9.

The top plate, referred to as chamber section 1 (a) is a water cooled plate which provides vacuum ports for thermocouple and pyrometer access for measurement of the temperature as well as for the gas input and measurements of growth velocity. This plate is fastened to chamber section 2 (b) which is also a double-walled stainless steel shell, with appropriate vacuum seals in place. The vacuum ports on the chamber section 2 (c) support the weight of the LMS, and also provides the possibility for incorporation of top hanging electrodes to support a furnace element above the crucible. The structure (d) has been designed for vertical mounting of linear drive devices (see Figure 10). Chamber section 2 (b) seals to chamber section 3 (e) via an O-ring seal. The weight of Chamber section 3 and its related elements are supported by the stainless steel braces (f) which are bolted directly to the mezzanine structure (see Figure 15). Chamber section 3 was designed as a double walled chamber with integral water cooling. The vacuum pass-through ports for the electrodes (g) and for the pyrometers (h) have their own distinct water cooling circuits. Two vacuum ports (j) have been included in the design to provide more symmetric gas flow through the system.

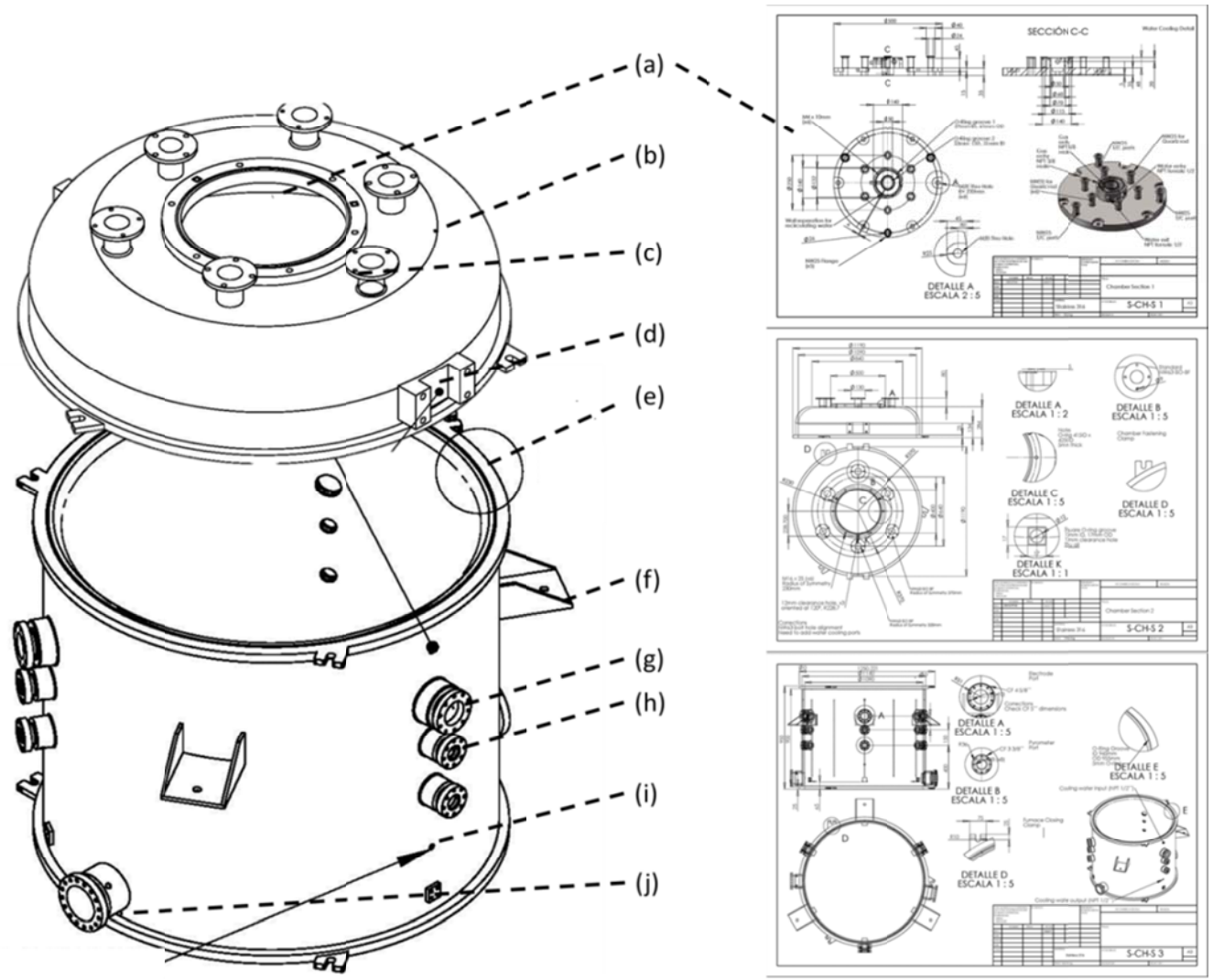

Figure 9 Left: (a) Chamber section 1, (b) chamber section 2, (c) vacuum flange for supporting insulation and hanging electrodes, (d) linear driving mounting face, (e) chamber section 3, (f) support flange for furnace, (g) vacuum port for electrode pass through, (h) vacuum port for pyrometer, (i) water inlet, (j) vacuum flange for connection to vacuum pumping system, Right: Examples of the detailed schematics developed for each of the chamber sections.

Table 1 Properties of Graphite Components used for the furnace heating element, insulation components, and the heat exchange block for vendors 1, 2, and 3.

GRAPHITE FOR HEATER							
	Designation	bulk density (g/cm³)	Thermal Cond W/m·K	Thermal Expansion Coeff. (10^{-6}/K)	Resistivity (μΩ·m)	Grain Size (μm)	Porosity (% vol.)
1	2020	1,77	85	4,3	15,5	15	9
2	CZ3 R6300	1,73	65	3,8	17	20	15
3	FU 8957	1,75	90	4,6	14	15	16

THERMALLY CONDUCTIVE GRAPHITE							
	Designation	bulk density (g/cm³)	Thermal Cond W/m·K	Thermal Expansion Coeff. (10^{-6}/K)	Compressive Strength (MPa)	Grain Size (μm)	Porosity (% vol.)
1	2020	1,77	85	4,3	99	15	9
2	CZ5 R6510	1,83	90	5,1	125	10	10
3	FU 2590	1,88	110	5,2	110	10	10

INSULATING GRAPHITE							
	Designation	bulk density (g/cm³)	Thermal Cond @ 1773 K (W/m·K)	Thermal Expansion Coeff. (10^{-6}/K)	Compressive Strength (MPa)	Moisture absor. (%)	Porosity (% vol.)
1	CBCF-15-2000	0,15	0,47	3	0,8	< 0,1	91
	CBCF-18-2000	0,18	0,63	3	1,1	< 0,1	89
2	MFA	0,2	0,45	—	1	< 1,0	—
	RFA	0,2	0,50	—	1	< 1,0	—
	GFA-10	—	0,56	—	—	—	—
3	FU 2914	—	0,45	—	—	—	—

1.4 LMS Drive subsystem (Linear actuation sub-systems)

The key functionality of the LMS drive Sub-system is the vertical displacement of the LMS insulation in order to achieve DSS modality through the mechanisms discussed above. However, this sub-system also provides several other capabilities which are critical to the operation and scientific investigation for which the system has been designed, such as monitoring the chamber temperature and pressure, or controlling the gas over-pressure. A schematic representation of this sub-system is presented in Figure 10.

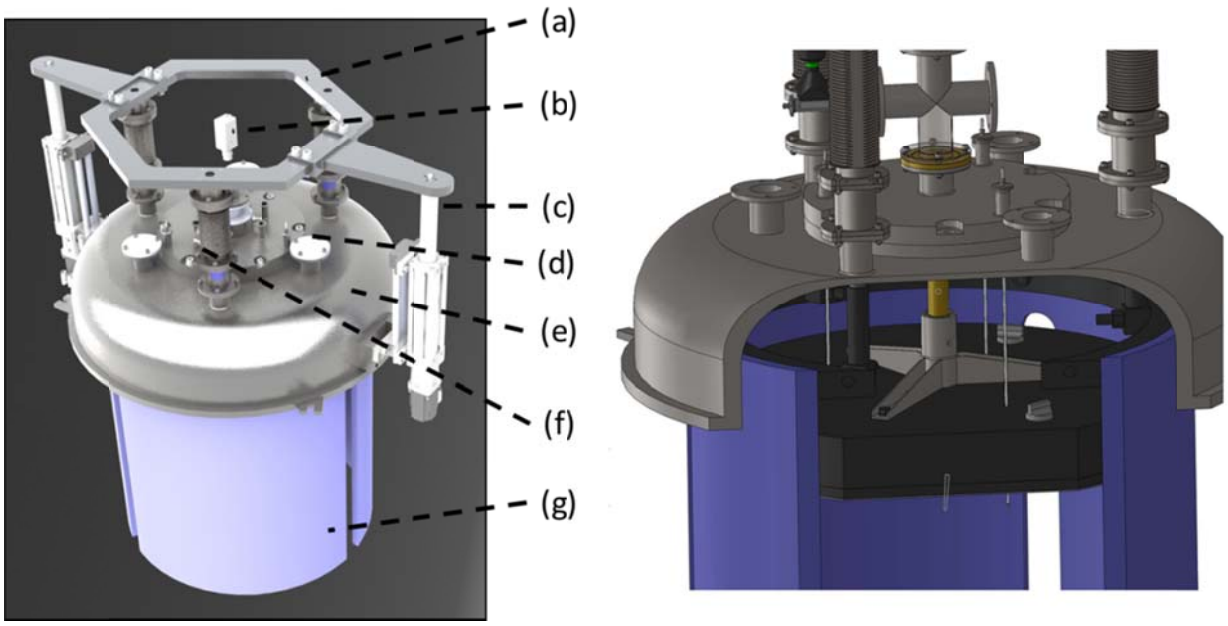

Figure 10 Left: (a) pressure distribution plate, (b) pyrometer, (c) linear actuator, (d) T/C and capacitive vacuum gauge feed-through, (e) double-walled water cooled stainless steel chamber, (f) DC motor, (g) LMS insulation. Right: Cut-away view of sub-system.

The chamber itself (e) consists of a double walled stainless steel shell, which is water-cooled using a recirculating water system. Mounted to the chamber shell are two powerful linear actuator columns (c) with DC motors which are oriented vertically and offset by 180^{o}. The force driven by these two columns provides the lift required move the pressure distribution plate (a) upwards. The required stroke length for the linear actuation columns has been calculated based on the requirements for translation of the LMS. The torque of each actuator has been determined following Equation 1. For example Siemens SINAMICS S120 Models 370 and 340,

can lift up to 480kg and 630kg respectively, which is more than sufficient lift given the application. The required lift was calculated taking into account material densities and volumes within the 3D model.

Equation 1 $$\boldsymbol{Torque} = \frac{\boldsymbol{F\,(N)\cdot 10\cdot(Screw\ Lead\ in\ mm)}}{\boldsymbol{2000\cdot\pi\cdot 0.8}}$$

The LMS (g) is coupled to the pressure distribution plate (a) via three molybdenum/graphite composite rods (not shown) which pass through a sophisticated vacuum bellows manifold sealed from possible air leaks by a stainless steel welded bellows (f). Capacitance pressure sensors and a thermocouple feed-through are mounted to the chamber wall (d) for measurement of chamber pressure and temperature near the crucible wall. Type R thermocouples were used in the design of this furnace, which can measure temperatures as high as 1760^{o}C. A KELLER PA40 2-COLOR pyrometer was located on top of the gas port for measurement of the surface temperature of the molten Si. This pyrometer has a dynamic range of measurement between 600 and 1700^{o}C.

A mass flow controller controls the delivery of argon and helium at appropriate stages of the growth process through the opening in the center of the top chamber wall (c). An external pyrometer (b) has also been integrated into the design, taking into account the focal distances, to provide the capability to measure the surface of the molten Si during the growth cycle.

1.5 Sub-system-Chamber Section

The HEM/DSS system was designed taking into account the difficulties with positioning the crucible within the furnace hot zone. As such, a bottom-loading capability was introduced in order to eliminate the necessity for overhead cranes or gantries which are necessary for lowering the crucible into the hot-zone from the top. In order to load the crucible from the bottom chamber, opening and closing functionality was required. Furthermore, independent of the chamber opening and closing functionality, precise positioning of the crucible within the hot-zone was required for both DSS & HEM modalities. Finally, linear translation of the bottom insulation was required for achieving the HEM modality. In total, three linear translation systems were designed for (1) opening and closing of the chamber (2) positioning of the crucible

and (3) positioning of the bottom insulation. Presented below in Figure 11 is the 3D CAD model of this sub-system.

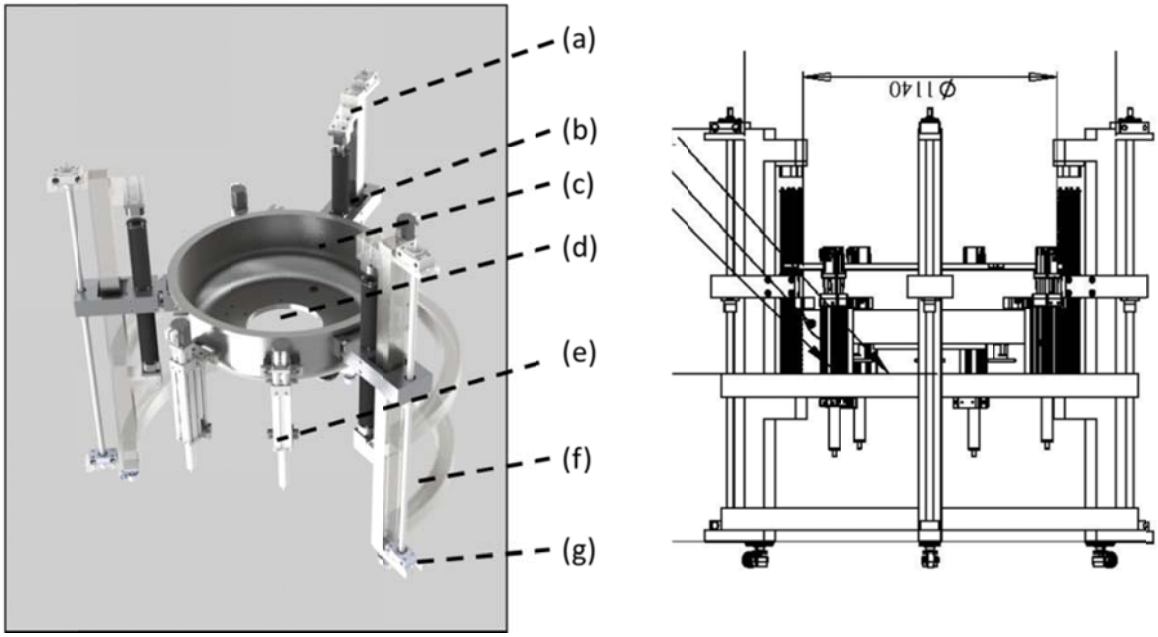

Figure 11 Left: (a) ball screw jack (b) flange with integral ball screw nut (c) water cooled stainless steel chamber wall (d) 50cm chamber opening (e) 2-axis linear actuation system (f) 3-axis linear actuation support structure (g) heavy duty casters.

A 3-axis linear actuation system and support structure (f) was designed to provide the open and closing functionality. The inverted bell shaped chamber wall (c) was coupled to three ball screw jacks (a) via a custom flange with integral ball screw nut (b).

Linear positioning of the crucible and the insulation within the furnace was achieved using two independent 2-axis linear actuation systems (e) coupled to pressure distribution plates (see Figure 6) which passes through the 50cm opening of the chamber wall (d) via welded bellows. The 2-axis linear actuation systems are oriented about 100º.

Other considerations taken into account in the design of this sub-system include adding additional ports for thermocouple connections, integral water cooling of the chamber, and an internal spill detection system which were designed for alerting the user in the case of crucible rupture, and heavy duty casters for improved access.

1.6 Sub-system 8- Vacuum Pumping and Overpressure Control Station

In order to achieve a process consistent with Industrial processes, it was necessary to achieve a pressure of 1×10^{-2} to 1×10^{-3} mbar within a time period not exceeding 7 – 10 hours for a chamber volume of 1.2-1.4 m^3. Furthermore, after the first stage of vacuum, the chamber is backfilled with Argon gas until a pressure of 600 mbar is reached which is maintained throughout the rest of the growth cycle.

To achieve this end, a vacuum pumping station was designed for use with the HEM/DSS furnace. Due to the large volume of the chamber, two vacuum pumping systems were integrated for achieving an acceptable level of vacuum, within the required amount of time. This pumping station consisted of a roots vacuum pump and a rotary vacuum pump. The 3D model of the sub-system which was developed for this application is presented below in Figure 12.

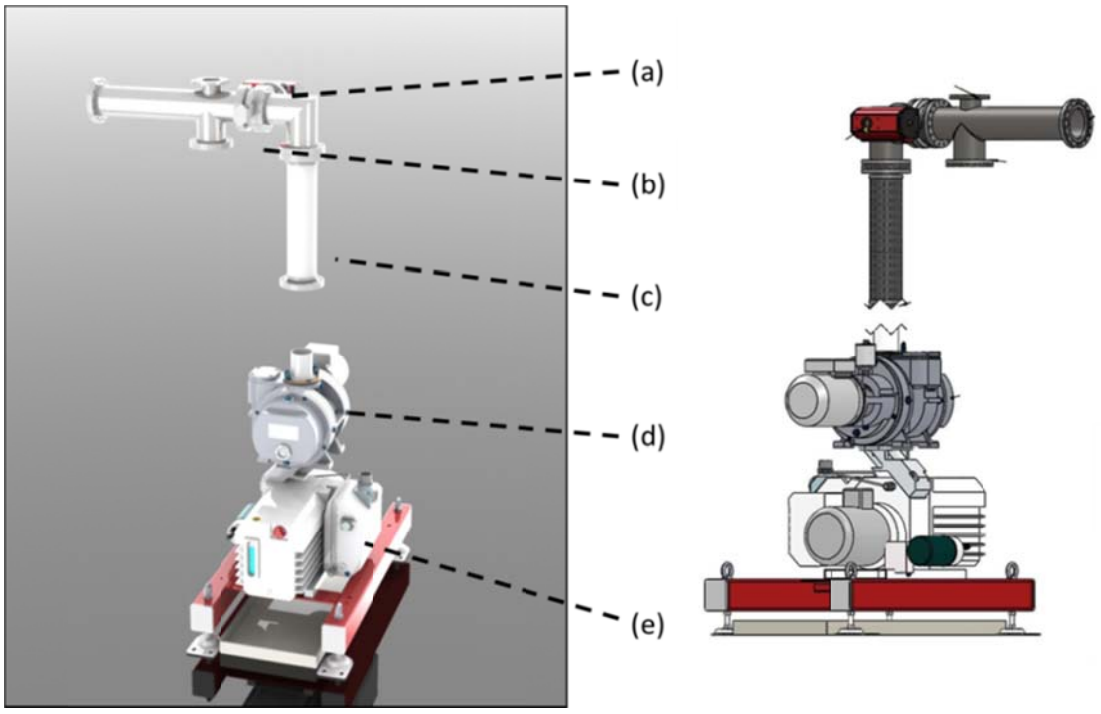

Figure 12 Vacuum pumping sub-system for achieving vacuum and gas over-pressure control consisting of (a) butterfly regulating valve, (b) ports for Pirani and capacitive vacuum gauges, (c) flexible braided vacuum line, (d) rotary vacuum pump, (e) roots vacuum pumping system.

The roots vacuum pumping system used was the OKTA 250A which had a pumping capacity of 270 m^3/hr using a 0.75kW motor. This system works in conjunction with the rotary vacuum pumping system which has a pumping capacity of 62m^3/hr using a 1.5kW motor. Using

these two systems together, a vacuum of less than 5×10^{-4} Torr would be achieved. It is important to comment that all of these considerations exceed the experimental requirements.

A capacitive vacuum gauge supplied by Pfiefer model CCR361 was used for measuring chamber pressure. This vacuum gauge has a range from 1000mbar to 1×10^{-1} mbar. A pirani vacuum gauge also supplied by Pfeifer model TPR280 with similar dynamic range was also considered.

Using a vacuum butterfly regulator valve, Model VAT612, the pressure within the chamber could be controlled. The integrated controller of the downstream pressure control valve calculates the required plate position of the baffle to achieve the set-point pressure, while an encoder monitors the position. Presented in Figure 13 is a vacuum schematic illustrating the in-line arrangement of the vacuum gauges, pumps, and regulator valves. Additional vacuum gauges were also installed on the furnace chamber wall.

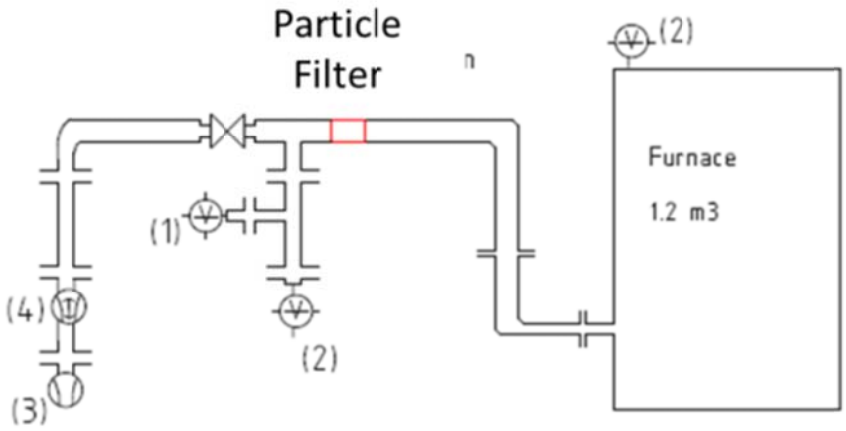

Figure 13 (1) Pirani vacuum gauge, (2) Capacitive vacuum gauge, (3) rotary vacuum pump, (4) roots vacuum pump.

1.7 Subsystem 4: S-HZ-PWR

One of the key components in the design of the hot-zone was the power delivery coupling between the transformer output and the graphite heating element. Due to the high intensity of current which may be possible, it was necessary to provide the capability for cooling of the electrodes using a deionized water cooling system. Presented below in Figure 14 is rendering of the final electrode design, with associated electrical isolation elements.

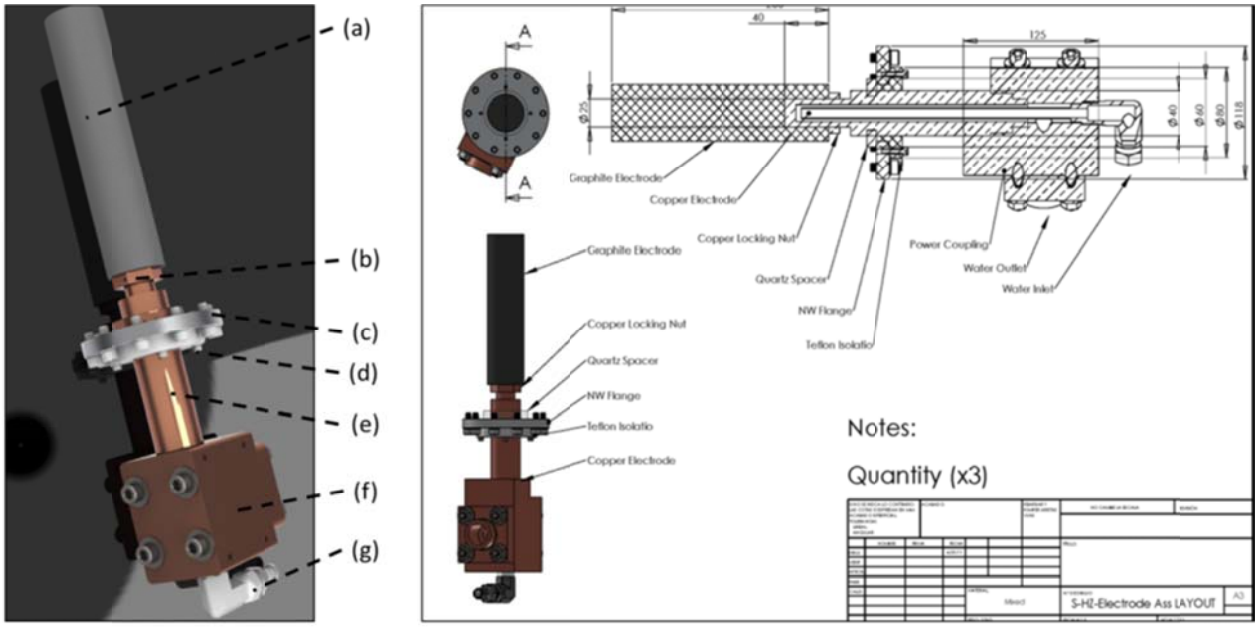

Figure 14 Left: Electrode used for coupling of the transformer to the graphite heating element (a) graphite electrode, (b) copper lock nut, (c) ISO vacuum flange, (d) Teflon and quartz isolation, (e) copper electrode, (f) copper housing, and (g) DI water input. Right: Cross section of electrode illustrating the different components and also the path of DI water through the electrode.

The graphite electrode (a) is mounted to the graphite heating element via a threaded fitting and nut. Before this connection is made however, graphite electrode (a) is mounted to a copper rod (e) using an internal threading and locknut (c). A Teflon isolation ring and quartz disc (d) is secured to the OD of these two components and fastened to an ISO vacuum flange (c) for coupling to the exterior vacuum wall. The copper rod (e) is then fastened to a copper housing (f), which provides the cooling water to the electrode from the input (g). The input water passes through a tube into the electrode and flows out of the electrode back towards the reservoir.

1.8 Sub-system 9-M-MZ

A mezzanine support structure was designed for supporting the weight of the chamber, transformers, and providing access to the system for maintenance. The mezzanine was designed using standard steel I-Bar and a 3D model is presented below in Figure 15.

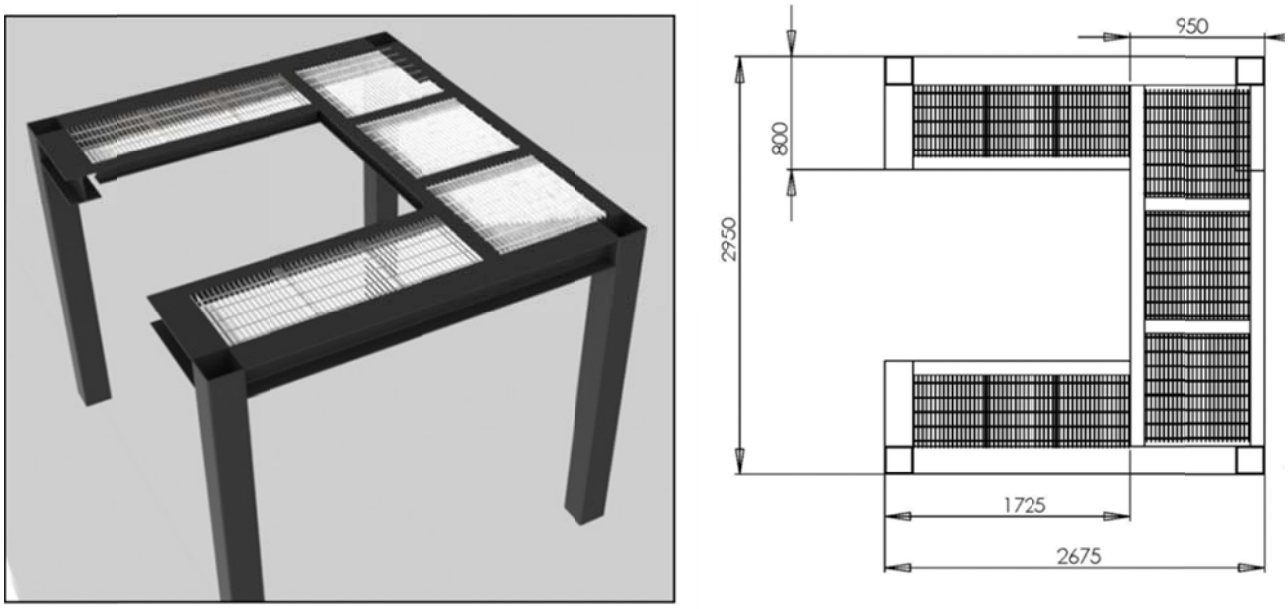

Figure 15 Mezzanine support structure. Units in mm.

1.9 Water Cooling System

One of the design challenges was to identify the needs of integral water cooling system for the HEM/DSS System. There were two kinds of systems identified which for which water cooling has been implemented, each with different requirements. The chamber itself was designed to be water-cooled using double wall geometry. Taking into account the heat dissipated by a single growth Q was 200,000 kJ, setting the maximum tolerable change in the water temperature, ΔT, at 15°C, and taking into account the heat capacitance of water, the necessary flow rate for the HEM/DSS system was determined to be 3.5 lpm. These calculations were carried out using Equation 2 to determine the water cooling requirements for the chamber. Presented below in Figure 16 is the water circuit and DI water system used for this work. The system consists of (a) water purification system (b) & (c) ball valves (d) the furnace wall (e) flow meters for measuring flow rates (g) temperature meters for measuring the water temperature in the return circuit (f).

Equation 2 $$\boldsymbol{Q = m \cdot c_p \cdot \Delta T}$$

In addition to this water cooling system a Millipore Super-Q Plus system was integrated for providing DI water with sufficiently high resistivity for use with the electrodes used in this work. This system provides a water inlet pressure of 5 bar, has a capacity of 5000 L, and can provide up to 12 LPM of DI water with 0.06μS/cm and is presented in Figure 16.

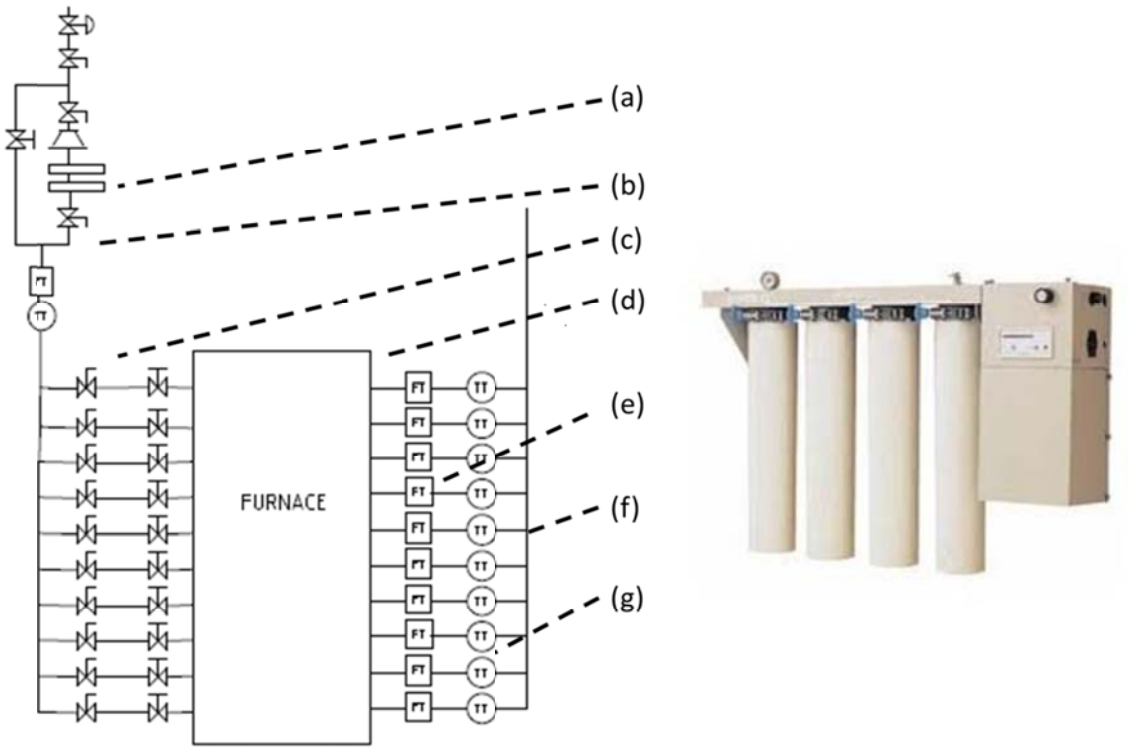

Figure 16 Left: Water circulation components consisting of (a) water purification system, (b) & (c) ball valves, (d) the furnace wall, (e) flow meters for measuring flow rates, (g) temperature meters for measuring the water temperature in the return circuit, (f). Right: Millipore Super-Q Plus system.